

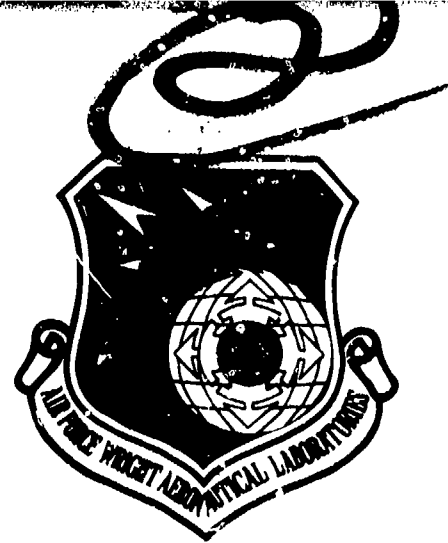
A7WAL-TR-81-3084, Volume III

ATMOSPHERIC ELECTRICITY HAZARDS ANALYTICAL  
MODEL DEVELOPMENT AND APPLICATION

VOLUME III: ELECTROMAGNETIC COUPLING MODELING  
OF THE LIGHTNING/AIRCRAFT INTERACTION  
EVENT

F. J. Eriksen  
T. H. Rudolph  
R. A. Perala

Electro Magnetic Applications, Inc.  
P.O. Box 26263  
1978 South Garrison Street  
Denver, Colorado 80226



August 1981

Final Report for Period August 1979 - June 1981  
Approved for public release; distribution unlimited

DTIC FILE COPY

FLIGHT DYNAMICS LABORATORY  
AIR FORCE WRIGHT AERONAUTICAL LABORATORIES  
AIR FORCE SYSTEMS COMMAND  
WRIGHT PATTERSON AIR FORCE BASE, OHIO 45433

DTIC  
ELECTE  
APR 30 1982  
S D

82 04 30 028

# NOTICE


When Government drawings, specifications, or other data are used for any purpose other than in connection with a definitely related Government procurement operation, the United States Government thereby incurs no responsibility nor any obligation whatsoever; and the fact that the government may have formulated, furnished, or in any way supplied the said drawings, specifications, or other data, is not to be regarded by implication or otherwise as in any manner licensing the holder or any other person or corporation, or conveying any rights or permission to manufacture use, or sell any patented invention that may in any way be related thereto.

This report has been reviewed by the Office of Public Affairs (ASD/PA) and is releasable to the National Technical Information Service (NTIS). At NTIS, it will be available to the general public, including foreign nations.

This technical report has been reviewed and is approved for publication.

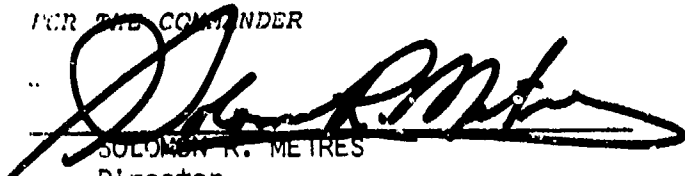


DONALD A. HIRST, 1LT  
Project Engineer



GARY A. QUERO, Chief  
Atmospheric Electricity Hazards Group  
Flight Vehicle Protection Branch  
Vehicle Equipment Division

FOR THE COMMANDER



SOLOMON R. METRES  
Director  
Vehicle Equipment Division

"If your address has changed, if you wish to be removed from our mailing list, or if the addressee is no longer employed by your organization please notify AFWL/FIESL, W-PAFB, OH 45433 to help us maintain a current mailing list".

Copies of this report should not be returned unless return is required by security considerations, contractual obligations, or notice on a specific document.

REPORT DOCUMENTATION PAGE		1. INSTRUCTIONS 2. COMPLETING FORM 3. CATALOG NUMBER
1. REPORT NUMBER	2. GOVT ACCESSION NO.	
AD-A114215		
4. TITLE (and Subtitle) ATMOSPHERIC ELECTRICITY HAZARDS ANALYTICAL MODEL DEVELOPMENT AND APPLICATION VOLUME III ELECTROMAGNETIC COUPLING MODELING OF THE LIGHTNING/AIRCRAFT INTERACTION EVENT		5. TYPE OF REPORT & PERIOD COVERED Technical-Final August 1979 - June 1981
		6. PERFORMING ORG. REPORT NUMBER EMA-81-R-21-006-3
7. AUTHOR(s) F.J. Eriksen T.H. Rudolph R.A. Perali		8. CONTRACT OR GRANT NUMBER(s) F-33615-79-C-3412
9. PERFORMING ORGANIZATION NAME AND ADDRESS Electro Magnetic Applications, Inc. P.O. Box 26263 Denver, Colorado 80226		10. PROGRAM ELEMENT, PROJECT, TASK AREA & WORK UNIT NUMBERS 24020212
11. CONTROLLING OFFICE NAME AND ADDRESS Flight Dynamics Laboratory (FIESL) Air Force Wright Aeronautical Laboratories Wright-Patterson Air Force Base, Ohio 45433		12. REPORT DATE June 1981
		13. NUMBER OF PAGES 313
14. MONITORING AGENCY NAME & ADDRESS (if different from Controlling Office)		15. SECURITY CLASS. (of this report) Unclassified
		15a. DECLASSIFICATION/DOWNGRADING SCHEDULE
16. DISTRIBUTION STATEMENT (of this Report)  Approved for public release; distribution unlimited.		
17. DISTRIBUTION STATEMENT (of the abstract entered in Block 20, if different from Report)		
18. SUPPLEMENTARY NOTES		
19. KEY WORDS (Continue on reverse side if necessary and identify by block number) Lightning Coupling Literature Review EMP Indirect Effects Maxwell's Equations External Coupling Aircraft Internal Coupling Internal Propagation		
20. ABSTRACT (Continue on reverse side if necessary and identify by block number) In this report, the state of the art of coupling of electromagnetic fields to aircraft is reviewed. The objective is to identify the best models available for assessing the electromagnetic interaction of lightning with aircraft. The coupling process is explained and the modelling requirements implied by the lightning environment are discussed. Finally, the description of models selected and implemented at the AFFDL Computing Center is given.		

**BLANK PAGE**



# FOREWORD

This report describes the results of a research effort sponsored by the Atmospheric Electricity Hazards Group of the Air Force Flight Dynamics Laboratory under Contract F33615-79-C-3412. This effort was entitled "Atmospheric Electricity Hazards Analytical Model Development and Application."

The principal investigator was Dr. Rodney A. Perala of Electro Magnetic Applications, Inc. He was assisted in this effort by two subcontractors. Mr. John D. Robb, of Lightning and Transient Research Institute, performed the part of the effort having to do with simulation. Drs. Martin A. Uman and E. Philip Krider of Lightning Location and Protection, Inc., performed the effort relating to environment definition. The results of their efforts are described in the following companion reports:

1. Volume I: "Lightning Environment Modeling," by M.A. Uman and E.P. Krider, of Lightning Location and Protection, Inc.
2. Volume II: "Simulation of the Lightning/Aircraft Interaction Event," by J.D. Robb, of Lightning and Transients Research Institute.

The authors wish to thank the Atmospheric Electricity Hazards Group for their support in this effort.

Accession For	
NTIS GRA&I	<input checked="" type="checkbox"/>
DTIC TAB	<input type="checkbox"/>
Unannounced	<input type="checkbox"/>
Justification	
By _____	
Distribution/	
Availability Codes	
Dist	Avail and/or Special
A	



**BLANK PAGE**

# TABLE OF CONTENTS

CHAPTER	TITLE	PAGE
1	INTRODUCTION	1
2	EVALUATION CRITERIA AND ENVIRONMENT	3
	2.1 Introduction	3
	2.2 Lightning Environment	3
	2.2.1 Quasi-Static Electric Fields	3
	2.2.2 Initiating Streamers	5
	2.2.3 Stepped Ladder	5
	2.2.4 Return Stroke	7
	2.2.5 Continuing Current and Restrikes	11
	2.2.6 Channel Impedance	11
	2.2.7 Summary	15
	2.3 The Coupling Process	15
	2.4 Evaluation Criteria	16
3	EXTERNAL COUPLING REVIEW	21
	3.1 Introduction	21
	3.2 General External Coupling Problem	21
	3.2.1 Problem Definition	21
	3.2.2 Forms of Maxwell's Equations	25
	3.2.3 Method of Moments	28
	3.3 Computational Methods	31
	3.3.1 Introduction	31
	3.3.2 Finite Difference	31
	3.3.2.1 General Method	31
	3.3.2.2 THREDE	34
	3.3.2.3 Taflove and Brodwin	51
	3.3.3 Magnetic Field Integral Equation (MFIE)	63
	3.3.3.1 Introduction	63
	3.3.3.2 Bennett and Weeks	63
	3.3.3.3 MFIE (Perala)	74
	3.3.3.4 (Sancer)	76
	3.3.4 Electric Field Integral Equation (EFIE)	85
	3.3.4.1 Introduction	85
	3.3.4.2 AMP/NEC [41-45]	85
	3.3.4.3 SYR [41-48]; CHAOS [49-50]	97
	3.3.4.4 Ohio State University [53-56]	112
	3.3.4.5 WIRANT [59-61]	119
	3.3.4.6 Thin Wire Time Domain (TSTD) [65-67]	135
	3.3.4.7 Thin Wire Models in General	142
	3.3.5 Singularity Expansion Method (SEM)	143
	3.3.6 Lumped Parameter Network (LPN)	155

# TABLE OF CONTENTS (CONT'D)

CHAPTER	TITLE	PAGE
	3.3.7 Additional External Coupling Methods	166
	3.3.7.1 Introduction	166
	3.3.7.2 Analytical Stick Model [77,78]	166
	3.3.7.3 Unimoment [79-81]	177
	3.3.7.4 Triangular Patch Method	182
	3.4 Corona Modeling	187
4	REVIEW OF INTERNAL COUPLING MODELING	191
	4.1 Apertures	191
	4.2 Seams and Joints	206
	4.3 Slots and Cracks	207
	4.4 Diffusion	213
	4.5 Radomes	215
	4.6 Deliberate Antennas	217
	4.7 Wing Wiring	217
	4.8 Internal Cable Propagation	219
5	SELECTED MODELING APPROACHES	223
	5.1 Introduction	223
	5.2 External Coupling Models	223
	5.3 Internal Coupling	242
	5.3.1 Background	242
	5.3.2 Apertures	242
	5.3.3 Seams and Joints	255
	5.3.4 Cracks and Slots	258
	5.3.5 Diffusion	258
	5.3.6 Radomes	261
	5.3.7 Deliberate Antennas	261
	5.3.8 Wing Wiring	261
	5.3.8.1 Introduction	261
	5.3.8.2 Theoretical Basis for CAPCODE	262
	5.3.8.3 Example Problem Using CAPCODE	270
	5.3.8.4 Determination of Coupling Parameters	272
	5.3.9 Internal Cable Propagation Model	277
6	CONCLUSIONS	281
7	REFERENCES	282
	APPENDIX A	296

# LIST OF FIGURES

FIGURE	TITLE	PAGE
2.1	Illustration of Lightning Attachment to Aircraft	4
2.2	Simple Computation of Electric Field for Approaching Stepped Leader [6]	6
2.3	Comparison of NEMP and Return Stroke LEMP Spectral Current at Various Ranges from the Stroke (LEMP Data from [7])	8
2.4	Comparison of NEMP and Return Stroke LEMP Electric Fields Measured at 50 km, and Extrapolated to 50 m by 1/R	9
2.5	Schematic Diagram of Swept Stroke	12
2.6	Analysis of Aircraft Coupling	17
2.7	Summary of Coupling Methodology	18
3.1	General NEMP-Type Scattering Problem	24
3.2	Typical Discretizing Mesh for a 1D (One Dimensional) Problem	32
3.3	The Model of the F-111 With Actual Profile [6]	35
3.4	THREDE Rectilinear Model of the F-111 [16]	36
3.5	Measured vs. Predicted Axial Current at Test Point 208 in the Time Domain [16]	37
3.6	Measured vs. Predicted Axial Current at Test Point 208 in the Frequency Domain [16]	38
3.7	Measured vs. Predicted Axial Current at Test Point R1 in the Time Domain [16]	39
3.8	Measured vs. Predicted Axial Current at Test Point R1 in the Frequency Domain [16]	40
3.9	A6 Aircraft with Measurement Locations [18]	41
3.10	Comparison of Measured and Predicted A6 Responses in EMPRESS Flyby [18]	42
3.11	Typical Current Injection Configuration [18]	44
3.12	Comparison of Experimental Versus Predicted SCIT A6 Responses. Test Points are Defined in Figure 3.9 [18]	45
3.13	Comparison of Experimental Versus Predicted SCIT A6 Responses. Test Points as Defined in Figure 3.9 [18]	46
3.14	A B-52 Model in a 30 x 30 x 30 THREDE Grid [20]	47
3.15	A B-52 Model in a 50 x 43 x 59 THREDE Grid [20]	48
3.16(a)	Normal Electric Field at Test Point 4 (Fuselage) on the B-52	49
3.16(b)	Axial Surface Current at Test Point 4 (Fuselage) on the B-52	49
3.17	Open-Ended Aluminum Cylinder Geometry (not to scale) [24]	53

# LIST OF FIGURES (CONT'D)

FIGURE	TITLE	PAGE
3.18	Cross-Section of Cylinder Model [24]	54
3.19	Comparison of Results for the Electric Field Along the Cylinder Axis [24]	55
3.20	Computed Electric Field Along Horizontal Radial Lines (Parallel to $H_{x_{inc}}$ ) of the Cylinder [24]	56
3.21	Computed Electric Field Along Vertical Radial Lines (Parallel to $E_{z_{inc}}$ ) of the Cylinder [24]	57
3.22	Nose Cone Geometry (Not to Scale) [24]	58
3.23	Key Cross-Sections of Nose-Cone Model [24]	59
3.24	View of Nose Cone Model at Horizontal Symmetry Plane [24]	60
3.25	Field Contours in Nose Cone Vertical Symmetry Plane. Only Sleeve-Fitting Aperture Open [24]	61
3.26	Geometry of Circular Cylinder	64
3.27	TM Approximate Impulse Response of Circular Cylinder [27]	65
3.28	TE Approximate Impulse Response of Circular Cylinder [27]	66
3.29	Time Domain Responses of the Circular Cylinder Compared to Other Computational Methods [27]	67
3.30	Frequency Domain Responses of the Circular Cylinder Compared to Other Computational Methods [27]	68
3.31	Functional Block Diagram of Time-Domain Reflectometry Scattering Range [34]	70
3.32	Comparison of Responses of Several Finned Cylinders at Axial Incidence [34]	71
3.33	Calculated MIG-21 Response, $\alpha = 90^\circ$ [34]	72
3.34	Fat Cylinder Diagram and Coordinate System	75
3.35	Variations of Surface Current Peak Amplitudes with $\phi$ and $z$ . Incident Field Polarized Parallel to $z$ Axis [30]	75
3.36	Schematic Diagram of Scattering Cylinder on Ground Plane [39]	78
3.37(a)	Measured Amplitude of Axial Surface Density of Outside Current on Tubular Cylinder, E-Polarization (Large Outdoor Ground Screen) [39]	79
3.37(b)	Calculated Amplitude of Axial Surface Current Density on a Finite Circular Cylinder [39]	79
3.38	Magnetic Field Integral Equation Aircraft Model [40]	80

# LIST OF FIGURES (CONT'D)

FIGURE	TITLE	PAGE
3.39	Top of Fuselage, $kh = 0.82$ . ( $h$ : Fuselage Half Length) [40]	82
3.40	Bottom of Fuselage, $kh = 0.82$ . ( $h$ : Fuselage Half Length) [40]	83
3.41	Development of Surface Model for Cylinder with Attached Wires [41]	88
3.42	Detail of the Connection of a Wire to a Surface at the $i^{\text{th}}$ Patch [41]	89
3.43	Stick Model of Aircraft Used to Test NEC2 [44]	90
3.44	A Diagram of the Patch Segmentation Used to Represent the Scattering from a Sphere [44]	93
3.45	Graph of the Bistatic Radar Cross Section as a Function of Angle $\theta$ Between Incident and Scattered Directions. The Solid and Dotted Lines are Analytical Results of the University of Michigan. Solid Line and Dots Represent E-Plane and Dashed Line and Crosses Represent H-Plane Scattering [44]	93
3.46	Diagram of the Cylinder/Wire Structure Used for Demonstrating the NEC, EFIE, and MFIE Hybrid Techniques [44]	94
3.47	Comparison of Calculations of Radiation Pattern from a Cylinder/Wire Structure to Measurements Made by Albertson [46]	95
3.48	Wire Cross Scatterer	99
3.49	Bistatic Radar Cross-Section $\sigma_{\theta\phi}/2$ Pattern in the Plane $\phi + 90^\circ, 270^\circ$ for the Wire Cross [47]	100
3.50	Wire Grid Model of a Fat Cylinder [49]	101
3.51	Predicted and Measured Time-Domain Response for Total Axial Current for the Dustbin. Double-Exponential Incident Field.	103
3.52	Predicted and Measured Frequency Domain Response for Vertical Wire Current for the Bird Cage [49]	104
3.53	CHAOS Wire Model of F111 Swing-Wing Aircraft. Length of Fuselage 22.4 m Wing Span 19.2 m. Total Number of Segments - 756	105
3.54	F111 Aircraft. Current in Wire Element 22 (Front - TP 208) E-Field Parallel to Fuselage. CHAOS 3 Program [50]	107
3.55	Measured vs. THREDE Calculations of Axial Current Rate of Charge at Test Point 208 in the Time Domain [16]	108
3.56	F111 Aircraft. Current in Wire Element 22 (Front) - TP 208 E-Field Parallel to Fuselage. CHAOS 3 Program	109
3.57	Measured, THREDE Calculated, and CHAOS Calculated Axial Currents at Test Point 208 in the Frequency Domain [16,50]	110
3.58	Representation of Fields and Sources Used in Deriving the Reaction Integral Equation	114
3.59	Test Source Configurations for the RIE	115

# LIST OF FIGURES (CONT'D)

FIGURE	TITLE	PAGE
3.60	Backscattering Echo Width of Circular Cylinder for TE Polarization from RIE Method [54]	117
3.61	Segmentation of Wire Model for Aircraft in Free Space Model for WIRANT [64]	120
3.62	Response of the WIRANT Aircraft Model to a Sinusoidal Plane Wave Incident on the Nose of the Aircraft [64]	121
3.63	Wing Current I in Segment 24, Wing Root [64]	122
3.64	In-Flight WIRANT Model of Learjet [62]	124
3.65	The Ground Test Configuration for WIRANT Analysis of a Learjet [62]	125
3.66	Aft Fuselage Sensor Skin Current Density (Time Derivative) for WIRANT Analysis of the Learjet [62]	126
3.67	F-111 Wire Mesh Model - Wings Extended [63]	127
3.68	F-111 Wire Mesh Model - Wings Swept [63]	128
3.69	B-1 Wire Mesh Model, Wings Extended [63]	129
3.70	B-1 Wire Mesh Model, Wings Swept [63]	130
3.71	Longitudinal Current Density on the F-111 Fuselage (FS 160), Top, Topside Incidence, E Parallel to Wings, Wings Extended [63]	131
3.72	Longitudinal Current Density on the F-111 Fuselage (FS 160), Top, Topside Incidence, E Parallel to Wings Extended [63]	133
3.73	Longitudinal Current Density on B-1, Forward Bulkhead (FS-160), Top, Topside Incidence, E Parallel to Fuselage, Wings Swept, Magnitude [63]	134
3.74	The Response of a Stick Model of a 747 to a NEMP Excitation as Calculated by the TWTB Code. The Perpendicular Lines on the Aircraft Segments Show the Bulk Current on that Member [67]	138
3.75	A Continuation of the NEMP Response from Figure 3.74 for a 747 as Calculated by the TWTB Code [67]	139
3.76	Comparison of Measured Pulse Response of Three Aircraft Models with TWTB Calculations [67]	140
3.77	Plane Wave Incident on Perfectly Conducting Sphere. The Angle Coordinates ( $\theta, \phi$ ) Locate Points on the Surface [69]	146
3.78	Natural Frequencies of the Perfectly Conducting Sphere in the Complex Plane (sa/c).	146
3.79	Step Function Response for Surface Current and Charge Density on a Perfectly Conducting Sphere, with $\theta=3\pi/4$ [69]	147
3.80	Geometry of the Wire Scatterer and Incident Field [69]	148



# LIST OF FIGURES (CONT'D)

FIGURE	TITLE	PAGE
3.81	Pole Locations in the Complex Frequency Plane for the Thin Wire of $d/L=0.01$ . The Poles are Grouped into Layers Denoted by $\alpha$ [69]	148
3.82	The Unit Step Response at $z/L = 0.75$ on the Thin Wire for One or Two Pole Pairs Compared to the Fourier Inversion Solution.	149
3.83	The Crossed Wire Configuration Over a Perfectly Conducting Ground Plane [70]	151
3.84	Junction Currents Versus Time for a Normally Incident Plane Wave [70]	152
3.85	Variation in the Natural Frequencies with Change in Relative Wire Lengths for Crossed Wires Over a Perfect Ground [70]	153
3.86	NASA Shuttle Vehicles; External Tank, SRB's and Orbiter as Configured at Launch [71]	156
3.87	FLTSATCOM Showing Important Dimensions (in Meters) [73]	158
3.88	FLTSATCOM LPN Model Used for SGEMP Excitation [73]	159
3.89	Overlay of Finite-Difference and Circuit Model Results for the Current Between the Main Body and the Right Hand Solar Panel [73]	160
3.90	An Example of a Patch on the LPN Surface Model [74]	162
3.91	Circumferential Surface Current Density at $\phi = 90^\circ$ as Calculated by the MFIE, and the Cylinder Circuit Model for Two Different Damping Values [74]	163
3.92	Circumferential Variation of Axial Current Density as Calculated by the MFIE and the Circuit Model for Two Damping Resistor Values	164
3.93	Complete Aircraft Represented by Parallel Current Carrying Filaments [76]	165
3.94	Stick Model Consisting of Six Elements Used in the Analytical Stick Model Analysis [77]	168
3.95	B-1 Natural Modes. The Dashed Lines Represent the Current Distribution on the Aircraft Segments at Resonance, While the Arrows Indicate Direction [77]	171
3.96	E-4 Natural Mode. The Dashed Lines Represent the Current Distribution on the Aircraft Segments at Resonance, while the Arrows Indicate Direction [77]	174
3.97	EC-135 Natural Modes. The Dashed Lines Represent the Current Distribution on the Aircraft Segments at Resonance, While the Arrows Indicate Direction [77]	175

# LIST OF FIGURES (CONT'D)

FIGURE	TITLE	PAGE
3.98	Axial Surface Current Density Measured on a B-52 on the Main Fuselage (TOP) Between the Wing and Stabilizer. See Figure 3.15 for Position of this Test Point (Test Point 4) [77]	176
3.99	Schematic of Scattering by a Dielectric Cylindrical Obstacle [79]	179
3.3.100	Far Field Scattering Pattern from a Cylinder [79]	181
3.3.101	Far Field Scattering Pattern from a Pair of Cylinders [79]	181
3.3.102	Arbitrary Surface Modeled by Triangular Patches [82]	183
3.3.103	Local Coordinates Associated with an Edge	184
3.3.104	Distribution of Current Components on a $0.2\lambda$ Radius Conducting Sphere Calculated by an Electric Field Integral Equation Formulation [82]	186
4.1	Cavity Backed Aperture	198
4.2	Illustration of Uniqueness Theorem	200
4.3	Application of Uniqueness Theorem to Aperture Problems	202
4.4	Example of Uniqueness Theorem Applied to an Annular Reentrant Cavity in Two Dimensions	203
4.5	$H_\phi$ Comparison	204
4.6	$E_r$ Comparison	205
4.7	Structural Joints for Quadmax Test Specimens [115]	208
4.8	Measured Joint Admittance of Structural Joints [115]	209
4.9	Measured Joint Admittance of Joint No. 5 [115]	210
4.10	A Slot Antenna and its Complementary Strip Pole	211
4.11	Equivalent Circuit Model of the Slot-Internal Cable Coupling	212
4.12	Statement of Shielding Problem for a Single Infinite Sheet	214
4.13	Example of Forward Radar Structures [124]	216

# LIST OF FIGURES (CONT'D)

FIGURE	TITLE	PAGE
4.14	Thevenin Equivalent Circuit of the Marker Beacon Antenna [125]	218
5.1	Generalized LPN Model	226
5.2	F-16 Aircraft System	227
5.3	LPN Model of F-16	228
5.4	Overlay of Finite-Difference and Circuit Model Results for EMP Excitation of F-16 at Test Point 3, for Incident E Field Parallel to Fuselage	230
5.5	Overlay of Finite-Difference and Circuit Model Results for EMP Excitation of F-16 at Test Point 3, for Incident E Field Perpendicular to Fuselage	231
5.6	Overlay of Finite-Difference and Circuit Model Results for EMP Excitation of F-16 at Test Point 3, for Incident E Field Perpendicular to Fuselage	232
5.7	Overlay of Finite-Difference and Circuit Model Results for EMP Excitation of F-16 at Test Point 3, for Incident E Field Perpendicular to Fuselage	233
5.8	Overlay of Finite Difference and Circuit Model Results for EMP Excitation of F-16 at Test Point 14, for Incident E-Field Parallel to Fuselage	234
5.9	C-130 in an Attached Lightning Channel	235
5.10(a)	Three-Dimensional Finite-Difference Representation of a C-130	236
5.10(b)	Three-Dimensional Finite-Difference Representation of a C-130	237
5.11	Comparison of Theoretical LPN and T3DFD H-Field Calculations at Sample Points 1(a) and 2(b)	238
5.11	(cont'd) Comparison of Theoretical T3DFD and LPN H-Field Calculations at Sample Point 3(c)	239
5.12	Comparison of Theoretical LPN and T3DFD E-Field Calculations at Sample Points 1(a) and 2(b)	240

# LIST OF FIGURES (CONT'D)

FIGURE	TITLE	PAGE
5.12	(cont'd) Comparison of Theoretical LPN and T3DFD E-Field Calculations at Sample Point 3	241
5.13	Comparison of Electric Field Responses for Different Risetimes	243
5.13	(cont'd) Comparison of Electric Field Response for Different Risetimes	244
5.14	Comparison of Magnetic Field Response for Different Risetimes	245
5.14	(cont'd) Comparison of Magnetic Field Response at Different Risetimes	246
5.15	Coupling Mode Architecture	247
5.16	Equivalent Circuit of a Small Hole ( $R_0 \gg$ Hole's Dimensions) [109]	249
5.17	3-D Finite Difference Equations in Rectangular Coordinates Set Up with Externally Supplied H-Fields [17]	252
5.18	3-D Finite Difference Equations in Rectangular Coordinates Set Up with Externally Supplied E-Fields [17]	253
5.19	Geometry for Cockpit Aperture Example (Dimensions in Meters)	254
5.20	Voltage on Wire Inside Cockpit as a Function of Stroke Risetime	256
5.21	Current on Wire Inside Cockpit as a Function of Stroke Risetime	257
5.22	Geometry Near the Line Charge $\rho_L$	264
5.23	Cross-Section of a Conductor	264
5.24	Cross-Section of N+1 Conductors	265
5.25	Subcontours of the Contour $C_j$	267
5.26	Example Conductor Cross-Sections	271

# LIST OF FIGURES (CONT'D)

FIGURE	TITLE	PAGE
5.27	Charge Density Distribution on Cable (Cable = 1 Volt, Airfoil = 1 Volt)	273
5.28	Charge Density Distribution on Airfoil (Cable = 1 Volt, Airfoil = 0 Volt)	274
5.29	Charge Density Distribution on Cable (Cable = 1 Volt, Airfoil = 0 Volt)	275
5.30	Charge Density Distribution on Airfoil (Cable = 1 Volt, Airfoil = 1 Volt)	276

# LIST OF TABLES

TABLE	TITLE	PAGE
2.1	Transmission Line Lightning Channel Models	14
2.2	Values of R and C for the Equivalent Impedance of the Channel Determined by Finite Difference Model	15
3.1	A Summary of the Computational Methods Reviewed	23
3.2	Values of Bulk Current for the Stick Model Aircraft Shown in Figure 3.43 [44]	92
3.3	A Comparison of Peak Surface Currents for the F111 as Calculated by CHAOS and Reported by Holland [50]	106
3.4	Comparison of External Surface Currents as Calculated by a LPN Method and as Measured by LTRI (Lightning and Transient Research Institute [72]	157
3.5	Parameters Used in the Analytical Stick Model of the B1 [77]	170
3.6	Parameters Used in Analytical Stick Model of the E4 [77]	172
3.7	Parameters Used in the Analytical Stick Model of the EC-135 [77]	173
4.1	Status of Literature as of 1976 [110] for Electro-magnetic Coupling through Apertures	197
5.1	Comparison of T3DFD and LPN Computer Requirements at AFFDL Computing Center for 300 ns of Problem Time	224
5.2	Aperture Polarization [109]	250

## CHAPTER 1

### INTRODUCTION

Recent technological developments have resulted in an increased interest in the coupling of lightning induced electromagnetic fields to aircraft. These developments include the use of advanced composite materials which provide less electromagnetic shielding than conventional aluminum or titanium structures, the increased use of low-level semiconductor circuits in many mission critical subsystems, and the trend towards completely fly-by-wire aircraft. In addition, recent data describing the lightning environment has shown that the environment has a much larger frequency content in the aircraft resonant regions (2-20 MHz) than was previously thought. The end result is that the lightning/aircraft electromagnetic interaction problem needs to be re-examined.

Previously, lightning coupling to aircraft has usually been accomplished by using low-frequency models which ignored airframe resonances and dynamic current and charge distributions. Models do exist however, which include these dynamic high-frequency effects. Ever since awareness of nuclear electromagnetic pulse (NEMP) effects began, attention has been focussed upon the problem of computing the coupling to aircraft when excited by transient electromagnetic fields having significant spectral content in the aircraft resonance region. Many models have been developed having various degrees of sophistication and advantages and disadvantages. The objective of this report is to review all of these models and select one which would be the most suitable for modeling the lightning/aircraft interaction event.

This report is divided into several chapters. A review of the lightning environment and model evaluation criteria is given in Chapter 2. The results of a literature survey of electromagnetic coupling models are then presented. This includes both the external (surface current and charges) and internal (interior fields, voltages, and currents) coupling models in Chapters 3 and 4, respectively. The models are compared to each other and are evaluated with respect to their applicability to the lightning environment.

The models which have been selected for application to the lightning/aircraft interaction problem are discussed in Chapter 5. These models are

implemented and installed at the Air Force Flight Dynamics Laboratory Computing Center. User's Manuals for these codes are given in separate documents [1,2,3].

This report is Volume III of a three volume set of reports. The other two volumes [4,5] are:

1. Volume I: "Lightning Environment Modeling," by M.A. Uman and E.P. Krider, of Lightning Location and Protection, Inc.
2. Volume II: "Simulation of the Lightning/Aircraft Interaction Event," by J.D. Robb, of Lightning and Transients Research Institute.

The first volume deals with the modeling of the lightning environment. The second volume deals with the development of aircraft test techniques.



## CHAPTER 2

### EVALUATION CRITERIA AND ENVIRONMENT

#### 2.1 Introduction

It will be the objective of the work in Chapter 3 to review external coupling methods presently used for lightning or NEMP calculations and to select one or more of these methods as the most appropriate for lightning coupling problems. In order to properly evaluate a coupling method, one first needs to know the character of the lightning environment for an aircraft or missile. This lightning environment differs from the NEMP environment especially in the generally lower frequency content of the lightning fields and the special phenomenon of an attached stroke. Although Volume I of this report gives an excellent description of all lightning processes, it is worthwhile here to first discuss some of the significant aspects of this environment in the context of interaction with aircraft. Also, an introduction to the basic coupling terminology is given. The coupling method to be selected will have to meet several requirements and a second objective of this chapter, therefore, is to present the evaluation criteria by which the coupling model will be judged.

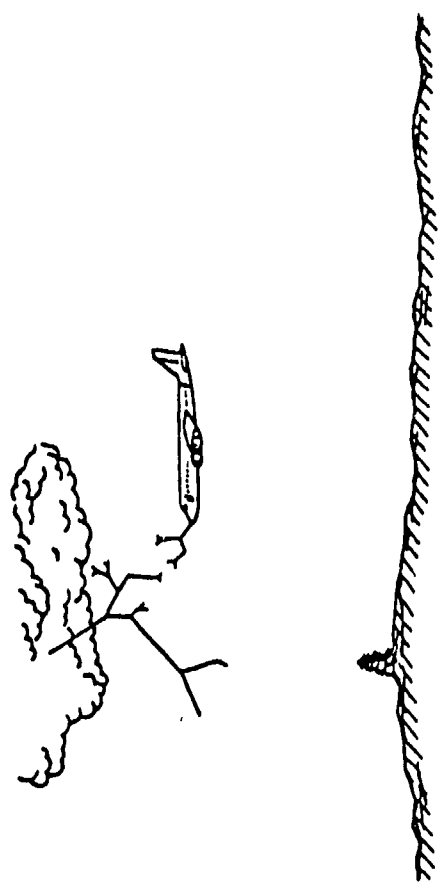
The rest of this chapter is organized into three sections: Section 2.2 which deals with the environment, Section 2.3 which gives an introduction to the coupling process, and Section 2.4 which deals with the evaluation criteria.

#### 2.2. Lightning Environment

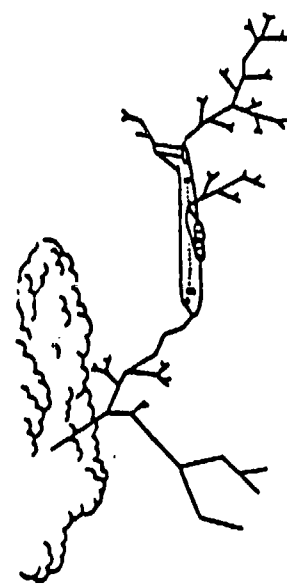
Consider an aircraft flying near a cloud in which charge has been separated, as is illustrated in Figure 2.1. Although most lightning flashes are intra-cloud, it is interesting to consider the sequence of events during a typical lightning flash connecting the aircraft to ground. The environment consists of various currents and fields which will now be discussed in the order they would naturally occur.

##### 2.2.1 Quasi-Static Electric Fields

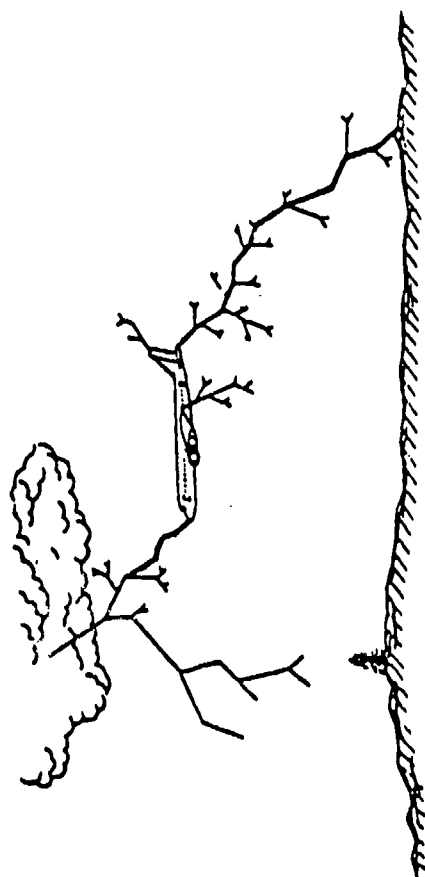
As charge initially separates within the cloud, static electric fields are formed. These fields may vary from as little as 300 V/m, which is the earth's fair weather field at ground level, to fields as high as 3 MV/m, (the nominal breakdown field of air at standard temperature and pressure). Typical values are generally in the range of 10-100 kV/m. An aircraft necessarily experiences these fields which usually do not present any great hazard to an aircraft because



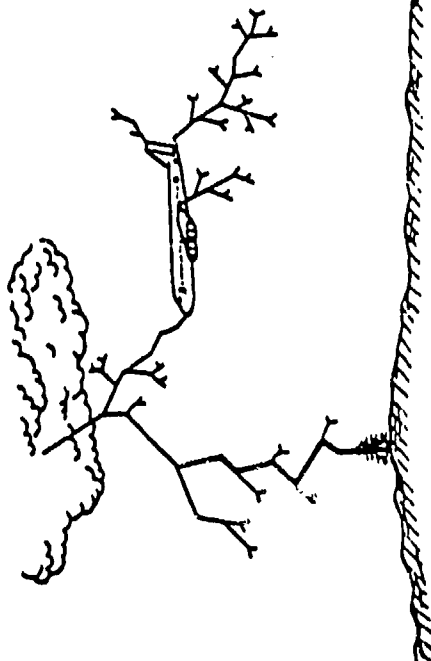
a. STEPPED LEADER APPROACHING AIRCRAFT



b. STEPPED LEADER ATTACHMENT AND CONTINUED  
PROPAGATION FROM AN AIRCRAFT



c. RETURN STROKE THROUGH THE AIRCRAFT



d. NO RETURN STROKE THROUGH THE AIRCRAFT

Figure 2.1 Illustration of Lightning Attachment to Aircraft

they are slowly varying, but they do induce a charge distribution (polarization) on the aircraft surface.

### 2.2.2 Initiating Streamers

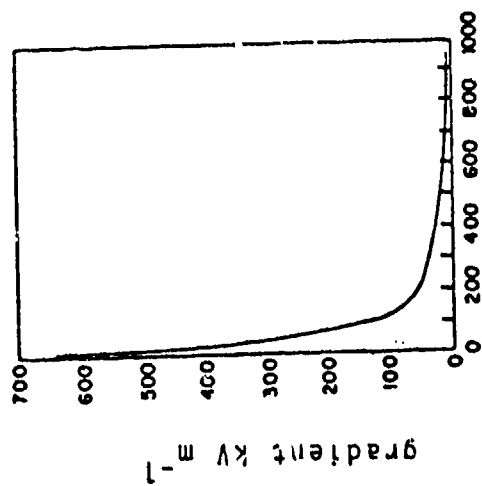
If the fields in the cloud become large enough, streamers begin to develop within the cloud. It is hypothesized that the normally downward moving stepped leader begins as a result of certain streamers which neutralize positive charge from the bottom-most pocket and negative charge from the main cloud volume. In addition to cloud streamers, if the fields around the aircraft are sufficiently large, streamers can form from the sharper extremities of the aircraft itself. Either of these phenomena can produce a response in the aircraft, the cloud streamers by production of electromagnetic radiation and the aircraft streamers by production of currents directly on the aircraft skin.

### 2.2.3 Stepped Leader

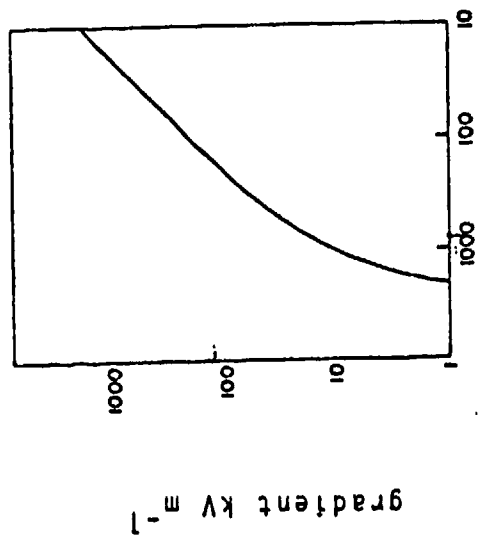
The stepped leader is a discharge which moves generally downward in steps of about 50 m, at an average rate of about  $10^5$  m/s, and carries a modest current of one or two thousand amperes. In spite of this relatively small current, there is substantial charge stored in the leader channel and its approach and/or attachment to an aircraft can be a major hazard. Because the end of the stepped leader can have very large electric fields near it, large changes in the electric field at the attachment point on the aircraft surface can result. The large change in electric field expected at the attachment point can induce substantial currents in such protuberances as deliberate antennas. In addition to these induced currents, EM radiation is produced at each leader step and this radiation can also couple to the aircraft.

Figure 2.2 illustrates a simple computation of the approaching leader electric fields based on data from Reference 6. The values of  $\partial E/\partial t$  so obtained ( $10^{10}$  V/m/sec) are not very large compared to those from NEMP ( $\sim 10^{13}$  V/m/sec).

When the stepped leader is about 50 meters or so from the aircraft, a streamer from the aircraft will propagate toward the approaching leader. When they meet, the aircraft is then attached to the leader channel. The channel then acts like a current source which elevates the aircraft potential by injecting current into it, in much the same way as a current



(a) Distance, meters



(b) Height Above Ground, meters

Assume  $\frac{\partial E}{\partial t} = \frac{\partial E}{\partial h} \frac{\partial h}{\partial t}$  and  $\frac{\partial h}{\partial t} = 1.5 \times 10^5 \text{ m/sec}$

One obtains  $\frac{\partial E}{\partial t} = 1.2 \times 10^7$  at 1000 m  
 $= 1.5 \times 10^{10}$  at 10-20 m

Figure 2.2 Simple Computation of Electric Fields for Approaching Stepped Leader [6]

source charges a capacitor. Although this process is not greatly understood (there is no data) and is subject to debate, simple calculations can be done to estimate  $\partial E/\partial t$  on the aircraft surface for this process. If one assumes a 500 pf capacitance for the aircraft (corresponding to a small fighter), and 1000 amperes in the leader current having a 100 ns rise time, the charging time is about 150 ns for 100  $\mu\text{C}$  of charge deposition. If one assumes a nominal value for the breakdown field of 3 MV/m (this can actually be much lower because of altitude and radius of curvature effects), one obtains values for  $\partial E/\partial t$  which are greater than  $10^{13}$  V/m/sec, which is comparable or even larger than that caused by NEMP. This attachment process is of course an area in which data should be obtained, but that is a very difficult task.

It is also important to point out that the aircraft is in a state of corona during this phase. Corona formation is a nonlinear process, and it can affect how the fields couple to the aircraft interior. Corona can affect coupling by either providing shielding by virtue of the inherent air conductivity, or else it may enhance coupling in certain spectral ranges by means of radiation from the corona process itself. Again, there is almost no data for this effect, but any coupling model must be able to account for non-linear effects such as corona and streamer formation and propagation.

#### 2.2.4 Return Stroke

After the stepped leader propagates through the aircraft and down to the earth, a large current (the return stroke) begins to flow in the leader channel at about 1/3 to 1/10 the speed of light. The return stroke current will also flow on the aircraft skin. Typical return stroke currents measured on the earth's surface are 10-20 kA but values larger than 200 kA have been observed. Electromagnetic field measurements at ground level for these strokes show fast rise times and slow decay times.

Previously, the fastest components of the return stroke rise time were thought to be on the order of microseconds. Recent measurements [4] however, show that substantial components of this rise time can be as small as 40 ns, with an average of 90 ns. The observations clearly show that there can be substantial frequency components of return strokes in the resonance region of the aircraft. Figure 2.3 shows an overlay of the high-altitude NEMP spectrum and LEMP (Lightning Electromagnetic Pulse) spectrum at various distances from a ground return stroke. These LEMP spectra are directly computed from measured vertical electric field waveforms at the distances indi-

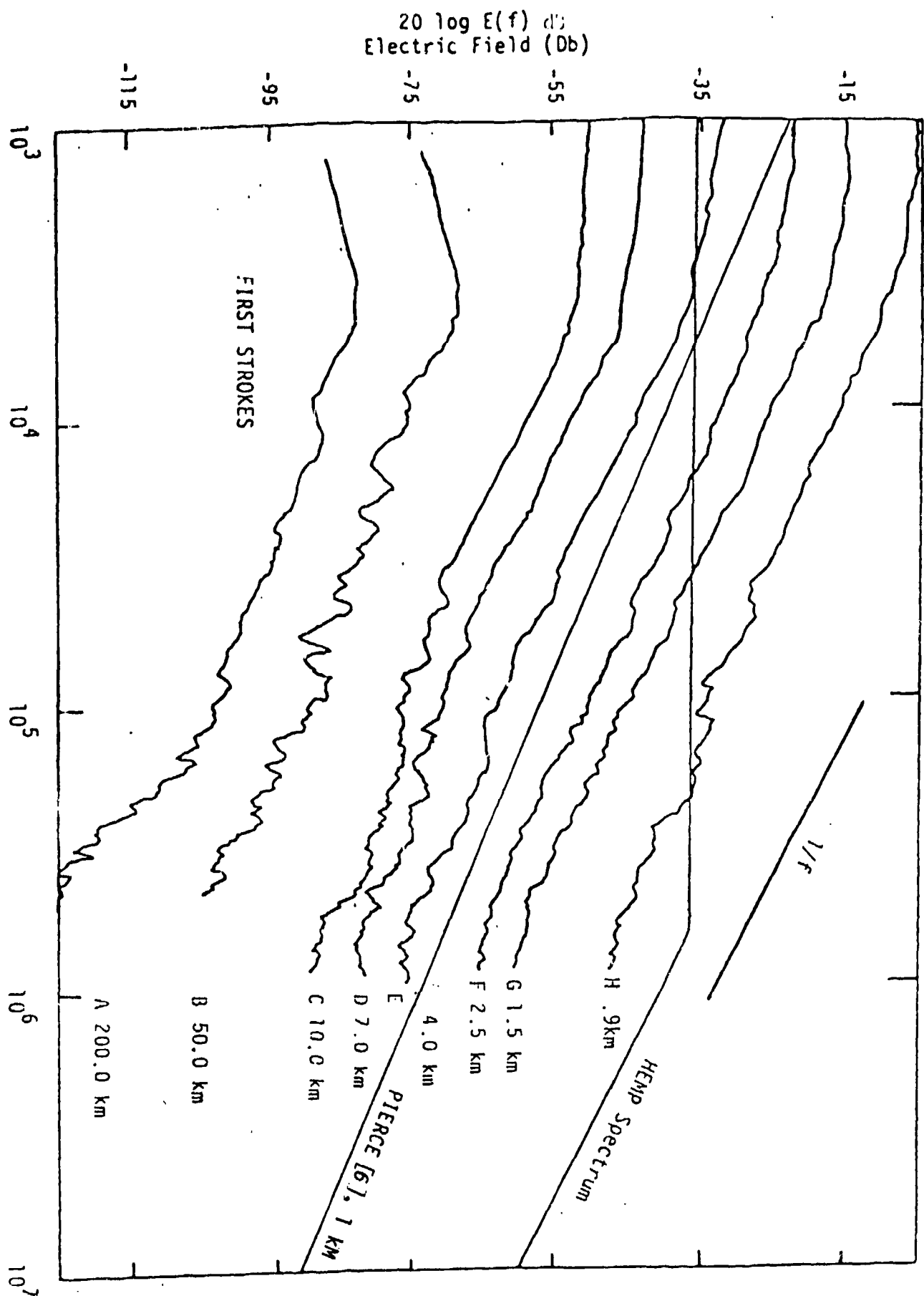


Figure 2.3 Comparison of HEMP and Return Stroke LEMP Spectral Current at Various Ranges from the Stroke (LEMP data from [7])

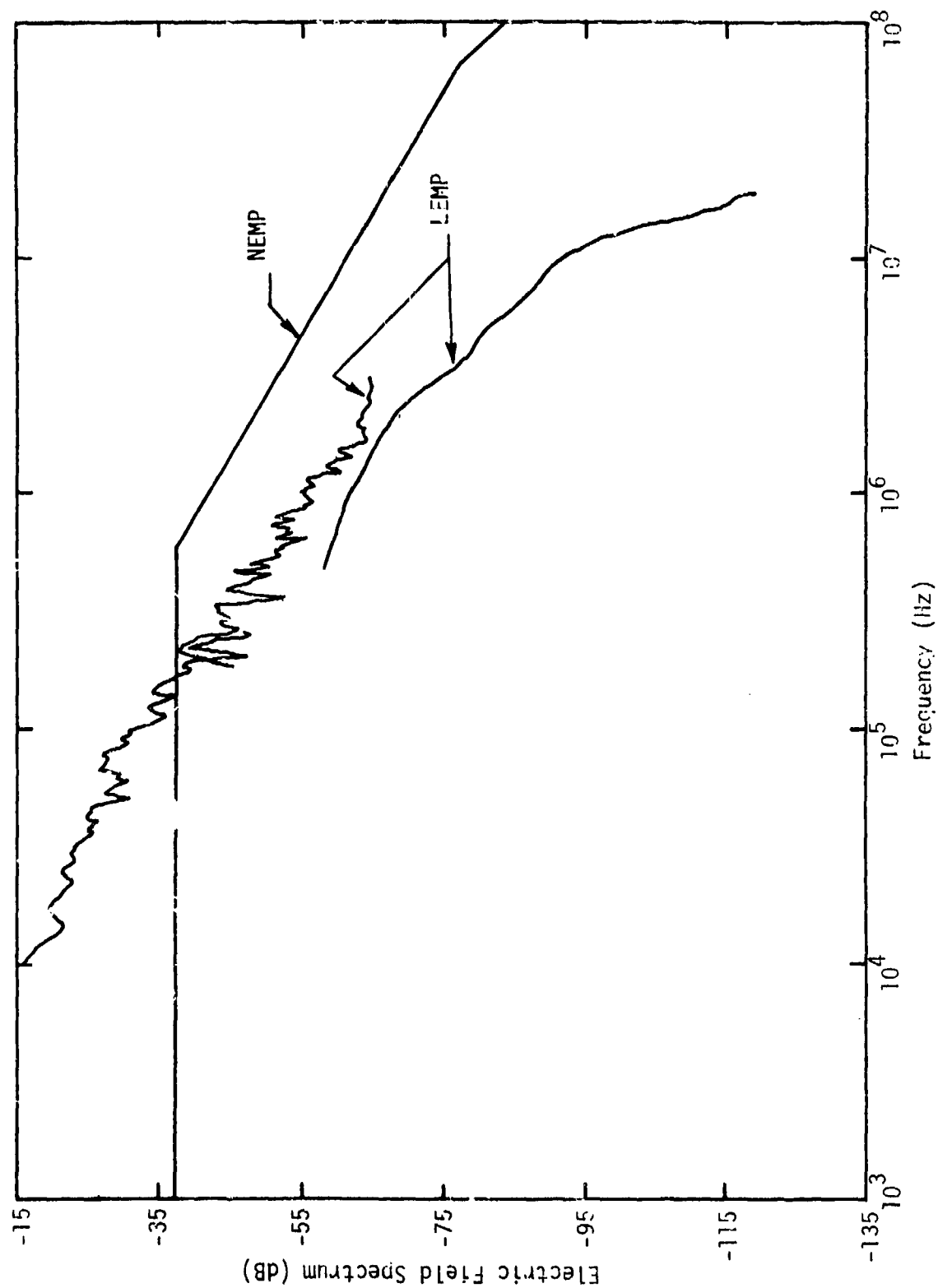


Figure 2.4 Comparison of NEMP and Return Stroke LEMP Electric Fields Measured at 50 km, and Extrapolated to 50 m by 1/R.

cated [7]. Also included is Pierce's narrow band data at 1 km [6]. Figure 2.4 shows a similar overlay except that the LEMP data is measured at 50 km and extrapolated by  $1/R$  to 50 m range, but is extended to 20 MHz, well beyond the first resonance of typical aircraft [4]. It is noted that the LEMP curve of Figure 2.4 also describes the spectrum of the intracloud discharge [4].

These two figures illustrate a current problem in the identification of the spectral content in the aircraft resonance region. It is clear that the values obtained by extrapolating 50 km data to small ranges by a  $1/R$  relationship do not give the same result as is obtained by transforming data at close ranges; the former method yields results much smaller than those obtained by the latter method. The discrepancy can possibly be explained by the method in Fourier transforming the close data, which has to be truncated in some manner [4], which produces false information. Also, the  $1/R$  rule is valid only at large distances from the channel. This problem is obviously one of current interest and is hoped to be resolved soon.

One can at least observe that, from the extrapolated 50 km data, which is for average lightning events, the LEMP spectral content at 50 m range in the aircraft resonance region for a worst case lightning stroke is comparable to that of NEMP. This means that the lightning current itself has a similar content, and an attached stroke can be expected to excite aircraft resonances at least as much as that caused by NEMP. The lightning current does have, however, a much greater low frequency content than does NEMP, and the low frequency response might obscure the resonant response.

An attached return stroke presents the most obvious and severe hazard to the aircraft. The large currents flowing on the aircraft skin generate large E and B fields, which in turn penetrate the aircraft skin via cockpits, apertures, deliberate antennas, cracks, slots, joints or radomes inducing currents or voltages in the electrical/electronic systems inside.

In addition to an attached stroke, near-miss return strokes will induce currents and charges on the external surface and consequent internal voltages and currents. Such a LEMP has in one case been measured to be nearly as effective in producing internal response as an attached stroke [8]. The LEMP fields, unlike the NEMP, may not be plane waves because the aircraft may be close enough to the stroke to encounter the near fields.



Attached strokes can also cause physical damage. For example locally large electric fields exist across insulating materials exposed to the aircraft's exterior. Under proper conditions of aircraft speed and return stroke duration, the attachment point to the aircraft can be swept many feet along the surface during the life of the return stroke channel. If the attachment point is near an insulating surface, the return stroke channel can be swept over the insulating surface as shown in Figure 2.5. Due to the substantial electric fields generated along the length of the stroke by  $\partial I/\partial t$ , the insulating material must be able to withstand the electric fields between points A and B. These fields can be on the order of a million volts per meter. Also, if an antenna were below an insulating radome, for example, the time rate of change of these fields caused by a stroke sweeping over the radome can be extremely large, and coupling to the antenna could also be large.

#### 2.2.5 Continuing Current and Restrikes

As the return stroke depletes charge from the channel, the return stroke current decays from its initial peak value towards zero. However, it is found that before the current ends, a relatively small current (several hundred amperes) can last for 10's or 100's of milliseconds. This current, called the continuing current, often carries over 50% of the total charge that is transferred from cloud to ground. During the period of continuing current flow, new additional streamers in the cloud can contribute charge to the upper end of the lightning channel. If the added charge is great enough, a dart leader propagates down the old channel at a uniform velocity and a restrike (subsequent return stroke) occurs. Restrike currents are large but generally smaller than the original return stroke, maximum values being on the order of 100 kA. Several such restrikes may occur 100's of milliseconds apart.

#### 2.2.6 Channel Impedance

When an aircraft is in an attached channel, the coupling to the aircraft depends upon channel impedance. For example, immediately after the leader attaches to the aircraft the rate of charge transfer to the aircraft depends upon the aircraft capacitance and the impedance of the channel. Similarly, for an aircraft in a return stroke channel, if one imagines to

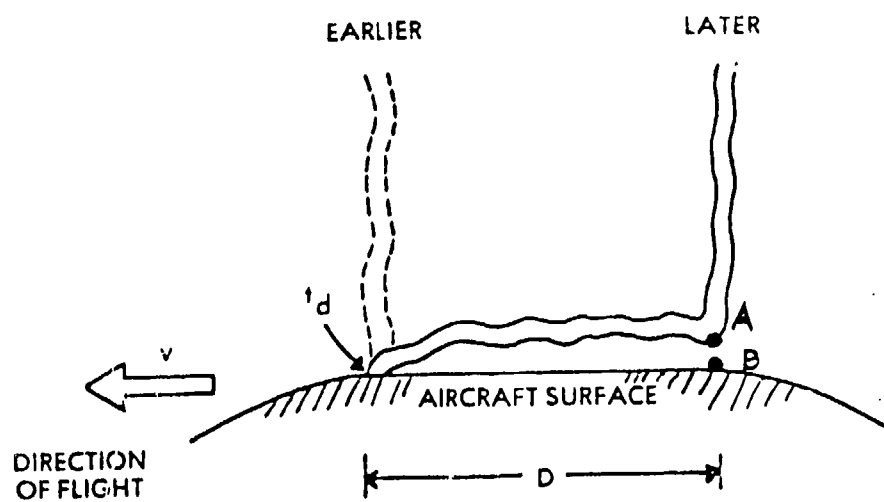


Figure 2.5. Schematic Diagram of Swept Stroke

a first order that the channel and the aircraft are two different impedance transmission lines, the resonant structure of the aircraft response is dependent upon the channel impedance.

The problem of determining the channel impedance is complicated by the structure of the channel. The channel consists of a somewhat narrow (a few centimeters diameter) hot conducting core surrounded by a corona sheath which can be several meters in diameter. Because little axial current flows in the corona sheath one might conclude that, if one were imagining the channel to be a transmission line, then the inductance would be given in terms of the diameter of the hot core, and the capacitance by the diameter of the corona sheath. Also, the resistance per unit length of the core is not well defined, and may vary from  $500\Omega/\text{m}$  to  $1\Omega/\text{m}$  [9]. Finally, only parameters which are used to characterize the channel are certainly time varying and spatially inhomogeneous.

Nevertheless, one can make estimates of this impedance and find its range of possible values by applying electromagnetic theory to what is understood about the channel. For example, in references 10 and 11, three methods of obtaining the channel impedance are given: transmission line model, dipole model with assumed sinusoidal current distribution, and a model based on two-dimensional time domain finite difference approach.

Table 2.1 summarizes the results for a transmission line and dipole approach, and Table 2.2 summarizes the results for the finite difference approach. In the latter case, the results are obtained by exciting a dipole at the center with a transient current source having a lightning-type pulse drive, and computing the drive point voltage. It was found that a series capacitance also given in Table 2.2 was required to duplicate the waveforms.

These studies seem to indicate that the source impedance of the lightning channel should be in the range of 100-700 ohms. This differs from the higher value of  $3000\Omega$  given by Wagner [12], although the value given in the latter is for the impedance seen by the return stroke wave as it propagates up the leader channel. Because its velocity is much less than that of light, its impedance is much higher. The impedance seen by an aircraft however, is that seen at the attach points by waves on the aircraft, and the smaller values would apply.

Table 2.1 Transmission Line Lightning Channel Models [10,11]

$\ell$ =channel length,  $a$ =core radius  
 $a_s$ =corona sheath radius

Case	Parameters	Transmission Line Model		Dipole Model*
1a	$\ell=300 \text{ m}$	L		
	$a=0.03\text{m}$	C		
	$a_c=0.03\text{m}$	Z	542 $\Omega$	451 $\Omega$
2a	$\ell=300\text{m}$	L		
	$a=0.03\text{m}$	C		
	$a_c=1\text{m}$	Z	422 $\Omega$	241 $\Omega$
3a	$\ell=300\text{m}$	L		
	$a=0.03\text{m}$	C		
	$a_c=10\text{m}$	Z	319 $\Omega$	102 $\Omega$
1b	$\ell=3000\text{m}$	L		
	$a=0.03\text{m}$	C		
	$a_c=0.03\text{m}$	Z	691 $\Omega$	680 $\Omega$
2b	$\ell=3000\text{m}$	L		
	$a=0.03\text{m}$	C		
	$a_c=1\text{m}$	Z	564 $\Omega$	310 $\Omega$
	$\ell=3000\text{m}$	L		
	$a=0.03\text{m}$	C		
	$a_c=10\text{m}$	A	472 $\Omega$	172 $\Omega$

\*At a frequency of 1 MHz

Table 2.2 Values of R and C for the Equivalent Impedance of the Channel Determined by Finite Difference Model [10,11]

CASE	R	C
a = 10m H = 55m	49 $\Omega$	$8.2 \times 10^2$ pfd
a = 1m H = 55m	$2.8 \times 10^2 \Omega$	69 pfd

#### 2.2.7 Summary

The lightning environment is extremely complex when viewed from a coupling point of view. There are both high E field (at attachment) and high H field (at return stroke) portions widely separated in time. The aircraft is in an attached channel whose impedance, which is time varying, is only partially understood. The coupling process is a non-linear phenomenon because of corona and streamer events. Spectral content is greatest in the low frequency range (1-100 kHz), yet is similar to or greater than that of NEMP at aircraft resonances. Alternately, one may say the coupling model should be able to handle early time ( $\sim 30$ ns) and late time ( $\sim$  several hundred microseconds) effects.

#### 2.3 The Coupling Process

In order to fully understand the following chapters which review and discuss coupling models, one needs to first have an overview of the coupling process and how it is reduced to smaller parts. The objective of this section is to provide this review.

In Figure 2.6(b) an aircraft is shown with an attached lightning arc channel. The coupling process may be viewed in three parts. First, the lightning channel causes electrical charge to flow on the surface of the aircraft, resulting in a surface current density (a vector quantity) and a charge density (a scalar quantity) which correspond to tangential magnetic fields ( $H_t$ ) and normal electric fields ( $E_n$ ), respectively. This is the external coupling process.

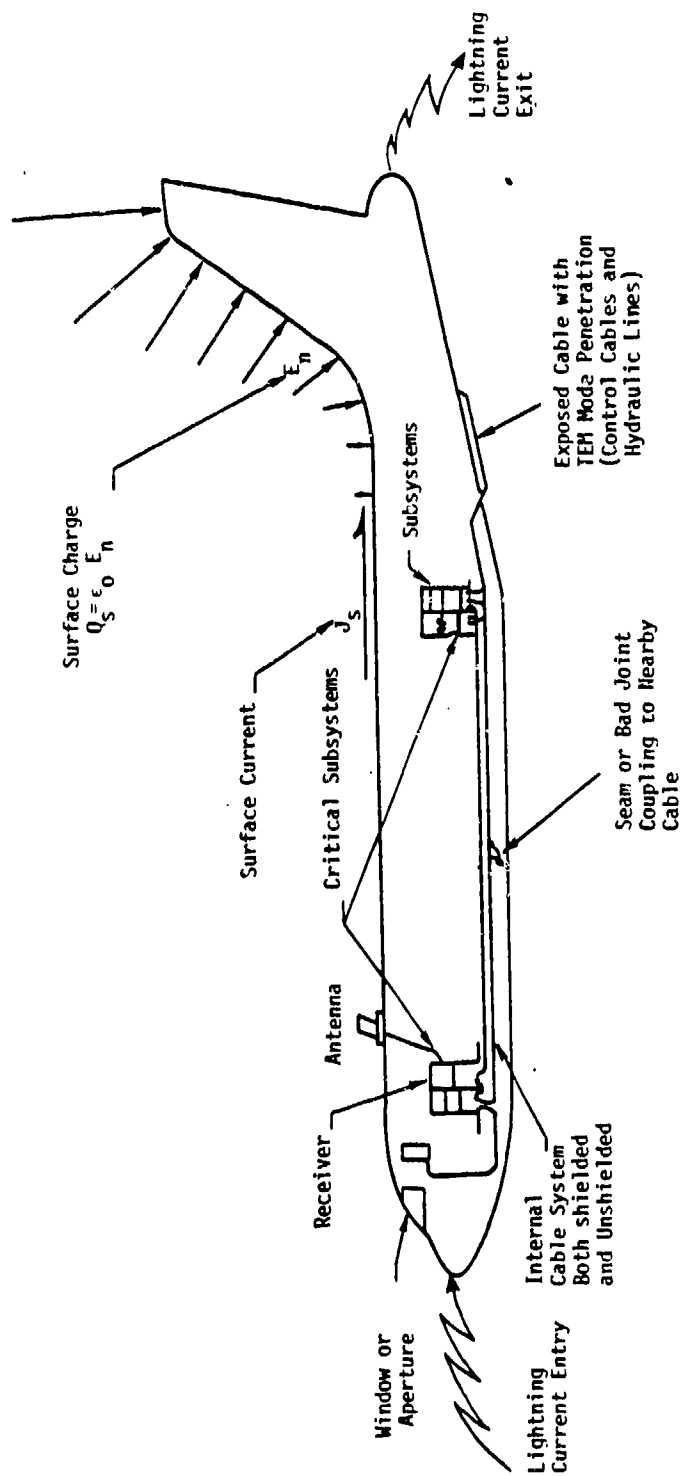
The second process, called internal coupling, refers to the penetration of energy through the shell or envelope of the aircraft. The penetration occurs because of apertures (windows, bomb bays, etc.), antennas, exposed cables or other conductors (such as fluid or control cables), seams and joints in the panels, or diffusion through the skin.

Finally, once the energy penetrates into the interior, the third process occurs, which is the internal propagation of the energy. The energy is propagated most efficiently by the internal cables, which form transmission lines along which the energy is transported. The energy is ultimately carried to the pins of electronic boxes which can be either temporarily upset or permanently damaged.

The process is summarized in Figure 2.6. It should be pointed out, however, that although the three processes are viewed as being independent and are usually solved separately, from a strictly theoretical point of view, they are not. The reason why the solutions can usually be done separately is that the mutual coupling between the processes is weak. For example, the presence of internal wiring is assumed to not greatly affect the external charge distribution, etc. One important case in which this does not hold is when an aircraft has a large aperture, such as a bomb bay or wheel well, whose presence significantly perturbs the external coupling response. In a case like this, the external coupling problem needs to be solved with the aperture present.

#### 2.4 Evaluation Criteria

The coupling method to be chosen must be able to treat the environment just described. In addition, the methods to be reviewed will be assessed according to several criteria. For example, the method should be able to predict the response of aircraft or missiles to lightning tests. Tests



- Incident lightning environment causes current and charge on external surface of aircraft.
- Surface currents and charges excite antennas and inadvertent penetrations.
- Penetrations couple to internal cabling.
- Cable systems couple to critical subsystems.

Figure 2.6 Analysis of Aircraft Coupling

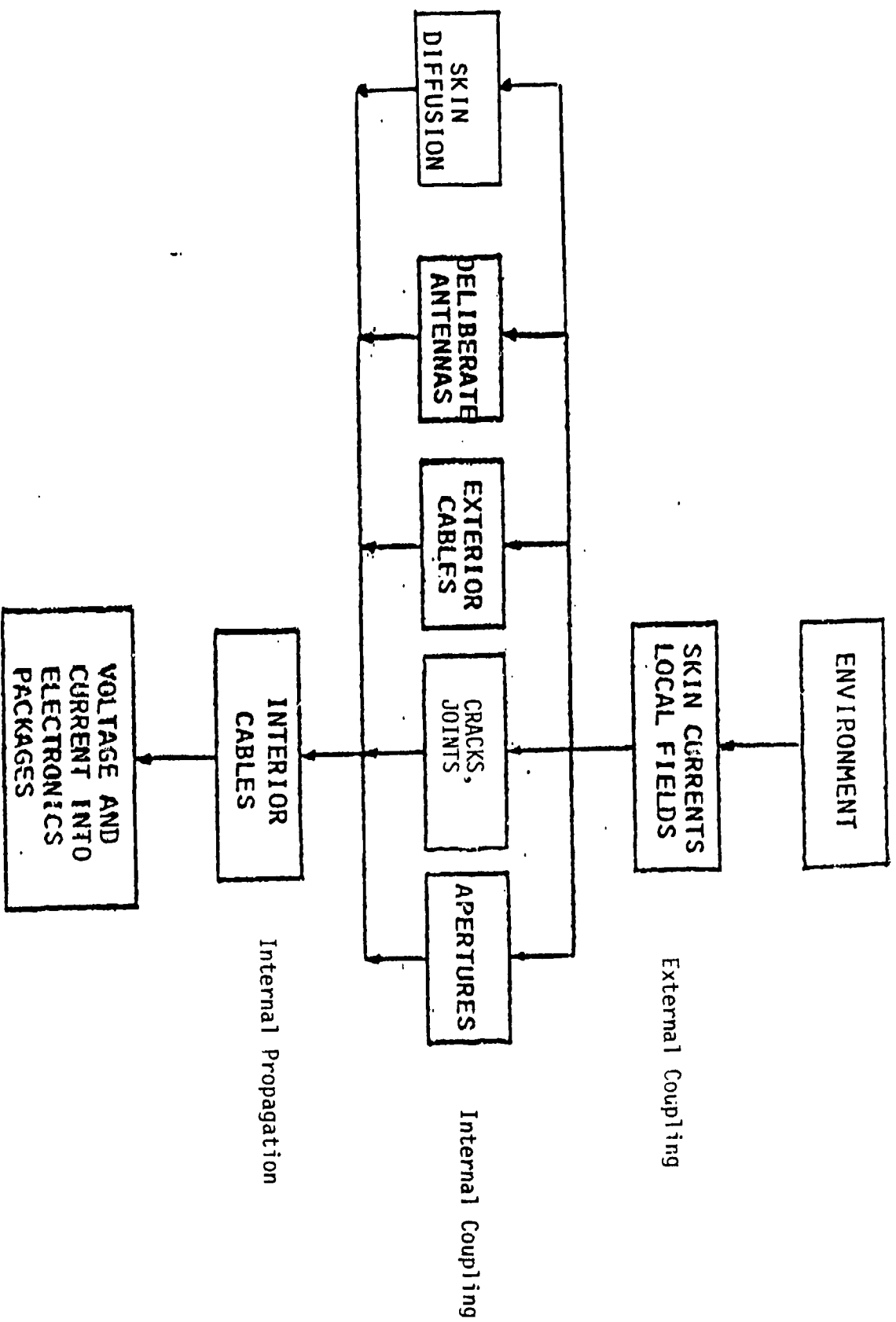


Figure 2.7 Summary of Coupling Methodology.



are often conducted over a ground plane, for example, and so the method selected should be able to include the peculiarities of a test fixture such as a ground plane. There are also certain software and numerical considerations that would be desirable in the selected code. These are principally computer memory and time constraints. Also, a code should be simple enough for non-specialists to use. These criteria have been explicitly applied to the external coupling modeling which forms the foundation for the overall model. Because the criteria do not all apply to the internal coupling and propagation models, they all are not explicitly applied there. The eleven criteria that have been chosen are listed below:

1. Do the computer codes which implement the method require more than 100kg memory?
2. Will a complete version of the code run a full analysis in two hours of CP time on a machine at the level of a CDC 6600?
3. Does the code achieve state-of-the-art numerical accuracy?
4. Does the code represent the aircraft with good physical accuracy?
5. Is the code user oriented?
6. Can the code treat both the high ( $>1$  MHz) and low ( $<10$  kHz) frequency components of the lightning fields?
7. Can the code treat a stroke attached to an aircraft in free space ?
8. Can the code treat the peculiarities of a test configuration?
9. Can the code handle both large and small aircraft?
10. Can the code incorporate the unique aspects of the lightning environment such as nonlinearities, time dependent air conductivity and near field effects?
11. Has the code been compared to experimental results ?

## CHAPTER 3

### EXTERNAL COUPLING REVIEW

#### 3.1 Introduction

The objective in this chapter is to assess methods of performing external coupling calculations. The assessment will be made for coupling of lightning to aircraft and/or missiles in the environment described in Section 2.2, and the assessment will be made using the eleven criteria listed in Section 2.4.

To fulfill this objective each computational method will be reviewed individually. The review will include a discussion of the mathematical basis of the method, examples of calculations that have been performed using the method, and a discussion of the method from the point of view of each of the eleven evaluation criteria. Many of the methods reviewed were originally developed for coupling of NEMP to missiles or aircraft.

In the course of performing the literature review, many references were gathered and reviewed. These references have been assembled in a bibliography which appears in Appendix A. For convenience, the references are listed by author as well as by subject matter.

The remainder of Chapter 3 is organized in the following manner. In Section 3.2 a general external coupling problem is defined, and various forms of Maxwell's equations are reviewed. Section 3.3 includes the review of each computational method along with a summary of the method according to each of the eleven evaluation criteria. In Section 3.4 there is a discussion of corona modeling. The final selection of the state-of-the-art external coupling method will be discussed later in Chapter 5.

#### 3.2 General External Coupling Problem

##### 3.2.1 Problem Definition

The objective of an external coupling calculation is to determine the exterior surface current and charge densities on the conductor of interest and this naturally requires the solution of Maxwell's equations

in the presence of arbitrarily shaped conductors. For convenience the various computational methods have been grouped into four categories. These four categories are 1) methods which solve differential equations, 2) methods based on the solution of an integral equation (or an integro-differential equation), 3) hybrid methods using combinations of integral equations, 4) and miscellaneous other methods. All of the methods aim to solve Maxwell's equations, and so apart from any numerical or physical approximations they are equivalent. Table 3.1 summarizes the methods reviewed.

A general external coupling problem can be described in the following way. Suppose a wave,  $\vec{E}_0(\vec{r}, t)$  and  $\vec{H}_0(\vec{r}, t)$ , is incident on a scatterer having a surface  $S$  (Figure 3.1), and suppose that some time in the past,  $t_0$ , the fields near  $S$  and the currents and charges on  $S$  are zero. When the incident fields reach the scatterer they induce surface currents  $\vec{J}_s$  and surface charges  $\sigma$  on  $S$  which flow for some time. The fields caused by the current  $\vec{J}_s$  and charge  $\sigma$  sum with the incident field to produce total fields  $\vec{E}_T(\vec{r}, t)$  and  $\vec{H}_T(\vec{r}, t)$  as shown in Figure 3.1. For a lightning attachment problem, the driving fields  $\vec{E}_0$ ,  $\vec{H}_0$  are really the fields from an attached arc channel.

For scattering problems the total fields  $\vec{E}_T$ ,  $\vec{H}_T$ , the scattered fields  $\vec{E}_s(\vec{r}, t)$  and  $\vec{H}_s(\vec{r}, t)$  produced by the currents and charges  $\vec{J}_s$  and  $\sigma$ , and the incident fields are related as follows:

$$\begin{aligned}\vec{E}_T(\vec{r}, t) &= \vec{E}_s(\vec{r}, t) + \vec{E}_0(\vec{r}, t) \\ \vec{H}_T(\vec{r}, t) &= \vec{H}_s(\vec{r}, t) + \vec{H}_0(\vec{r}, t)\end{aligned}\tag{3.2.1}$$

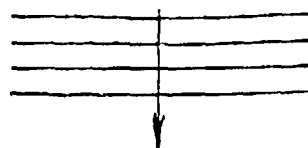
For perfect conductors, the problem of finding  $\vec{J}_s$  and  $\sigma$  is equivalent to finding the electric and magnetic fields on the surface of the conductor; the relationships are

Table 3.1 A Summary of the Computational Methods Reviewed.

BASIS OF METHOD	IDENTIFICATION/AUTHOR	NOTES
DIFFERENTIAL EQUATION.	THREDE/Mission Research Corporation	DFME/TD, FTD
	THREDE (update)/Same	Same
	-/Taflave and Brodwin	Same
MAGNETIC FIELD INTEGRAL EQUATION	-/Bennett & Weeks -/Peralta	MFIE/TD
ELECTRIC FIELD INTEGRAL EQUATION	AMP (Antenna Modelling Program)/M&A	EFIE/TW, FD
	TWTD/Lawrence Livermore Ohio State/Richmond -/Wilton	EFIE/TW, TD RIE/TW, FD EFIE/FD
HYBRID METHOD	AMP2/NBA NEC(Numerical Electromagnetic Code)/Lawrence Livermore -/Bennett	EFIE-TW, MFIE/FD Same EFIE, MFIE/TD
MISCELLANEOUS	Analytical Stick Model/Redrozan Unimoment/Mei Singularity Expansion Method/Bacon Finite Element/e.g., Silvervester et al. Lumped Parameter Network Models Wilton, Triangular Patch	Integral for current in an Antenna/FD Eigen function Expansion and Another Method of Choice/FD Variational Integral Eqn/FD EFIE/FD

Notes: The Following Abbreviations Have Been Used Above: Differential Form of Maxwell's Equations (DFME), Electric Field Integral Equation (EFIE), Finite Difference (FTD), Frequency Domain (FD), Magnetic Field Integral Equation (MFIE), Thin Wire (TW), Time Domain (TD), and Reaction Integral Equation (RIE).

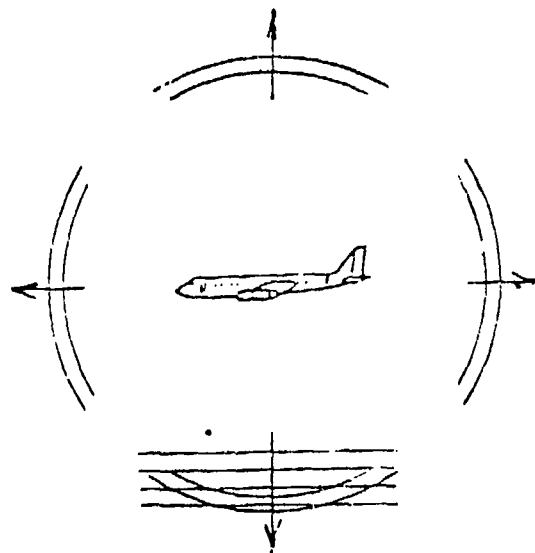
$$\vec{E}_0(r,t), \vec{H}_0(r,t)$$



Incident Fields



$$\vec{E}_T(r,t), \vec{H}_T(r,t)$$



Total Fields

Figure 3.1 General NEMP-Type Scattering Problem.

$$\left. \begin{aligned} \vec{J}_S(\vec{r}_S, t) &= \hat{n} \times \vec{H}_T(\vec{r}_S, t) \\ \sigma(r_S, t) &= \epsilon_0 \hat{n} \cdot \vec{E}_T(\vec{r}_S, t) \end{aligned} \right\} \quad (3.2.2)$$

where  $\vec{r}_S$  is on the surface  $S$ , and  $\hat{n}$  is the unit vector normal to the surface.

### 3.2.2 Forms of Maxwell's Equations

To determine the fields  $E_T$  and  $H_T$ , it is necessary to find a solution of Maxwell's equations consistent with the incident fields and the boundary conditions required at the surface of the scatterer. Three forms of Maxwell's equations will be discussed here.

First, consider the differential form of Maxwell's equations,

$$\left. \begin{aligned} \vec{\nabla} \cdot \vec{E} &= \rho/\epsilon_0 & \vec{\nabla} \times \vec{E} &= -\frac{\partial \vec{B}}{\partial t} \\ \vec{\nabla} \cdot \vec{B} &= 0 & \vec{\nabla} \times \vec{H} &= \vec{J} + \frac{\partial \vec{D}}{\partial t} \end{aligned} \right\} \quad (3.2.3)$$

These equations, especially the two curl equations, are used to obtain a solution in free space using finite difference techniques.

The two source free equations suggest defining potentials  $\phi(\vec{r}, t)$  and  $\vec{A}(\vec{r}, t)$  as follows:

$$\left. \begin{aligned} \vec{B} &= \vec{\nabla} \times \vec{A} \\ \vec{E} &= -\vec{\nabla} \phi - \frac{\partial \vec{A}}{\partial t} \end{aligned} \right\} \quad (3.2.4)$$

These potentials then satisfy the equations

$$\left. \begin{aligned} \nabla^2 \vec{A} - \mu_0 \epsilon_0 \frac{\partial^2 \vec{A}}{\partial t^2} &= -\mu_0 \vec{J} \\ \nabla^2 \phi - \mu_0 \epsilon_0 \frac{\partial^2 \phi}{\partial t^2} &= -\rho/\epsilon_0 \end{aligned} \right\} \quad (3.2.5)$$

These equations have known retarded time solutions

$$\left. \begin{aligned} \vec{A}(\vec{r}, t) &= -\frac{\mu_0}{4\pi} \int \frac{\vec{J}(\vec{r}', \tau)}{R} dV' \\ \phi(\vec{r}, t) &= \frac{1}{4\pi\epsilon_0} \int \frac{\sigma(\vec{r}', \tau)}{R} dV' \end{aligned} \right\} (3.2.6)$$

where  $\tau = t - R/c$  and  $R = |\vec{r} - \vec{r}'|$ . Substituting these expressions into the defining equations for  $\vec{A}$  and  $\phi$  gives for the scattered fields

$$\left. \begin{aligned} \vec{H}_s(\vec{r}, t) &= \frac{1}{4\pi} \int_V \left( \frac{\vec{J}(\vec{r}', \tau)}{R^2} + \frac{1}{Rc} \frac{\partial \vec{J}}{\partial \tau} \right) \times \frac{\vec{R}}{R} dV' \\ \vec{E}_s(\vec{r}, t) &= \frac{1}{4\pi\epsilon} \int_V \left( \frac{1}{Rc} \frac{\partial \sigma}{\partial \tau} \vec{R} + \frac{\sigma(\vec{r}', \tau)}{R^2} \vec{R} + \frac{\mu\epsilon}{R} \frac{\partial \vec{J}}{\partial \tau} \right) dV' \end{aligned} \right\} (3.2.7)$$

For the fields on the surface of a perfect conductor, equations (3.2.7) reduce to

$$\left. \begin{aligned} \vec{H}_s(\vec{r}, t) &= \frac{1}{4\pi} \int \left( \frac{\vec{J}_s(\vec{r}', \tau)}{R^2} + \frac{1}{Rc} \frac{\partial \vec{J}_s}{\partial \tau} \right) \times \frac{\vec{R}}{R} da' \\ \vec{E}_s(\vec{r}, t) &= \frac{1}{4\pi\epsilon} \int \left( \frac{1}{Rc} \frac{\partial \sigma}{\partial \tau} \vec{R} + \frac{\sigma(\vec{r}', \tau)}{R^2} \vec{R} + \frac{\mu\epsilon}{R} \frac{\partial \vec{J}_s}{\partial \tau} \right) da' \end{aligned} \right\} (3.2.8)$$

From these two equations, it is possible to derive two integral equations for the unknown surface current. Consider first the E-field equation in (3.2.8). The tangential component of the total electric field must be zero at the surface of a perfect conductor. Using the E-field equation of (3.2.8) and the relation for  $E_T$  in (3.2.1) gives

$$\left. \begin{aligned} \hat{n} \times \vec{E}_T &= 0 \\ \hat{n} \times (\vec{E}_0 + \vec{E}_s) &= 0 \\ \hat{n} \times \vec{E}_0 &= -\hat{n} \times \vec{E}_s \end{aligned} \right\} (3.2.9)$$

and

$$\hat{n} \times \vec{E}_0(\vec{r}, t) = \frac{\hat{n}}{4\pi} \times \int \left[ \frac{\mu}{R} \frac{\partial \vec{J}_s(\vec{r}', \tau)}{\partial \tau} + \frac{\sigma(\vec{r}', \tau)}{\epsilon} \frac{\vec{R}}{R^3} + \frac{1}{c\epsilon} \frac{\partial \sigma(\vec{r}', \tau)}{\partial \tau} \frac{\vec{R}}{R^2} \right] da' \quad (3.2.10)$$

This is an integral equation in the related unknowns  $\vec{J}_s(\vec{r}, \tau)$  and  $\sigma(\vec{r}, \tau)$  and is commonly called the Electric Field Integral Equation (EFIE). It is the time domain form of the EFIE. If a sinusoidal dependence is assumed, then the frequency domain version of (3.2.10) is obtained:

$$\hat{n} \times \vec{E}_0(\vec{r}, t) = \frac{1}{2\pi j \omega \epsilon_0} \hat{n} \times \int \left\{ -\omega^2 \mu_0 \epsilon_0 \vec{J}_s(\vec{r}', t) \phi + (\vec{\nabla} \phi) \left[ \vec{\nabla} \cdot \vec{J}_s(\vec{r}', t) \right] \right\} da' \quad (3.2.11)$$

where  $\phi$  represents  $\exp(jkR)/R$ .

A second integral equation results from the H-field equation of equations (3.2.8). From (3.2.2), the surface current on the conductor is related to the tangential component of the total H field at the surface. Therefore

$$\vec{J}_s(\vec{r}, t) = \hat{n} \times \vec{H}_T = \hat{n} \times (\vec{H}_0 + \vec{H}_s) \quad (3.2.12)$$

Using the expression for  $\vec{H}_s$  from (3.2.8), and following [13], it can be shown that

$$\vec{J}_s(\vec{r}, t) = 2\hat{n} \times \vec{H}_0 + \frac{1}{2\pi} \hat{n} \times \int \left( \frac{1}{Rc} \frac{\partial \vec{J}_s(\vec{r}', \tau)}{\partial \tau} + \frac{\vec{J}_s(\vec{r}', \tau)}{R^2} \right) \times \frac{\vec{R}}{R} da' \quad (3.2.13)$$



If harmonic time dependence is assumed for the fields, then

$$\vec{J}_S(\vec{r}, t) = 2\hat{n} \times \vec{H}_0 + \frac{\hat{n}}{2\pi} \times \int \vec{J}_S(\vec{r}, \tau) \vec{x} \nabla \phi \, da', \quad (3.2.14)$$

where  $\phi$  is  $\exp(jkR)/R$ . Equations (3.2.13) and (3.2.14) are denoted the Magnetic Field Integral Equation (MFIE) in the time or the frequency domain, respectively.

### 3.2.3 Method of Moments

Because many of the methods to be reviewed rely on the Method of Moments (MoM) to solve integral equations, the method is reviewed briefly here following [14]. Consider an integral equation of the form

$$V(x) = \int_a^b K(x, x') J(x') \, dx \quad (3.2.15)$$

where  $V(x)$  is a known function,  $K$  is the kernel, and  $J(x)$  is unknown.  $J(x)$  will be a surface current density. The integral in (3.2.15) is a linear operator, and so the equation can be written in a more concise form,

$$\underline{L} J(x) = V(x) \quad (3.2.16)$$

where  $\underline{L}$  is an operator, its domain being a function like  $J$  and its range functions like  $V$ . Customarily one expands the function  $J$  in a series of known functions, denoted by  $J_n(x)$ , so

$$J(x) = \sum_{n=1}^N I_n J_n(x) \quad (3.2.17)$$

The functions  $J_n(x)$  are called basis functions or expansion functions. Substitution of (3.2.17) into (3.2.16) gives

$$\sum_{n=1}^N I_n \underline{L} J_n(x) = V(x) \quad (3.2.18)$$

Define an inner product between two functions  $\langle w, v \rangle$  to be

$$\langle w, v \rangle = \int_{\ell_1}^{\ell_2} w(x') V(x') dx'. \quad (3.2.19)$$

Then it is possible to construct a system of linear equations from the original algebraic equation by multiplying (3.2.18) by  $w_m(x')$  and integrating both sides from  $\ell_1$  to  $\ell_2$ ,

$$I_n \int_{\ell_1}^{\ell_2} w_m(x') \underline{L}(x') J_n(x') dx' = \int_{\ell_1}^{\ell_2} w_m(x') V(x') dx' \quad (3.2.20)$$

The functions  $w_m(x)$  are in the range of the operator  $\underline{L}$  and are denoted weighting or testing functions. Define a matrix element  $Z_{nm}$  and a vector element  $V_m$  as follows:

$$\begin{aligned} Z_{nm} &= \int_{\ell_1}^{\ell_2} w_m(x') \underline{L}(x') J_n(x') dx' \\ V_m &= \int_{\ell_1}^{\ell_2} w_m(x') V(x') dx' \end{aligned} \quad (3.2.21)$$

Then (3.2.20) can be written

$$\begin{bmatrix} V_m \end{bmatrix} = \begin{bmatrix} Z_{mn} \end{bmatrix} \begin{bmatrix} I_n \end{bmatrix} \quad n, m = 1, 2, \dots, N \quad (3.2.22)$$

where  $Z_{mn}$  and  $V_m$  are known, and the constants  $I_n$  are to be determined. There are  $N$  unknown  $I$ 's, one for each  $J_n(x)$ . If we choose at least  $N$  testing functions then there will be a solution for  $I_n$  although the solution may not be unique depending on the matrix  $Z_{mn}$ . The solution to (3.2.22) is obviously given by

$$\begin{bmatrix} I_n \end{bmatrix} = \begin{bmatrix} Z_{mn} \end{bmatrix}^{-1} \begin{bmatrix} V_m \end{bmatrix}, \quad (3.2.23)$$

which is the desired solution presuming that  $\begin{bmatrix} Z_{mn} \end{bmatrix}^{-1}$  exists.

Several common choices for the testing and expansion functions deserve mention. If the basis functions are the same as the testing functions, the method is known as Galerkin's method. Galerkin's method is equivalent to the Rayleigh-Ritz variational method, which in this case is the minimization of the functional  $\frac{\langle J, LJ \rangle}{\langle J, J \rangle}$ . A common choice for the weighting

functions, independent of whether Galerkin's method is used, are Dirac delta functions

$$w_m(x) = \delta(x - x_m) \quad (3.2.24)$$

This effectively requires that the linear equation holds only at the set of points  $\{x_m, m=1,2,\dots,N\}$ . The name for this method is collocation or point matching. It is sometimes sufficient to choose basis functions which are constants for regions of the  $x$  variable, namely

$$J_n(x) = \begin{cases} J_0^n = \text{const} & \text{if } x \in S_n \\ 0 & \text{otherwise} \end{cases} \quad (3.2.25)$$

and where  $\bigcup_{n=1}^N S_n$  includes the entire range of  $x$  but  $S_n \cap S_m = \emptyset$  if  $n \neq m$ .

This choice of  $J_n$  has the effect of substantially simplifying the integrals for  $Z_{mn}$ , in fact making  $Z_{mn}$  a sum of simpler integrals.

This completes the discussion of a general external coupling problem and the forms of Maxwell's equations which are most commonly used in the methods that are reviewed here. In the next section the individual methods are discussed.

### 3.3 Computational Methods

#### 3.3.1 Introduction

It is the objective of Section 3.3 to discuss separately each of the computational methods that have been reviewed. For convenience, the methods have been divided into groups and treated in individual subsections. The groups are Finite Difference (Section 3.3.2), Magnetic Field Integral Equation (MFIE, Section 3.3.3), Electric Field Integral Equation (EFIE, Section 3.3.4), Singularity Expansion Method (SEM, Section 3.3.5), Lumped Parameter Network (LPN, Section 3.3.6) and Miscellaneous Methods (Section 3.3.7).

#### 3.3.2 Finite Difference

##### 3.3.2.1 General Method

From equations (3.2.3), the two Maxwell curl equations are

$$\begin{aligned}\vec{\nabla} \times \vec{E} &= - \frac{\partial \vec{B}}{\partial t} \\ \vec{\nabla} \times \vec{H} &= \vec{J} + \frac{\partial \vec{D}}{\partial t}.\end{aligned}\tag{3.3.1}$$

Following the suggestion of Yee [15] the derivatives in these two equations can be expressed as differences of field values at neighboring spatial and temporal positions. The difference equations which result can be used to obtain the fields at some time if the fields everywhere are known at an earlier time. To illustrate how the solution proceeds, consider a problem with cylindrical symmetry in which the material properties  $\epsilon$ ,  $\mu$  and  $\sigma$  depend at most on  $|\vec{r}|$  only. Furthermore, suppose that only  $H_\phi$  and  $E_z$  are non-zero and that these fields have no  $\phi$  or  $z$  dependence, i.e. a one-dimensional problem in the variable  $r$  (the cylindrical radius). The equations (3.3.1) then become

$$\begin{aligned}\frac{\partial}{\partial r} E_z(r,t) &= - \mu \frac{\partial}{\partial t} H_\phi(r,t) \\ \frac{\partial}{\partial r} [r H_\phi(r,t)] &= J_z + \sigma E_z + \epsilon \frac{\partial}{\partial t} E_z(r,t).\end{aligned}\tag{3.3.2}$$

To convert these equations to difference form, two sets of points are imagined to fill Euclidian space. The sets of points are called a discretizing mesh and an example is shown in Figure 3.2. The electric field  $\vec{E}$  will be evaluated at points labelled (x) and the magnetic field  $\vec{H}$  will be evaluated at points labelled (·). The spatial derivatives in (3.3.2) are approximated by differences



of the field values at neighboring points (x) or (0). Central differencing is used to reduce the numerical errors. If  $\Delta r$  and  $\Delta t$  are the distances between grid points in Figure 3.2, then Maxwell's equations in the form of (3.3.2) can be written in the following way:

$$\begin{aligned} \mu \frac{H_{\varphi}(r, t+\frac{1}{2}\Delta t) - H_{\varphi}(r, t-\frac{1}{2}\Delta t)}{\Delta t} &= \frac{E_z(r+\frac{1}{2}\Delta r, t) - E_z(r-\frac{1}{2}\Delta r, t)}{\Delta r} \\ \epsilon(r) \frac{E_z(r, t+\frac{1}{2}\Delta t) - E_z(r, t-\frac{1}{2}\Delta t)}{\Delta t} &+ \sigma(r) \frac{E_z(r, t+\frac{1}{2}\Delta t) + E_z(r, t-\frac{1}{2}\Delta t)}{2} = -J_z(r, t) \\ &+ \frac{1}{r} \frac{(r+\frac{1}{2}\Delta r)H_{\varphi}(r+\frac{1}{2}\Delta r, t) - (r-\frac{1}{2}\Delta r)H_{\varphi}(r-\frac{1}{2}\Delta r, t)}{\Delta r} \end{aligned} \quad (3.3.3)$$

Solving for  $H_{\varphi}(r, t+\Delta t/2)$  in the first equation and for  $E_z(r, t+\Delta t/2)$  in the second gives two equations with the following functional dependence:

$$\begin{aligned} H_{\varphi}(r, t+\frac{1}{2}\Delta t) &= H_{\varphi} \left( H_{\varphi}(r, t-\frac{1}{2}\Delta t), E_z(r+\frac{1}{2}\Delta r, t), E_z(r-\frac{1}{2}\Delta r, t), \epsilon, \mu \right) \\ E_z(r, t+\frac{1}{2}\Delta t) &= E_z \left( E_z(r, t-\frac{1}{2}\Delta t), H_{\varphi}(r+\frac{1}{2}\Delta r, t), H_{\varphi}(r-\frac{1}{2}\Delta r, t), J_z(r, t), \sigma, \epsilon, \mu \right) \end{aligned} \quad (3.3.4)$$

The important feature of these equations is that the fields at time  $t+\Delta t/2$  are given entirely in terms of fields at earlier times ( $t$  and  $t-\Delta t/2$ ). Thus if one knows the fields at a time  $t_0$ , equations (3.3.4) can be used to calculate the new fields at later times  $n\Delta t$ , where  $n$  is a positive integer.

The above procedure for calculating the fields at time  $t+\Delta t/2$  from those at time  $t-\Delta t/2$  can be implemented nicely by computer. Owing to the finite size of computer memories however, it is necessary to limit the size of the Euclidian space. The limit is defined by a problem space boundary but this introduces a difficulty in performing the step-by-step solution. In order to

avoid solutions for the fields which depend strongly on the problem space boundary, it is necessary to impose some type of boundary condition at the problem space boundary.

### 3.3.2.2 THREDE

For three dimensional problems finite difference expressions can be calculated in an entirely analogous manner. This has been described by Holland [16] and Merewether [17] in a finite difference handbook. The expressions are substantially more complicated. A computer code based on this method has been developed and tested on several aircraft for nuclear EMP coupling. The code is called THREDE [16] and has been used to investigate the response of an F-111 [16] and an A6 [18] to a NEMP environment, and the Advanced Design Composite Aircraft (ADCA) to a lightning environment [19].

Calculations of the surface current density  $J_s$  and the surface charge density  $\sigma$  have been made for an F-111 fighter aircraft [16]. The representation of the aircraft is shown in Figures 3.3 and 3.4. Figure 3.3 shows the gridding and the F-111 profile, and Figure 3.4 identifies the test points TP 208 and TP R1. Calculations using THREDE were compared to measurements made at the Horizontal Polarized Dipole (HPD) EMP simulator at Kirtland AFB. The actual measurements and comparison with THREDE were made for the time derivatives,  $\dot{J}_s$  and  $\dot{\sigma}$ , because of the higher frequency response that was available by measurement of these quantities.

The data and THREDE calculations of  $J_s$  are compared in Figures 3.5 to 3.8. For the measurements reported in these figures, the driving field was the simulator wave incident on the top of the aircraft polarized parallel to the fuselage. The agreement between the calculations and the tests is good, except perhaps for TP R1 near 20 MHz.

THREDE calculations have also been compared to measurements for the A6 aircraft by Kunz et al. [18]. The main purpose of this work was to identify requirements for a Surface Current Injection Technique (SCIT) to substitute for the expensive and elaborate EMP electromagnetic field simulators. However, as a part of the work, comparisons have been made of THREDE predictions with both SCIT and simulator measurements on an A6 aircraft to verify THREDE's accuracy. The gridding used for the A6 and the relevant results are shown in Figures 3.9 and 3.10. The measurements were taken for an A6 flying over the EMPRESS (a horizontal dipole) simulator. For test points 1, 2 and 4 the agreement

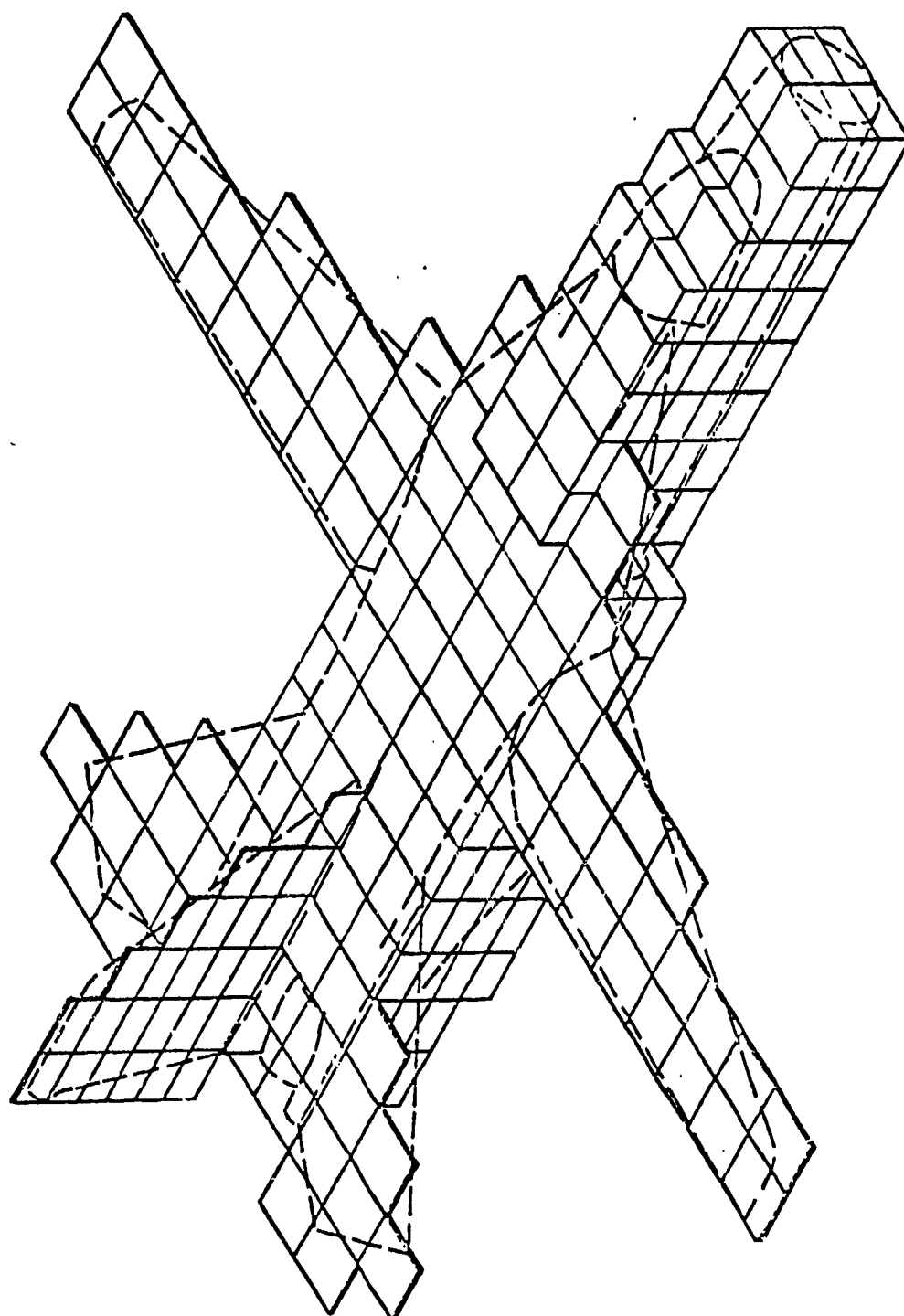


Figure 3.3 The Model of the F-111 With Actual F-111 Profile [16]



Figure 28. THREDE Rectilinear Model of the F111

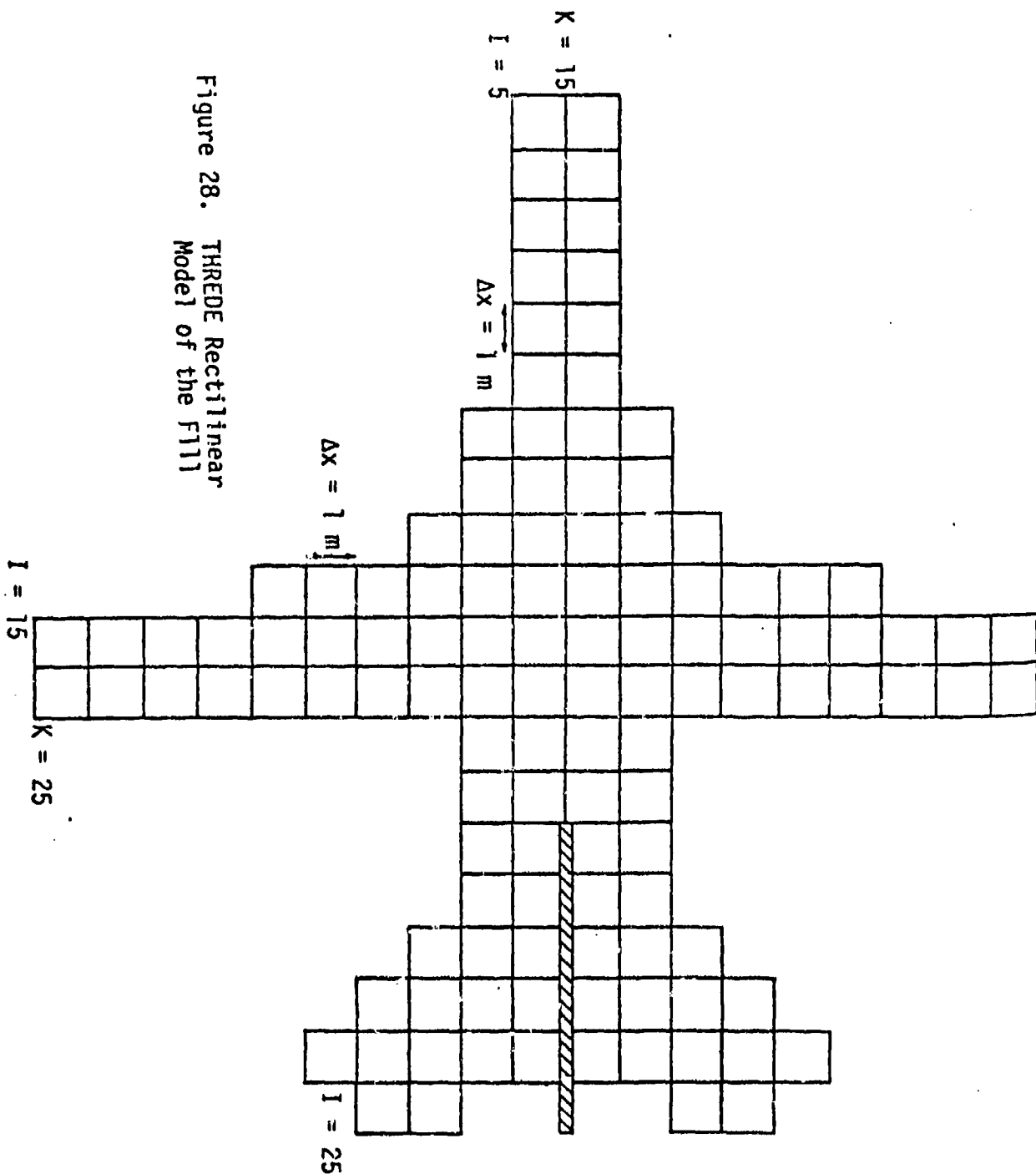
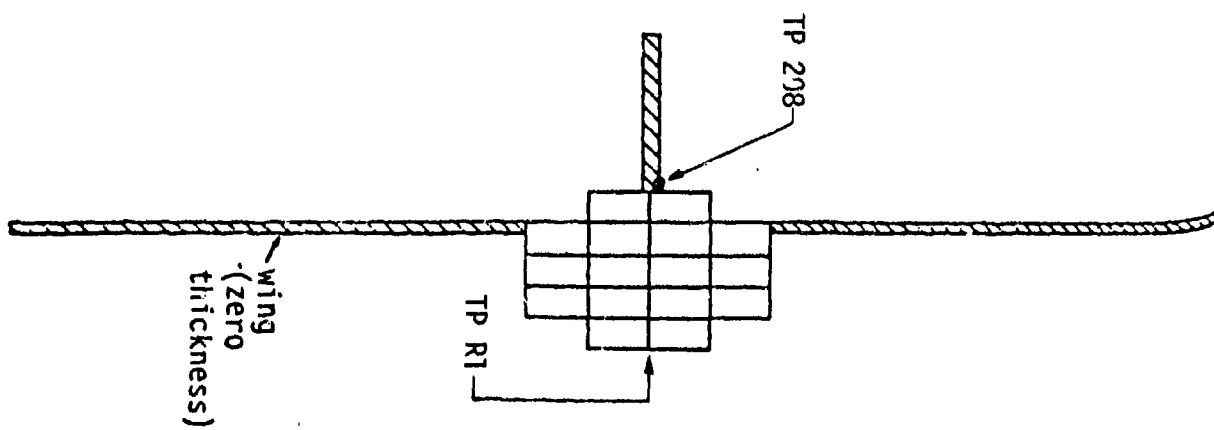


Figure 3.4 THREDE Rectilinear Model of the F-111 [16]



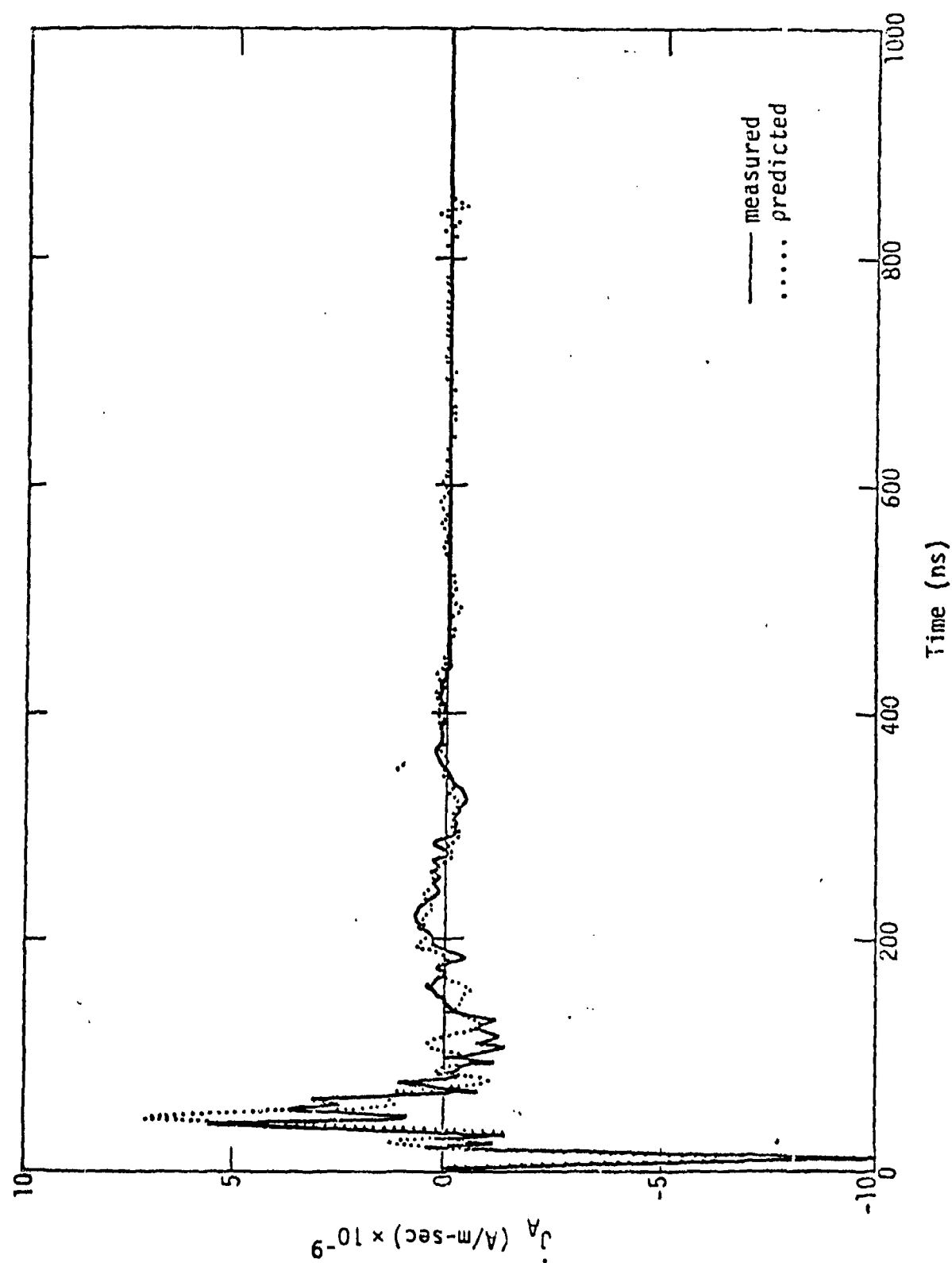


Figure 3.5 Measured vs. Predicted Axial Current at Test Point 208 in the Time Domain [16]

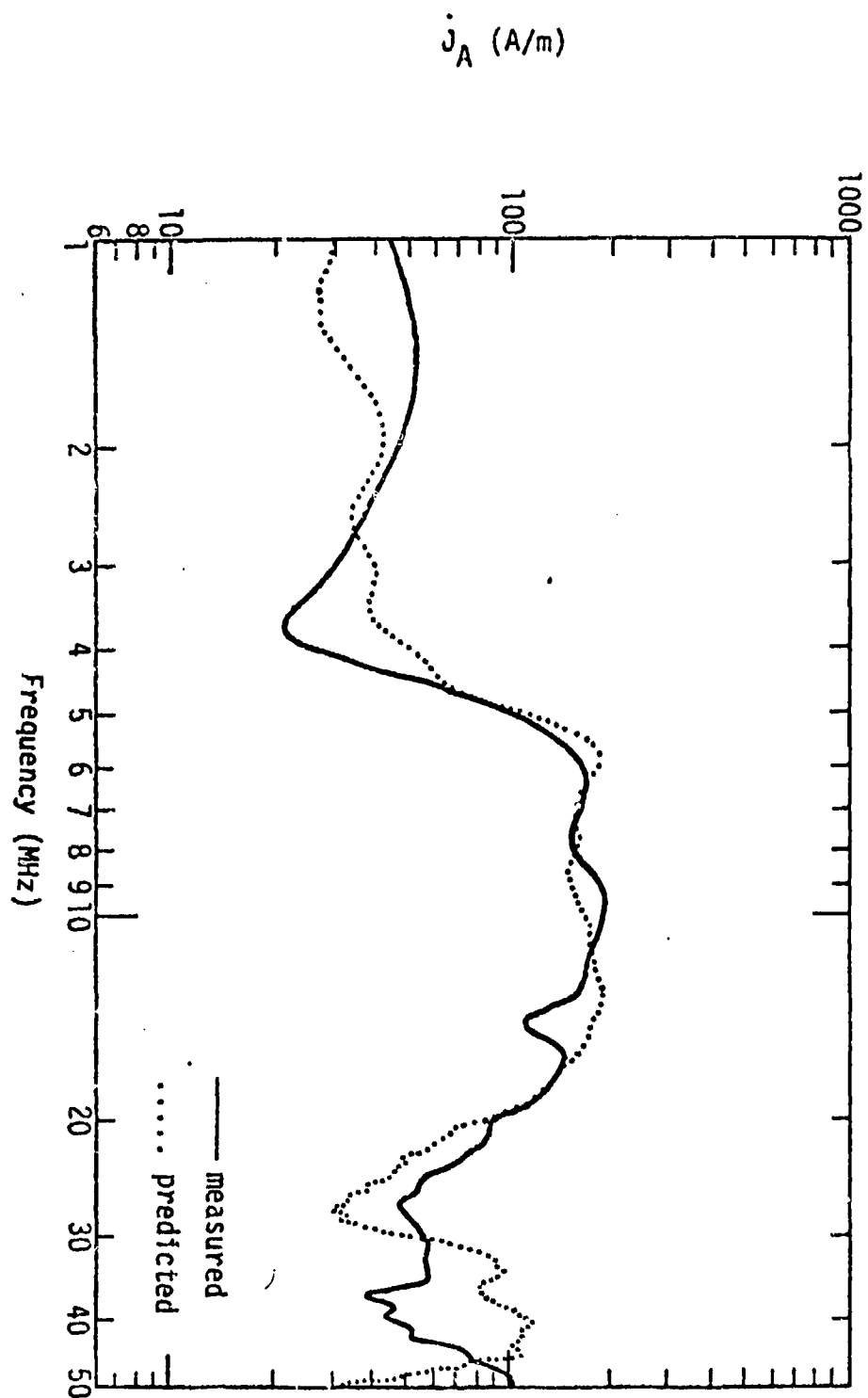


Figure 3.6 Measured vs. Predicted Axial Current at Test Point 208 in the Frequency Domain [16]

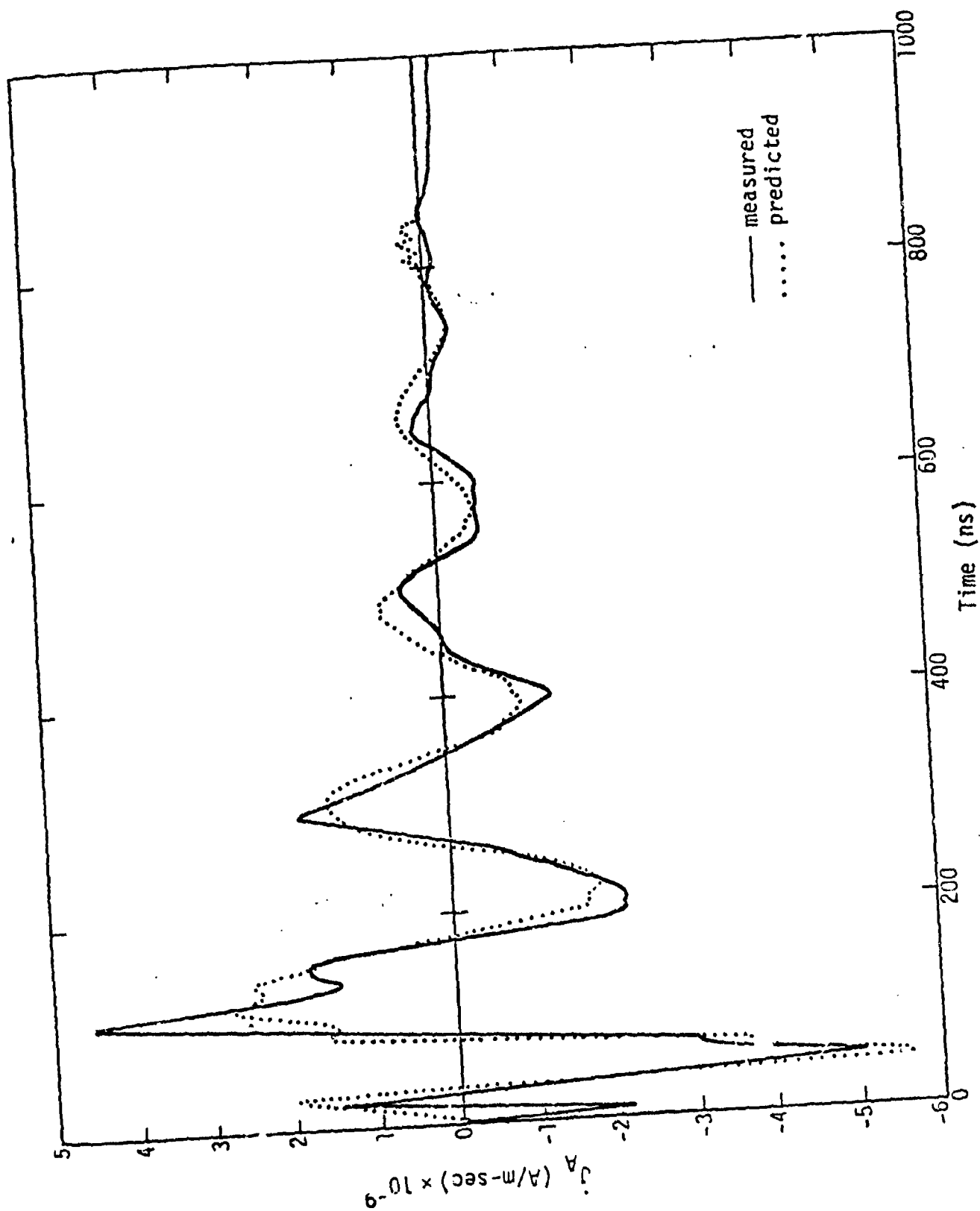


Figure 3.7 Measured vs. Predicted Axial Current at Test Point R1 in the Time Domain [16]

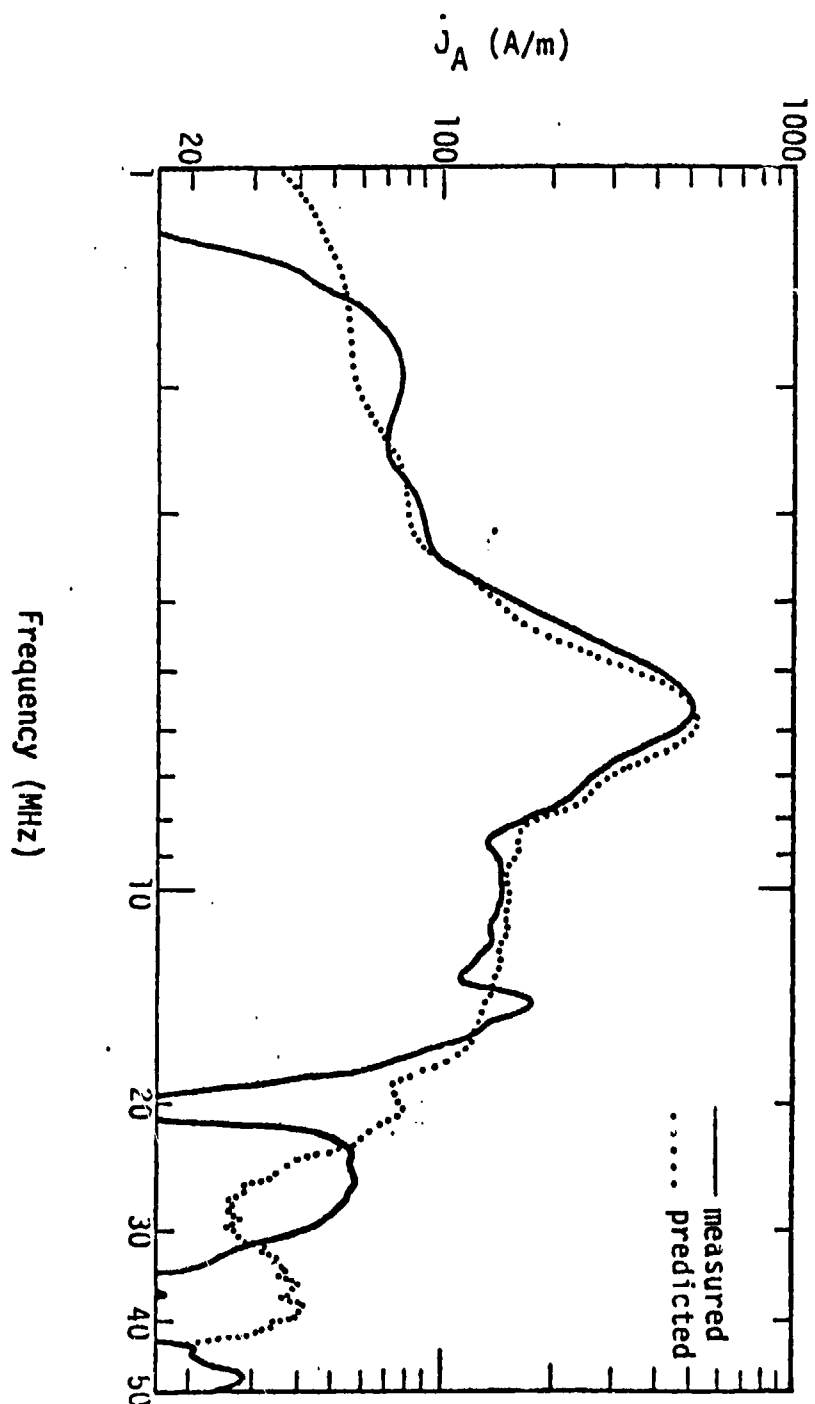


Figure 3.8 Measured vs. Predicted Axial Current at Test Point R1 in the Frequency Domain [16]

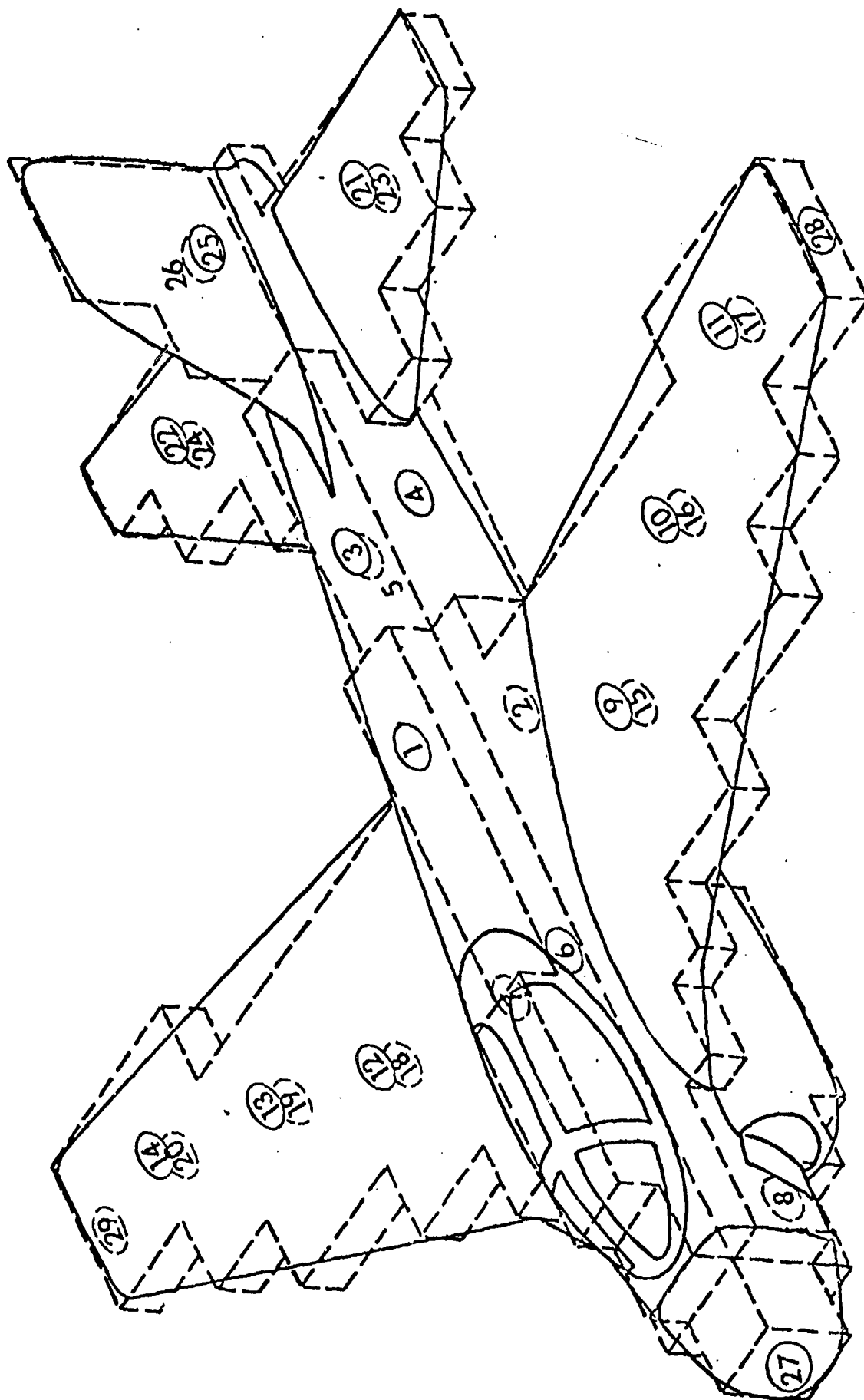
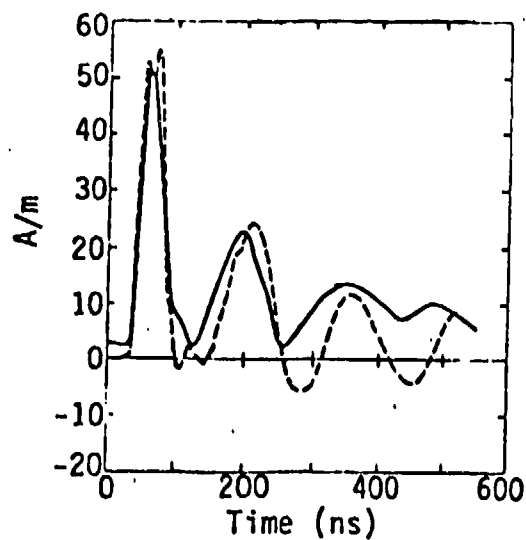
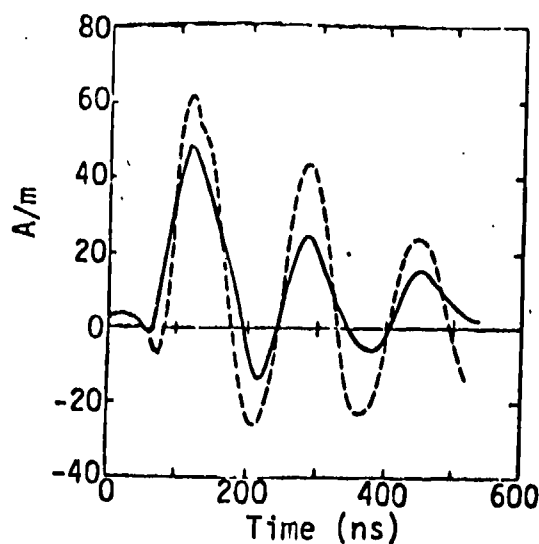


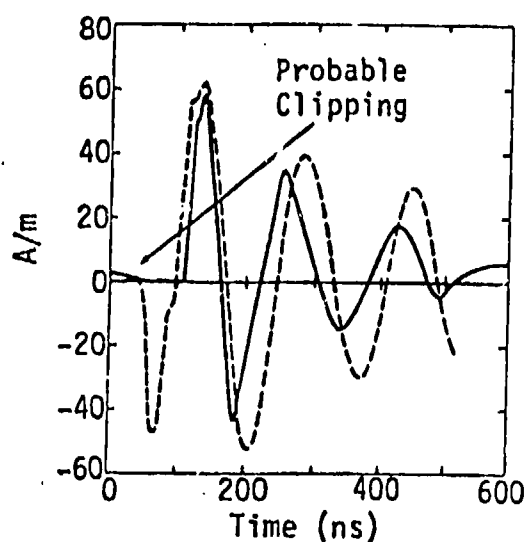
Figure 3.9 A6 Aircraft with Measurement Locations [18]



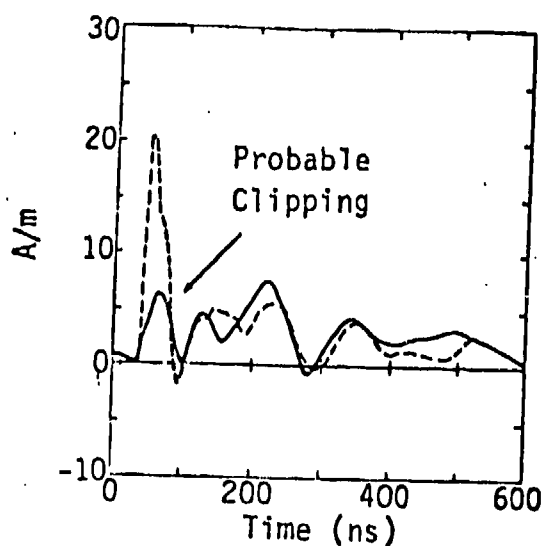
(a) Test Point 1 -  $I_{axial}$



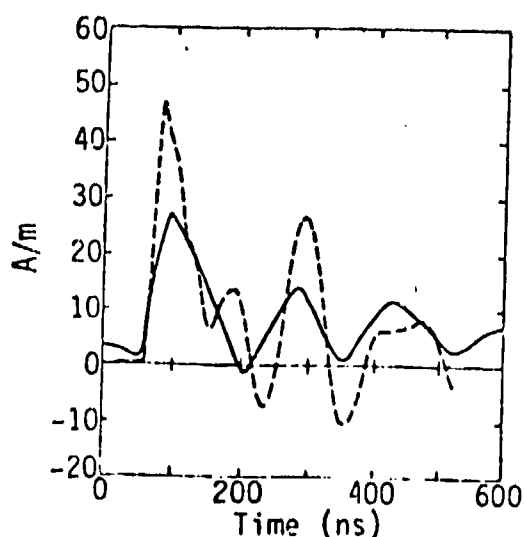
(b) Test Point 2 -  $I_{axial}$



(c) Test Point 4 -  $I_{axial}$



(d) Test Point 7 -  $I_{axial}$



(e) Test Point 8 -  $I_{axial}$

— Measured  
- - - Predicted

Figure 3.10 Comparison of Measured and Predicted A6 Responses in EMPRESS Flyby [18]

is good but for test points 7 and 8 near the cockpit the agreement is poor. In a more accurate representation of the aircraft, the computational model would taken the cockpit into account. Figure 3.11 shows the configuration of the aircraft and injection sources used as a model for the calculations and used to measure the SCIT response. Figures 3.12 and 3.13 compare the measurements and predictions, again showing good agreement for some test points (TP's 1, 2, 5, 6 and 8) but only fair agreements for others (TP's 4 and 7).

The main limitation with THREDE is computer memory. For certain machines, the code can be "packed" into the memory by taking advantage of the machine architecture. The method is obviously machine-dependent, but a significant advantage in physical resolution can be obtained. This technique has been used to model the B-52 [20]. The improvement in the physical modeling accuracy that can be accomplished with the compacted code is shown in Figures 3.14 and 3.15. Figure 3.16 shows the results of THREDE calculations for a charge density (normal  $\vec{E}$ ) and surface current ( $J_s$ ) at test point 4 (as identified in Figure 3.15). For reference, the resonances calculated using an analytical stick model are shown marked on the frequency scale of Figure 3.16(b).

THREDE has also been used by Peraia et al. [19] to calculate external current and charge densities on an all composite aircraft struck by lightning. Internal cable responses were calculated from the external sources using the transfer impedance of the composite material, but no comparisons with experiment have been made. The source of the external currents was either a near-miss LEMP or the currents injected by an attached return stroke.

In view of the previous discussion, we now summarize THREDE according to each of the evaluation factors listed in Chapter 2.

1. Computer Memory: For a complete analysis of an external coupling problem, THREDE will certainly require computer memory in excess of 100k<sub>g</sub>. In the example of the A6, which was run on a CDC 6600, the code used 44k<sub>g</sub> small core memory (SCM) and 1M<sub>g</sub> large core memory (LCM). The B-52 problem using the upgraded version of THREDE required 158k<sub>g</sub> SCM and 1.4M<sub>g</sub> LCM. In general, for an N x M x P dimensional gridding, there will have to be at least a 6 x N x M x P dimensional matrix to store the field components. In the compacted version of THREDE two field components are stored in one CDC word, however, which reduces the amount of LCM required.



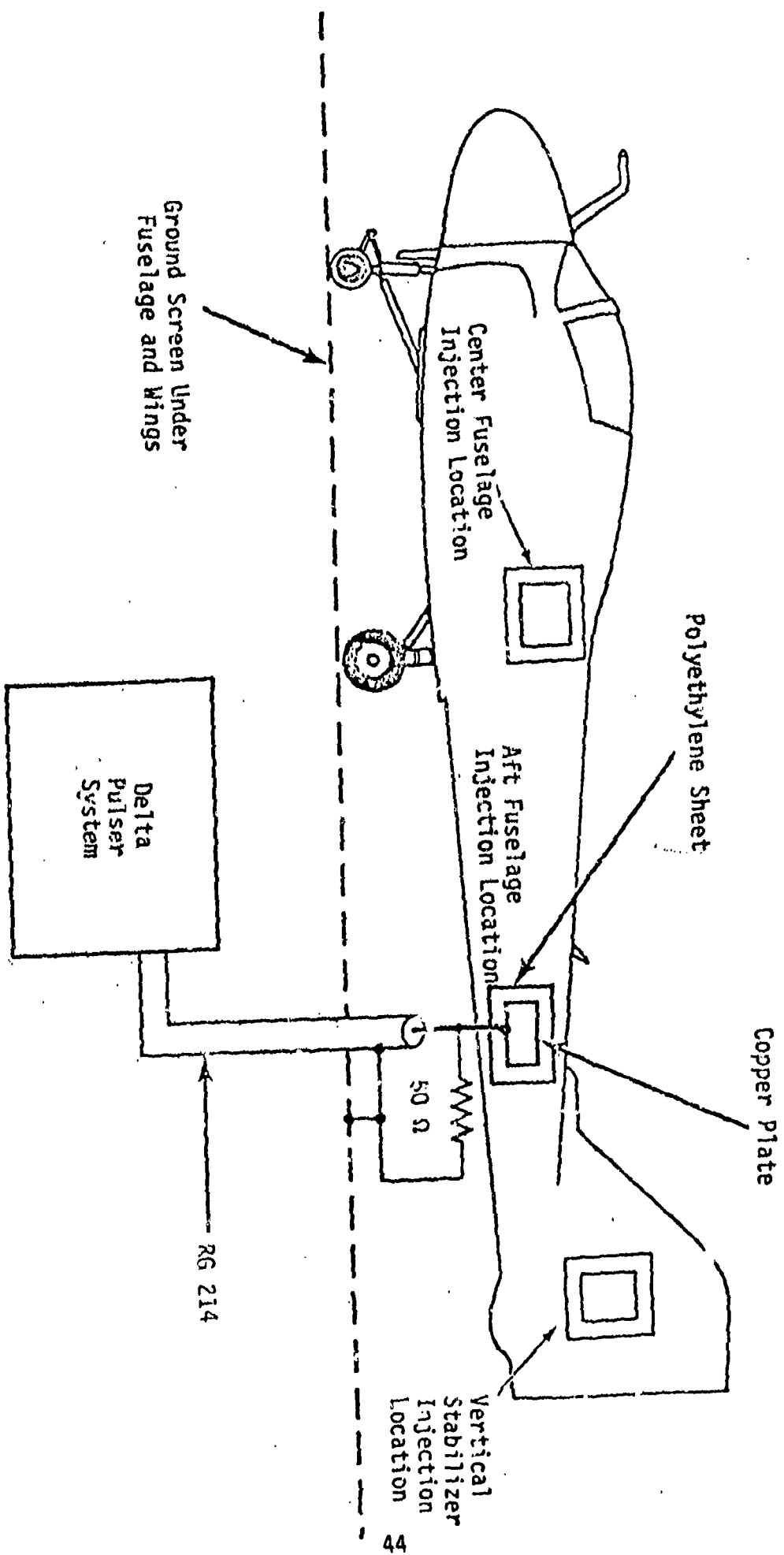


Figure 3.11 Typical Current Injection Configuration [18]

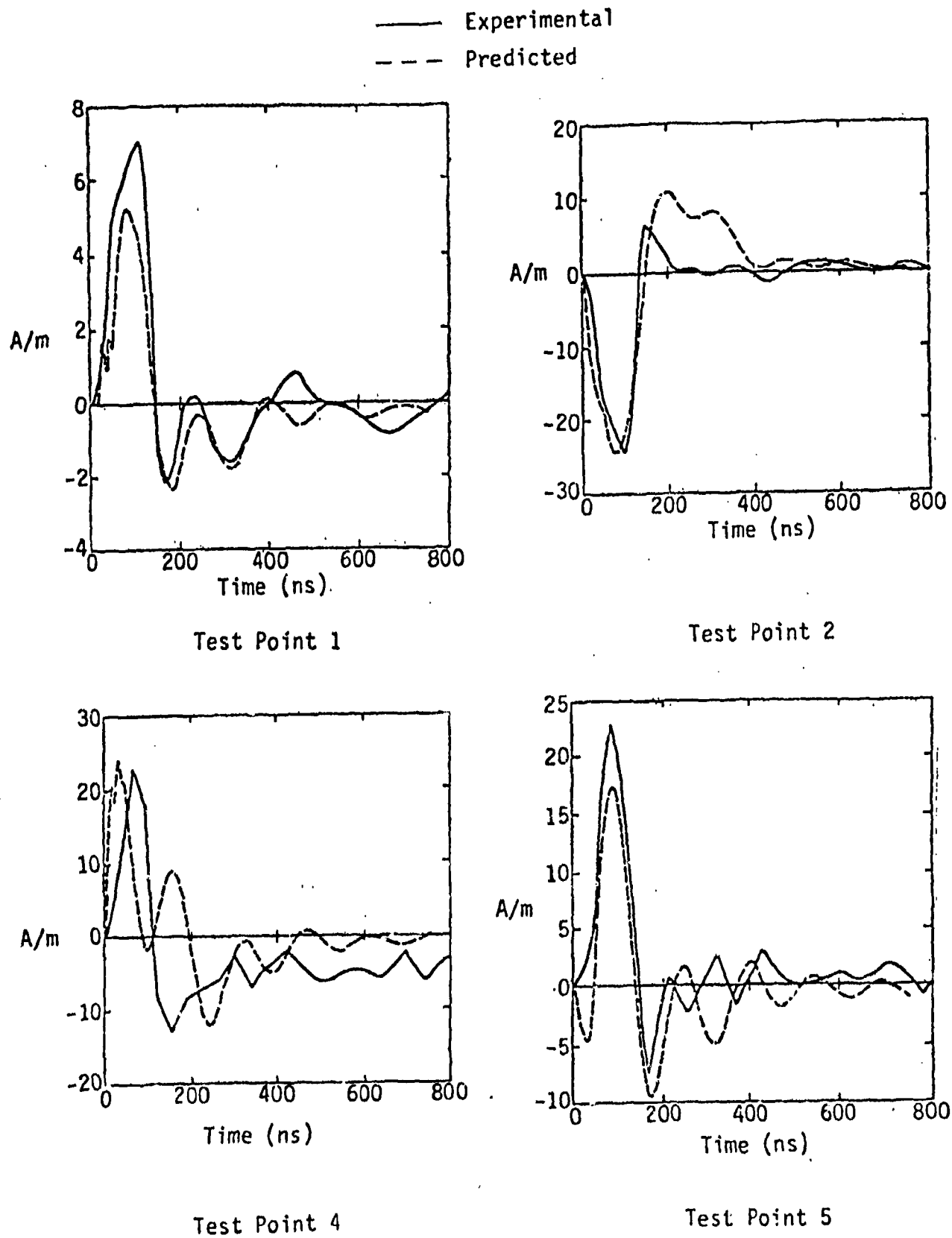
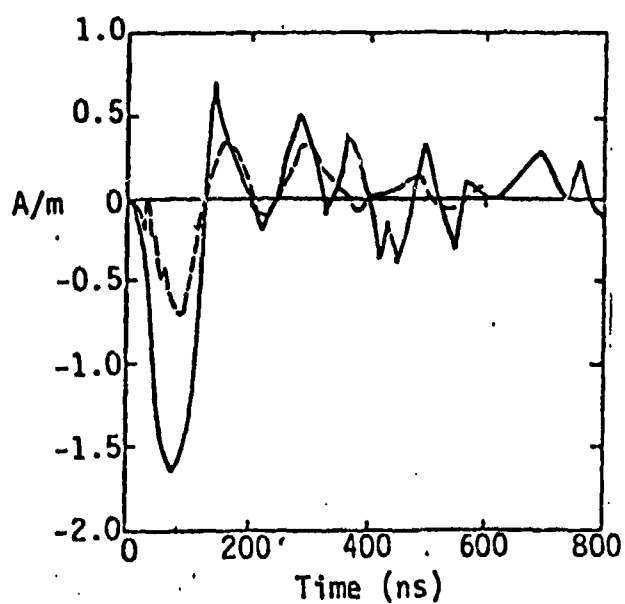
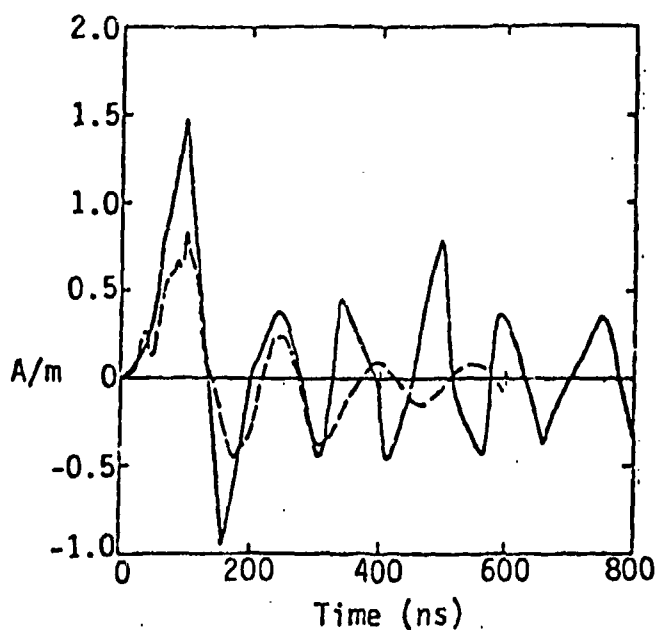


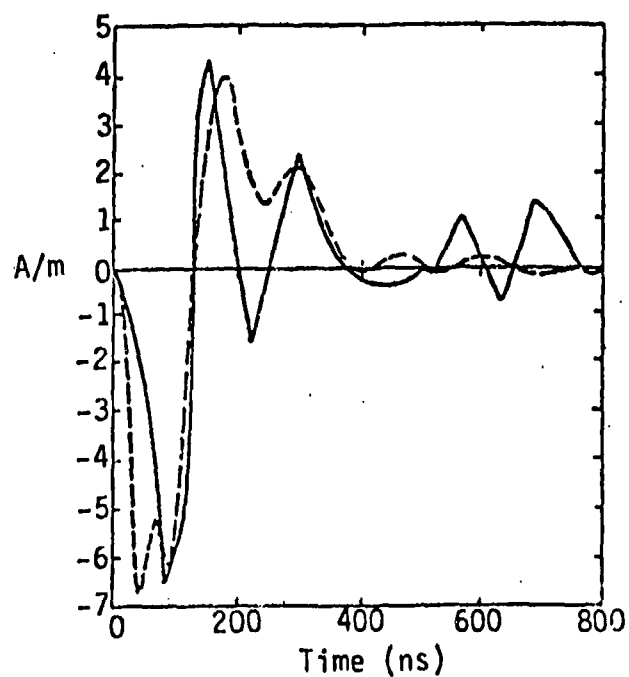
Figure 3.12 Comparison of Experimental Versus Predicted SCIT A6 Responses.  
Test Points are Defined in Figure 3.9 [18]



Test Point 6



Test Point 7



Test Point 8

— Experimental  
 - - - Predicted

Figure 3.13 Comparison of Experimental Versus Predicted SCIT A6 Responses. Test Points as Defined in Figure 3.9 [18]

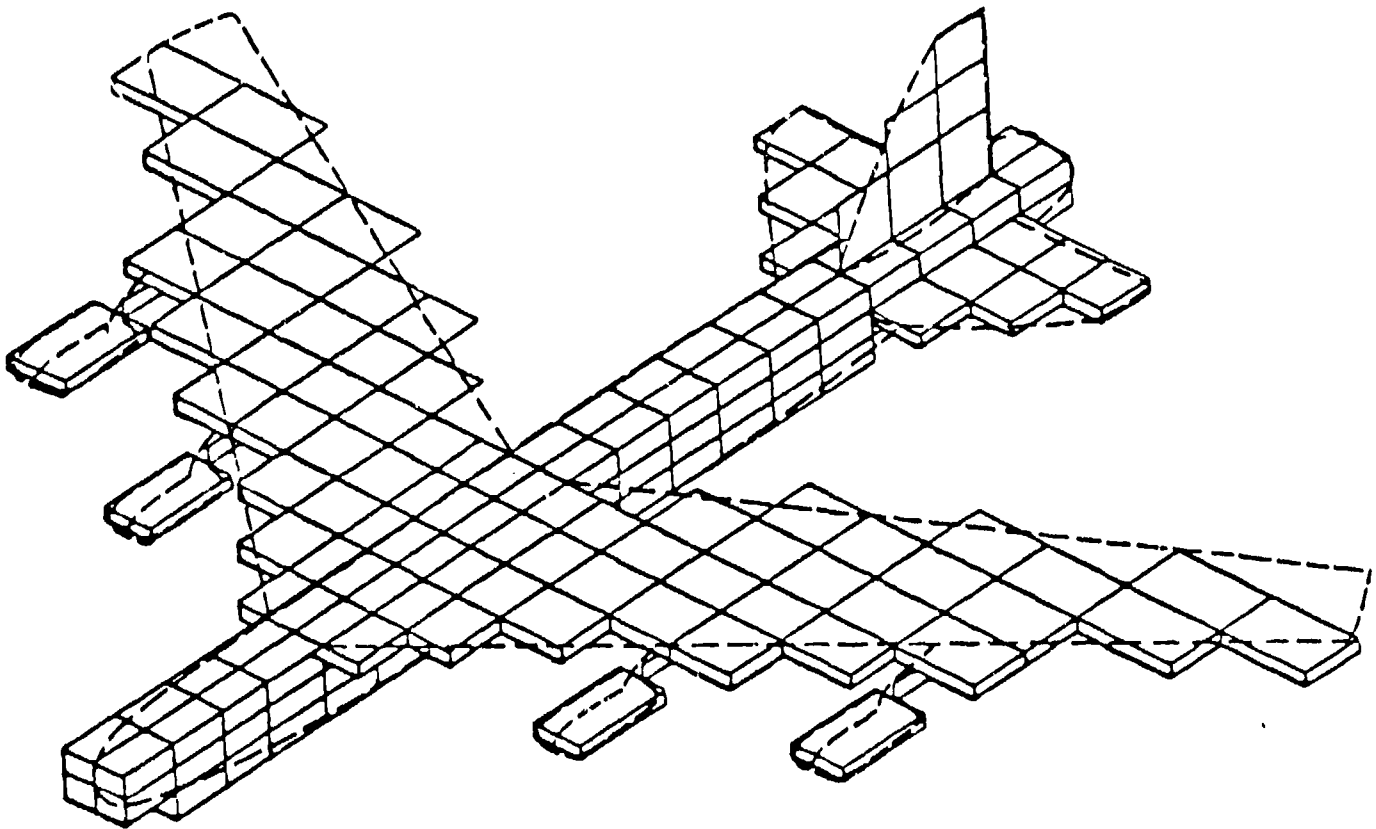


Figure 3.14 A B-52 Model in a 30 x 30 x 30 THREDE Grid [20]

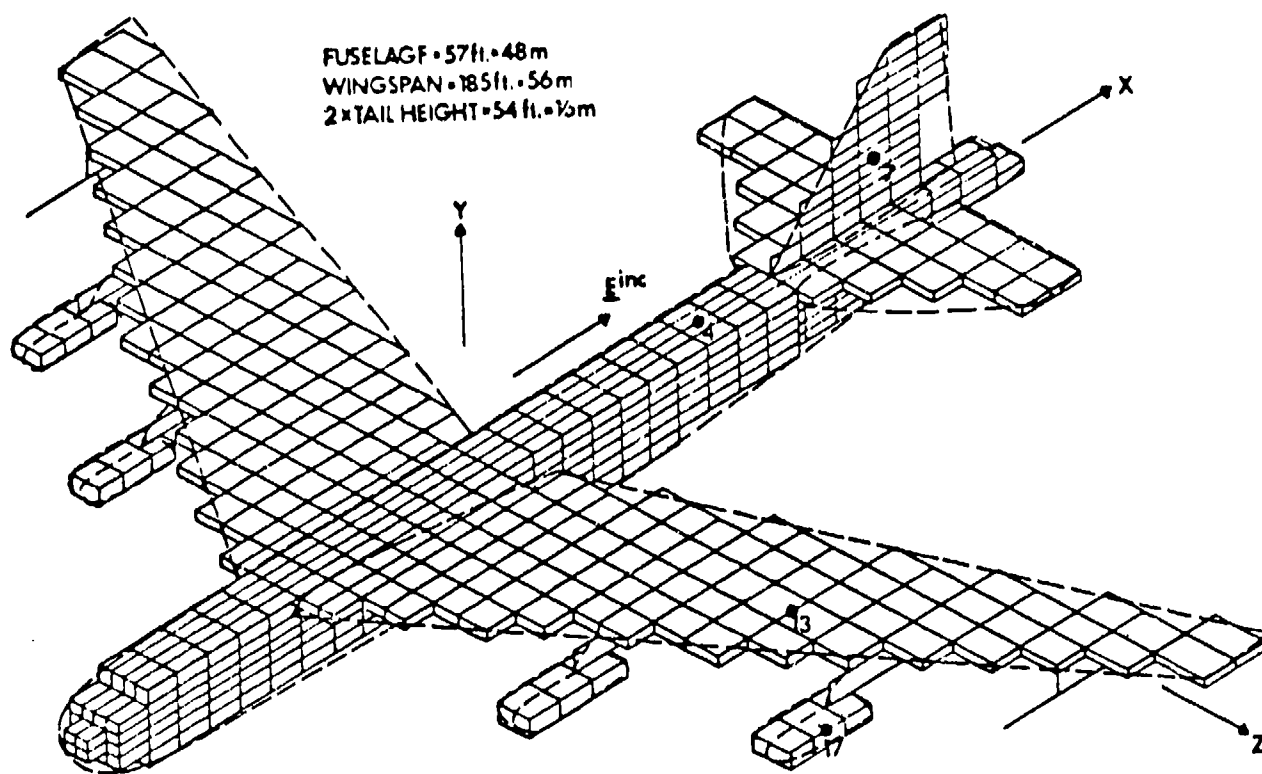
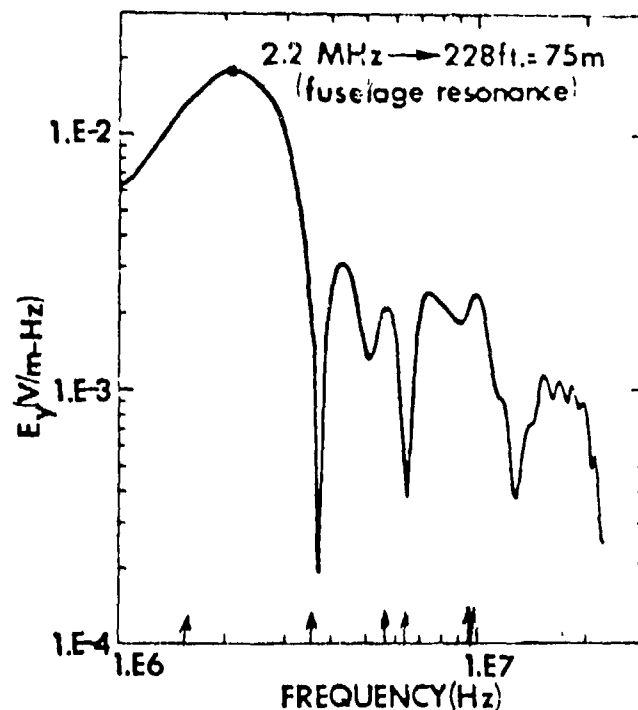
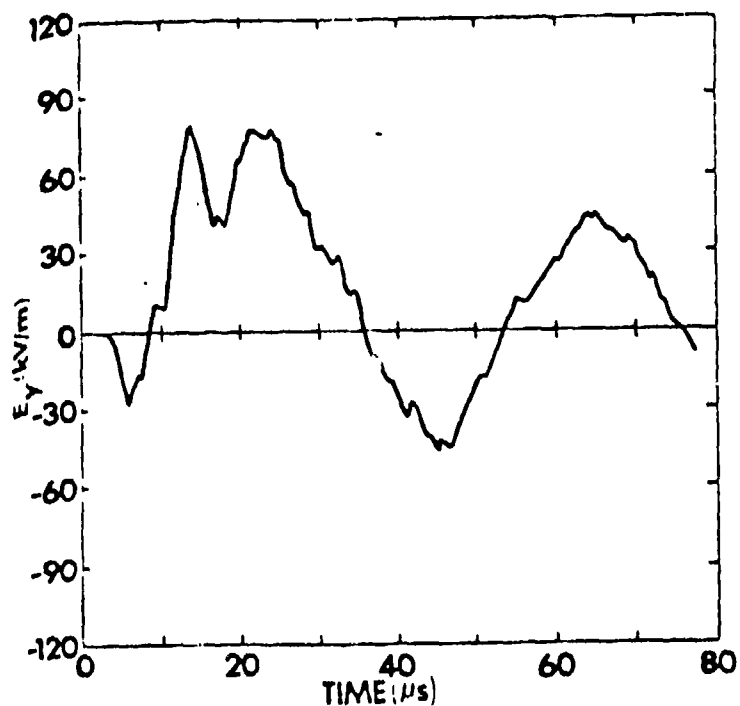
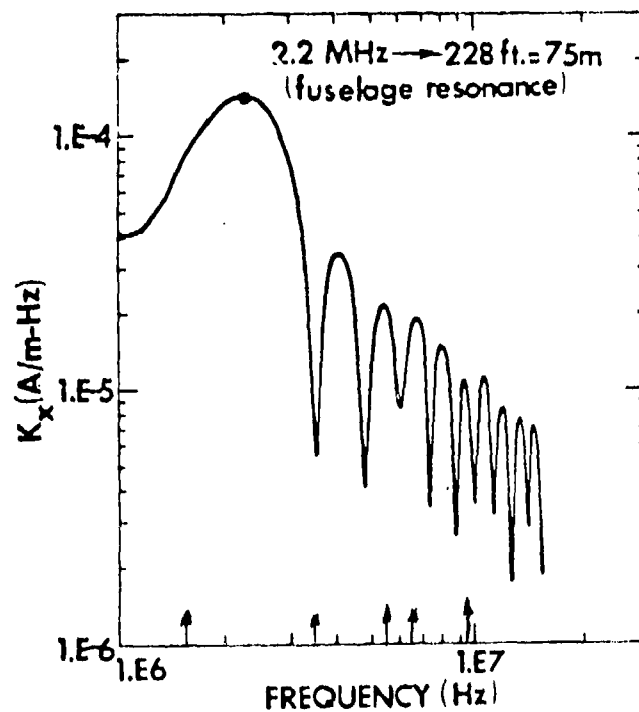
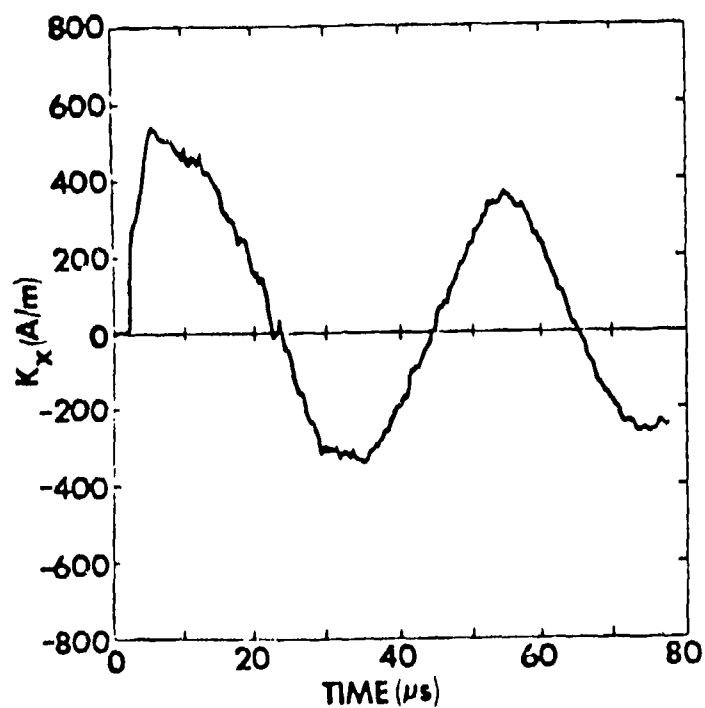


Figure 3.15 A B-52 Model in a 50 x 43 x 59 THREDE Grid [20]



$E_n$  TEST POINT 4

Figure 3.16(a) Normal Electric Field at Test Point 4 (Fuselage) on the B-52



$J_s$  TEST POINT 4

Figure 3.16(b) Axial Surface Current at Test Point 4 (Fuselage) on the B-52  
[20]

2. Central Processor (CP) Time: Execution time for all the cases, including the upgraded version, was about one second of CDC 6600 time for one timestep of the code. Typically, a NEMP response requires 15-20 minutes of CP time, which is good because the entire transient response is obtained from such a calculation. For frequency domain codes, the response must be determined at many ( $\sim 200$ ) frequencies and the Fourier inverse taken to get the transient response. The THREDE code is limited, however, to total run times of several  $\mu$ secs or less due to numerical errors that accumulate for longer run times.

3. Numerical Accuracy: The numerical accuracy of the code is limited by the accuracy of the "word" used to store a field component, by the radiating boundary condition, by the choice of central differencing to represent time and spatial derivatives, and by the time step  $\Delta t$ . Numerical inaccuracies limit the running time of the code to a few  $\mu$ sec with radiation boundary conditions.

4. Physical Accuracy: The compacted version represents probably the best physical approximation of aircraft available. Some calculations with special physical models are also very good, but are limited to certain shapes of revolution for aircraft structure and usually right angles for wing-fuselage and stabilizer-fuselage interfaces.

5. User Orientation: The code is well documented including descriptions and flow diagrams of all subroutines and identification of the variables used. Information is provided in two publications, a user's manual [21] and a maintenance manual [22]. In general the operation of the code will require a skilled user, for example to choose a proper grid for the aircraft, but most importantly to recognize that the results of the calculations are sensible. In choosing the expanding portion of the grid, for example, it is possible to generate misleading values of  $\vec{E}$  and  $\vec{H}$ .

6. Frequency Range: THREDE is limited to the high frequency part of the lightning spectrum. The time domain response can be calculated for only a limited time after excitation, and so only a small fraction of a cycle of low frequency response is included in the transient waveform. If  $f_L$  is the frequency having at least a quarter cycle in the time domain response, then  $f_L$  is about 250 kHz for THREDE. Since this is much higher than the 10 kHz components known to comprise return strokes, an unmodified form of THREDE is clearly not suited for the entire lightning spectrum. On the other hand, THREDE's upper frequency limit typically exceeds 30 MHz, and thus it can handle the resonant response. Extensions of the code may be able to handle low frequencies.

7. Attached Stroke: The THREDE code can include a ground plane or leave it out. An attached channel can be coded by specifying (impressing) a magnetic field about a line in space which defines the channel.

8. Test Case: Since the code has been used to predict SCIT responses accurately, it should be a good choice for treating most lightning test analysis methods. Also, THREDE's ability to treat non-linear behavior should be of value because of the non-linear nature of proposed test methods. THREDE could incorporate such non-linear elements, for example spark gaps, in its analysis.

9. Aircraft Size: The THREDE code can treat large aircraft as well as small. The analysis of the B-52, and the good physical modeling accuracy demonstrated there, proves THREDE's ability to handle even the largest aircraft as well as small fighters.

10. Lightning Environment: The lightning environment includes slow and relatively rapid changes in electric fields and current density (attached stroke) and possible non-linear effects such as streamers and corona. Unlike frequency domain calculations where the transient response must be determined by a Fourier inversion (and so are limited to linear models), THREDE can incorporate nonlinearities in its solution. THREDE can also include the near fields of a near-miss return stroke.

11. Experimental Verification: THREDE has probably been compared successfully with more experimental information than any other external coupling code; at least four aircraft have been treated by the code, the F-111, A6, B-52 and F-16 [23].

### 3.3.2.3 Taflove and Brodwin

Another method of solution, very similar to the THREDE code, has been developed by Taflove [24], and Taflove and Brodwin [25], specifically for the determination of the time harmonic fields inside conductors and dielectrics. The method uses the same central differencing as described for THREDE but uses somewhat different boundary conditions on the problem space surfaces. Instead of requiring that the far fields vary like radiation from a monopole, the boundary fields are calculated at neighboring points using averages of earlier fields at neighboring points. The averages are chosen in a special way so that a wave traveling in an opposite direction to the incident field will be totally absorbed at the problem space boundary. In addition, the region outside the problem space is chosen to have an anisotropic conductivity that attenuates just those components of  $\vec{E}$  perpendicular to the incident polarization direction. The



method has the normal advantages of a finite-difference code such as speed, accuracy, the ability to treat non-linearities, and the ability to treat inhomogeneities. It has been used to calculate the response of dielectric slabs, cylinders and spheres to sinusoidal excitation, and has been used to calculate the absorption of microwave radiation by the human eye. The method has not been used for NEMP-like impulsive excitation, although in principle there is no reason why the code couldn't be rewritten for such cases.

Calculations of the fields internal to an open cylinder and a model of a nose cone have also been made by Taflové [24]. The cylinder is shown in Figure 3.17 and the gridding in Figure 3.18. The excitation is a 300 MHz plane wave (10 cm wavelength) and the method is used to calculate the internal fields for about two cycles of the incident wave. The time steps are on the order of 5 psec. Results of the calculations are shown in Figure 3.19 along with measurements [21]. The poor agreement deep inside the cylinder is attributed to the difficulty in measuring the small fields. The radial dependence of the field, on the other hand, compares favorably with experiment and is shown in Figures 3.20 and 3.21. A second geometry has been considered and is pictured in Figure 3.22. Using the gridding in Figures 3.23 and 3.24, the electric and magnetic field contours have been calculated as in Figure 3.25(a). However, there are no experimental data for comparison. The method has not been used for any aircraft.

The summary of this method according to the criteria of Chapter 2 is very similar to THREDE and appears below.

1. Computer Memory: As they were for THREDE, computer memory requirements are substantial. For example, the problem space for the cylinder was a  $24 \times 163 \times 24$  mesh (994,000 segments), roughly 25% smaller than that used by THREDE for the B-52. The code required  $10^6$  words of memory, or about 3.8M<sub>8</sub>, on a Control Data STAR 100.

2. CP Time: Execution times for both the cylinder problem and the nose cone were under 3.5 minutes, reasonably quick runs. The code might be rewritten using data packing techniques and so reduce the memory requirements at the cost of slightly increasing the run time.

3. Numerical Accuracy: The code has about the same numerical limitations as THREDE. Comparisons of the boundary conditions indicate that the

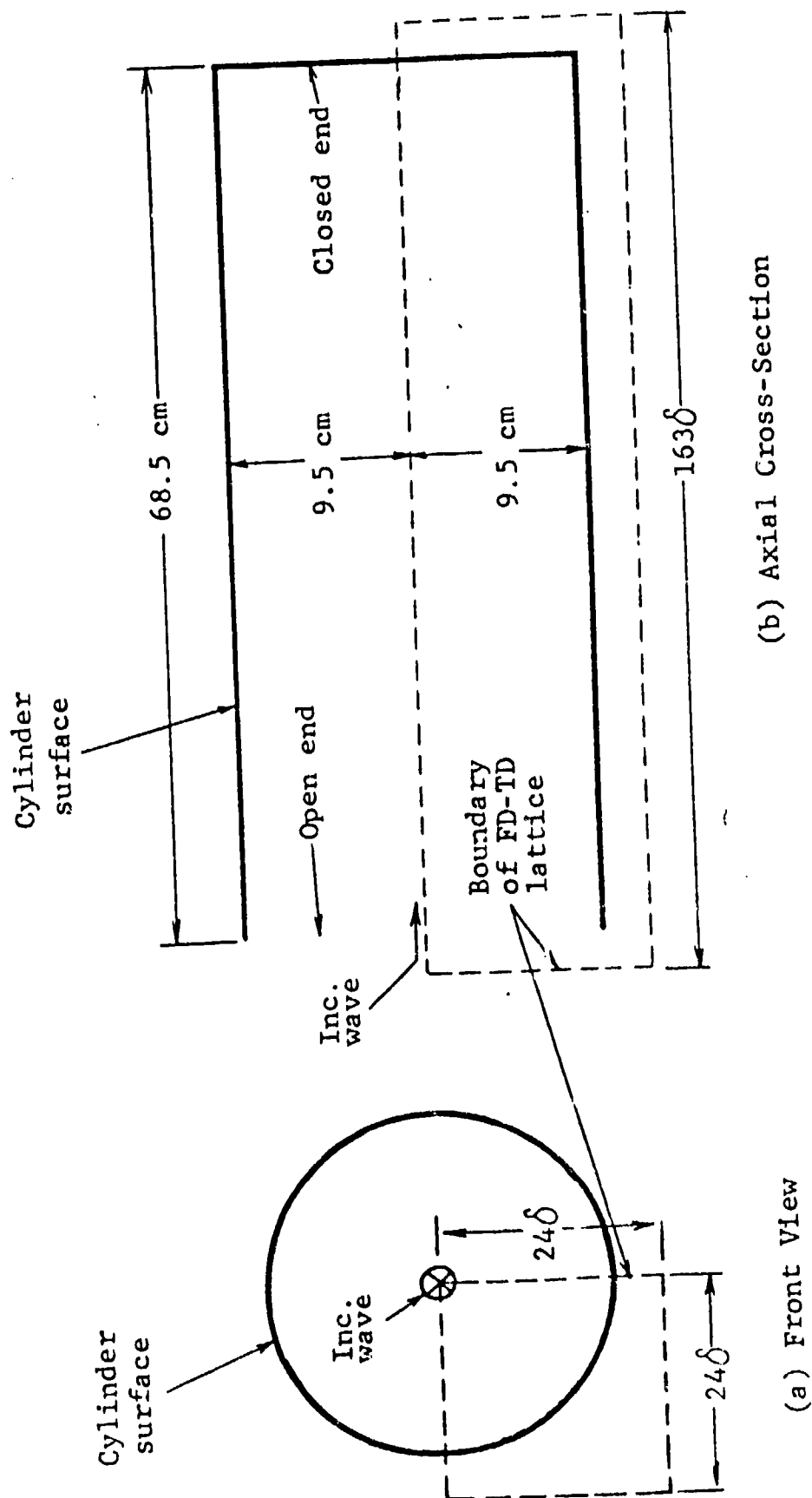


Figure 3.17 Open-Ended Aluminum Cylinder Geometry (not to scale) [24]

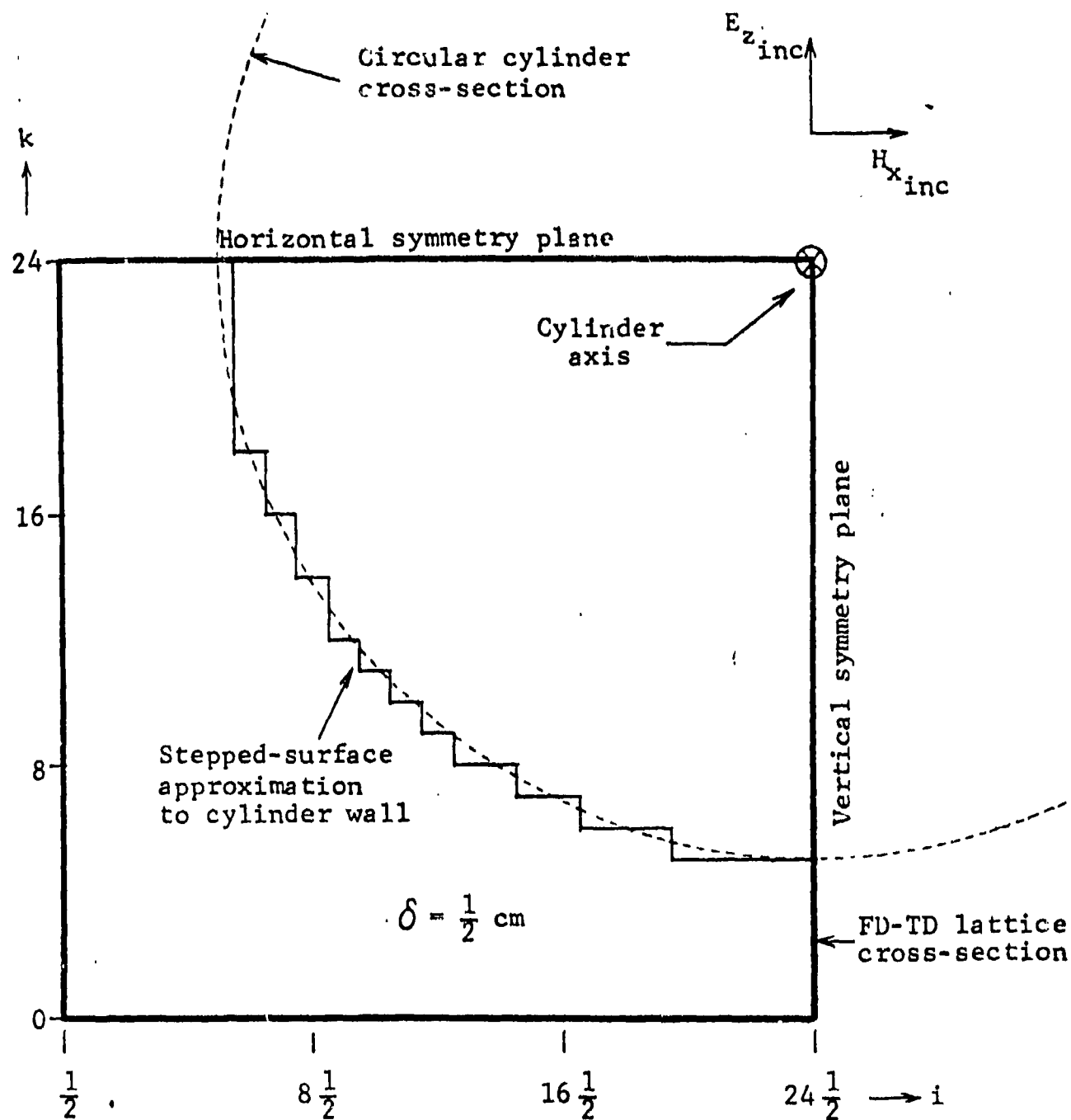


Figure 3.18 Cross-Section of Cylinder Model [24]

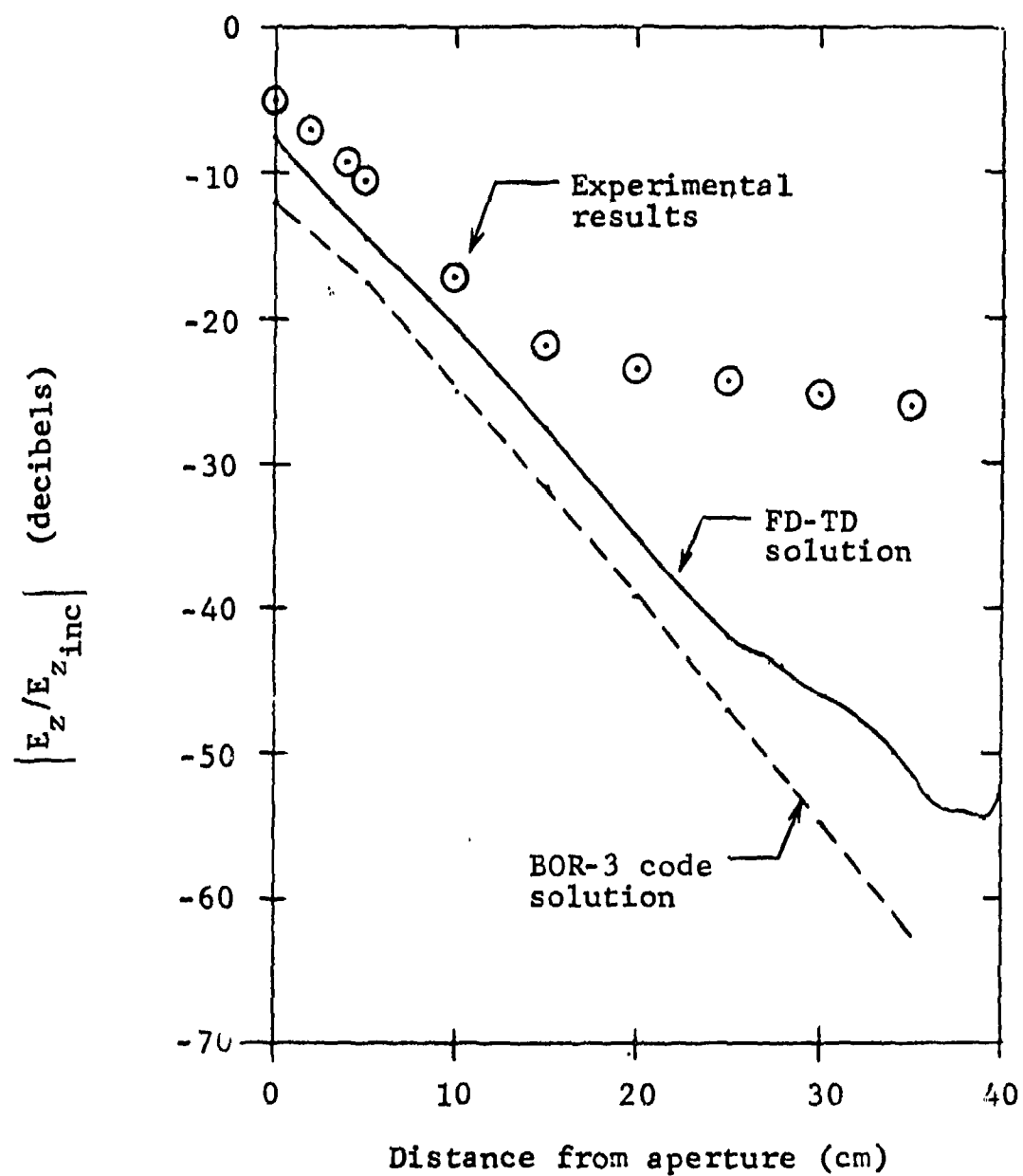


Figure 3.19 Comparison of Results for the Electric Field Along the Cylinder Axis [24]

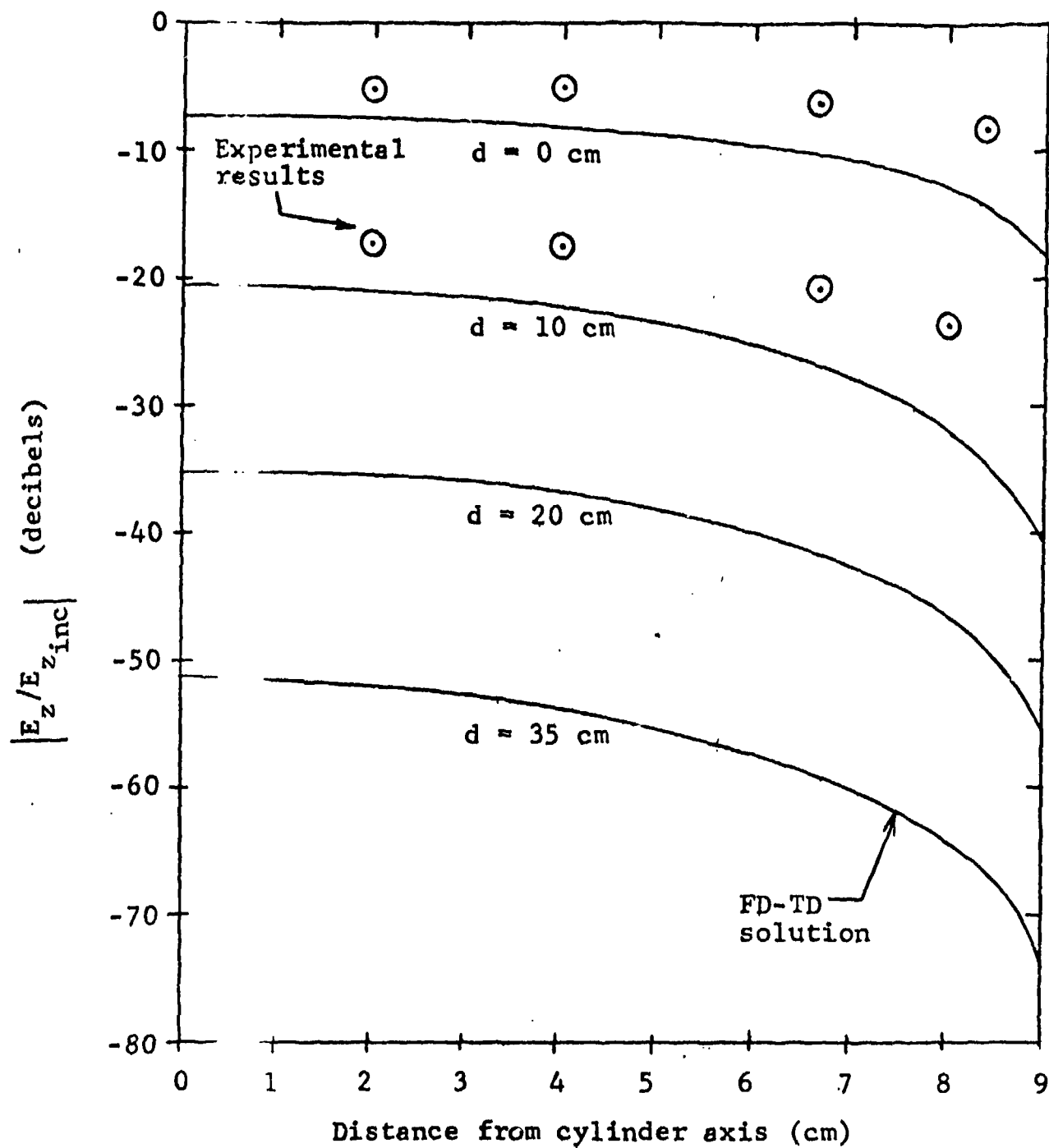


Figure 3.20 Computed Electric Field Along Horizontal Radial Lines (Parallel to  $H_{x,inc}$ ) of the Cylinder [24]

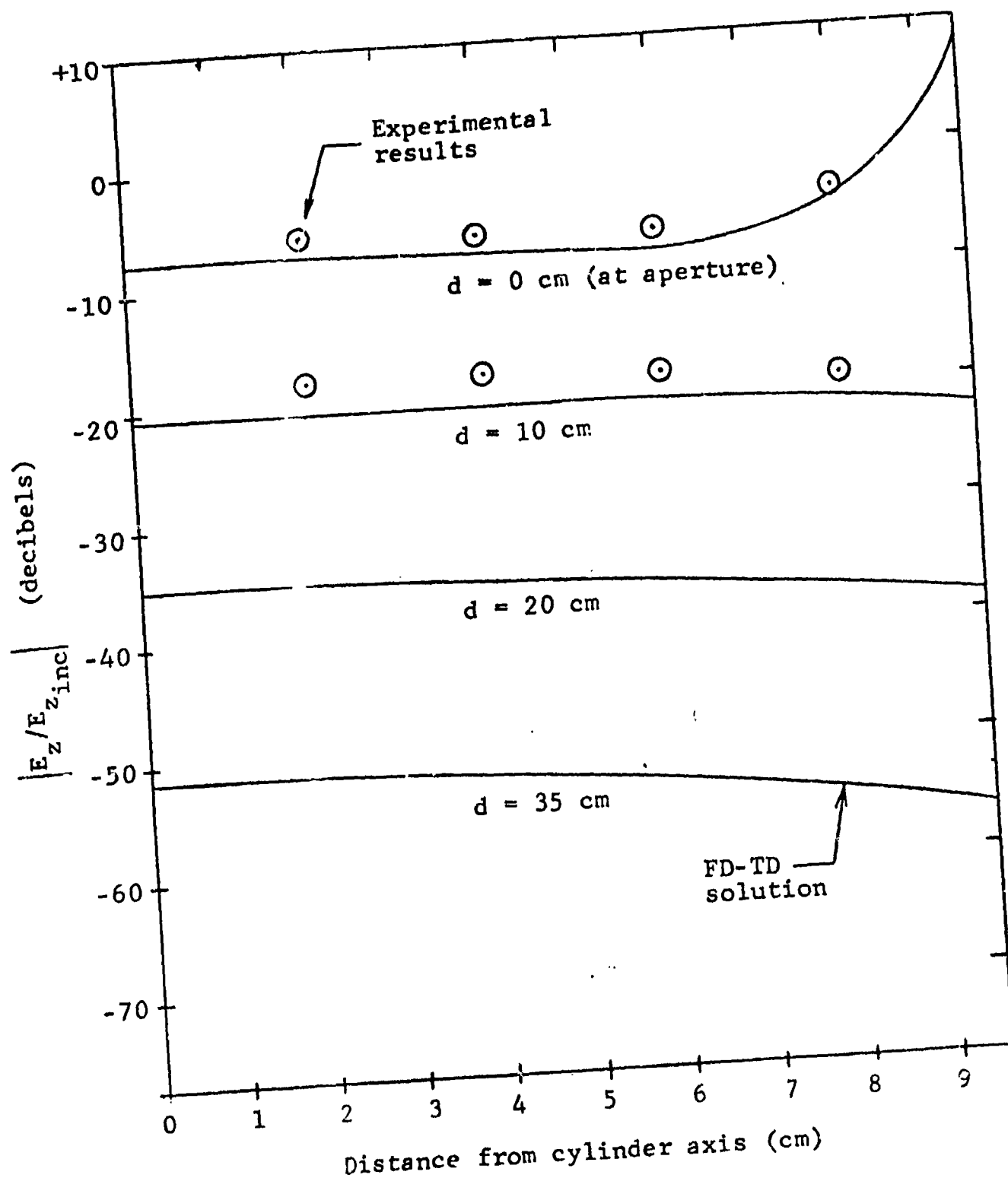


Figure 3.21 Computed Electric Field Along Vertical Radial Lines (Parallel to  $E_{z_{inc}}$ ) of the Cylinder [24]

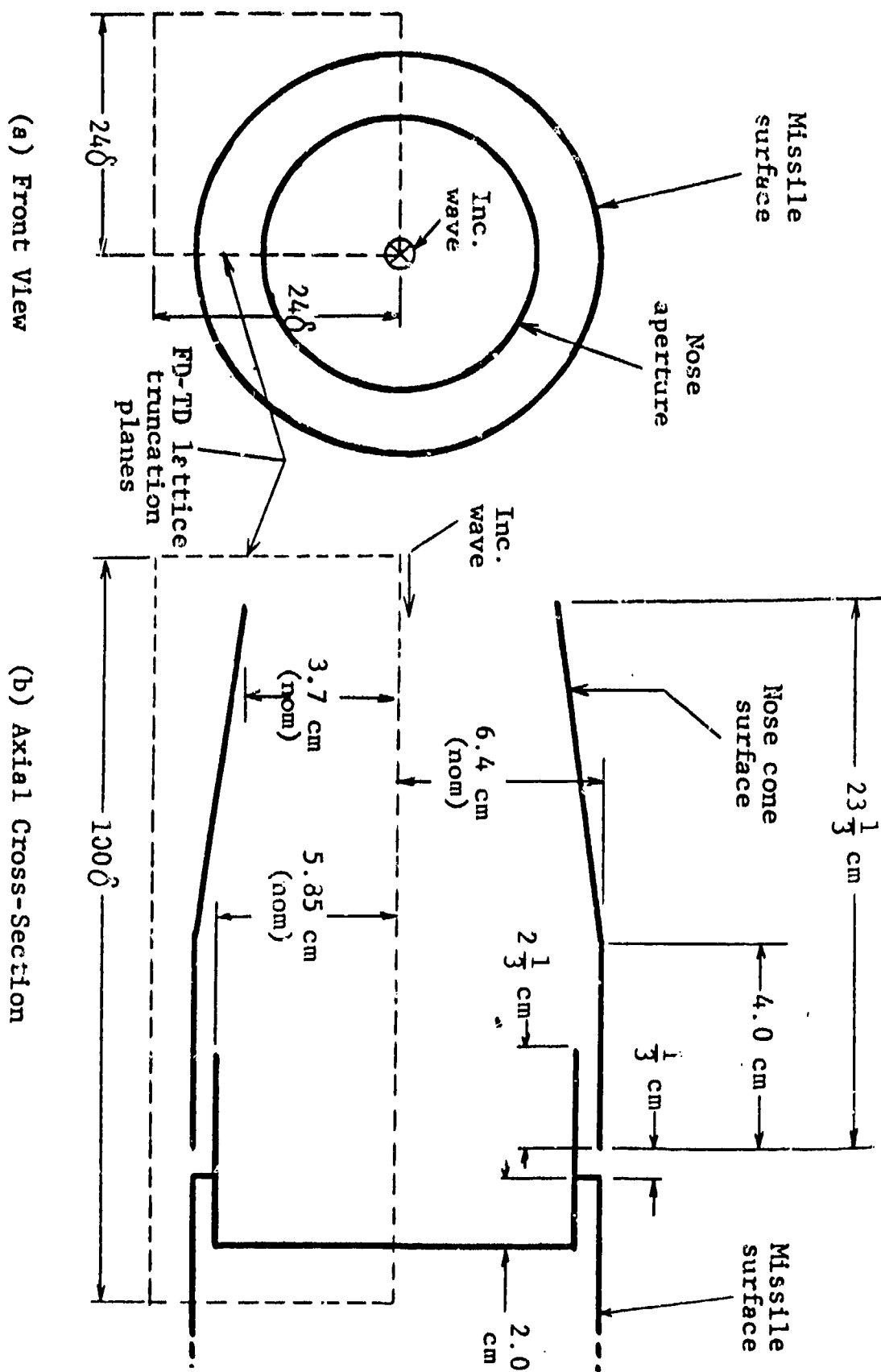


Figure 3.22 Nose Cone Geometry (Not to Scale) [24]

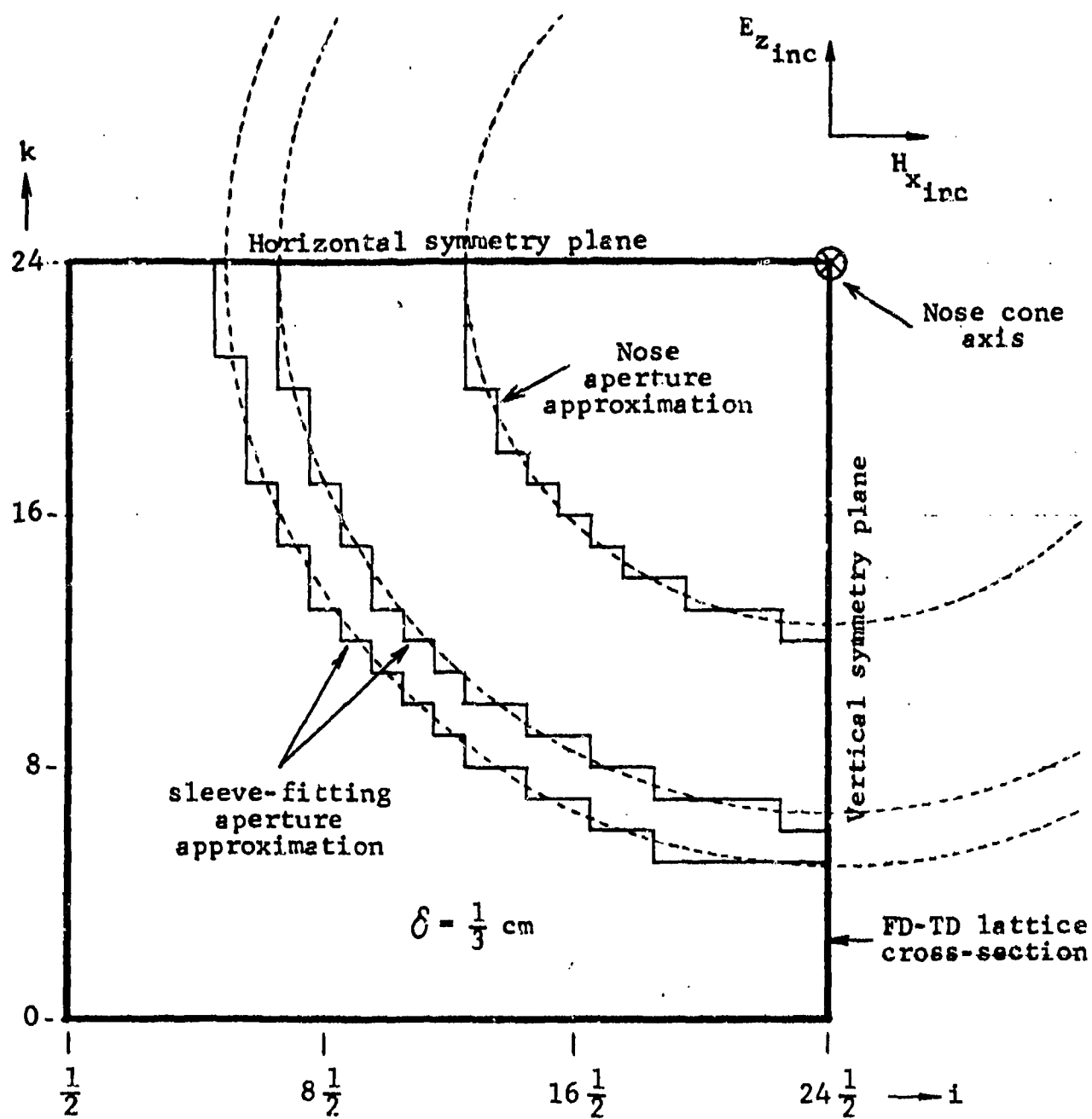


Figure 3.23 Key Cross-Sections of Nose-Cone Model [24]



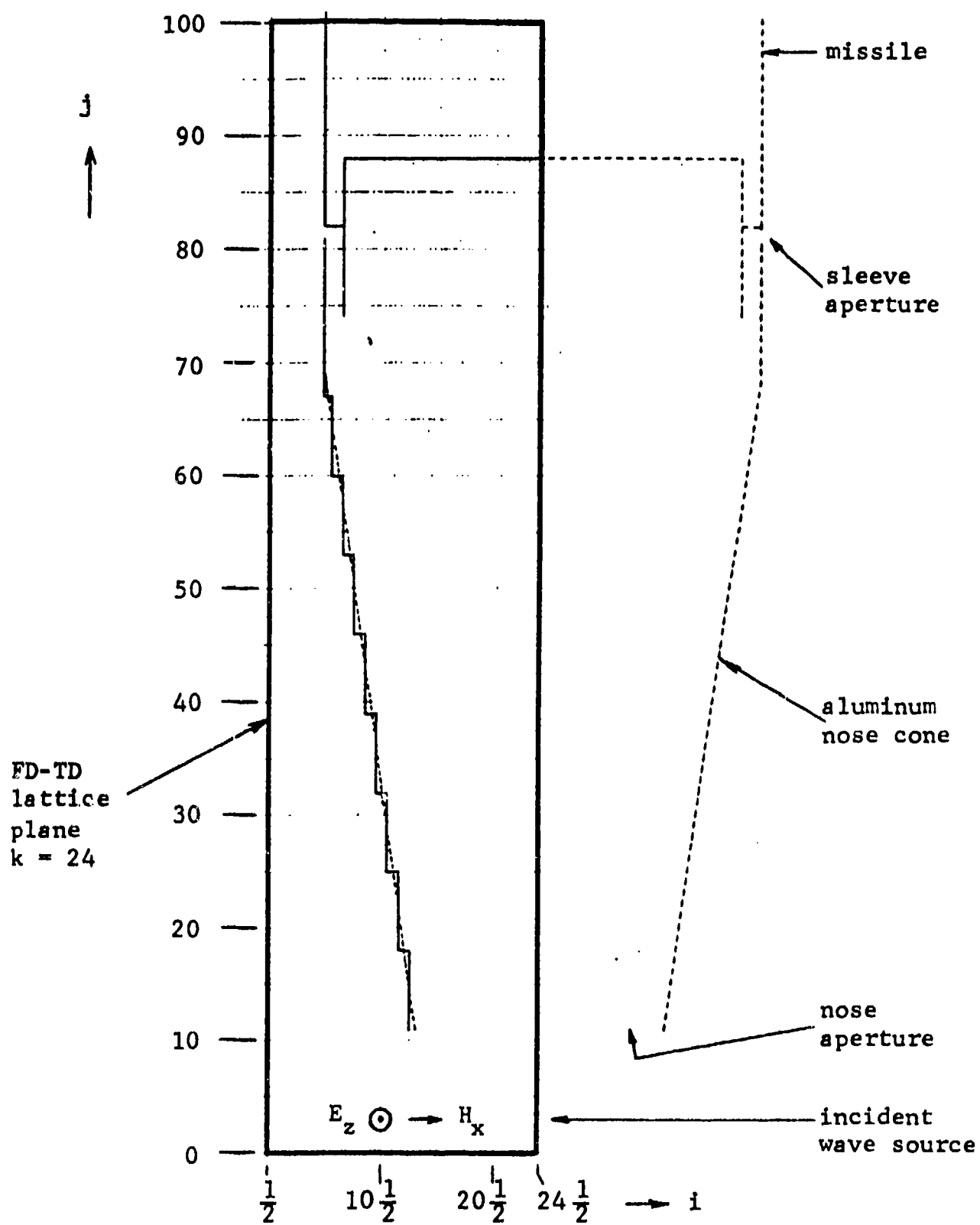


Figure 3.24 View of Nose Cone Model at Horizontal Symmetry Plane [24]

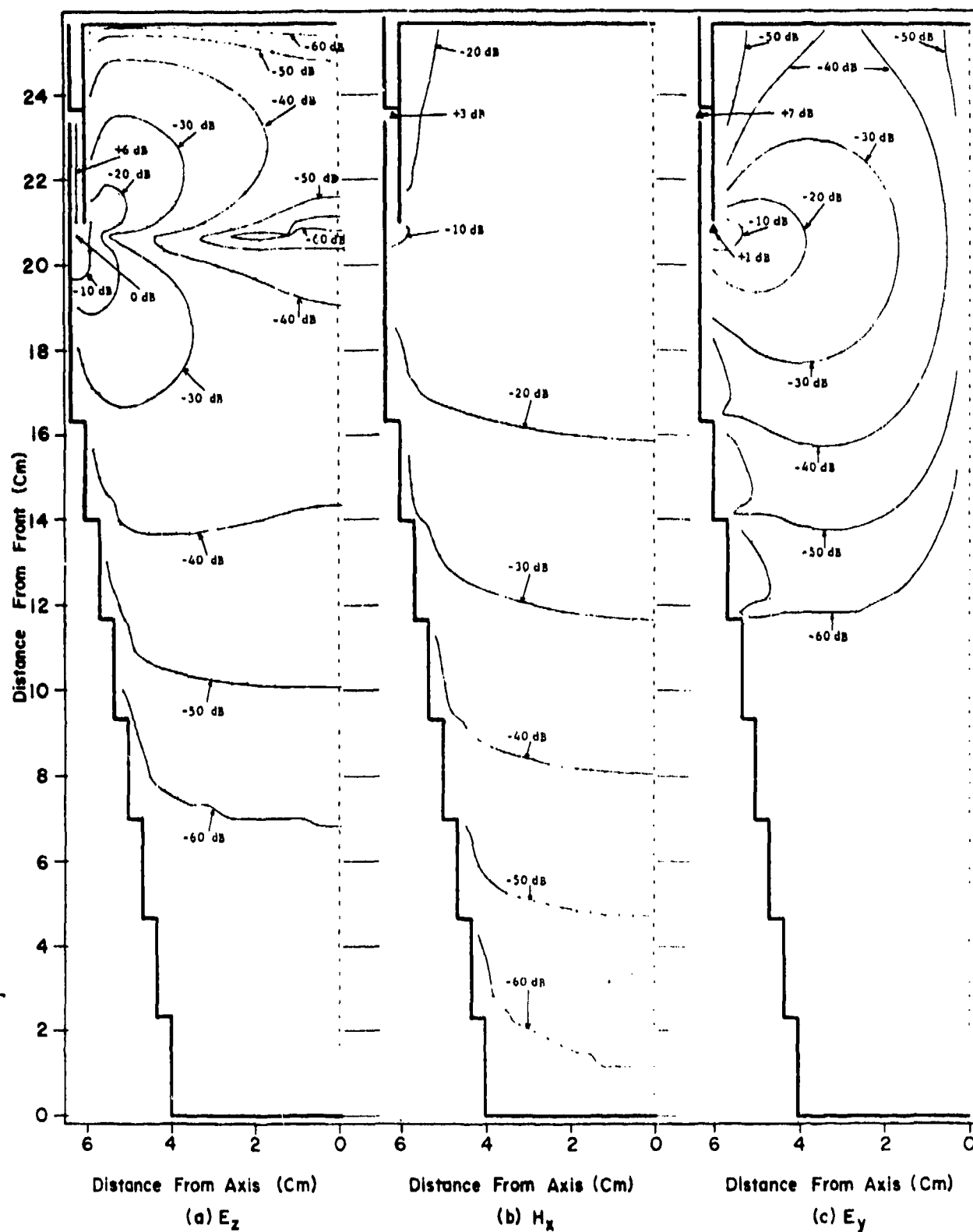


Figure 3.25 Field Contours in Nose Cone Vertical Symmetry Plane.  
Only Sleeve-Fitting Aperture Open [24]

radiating boundary condition is comparable to methods used by Taflove, and so little or no difference in the numerical accuracy is expected [17].

4. Physical Accuracy: As demonstrated in the cylinder problem, the gridding used is comparable to THREDE.

5. User Orientation: Although a listing of the code is available, there is not any extensive documentation. The user of this code will need to be able to grid up an aircraft intelligently and will have to recognize numerical instabilities if they occur.

6. Frequency Range: The code will be most useful at high frequencies; however, extensions to long running time may be feasible and so the code might be able to treat the low frequencies also. At this time, however, only high frequency content has been addressed in any calculations.

7. Attached Stroke: This code has the potential to treat an attached stroke in the same manner as THREDE, although it has not been tried for such excitations.

8. Test Case: The code can in principle handle ground planes and attached strokes which are features of the test case.

9. Aircraft Size: The code could treat large and small aircraft with good physical accuracy.

10. Lightning Environment: The code has the ability to model non-linear and time dependent media, and therefore has advantages over frequency domain calculations as described earlier.

11. Experimental Verification: The code has not been used for aircraft but there are a few comparisons with experiment for metallic conductors.

### 3.3.3 Magnetic Field Integral Equation (MFIE)

#### 3.3.3.1 Introduction

The time and frequency domain forms of the MFIE were derived in Section 3.2 and were given in equations (3.2.13) and (3.2.14). In this section three methods of employing the MFIE to obtain solutions of coupling problems will be reviewed. The most extensively developed method is originally due to Bennett and Weeks [27,28,29] and was used to calculate the scattered fields from conducting objects. This method is reviewed in Section 3.3.3.2. Using a nearly identical model, Perala [30] has calculated the induced currents on a cylinder and these results are discussed in Section 3.3.3.3. A third method, which uses the frequency domain MFIE to determine the fields around a model aircraft, has been developed by Sancer [30] and is discussed in Section 3.3.3.4.

#### 3.3.3.2 Bennett and Weeks

Using the time domain form of the MFIE, Bennett and Weeks [27] have solved for the scattered fields from cylindrical and spherical shaped conductors which are illuminated by a Gaussian shaped plane wave. The major objective of their work was to understand the physical mechanisms of plane wave (radar) scattering by conducting objects. As an intermediate step in the method, however, surface current densities are calculated so the method could be used to calculate the parameters  $J_s$  and  $\sigma$  which are required for a lightning coupling analysis.

The MFIE itself is not well suited to treating wire-like structures. Because the EFIE is much better suited to these geometries, Bennett [32,33] was led to develop a hybrid method which incorporated both the MFIE and the EFIE. The hybrid method can treat structures of more general shape than either the EFIE or MFIE alone. Bennett has also made extensive measurements of the reflections from various geometrical shaped objects and from scale models of aircraft [34].

The original method developed by Bennett and Weeks [27] begins with the time dependent MFIE derived in Section 3.2 but simplifies the equation for cylindrical or spherical symmetry. The basic equation is

$$\vec{H}(\vec{r}, t) = \vec{H}_0(\vec{r}, t) + \lim_{\vec{r}'' \rightarrow \vec{r}} \frac{1}{4\pi} \times \int_S \left[ \frac{J_s(\vec{r}', \tau)}{R^2} + \frac{1}{Rc} \frac{\partial J_s(\vec{r}', \tau)}{\partial \tau} \right] \times \hat{a}_R dS' \quad (3.3.3.1)$$

where  $S'$  is the surface of the conducting scatterer,  $t$  is the retarded time,  $t-R/c$ ,  $\hat{a}_R$  is a vector normal to the surface, and  $R$  is  $|\vec{r}'-\vec{r}|$ , the distance between the source and observation points. If the driving field  $H_0(\vec{r},t)$  is known and the surface current is known at earlier time (i.e.,  $t'<t$ ), then equation 3.3.3.1 can be solved by "marching-in-time." The cylindrical or spherical symmetry was used to reduce the integral in (3.3.3.1) analytically, the remaining integrals being calculated numerically by partitioning the surface area into patches and assuming  $J_s$  constant on a patch (rectangular rule). The solution then proceeds by computer using the initial conditions that all fields and currents are zero before the excitation arrives. Just as in the finite difference method, the time step  $\Delta t$  must be smaller than the time it takes light to travel from one patch to another; otherwise the solution is not stable numerically.

Bennett has solved for the scattering from a long circular cylinder. The cylinder was partitioned into twenty-four segments as shown in Figure 3.26. Figures 3.27 and 3.28 show the scattered fields as a function of angle. The time dependence of these fields, especially in the backscatter direction, shows the direct reflection plus the radiated fields from the "creeping" currents which are excited on the scatterer. Figures 3.29 and 3.30 show a comparison of fields with results from other computational methods. The agreement is good to excellent.

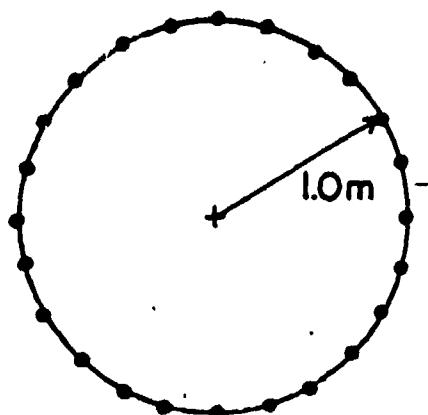


Figure 3.26 Geometry of Circular Cylinder

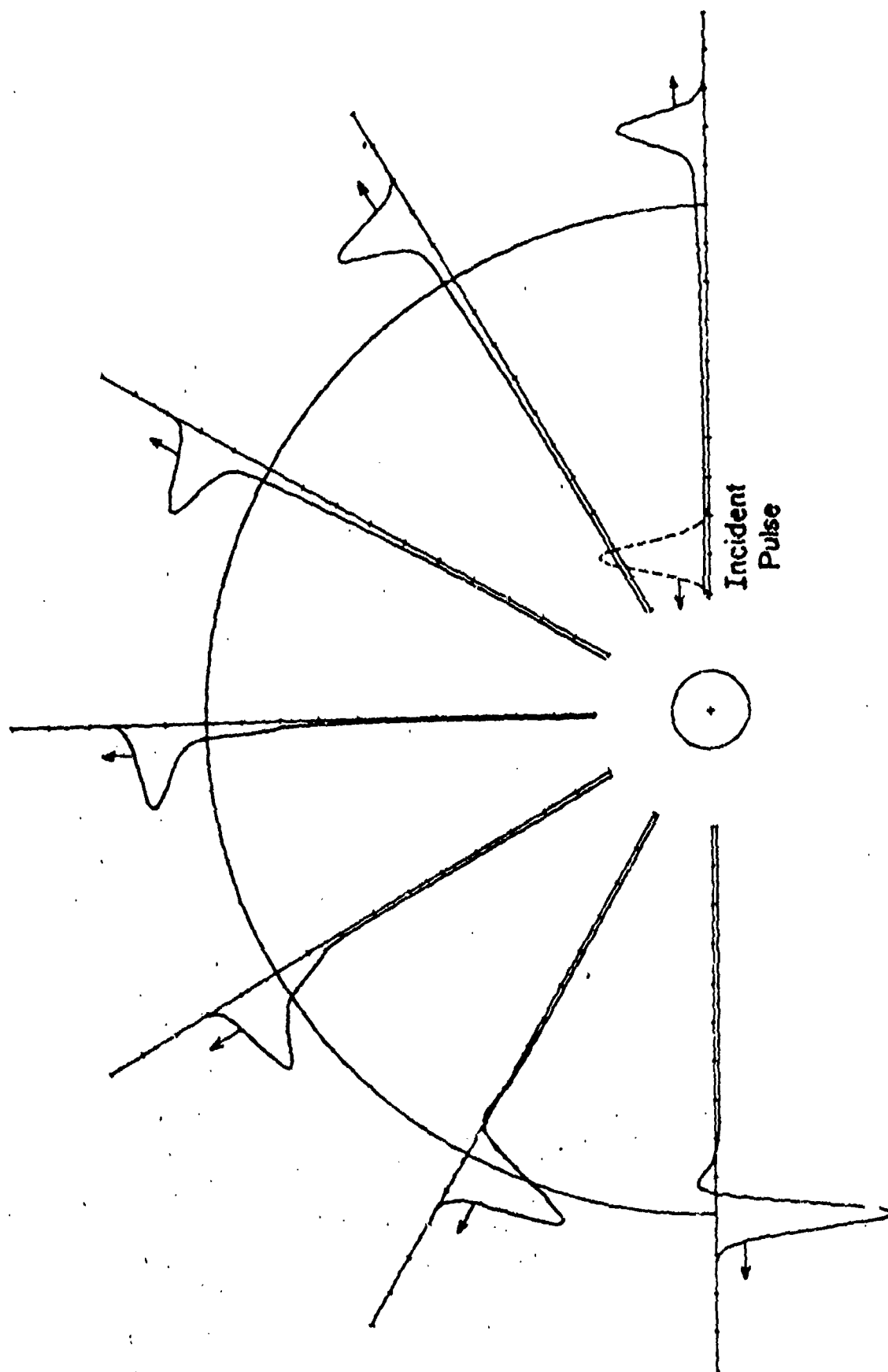


Figure 3.27 TM Approximate Impulse Response of Circular Cylinder [27]

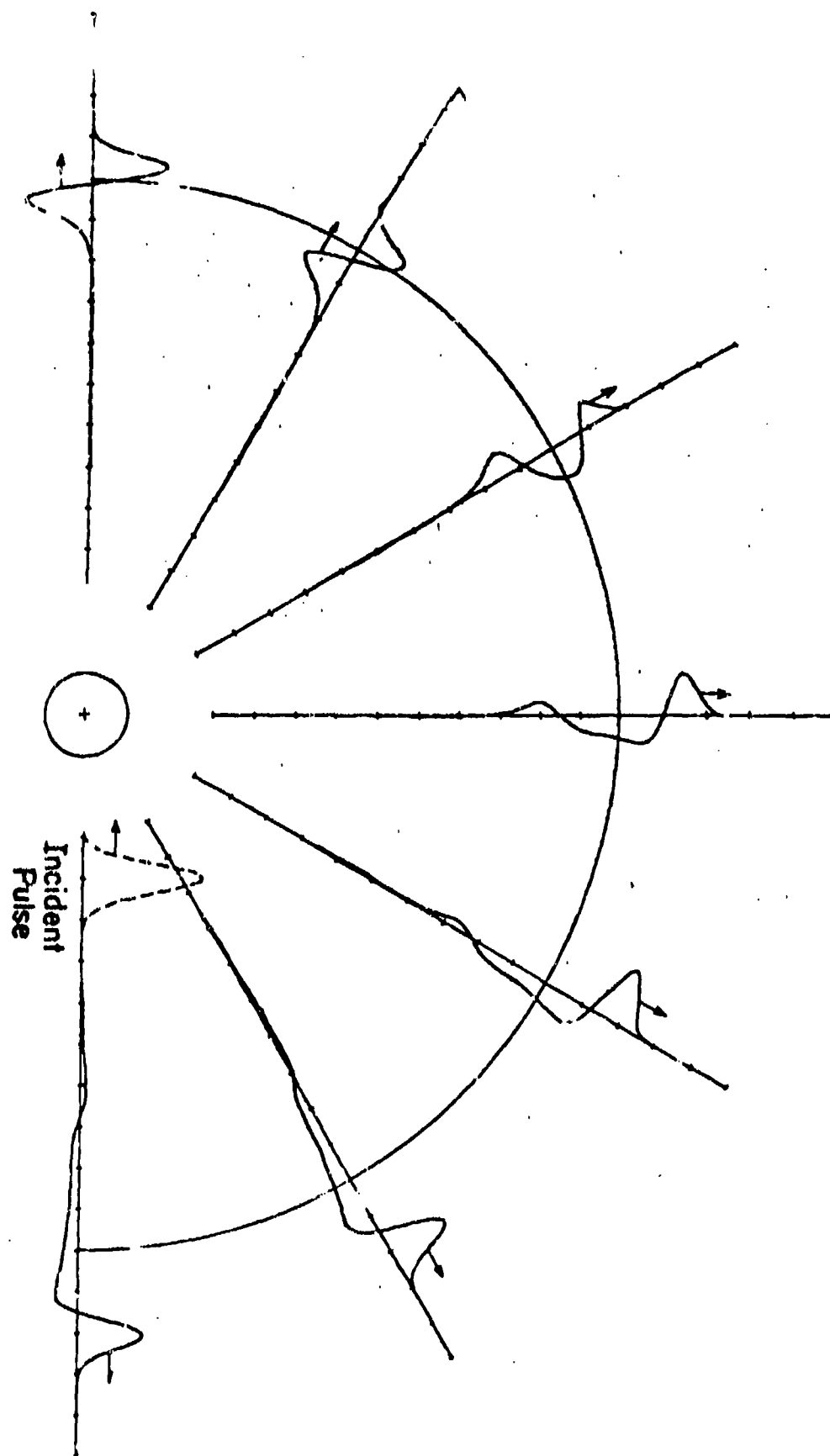
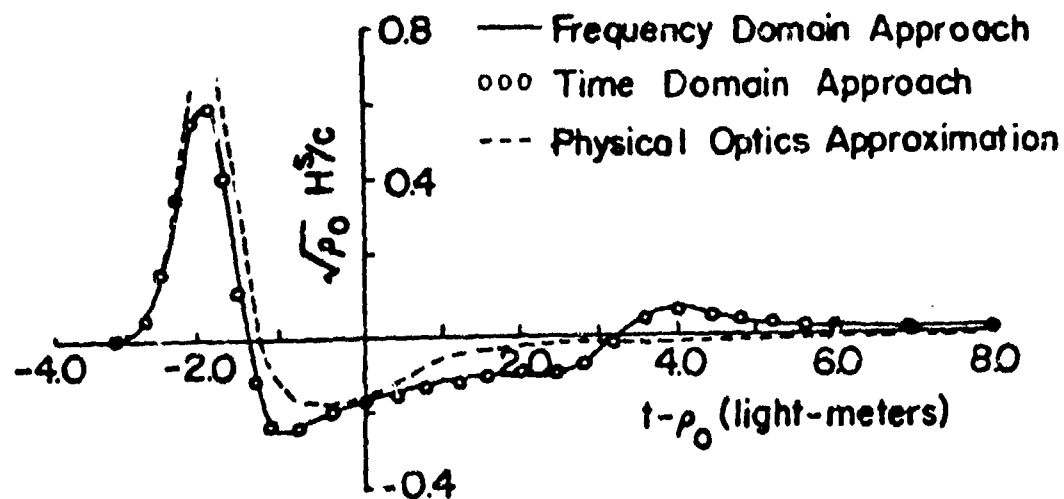
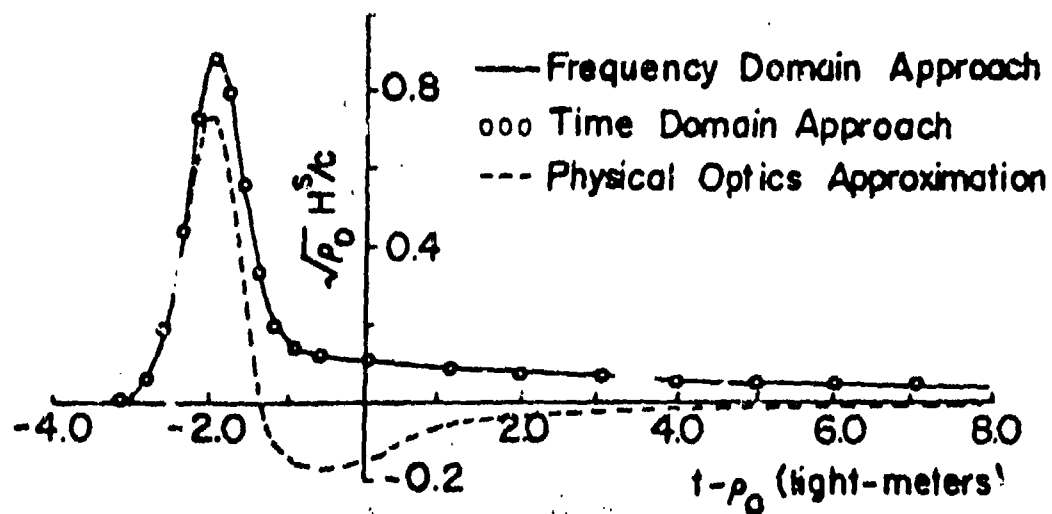


Figure 3.28 TE Approximate Impulse Response of Circular Cylinder [27]



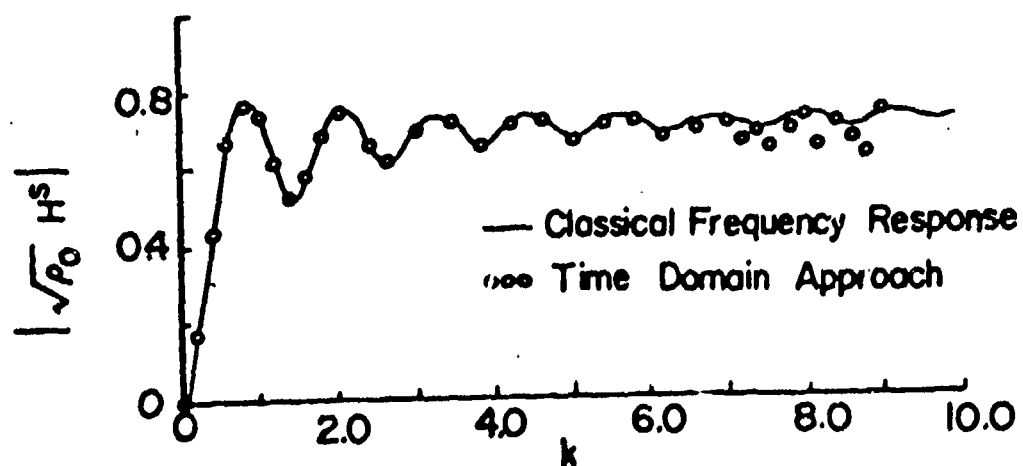
(a) TE Approximate Impulse Response of Circular Cylinder in Backscatter Direction [27]



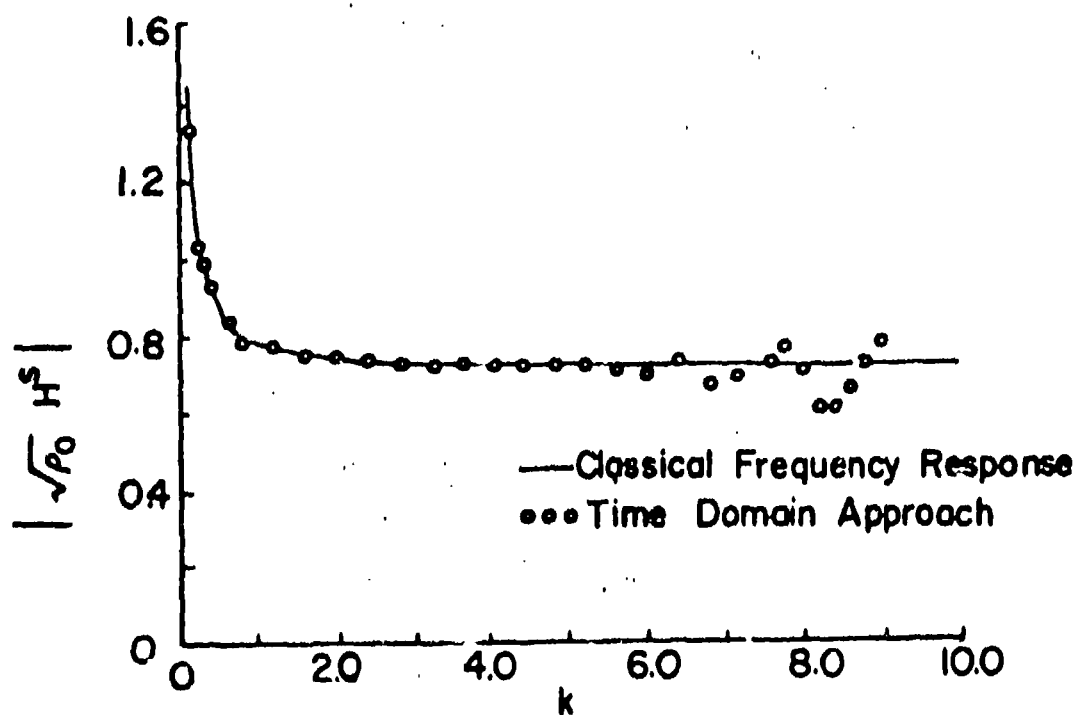
(b) TM Approximate Impulse Response of Circular Cylinder in Backscatter Direction

Figure 3.29 Time Domain Responses of the Circular Cylinder Compared to Other Computational Methods [27]





(a) TE Frequency Response in Backscatter Direction of Circular Cylinder with One Meter Radius [27]



(b) TM Frequency Response in Backscatter Direction of Circular Cylinder with One Meter Radius

Figure 3.30 Frequency Domain Responses of the Circular Cylinder Compared to Other Computational Methods [27]

The hybrid method developed by Bennett [32] uses the solution of the MFIE as just described and appends a solution of the time dependent EFIE for parts of the scatterer that resemble plane surfaces or wire like structures. The form of the EFIE that has been used is

$$0 = \epsilon \frac{\partial \vec{E}_{\text{tan}}^i}{\partial t} + \left\{ \left[ \vec{\nabla}(\vec{\nabla} \cdot) - \frac{1}{c^2} \frac{\partial^2}{\partial t^2} \right] \frac{1}{4\pi} \int_{S'} \frac{\vec{J}_s(\vec{r}', \tau)}{R} ds' \right\} \quad (3.3.3.2)$$

where  $\vec{E}^i$  is the incident electric field, and  $\vec{J}_s$  and  $S'$  are as in equation (3.3.3.1). This equation is solved in the time domain by a marching-in-time procedure also. The solutions from the MFIE and EFIE are matched at interface points between the plane (EFIE) and voluminous (MFIE) surfaces. The solutions are matched by requiring

$$\begin{aligned} \frac{\partial (\vec{J}_{s\perp})}{\partial n} &= 0 \\ (\vec{J}_s)_{//} &= 0 \end{aligned} \quad (3.3.3.3)$$

where  $\hat{n}$  is the normal vector to the voluminous surface at the line formed by the intersection of the plane and voluminous surfaces.  $(\vec{J}_s)_{\perp}$  and  $(\vec{J}_s)_{//}$  are the vector components of  $\vec{J}_s$  perpendicular and parallel to the line above.

Bennett [34] has compared calculations of scattered fields using the above method with measurements of his own on a scale model aircraft. The measurements were made by the time domain reflectometry method and a block diagram of the measuring equipment is shown in Figure 3.31. Basically, transmitting and receiving antennas are used to illuminate an object and record the reflected pulse from the scattering object. Figure 3.32 shows the backscatter response of several shapes. The sequence shows the relative importance of scatterer edges to the reflected response. Figure 3.33 shows the reflection from a MIG-21 model as compared to calculations using the hybrid method. The calculated response compares well with the measurements except for the phase of the tail section reflections. This discrepancy is believed to be due to the imperfect representation of the coupling between the fins and the fuselage.

In the following sections, the various evaluation criteria are discussed.

#### 1. Computer Memory: There is little information on computer memory

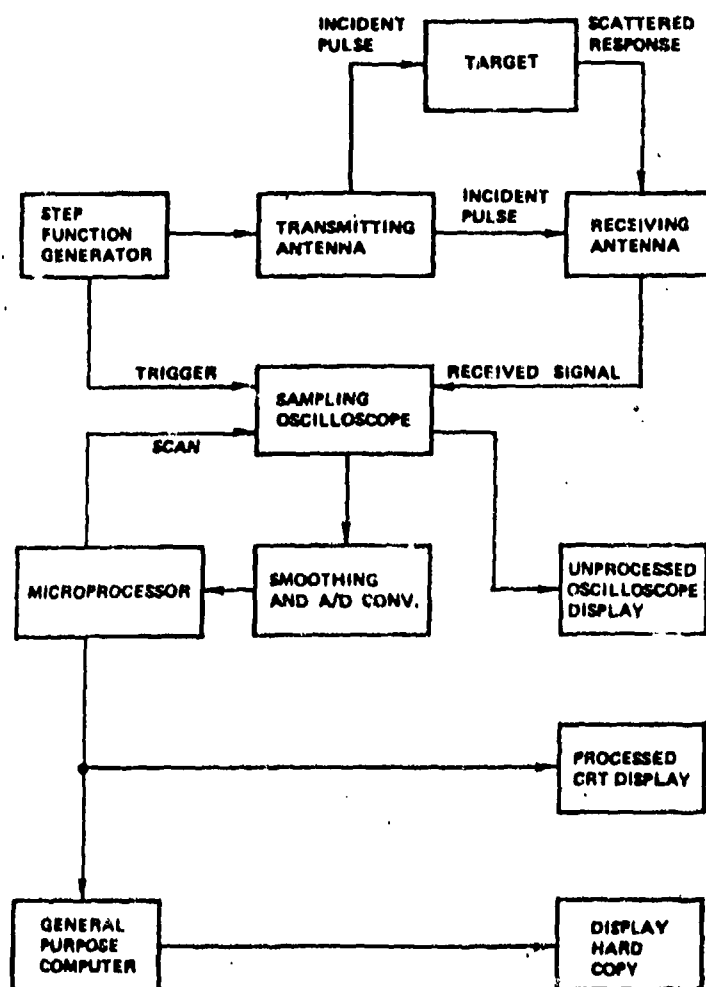


Figure 3.31 Functional Block Diagram of Time-Domain Reflectometry Scattering Range [34]

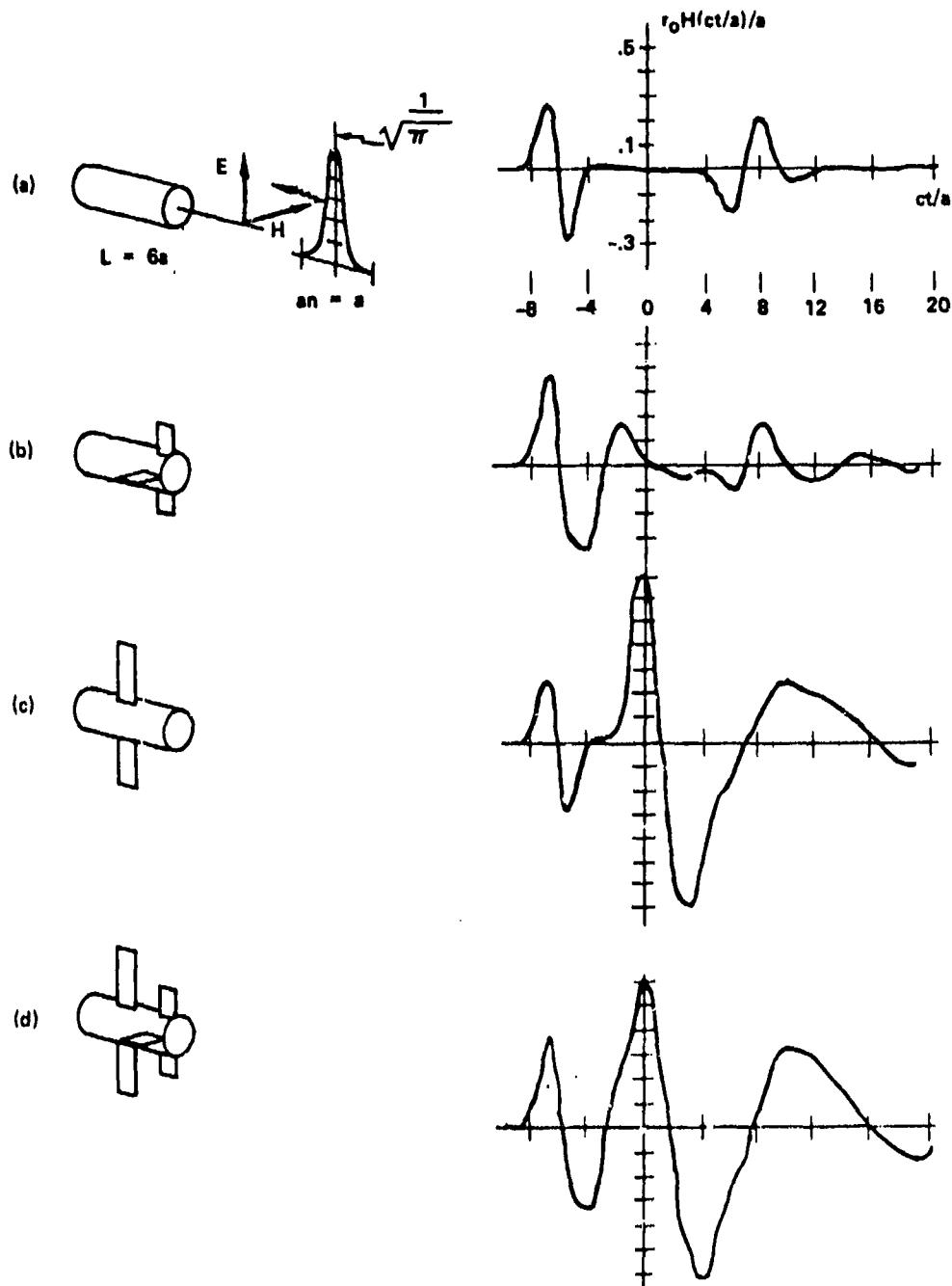
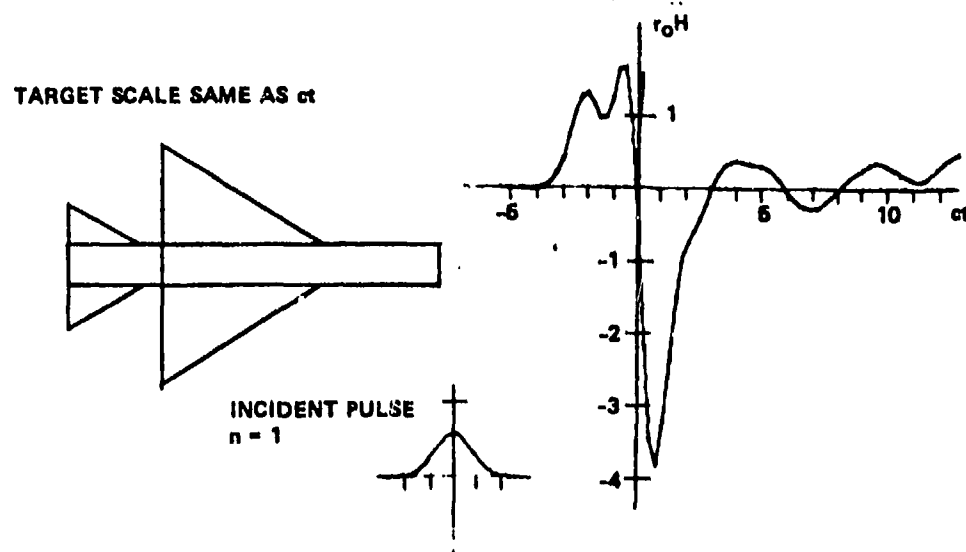
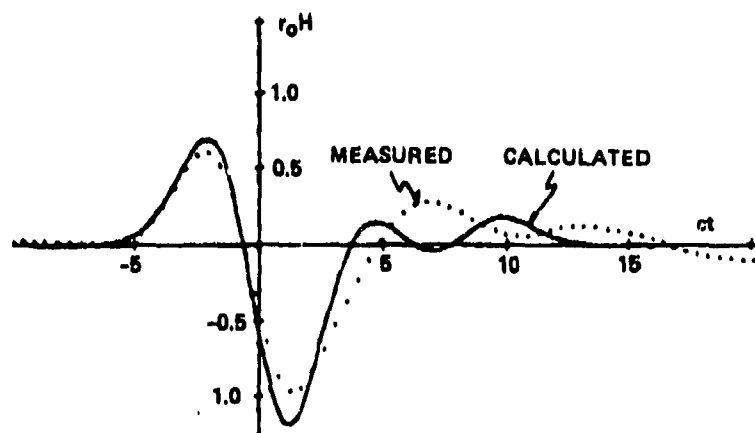


Figure 3.32 Comparison of Responses of Several Finned Cylinders at Axial Incidence [34]



(a) CALCULATED



(b) CALCULATED COMPARED WITH MEASUREMENT  $n = 0.5$

Figure 3.33 Calculated MIG-21 Response,  $\alpha = 90^\circ$  [34]

requirements for either the MFIE or the hybrid method. Bevensee and Brittingham [35] have performed test calculations of the scattering by a sphere. The sphere was partitioned into 160 patches and calculations of 60 time steps were performed on a CDC 6600. The code ran in  $18k_{10}$  words so it would run in  $100k_8$  words on most machines. The hybrid method is expected to use more than  $100k_8$  words for a reasonable representation of a real aircraft, however.

2. CP Time: For the above example of scattering from a sphere, it took 10 minutes to calculate the radiated fields for one incident and one scattering angle. This was for 60 time steps only. For a lightning strike it might be necessary to run 1000 time steps and so the computer time required to run the MFIE alone could be long. The hybrid method is expected to be longer although no example runs were found.

3. Numerical Accuracy. The numerical accuracy of results from the MFIE method is determined by several approximations. One is the representation of the current on a patch by a constant value. Another is the approximation of the angular dependence of an integrand by a Fourier series. The hybrid method includes the above approximations as well as the boundary condition on vector components of the surface current at boundaries between the plane surfaces treated by the EFIE and the voluminous ones treated by the MFIE. The errors do not seem large. Scattering from a sphere is predicted to within a few percent of the exact expression and the agreement between the calculations and measurements for the MIG-21 model is also good.

4. Physical Accuracy: The MFIE method and the hybrid method are limited in their physical accuracy by the number of patches used to represent a surface. In the example of scattering from a 1 m radius sphere, the surface of the sphere was divided into 160 patches. Unfortunately the gridding used for the MIG-21 was not given.

5. User Orientation: The code is available with limited support from Lawrence Livermore Laboratory, and is referred to as S3T-CLB [36].

6. Frequency Range. The MFIE and hybrid methods are both good at high frequencies. The high frequency limit is determined by the patch spacing because the step time  $\Delta t$  must be less than the time it takes light to travel from one patch to a neighboring patch. As a practical matter, for 1m patches, the upper frequency limit is on the order of several hundred MHz. The low frequency limit

of the code is determined by the number of time steps that can be run before numerical errors mask the results. The lower frequency limit is not known.

7. Attached Stroke: At the present time, the code is used only for field illumination and has not been used for current injection. The codes would have to be rewritten for an attached stroke.

8. Test Case: The test configuration includes a ground plane and return conductors and will be a current injection test rather than field illumination. Neither the MFIE nor the hybrid method can incorporate these features without modification.

9. Aircraft Size: Small aircraft models have been treated. However, for real sized aircraft, it is not clear whether this code can handle very large aircraft such as a B-52.

10. Lightning Environment: As the methods are presently written, non-linear conductivity and time dependent media cannot be incorporated into the solution without a non-trivial change in the integral equations being solved. Without much trouble, lightning near fields could be incorporated as the driving fields.

11. Experimental Verification: The hybrid method has been compared to extensive measurements by Bennett. The verification has been performed with arbitrarily shaped geometrical objects like plates and with model aircraft such as the MIG-21 model discussed in the text. The comparisons have been for scattered fields however. This may not be a sensitive test of surface current or charge density on the aircraft which are important for a lightning coupling calculation.

### 3.3.3.3 MFIE (Perala)

Using a method of solving the time domain MFIE very similar to that of Bennett and Weeks, Perala [30] has studied the response of a fat cylinder to a NEMP excitation. The object of this work was the explicit calculation of surface currents rather than scattered fields.

The cylinder which has been illuminated by a NEMP pulse is shown in Figure 3.34. The length to diameter ratio of the cylinder is about 1.0. This shape cylinder is difficult to treat by other computational methods and is well suited to the MFIE solution. The surface of the cylinder was broken up into 324 patches. The incident field was a Gaussian plane wave approaching the cylinder broadside (approaching from the + x axis in Figure 3.34.). Studies

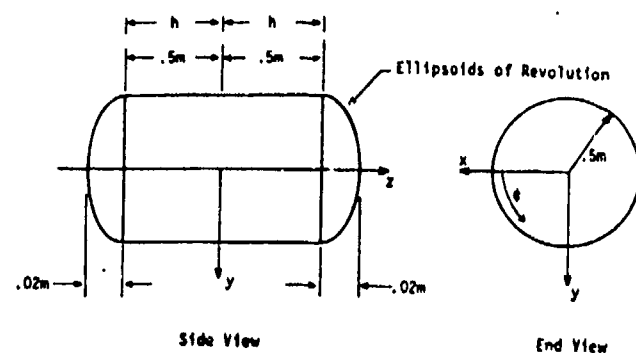


Figure 3.34 Fat Cylinder Diagram and Coordinate System [30]

were performed for both polarization parallel and perpendicular to the cylinder  $z$  axis. Figure 3.35 shows various vector components of the surface current as a function of the circumferential angle around the cylinder for an incident field with polarization parallel to the  $z$  axis. The results show the dip in  $J_z$  at  $90^\circ$  as expected from the vanishing of  $\hat{n} \times \mathbf{H}_0$  at  $90^\circ$ . In addition to the response shown in Figure 3.35, other responses were calculated including surface currents in the frequency and time domain for many positions on the cylinder.

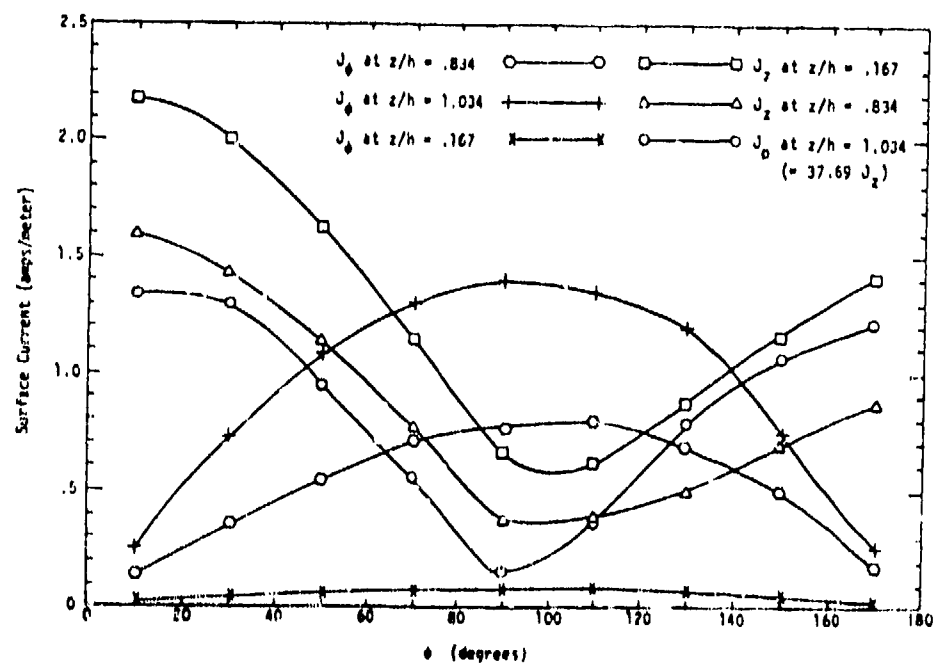


Figure 3.35 Variations of Surface Current Peak Amplitudes with  $\phi$  and  $z$ . Incident Field Polarized Parallel to  $z$  axis [30]



The discussion of this code with regard to the eleven evaluation criteria is very similar to the discussion for the MFIE of Bennett and Weeks.

1. Computer Memory: For the cylinder example described in the text, the computer code required 243k<sub>8</sub> words on a CDC 6600. There have been no aircraft treated by this method. Clearly the memory requirements are very large.

2. CP Time: For the fat cylinder, the runs described in the article by Perala took about 1 hour of CP time.

3. Numerical Accuracy: The numerical accuracy of the method is limited by the rectangular approximation used to evaluate the integral, by a parabolic fit of the time dependence of  $\vec{J}$ , and, by an approximation used to evaluate the Fourier transform integrals to get frequency domain results.

4. Physical Accuracy: The cylinder is well represented by the 324 patches which are used in the example described in the text. Aircraft would have to be partitioned into surface patches and the method would have the same physical accuracy limits as the MFIE method of Bennett.

5. User Orientation: There are no user manuals or documentation for this code and so it is not user oriented at the present time. The method would probably require a skilled user to partition a complicated surface such as that of an aircraft.

6. Frequency Range: Same as Bennett and Weeks.

7. Attached Stroke: Same as Bennett and Weeks.

8. Test Case: Same as Bennett and Weeks.

9. Lightning Environment: Same as Bennett and Weeks.

10. Aircraft Size: Same as Bennett and Weeks.

11. Experimental Verification: Armour [37] has made measurements of the current distribution on a wire grid model of the fat cylinder. The measured results are in fair agreement with Perala's calculations, although the wire grid model is itself only an approximation to the fat cylinder.

#### 3.3.3.4 MFIE (Sancer)

The response of an aircraft to a NEMP excitation is sometimes calculated using a stick model of the gross features of the aircraft. The currents

flowing on the segments of the stick model represent the bulk currents on the real aircraft fairly accurately. When surface current densities on the aircraft are required from such a model, it is customary to assume that  $I_{\text{bulk}}/2\pi r$  gives the surface current density on a structural member of radius  $r$ . This approximation was believed to improve as the wavelength of the driving fields became larger. However, Sancer [38] has shown that the current density on an object, specifically a cylinder, can be very different from  $I_{\text{bulk}}/2\pi r$  even at low frequencies. This observation led Sancer to employ the MFIE in an analysis of the coupling of a NEMP pulse to an aircraft because the MFIE would provide the correct low frequency behavior.

Sancer's approach was to use the frequency domain MFIE and solve the integral equation by the Method of Moments technique discussed in Section 3.2.3. The integral equation was transformed into a system of linear equations by dividing the surface of the scatterer into patches and evaluating the integral over each patch under the assumption that the surface current on each patch is constant. Excellent, but very elaborate, methods were employed to take into account all the simplifications afforded by the symmetries of the scatterer. Systems of equations were derived for objects with a single plane of symmetry and with three planes of symmetry. These equations are complex and can be found in Sancer's work [31]. The partitioning of the scatterer's surface has been accomplished in a way so that small patch sizes can be used near junctions and boundaries where the surface current is a strong function of position.

The method has been applied to plane wave excitation of a cylinder and the results have been compared to measurements by Burton et al. [39]. The experimental arrangement is shown in Figure 3.36. A sinusoidal plane wave is generated at the corner reflector and excites currents in a scattering object (cylinder) a distance  $d$  from the source. The surface current density on the cylinder is measured by a probe which can be moved up and down the length of the cylinder. The cylinder can also be rotated through an angle  $\theta$ . Figure 3.37(a) and 3.37(b) show the measured and calculated amplitudes of the surface current as a function of height. The calculations have been scaled by a single multiplicative constant to account for a lack of calibration. The agreement is excellent.

Sancer has also made calculations of the current density of a model aircraft. The aircraft is shown in Figure 3.38 and consists of structural

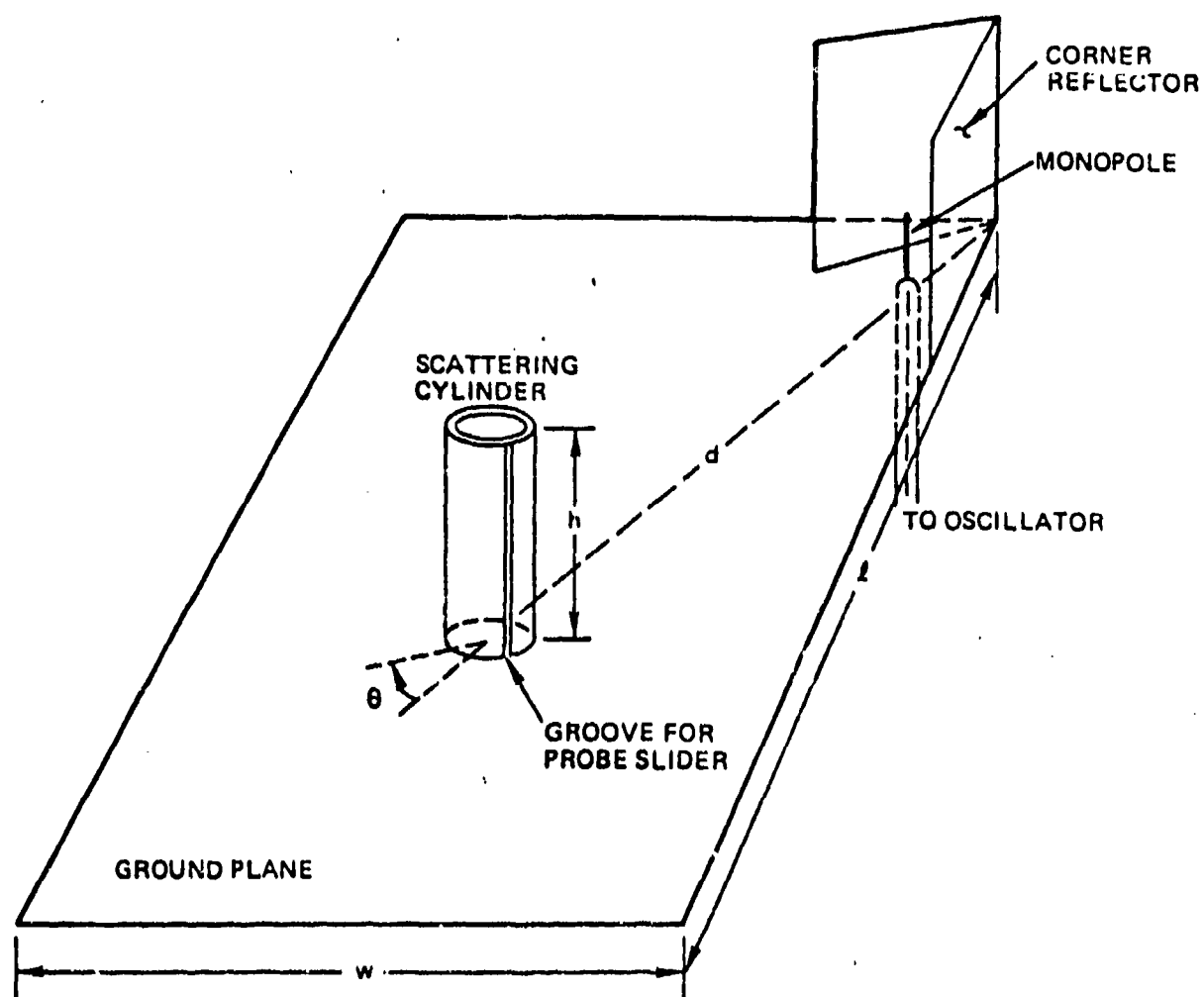


Figure 3.36 Schematic Diagram of Scattering Cylinder on Ground Plane [39]

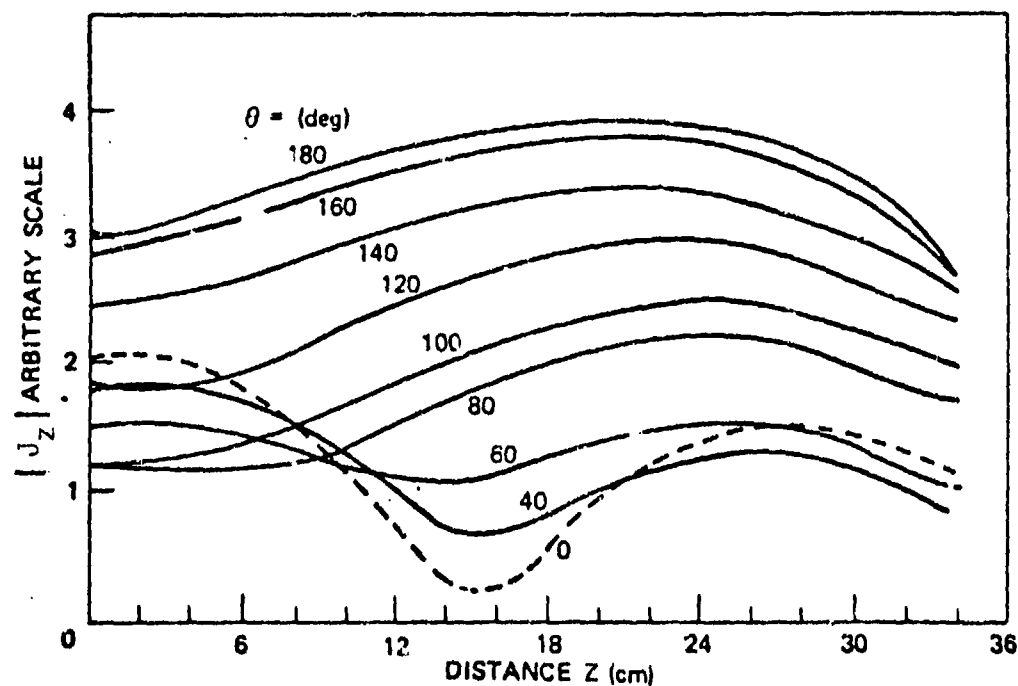


Figure 3.37 (a) Measured Amplitude of Axial Surface Density of Outside Current on Tubular Cylinder, E-Polarization (Large Outdoor Ground Screen) [39]

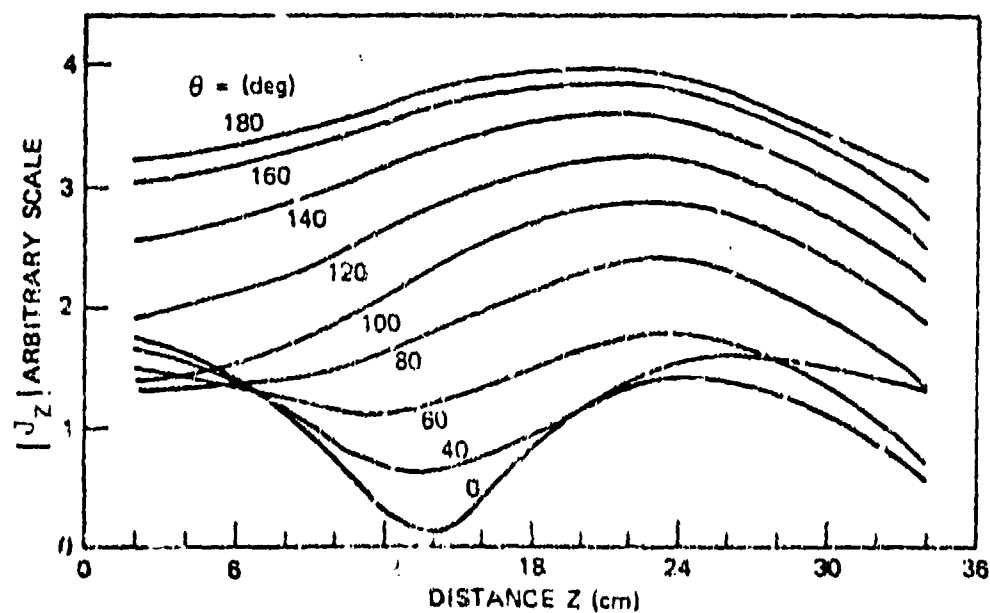


Figure 3.37 (b) Calculated Amplitude of Axial Surface Current Density on a Finite Circular Cylinder [39]

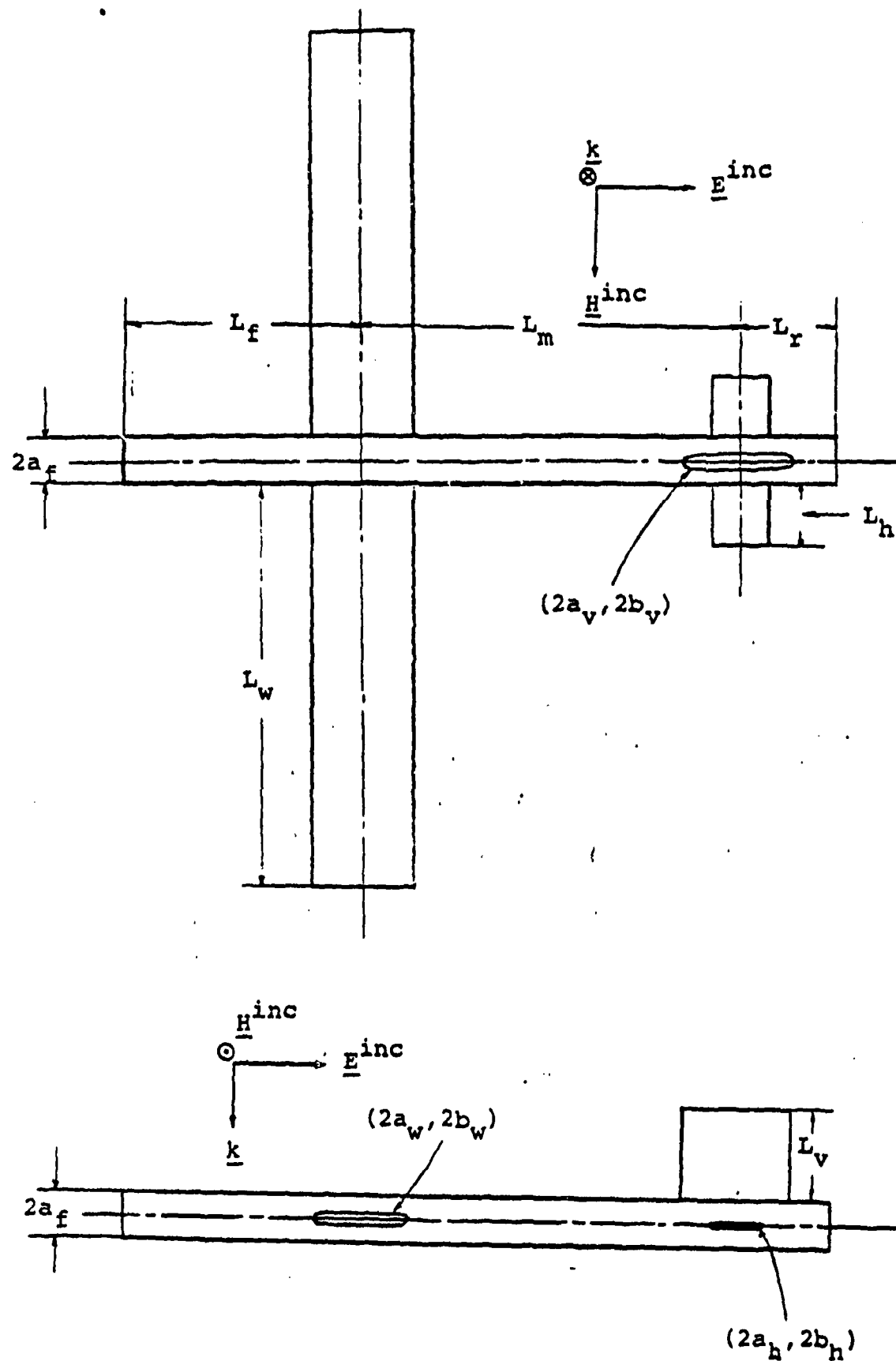


Figure 3.38 Magnetic Field Integral Equation Aircraft Model [40]

elements (wings, fuselage and stabilizers) which are cylinders of elliptic cross section. The structural members intersect at right angles only. Over 100 patches of variable size were used to represent the surface areas required in the calculation. Figure 3.39 shows the surface current density along the top of the fuselage as a function of the position along the fuselage. Figure 3.3.40 shows similar surface current density along the bottom of the fuselage. The calculations compare very well with the measurements which were made by Liepa [40] at the University of Michigan. The current density near the vertical stabilizer is expected to be in error because of the singular behavior of solutions using this method near edges.

Next, the eleven evaluation criteria are discussed.

1. Computer Memory: There is no definite information on the computer memory required for a calculation such as the one for the model aircraft. However, the use of symmetries in the simplification of the integral equation would reduce the required computer storage.

2. CP Time: Again there is no information on the computer time required to perform a calculation. Large matrices (400 x 400) have to be inverted, however. Also, the result of a calculation is the current density at one frequency. To obtain a time dependent response, the current density will be required at a few hundred frequency points so the computer time required for a time dependent solution will be substantial.

3. Numerical Accuracy: The numerical accuracy depends on such factors as the matrix inversion method, the number of patches used to represent the aircraft area, approximations used to match the solution between various structural parts of the aircraft and the approximations used to represent the functional dependence of  $J_s$  between patches. Numerical errors were investigated very carefully and it was demonstrated, for example, that the solution was independent of patch position and size. The method, however, does not determine the surface currents near junctions or boundaries because of the singular behavior of certain matrix elements.

4. Physical Accuracy: Using the model, a solution can be obtained only for an aircraft with uniform, elliptical cross section cylinders as structural parts. Furthermore, the model cannot represent aircraft with structural members

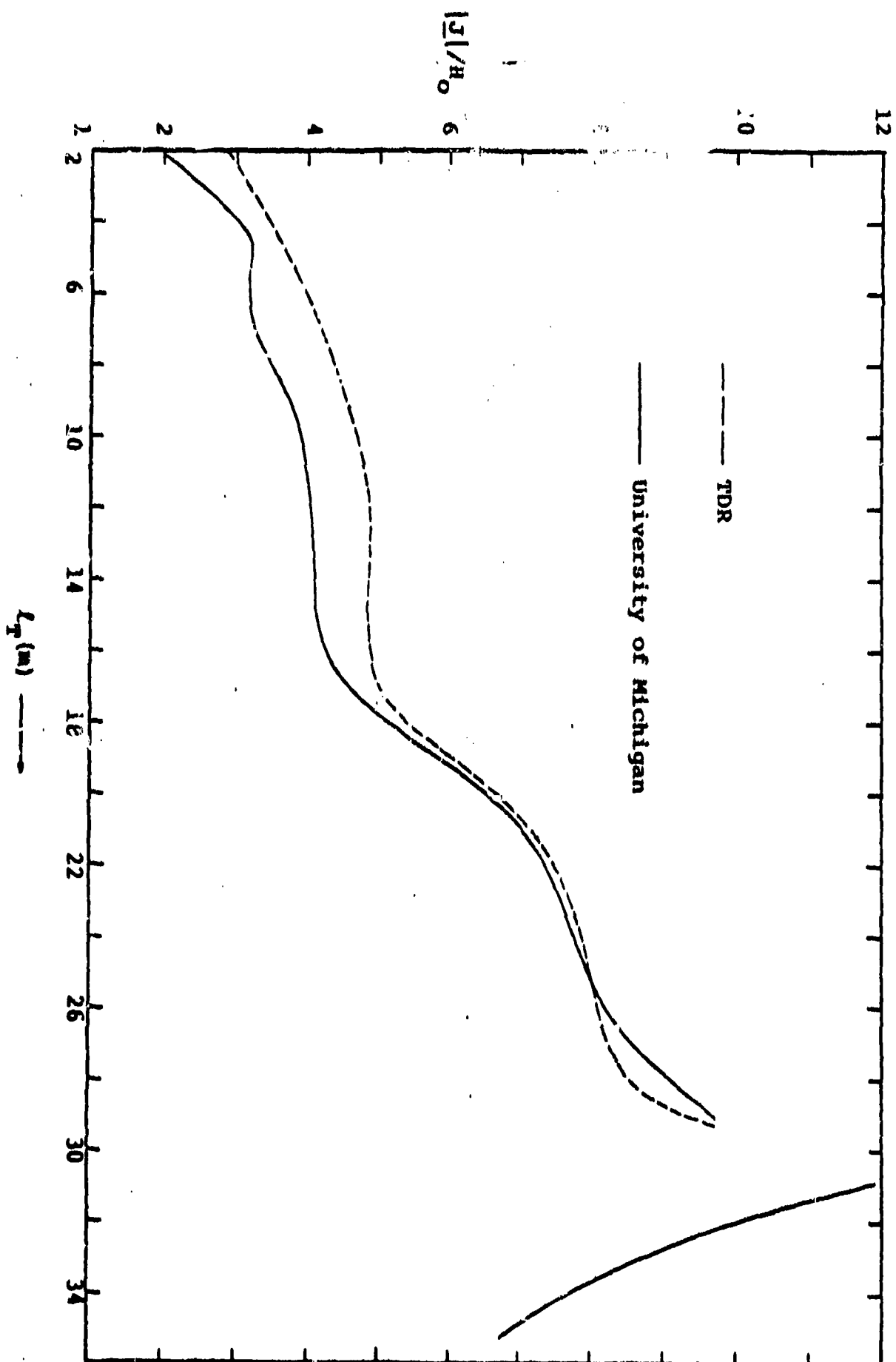


Figure 3.39 Top of Fuselage,  $kh = 0.52$ . ( $h$ : Fuselage Half Length) [40]

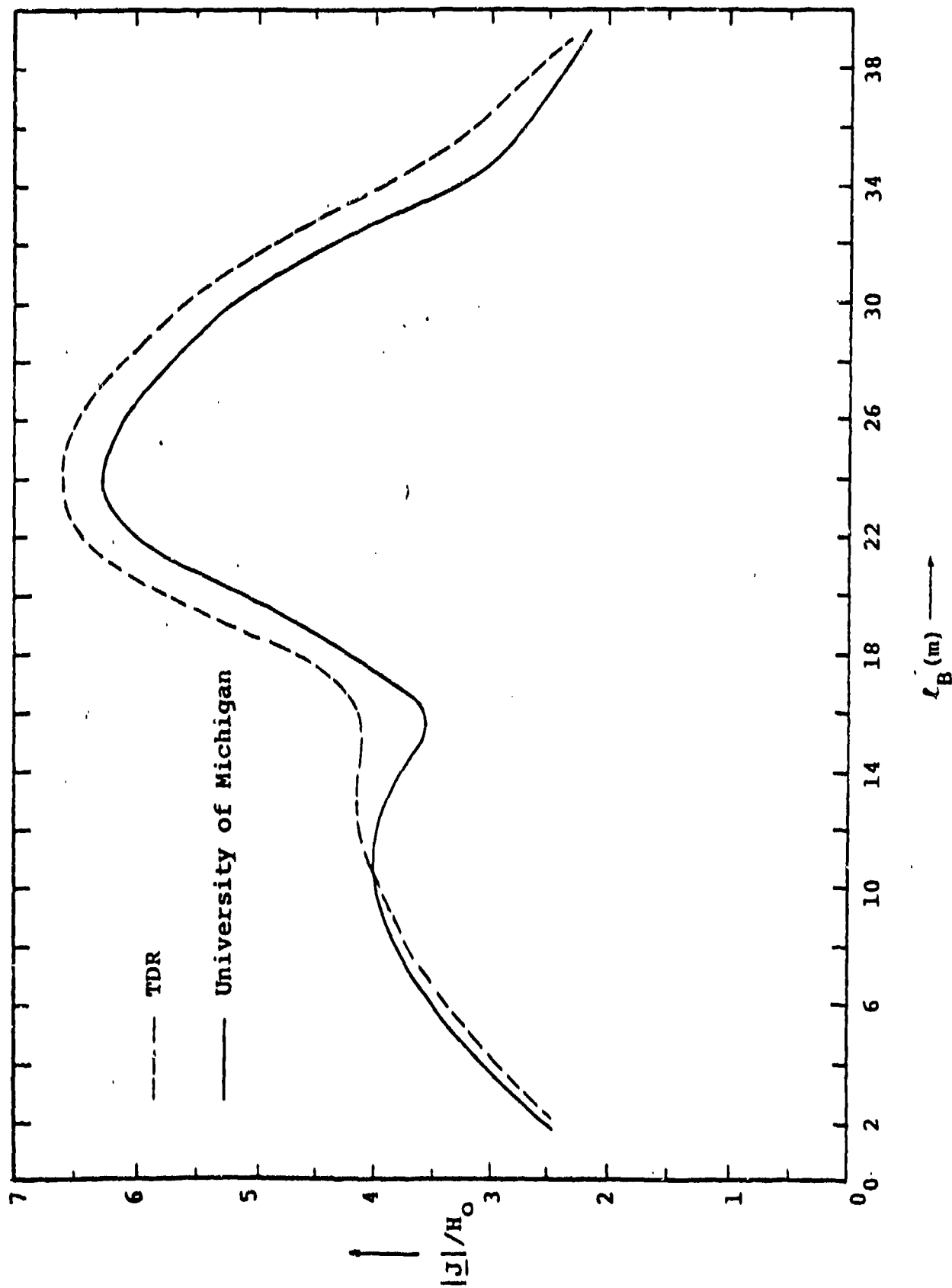


Figure 3.40 Bottom of Fuselage,  $kh = 0.82$ . (h: Fuselage Half Length) [40]



which intersect at other than right angles. The solution near junctions and boundaries is not reliable.

5. User Orientation: The original MFIE method of Sancer is not documented. It was written with input options to change the patch spacing and size near edges where the surface current density is a strong function of position. A computer code NEC which will be described in Section 3.4.2 has incorporated this method, or a similar one, to solve for surface current density on voluminous objects. The code NEC is well documented and is relatively user oriented, considering its size and complexity.

6. Frequency Range: This method of determining surface currents is particularly suited to lightning because of the relatively low frequency content of the lightning stroke and the exact treatment by this method of the coupling at low frequencies. The high frequency limit is not known but for similar NEC methods [41] the requirement is that  $\lambda > 5 \times$  (patch size). For a 1 m patch size, this restricts the frequency to less than 60 MHz.

7. Attached Stroke: Sancer's method does not include a direct drive of the aircraft or scatterer and so to incorporate attached stroke phenomena the method would have to be rewritten.

8. Test Case: The method has been used for NEMP illumination of an aircraft model over a lossy earth. However the method is not presently designed to handle direct drive. Return conductor wires would be hard to treat.

9. Lightning Environment: Although the method can probably treat lightning near fields without a great deal of modification, it cannot treat the attached stroke. A more serious failing, however, is that the calculations are made in the frequency domain. Therefore, a time domain response must be obtained by a Fourier inverse procedure and this precludes treating non-linearities or time dependent media properties (air conductivity) in a straightforward manner.

10. Aircraft Size: The method has been used to treat model aircraft but it is not clear what limitations there are on the size of the aircraft it can handle.

11. Experimental Verification: The method has been verified experimentally for plane wave illumination of a cylinder over a ground plane and of a model aircraft.

### 3.3.4 Electric Field Integral Equation (EFIE)

#### 3.3.4.1 Introduction

There are several methods which use forms of the EFIE as derived in Section 3.2.2 or which use a combination of the EFIE and MFIE. These methods are reviewed in this section and they include AMP/NEC (Section 3.3.4.2), a code developed by Chao and Strait (Section 3.3.4.3), a code developed by Curtis at Boeing, and a Thin Wire Time Domain (TWTN) code developed at Berkeley (Section 3.3.4.5). Because many of the codes use a wire grid structure to model an object, some general considerations on wire grid models have been discussed in Section 3.3.4.6. Finally, the EFIE methods use an approximation called the thin wire approximation and this has been described in Section 3.3.4.2.

#### 3.3.4.2 AMP/NEC [41-45]

There is an evolution of computer codes primarily developed by MB Associates, one code of which is the Antenna Modeling Program (AMP and AMP2) [45]. The Numerical Electromagnetic Code (NEC1 and NEC2) is an outgrowth of AMP but has been developed at the Lawrence Livermore Laboratory [41-44]. All of these codes provide frequency domain solutions. AMP and its predecessors were restricted to thin wire models and solution of the EFIE by the method of moments. AMP2, NEC1 and NEC2 have added the ability to treat voluminous surfaces by patch segmentation of the surface using a solution of the MFIE (also by the method of moments) [41-45].

In the following paragraphs, the thin wire EFIE method will be described. The MFIE solution by means of patching was discussed in Section 3.3.3.3 (Sancer's Model Aircraft). The most advanced of the codes is NEC2 [41-44] and it is the only one that needs to be considered as a candidate for a lightning external coupling calculation. Important features of the other codes are included in NEC2.

From Section 3.2.3, the EFIE in the frequency domain is

$$\hat{n} \times \vec{E}_0 = \frac{1}{4\pi j\omega\epsilon_0} \hat{n} \times \int_S \left[ -\omega^2 \mu_0 \epsilon_0 \phi(r, r') \vec{J}_s(\vec{r}, \vec{r}') + \vec{\nabla}\phi(r, r')(\vec{\nabla}' \cdot \vec{J}_s) \right] ds' \quad (3.3.4.1)$$

where  $\phi$  is  $\exp(jkR)/R$  and  $\vec{J}_s$  is the unknown surface current. The driving field is  $\vec{E}_0$ . Consider the problem of finding the current  $\vec{J}_s$  on the surface of a cylinder (circular cross section) whose radius "a" is small compared to a wavelength. Following the discussion in [41], take  $\vec{J}_s$  to be concentrated at the center of the wire and assume that the current  $J_s$  flows only in the axial direction. That is,

$$I(s) \hat{s} = 2\pi a \mathbf{J}_s(\vec{r}) \quad (3.3.4.2)$$

where  $\hat{s}$  is a vector in the direction of the axis of the wire. The vector cross products in equation (3.3.4.1) arise because the tangential component of  $\vec{E}_{TOT}$  must vanish on the conducting surface  $S'$ . For a straight cylindrical wire, this boundary condition can be written in terms of a dot product of  $\vec{E}$  with  $\hat{s}$ . Using this fact and equation (3.3.4.2), one obtains

$$-\hat{s} \cdot \vec{E}_0 = \frac{1}{j4\pi\omega\epsilon_0} \int_L I(s) \left( k^2 \hat{s} \cdot \hat{s}' - \frac{\partial}{\partial s \partial s'} \right) \phi(r, r') ds' \quad (3.3.4.3)$$

where the integration is over the length  $L$  of the wire. Equation (3.3.4.3) is an integral equation in the unknown current  $I(s)$  with  $\vec{E}_0$  as the driving term. The following is a list of the assumptions used in deriving the EFIE for thin wires, i.e. equation (3.3.4.3):

- (1) Transverse currents can be neglected relative to axial currents on the wire.
- (2) The circumferential variation of axial current can be neglected.
- (3) The current can be represented by a filament on the wire axis.
- (4) The boundary condition on the electric field needs to be enforced in the axial direction only.

Equation (3.3.4.3), and the frequency domain MFIE which is used in AMP2, NEC1 and NEC2, are solved by the method of moments. The EFIE is used to treat thin wire structures only. Wire structures are partitioned into segments, and point matching or collocation is used, that is, the weighting functions in the method of moments are delta functions. The basis functions used to represent the currents on a wire have constant, sine, and cosine terms. Mathematically,

$$I_n(s) = A_n + B_n \sin(s-s_n) + C_n \cos(s-s_n) \quad (3.3.4.4)$$

where  $I_n(s)$  is the current on the  $n^{\text{th}}$  wire segment,  $A_n$ ,  $B_n$  and  $C_n$  are constants, and  $s_n$  is the position of the middle of the  $n^{\text{th}}$  wire segment. The variable  $s$  is a measure of distance along the wire segment. The current and charge density are matched at joints between wire segments.

The same collocation method is applied to the MFIE except in this case the basis functions are a set of pulse functions. If  $\vec{J}_s$  is the surface current density, then

$$\vec{J}_s(\vec{r}) = \sum_{i=1}^{N_p} (J_{1i} \hat{t}_{1i} + J_{2i} \hat{t}_{2i}) v_i(\vec{r}) \quad (3.3.4.5)$$

where  $N_p$  is the number of patches,  $J_{1i}$  and  $J_{2i}$  are constants,  $\hat{t}_{1i}$  and  $\hat{t}_{2i}$  are orthogonal unit vectors parallel to the surface of the  $i^{\text{th}}$  patch, and  $v_i(r)$  is a function that is 1 on the  $i^{\text{th}}$  patch and zero elsewhere. Equation (3.3.4.5) is used for all patches except those to which a wire is connected. A wire is allowed to connect to a patch only at the center of the patch. This is shown in Figure 3.41(d) for a cylinder with a wire attached. Furthermore, those patches which have a wire attached are further broken down into quarters as shown in Figure 3.41(d) and also in Figure 3.42.

NEC2 has the provision to include drive by a voltage or current source between wire segments, or, by an incident radiation field. Also, NEC2 can include the effect of a ground plane by either of three methods:

- 1) the method of images can be used for a perfectly conducting ground plane;
- 2) Sommerfeld's method can be used for small ( $< 1\lambda$ ) interaction distances and an asymptotic expansion used elsewhere; or
- 3) a modified method of images using Fresnel reflection coefficients can be used.

Sommerfeld's method is the most demanding on computer resources and the Fresnel reflection coefficient method gives the best compromise between accuracy and computation time.

Three example calculations will now be described. The first is scattering of a plane wave by a stick model of an aircraft, the second is scattering of a plane wave by a sphere, and the third is the radiation pattern of the cylindrical satellite with two whip-type antennas. The first example uses only the EFIE solution of NEC, the second uses only the MFIE solution, and the third example uses the hybrid capabilities of NEC.

Figure 3.43 shows the stick model of an aircraft that has been analyzed. The aircraft sections are broken up into a total of 29 segments. The driving field is shown incident on the front of the aircraft with its electric

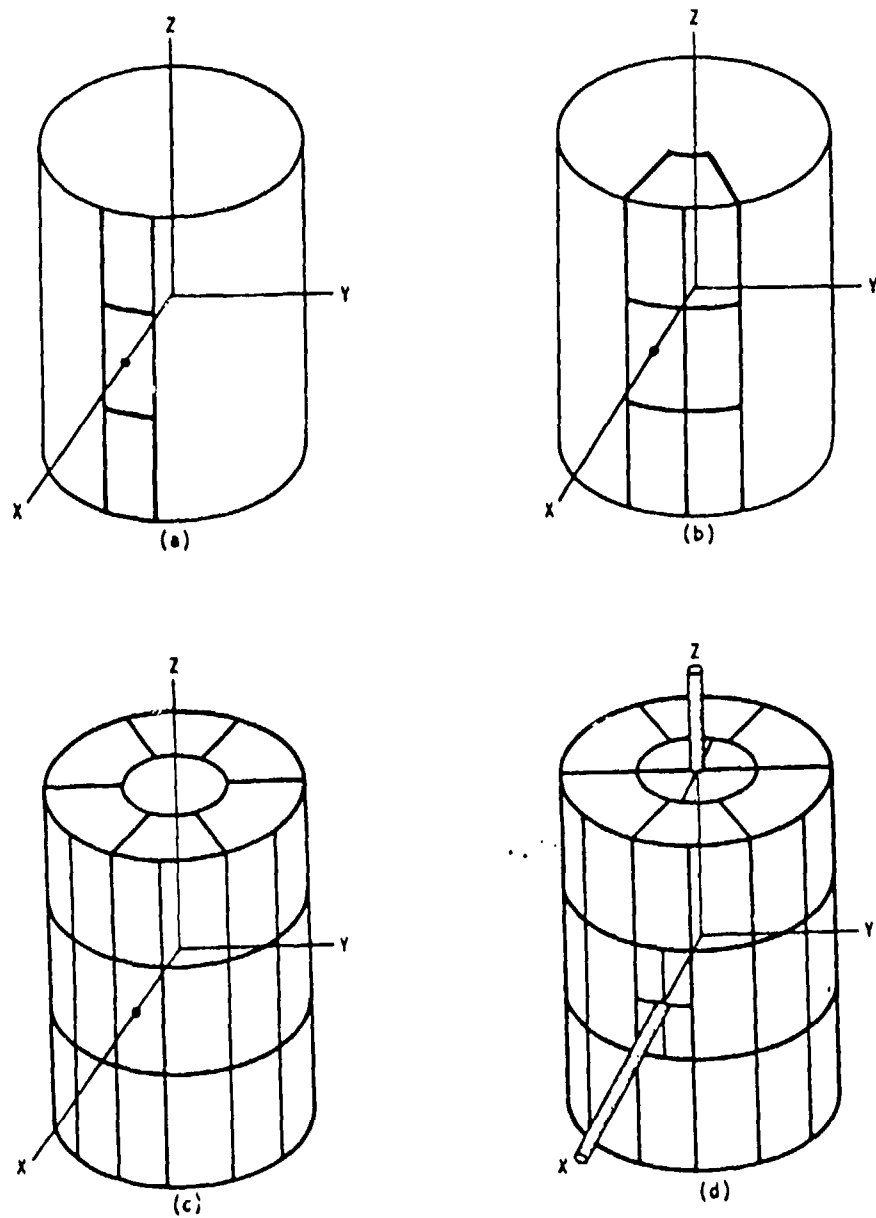


Figure 3.41 Development of Surface Model for Cylinder with Attached Wires [41]

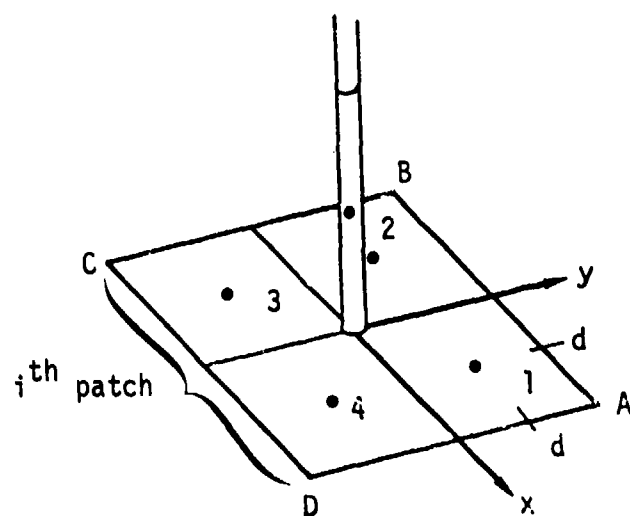


Figure 3.42 Detail of the Connection of a Wire to a Surface at the  $i^{\text{th}}$  Patch [41]

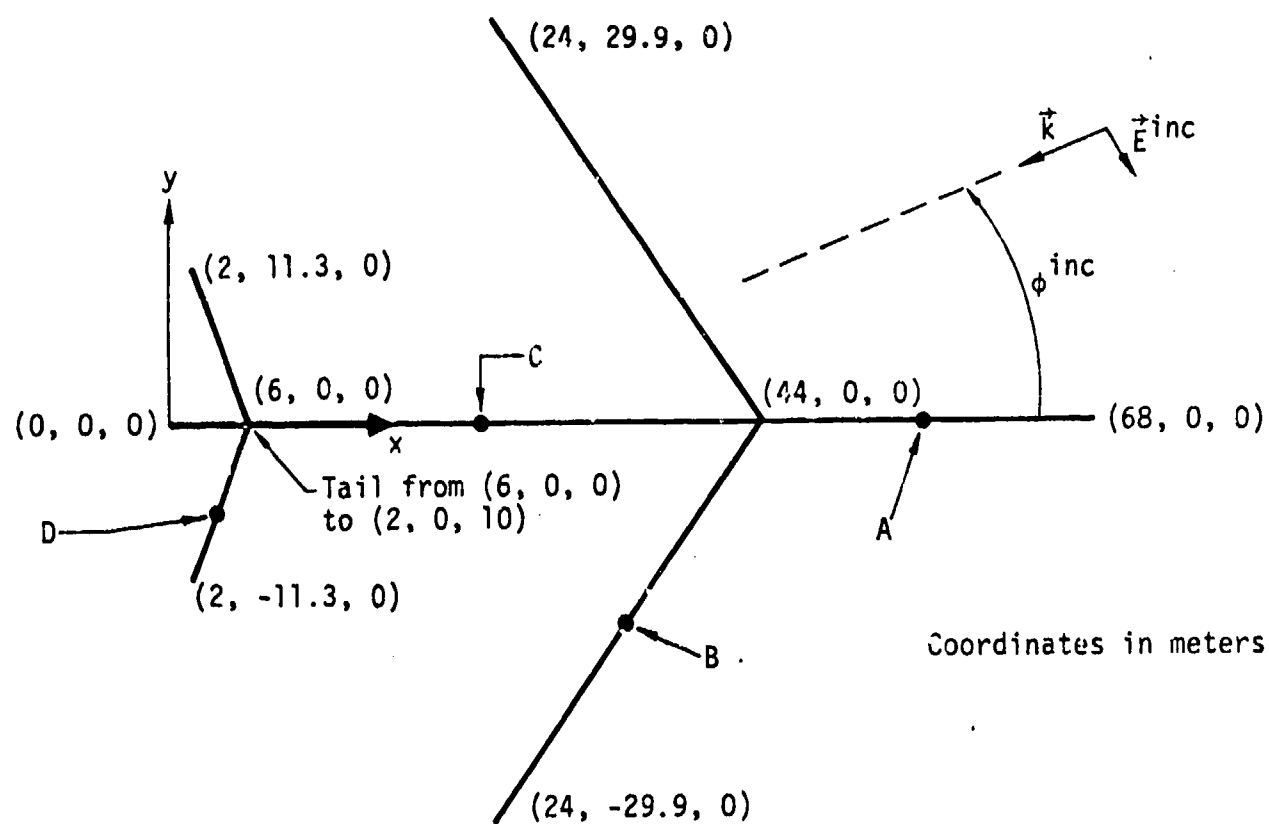


Figure 3.43 Stick Model of Aircraft Used to Test NEC2 [44]

field in the plane of the wings and fuselage. For the example calculation,  $\theta_{inc}$  was taken equal to zero, i.e. head-on incidence. The frequency of the exciting field was 3 MHz ( $\lambda = 100$  m) and the overall length of the aircraft was 68 m. Table 3.2. shows bulk currents at four positions on the aircraft. There were no measurements or calculations with which to compare these results.

The next example calculation was the scattering of a plane wave by a sphere. Figure 3.44 shows the patch selection used for this problem. The patches are selected to have approximately square shape at all latitudes. There were 80 patches total. The wavelength of the incident radiation was 100 m and the sphere had a radius of 46 m. Figure 3.45 shows the scattering cross section as a function of angle compared to analytical results from the University of Michigan. There are two cross sections represented in Figure 3.45. The first set of results are represented by a solid line (analytical result) and the dots (NEC calculation). These are results for scattering to an angle  $\theta$  in the plane of the incident  $\vec{k}$  and incident  $\vec{E}_0$  (E-field scattering). The second set of results includes the dotted line (analytical results) and crosses (NEC calculation) which represent H-field scattering, that is scattering at an angle  $\theta$  but in the plane of the incident  $\vec{k}$  and incident  $\vec{H}_0$ . The agreement with analytical results is excellent.

The third example uses both the EFIE and MFIE solution capabilities of NEC. Figure 3.46 shows a cylinder with two attached wires. This is the same object which was shown in Figure 3.3.40 as an example of MFIE patching. The radiation pattern from this structure has been calculated and the values compared to measurements made by Alberston et al. [46]. Figure 3.47 shows a comparison of the calculated intensity distribution (solid line) with the measurements (dots). The distribution is calculated as a function of angle  $\theta$  in the plane of the two antennas.

Next the eleven evaluation criteria are discussed.

1. Computer Memory: This code will require more than 100k<sub>8</sub> words except for certain small problems. Recommendations from the AMP User's Manual for a CDC 6700 state that 210k<sub>8</sub> words should be reserved for loading the program. The NEC program listing has over 5000 cards.

2. CP Time: The CP times which are available for the examples are for one frequency only. For the stick model of the aircraft the matrix fill and inversion time was 1.2 sec and for the sphere problem it was 1.1 sec. For the



Table 3.2 Values of Bulk Current for the Stick Model Aircraft  
Shown in Figure 3.43 [44]

Physical Position (see Figure 3.43)	Bulk Current (Arbitrary Units)
A	0.18
B	0.08
C	0.07
D	0.005

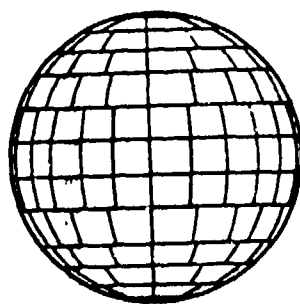


Figure 3.44 A Diagram of the Patch Segmentation Used to Represent the Scattering From a Sphere [44]

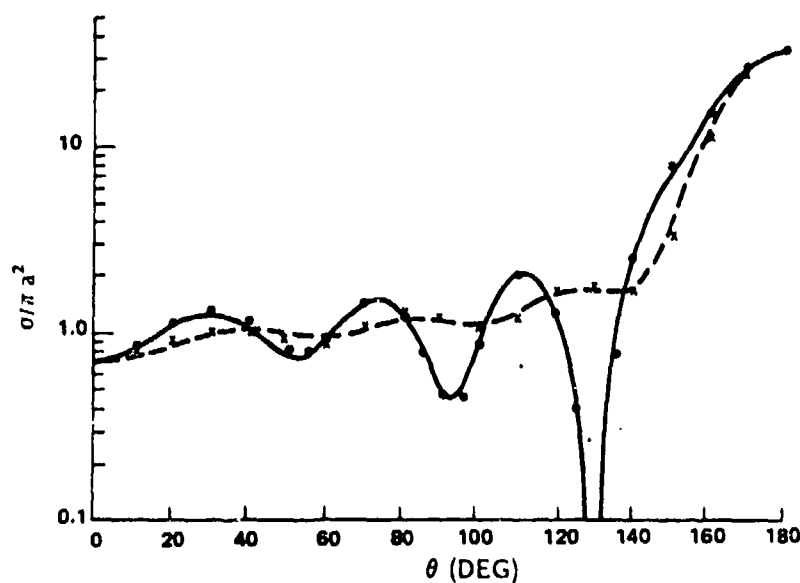


Figure 3.45 Graph of the Bistatic Radar Cross Section as a Function of Angle  $\theta$  Between Incident and Scattered Directions. The Solid and Dotted Lines are Analytical Results of the University of Michigan. Solid Line and Dots Represent E-Plane and Dashed Line and Crosses Represent H-Plane Scattering [44].

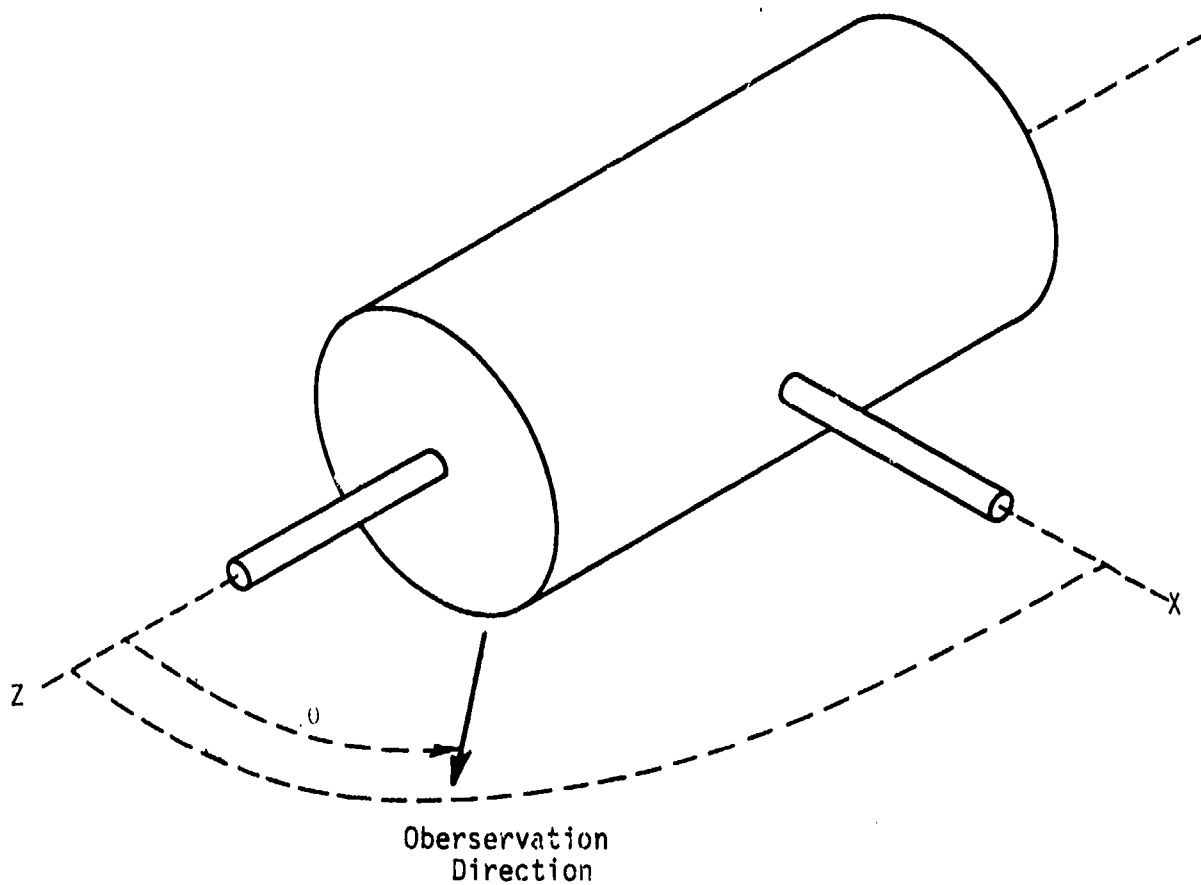


Figure 3.46 Diagram of the Cylinder/Wire Structure Used for Demonstrating the NEC, EFIE, and MFIE Hybrid Techniques [44]

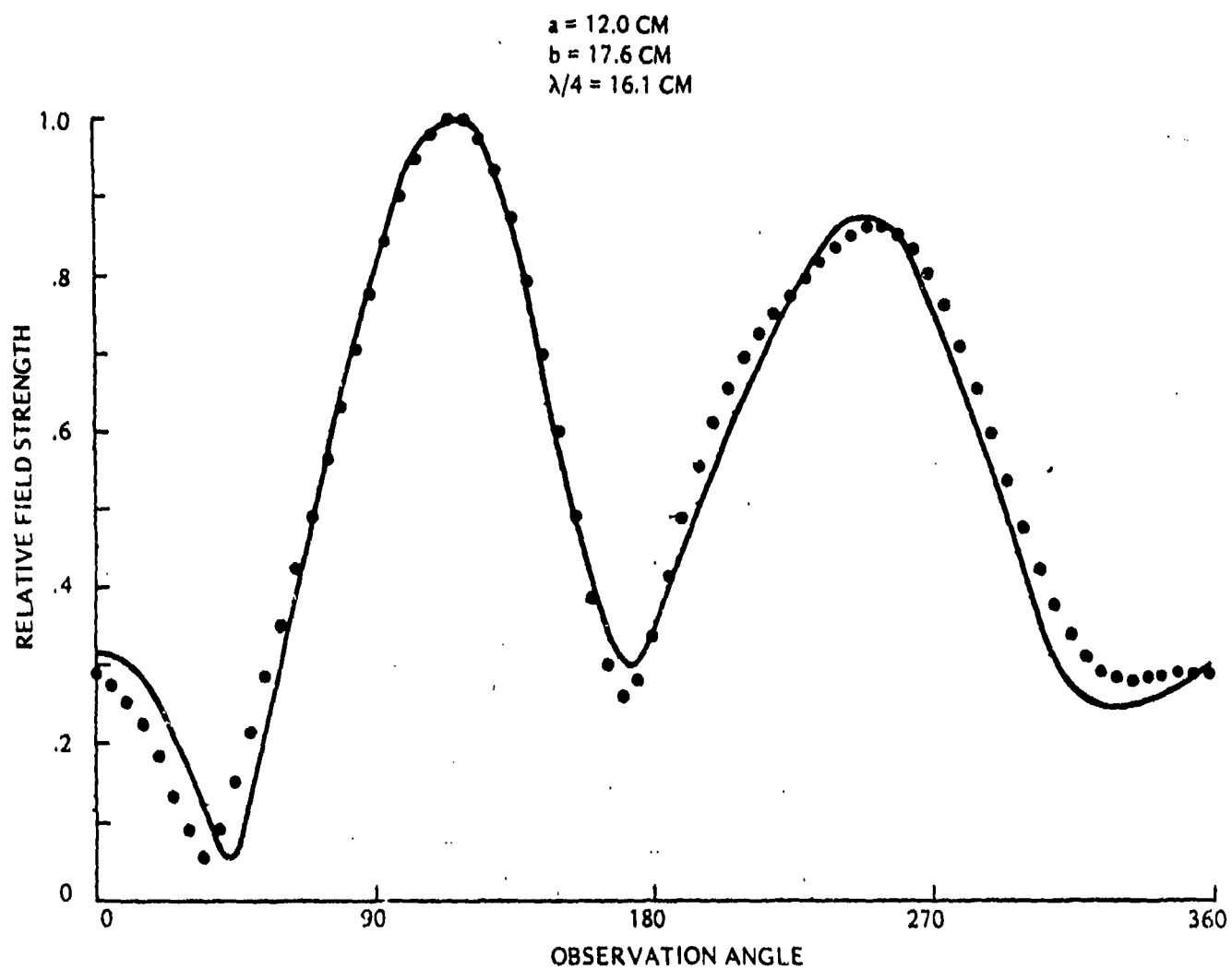


Figure 3.47 Comparison of Calculations of Radiation Pattern from a Cylinder/Wire Structure to Measurements Made by Albertson [46]

cylinder/wire problem, however, the time was 12.6 sec. In order to determine a time dependent transient response, a Fourier inversion will have to be performed. This requires typically 200 frequency calculations so therefore the actual execution time would be longer. The execution times would be more than about 4 minutes for the stick model and the sphere, and would be more than about 40 minutes for the cylinder/wire. An aircraft model for a lightning coupling model would almost certainly require detail exceeding that used in the cylinder/wire problem.

3. Numerical Accuracy: NEC2 is probably one of the most accurate codes discussed in this report. There have been extensive efforts to reduce numerical errors in integration routines, for example. The good comparison with sample calculations (Figure 3.45) and with experimental data (Figure 3.47) supports this conclusion. There is one problem. For certain voluminous structures, the calculated response can be dominated by spurious internal resonances. Care must be taken to avoid calculations at these frequencies or to include extra physical structure inside the cavity to destroy the resonance.

4. Physical Accuracy: Because NEC2 has both EFIE and MFIE solution ability, the physical representation of both thin structure (by wires) and bulky structure (by patches) is very accurate. The patch representation of the cylinder/wire combination is shown in Figure 3.41.

5. User Orientation: Both AMP and NEC have the best documentation of any of the codes which have been reviewed, except possibly for THREDE. For both codes there is a user manual with example inputs and outputs, a systems manual which describes the subroutines and variable names, and an engineering manual which describes the theory on which the code is based. The code itself is very large, about 5000 cards, and so any modifications will require an intelligent user.

6. Frequency Range: The code can handle fairly high frequencies,  $\sim 100$ 's MHz, provided that the diameter of all wire segments remain small compared to the wavelength of the exciting radiation. As described in (3) some physical structures may show artificial resonances at frequencies where the structure has internal resonances.

7. Attached Stroke: NEC could model an attached stroke very well using wire segments to model the return stroke channel and using NEC's capability

to load the wire segments inductively, resistively or capacitively. Distributed or discrete voltage and/or current sources can simulate the source.

8. Test Case: NEC has extensive methods to treat lossy ground planes. Also, it could represent the return conductors that are usually employed in a test case and it can represent current injection. Only non-linear features of the test procedure, spark gaps for example, could not be modeled. This is a severe restriction because spark gaps will almost certainly be used in the test configuration to produce large rates of change of electric field.

9. Aircraft Size: The code can model both large and small aircraft, but large aircraft might require excessive computer memory.

10. Lightning Environment: A limitation of the NEC code is that it is written in the frequency domain. In order for the time domain response to be calculated, the system must be a linear one in order that a Fourier inversion can be performed. Therefore, NEC will not be able to treat the non-linear parts of the lightning environment. Some modification of the code would be required to treat near field excitation.

11. Experimental Verification: There has been substantial verification of NEC calculations although the verification has been by comparison with analytical solutions of problems as much as by experiment. NEC has not been used to model the full detailed structure of any aircraft.

#### 3.3.4.3 SYR [41-48]; CHAOS [49-50]

Chao and Strait [47] at Syracuse have developed a method (which we will denote SYR) of solving the EFIE for general structures composed of wire segments. The method has been extended by Armour [49-50] and a computer code CHAOS based on the method has been written by Armour. The original work by Chao and Strait focused on radar cross sections and radiation patterns from antennas. Armour's published work has focused on the NEMP response of geometrical objects and aircraft.

The method developed by Chao and Strait uses the frequency domain EFIE in the thin wire approximation. The form of the EFIE used in the SYR method is similar to equation (3.2.11). The integral equation in the one dimension of the wire length has been reduced to a set of linear equations by

the method of moments. Galerkin's method has been used rather than point matching, and the test and weighting functions employed are triangle functions. The use of Galerkin's method with triangle functions enabled the integrals to be performed analytically. The expansion functions were chosen to conserve current at a junction of several wire segments. The method includes the possibility of loading each wire segment by defining the impedance relationship on a segment.

A computer code has been written to implement a numerical solution by the method described above. The code was written to determine radiation fields produced by discrete sources in the wire structures or by scattering of an incident plane wave. A listing and some documentation on the code are available, but the information is not nearly as extensive as that provided with NEC. The problems which have been solved are mostly antenna radiation problems. Figure 3.48 shows a wire cross scatterer that has the basic shape of an aircraft. The scattered radiation fields have been calculated for a plane wave excitation incident on the cross from the top as shown in Figure 3.48. Figure 3.49 shows the bistatic radar cross section or scattering pattern for the cross. Chao and Strait have calculated other radar cross sections but none of significance to aircraft or lightning coupling. There was no explicit comparison to any other calculation or to experimental work.

In work performed at the Atomic Weapons Research Establishment (AWRE), Armour has used the same basic method to develop a code named CHAOS that solves for induced currents and scattered fields from wire grid structures. There are improved routines that treat junctions between wire segments and there is an added capability to invert large, dense matrices. There is no listing or documentation for the code [49-50].

Computations of EMP induced surface currents using CHAOS have been performed for several geometrical structures and several aircraft. In addition, some measurements on a wire grid cylindrical structure have been made.

Figure 3.50 shows a wire grid model of a fat cylinder which has been used to evaluate the errors in wire grid modelling of surfaces. Both calculations and measurements have been performed using the model. The measurements were performed in a travelling-wave simulator which produced a plane wave excitation with a double exponential time dependence similar to a NEMP. Figure

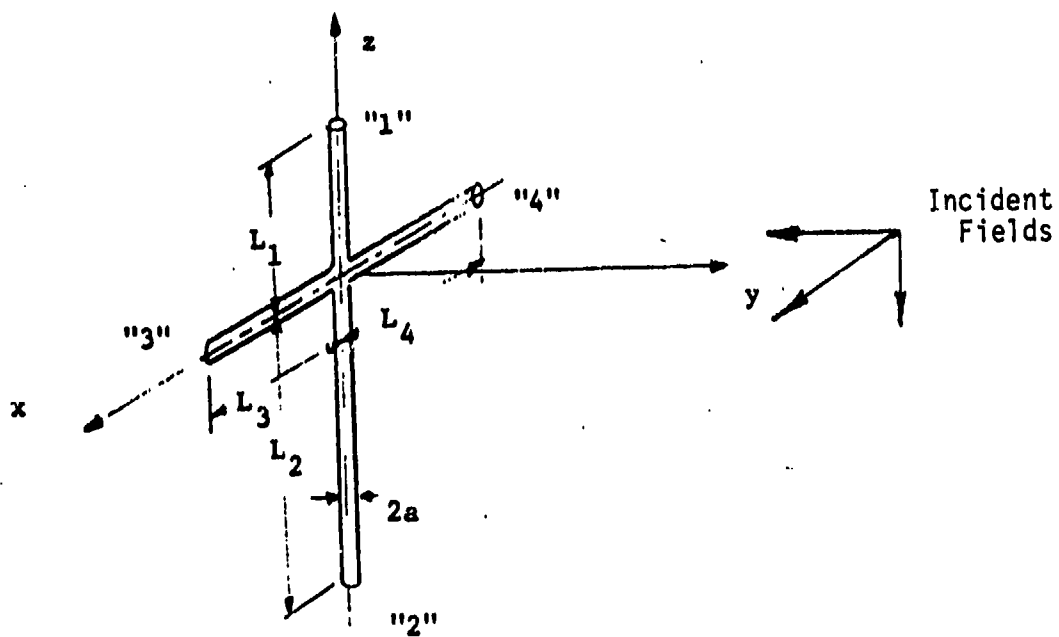


Figure 3.48 Wire Cross Scatterer



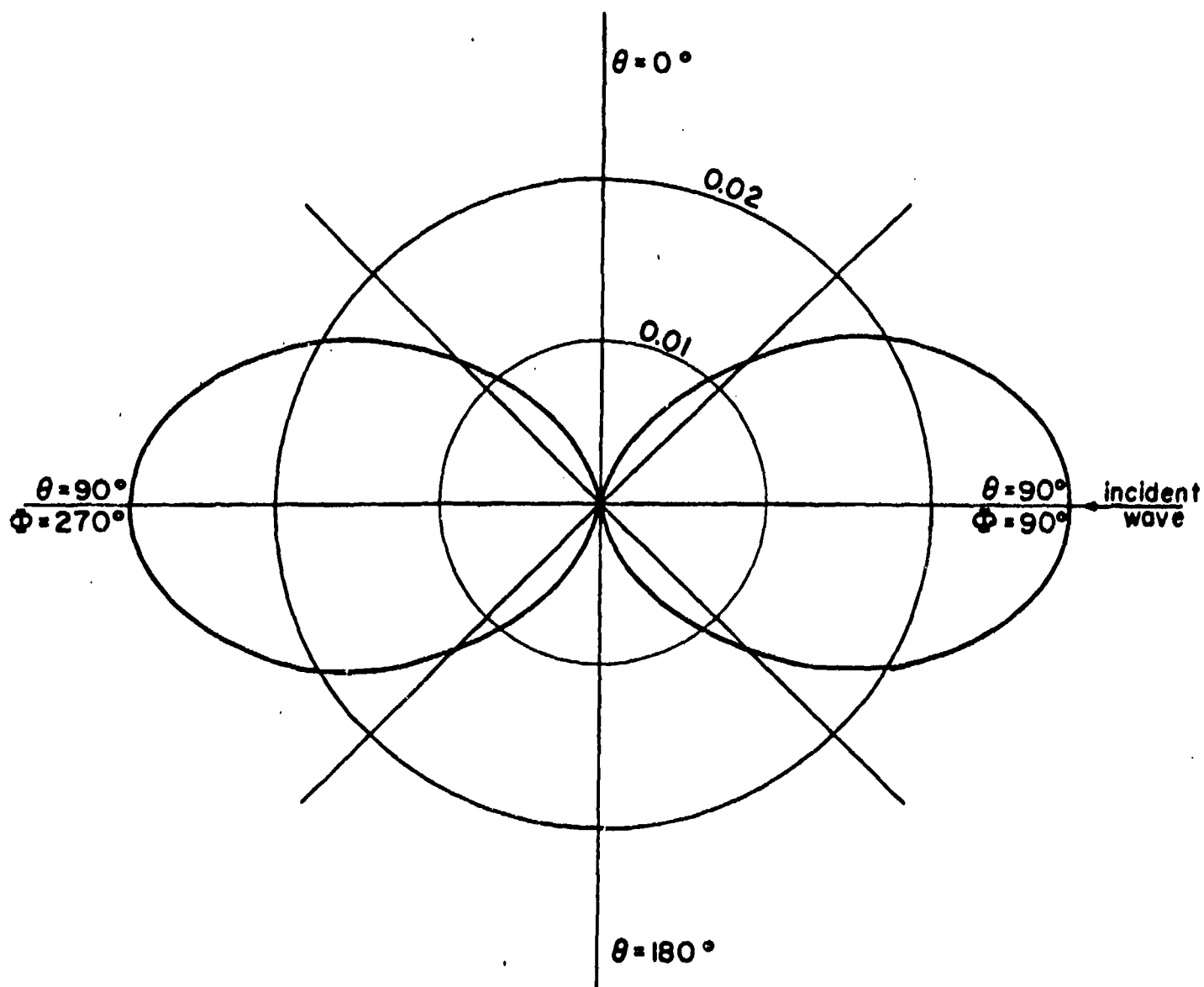


Figure 3.49 Bistatic Radar Cross-Section  $\sigma_{\theta\theta}/2$  Pattern in the Plane  $\phi + 90^\circ, 270^\circ$  for the Wire Cross [47]

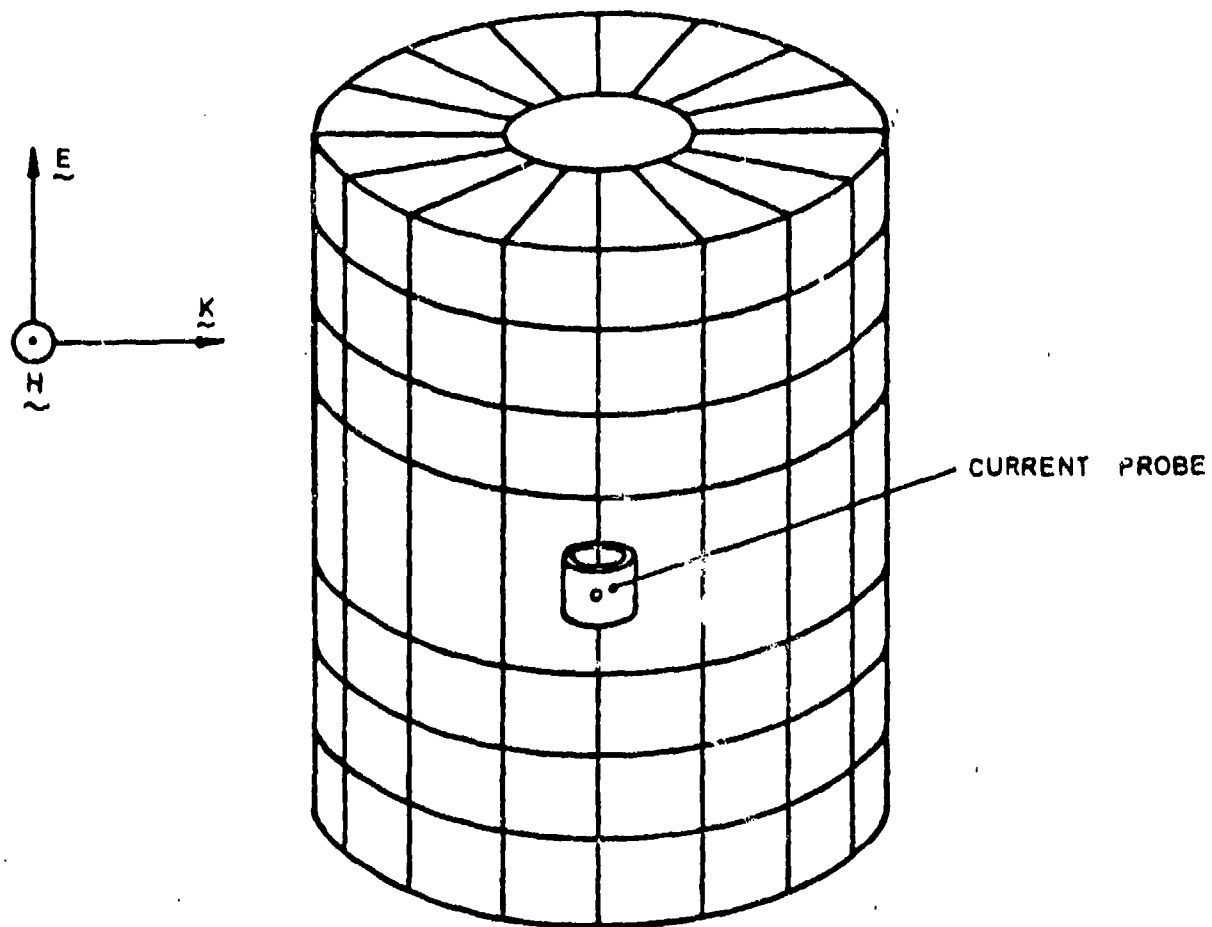


Figure 3.50 Wire Grid Model of a Fat Cylinder  
[49]

3.51 shows a comparison of the total axial current as measured in the simulator and calculated using CHAOS. The agreement in pulse shape is fairly good. Figure 3.52 shows the comparison of CHAOS calculations with measurements for the frequency domain. The predicted frequency spectrum has the overall basic shape of the measured response, but doesn't show the fine structure that appears in the measurements.

CHAOS has also been used to model the F111 fighter. A diagram of the wire grid structure that has been used in this model is shown in Figure 3.53. This model represents a fairly complete model of an aircraft for the wire grid technique. There were 756 wire segments used in the model and the aircraft was 22.4 m long. The wire radius was chosen so that the area of all the wires is equal to that of the modelled surface. The effects of wire radius have been discussed by Castillo et al. [51]. The F111 model was illuminated by a NEMP excitation. The EMP fields were incident on the top of the aircraft and had a polarization either parallel or perpendicular to the fuselage. Table 3.3 shows a comparison of the peak transient surface currents predicted by CHAOS and reported by Holland [16]. The agreement is fairly good for peak values. Figures 3.54 and 3.55 show the current density as a function of time for TP 208. The data reported by Holland in Figure 3.55 include both calculations by THREDE (discussed in Section 3.3.2) and measurements made at an HPD facility at AFWL. The agreement between the measurements and the two calculations is good. Note that the THREDE and measured data are the time derivative of the surface current density,  $\dot{J}$ , whereas for the CHAOS' data, the surface current density  $J_s$  has been calculated. Figures 3.56 and 3.57 show the frequency spectra for CHAOS and for the data reported by Holland. The frequency spectra are difficult to compare. The data in Figure 3.56 need to be multiplied by angular frequency  $\omega$  before they are compared to Holland's data in Figure 3.57. The CHAOS data, after being multiplied by frequency and given an arbitrary vertical position, are shown in Figure 3.57. These data do not compare as well to the measurements as do the THREDE data, especially in the region of 10-30 MHz. The Anglo-French Jaguar aircraft has also been analyzed using CHAOS but there are no measurements or other calculations with which to compare the CHAOS results.

Next, the eleven evaluation criteria are discussed.

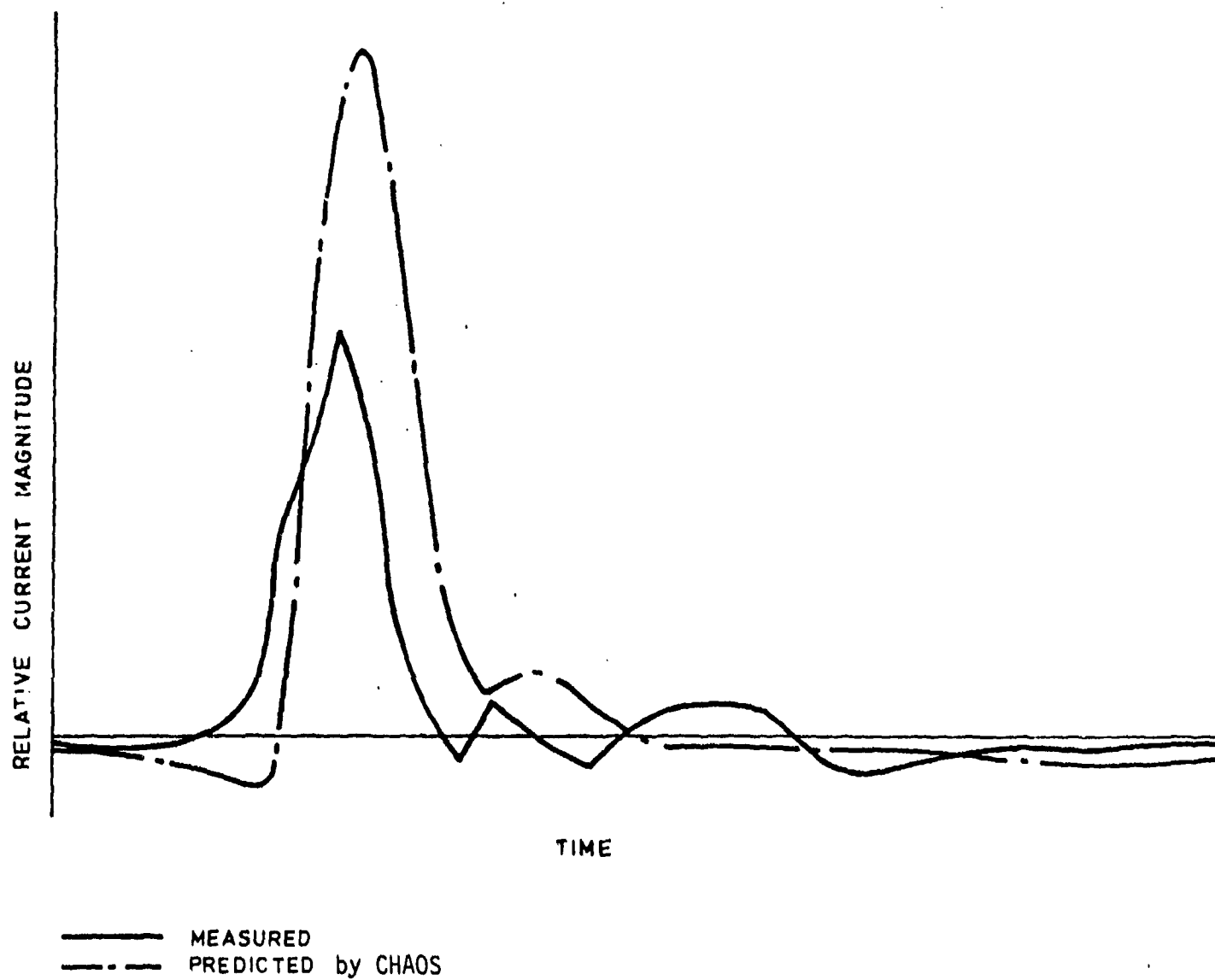
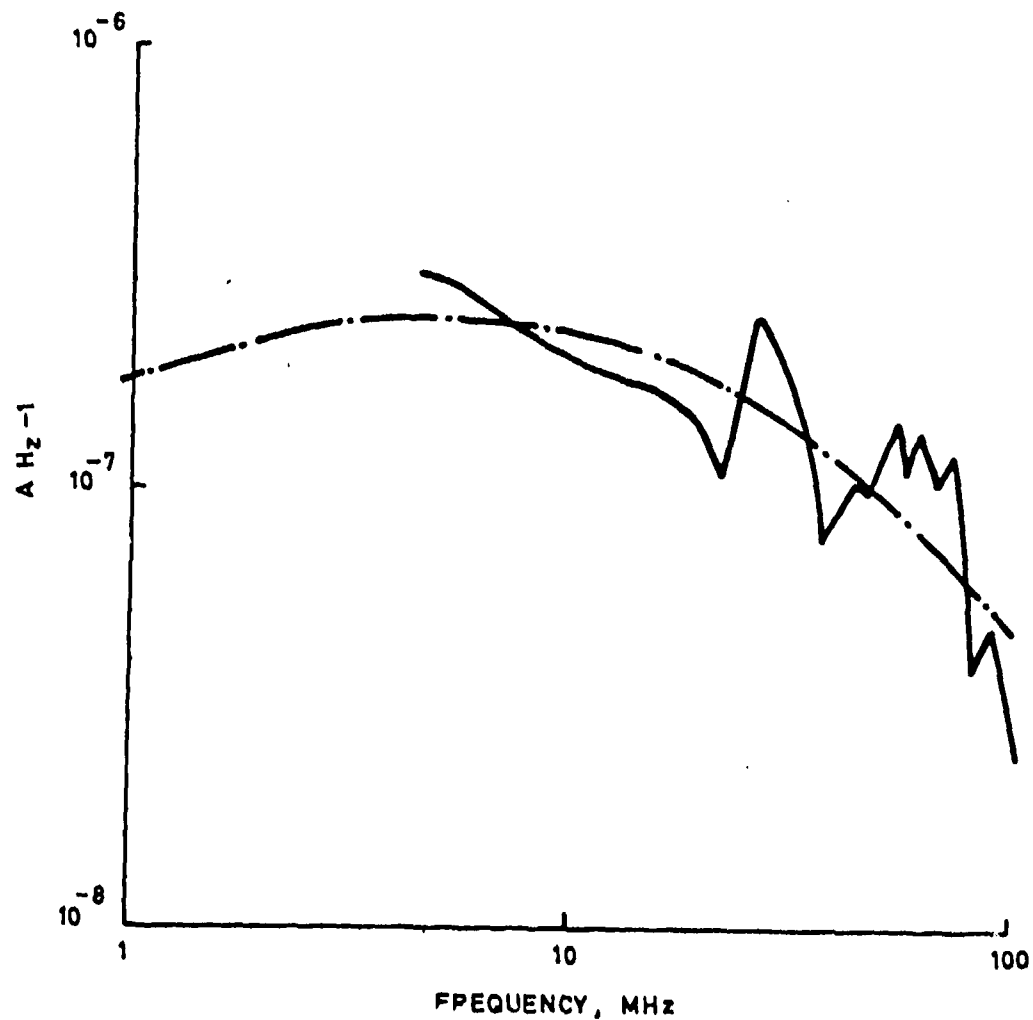


Figure 3.51 Predicted and Measured Time-Domain Response for Total Axial Current for the Dustbin. Double-Exponential Incident Field. Vertical Scale Shows Relative Current Magnitudes [49]



— . — Predicted by CHAOS  
 — Measured

Figure 3.52 Predicted and Measured Frequency Domain Response for Vertical Wire Current for the Bird Cage [49]

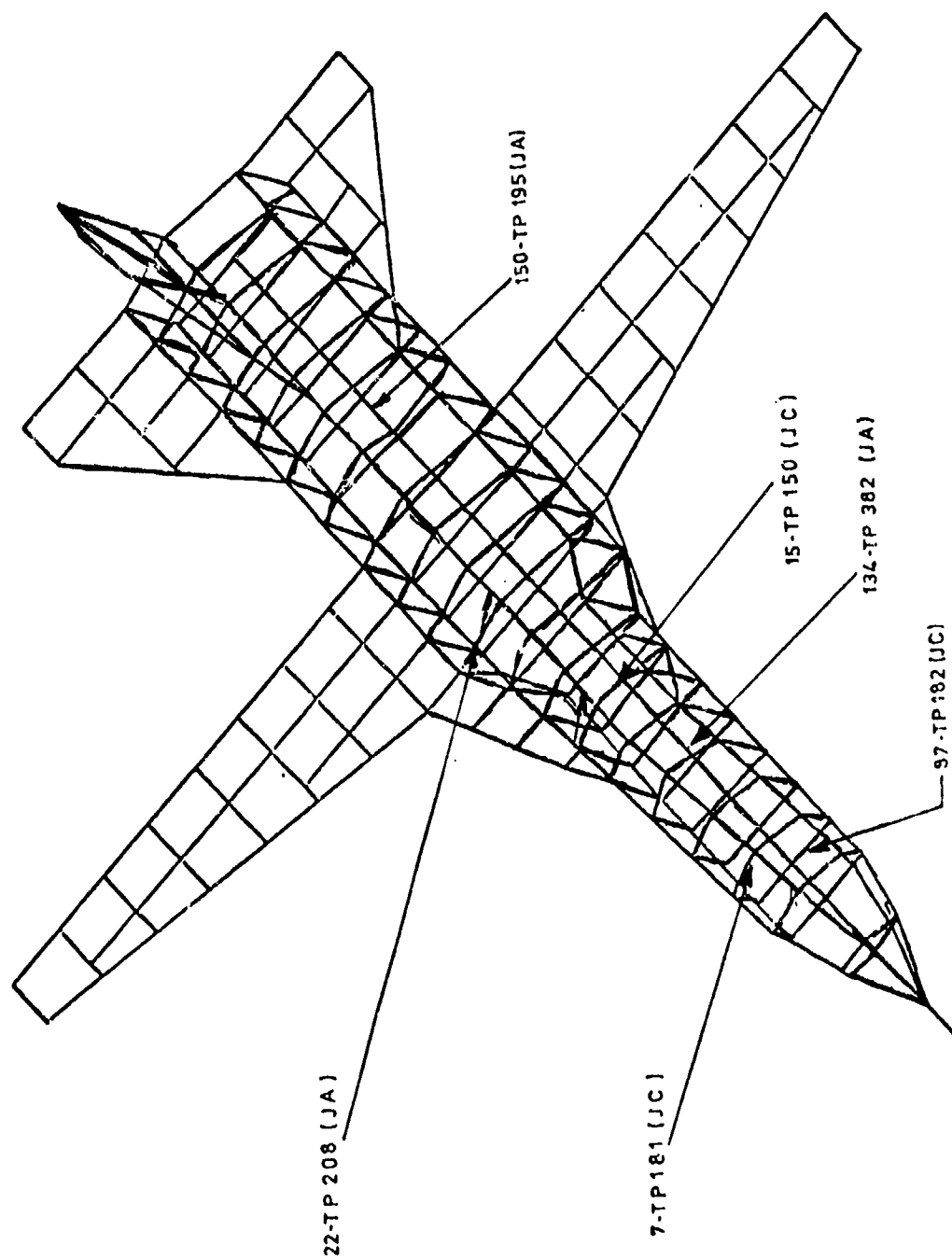


Figure 3.53 CHAOS Wire Model of F111 Swing-Wing Aircraft. Length of Fuselage 22.4 m  
Wing Span 19.2 m. Total Number of Segments - 756 [50]

Table 3.3 A Comparison of Peak Surface Currents for the F111 as  
Calculated by CHAOS and Reported by Holland [50]

(a) E-field parallel to fuselage (axial current).

Test Point	Wire Number	Current Density A/M	
		Measured	Predicted
TP 382	134	285	400
TP 208	22	300	310
TP 195	150	220	285

(b) E-field perpendicular to fuselage (circumferential current)

Test Point	Wire Number	Current Density A/M	
		Measured	Predicted
TP 181	7	150	85
TP 182	87	115	80
TP 150	15	125	125

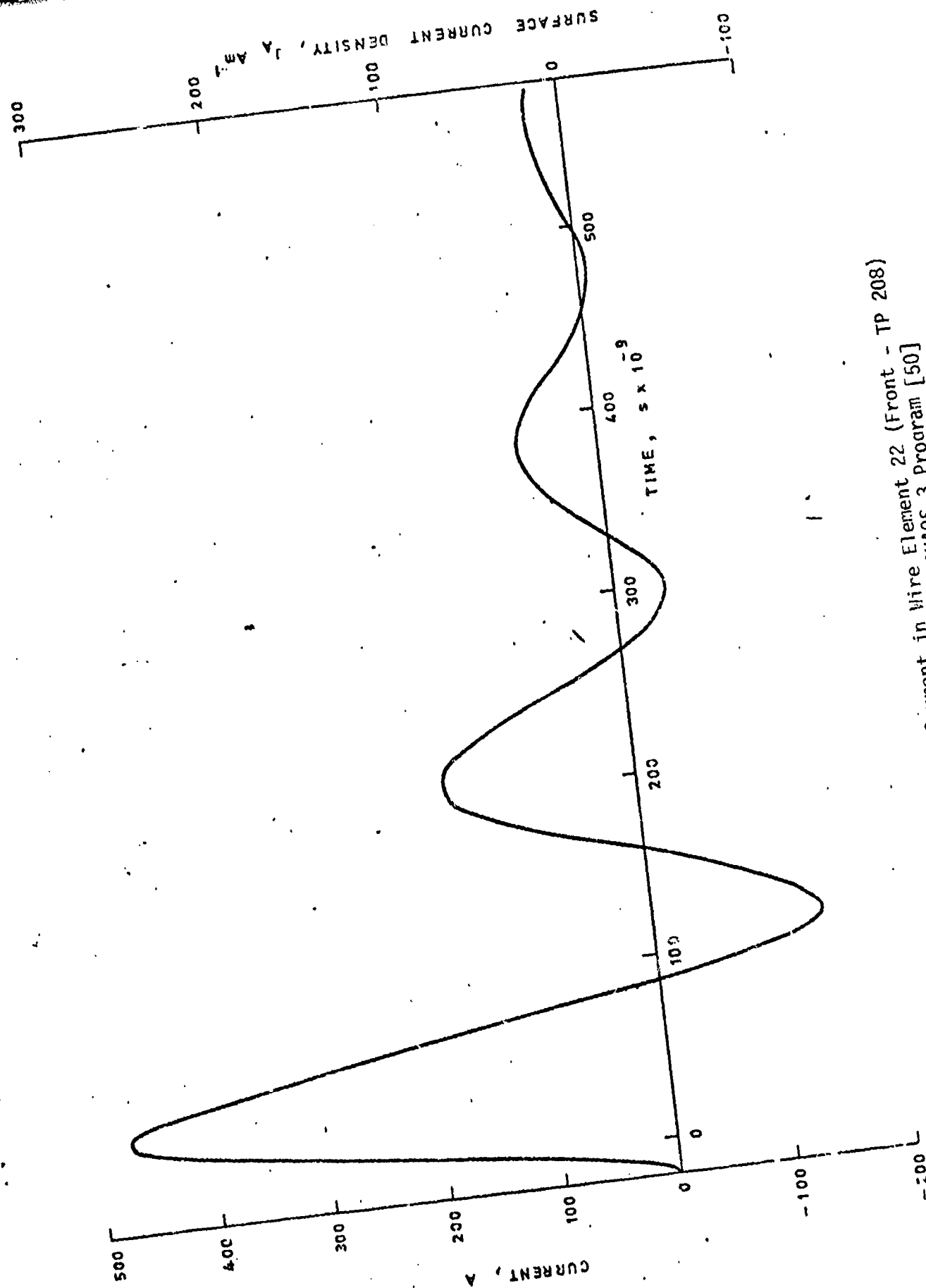


Figure 3.54 F111 Aircraft. Current in Wire Element 22 (Front - TP 208)  
E-Field Parallel to Fuselage. CHAOS 3 Program [50]



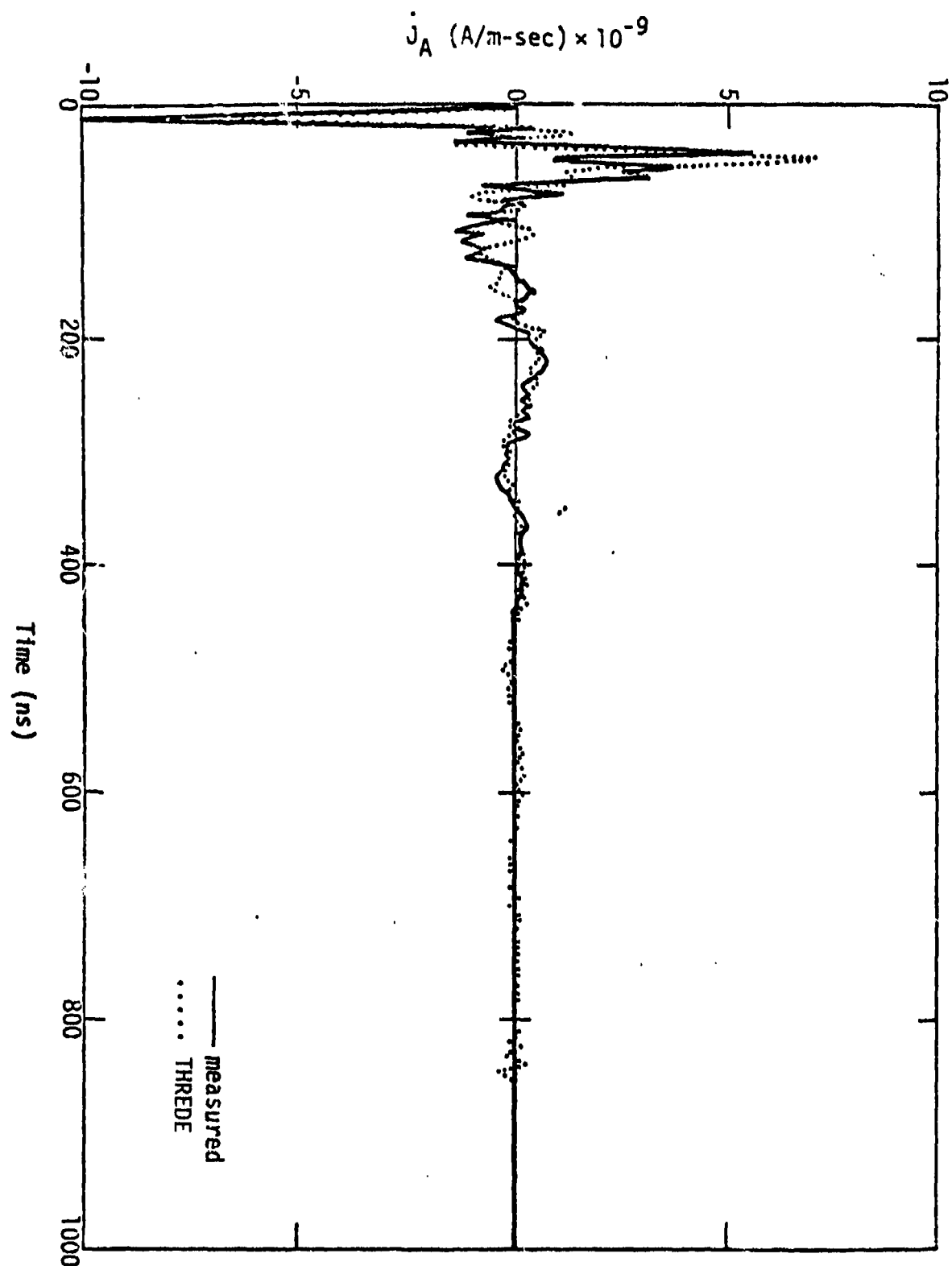


Figure 3.55 Measured versus THREDE Calculations of Axial Current Rate of Change at Test Point 208 in the Time Domain [16]

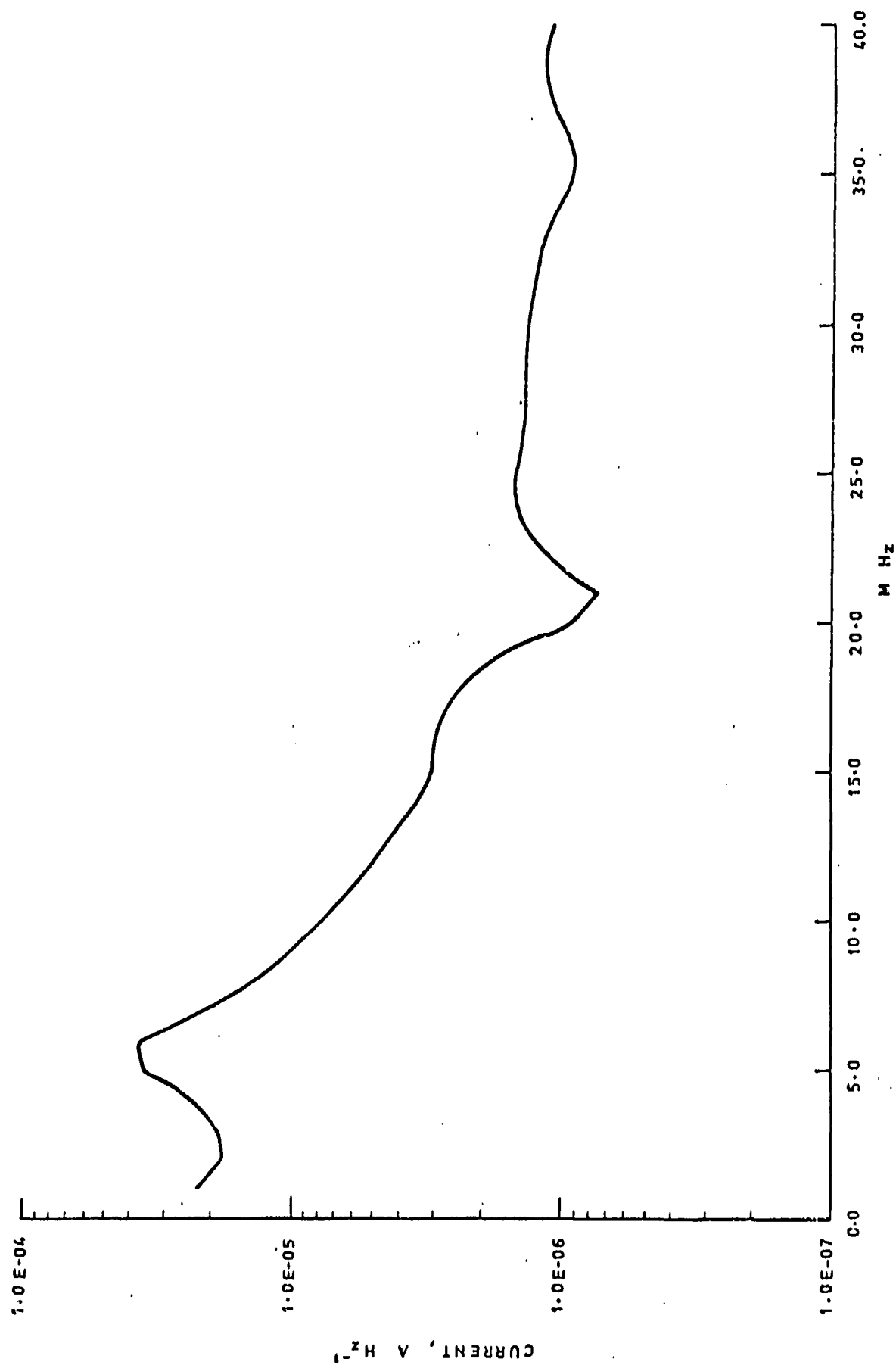


Figure 3.3.55 F111 Aircraft. Current in Wire Element 22 (F-ent) - TP 208  
E-Field Parallel to Fuselage. Chaos 3 Program

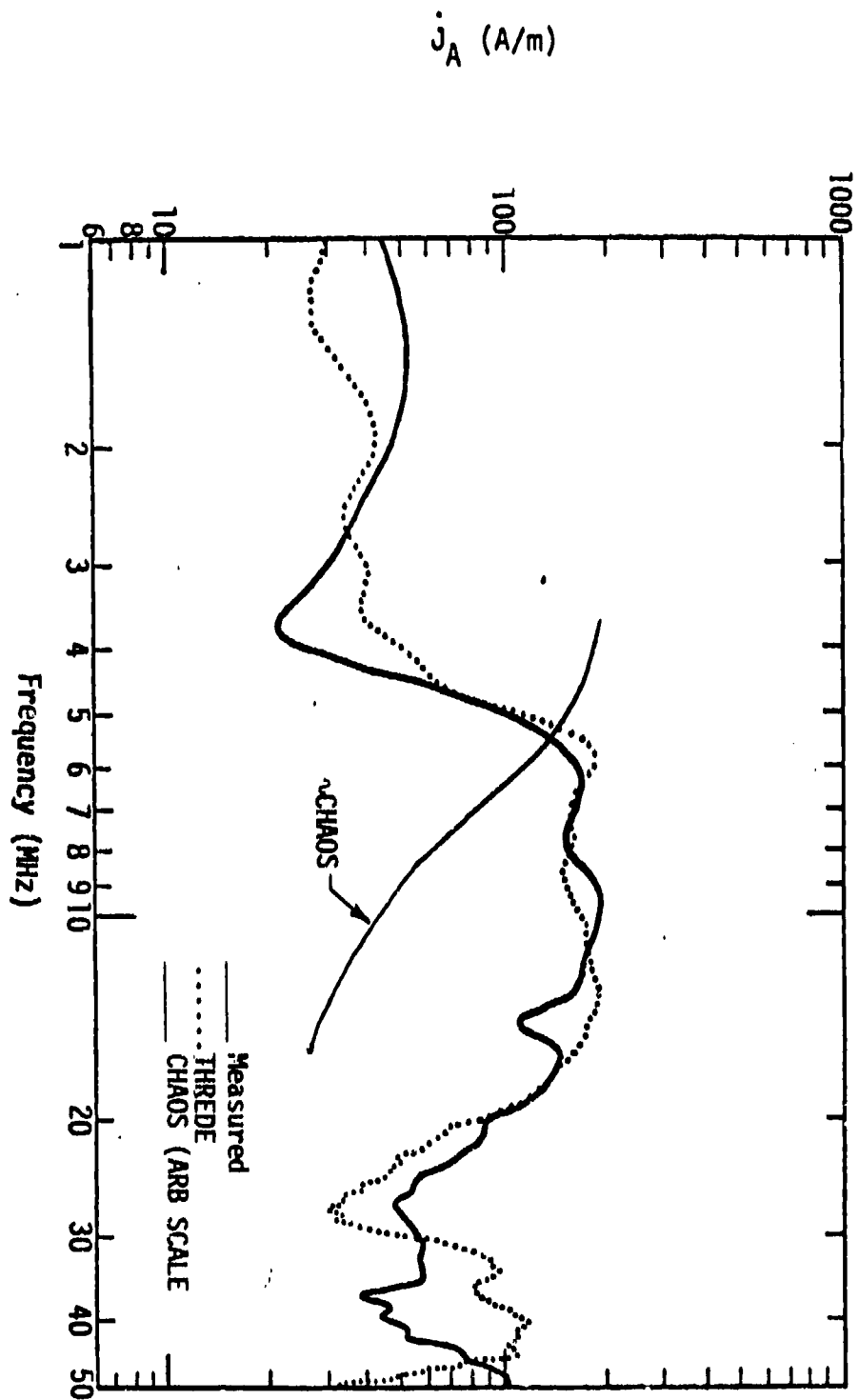


Figure 3.57 Measured, THREDE Calculated, and CHAOS Calculated Axial Currents at Test Point 208 in the Frequency Domain [16,50]

1. Computer Memory: There is no mention of computer memory requirements for the original Chao and Strait work which was implemented on an IBM 360/50 computer. For a simple structure of 50 wire segments or less, the code probably uses less than  $100k_8$  words. Bevensee and Brittingham [35] have taken a version of the Chao and Strait program (1100 cards) and performed benchmark calculations on a CDC7600. The code required  $31k_8$  words of memory for a structure with less than 50 wire segments. The CHAOS code certainly requires more than  $100k_8$  words since it has the ability to invert large, dense matrices and can include  $>700$  elements. The code is currently implemented on a Cray I computer at AWRE.

2. CP Time: There is no mention of computer run time in any of the reports available. However, for a problem such as the F111, very large matrices will have to be inverted, perhaps as large as  $700 \times 700$ . This must be done at many frequencies in order to get a time domain response.

3. Numerical Accuracy: The codes are limited in their accuracy by the type of expansion function chosen to represent the current and by the boundary conditions used at wire junctions. CHAOS has similar limitations. Both methods, when applied to wire grid models of closed voluminous surfaces, are susceptible to spurious resonances inside the structure. Also, in a comparison of SYR with WIRANT, OSU and BRACK [52], the SYR code was not as accurate as the OSU code.

4. Physical Accuracy: In order for an aircraft coupling calculation to be performed, an all wire grid model of the aircraft needs to be constructed. These methods, therefore, probably cannot treat complicated surfaces as efficiently or as well as codes such as NEC2 which employs both surface and wire elements to model an object.

5. User Orientation: There is a listing of the SYR code with some documentation, however, there is no listing or documentation for the CHAOS code.

6. Frequency Range: The CHAOS code has the ability to do both high and low frequencies. The upper frequency for a wire grid model is determined by the wire radius "a" since it must remain large compared to "a". typically, the upper limit is 50 MHz or larger. Armour recommends that a minimum frequency of  $C/(1000L)$  be used. For lengths of 1 m, the minimum frequency is 0.3 MHz.

7. Attached Stroke: A lightning attached stroke channel could be modelled as wire segments. The Syracuse code can model the channel as reactively loaded wire segments. CHAOS doesn't have this ability although it could probably be incorporated in the code. Non-linear aspects of the attached stroke could not be treated, however, since both codes are written in the frequency domain.

8. Test Case: Both the Syracuse and CHAOS codes could model some aspects of the test case. They could model the current injection as a wire segment (the Syracuse code can have a loaded wire segment if appropriate) and they could represent the return conductors that will probably be used around the aircraft. Neither code has the provision to do a ground plane, however. Also, both codes are written in the frequency domain and so they cannot handle the non-linear behavior that would occur in the test fixture.

9. Aircraft Size: CHAOS has been applied to fighter aircraft such as the F111 and the Jaguar. The code could model large aircraft except the spatial resolution and the upper frequency limit would be degraded.

10. Lightning Environment: Both codes can treat the current injection aspect of an attached stroke and both could handle the near fields of a return stroke with some rewriting of the codes. However, the codes are written in the frequency domain and rely on the linearity of the system to be able to construct the time domain response. Therefore, non-linear aspects of the lightning environment such as streamer and corona formation cannot be treated in a straightforward manner.

11. Experimental Verification: The method has been compared to measurements on geometrical shapes such as the bird cage (Figure 3.50) and the F111 aircraft. Frequency domain data for the F111 do not agree as well with experiment as THREDE predictions.

#### 3.3.4.4 Ohio State University [53-56]

Richmond [53-56] at Ohio State has solved an integral equation formulation of Maxwell's equations by the method of moments and has employed the thin wire approximation to treat wire structures. The method includes isotropic media and ground plane structures, and has been used to determine

antenna radiation patterns as well as scattered fields (bistatic radar cross sections, for example).

A unique and general integral equation called the Reaction Integral Equation (RIE) has been derived by Richmond. The RIE method encompasses both the EFIE and MFIE depending on a choice of test function. Although the method is more general than the EFIE or MFIE, it has been included in the EFIE section because the actual solution is implemented using the thin wire approximation and the method of moments. The class of problems that have been treated using this method is therefore very similar to those treated by the EFIE methods.

The fundamental principles used in deriving the RIE are the Reaction Theorem of Rumsey [57] and the Surface Equivalence Theorem of Schelkunoff [58]. Figure 3.58(a) shows a scattering problem in which sources  $M_0, J_0$  produce incident fields  $E_0, H_0$  which scatter from an object having surface  $S$  and volume  $V$ . Let  $E_s, H_s$  be the fields produced by the induced currents on surface  $S$ , and let  $E_t, H_t$  be the total fields. The equivalence theorem states that sources  $J_s, M_s$  given by

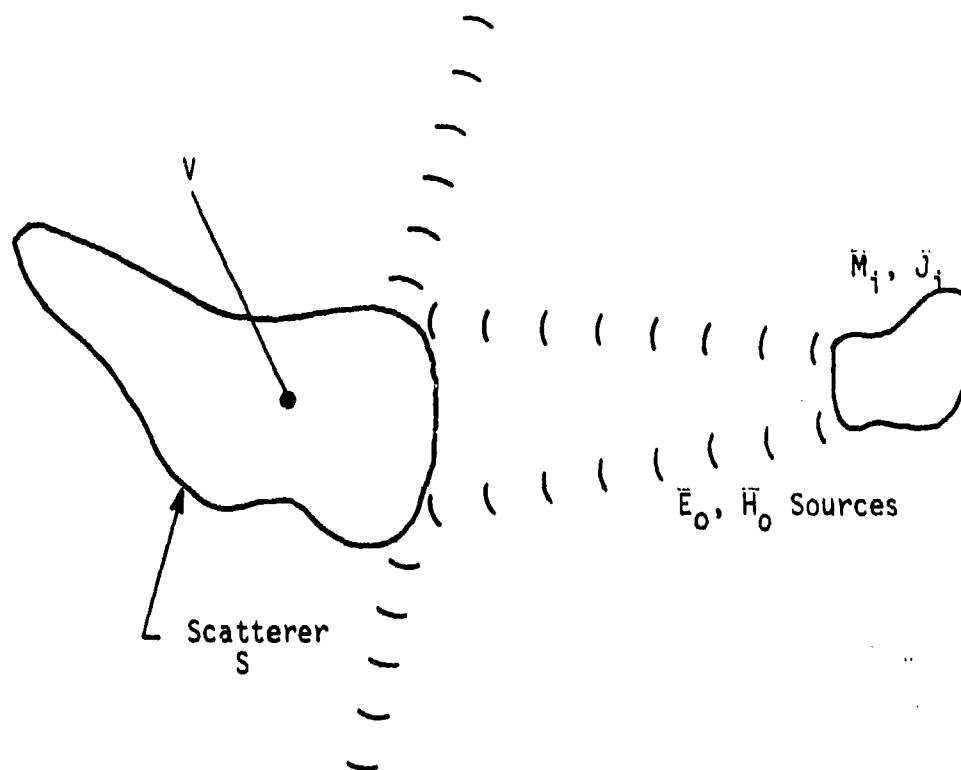
$$\begin{aligned} J_s &= \hat{n} \times \vec{H}_t \\ M_s &= \vec{E}_t \times \hat{n}, \end{aligned} \quad (3.3.4.4.1)$$

when installed in place of the scattering surface  $S$ , produce the same scattered fields outside the scattering surface  $S$  and produce fields  $-E_0, -H_0$  inside. This is shown in Figure 3.58(b).

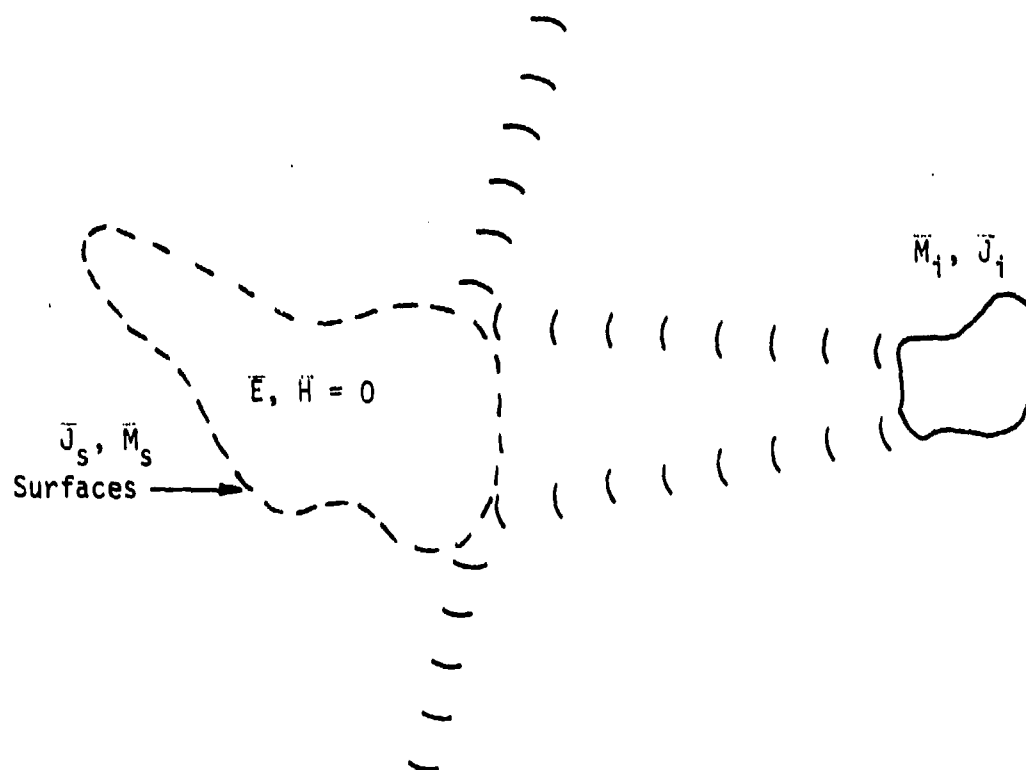
Now suppose that a test distribution of sources,  $J_t, M_t$ , are placed inside the surface  $S$  as shown in Figure 3.59. The Reaction Theorem now requires

$$\int (J_s \cdot \vec{E}_t - M_s \cdot \vec{H}_t) dS_t = - \int (J_0 \cdot \vec{E}_t - M_0 \cdot \vec{H}_t) dV \quad (3.3.4.2)$$

where  $S_t$  is the surface on which the test sources reside,  $E_t$  and  $H_t$  are free space fields from the test series, and  $V_0$  is the volume enclosing the sources  $J_0, M_0$  of the incident field. By an appropriate choice of test function, this equation can be cast into the form of the EFIE or the MFIE.



(a) Initial Physical Configuration



(b) Scatterer Replaced by Equivalent Sources

Figure 3.3.58 Representation of Fields and Sources Used in Deriving the Reaction Integral Equation

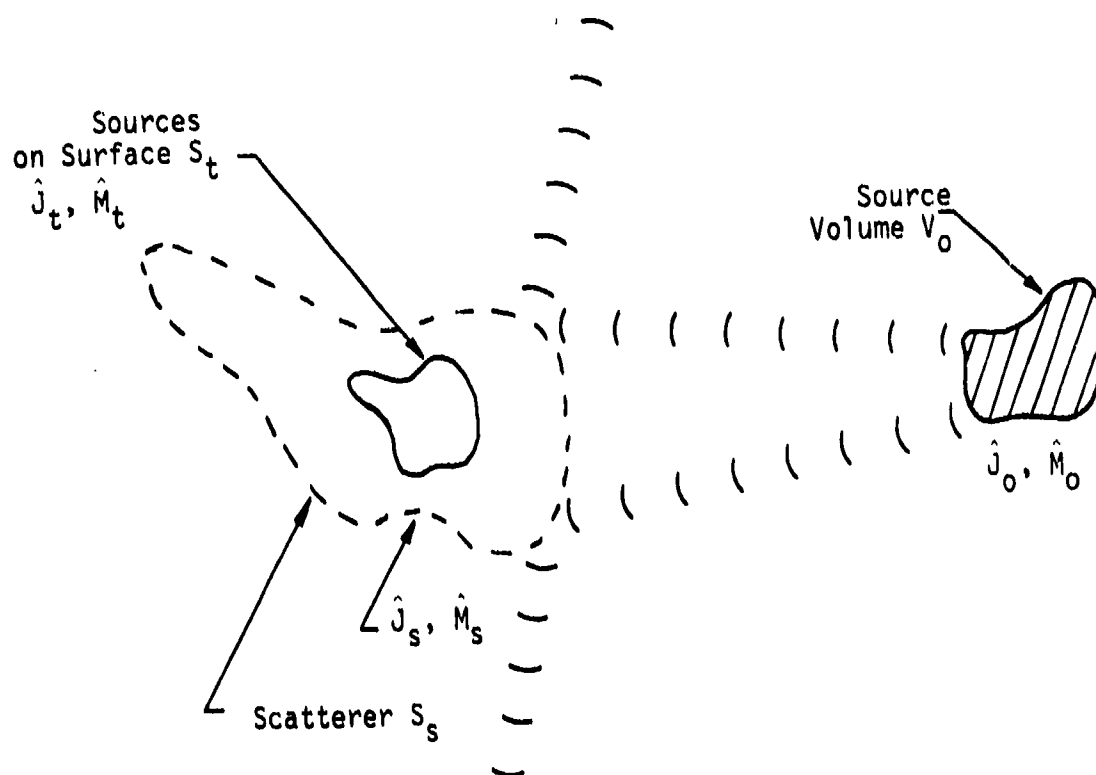


Figure 3.3.59 Test Source Configurations for the RIE



The scattering geometry is restricted to wire segments and the test sources are chosen to be filamentary electric dipoles with sinusoidal current distribution. The unknown currents  $J_s$  are described by a sum of sinusoidal expansion functions and using the thin wire approximation discussed earlier (Section 3.3.4.2), the RIE can be transformed to a set of linear equations

$$[Z] \underline{I} = \underline{V} \quad (3.3.4.3)$$

where the elements  $I_n$  of the vector  $\underline{I}$  are the coefficients of the expansion of  $J_s$ , the elements of  $[Z]$  are in the terms of integrals of test and expansion functions, and the elements  $V_n$  of  $\underline{V}$  are in terms of the driving source parameters  $J_0, M_0$ . This set of linear equations is similar to the set of equations which would result from the solution of the EFIE by Galerkin's method with sinusoidal test and by expansion functions. The constants  $I_n$  are the unknowns and can be determined from equation (3.3.4.3) if  $[Z]^{-1}$  exists.

A computer code based on this method has been written by Richmond. It is fairly well documented and many examples of the code's operation are given [53-56]. The code can treat antennas or scattering objects represented by wire grid structures. It can include homogeneous, linear, conducting materials around the wire segments and can include a ground plane. The wire segments may have finite conductivity and may have dielectric material around them.

According to Richmond [53] the method has been used to calculate radiation patterns and scattering cross sections for antennas and wire grid models of plates, spheres, cones, aircraft and ships. However, in the publications reviewed here, no aircraft models have been found. The data for scattering from a 2D circular cylinder for TE incident polarization has been calculated and compared to an eigenfunction method of solution. The data are shown in Figure 3.60 and the agreement between the OSU and eigenfunction methods is excellent for this example.

The eleven evaluation criteria will now be discussed.

1. Computer Memory: The program is described and compared to other NEMP codes in a review article by Bevensee and Brittingham [35]. Several versions of the OSU code have been run. A small version (1100 cards) used about 50kg words of memory on a CDC7600 for a bistatic scattering calculation from a

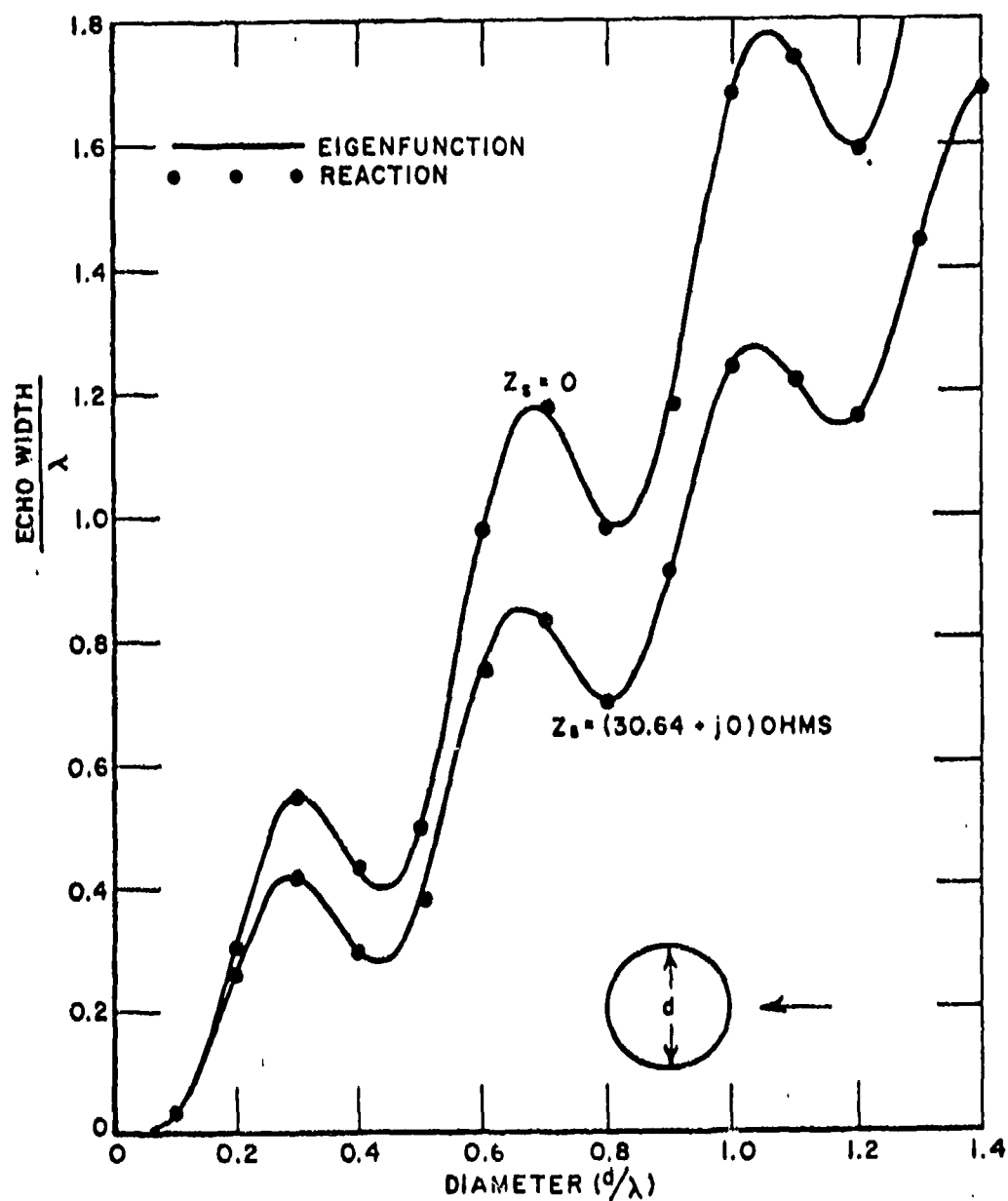


Figure 3.60 Backscattering Echo Width of Circular Cylinder for TE Polarization from RIE Method [54]

structure having less than 55 points and 50 segments. A more elaborate version, run again on a CDC7600, had about 3000 cards in the program and used 110k<sub>o</sub> of memory for a similar scattering problem. The second version was a user-oriented modification of the code which could treat a lossy ground.

2. CP Time: An example calculation of back-scattering from a 60 segment wire grid model of a plane took 100 sec for one frequency. This version of the code was not well optimized, however, and some extra parameters were calculated that were not required for that specific problem. In any event, a time domain response would require several hundred frequency points to be calculated, and for such a task the CP time would probably be in excess of 1 hour.

3. Numerical Accuracy: The numerical accuracy of the solution is limited by the sinusoidal expansion functions and by the use of Simpson's Rule to evaluate certain integrals. A comparison of several frequency domain codes has been performed by Miller et al. [52] and the OSU was found to be good numerically compared to versions of the Syracuse code, BRACK (a forerunner of AMP) and WIRANT. The comparison was made for scattering from three wire shapes: a straight wire, an L, and a cross. The numerical accuracy is therefore as good or better than these other codes for the three examples given.

4. Physical Accuracy: The method has the same modeling inaccuracies as any other code which relies strictly on wire grid representations of a structure. Therefore, the same discussion made for the Syracuse code applies here. The physical modelling accuracy is not as good as a hybrid code such as NEC2.

5. User Orientation: The original code developed by Richmond is well documented including listings and descriptions of various example problems. Richmond states that "an experienced engineer" would be required to use the code properly.

6. Frequency Range: Like the other wire grid models, this method has a broad frequency range limited principally by computer capabilities.

7. Attached Stroke: The OSU code can model current injection but cannot model the non-linearities in the attached stroke. The discussion is the same as for the Syracuse code.

8. Test Case: The discussion is the same as for the Syracuse code, namely, current injection and the return conductors can be treated nicely but the non-linearities such as spark gaps cannot be handled easily.

9. Aircraft Size: As with other wire grid modeling approaches, large aircraft are likely to require prohibitive amounts of computer memory.

10. Lightning Environment: The discussion is similar to the Syracuse code. The major limitation of the code is its inability to treat the non-linear aspects of the lightning environment. With minor modifications, it should be able to treat the near fields of a return stroke.

11. Experimental Verification: There is little experimental verification of the code, especially for aircraft shaped objects.

#### 3.3.4.5 WIRANT [59-61]

Curtis et al. [59-61] at Boeing have developed a computer code WIRANT which has been used for external coupling calculations of EMP and lightning to aircraft. The code is based on a standard method of moments solution of the EFIE in the thin wire approximation. Pulse functions are used to approximate the unknown currents on wire segments and the reduction of the integral equation to a set of linear equations is accomplished by point matching. Because the code is the property of Boeing and is considered proprietary, listings and documentation are not generally available. However, the code has been used for EMP and lightning susceptibility studies of many aircraft including the F111, 747, YC14, AWACS P3, the B1 and a Learjet. Some of these analyses will now be considered.

Figure 3.61 shows a stick model of a 747 which has been analyzed for its NEMP response [64]. The model consists of 46 straight, cylindrical wire segments. The current in the wing root (Section 24 in the stick model) as excited by a 1.8 MHz plane wave incident head-on to the aircraft is shown in Figure 3.62. For polarization in the geometric plan of the wings and fuselage the wings experience large resonant currents. The 747 response has been calculated at many frequencies and from these data the time domain response has been determined by a Fourier inversion. This time domain response is shown in Figure 3.63. It has a nearly damped sinusoidal waveshape. Other responses have also been calculated, in particular the response of the aircraft while it is on the ground.

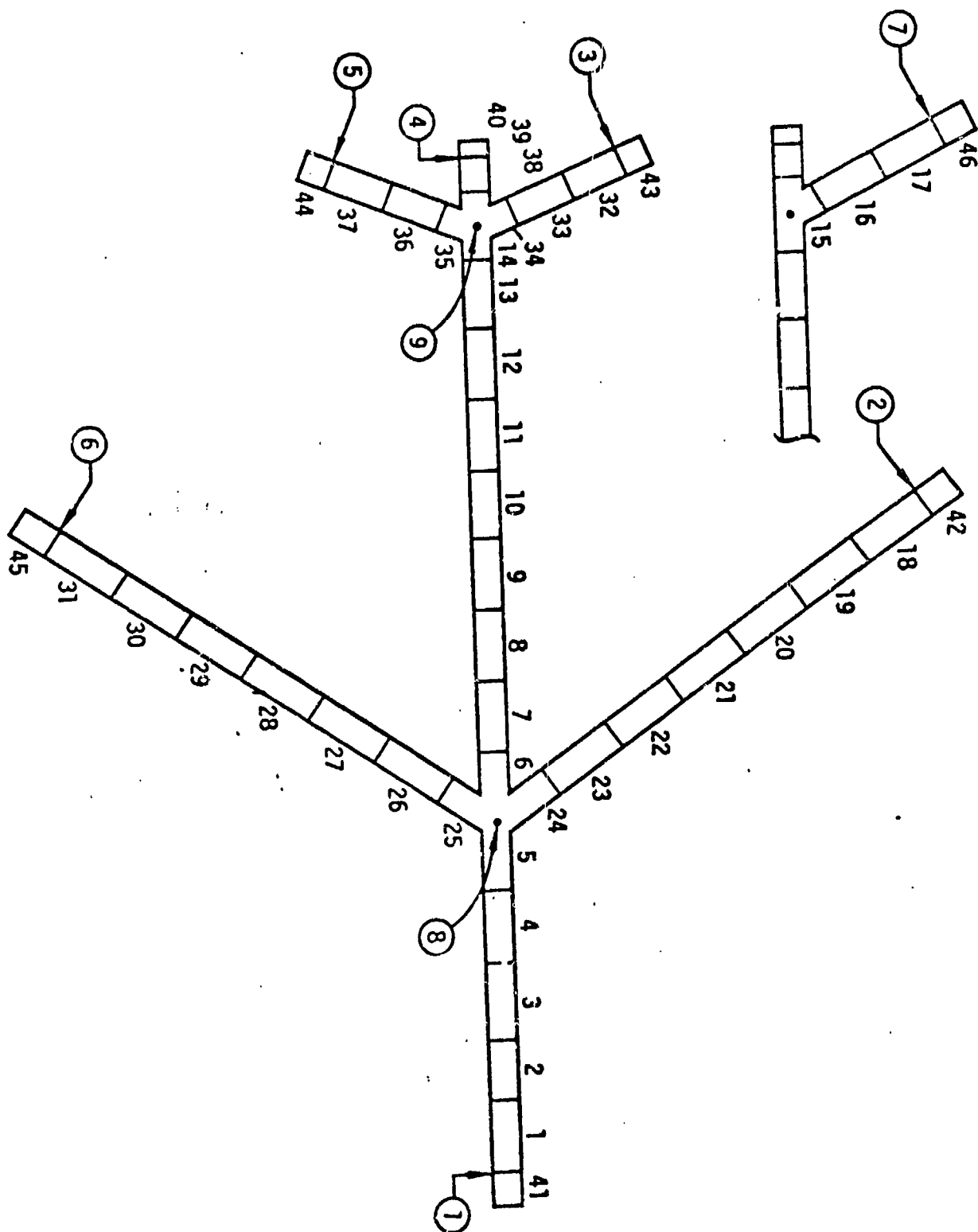


Figure 3.61 Segmentation of Wire Model for Aircraft in Free Space Model for WIRANT [64]

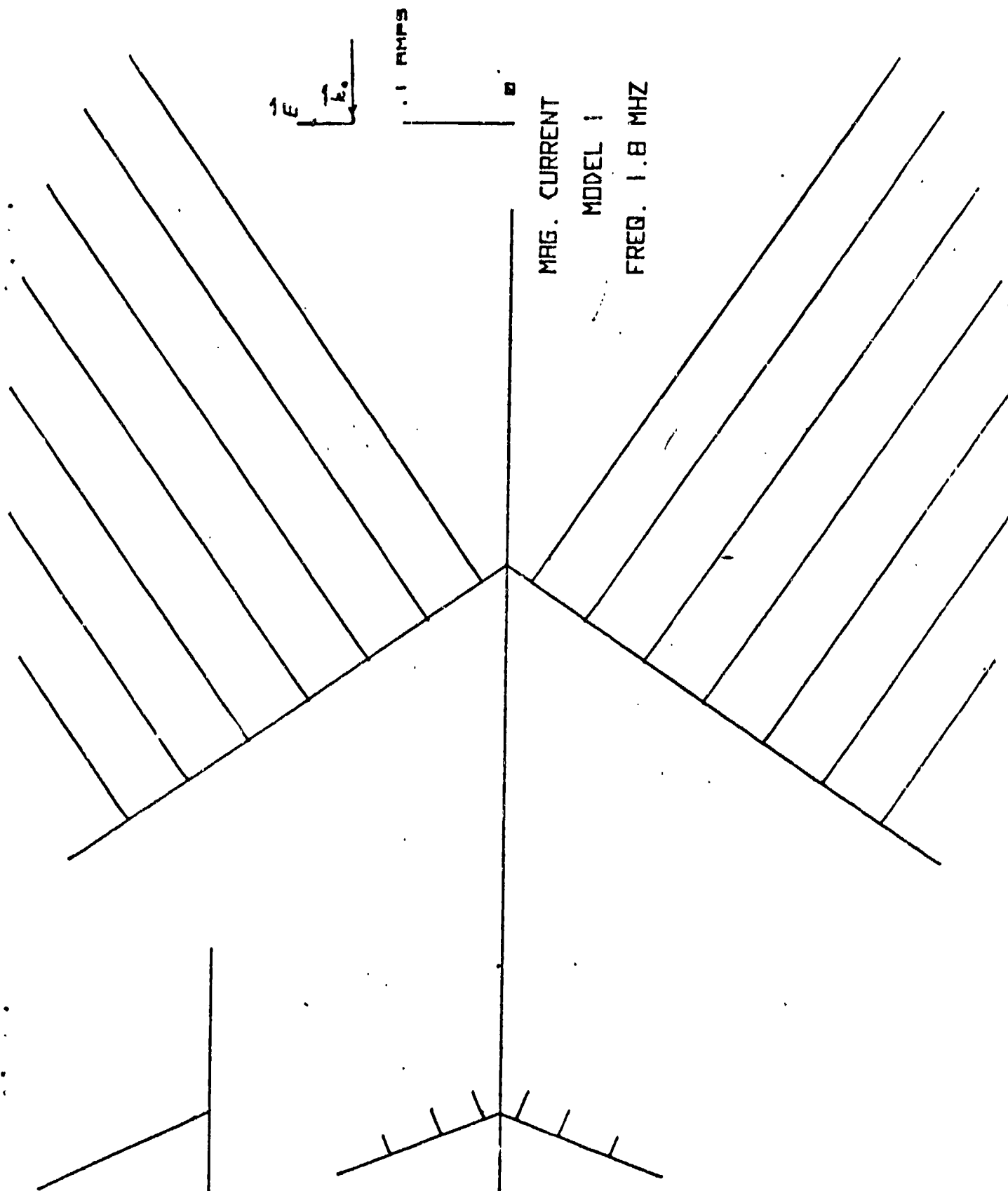


Figure 3.62 Response of the WIRANT Aircraft Model to a Sinusoidal Plane Wave Incident on the Nose of the Aircraft [64]

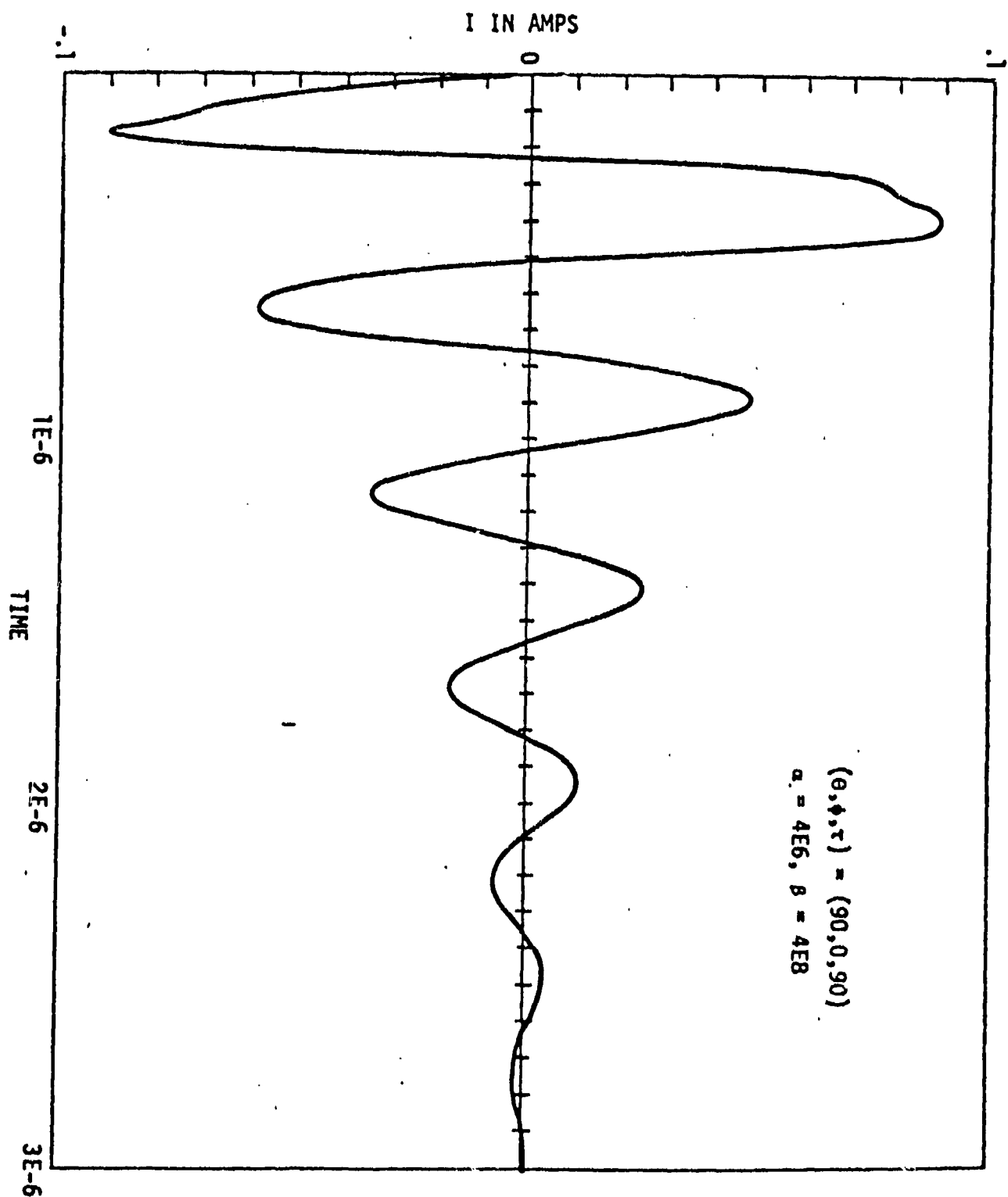


Figure 3.63 Wing Current I in Segment 24, Wing Root [64]

A more complete wire grid model of a Learjet aircraft has been constructed to analyze the TRIP-76 in-flight lightning strike data [62]. The in-flight WIRANT model is shown in Figure 3.64. This model represents the aircraft fuselage fairly accurately and represents the wings as plane wire grid surfaces. In addition to the in-flight analysis, the Learjet was also analyzed in a test configuration as shown in Figure 3.65(a). The computational model for the test configuration is simplified from the in-flight model and is shown in Figure 3.65(b).

It was the original hope to compare the measurements and calculations for both in-flight and test configurations. Unfortunately, there were negligible in-flight data obtained that year and so no calculations of the external coupling parameters for the in-flight model were reported. Comparison of the limited test configuration model and test data are available, however. Figure 3.66 shows a comparison of the measured skin current density on the aft fuselage compared to the measured response for the ground test. The data plotted in Figure 3.66 are time derivatives of the skin current. The measured and calculated data compare well in peak amplitude but not in pulse shape.

Models of the F111 and B1 have also been developed using WIRANT [63]. The models use wire grid structures to represent the aircraft and are shown in Figures 3.67 through 3.70 for the conditions of wings swept or wings extended. The F111 models contain 103 wire elements and the B1 nearly the same. A large number of calculations for NEMP excitation have been performed and reported in Ref. [63]. These data have been compared to measurements made on a real F111 aircraft at ARES and on a scale model of the B1 at ALECS. The F111 measurements used a pulse excitation whereas those on the B1 used swept CW. In general, the agreement between experiment and theory is good.

There are too many responses to report many of them here. There are 30 graphs for the B1 alone, for example. Therefore, only several representative responses will be discussed. Figure 3.71 shows the longitudinal current density excited on the F111 fuselage for top-side NEMP incidence with polarization parallel to the fuselage. The test point FS 160 is on the top of the fuselage just forward of the cockpit approximately as shown in Figures



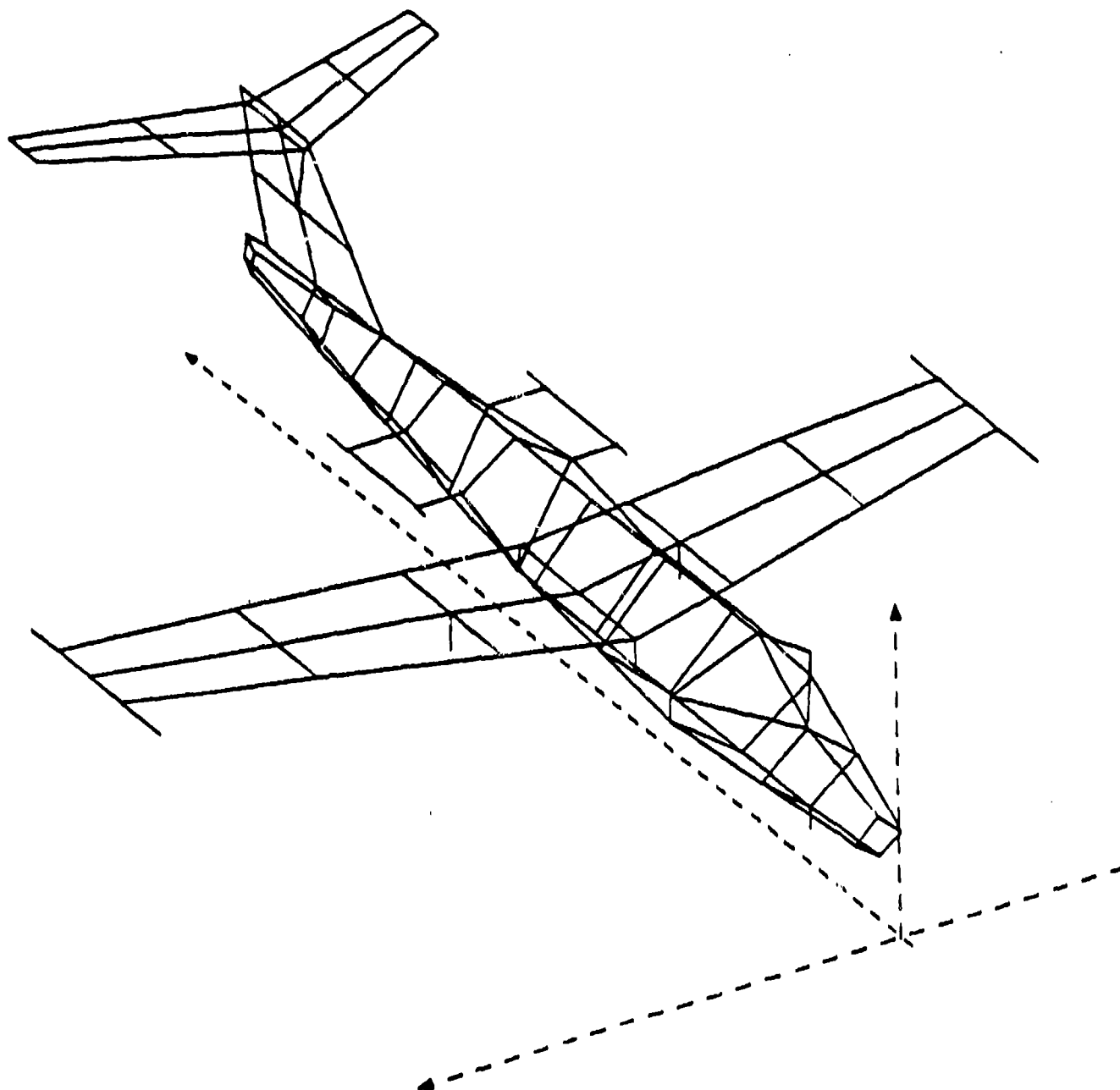
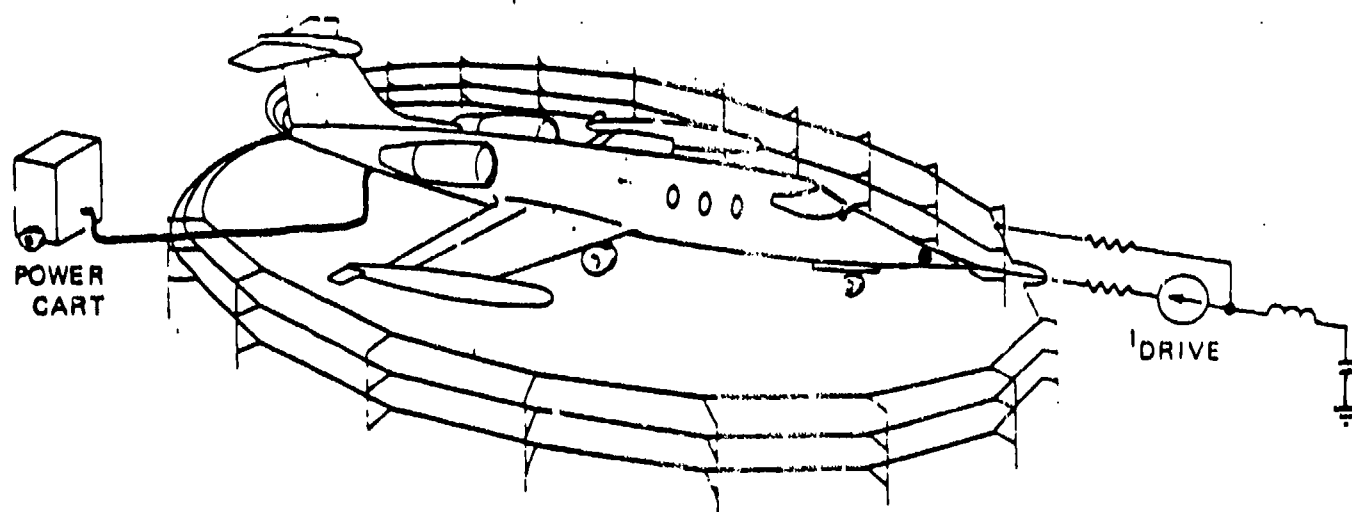
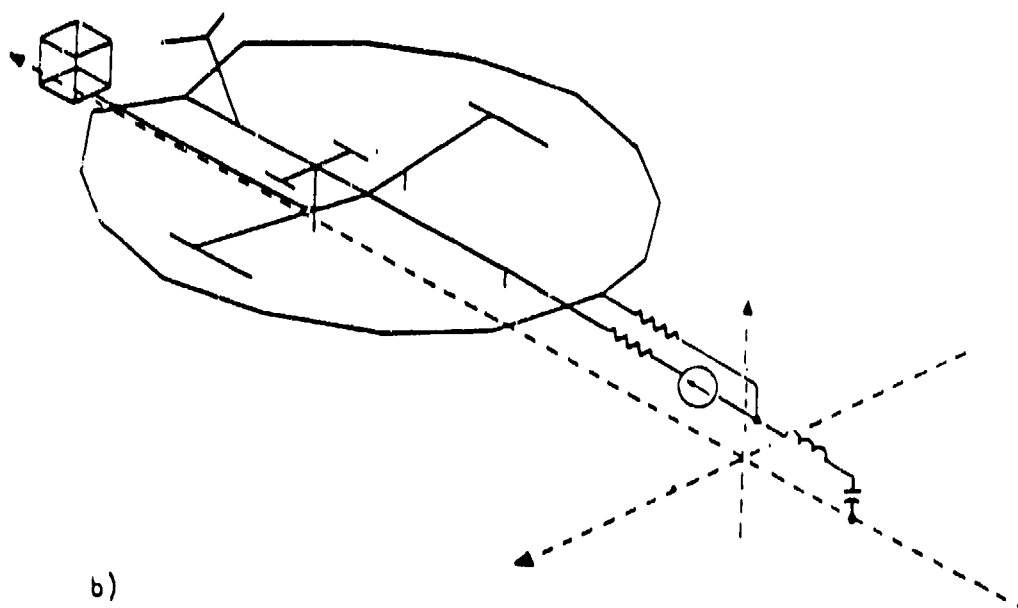


Figure 3.64 In-Flight WIRANT Model of Learjet [62]

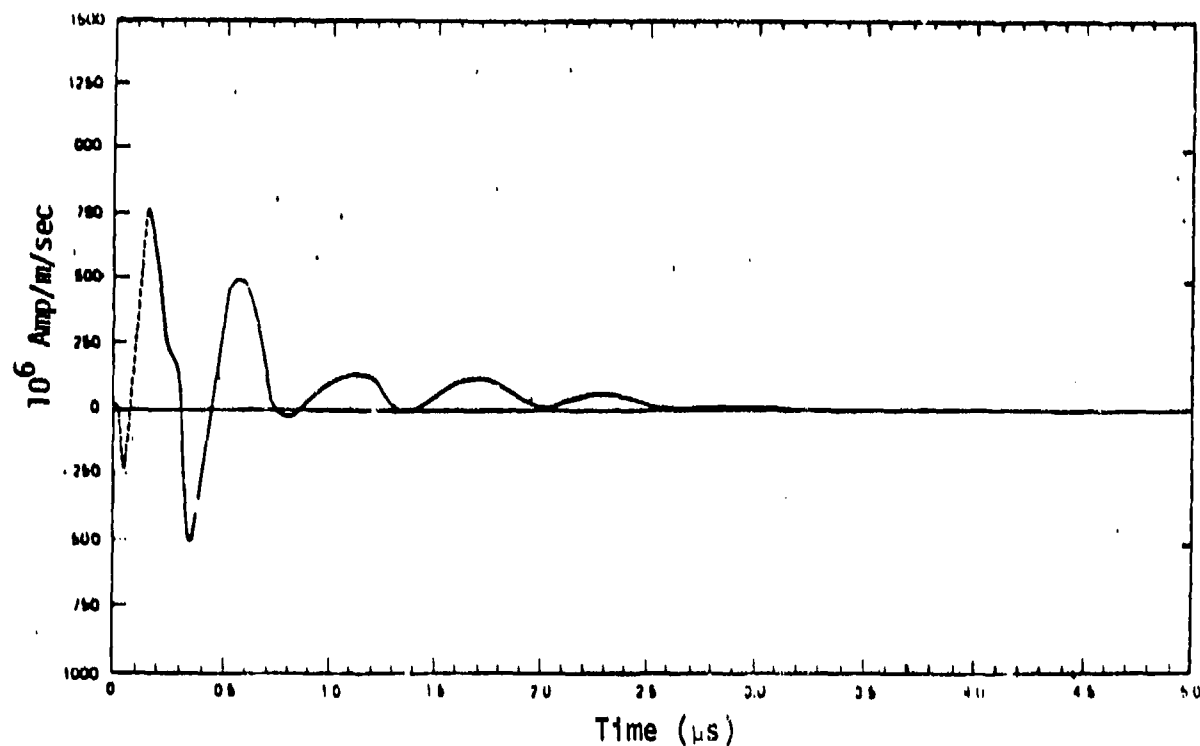


a)

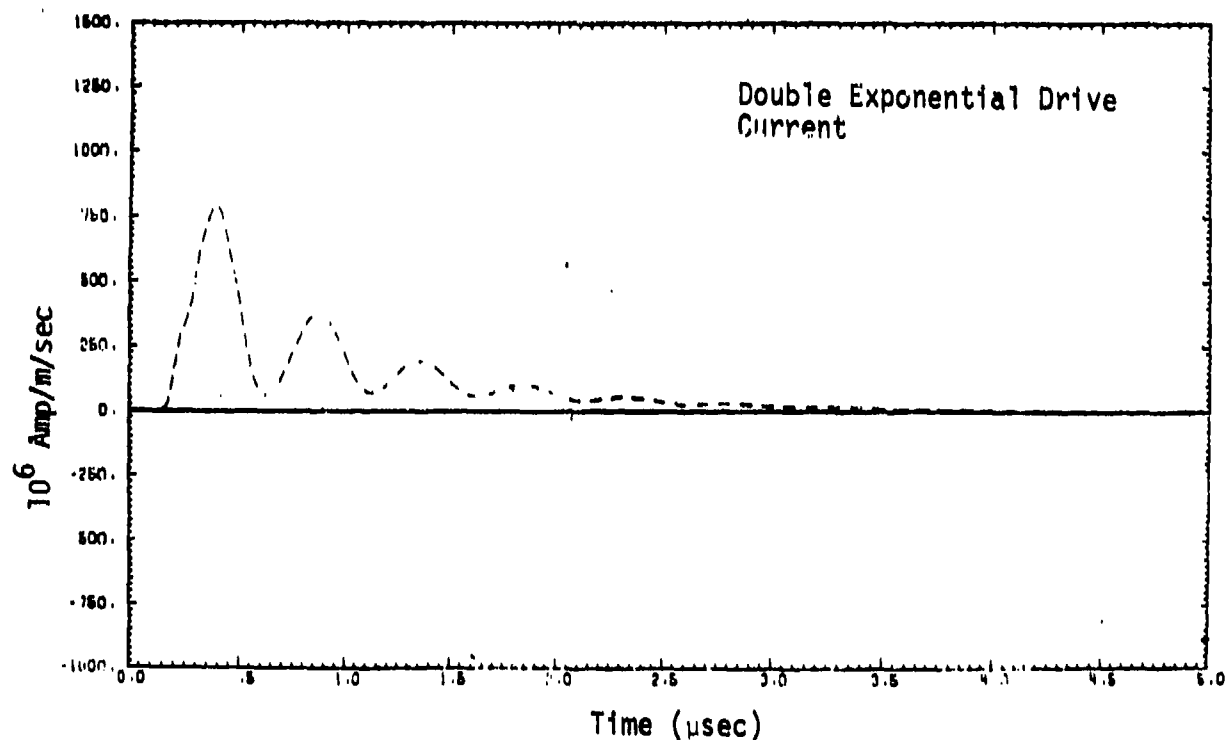


b)

Figure 3.65 The Ground Test Configuration for WIRANT Analysis of a Learjet [62]



(a) Ground Test Data



(b) Calculated Response

Figure 3.66 Aft Fuselage Sensor Skin Current Density (Time Derivative)  
For WIRANT Analysis of the Learjet [62]

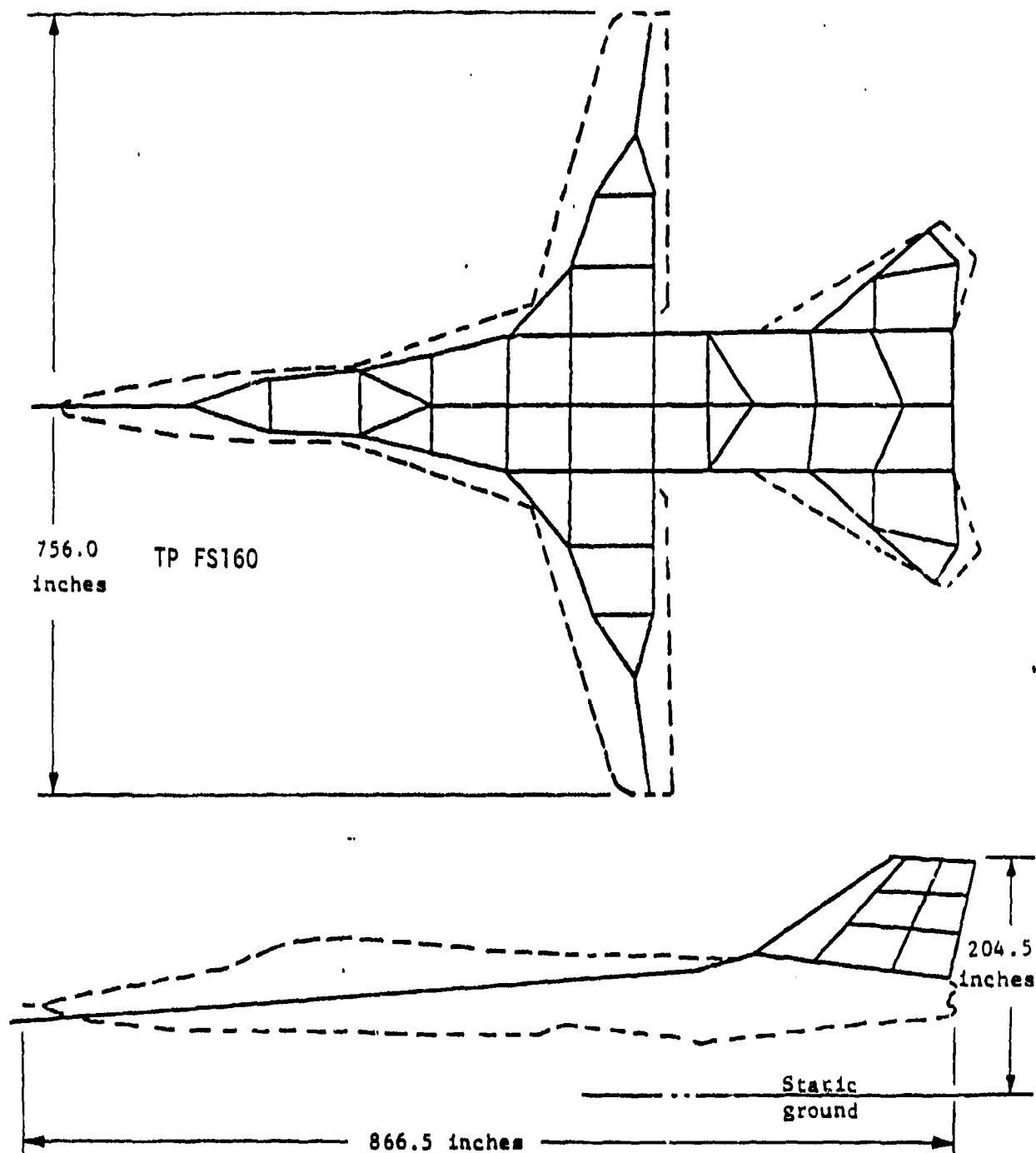


Figure 3.67 F-111 Wire Mesh Model - Wings Extended [63]

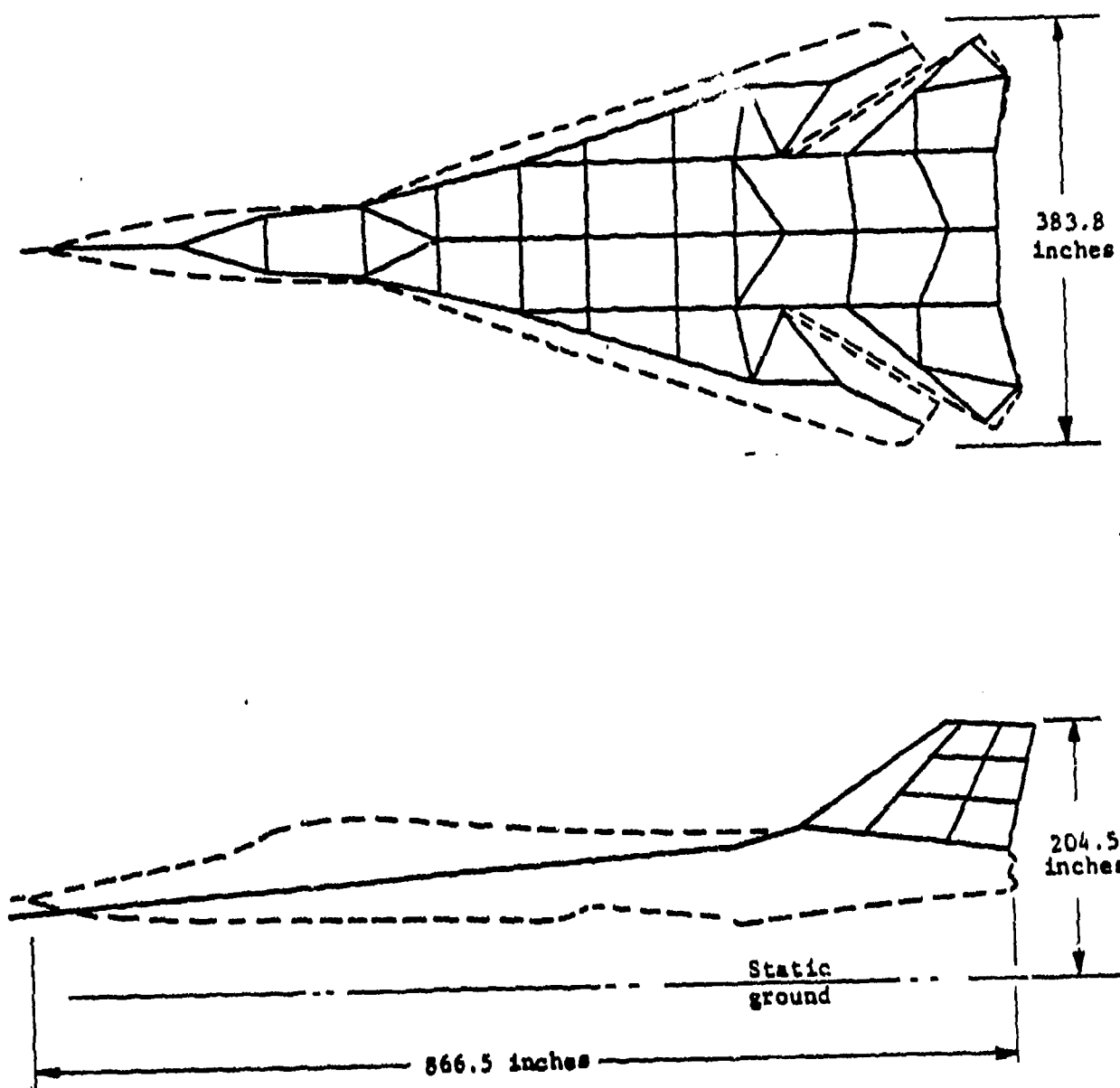


Figure 3.68 F-111 Wire Mesh Model, Wings Swept [63]

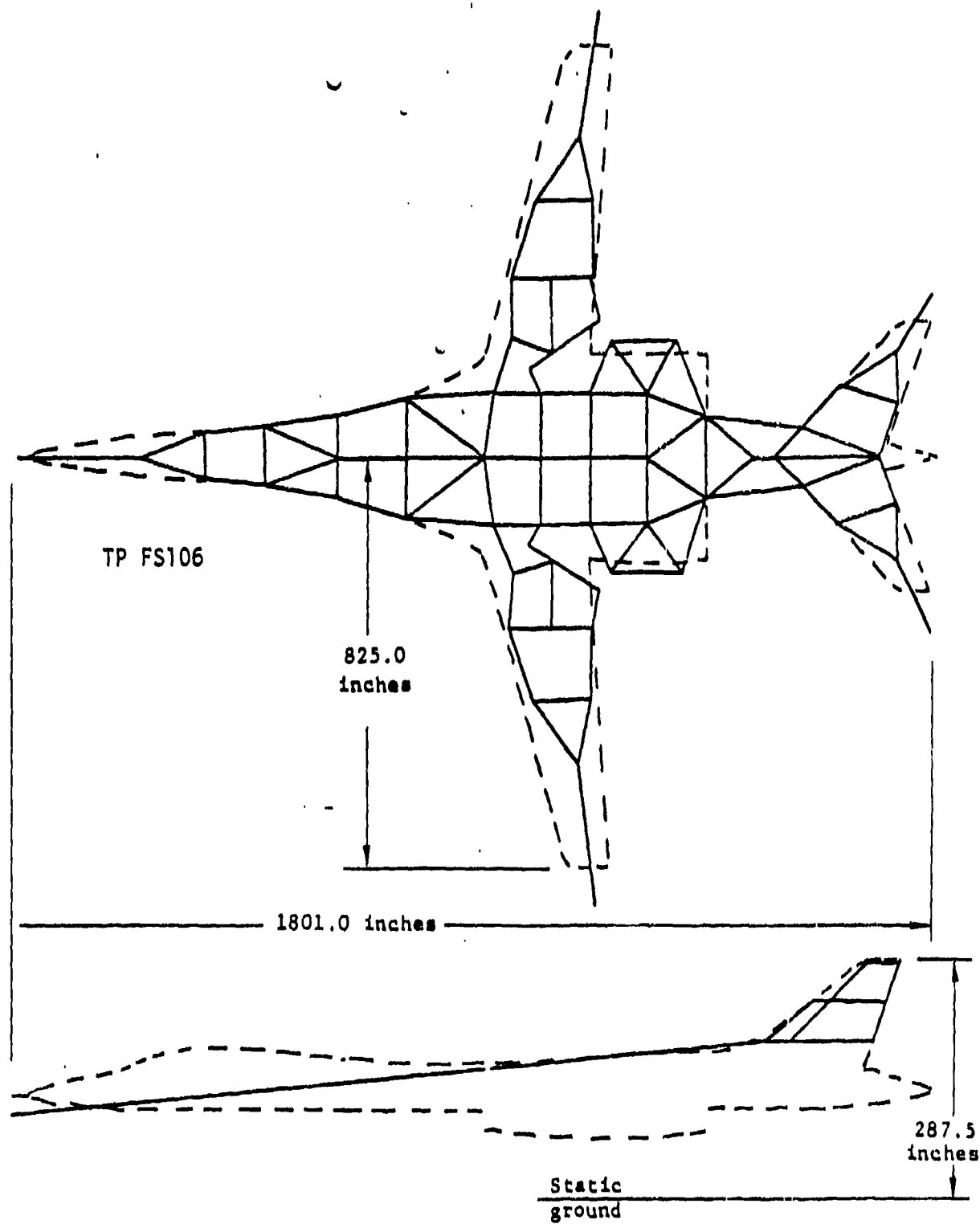


Figure 3.69 B-1 Wire Mesh Model, Wings Extended [63]

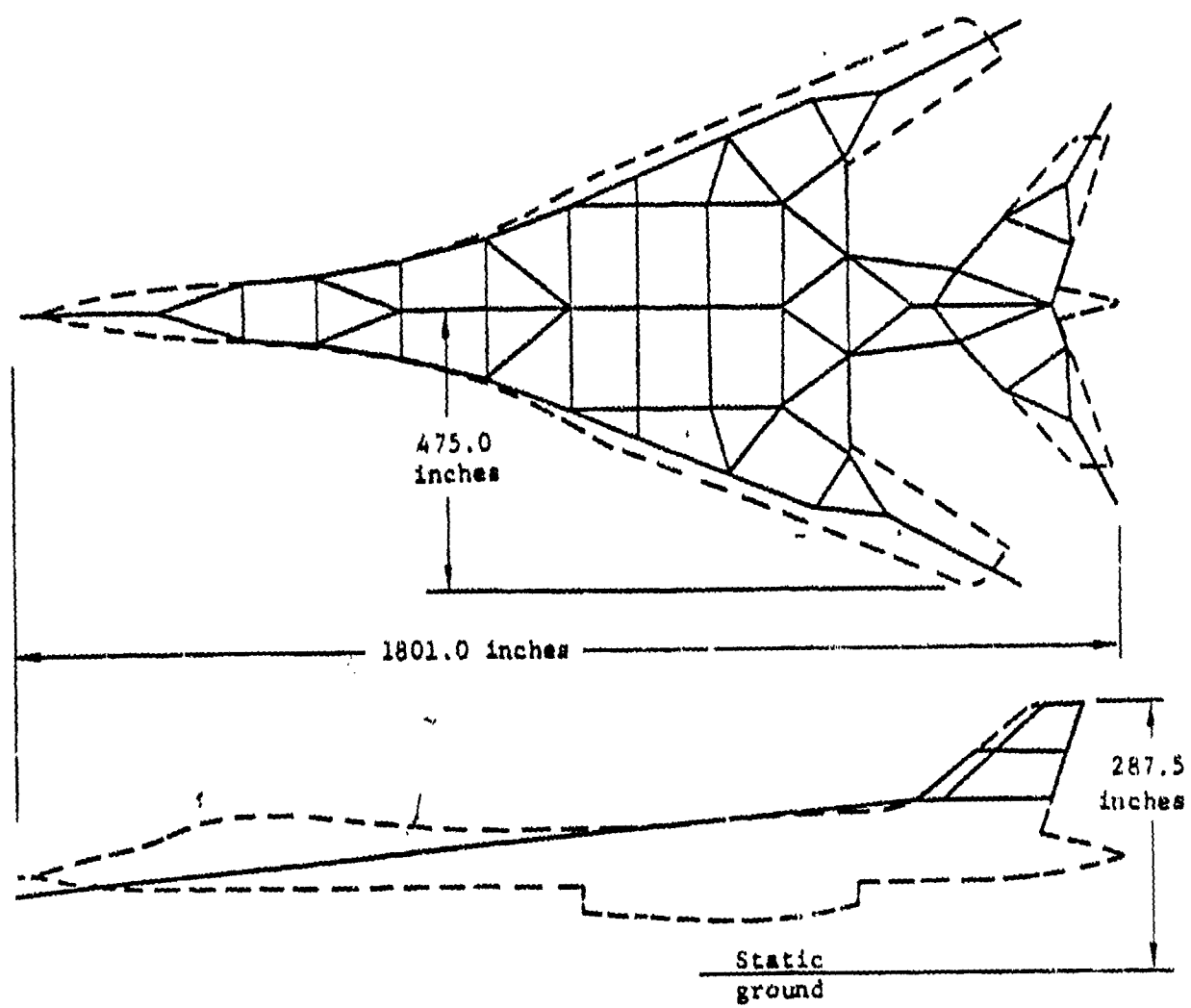
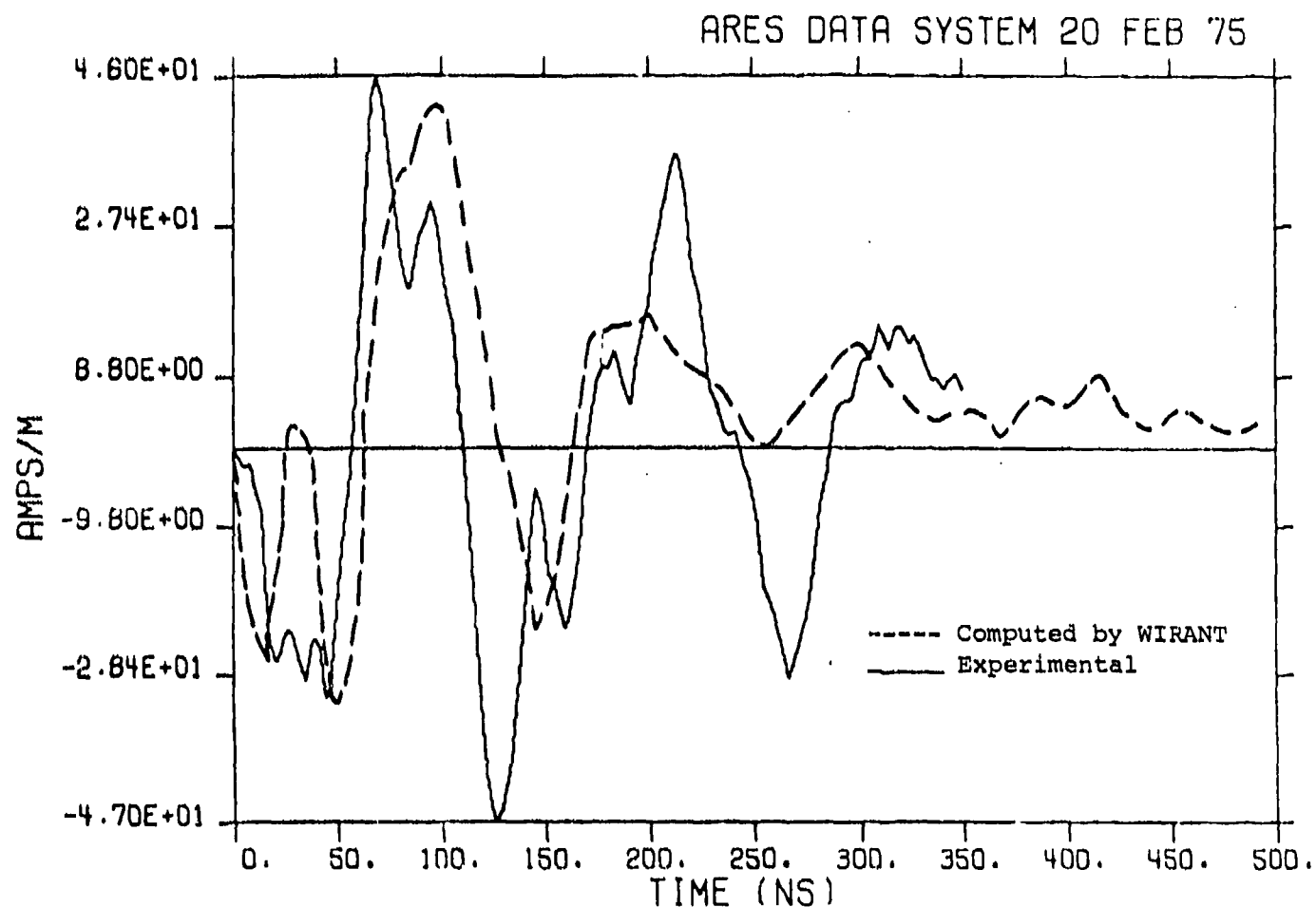


Figure 3.70 B-1 Wire Mesh Model, Wings Swept [63]



ARES F-111 TEST  
CALIBRATED DATA  
RESPONSE

Figure 3.71 Longitudinal Current Density on the F-11 Fuselage (FS 160),  
Top, Topside Incidence, E Parallel to Wings, Wings Extended  
[63]



3.67 and 3.69. The data in Figure 3.71 shows the time dependence of the axial current density. The data in Figure 3.72 shows the frequency spectrum of this axial current. The calculated data are limited to frequencies below 20 MHz by wire grid modeling. Figure 3.73 shows the frequency domain response for the surface current density on a similar test point for the B1. The agreement between the computations and the test data is good for both the B1 and F111.

The eleven evaluation criteria will now be discussed.

1. Computer Memory: As with other thin wire codes which rely strictly on wire grid structures, the computer code WIRANT will require substantial computer memory for a physically complete representation of an aircraft surface. A benchmark test of WIRANT [35] for a fairly large model, 147 unknown current elements, took 175 k<sub>8</sub> words of memory on a CYBER 174. The program used to analyze the F111 requires 170 k<sub>8</sub> words of memory (almost the entire size of SCM) of a CDC 7600.

2. CP Time: A run for WIRANT using 140 wire segments took 5 CP seconds. For the benchmark test described above (147 elements), it took 89 seconds of CP time for five frequency points. For a large structure, the matrix inversion time limits speed of the code.

3. Numerical Accuracy: In another benchmark test [52], the OSU, SYR and BRACK codes were compared to WIRANT. The OSU code showed the greatest numerical accuracy. The limiting features of WIRANT are the choice of pulse test functions and the decision to use point matching. The OSU code, for example, uses sinusoidal expansion functions and Galerkin's method which are more accurate.

4. Physical Accuracy: Methods such as WIRANT which use wire grid modelling are limited to the resolution that can be obtained for large voluminous surfaces. The resolution of the F111 and B1 is fairly good, however.

5. User Orientation: WIRANT has been developed by Boeing and is a proprietary product of that company. Therefore, listings and documentation on the code are not available.

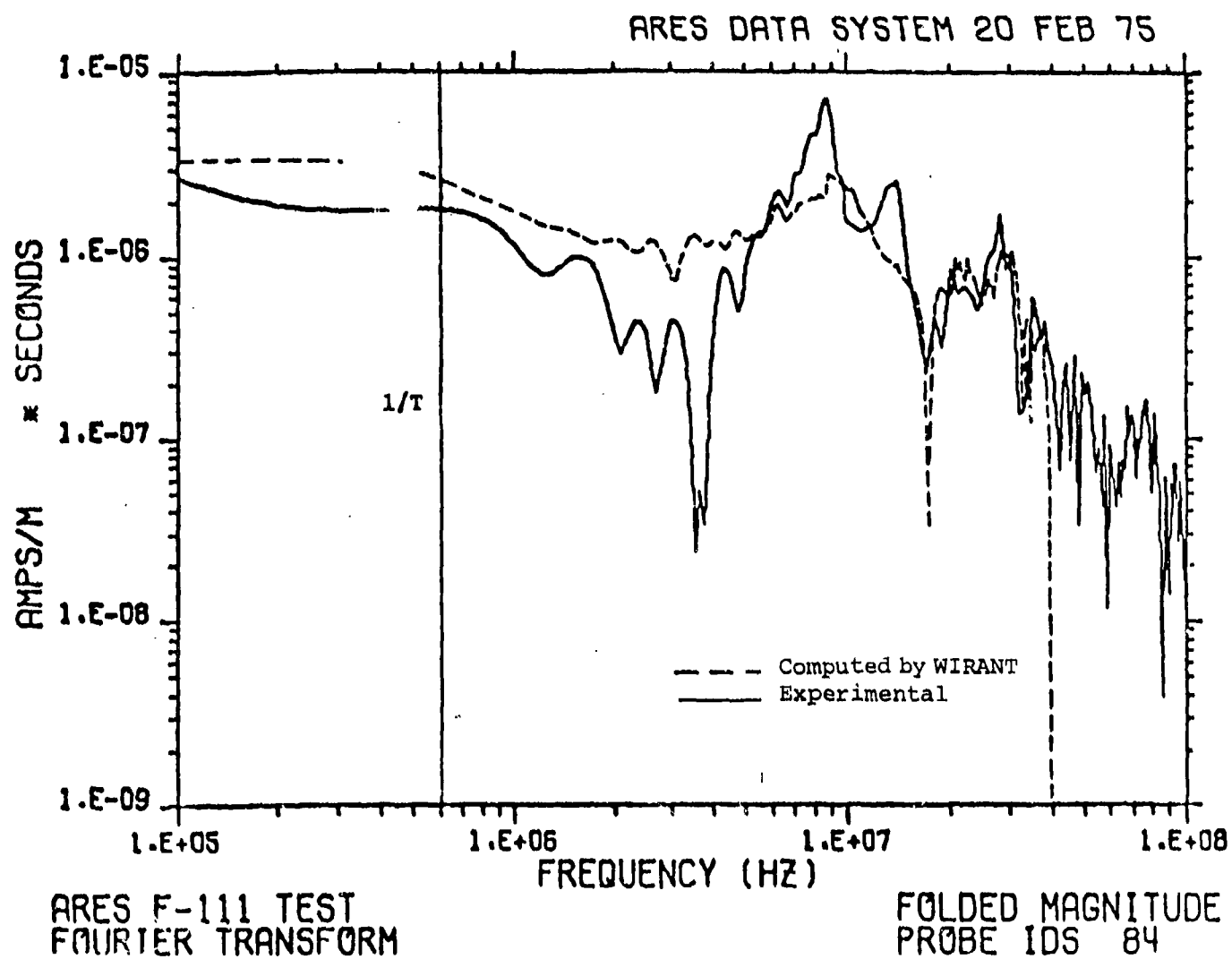


Figure 3.72 Longitudinal Current Density on the F-111 Fuselage (FS 160), Top, Topside Incidence, E Parallel to Wings Wings Extended [63]

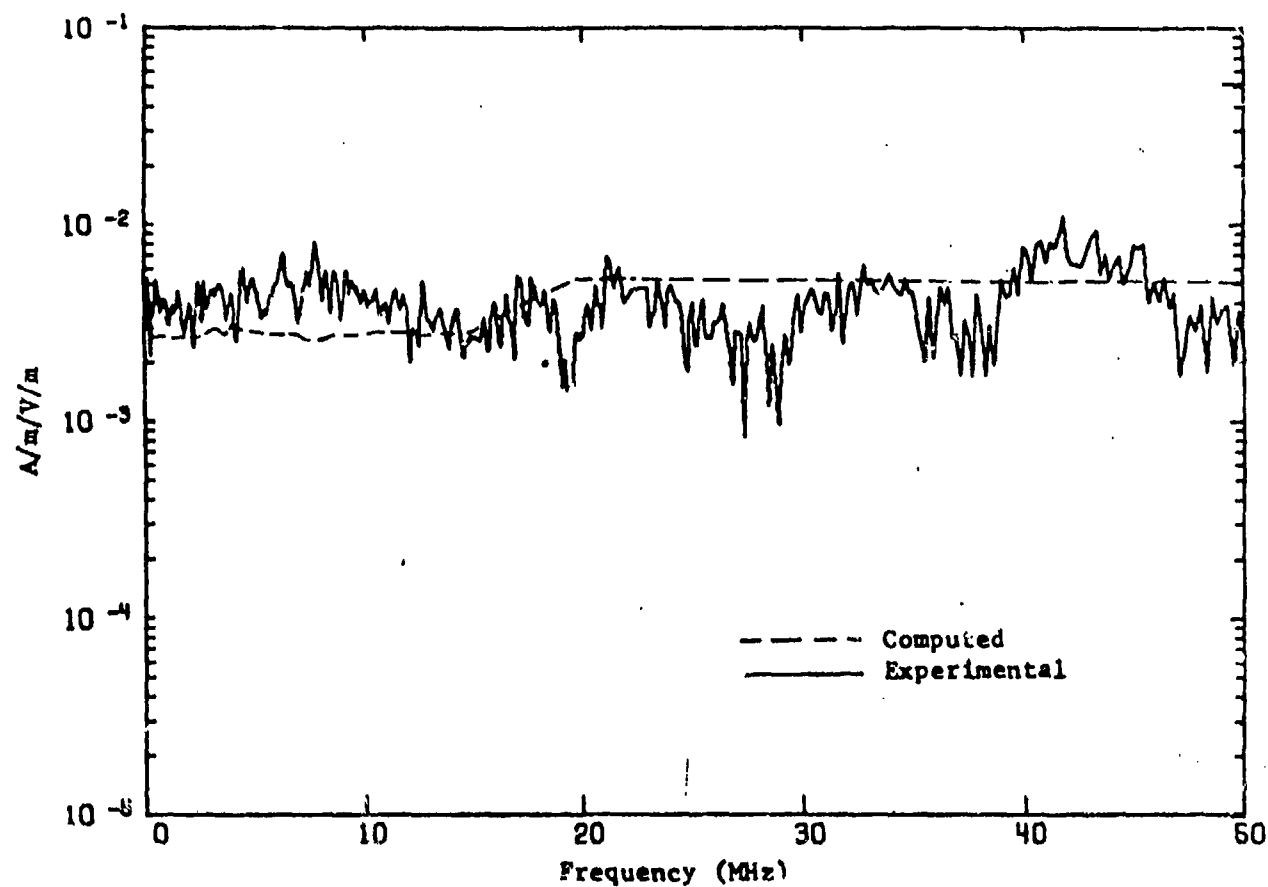


Figure 3.73 Longitudinal Current Density on B-1, Forward Bulkhead (FS 150), Top, Topside Incidence, E Parallel to Fuselage, Wings Swept, Magnitude [63]

6. Frequency Range: The code has a broad frequency range as do other frequency domain EFIE methods. In the case of the F111, the frequency range is from 10 kHz to 20 MHz. The upper frequency limit is determined by the largest wire segment of the grid structure.

7. Attached Stroke: The code can model current injection using wire segments. However, the method relies on system linearity to enable the calculation of a time dependent response. Therefore, the non-linear characteristics of an attached stroke cannot be modelled.

8. Test Case: WIRANT can model the test case fairly well, for example, it can handle current injection and could model the return conductors. However, it cannot treat non-linear behavior, which is expected to occur in test fixtures.

9. Aircraft size: This method can be used to model small aircraft but it probably cannot model a large aircraft like a B52 or a 747 with the same accuracy as THREDE. Stick models of large aircraft could be employed, however.

10. Lightning Environment: The code can treat current injection and it could probably handle the near fields of a lightning strike. However, non-linear aspects of the lightning environment cannot be treated because the linearity of the system is required to calculate the time domain response. Therefore, the code cannot treat streamers or corona.

11. Experimental Verification: The code has been extensively compared to experiment for for the F111 and B1.

#### 3.3.4.6 Thin Wire Time Domain (TWTD) [65-67]

MB Associates and Lawrence Livermore Laboratories [65-67] have developed a method of solving scattering problems using the time domain EFIE. The solution utilizes the thin wire approximation described in Section 3.3.4.2 and employs a matrix solution in the time domain. A computer code (TWTD) has been written based on the method and a complete listing and documentation are available [67].

The technical approach uses the time dependent EFIE in the form

$$\hat{s} \cdot \vec{E}_0 = \frac{1}{4\pi} \int_L \left[ \frac{\hat{s} \cdot \hat{s}'}{R} \frac{\partial}{\partial \tau} I(\hat{s}', \tau) + \frac{C}{R^2} \hat{s} \cdot \vec{R} \frac{\partial}{\partial \tau} I(s', \tau) + \frac{C'}{R^3} \hat{s} \cdot \vec{R} q(s', \tau) \right] d\tau \quad (3.3.4.6.1)$$

where  $\hat{s}$  and  $\hat{s}'$  are tangent vectors to a wire segment,  $R$  is the distance from  $\hat{s}'$  to  $\hat{s}$ ,  $\tau$  is the retarded time  $t = R/c$ ,  $q$  is charge density and  $L$  represents an integral over the full length of a piece of wire. The quantity  $E_0$  is the incident field which gives rise the unknown current  $I$ . This equation is of the form

$$\hat{s} \cdot \vec{E}_0 = \int f(I, s, s', ) ds' \quad (3.3.4.6.2)$$

where the function  $f$  represents the integrand of equation (3.3.4.6.1). This integral equation is reduced to a set of linear equations by subsectional collation. The wire  $L$  is divided into sections, the unknown current on each section is approximated by a sum of expansion functions, and the integral equation is enforced in a point-wise manner over the physical structure. The result is that the integral equation for the unknown current reduces to a set of linear equations of the form

$$I_{11}(t + \Delta t) = (\underline{Z}^{-1})_{mn} V_n(t) = Y_{mn} V_n(t) \quad (3.3.4.6.3)$$

where  $I_n$  represents the amplitude for the  $n^{\text{th}}$  expansion function,  $V_m(t)$  is a function of the driving source, and  $Y_{mn}$  is a space matrix which depends on the geometry and  $\Delta t$  but not on time. The solution at a time  $t = n\Delta t$ , where  $n$  is an integer, is therefore given by

$$\underline{I}(t = n\Delta t) = [\underline{Y}]^n \underline{V}(t) \quad (3.3.4.6.4)$$

where  $[\underline{Y}]^n$  stands for  $[\underline{Y}] \cdot [\underline{Y}] \cdot \dots [\underline{Y}]$  ( $n$  times) and the equation has been written in a more concise matrix notation. In the computer implementation of the solution, the matrix inversion  $\underline{Z}^{-1}$  needs to be performed only once as long as the geometry is not changed. This represents a substantial time savings. In a frequency domain method, a matrix inversion generally needs to be performed for each frequency and there may be calculations at several hundred frequencies in order to obtain an accurate time domain result.

The expansion functions used in the solution are second order polynomials in the length along the wire segment.

The TWT code is especially useful for giving quick, approximate information on the resonance response of an aircraft. Two example calculations typify the kind of results that can be obtained with the TWT code [67]. The first is a calculation of the NEMP response of a stick model of a 747. The response has been calculated as a function of time and is shown in the sequence of drawings in Figures 3.74 and 3.75. The incident EMP strikes the front of the aircraft. The second example shows the physical and numerical modeling errors that can be expected with stick model calculations. Three models of a 747 as shown in Figure 3.76(a) have been studied both experimentally and theoretically. From left to right, the models are a stick model, a scale model of a 747, and a pipe model. The pipe model uses larger diameter cylinders than employed in the stick model but otherwise it has the same shape and size. The excitation for the aircraft models is a plane wave incident on the top of the aircraft with polarization parallel to the fuselage. The measured current in the nose of the aircraft is shown in Figure 3.76(b). There is clearly very little physical modeling error for this response. Furthermore, there is little numerical error because the calculated response fits the measured response as shown in Figure 3.76(c).

The eleven evaluation criteria will now be discussed.

1. Computer Memory: The program listing for this code is 2000 cards long, and for a 60 segment wire structure 370 k<sub>8</sub> words were required on a CDC 7600 in a benchmark test by Bevensee and Brittingham [35]. The memory requirement can be reduced below 100 k<sub>8</sub> by reducing the number of wire segments.

2. CP Time: As pointed out previously, the code is very time efficient. For example, a 20 segment model of a 747 ran in 1.8 seconds. This run gave the bulk currents on 20 wire segments at each of 600 time steps ( $t_{\max}$  was 2.4  $\mu$ sec).

3. Numerical Accuracy: The method is primarily limited by the discretization error in choosing the wire segments and in the time steps. Also, numerical error is introduced into the solution by a Lagrangian interpolation

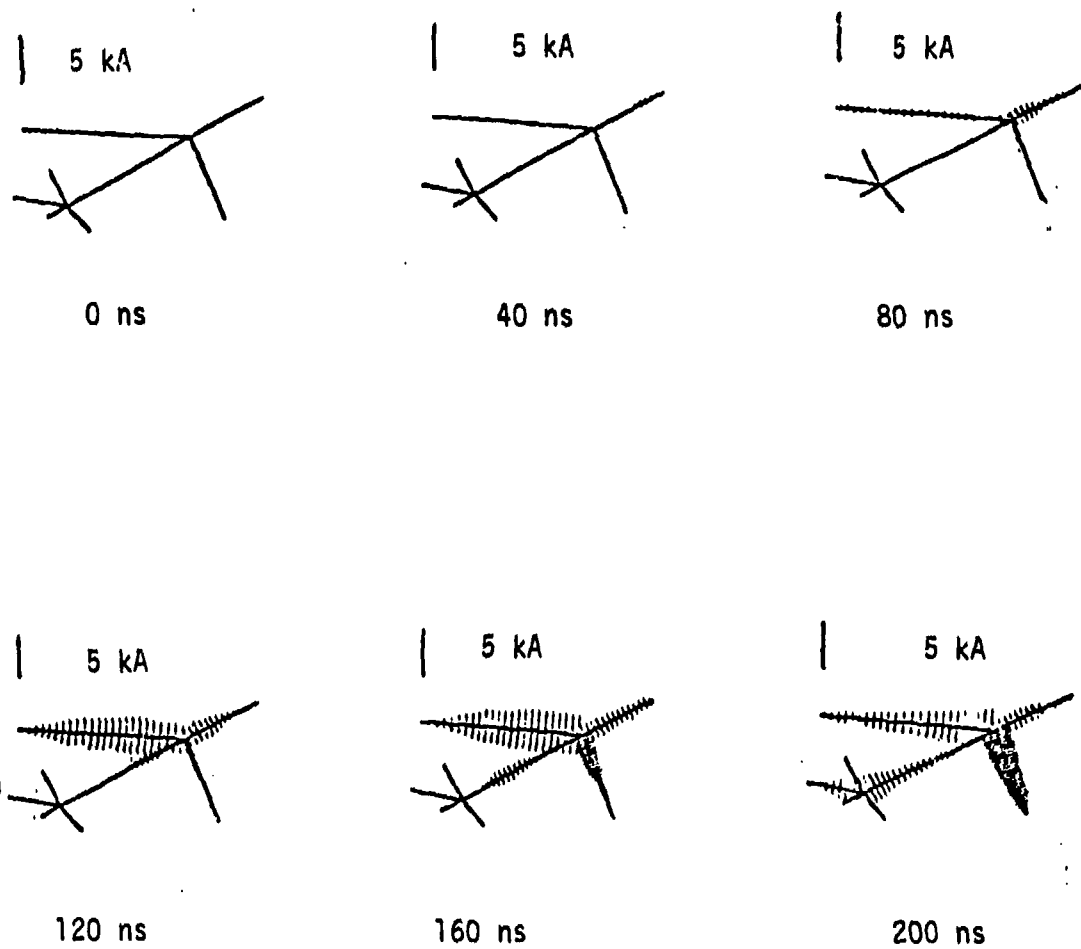
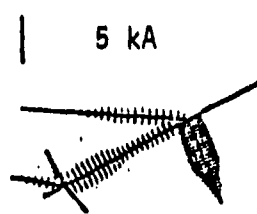
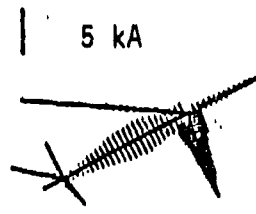


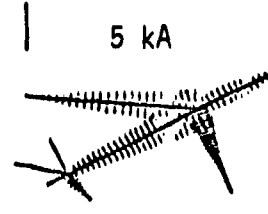
Figure 3.74 The Response of a Stick Model of a 747 to a NEMP Excitation As calculated by the TWT Code. The Perpendicular Lines on The Aircraft Segments show the Bulk Current on That Member. [67]



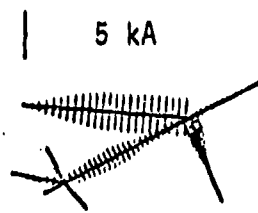
240 ns



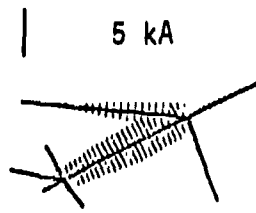
280 ns



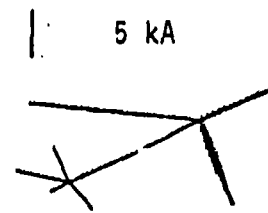
320 ns



400 ns



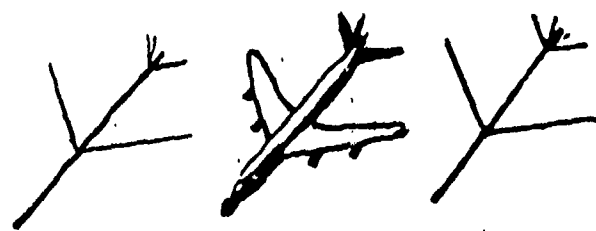
600 ns



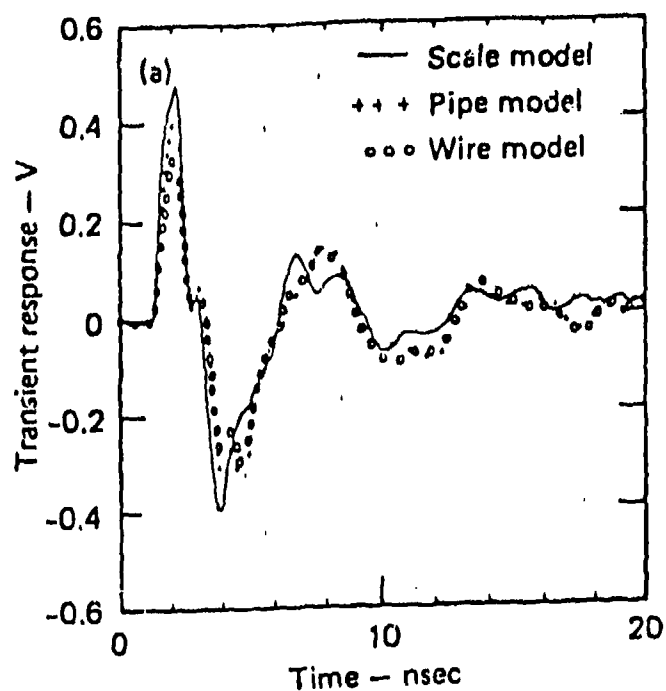
800 ns

Figure 3.75 A Continuation of the NEMP Response from Figure 3.74 for a 747 ns Calculated by the TWTN Code [67]

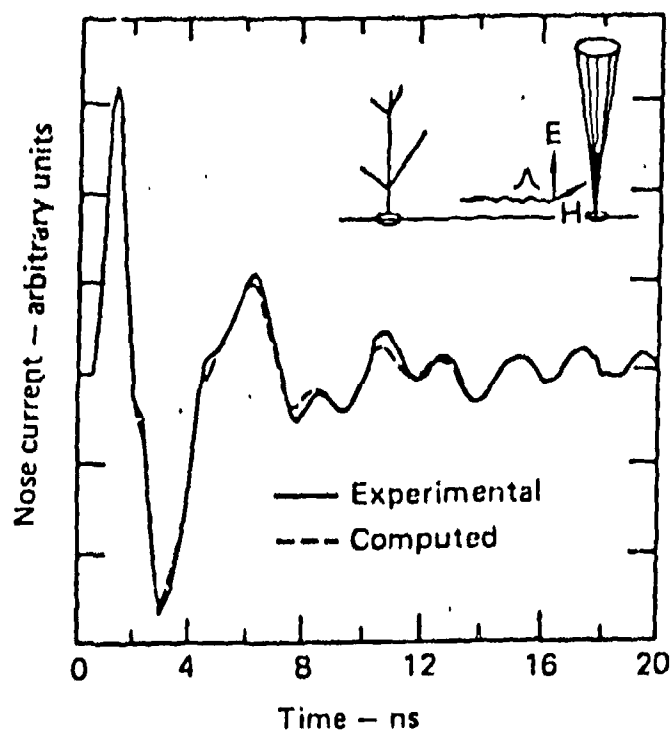




(a) Models Used in Measurements: Wire Model, Scale Model and Pipe Model from Left to Right.



(b) Results of Measurements on the Models Shown in (a).



(c) Comparison of TWT Calculations with Measurements Shown in (b)

Figure 3.76 Comparison of Measured Pulse Response of Three Aircraft Models With TWT Calculations [67]

scheme which determines certain current values in the solution. The numerical error, however, is not very large if the results in Figure 3.76(c) are truly representative.

4. Physical Accuracy: The physical accuracy of the stick model for predicting bulk currents is not very good although bulk currents are predicted well as can be seen from Figure 3.76(c). However, when a point of entry calculation requires a surface current density that may vary circumferentially, the stick model bulk currents cannot give an accurate value for  $J_s$ . Therefore, the stick model is limited in accuracy for predicting such parameters as surface current density which may be important for a full coupling calculation.

5. User Orientation: This code is relatively user oriented when applied to stick models. There are complete listings and documentation available on the code [52]. Furthermore, the stick model dimensions and segmentation are basically the only parameters that need to be changed from aircraft to aircraft. This will not require a user experienced in EMP or lightning external coupling problems.

6. Frequency Range: The frequency limits of this code are not known. However, there is an upper frequency limit determined by the time step and a lower frequency limit determined by the number of time steps that can be run before excessive numerical error begins to accumulate. This code is probably good in the range 0.1 MHz to 50 MHz.

7. Attached Stroke: The code as presently written treats only applied field illumination and it would have to be rewritten to include the discrete sources that would be convenient in modelling current injection. In principle circumferential magnetic fields around a wire segment could be used as a current source. There is no provision in the method to take into account streamers or corona formation.

8. Test Case: The code would not be good for the test case since it cannot treat spark gaps or current injection without some modification. The physical modelling of the return conductors could be accomplished easily.

9. Aircraft Size: The method can be used for stick models of large and small aircraft.

10. Lightning Environment: The code is not well suited for the lightning environment since it cannot treat current injection on the time dependent media expected in the lightning environment. It could treat lightning near fields with some modifications.

11. Experimental Verification: Some verification of bulk current has been made for the stick models of Figure 3.76.

#### 3.3.4.7 Thin Wire Models in General

There are several considerations which have been noted in the literature and which are discussed here. They apply to any model which requires a wire grid structure to model a closed surface, and this includes most of the methods reviewed in Section 3.3.4.

First, the surface current density on an aircraft structure of approximate radius  $r$  is sometimes calculated from a bulk current by using the expression  $I_{\text{bulk}}/2\pi r$ . Sancer [38] has pointed out, however, that this result can be very misleading for induced currents from field illumination, even at very low frequencies. The circumferential dependence for  $I$  on a cylinder at low frequencies can be calculated from the magnetostatic solution. If the surface current density is required for a lightning coupling calculation, then one must beware of using stick model bulk currents to infer  $J_s$  at critical points of entry.

Second, wire grid models underestimate the surface current density. Lee, Marin and Castillo [68] have calculated the currents in a wire grid model and have compared these to current calculated for an actual surface by the EFIE. The comparison shows that the wire grid model underestimates the surface current density. Examination of the impedance matrix elements showed that the diagonal and near diagonal terms of the wire grid were smaller than the actual surface and that the far off diagonal terms were nearly the same. The conclusion is that the wire grid model underestimates the coupling between neighboring parts of the surface.

Third, artificial resonances can occur inside a wire grid structure that is intended to model a closed, voluminous surface. This has been observed by Armour [37] among others. The resonances can be avoided by including

some structure inside the wire grid cavity, however care must be taken in the interpretation of the wire grid results to avoid such spurious results.

Fourth, the verification of a model by comparison of calculated and measured data in the far field may not be as sensitive a test of a model as comparison of surface current density. Therefore, models which work well for radar echo calculations may not necessarily be good for coupling calculations.

### 3.3.5 Singularity Expansion Method (SEM)

From studies of the interaction of NEMP with conducting objects, it was observed that the response of an object often showed a multicomponent damped sinusoidal behavior. The scattering objects considered in these studies were aircraft, missiles or satellites and the response was typically a surface current density or surface charge density to be used in an internal coupling analysis. Expressed mathematically,

$$J(\vec{r}, t) = \sum_{i=1}^N A_i(\vec{r}) e^{-\alpha_i t} \sin \omega_i t \quad (3.3.5.1)$$

where  $J(\vec{r}, t)$  is some response,  $\vec{r}$  and  $t$  are position and time, and  $\alpha_i$  and  $\omega_i$  are real numbers. This time domain function has a Fourier transform,  $\hat{J}(\vec{r}, \omega)$ , given by

$$\hat{J}(\vec{r}, \omega) = \sum_{i=1}^N \frac{A_i(\vec{r})}{(\omega + j\alpha_i)} = \sum_{i=1}^N \frac{B_i(\vec{r})}{(\omega - \bar{\omega}_i)} \quad (3.3.5.2)$$

where a hat symbol (^) means Fourier transform, and  $A_i$ ,  $B_i$ ,  $\bar{\omega}_i$  and  $j$  are complex numbers. Plotted in the complex  $\omega$ -plane,  $\hat{J}(\vec{r}, \omega)$  has simple poles at the points  $\bar{\omega}_i$ .

Motivated by this observation, Baum [69] and others sought to cast the normal frequency domain solution methods into a form which would provide the parameters  $B_i$  and  $\bar{\omega}_i$  directly as a part of the solution. The result of this effort is the Singularity Expansion Method (SEM). The formulation provides a concise and elegant form of the transient response for certain problems.

There is an extensive literature to the SEM which is well referenced in Appendix A. The discussion which follows here can be found in the review article by Baum [69]. As Baum has pointed out, the "... SEM is not so much an alternate method for solving boundary value problems but one which should

be used in conjunction with other methods to cast the solution for broadband frequency and time response in a more useful form." In fact the actual solution of the boundary value problem by the SEM may proceed more efficiently by a formulation that does not directly attempt to determine the poles and residues of the expansion in equation (3.3.5.2). It may only be after the actual solution has been obtained that it is efficient to calculate the SEM parameters. In some cases, where the response is not dominated by the system resonances, it may not even be helpful to calculate the SEM parameters at all. The great value of SEM is not in providing new computational techniques but as a way of providing insight into the physical mechanisms of the resonant part of the transient scattering response.

A formulation of a boundary value problem, which would give the SEM parameters directly, starts with the frequency domain integral equations derived in Section 3.2.2. These equations are of the form

$$\int_{S'} \hat{K}(\vec{r}, \vec{r}'; \omega) \hat{J}(\vec{r}'; \omega) ds' = \hat{F}(\vec{r}, \omega) \quad (3.3.5.3)$$

where  $(\hat{\phantom{x}})$  indicates a Fourier transform,  $\hat{K}(\vec{r}, \vec{r}'; \omega)$  is a kernel,  $\hat{J}$  is the system response (perhaps a surface current density), and  $\hat{F}(\vec{r}, \omega)$  is a forcing function (driving field in a NEMP excitation problem). For simplicity the vector character has been suppressed. This integral equation can be reduced to a set of simultaneous linear equations by the method of moments described in Section 3.2.3. Upon the selection of appropriate basis functions,  $f_n(\vec{r}, \omega)$ , and choosing point matching weighting functions, the integral equation becomes

$$\hat{K}_{nm}(\omega) \hat{J}_m(\omega) = \hat{F}_n(\omega) \quad (3.3.5.4)$$

where

$$\begin{aligned} \hat{K}_{nm} &= \int_{S'} K(r_m, r') f_n(r', \omega) ds' \\ \hat{J}(\vec{r}, \omega) &= \sum \hat{J}_n f_n(\vec{r}, \omega) \end{aligned} \quad (3.3.5.5)$$

and

$$\hat{F}_n(\omega) = \hat{F}(r_n, \omega).$$

Equations (3.3.5.4) can be inverted to give the solution for  $\hat{J}_n(\omega)$  provided  $\hat{K}^{-1}$  exists.

The singular character of  $\hat{J}_n(\omega)$  has been thoroughly investigated -- for example, finite-sized perfectly conducting objects in free space are known to give a response which has only simple pole singularities. Essential and branch point singularities are excluded for this case. For such problems, therefore, the solution  $\hat{J}(\vec{r}, \omega)$  can be expanded in the form

$$J(\vec{r}, \omega) = \sum_{\alpha=1}^N \eta_{\alpha}(\omega) V_{\alpha}(\vec{r}) (\omega - \omega_{\alpha})^{-m_{\alpha}} + J_0(\vec{r}, \omega) \quad (3.3.5.6)$$

where  $\eta_{\alpha}(\omega)$  is called the coupling coefficient,  $V_{\alpha}(\vec{r})$  is the natural mode solution,  $m_{\alpha}$  is an integer,  $J_0(\vec{r}, \omega)$  is a function with no singular behavior,  $\alpha$  labels the order of the pole, and  $\omega_{\alpha}$  is the pole. For the special case above,

$$\int_{S'} \hat{K}(\vec{r}, \vec{r}'; \omega_{\alpha}) V_{\alpha}(\vec{r}') ds' = 0 \quad (3.3.5.7)$$

so the natural modes and natural frequencies can be calculated from this equation. The coupling coefficients,  $\eta_{\alpha}(\omega)$ , are given explicitly by Baum [69] and involve complicated integrals of the kernel  $K(\vec{r}, \vec{r}'; \omega)$ ,  $V_{\alpha}(\vec{r}')$  and other auxiliary functions. The exact expressions for the coupling coefficients are not essential to our discussion here. As a practical matter, the direct evaluation of  $V_{\alpha}(\vec{r})$ ,  $\omega_{\alpha}$  and  $\eta_{\alpha}(\omega)$  for an object with a non-trivial shape is very difficult. The procedure has not been carried out for an aircraft, for example.

One of the advantages of the SEM, however, is the overview it provides from solutions of canonical problems such as the scattering of a NEMP pulse from a sphere or a cylindrical antenna. This is especially true with regard to the resonance character of the transient response. Figure 3.77 shows the geometry for scattering by a conducting sphere and Figure 3.78 shows some of the lower order natural frequencies of the sphere [69]. These frequencies have been used to construct the time dependent surface charge density on the sphere. Figure 3.79 shows the charge density as a function of time at an angle  $\theta$  of  $3\pi/4$  with the  $\phi$  dependence normalized out. The curves show the convergence of the SEM solution as  $N$ , the number of pole pairs in the sum (3.3.5.6), is increased. The curve labelled  $\infty$  is the exact solution.

Figure 3.80 shows another scattering geometry which has been investigated [69]. Figure 3.81 shows the lower order poles and Figure 3.82 shows the electrical current response on the wire as a function of the number of pole pairs. The

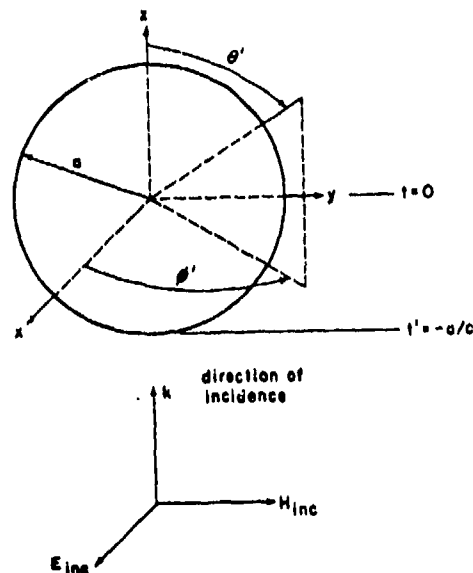


Figure 3.77 Plane Wave Incident on Perfectly Conducting Sphere. The Angle Coordinates  $(\theta, \phi)$  Locate Points on the Surface [69]

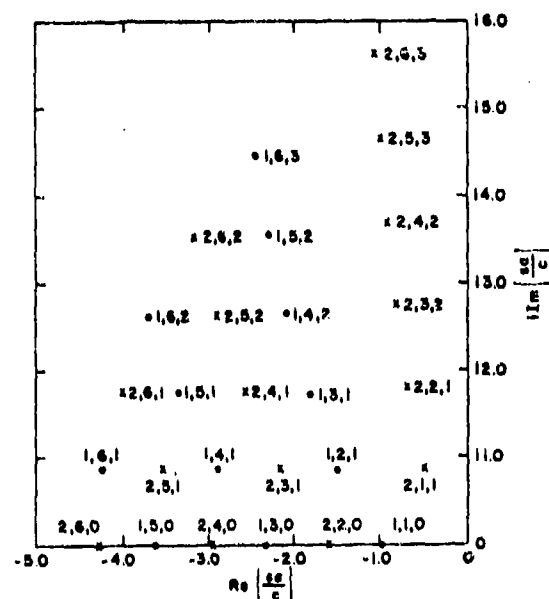


Figure 3.78 Natural Frequencies of the Perfectly Conducting Sphere in the Complex Plane  $(sa/c)$ . For Use with Exterior Incident Wave,  $1 < n < 6$ , Index Set is Three Numbers  $q, n, n'$ .  $q=1$  Denotes the Case where there is no Surface Charge Density.  $q=2$  Denotes the Case of Non-Vanishing Charge Density. The Index  $n$  Identifies the Pole Grouping Associated with an  $n$ -th Order Bessel Function; the  $n'$  Identifies a Particular Pole within that Group [69]

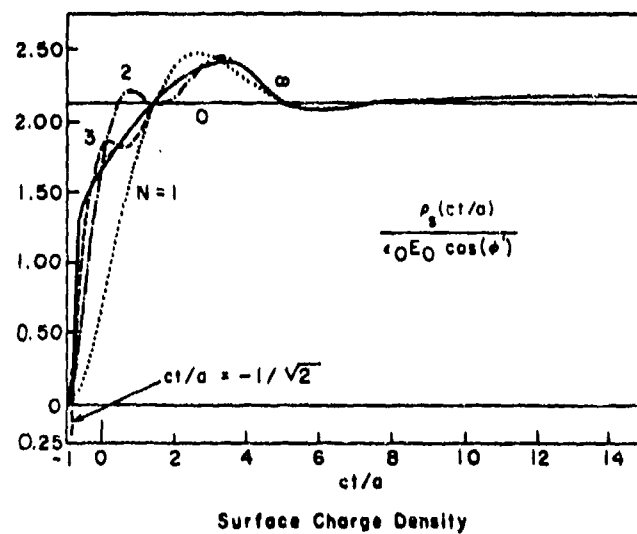


Figure 3.79 Step Function Response for Surface Current and Charge Density on a Perfectly Conducting Sphere, with  $\theta=3\pi/4$  [69]



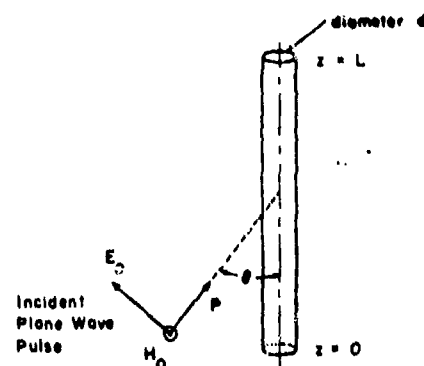


Figure 3.80 Geometry of the Wire Scatterer and Incident Field [69]

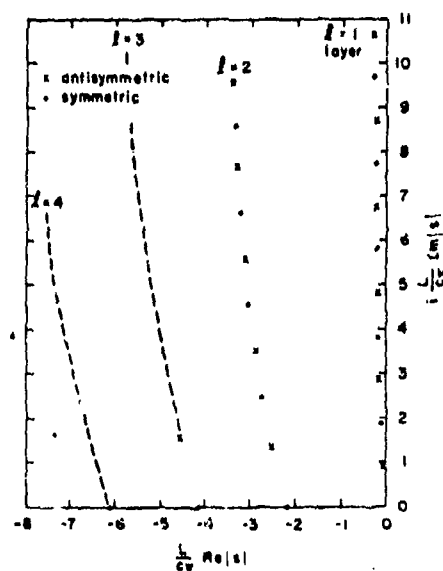


Figure 3.81 Pole Locations in the Complex Frequency Plane for the Thin Wire of  $d/L=0.01$ . The Poles are Grouped into Layers Denoted by  $l$  [69]

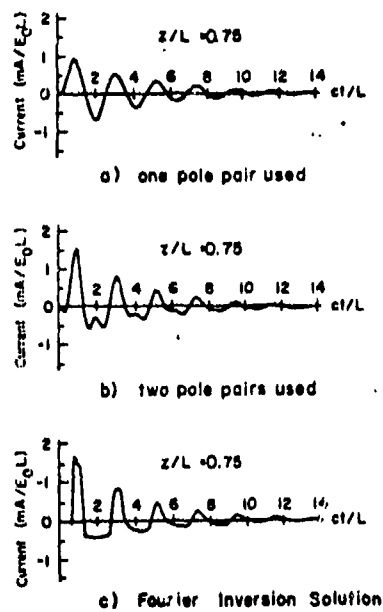


Figure 3.82 The Unit Step Response at  $z/L = 0.75$  on the Thin Wire for One or Two Pole Pairs Compared to the Fourier Inversion Solution. The Angle of Incidence is  $\theta = 30^\circ$ , and  $d/L = 0.01$ . [69]

curve labelled Fourier Inversion Solution is the exact solution. It does not take many pole pairs in either the sphere or wire cases to represent the time domain response fairly accurately.

The SEM has also been applied to the excitation of perpendicular crossed wires [70] over a perfectly conducting ground plane. Figure 3.83 shows the geometrical arrangement of the two wires. For this configuration, the EFIE was solved by a moment method and the natural resonant frequencies were calculated. A parametric study of the pole positions was made and Figure 3.84 shows the variation in the pole positions with the lengths of the elements of the crossed wires. Using these results and results for the natural modes, the time dependence of the transient response for a NEMP illumination was determined. The results for currents as a function of time on various parts of the crossed wires are shown in Figure 3.85. No comparison with measurement or other calculation was made at this time.

As explained earlier, the SEM is not really as much a method of solving boundary value problems as it is an illuminating way of expressing certain transient responses. The method is only helpful in understanding a coupling problem when just a few of the system resonances are excited. Because of the significant low frequency content of a lightning return stroke compared to NEMP, the resonant response of an aircraft or missile may not be the dominating concern it was for NEMP coupling. Therefore, the SEM description of the lightning coupling problem will not be particularly useful unless the resonances of the system are strongly excited. More importantly, however, the SEM method relies on the linearity of the system to construct the time dependent response. The presence of streamers, corona, arcing and the strong time dependence of the air conductivity around a lightning return stroke channel makes a lightning coupling problem non-linear. The SEM method cannot treat these features of the lightning environment.

1. Computer Memory: Information on the amount of computer memory depends on the type of method used to solve the integral equation. Typical moment methods for a wire grid model of an aircraft use more than 100 kg.

2. CP Time: Again the answer to this question is not unique because various methods may be employed. To implement a solution for a wire grid model of an aircraft (not a simple stick model), would require a great deal of CP time.

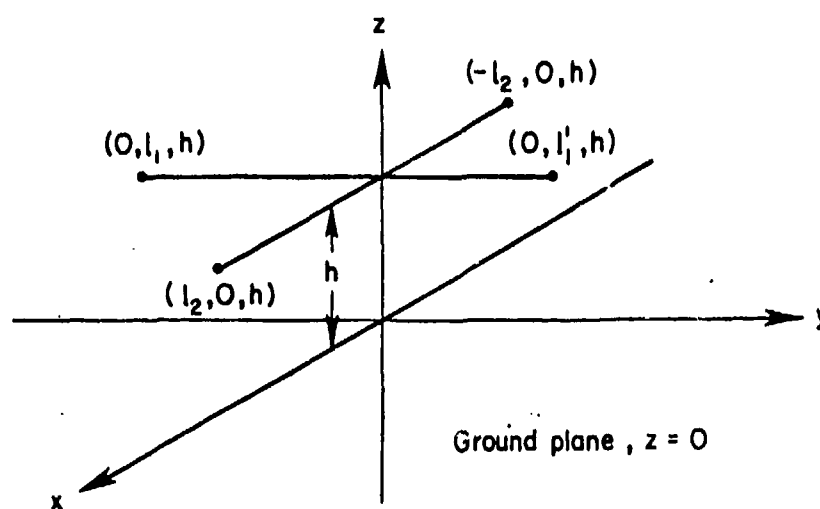
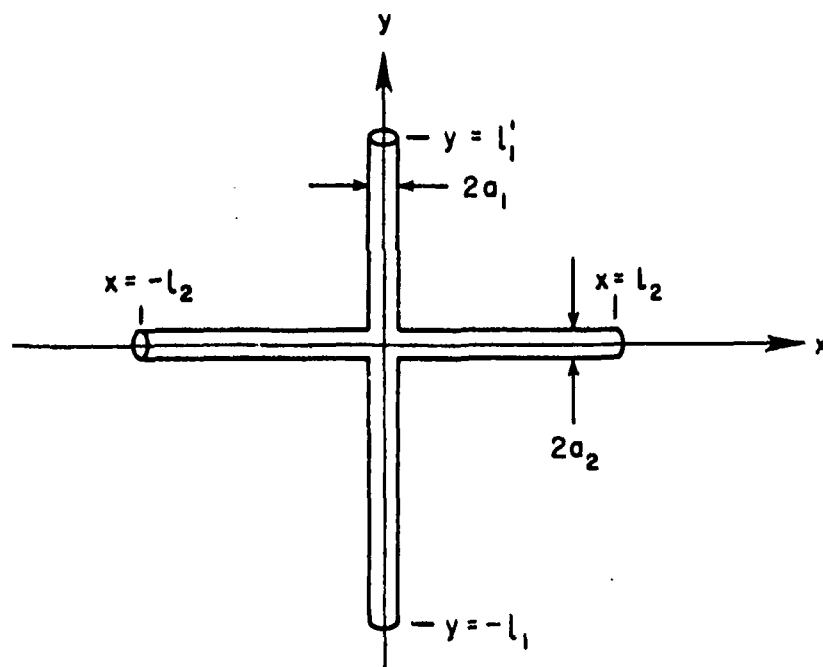


Figure 3.83 The Crossed Wire Configuration Over a Perfectly Conducting Ground Plane [70]

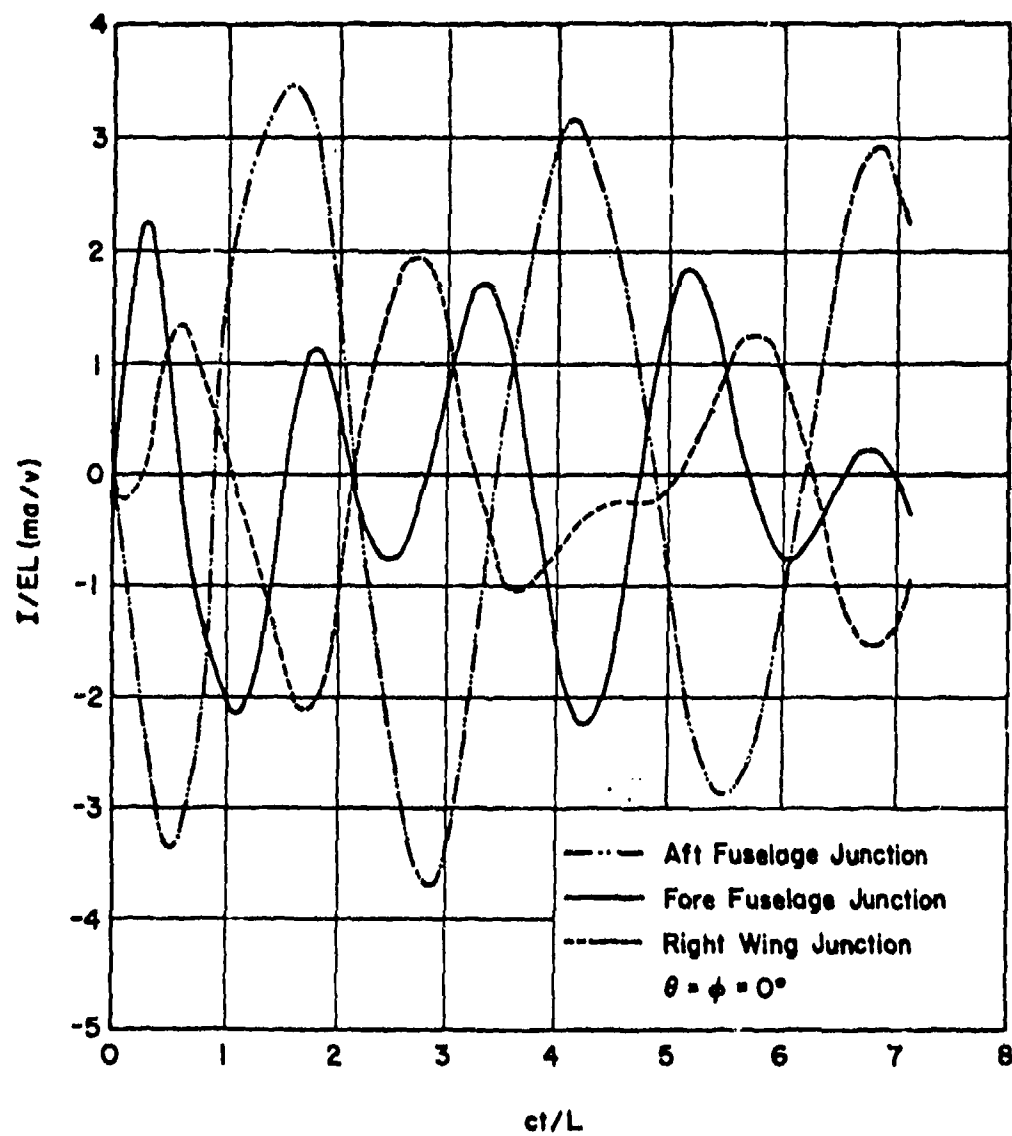


Figure 3.84 Junction Currents Versus Time for a Normally Incident Plane Wave [70]

----- Real Component (Right Scale)

———— Imaginary Component (Left Scale)

$$L = 2l_2, l'_1/l_1 = 0.5, a_1 = a_2, L/a_2 = 20, h/L = 0.2$$

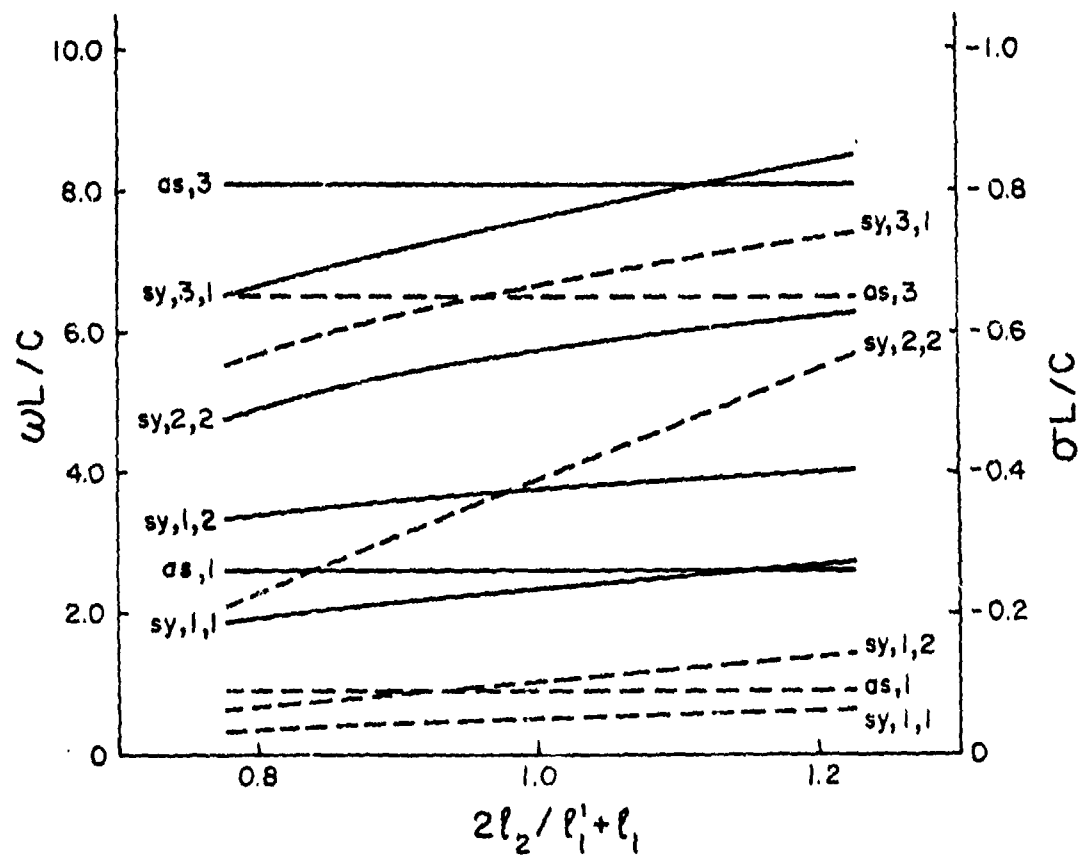


Figure 3.85 Variation in the Natural Frequencies with Change in Relative Wire Lengths for Crossed Wires Over a Perfect Ground [70]

3. Numerical Accuracy: Again this depends upon the method of solution employed. The solutions for the sphere and dipole scatterer shown in Figures 3.50 and 3.51 compare well with exact solutions.

4. Physical Accuracy: Again this depends on the method used. Wire grid models which are likely choices for the SEM method have limitations as described in Section 3.3.4.7.

5. User Orientation: There is no documented code with general availability. Almost certainly the code would require an expert user.

6. Frequency Range: Again, there is no unique answer to this question. A patch segmentation with the MFIE (Sancer) could treat very low frequencies and a wire grid model could provide high frequency response (30 MHz).

7. Attached Stroke: Direct drive of scatterers has not been treated by the SEM method, except that the transient results of calculations such as THREDE have been cast into a form showing the poles and residues in the frequency domain for a direct drive problem. Since wire grid models can incorporate direct drive of the structure, SEM can probably also. However, SEM cannot treat the nonlinear aspects of attached stroke because it is a linear method.

8. Test Case: The SEM could probably not treat the nonlinear aspects of the test case, namely streamer formation, corona, and spark gaps. A wire grid model would be appropriate for modeling an aircraft with return conductors placed around it, however.

9. Aircraft Size: No direct calculations of the SEM parameters have been reported in the literature and so it is difficult to evaluate the size of aircraft that can be treated with the SEM method. For wire grid models, both large and small aircraft can be treated.

10. Lightning Environment: The attached stroke aspect and the near field aspect of the lightning environment can be treated by the SEM. However, nonlinear aspects cannot be treated in a straight forward manner.

11. Experimental Verification: There are no comparisons of the SEM to experimental data for aircraft in the open literature.

### 3.3.6 Lumped Parameter Network (LPN)

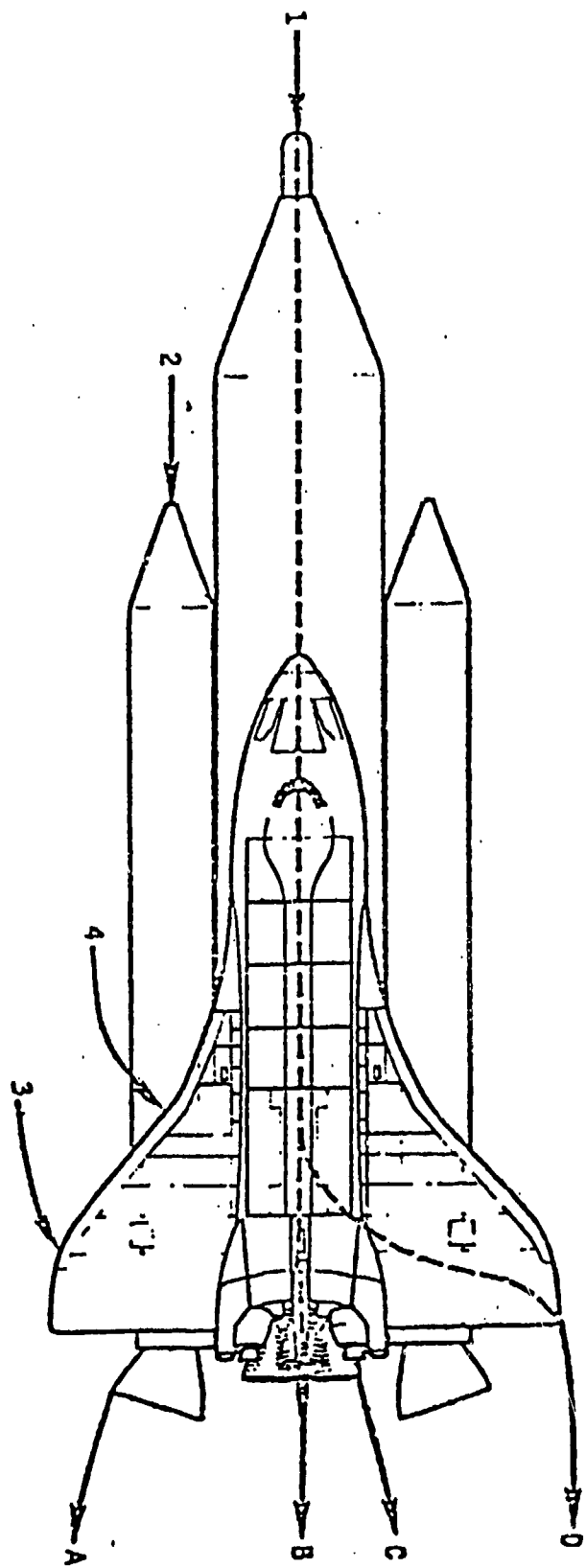
It is possible to model the electromagnetic behavior of a physical structure with an equivalent circuit network whose elements (inductance, capacitance and resistance) represent the distributed properties of the structure. This type of model has been used extensively for both NEMP and lightning coupling problems and the predicted bulk currents compare favorably with experiment and with other proven computational methods.

These methods are often based on insight and intuition, and are usually not derived directly from Maxwell's equations. Their chief advantage is that they are simple to develop and implement, and often provide good insight into the gross response of an object. There are many ways to formulate these models, and the ones presented here are typical examples.

The coupling of lightning to the Solid Rocket Boosters (SRB) of the NASA Space Shuttle has been analyzed using an LPN method [71-72]. At launch the Shuttle system is comprised of several vehicles, the external tank, the SRB's, and the orbiter vehicle. The physical structure of these vehicles is shown in Figure 3.86. The structure has been modeled as a nonuniform transmission line. The inductance and capacitance matrices for the transmission line segments were calculated with a computer code which solves Laplace's equations, and the transmission line response was calculated using the circuit code SCEPTRE. Since the network included nearly 200 elements, a schematic diagram has not been included here. For the purpose of this report, one of the most significant results of the analysis was the agreement between bulk currents as calculated by the LPN method and the currents measured on a Shuttle model by Robb [71-72]. Table 3.4 summarizes the computed and measured peak currents and it can be seen that the agreement is within 15% for each case studied.

SGEMP (System Generated EMP) excitation of the FLTSATCOM satellite has also been studied using the LPN method [73]. The satellite is shown in Figure 3.87. Calculations of the gamma ray induced currents (SGEMP) have been made using a 2D finite difference method and the LPN method. Figure 3.88 shows a schematic diagram of the circuit network used to model the structure and Figure 3.89 is the current flowing in a strut between the main body of the satellite and of the solar panels. The agreement is generally good, although there are differences in waveform structure.





Notes:

1. Most likely stroke entry points are at 1, 2, 3, 4, and 5 with highest probability at 1, followed by 2 and 3 and then 4 and 5.
2. The least likely exit point is the orbiter main engine - C.
3. Probabilities of damage are equal at an entry or an exit point.

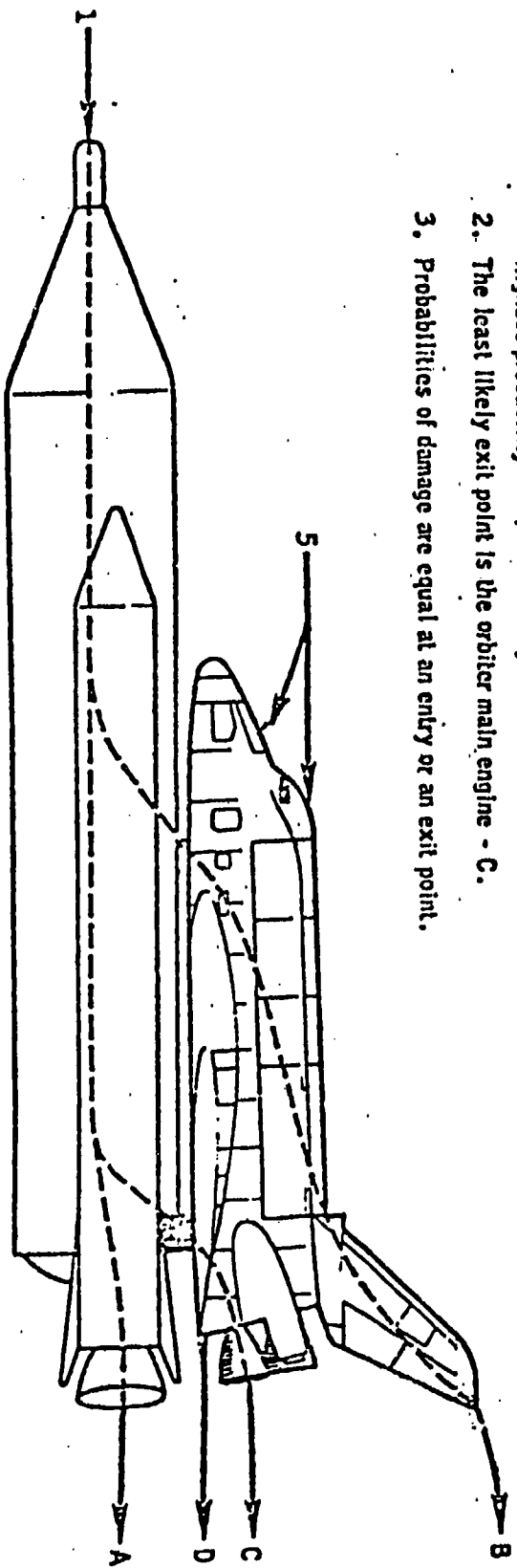


Figure 3.86 NASA Shuttle Vehicles; External Tank, SRB's and Orbiter as Configured at Launch [71]

Table 3.4 Comparison of External Surface Currents as Calculated by a LPN Method and as Measured by LTRI (Lightning and Transient Research Institute [72])

Entry Point	Exit Point	SRB Attach Points				Orbiter Attach Points		SRB Current Density at Cable Tunnel KA/m
		FWD		AFT				
		Left KA	Right KA	Left KA	Right KA	FWD KA	AFT KA	
Forward ET	Left SRB	62 52   9	25 37   9	127 150   9	30 36   9	56 60   3	54 58   4	11.2 10.5   3
Left SRB	Left SRB	115 120   2	30 37   10	101 130   3	26 36   6	55 57   2	53 56   3	----
Forward Orbiter	Left SRB	56 45   1	29 30   2	117 155   4	22 29   4	94 110   8	99 90   5	----

\* Exp. Value  
Anal. Value

— Error Percentage

\*\*Normalized to 68KA flowing on SRB between attach points

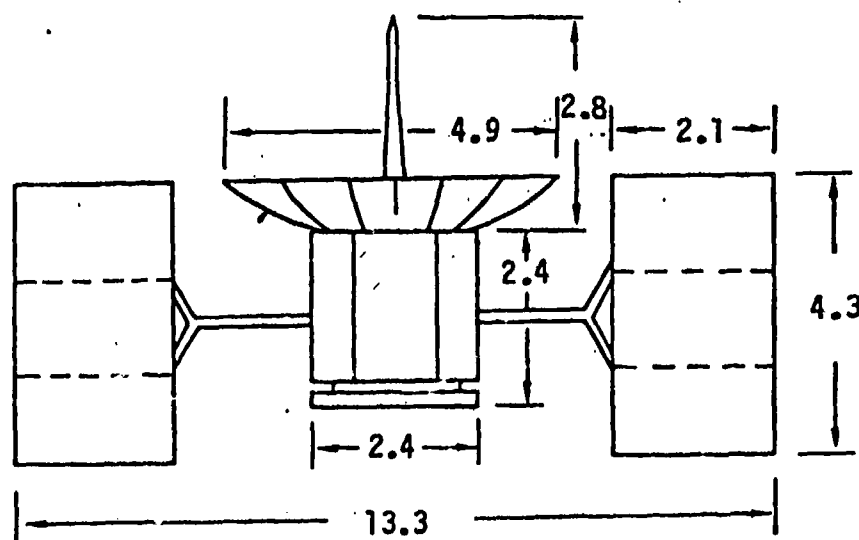
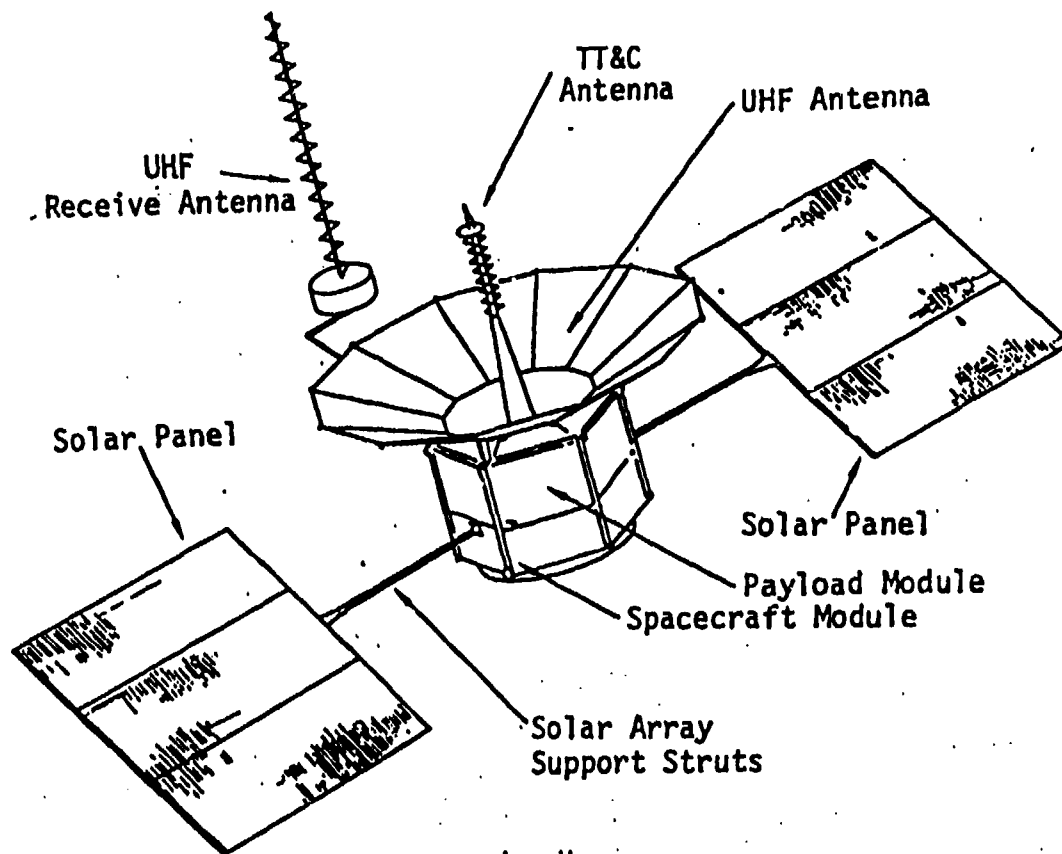


Figure 3.87 FLTSATCOM Showing Important Dimensions (in Meters)

Note: Units are pf, nH,  $\Omega$

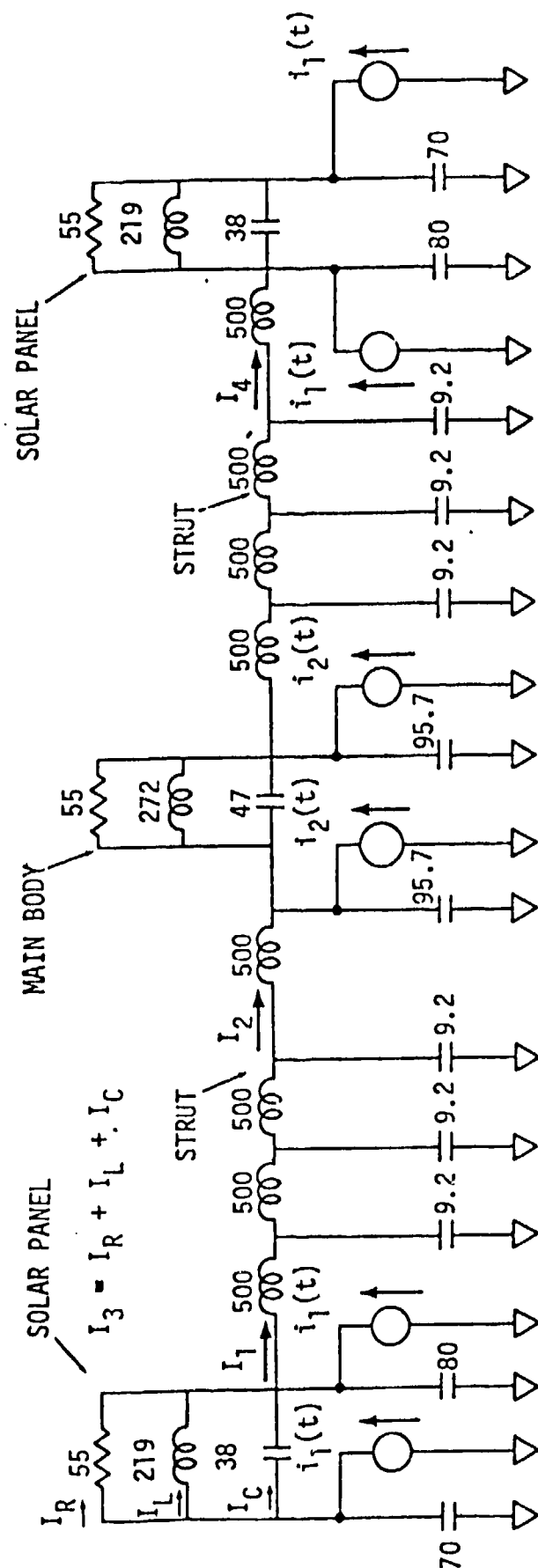


Figure 3.83 FLTATCOM LPN Model Used for SGEMP Excitation [73]

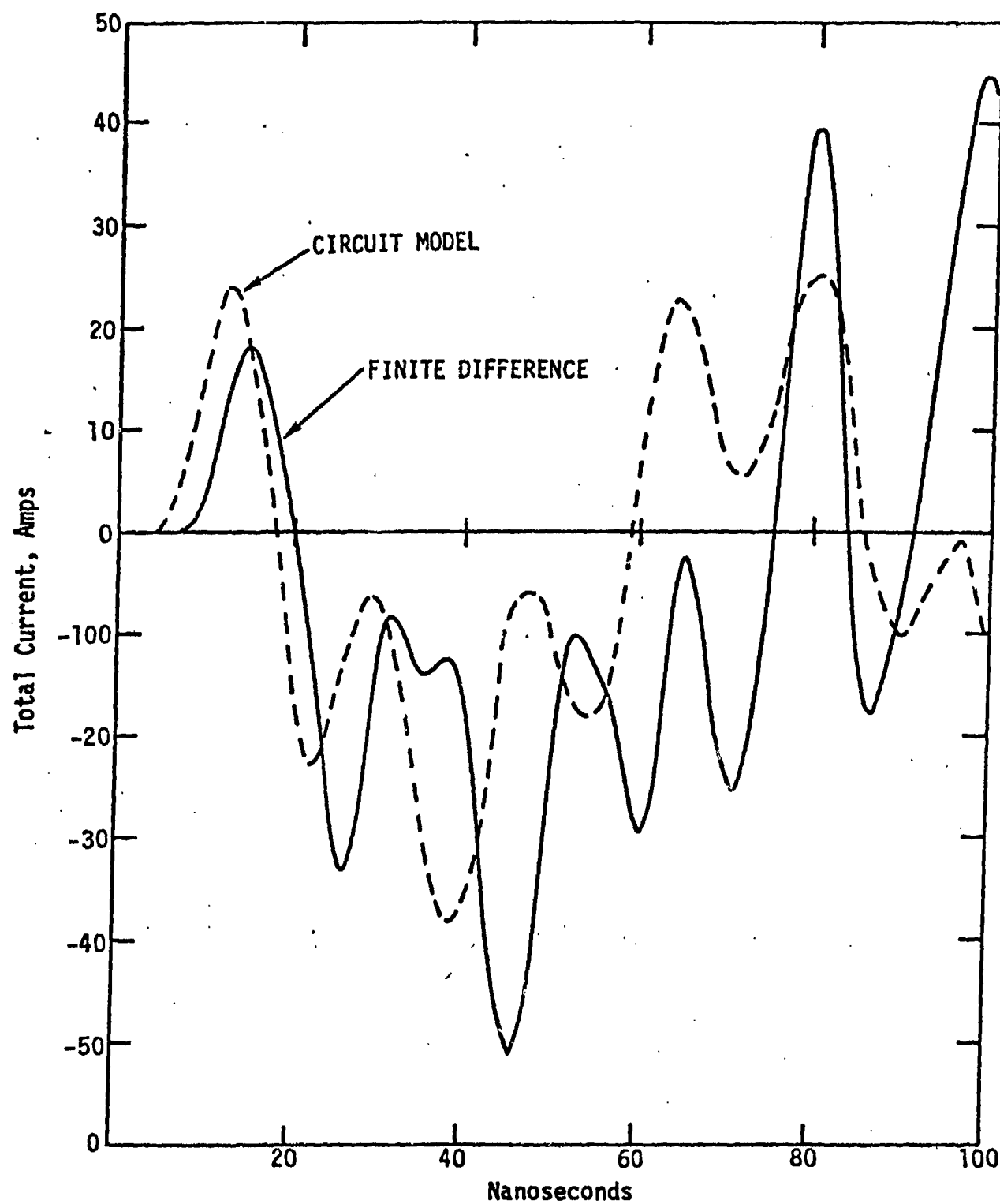


Figure 3.89 Overlay of Finite-Difference and Circuit Model Results for the Current Between the Main Body and the Right Hand Solar Panel [73]

An LPN model has also been used to analyze NEMP currents induced on a fat cylinder [74]. These results have been compared to calculations by the MFIE method of Perala [30] described in Section 3.3.3.3. For this LPN model, the surface of the cylinder was partitioned into patches and the effect of each patch was simulated by a network as shown in Figure 3.90. Plane wave excitation having a standard EMP double exponential time dependence was used to drive the network and SCEPTRE was used to solve for the currents. Figure 3.91 shows the circumferential surface current density as a function of time for the MFIE results of Perala [30] and for the LPN network with two choices of the damping resistance. The agreement is only fair. However, the shadowing effect at the rear of the cylinder is predicted well by the LPN method as shown in Figure 3.92.

One type of LPN model which has been previously used in the lightning community may be termed a filamentary model [75,76]. This is a model for late time and computation of only magnetic fields. In this model, aircraft surfaces are represented by parallel axial conductors which approximate the aircraft surface (Figure 3.93). The conductors are only magnetically coupled to each other. Imperfectly conducting skins can be modeled by incorporating a resistor in series with a conductor's inductance. In this way inhomogeneous materials such as metal and composite airframes can be included, and current redistribution as a function of time can be estimated, along with the resulting internal magnetic fields. These models cannot predict resonant behavior but they are useful for estimating late time effects.

The eleven evaluation criteria will now be discussed for the LPN model.

1. Computer Memory: The LPN method requires very little computer memory. Comparisons between an LPN and a three-dimensional finite difference model of an F16 and C130 are given in Section 5.2.

2. CP Time: The LPN method also requires much less CP time than other techniques. Again, comparisons are given in Section 5.2.

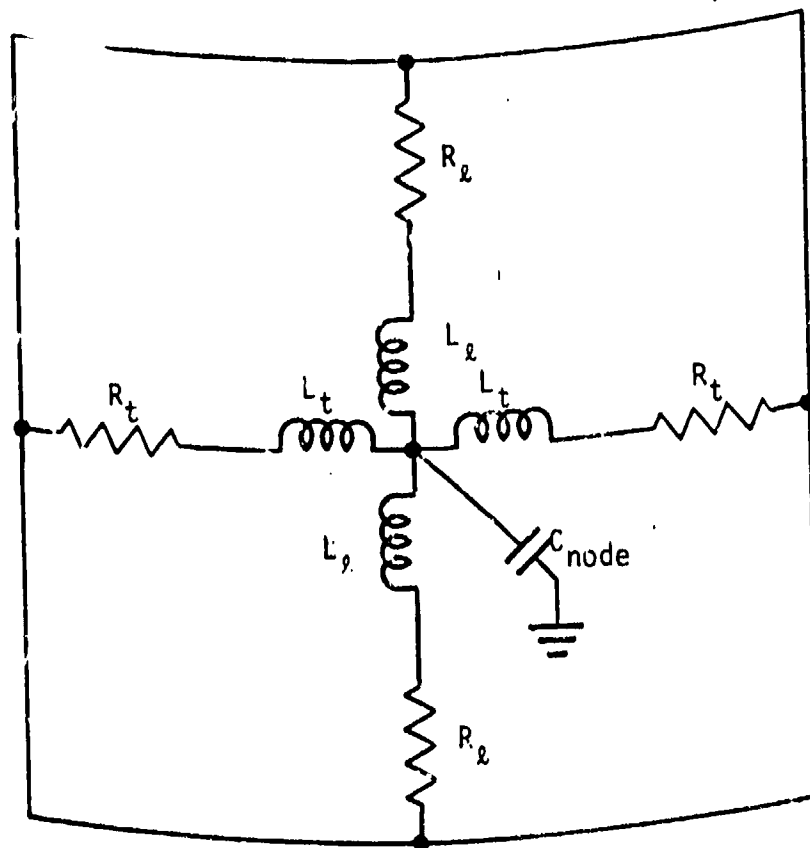


Figure 3.90 An Example of a Patch on the LPN Surface Model [74]

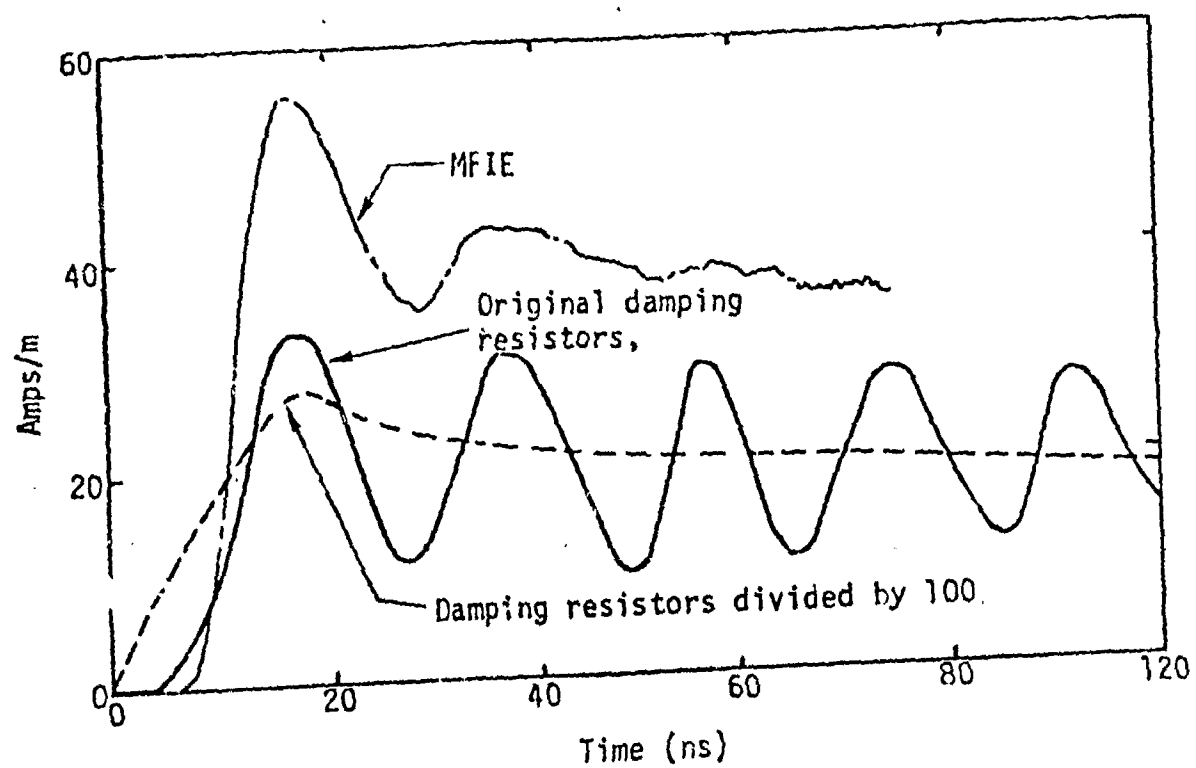


Figure 3.91 Circumferential Surface Current Density at  $\phi = 90^\circ$  as Calculated by the MFIE, and the Cylinder Circuit Model for Two Different Damping Values [74]



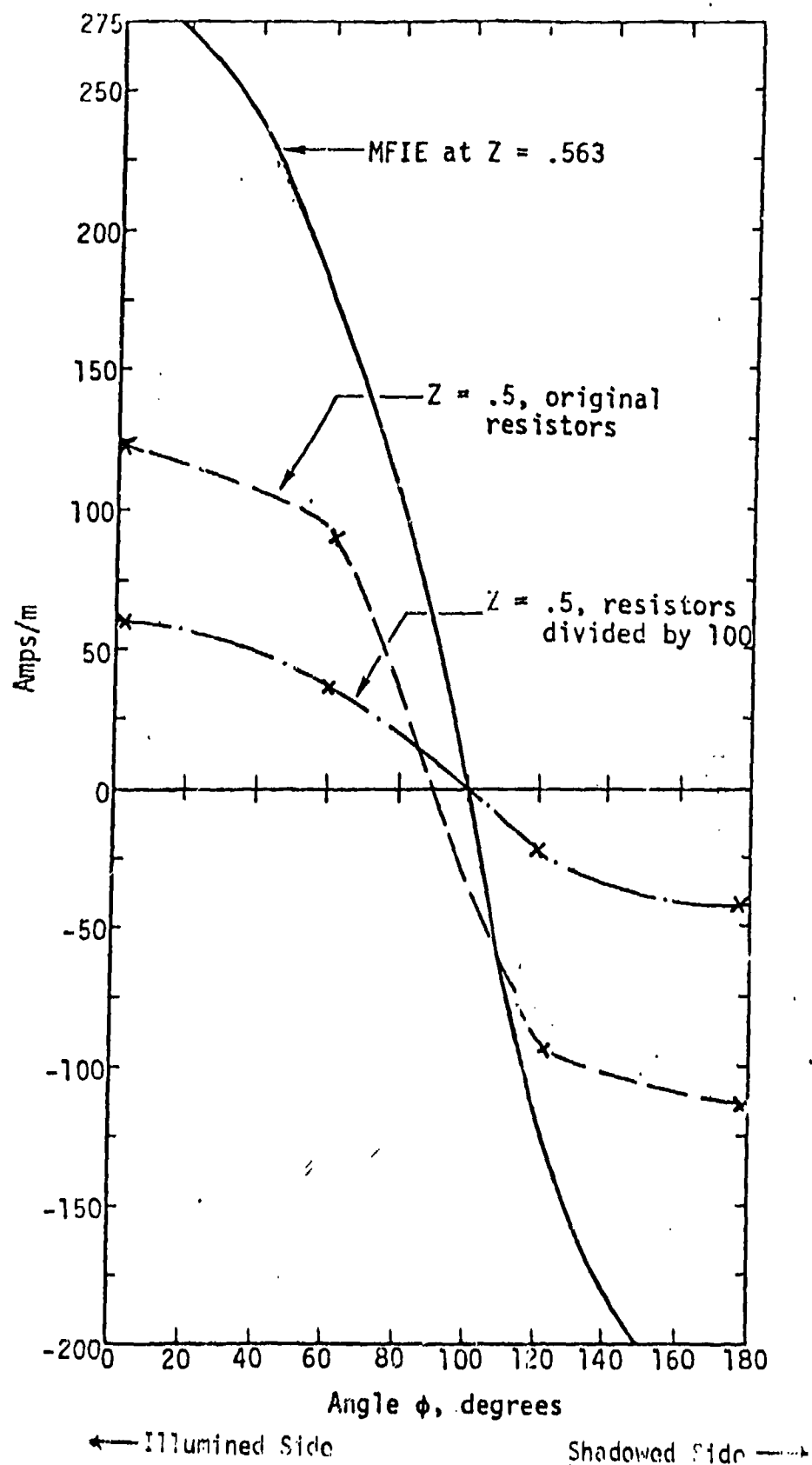


Figure 3.92 Circumferential Variation of Axial Current Density as Calculated by the MFIE and the Circuit Model for Two Damping Resistor Values

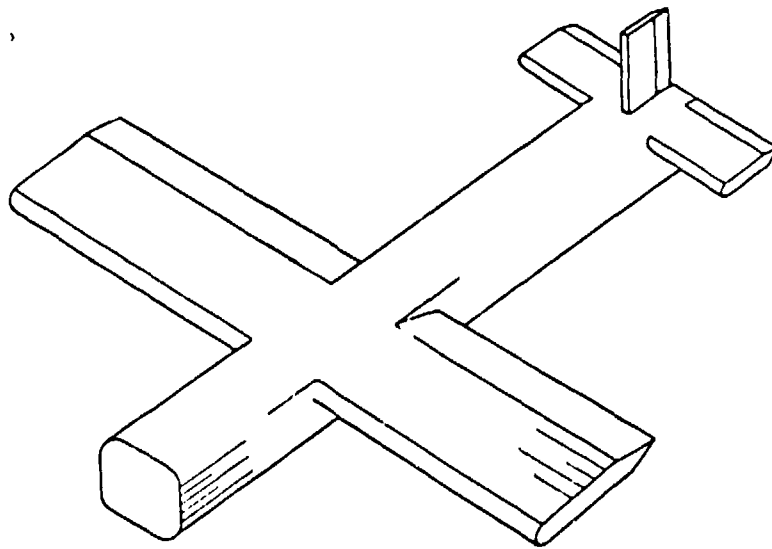


Figure 3.93 Complete Aircraft Represented by Parallel Current Carrying Filaments [76]

3. Numerical Accuracy: The numerical accuracy of the code is limited by the method used to solve the network equations. These methods are well developed, so the LPN method has potentially little numerical error.

4. Physical Accuracy: The LPN method is most severely limited in its physical accuracy. It usually represents only the bulk structure of the aircraft and does not generally include all the interactions between the physical members (wings, fuselage, tail, etc.).

5. User Orientation: There is presently no well documented code to represent aircraft. Furthermore, the user will need to select the lumped parameter values intelligently. Therefore, the LPN method is a simple, user oriented method, but requires judgement on the part of the user to determine the parameter values and interpret the results.

6. Frequency Range: The code can treat both low and high frequencies (10 kHz to 30 MHz) consistent with other modeling errors.

7. Attached Stroke: The code can treat an attached stroke, and it can treat the nonlinearities of the attached lightning channel if the circuit network solution is implemented by a time domain code such as SCEPTRE.

8. Test Case: The LPN method can model the direct drive and non-linear aspects (spark gaps) of the test case. It may not be very good, however, at modeling the details of the physical structure of an aircraft with return conductors.

9. Aircraft Size: The method can model both small and large aircraft.

10. Lightning Environment: One of the attractive features of the LPN model is that it can treat the near field, attached stroke and non-linear aspects of the lightning environment.

11. Experimental Verification: The LPN model has been tested against experimental results for the NASA Shuttle SRB analysis, and the LPN and experimental data agree within 15%. The LPN method has also been tested against experimental results indirectly since it agrees well (see Section 5.2) with THREDE results and THREDE has been compared extensively with experiment.

### 3.3.7 Additional External Coupling Methods

#### 3.3.7.1 Introduction

Several additional methods, some of which have been used for external coupling calculations, are relatively new or do not fit readily into the categorization that has been chosen for Chapter 3. These methods are described in this section. They include an Analytical Stick Model (Section 3.3.7.2), the Unimoment Method (Section 3.3.7.3), a Triangular Patch Method due to Wilton (Section 3.3.7.4) and the Finite Element method (Section 3.3.7.5).

#### 3.3.7.2 Analytical Stick Model [77,78]

To characterize the EMP response of an aircraft it is helpful to have a simple theory which will enable a calculation of the basic system resonances. In two papers [77,78] applied to a stick model, Bedrosian has calculated expressions for the resonant frequencies and damping constants of an aircraft. The expressions are easy to solve and give realistic values for the basic resonances of the aircraft.

Figure 3.94 shows the physical construction of the stick model that has been analyzed. It consists of six wire segments representing the wings, fuselage and stabilizers. The expressions that have been derived give the structure currents when the model is illuminated by a NEMP plane wave.

The essential element in the solution is an analytical expression for the inhomogeneous solution to the current in a wire segment due to the incident field. The expression is

$$I_{ind}(k, x, \theta) = \frac{4\pi j E_0}{k Z_0 \Omega \sin \theta} e^{jkx \sin \theta} \quad (3.3.7.1)$$

where  $I_{ind}$  is the induced current on a wire segment,  $k$  is the wave number of the incident wave, the coordinate  $x$  identifies the position along a wire segment,  $E_0$  is the incident field strength, and  $\theta$  is the angle between the structure and the wave vector as defined in Figure 3.94.  $Z_0$  is the impedance of free space and  $\Omega$  is the fatness parameter

$$\Omega = 2 \ln[2 (\text{stick length})/(\text{stick radius})]. \quad (3.3.7.2)$$

The total solution for the current in the  $n^{\text{th}}$  wire segment is written

$$I_m(\xi) = I_{ind,n}(\xi, \theta) + S_n \sin[k(\xi - \xi_n)] + C_n \cos[k(\xi - \xi_n)] \quad (3.3.7.3)$$

to first order in the parameter  $\Omega$ . This expression has unknown constants  $S_n$  and  $C_n$  for the  $n^{\text{th}}$  segment. By requiring that the current vanish at any unterminated end of a wire segment, and that the current and charge density be conserved at junction points of wires, a set of linear equations for the parameters  $S_n$  and  $C_n$  can be generated. Written in matrix form, these equations are

$$[M] \begin{pmatrix} S \\ C \end{pmatrix} = \frac{4\pi j E_0}{k \Omega Z_0} \begin{pmatrix} V_s \\ V_c \end{pmatrix} \quad (3.3.7.4)$$

where the matrix  $[M]$  depends on the geometry of the stick model, and  $\begin{pmatrix} S \\ C \end{pmatrix}$  and  $\begin{pmatrix} V_s \\ V_c \end{pmatrix}$  are column vectors for the unknown constants and for the source, respectively. The natural modes of oscillation are determined by finding the eigenvalues and eigenfunctions of the matrix  $[M]$ . The damping constants are determined from expressions for the average radiated power and the stored magnetic energy.

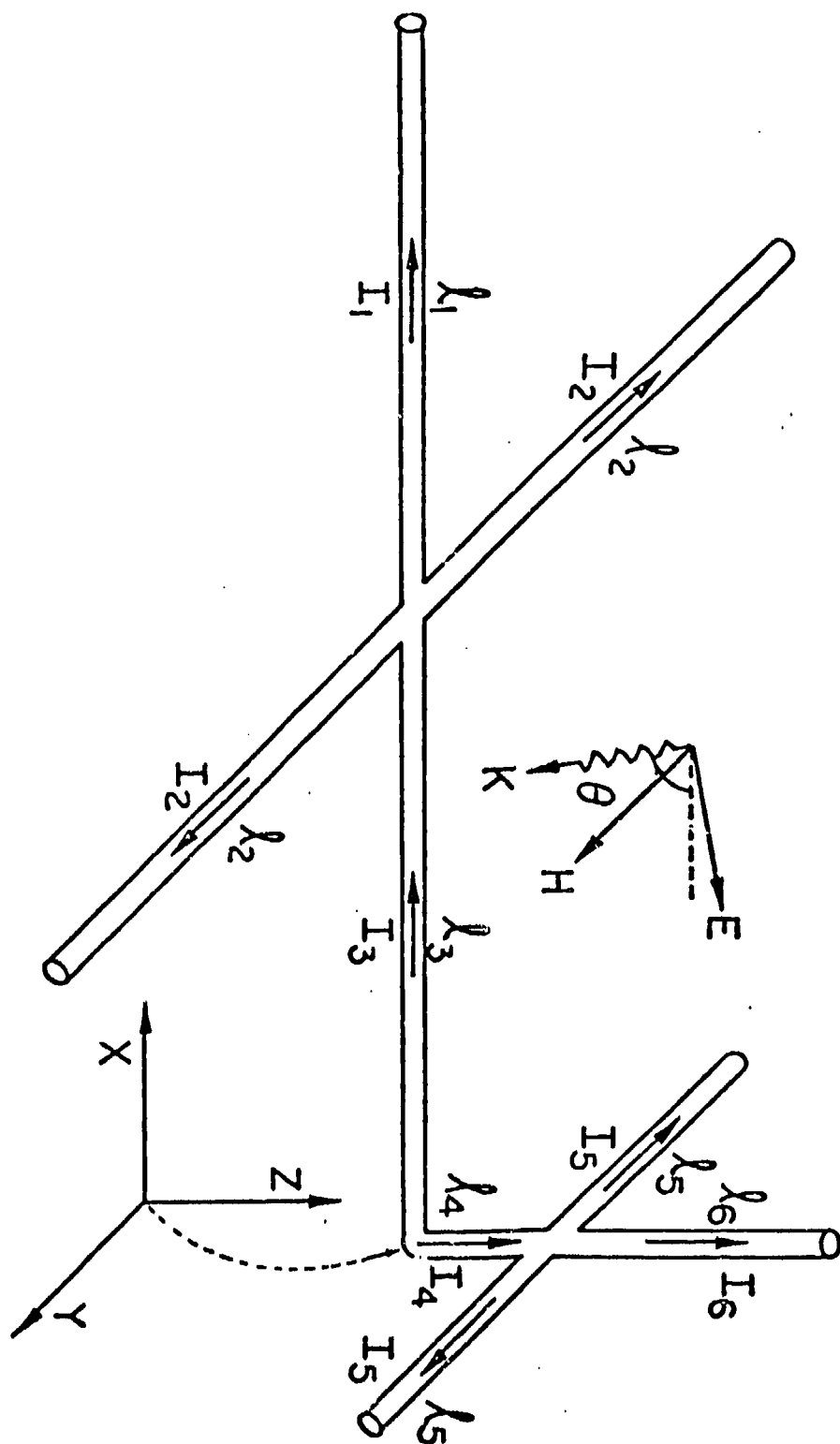


Figure 3.94 Stick Model Consisting of Six Elements Used in the Analytical Stick Model Analysis [77]

Solutions for stick models of the B1, E4, and EC135 have been calculated by Bedrosian [77]. Table 3.5 and Figure 3.95 show the parameters used in the model of the B1 and show the frequencies for the first few resonances. Tables 3.6 and 3.7 and Figures 3.96 and 3.97 provide similar information for the E4 and EC135, respectively. Figure 3.98 shows a comparison of the axial surface current density on the top of the main fuselage of a B52 as calculated by THREDE and the positions of the resonances as calculated by the analytical stick model. Below 7-8 MHz there is a reasonable correspondence between the stick model resonances and the THREDE calculations.

The eleven evaluation criteria for the analytical stick model will now be discussed.

1. Computer Memory: The most significant advantage of the analytical stick model is that it requires very modest computer resources. For a version of this method implemented by EMA, the storage required was 60 k<sub>g</sub> words and this storage included a Fourier inverse subroutine to calculate the time dependent response.

2. CP Time: For the above analysis on the B52, about 10 minutes of CP time on a Data General Nova minicomputer were required to calculate the currents in all six segments and to determine the time domain response.

3. Numerical Accuracy: The method is limited in its numerical accuracy by the expression which gives the wire segment drive in terms of the incident plane wave, by the approximation used to find the roots of the [M] matrix, and by the approximation used to evaluate the integrals for power in the calculation of the damping constant. However, the numerical error introduced by the above approximations is probably small compared to the drastic physical approximations that are made.

4. Physical Accuracy: This model, like any other stick model, can provide only bulk currents, and inferring surface current densities from the bulk currents can be misleading as discussed in Section 3.3.4.7. The physical accuracy is, therefore, not good.

5. User Orientation: There is no documented code generally available which is based on the method. However, the method is simple and it would be easy to write a well documented version. Furthermore, the selection of stick model elements to represent an aircraft is straightforward and the code has the potential of being very user oriented.

Table 3.5 Parameters Used in the Analytical  
Stick Model of the B1 [77]

Lengths (meters)

1. Forward fuselage..... 24.5
2. Wing..... 21.6
3. Aft fuselage..... 18.5
4. Vertical stabilizer (bottom)..... 2.0
5. Horizontal stabilizer..... 8.0
6. Vertical stabilizer (top)..... 6.5

$\Omega = 7.0$

Frequency (MHz)

Decay time ( $\mu$  sec)

2.2	0.73
3.2	0.65
6.0	0.40
8.2	0.27
9.6	0.13

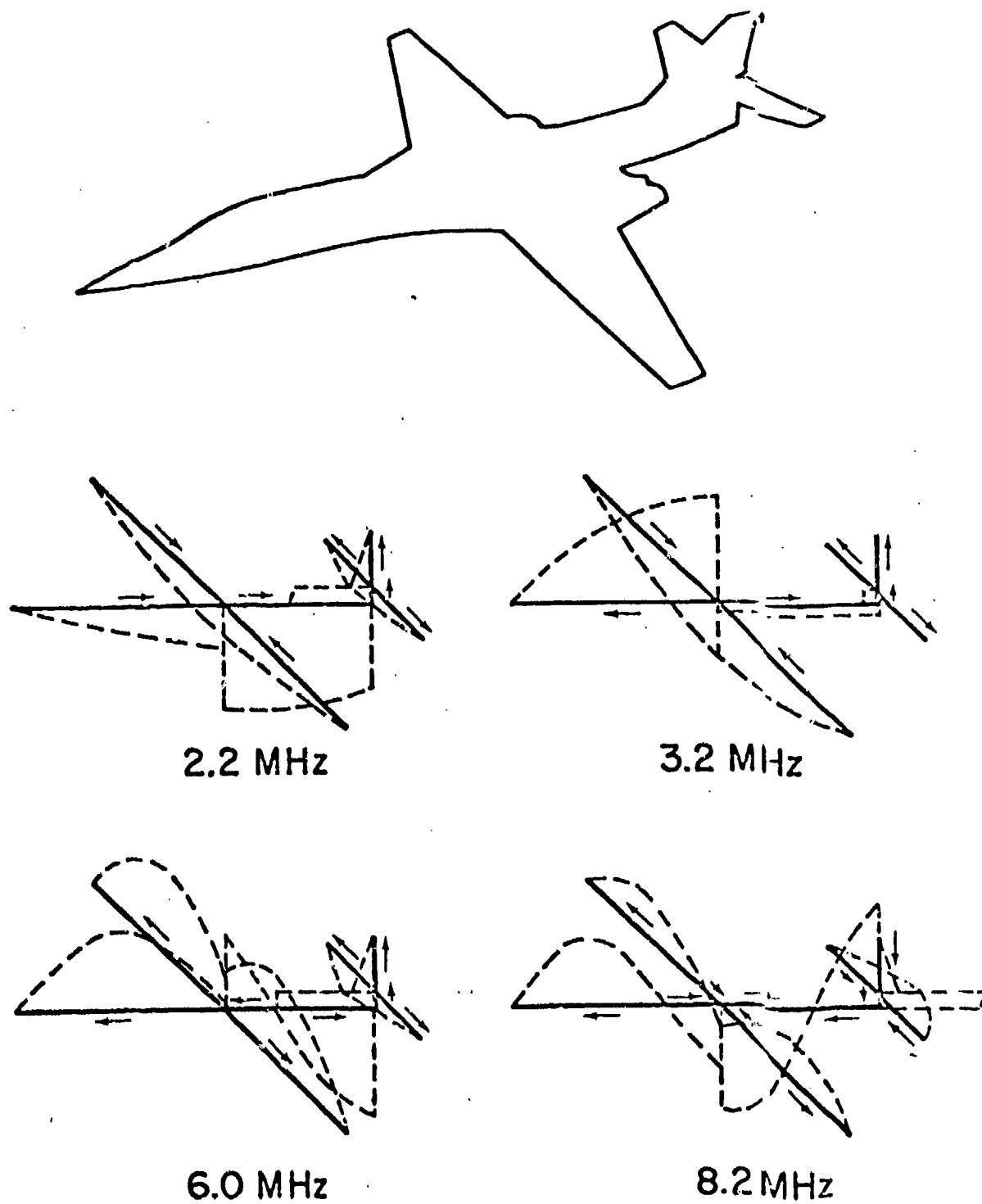


Figure 3.95 B-1 Natural Modes. The Dashed Lines Represent the Current Distribution on the Aircraft Segments at Resonance, While the Arrows Indicate Direction [77]



Table 3.6 Parameters Used in Analytical Stick Model of the E4 [77]

Lengths (meters)

1. Forward fuselage.....	25.0
2. Wing.....	36.0
3. Aft fuselage.....	36.0
4. Vertical stabilizer (bottom)....	0.0
5. Horizontal stabilizer.....	12.0
6. Vertical stabilizer (top).....	16.0

$$\Omega = 6.2$$

Frequency (MHz)

Decay time ( $\mu$  sec)

1.3	1.27
2.6	0.57
3.9	0.50
5.0	0.37
5.3	0.23

Table 3.7 Parameters Used in the Analytical Stick  
Model of the EC 135 [77]

Lengths (meters)

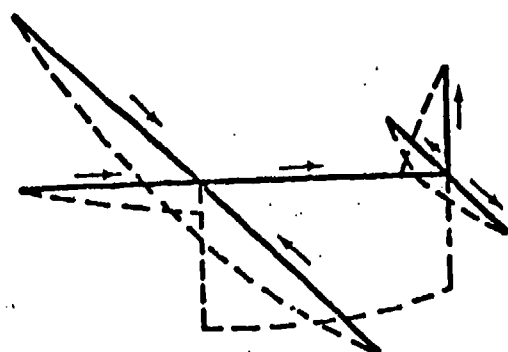
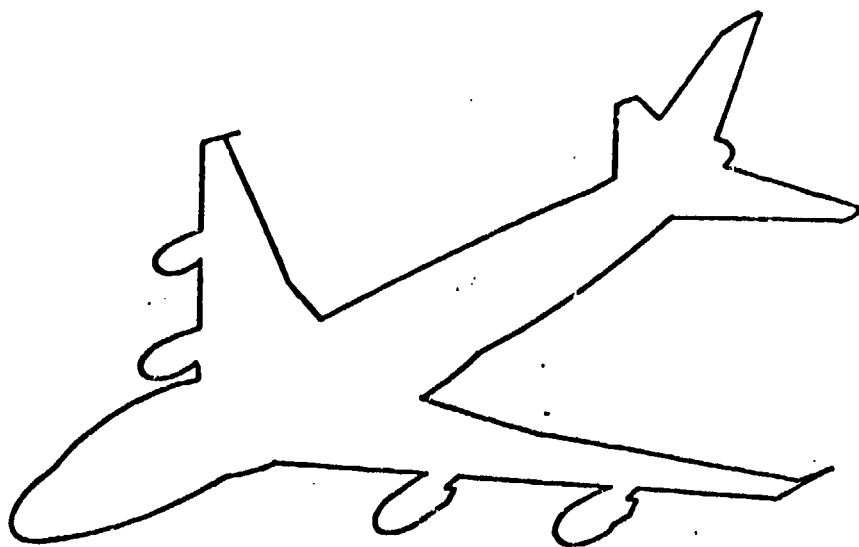
1. Forward fuselage.....	13.0
2. Wing.....	20.0
3. Aft fuselage.....	23.0
4. Vertical stabilizer (bottom).....	0.0
5. Horizontal stabilizer.....	7.0
6. Vertical stabilizer (top).....	11.0

$$\Omega = 6.5$$

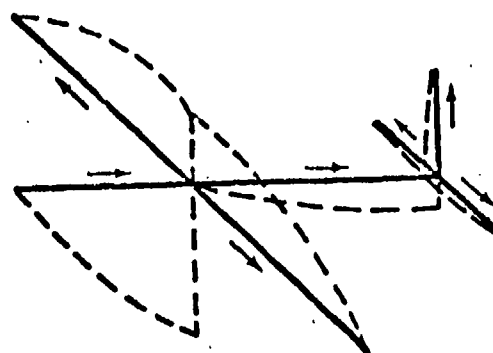
Frequency (MHz)

Decay time ( $\mu$  sec)

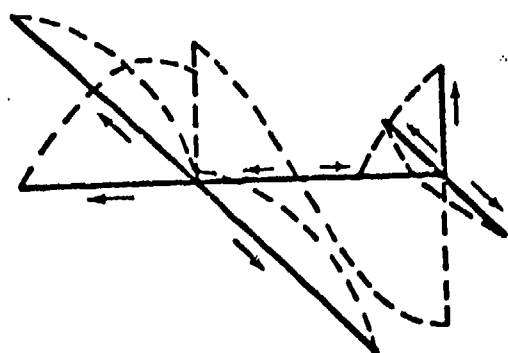
2.1	0.78
4.8	0.38
6.4	0.26
7.8	0.20
9.0	0.17



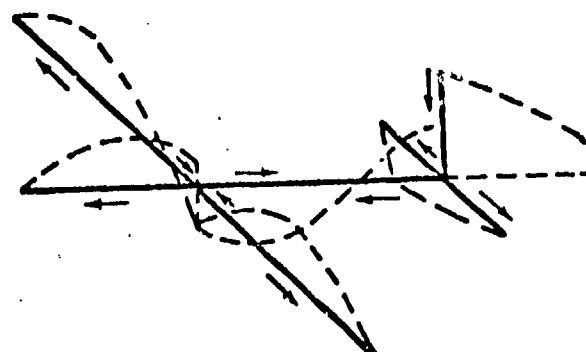
1.3 MHz



2.6 MHz

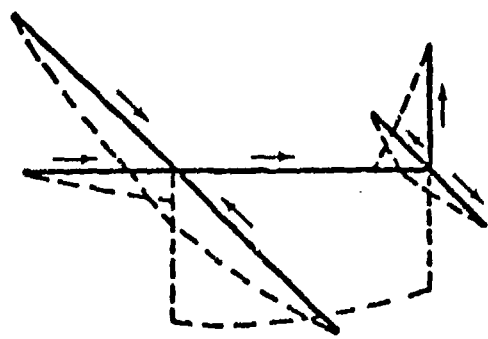
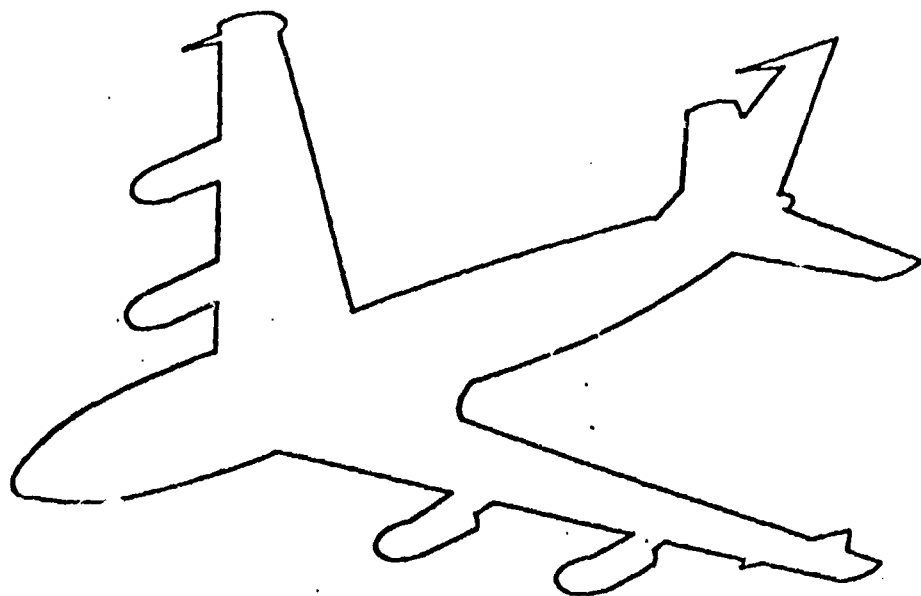


3.9 MHz

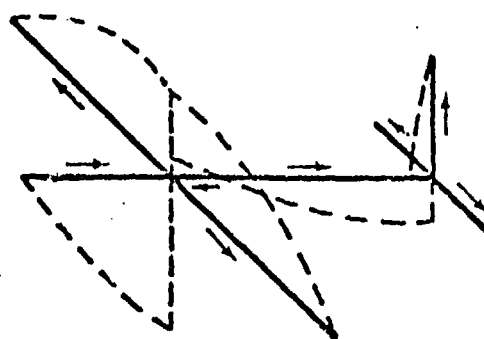


5.0 MHz

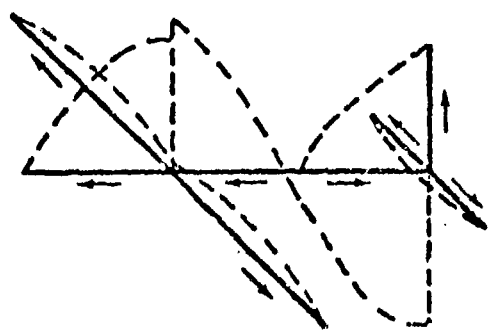
Figure 3.96 E-4 Natural Modes. The Dashed Lines Represent the Current Distribution on the Aircraft Segments at Resonance. While the Arrows Indicate Direction [77]



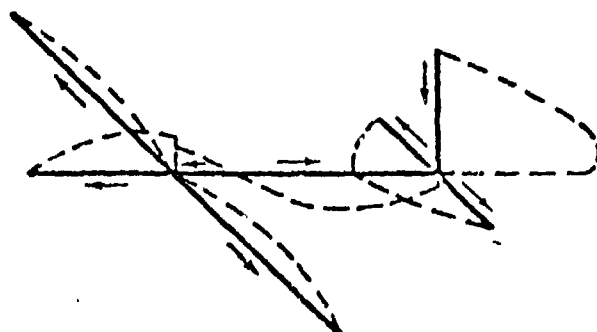
2.1 MHz



4.8 MHz



6.4 MHz



7.8 MHz

Figure 3.97 EC-135 Natural Modes. The Dashed Lines Represent the Current Distribution on the Aircraft Segments at Resonance, While the Arrows Indicate Direction [77]

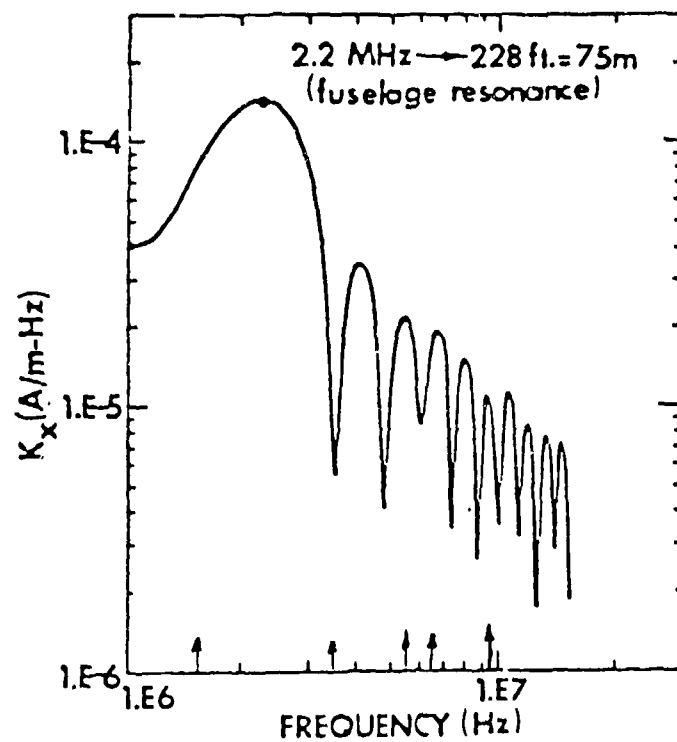


Figure 3.98 Axial Surface Current Density Measured on a B-52 on the Main Fuselage (TOP) Between the Wing and Stabilizer. See Figure 3.15 for Position of this Test Point (Test Point 4) [77]

6. Frequency Range: The code is applicable in the frequency range of aircraft resonances, namely 0.5 MHz to 20 MHz. In this range, the basic resonant frequencies are given fairly accurately although the damping constants are not.

7. Attached Stroke: The model is not presently able to treat current injection, and furthermore because it gives a frequency domain solution, it cannot treat the nonlinearities inherent in the attached stroke phenomenon.

8. Test Case: The method cannot treat current injection, the return conductors which will probably be used for the test case, nor the nonlinear aspects (spark gaps) of the test case. It is therefore not well suited to the test case.

9. Aircraft Size: Within the physical accuracy limitations of the stick model, this method can treat both large and small aircraft.

10. Lightning Environment: The model could treat the near fields of a lightning return stroke with some modification. Otherwise, the model is not well suited to the lightning environment since it cannot treat an attached stroke nor can it treat the nonlinear aspects of the environment.

11. Experimental Verification: The results for the B52 resonances have been compared to measurements and they compare fairly well.

#### 3.3.7.3 Unimoment [79-81]

Although there are well developed methods for solving integral equations, (e.g., the method of moments described in Section 3.2.3), integral equation formulations of scattering or coupling problems can not treat inhomogeneous or time dependent problems without extensive mathematical and/or numerical efforts. Finite element and finite difference techniques, however, can incorporate such inhomogeneities and time dependent media without serious problems. The unimoment method as developed by Mei [79-81] endeavors to utilize the strengths of finite difference or finite element solutions in bounded inhomogeneous regions, and integral equation solution methods in homogeneous, unbounded regions. This is done by partitioning the general scattering problem space into two parts by means of an artificial closed boundary  $C$ . The boundary  $C$  is chosen to enclose the physical parts of the scattering region which have the inhomogeneities. Then, the finite

difference or finite element methods are used for the interior region and integral equation methods are used outside  $C$ , and the solutions are matched on  $C$ .

Consider a two dimensional scattering problem as shown in Figure 3.99 where  $\phi^{inc}$  is an incident wave that is scattered by the dielectric  $\epsilon_1$ . Let the scattering region be divided into two parts by the contour  $C$  so that the dielectric  $\epsilon_1$  is entirely inside  $C$  and there is free space outside  $C$ . If  $G_1$  and  $G_0$  are the Green's functions for the inside and outside regions, respectively, then the scattered field  $\phi(\vec{r})$  is the solution of the coupled integral equations

$$\frac{1}{2} \phi(\vec{r}) = \phi^{inc}(\vec{r}) - \lim_{\sigma \rightarrow 0} \int_{C-\sigma} \left\{ G_0 \frac{\partial \phi}{\partial n} - \phi \frac{\partial G_0}{\partial n} \right\} dC' \quad (3.3.7.5)$$

and

$$\frac{1}{2} \phi(\vec{r}) = \lim_{\sigma \rightarrow 0} \int_{C-\sigma} \left\{ G_1 \frac{\partial \phi}{\partial n} - \phi \frac{\partial G_1}{\partial n} \right\} dC' \quad (3.3.7.6)$$

where  $\vec{r}$  and  $\vec{r}'$  are on the boundary  $C$ . In a conventional moment method solution, unknowns  $\phi$  and  $\partial\phi/\partial n$  are written in terms of expansion functions and the two integral equations are reduced to a set of linear equations. In the unimoment method, the expansion functions are determined by the solution of Maxwell's equations for the interior region (not necessarily by the solution of the integral equation in (3.3.7.6) however). The unknown fields in the problem are expanded in a finite series of the expansion functions and the expansion coefficients are determined by a method of moments solution of just one integral equation, namely equation (3.3.7.6), and hence the name unimoment.

The most attractive feature of the unimoment solution for a lightning coupling problem is the possibility of replacing equation (3.3.7.2) by a solution method which would be able to treat the nonlinearities and time dependent phenomena of the lightning environment. Unfortunately, the unimoment method is not developed completely enough that trial functions for such highly

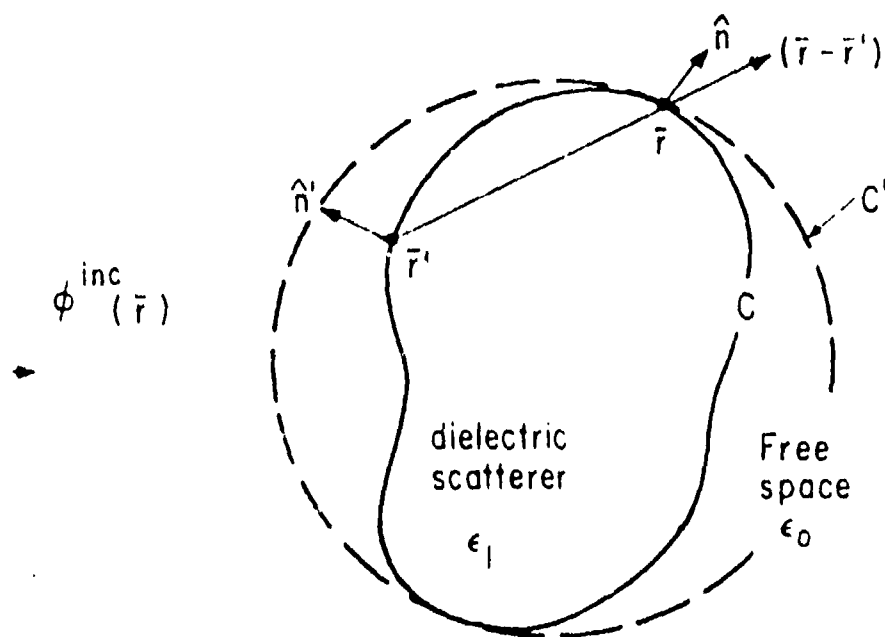


Figure 3.99 Schematic of Scattering by a Dielectric Cylindrical Obstacle [79]



nonlinear regions can be obtained easily. Furthermore, no aircraft or aircraft-like structures have been analyzed. The only examples of its application are two two-dimensional scattering problems. Figure 3.100 shows a comparison of the E-wave and H-wave for field scattering patterns for a plane wave incident on a conducting cylinder. There is very good agreement between the exact solution and the unimoment solution which here uses a finite element method for the interior solution. Figure 3.101 shows a more complicated scattering geometry, namely two parallel conducting cylinders, and again the comparison between the far field scattering patterns of the unimoment method and the exact solution is good. It should be kept in mind, however, that an external coupling problem for lightning will require surface current densities as an output, and comparison of far scattered fields may not be a good indicator of the accuracy of surface current density.

The eleven evaluation criteria for the unimoment method will now be discussed.

1. Computer Memory: The programs used for the two dimensional calculations described in Figures 3.3.103 and 3.3.104 were implemented on CDC 6400 and 7600 computers, however there is no information on the computer memory required.

2. CP Time: Likewise, there was no mention of computer run time.

3. Numerical Accuracy: The two dimensional examples described in the text were not optimized for efficiency nor numerical accuracy, however the agreement with exact results is good. The method was sensitive to a choice of interpolating polynomials to represent the interior solution (the finite element part of the solution).

4. Physical Accuracy: The example problems which have been solved by this method do not give an indication of the physical accuracy that could be obtained for a complicated scatterer such as an airplane.

5. User Orientation: At the present time, there are no well documented computer codes generally available which are based on the unimoment method. The use of this method will certainly require a skilled scientist to recognize a good choice of interior expansion functions.

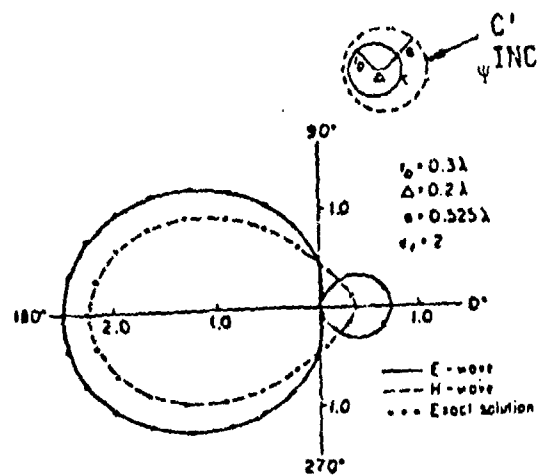


Figure 3.3.100 Far Field Scattering Pattern from a Cylinder [79]

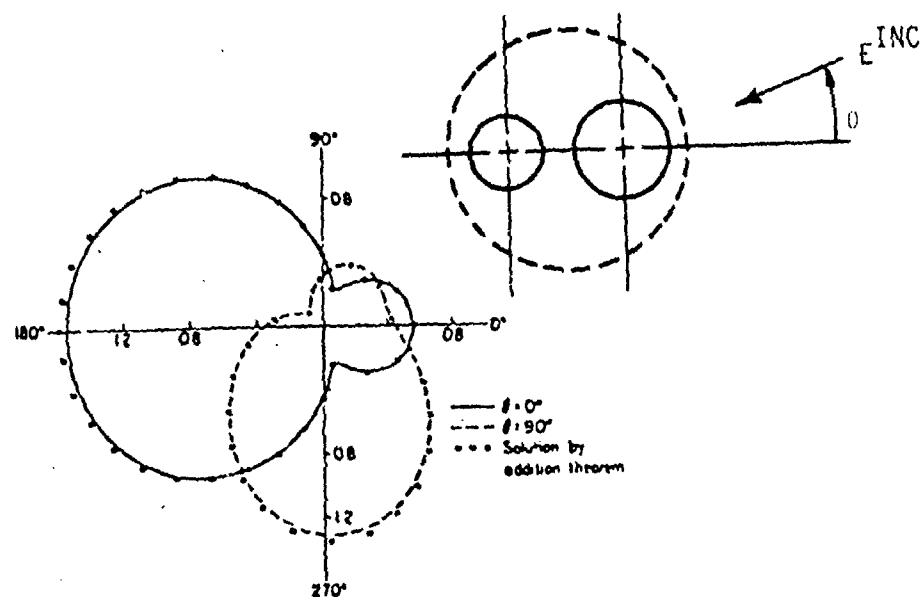


Figure 3.3.101 Far Field Scattering Pattern from a Pair of Cylinders [79]

6. Frequency Range: Information not available.
7. Attached Stroke: Current injection drive has not been attempted with this method.
8. Test Case: The method has not been used to treat current injection and, since the present implementation of the method is in the frequency domain, it cannot treat the nonlinear aspects of the test case.
9. Aircraft Size: Information not available.
10. Lightning Environment: In its present stage of development, the method cannot treat an attached stroke nor can it treat the nonlinearities of the lightning environment.
11. Experimental Verification: The method has not been used to model aircraft and so there are no data comparing the method with experimental results on aircraft.

#### 3.3.7.4 Triangular Patch Method

A somewhat unique method of solving either the EFIE, the MFIE, or a hybrid integral equation, has been developed by Wilton [82]. The method is implemented in the frequency domain and uses triangular patches to represent a surface. The electric field integral equation has received the most attention by Wilton since it can be used to treat both open and closed surfaces. The advantage of triangular patch modeling is that a better representation of a surface can be obtained (with triangles) than with quadrilateral patches. An example of the kind of surface that can be represented by this method is shown in Figure 3.102.

Wilton's approach is to use the method of moments to solve an integral equation and use a unique set of vector expansion functions to represent the surface current on the triangular patches. The  $n^{\text{th}}$  expansion function  $\vec{f}_n(\vec{r})$ , is associated with the  $n^{\text{th}}$  edge and with two triangular patches  $T_n^+$  and  $T_n^-$  as shown in Figure 3.103. The functions  $\vec{f}_n$  are defined in terms of the vectors  $\vec{\zeta}_n^+$  and  $\vec{\zeta}_n^-$  from the far vertices to the area of each patch, and are given by

$$\vec{f}_n(\vec{r}) = \begin{cases} (\ell_n/2A_n^+) \vec{\zeta}_n^+ & \vec{r} \in T_n^+ \\ (\ell_n/2A_n^-) \vec{\zeta}_n^- & \vec{r} \in T_n^- \\ 0 & \text{otherwise} \end{cases} \quad (3.3.7.7.)$$

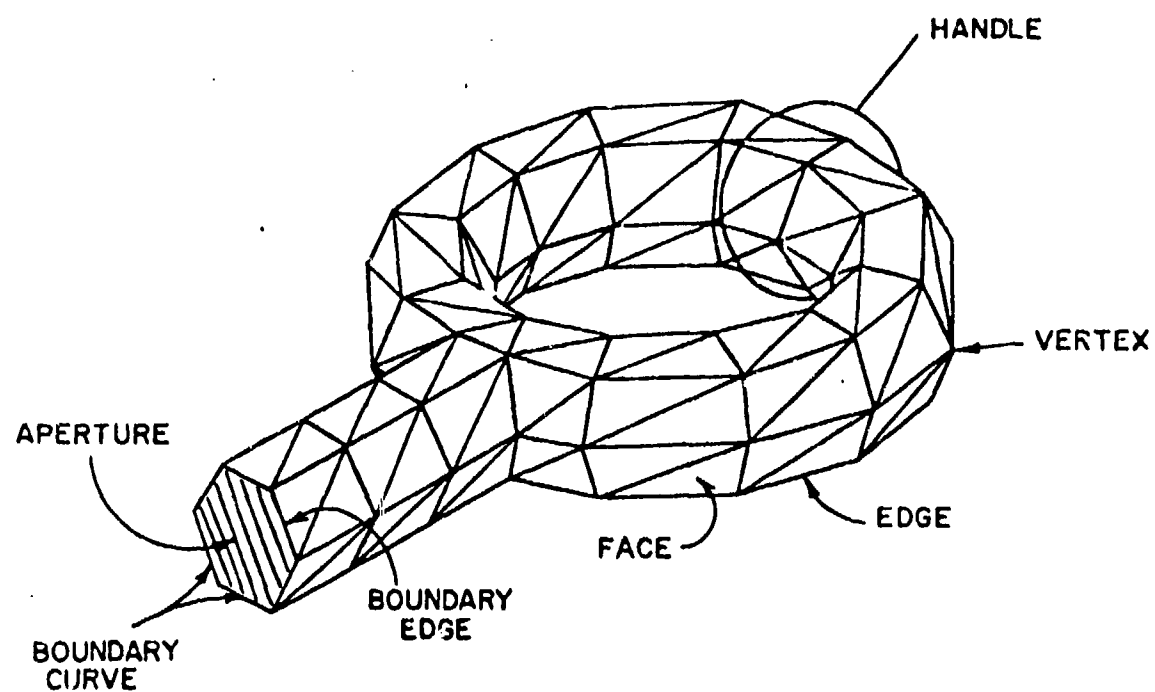


Figure 3.102 Arbitrary Surface Modeled by Triangular Patches  
[82]

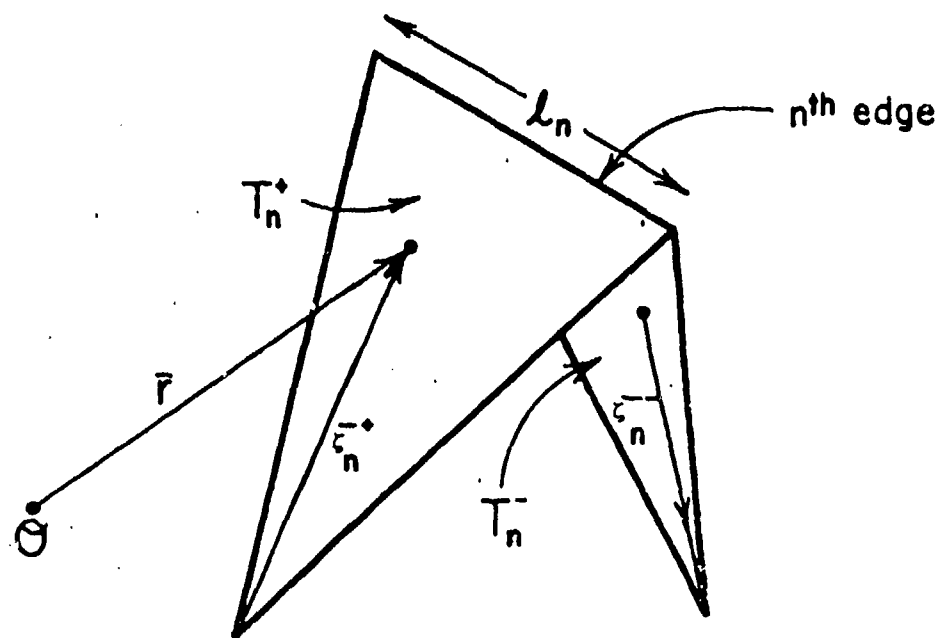


Figure 3.103 Local Coordinates Associated with an Edge [82]

These functions have no vector component normal to a patch edge, except for the  $n^{\text{th}}$  edge, and therefore no line charge densities are required to satisfy the continuity equation. For an interior patch, there are three vector functions defined on a patch. By using these expansion functions for the surface current density, and employing Galerkin's method (i.e. using the same functions for weighting functions), the EFIE has been reduced to a set of linear equations. The reduction includes the analytic evaluation of many of the resulting integrals but includes numerical evaluation of some. Approximation methods are used to avoid the numerical difficulties normally introduced by the derivatives of surface current density and scalar potential in the EFIE.

At the present time the method has not been used to analyze any aircraft. It has been used to calculate the induced currents on a conducting sphere due to an incident plane wave. Figure 3.104 shows the results calculated by the triangular patch method compared to an exact solution. The agreement is good and is shown not to be sensitive to the method of patching.

Next, the method will be reviewed according to the eleven evaluation criteria. Since the method is relatively new, complete information is not always available.

1. Computer Memory: Complete information is not available. However, to model a full aircraft with  $1 \text{ m}^2$  patches will almost certainly require more than 100 kg. There may be in excess of 1000 patches.

2. CP Time: Since the method is implemented in the frequency domain, calculations will have to be performed at many frequencies (100-200) in order to reconstruct the time domain transient response. This will require substantial CP time, however quantitative information is not available.

3. Numerical Accuracy: The method potentially has good numerical accuracy since techniques for implementing the method of moments solution are well developed. Numerical accuracy will also be limited by the integral approximations that are used.

4. Physical Accuracy: The triangular patch method of modeling a surface will give a good representation of an aircraft although no aircraft have been modeled at this time.

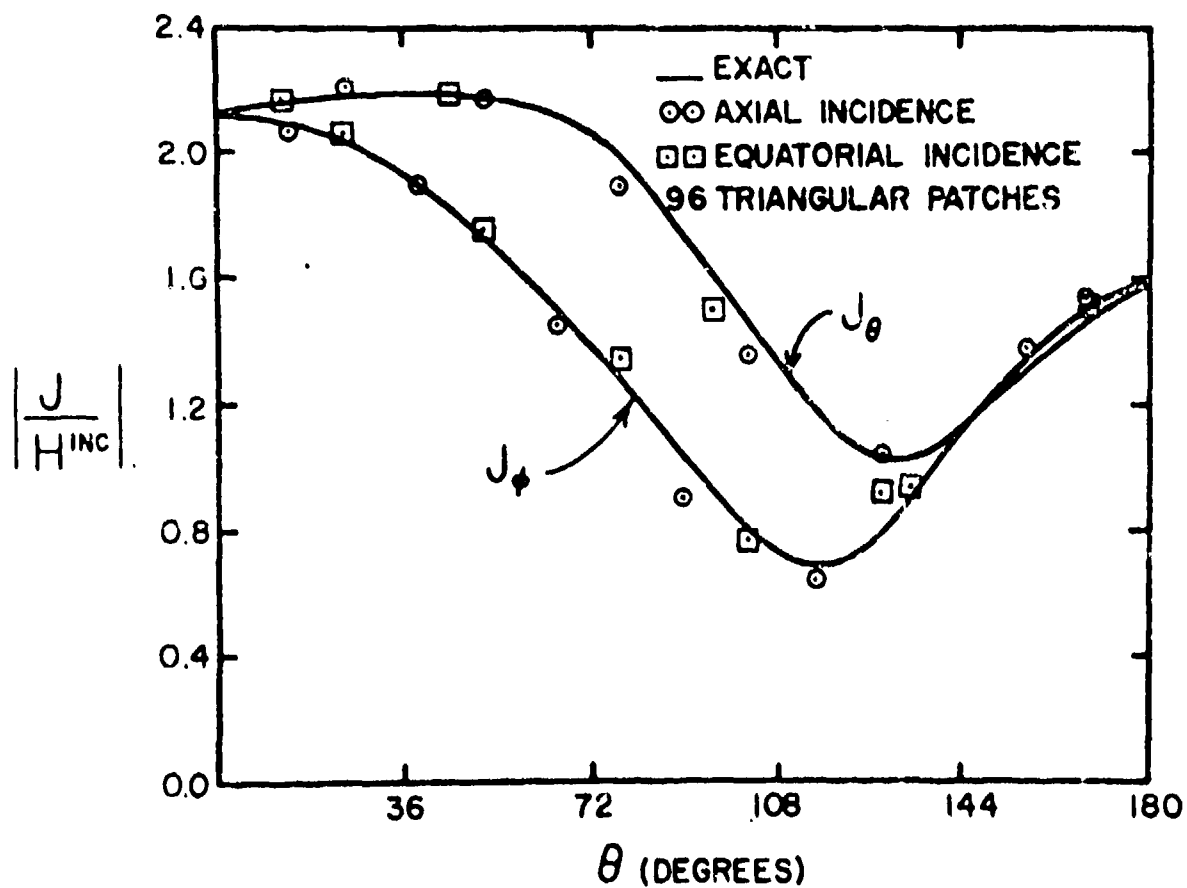
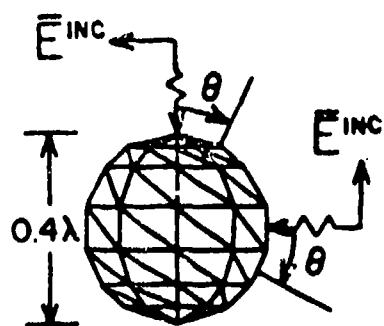


Figure 3.104 Distribution of Current Components on a  $0.2\lambda$  Radius Conducting Sphere Calculated by an Electric Field Integral Equation Formulation [82]

5. User Orientation: The code is not well developed at this time and so there is no documentation generally available. However there are automatic patching subroutines available and the method of moments is well developed. Therefore, the code may be eventually user oriented although it is not so at the present time.

6. Frequency Range: No quantitative information.

7. Attached Stroke: Current injection has not been implemented.

8. Test Case: Current injection has not been implemented and, since the method is a frequency domain method, nonlinearities cannot be treated easily.

9. Aircraft Size: No quantitative information.

10. Lightning Environment: Attachment and nonlinear behavior may be difficult to include in the method.

1. Experimental Verification: There has been no experimental verification of calculations for aircraft.

#### 3.3.7.5 Finite Element Method

Briefly, the finite element solves a differential equation such as Laplace's equation by reduction of the equation to a set of linear equations. The reduction is accomplished using variational expressions for the differential equation and a polynomial representation of the unknown field around some point in the problem space. This method is often used for problems such as the determination of fields around a strip transmission line. The method is not easily adapted to problems which require a field to satisfy radiation boundary conditions, however, and so it has not been used for coupling problems. No aircraft or missile structures have been analyzed for example. Therefore, the method is only mentioned here for completeness and will not be discussed in detail. A guide to the finite element literature is contained in Appendix A.

#### 3.4 Corona Modeling

One of the least understood aspects of the lightning interaction problem is corona. At present there is no definite lightning data on aircraft response which gives insight into this phenomenon. Certainly the aircraft is in corona during much of the interaction, yet its effects on the interaction have not really been studied.



Corona can have at least two effects. First, it can reduce the coupling of energy to the aircraft interior by providing electric field shielding by virtue of the presence of a time varying air conductivity. On the other hand, corona processes may radiate or inject spurious signals having a spectral content which is quite different from what would be expected in a totally linear interaction.

At present, there does not appear to be a corona model which has been applied to the lightning/aircraft interaction problem. However, corona models based on an air chemistry formulation developed for NEMP may provide at least a starting point in this direction.

Such an air chemistry formulation has been used to predict air conductivity produced by ionizing radiation. This dynamic solution to air conductivity problems considers the effects of the avalanche rate  $G(\text{sec}^{-1})$ , the electron attachment rate  $\alpha_e(\text{sec}^{-1})$ , electron-ion recombination  $\beta(\text{m}^3/\text{sec})$ , negative and positive ion recombination rate  $\delta(\text{m}^3/\text{sec})$ , electron mobility  $\mu_e(\text{m}^2/\text{V}\cdot\text{sec})$ , and ion mobility  $\mu_i(\text{m}^2/\text{V}\cdot\text{sec})$ .  $G$ ,  $\alpha_e$  and  $\mu_e$  are all functions of electric field  $E$ , relative air density  $\rho_r$ , and percent water vapor  $P$  (except for  $G$ ).  $\beta$  depends upon  $P$ , and  $\gamma$  and  $\mu_i$  depends upon  $\rho_r$ . Table 3.8 summarizes the formulas required to compute the air chemistry coefficients. These are based on analytical fits to measured data, and their bases are discussed elsewhere [83] and will not be repeated here.

The continuity equation appropriate for consideration of electrons only can be stated

$$\frac{dn_e}{dt} + (\alpha_e - G)n_e = Q(t) \quad (3.4.1)$$

where  $n_e$  is the number density of electrons ( $\text{m}^{-3}$ ) and  $Q(t)$  is the ionizing source function corresponding to the background radiation (cosmic rays) and is nominally  $10^7$  electron-ion pairs/ $(\text{m}^3\cdot\text{sec})$ .

One can consider, in addition, the effects of the positive ion density  $n_+$  and the negative ion density  $n_-$  and write the following coupled differential equations in a manner similar to equation (3.4.1):

Table 3.8 Air Chemistry Coefficient Formulas.  
All Units are esu.

Calculation of  $E_{rel}$ :

$$E_{rel} = \frac{E}{\rho_r} / (1 + 2.457P^{0.834}) \text{ for } \frac{E}{\rho_r} < 0.07853(1 + 2.457P^{0.834})$$

$$E_{rel} = \frac{E}{\rho_r} - 1.195P^{0.834} \text{ for } \frac{E}{\rho_r} > 3.015 + 1.195P^{0.834}$$

$$E_{rel} = \left( \sqrt{\frac{E}{\rho_r} + \left( \frac{0.6884P^{0.834}}{2} \right)^2} - \frac{0.6884P^{0.834}}{2} \right)^2 \text{ for all other } \frac{E}{\rho_r}$$

Where  $P$  is the per cent water vapor and  $\rho_r$  is relative air density. Note:  $E$  is in esu, where  $E_{esu} = E_{mks}/3 \times 10^4$

Calculation of Electron Attachment Rate  $\alpha_e$ :

$$\alpha_e = \frac{100-P}{100} (\alpha_3(1+0.344P) + \alpha_2)$$

$$\alpha_2 = 1.22 \times 10^8 \rho_r e^{-21.15/E_{rel}}$$

$$\alpha_3 = \rho_r^2 (6.2 \times 10^7 + 8. \times 10^{10} E_{rel}^2) / (1 + 10^3 E_{rel}^2 (E_{rel}(1 + 0.03 E_{rel}^2))^{1/3})$$

Calculation of Electron Mobility,  $\mu_e$ :

$$\mu_e = \frac{100\mu_a}{100-P+PXR}; R = 1.55 + 210 / (1 + 11.8 E_{rel} + 7.2 E_{rel}^2)$$

$$\mu_a = 10^5 ((16.8 + E_{rel}) / (0.63 + 26.7 E_{rel}))^{0.6} / \rho_r$$

Calculation of Avalanche Rate,  $G$ :

$$G = 5.7 \times 10^3 \rho_r Y^5 / (1 + 0.3 Y^{2.5}); Y = \frac{E_{rel}}{100}$$

Calculation of Ion Mobility,  $\mu_i$ :

$$\mu_i = 750 / \rho_r$$

Calculation of electron-ion recombination coefficient  $\beta$ , and ion-ion neutralization coefficient,  $\delta$ :

$$\delta = 2 \times 10^{-7} + \rho_r 2.1 \times 10^{-6}$$

$$\beta = 2 \times 10^{-7} + 2.8 \times 10^{-6} (P)^{1/3}$$

$$\left. \begin{aligned}
 \frac{dn_e(t)}{dt} + [\beta n_+(t) + \alpha_e - G] n_e(t) &= Q(t), \\
 \frac{dn_-(t)}{dt} + [\gamma_+(t)] n_-(t) &= \alpha_e n_e(t), \\
 \frac{dn_+(t)}{dt} + [\beta n_e(t) + \gamma_-(t)] n_+(t) &= Q(t) + G n_e(t), \\
 n_+(t) &= n_e(t) + n_-(t).
 \end{aligned} \right\} \quad (3.4.2)$$

In addition, one needs to solve for the air conductivity  $\sigma$  according to

$$\sigma = q(\mu_e n_e + \mu_i (n_- + n_+)) \quad (3.4.3)$$

where  $q$  is the fundamental electronic charge. It is clear that only three of equations (3.4.2) need to be solved, the other being redundant. It is interesting to solve these equations in the steady state ( $\frac{d}{dt} = 0$ ) with the ambient  $Q$  as stated. If this is done, one obtains  $n_e = .2/m^3$ , and  $n_+ \sim n_- = 7.3 \times 10^9/m^3$ , and  $\sigma = 2 \times 10^{-13}$  mho/m. Thus, there are very few free electrons in ambient air, and the ambient air conductivity is mainly due to the presence of ions.

It is noted that the air chemistry formulation does not include photoionization of the air caused by photons generated in the electron avalanche. The formulation then will not predict streamering or arcing.

This method has mainly been used for the prediction of NEMP response in source region environments [84]. However, it has been applied to NEMP free space scattering problems, much as a transmission line [85] and simple monopole antennas [86, 87]. Such a model could also be applied to a three-dimensional finite difference solution of Maxwell's equations for lightning interaction with an aircraft.

## CHAPTER 4

### REVIEW OF INTERNAL COUPLING MODELING

#### 4.1 Apertures

Apertures are openings in the structure of an aircraft that allow electromagnetic energy to couple to the interior. Examples include bomb bays, windows, and wheel wells. These types of apertures are extremely complex electromagnetically. The apertures are backed by irregular shaped cavities and contain many conductors such as electrical wiring, fluid lines, and control lines. The apertures themselves can be of odd shape, and the dimensions of a cavity and its aperture may not be small compared to wavelength. The aperture coupling problem is thus formidable, and is probably one of the least understood. The problem is usually reduced to an idealized representation called a canonical representation of the problem. These representations are designed to make the problem tractable, and may not always be an adequate formulation of the real physical situation.

The electrical quantities usually desired from an analysis are the following:

1. Total energy transmitted through the aperture for an incident pulse.
2. Electric and magnetic fields behind the aperture.
3. Transient response and transfer function of the current in the load and the voltage across the load when loaded wires are placed behind the aperture.
4. Energy dissipated in terminations of wires placed behind the aperture.

These quantities, when determined for canonical problems, can give, at least, bounds on what can be expected for physical problems.

There are four classes of canonical problems that have been dealt with in the literature.

1. Apertures in a perfectly conducting plane of infinite extent.
2. Apertures in two-dimensional perfectly conducting bodies.
3. Apertures in three-dimensional perfectly conducting bodies.
4. Apertures with wires behind the opening.

Each of these classes will be discussed separately in the text. In addition, some new approaches for modeling real apertures are presented.

The problem of apertures in an infinite perfectly conducting plane has received the most attention. The solutions can be divided into two types:

1. Low frequency approximation.
2. Moment method solutions of integral equations.

The first method, which is limited to apertures which are small compared to the wavelength of the incident pulse, uses the approximation that the incident field across the aperture is essentially uniform. When these field variations across the spatial extent of the aperture need not be accounted for, the problem is enormously simplified.

The low frequency approximation is used in Babinet's equivalence principle, which allows an aperture in an infinite plane to be represented by a perfectly conducting disk of the same shape as the aperture. On the back side of the aperture the sum of the fields for the disk problem and for the aperture problem are equal to the incident field. This allows one to calculate the aperture fields from the fields scattered by the disk. A good discussion of this method is given in [38].

The low frequency approximation is originally due to Lord Rayleigh [98]. He used it to investigate the problem of a circular aperture. He expanded the solution in what has become known as a Rayleigh series. This is a power series in  $ka$ , where  $k$  is the wave number of the incident pulse and  $a$  the radius of the aperture. He obtained only the first term of the series. Bethe [90], in a classic paper, wrote the solution for the fields behind the plane in terms of electric and magnetic dipoles in place of the aperture. Bouwkamp [91, 92] obtained some of the higher-order terms in the Rayleigh power series, and in doing so, was able to show that Bethe had an error in his development.

The low frequency approximation has also been used to develop integral equations for the aperture problem. Umashankar and Butler [93] found an integral equation solution in terms of the equivalent magnetic currents in the aperture. The coefficients in the Rayleigh series are written as integral equations and these are then solved numerically for a given configuration. Ramat-Sami and Mittra [94] dealt with the case of a circular aperture by writing an integral equation in terms of the tangential

electric fields in the aperture. These fields are then expanded in a Rayleigh series which gives a set of integral equations for the coefficients of the Rayleigh series. The first three terms of the series can then be found analytically for this special case. In principle, however, the method can be applied to arbitrarily shaped apertures.

The methods discussed so far all require that the aperture be small, because this is the condition on convergence of the Rayleigh series. Methods which are applicable to any size aperture will be discussed next.

A solution for a circular aperture was developed by Taylor, Crow and Chen [95, 96]. They wrote the solution in terms of the current on a Babinet's equivalent disk with the current on the disk being written in terms of an electric field integral equation. The disk's current and the incident fields were then expanded in terms of transverse electric and magnetic cylindrical modes at the surface of the disk. This gave a new set of integral equations for the current modes on the disk. The equations are then solved numerically using a moment method.

Wilton and Dunaway [97] formulated the problem of an aperture in a plane in a way that is not limited to circular apertures. They wrote the fields on both sides of the aperture in terms of the electric vector potential and derived an integral equation by forcing the electric field to be continuous through the aperture. The moment method approach was then used to handle numerical calculations.

The above analyses are frequency domain solutions. A time domain solution can be obtained by using Babinet's principle to represent the aperture problem as an equivalent plate in free space. This problem has been solved by Menger, Bennett, Peterson, and Maloy [98]. They formulated the problem in terms of the unknown current on the plate. The electric field was written as an integral-differential equation in terms of the unknown current. The expression for the current was found using the boundary condition at the surface of the plate, and the equation for the current was solved using numerical methods.

For apertures in two dimensional bodies, almost all work in this area has concentrated on slots in infinitely long cylinders. Analyses of this problem have been done by Bombardt and Libelo [99, 100], Kligman and Libelo [101], and Senior [102]. The methods of solution essen-

tially consist of deriving an integral equation for the unknown fields in the aperture, or equivalently, unknown surface currents, and solving these equations numerically by moment methods.

More important than the problem of apertures in two-dimensional bodies is that of apertures in three-dimensional bodies. Here one begins to approximate realistic physical situations. Most of the approaches in the literature are in the frequency domain, but of course these can be transformed to the time domain when desired.

Chang and Senior [103] have studied the case of a circular aperture in a spherical shell. They write the fields inside and outside the sphere in terms of an infinite series of wave functions. The coefficients in the series are determined by using boundary conditions and requiring that the magnetic and electric fields be continuous through the aperture. An error function is derived in order to truncate the infinite series, and this error function is minimized in a least squares sense with respect to the coefficients. This results in a set of equations for the coefficients in the truncated series.

Of more practical interest is the case of an aperture in a perfectly conducting box. This is usually handled by dividing the problem into internal and external regions. Chen [104] used Bethe hole theory to approximate the coupling between the two regions. The external problem is assumed to be a plane wave incident on a small hole in a plate of infinite extent. The induced currents on the plate are then used to find the equivalent magnetic source from Bethe hole theory, and this source is used to excite fields in the interior of the box. The approach neglects coupling from the inside of the box to the aperture and requires that the aperture be small electrically.

To account for coupling between the internal and external regions Rahmat-Samii and Mittra [94] use the same kind of development as was used for the infinite plane to derive a set of integral equations in terms of tangential electric fields in the aperture. A moment method is used to solve the equations numerically. The problem is simplified by making the interior region the space between two infinite plane sheets, rather than a finite sized box.

To understand how energy couples through apertures and into electrical systems, it is necessary to calculate voltages and currents on wires which may be placed behind apertures. The simplest situation is that of a straight wire behind an aperture in a perfectly conducting infinite screen. Lin, Curtis, and Vincent [105] approached the problem by finding the fields behind the aperture using Babinet's principle and neglecting the presence of the wire. The wire is then treated as a transmission line with the fields as sources. This allows the voltage on the ends of the wire to be calculated numerically. Clearly, the method lacks mutual coupling between the aperture and the wire.

Butler and Umashankar [106] derived coupled integral equations for the current on a single finite wire segment behind an arbitrarily shaped aperture in an infinite sheet. These equations have been solved numerically for a slot aperture and extensive results are given.

Seidel, Dudley, and Butler [107] analyzed the problem of an aperture in an infinite plane sheet with a rectangular enclosure behind the aperture and a wire inside the enclosure. Coupled integral equations are derived and numerically solved for the current on the wire. However, the aperture is approximated using Bethe hole theory, so there is no coupling between internal and external regions.

Umashankar and Wait [108] have developed a general integral equation for an arbitrary aperture in a plane conducting screen with an arbitrary conductor behind the screen. The equations are cast in a form particularly suitable for use with the singularity expansion method. Numerical work has been done for the cases of the fields in an aperture alone, the fields in a region between a screen (no aperture) and a wire, and for a wire behind a slot aperture.

It should be pointed out that formulas for coupling through canonical-type apertures have been recently developed and incorporated into a NEMP coupling handbook [109]. These formulas can provide useful estimates and bounds for aperture coupling, and are also given in Section 5.3.2 of this report.

It should also be noted that large apertures can often be treated as part of the external coupling problem. Finite difference codes or wire grid codes are often capable of dealing with large apertures by simply including



them in the overall external coupling model, and the internal fields are obtained directly.

The problem of coupling of electromagnetic energy through apertures is still a developing field. Most classical methods either make sweeping approximations or are limited to canonical shapes. Table 4.1 summarizes the state of the literature for the various problems associated with apertures [110] as of 1976. Although somewhat outdated, the chart does summarize the types of problems yet to be solved and it is still true that there are more zeroes in the chart than numbers.

It has been shown that classical methods (integral equation techniques, small hole theory) of analyzing apertures are confounded by the presence of irregular shaped cavities which contain wires. Straightforward numerical techniques, such as finite difference, can in principle, solve irregular geometries. The limitation, however, is that in order to resolve small geometrical features, small grid size and, consequently, small time steps, must be used which places unreasonable demands on computer resources. There are techniques, however, which can be used to solve the aircraft external coupling response with a large grid, and then use the large grid results to solve a small subset (e.g., an aperture) of the aircraft with a much smaller grid which can resolve the geometrical details. Two approaches are presented here, an exact technique (in the numerical sense) based on the equivalence principle, and an approximate technique, based on the uniqueness theorem.

First, the approach developed by Merewether [111] based on the equivalence principle is discussed. Consider the generalized conducting body containing a cavity backed aperture (Figure 4.1). Let  $S$  be the surface of the body,  $S_1$  the surface of the aperture, and  $V$  and  $V_1$  be the volume of the body and the enclosed cavity, respectively. The field everywhere in space is broken up into three components:

Table 4.1 Status of Literature as of 1976 [110] for Electromagnetic Coupling through Apertures

	Theoretical formulation				Closed-form results				Numerical implementation				Validation of approximations				Experimental data		Data on canonical problems	
	FD		TD		FD		TD		FD		TD		FD		TD		FD	TD	FD	TD
	SA	AA	SA	AA	SA	AA	SA	AA	SA	AA	SA	AA	SA	AA	FD	TD	FD	TD	FD	TD
Aperture in plane	5	5	5	5	5	0	0	0	5	5	5	5	3	0	3	3	3	3	3	3
Aperture in plane with loaded wire behind	3	0	3	0	0	0	0	0	3	0	3	0	1	0	2	0	3	0	3	0
Aperture in plane with cavity behind	3	0	3	0	0	0	0	0	3	0	0	0	0	0	0	0	0	0	0	0
Aperture in plane with loaded wire contained in a cavity behind the aperture	0	0	0	0	0	0	0	0	0	0	0	0	0	0	0	0	0	0	0	0
Aperture in three-dimensional bodies	3	0	0	0	0	0	0	0	3	0	0	0	0	0	0	0	0	0	0	0
Aperture in three-dimensional bodies with loaded wire inside the body	3	3	0	0	0	0	0	0	3	3	0	0	0	0	0	0	2	0		
Aperture in three-dimensional bodies with different shaped cavity inside the body	0	0	0	0	0	0	0	0	0	0	0	0	0	0	0	0	0	0		
Apertures in three-dimensional bodies with cavity inside the body where the cavities contain loaded wires	0	0	0	0	0	0	0	0	0	0	0	0	0	0	0	0	0	0	0	0

- 0 Nothing in literature.  
1 Denotes very little formulation, information or results.  
2 Denotes some formulation, information or results do exist, but it is limited to unimportant cases.  
3 Denotes a limited amount of formulation, information or results do exist for a small number of important cases.  
4 Denotes a good amount of formulation, information or results do exist on most cases, but needs a little work to be complete.  
5 Denotes a fairly complete formulation, information or results on all important cases.

$$\vec{E} = \vec{E}^i + \vec{E}^s + \vec{E}^p, \quad (4.1)$$

and

$$\vec{H} = \vec{H}^i + \vec{H}^s + \vec{H}^p. \quad (4.2)$$

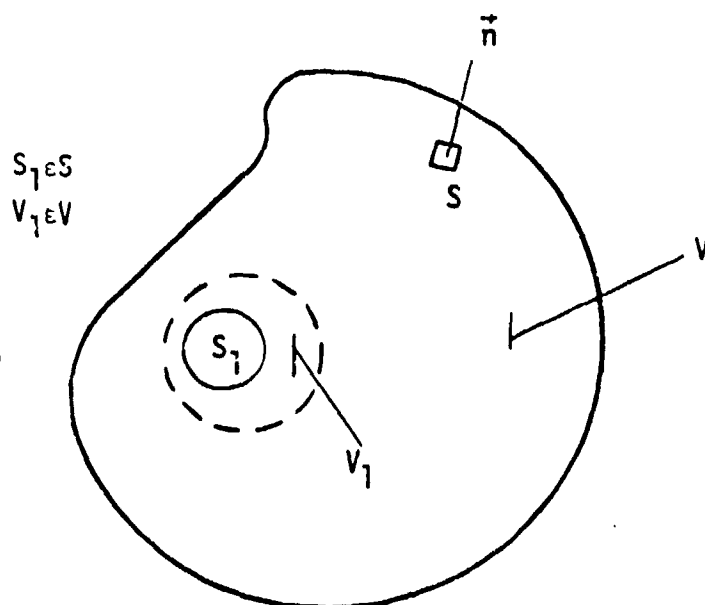


Figure 4.1 Cavity Backed Aperture

where  $\vec{E}$ ,  $\vec{H}$  is the total field,  $\vec{E}^i$ ,  $\vec{H}^i$  is the incident field produced by a distant transmitter,  $\vec{E}^s$ ,  $\vec{H}^s$  is the field scattered by the body with no aperture and no cavity present, and  $\vec{E}^p$ ,  $\vec{H}^p$  is the "perturbed field" - the difference between the scattered field with and without the aperture and cavity present.

According to the equivalence theorem, the surface electric and magnetic current densities

$$\vec{J}_s = (\vec{H} \times \vec{n}) \quad (4.1.3)$$

and

$$\vec{M}_s = (\vec{n} \times \vec{E}), \quad (4.1.4)$$

introduced in the surface  $S$  in place of the distant transmitter will produce the correct  $\vec{E}$ ,  $\vec{H}$  field inside  $S$ , and zero field outside [17]. Here the media inside  $S$  is the media of the body including the cavity behind the aperture.

Because the polarization and conduction currents that are responsible for the  $\vec{E}^p$ ,  $\vec{H}^p$  component of the field are contained within  $S$ , one can define surface current densities

$$\vec{J}_S^P = \vec{n} \times \vec{H}^P, \quad (4.1.5)$$

$$\vec{M}_S^P = \vec{E}^P \times \vec{n}. \quad (4.1.6)$$

These produce the  $\vec{E}^P$ ,  $\vec{H}^P$  component of the fields outside S with no fields inside. If these two components are added together, the resultant current densities

$$\vec{J}_S' = \vec{J}_S + \vec{J}_S^P = (\vec{H} - \vec{H}^P) \times \vec{n}, \quad (4.1.7)$$

$$\vec{M}_S' = \vec{M}_S + \vec{M}_S^P = \vec{n} \times (\vec{E} - \vec{E}^P), \quad (4.1.8)$$

distributed over S, produce the correct total field inside S ( $\vec{E}$  and  $\vec{H}$ ) and the perturbed field ( $\vec{E}^P$  and  $\vec{H}^P$ ) outside S. Substituting (4.1.1) and (4.1.2) into (4.1.3) and (4.1.4) yields

$$\vec{J}_S' = (\vec{H}^i + \vec{H}^S) \times \vec{n}, \quad (4.1.9)$$

and

$$\vec{M}_S' = \vec{n} \times (\vec{E}^i + \vec{E}^S). \quad (4.1.10)$$

Considerable simplification in these formulas result. First, because  $\vec{E}^i + \vec{E}^S = 0$  on a good conductor and, secondly, because  $\vec{J}_S'$  impressed on the surface of a conductor produces no field (by application of the reciprocity theorem). Therefore, the correct "total field" ( $\vec{E}$ ,  $\vec{H}$ ) inside the cavity and the correct "perturbed field" outside the body,  $\vec{E}^P$ ,  $\vec{H}^P$ , are obtained by impressing a source current  $\vec{J}_S' = (\vec{H}_{\text{tan-sc}}) \times \vec{n}$  over the aperture  $S_1$  in the body.

The approach based on the uniqueness theorem is now described. Figure 4.2 illustrates the theorem. The theorem is used to first solve for the external coupling response of the aircraft with a large grid, with

UNIQUENESS THEOREM:

THE FIELDS WITHIN A REGION  $R$  ARE COMPLETELY AND UNIQUELY SPECIFIED BY THE INITIAL VALUES OF THE FIELDS WITHIN  $R$  AND EITHER THE TANGENTIAL  $E$  OR  $H$  FIELDS (OR A COMBINATION) ON THE BOUNDARY AS A FUNCTION OF TIME.

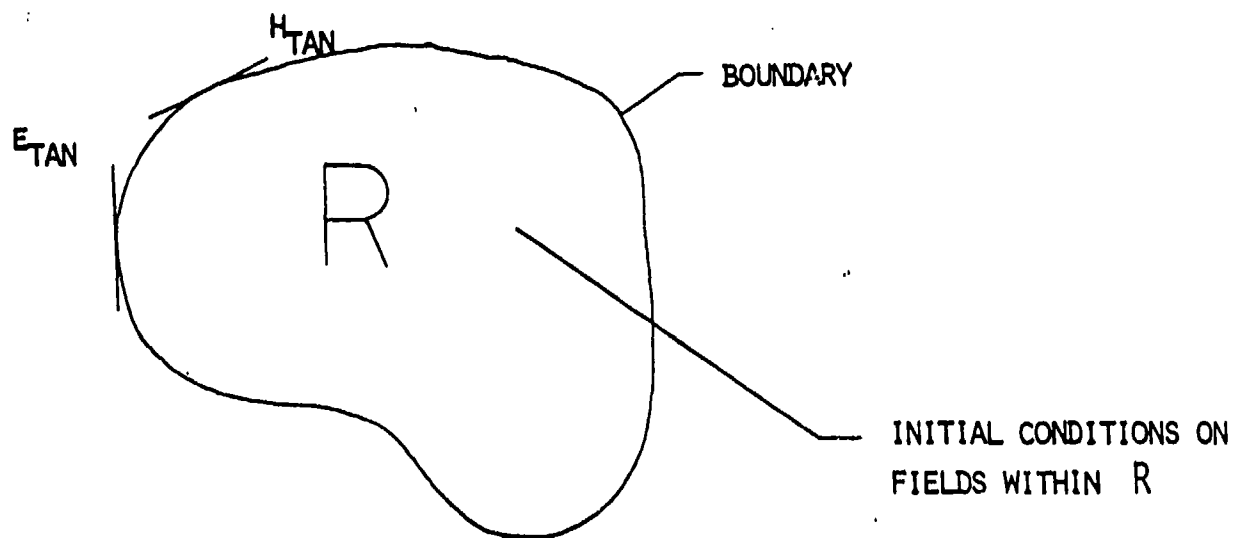


Figure 4.2 Illustration of Uniqueness Theorem

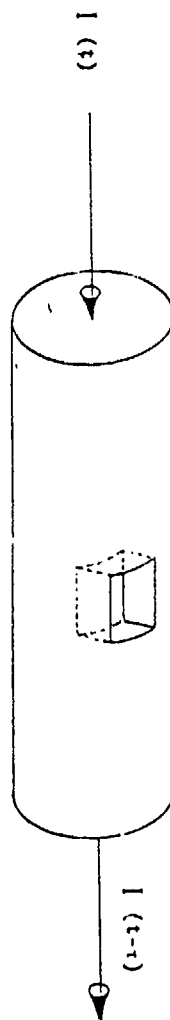
all apertures shorted. Then a region about the aperture is defined and the initial fields within the region  $R$  (usually  $= 0$ ) and the boundary fields (for all time) are stored. Then a second problem is solved which grids up only the aperture and the region  $R$  but with a much finer grid size. This is illustrated in Figure 4.3. The disadvantage of this approach is that it is an approximation which assumes that the boundary fields do not significantly depend upon the presence or absence of the aperture.

The main advantage is that the solution does not require a radiation boundary condition (as does the equivalence principle approach) which greatly eases the computer requirements.

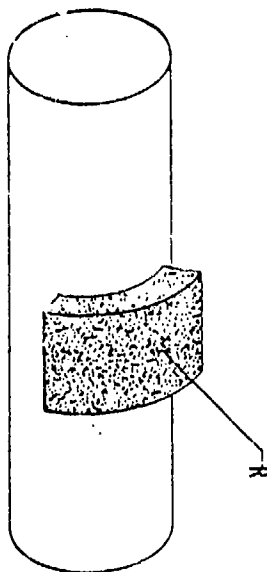
An example is given in Figure 4.4. The approach is to solve the smooth cylinder with a large grid and store the tangential fields on the boundary. Then only the region  $R$  is gridded, with a finer grid, and the response inside the cavity is computed. It is noted that in order to solve the second problem, the results from the first problem need to be spatially and temporally interpreted. It is observed also, that the valid spectral content of the second problem is limited by the grid size of the first problem. In the results presented here, the waveforms have been passed through an ideal numerical bandpass filter which eliminates the noise from the finite difference grid.

Figures 4.5 and 4.6 compare the results obtained by two methods. The method called "direct" is a direct solution of the problem with a fine grid, and the other one is obtained from a solution of the smooth cylinder with a coarse grid and then using these results and the uniqueness theorem to get the internal response with the fine grid. The injected current is a step function with a 36 ns risetime. The comparisons are the worst case, in that they are an observation point which is farthest away from the open aperture. The results nearly overlay at the aperture mouth. The comparisons show discrepancies at late time amplitude, but resonant features are similar. The approach is adequate when absolute accuracy is not required and order of magnitude or better estimates are appropriate. It should be noted that the cavity is only resolved by three cells, a very coarse gridding, and results are expected to improve with a finer mesh.

1. ORIGINAL PROBLEM



2. SOLVE WITH APERTURE SHORTED AND STORE INITIAL VALUES (USUALLY  $E$  OR  $H$  WITHIN  $R$  AND TANGENTIAL  $E$  OR  $H$  FIELDS ON BOUNDARY OF  $R$ , WHERE  $R$  ENCLOSES APERTURE OF INTEREST



3. FILL UP PROBLEM SPACE WITH ONLY REGION  $R$  AND APERTURE OF INTEREST AND SOLVE FOR FIELDS WITHIN  $R$

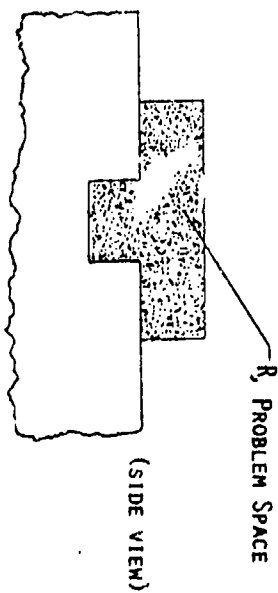
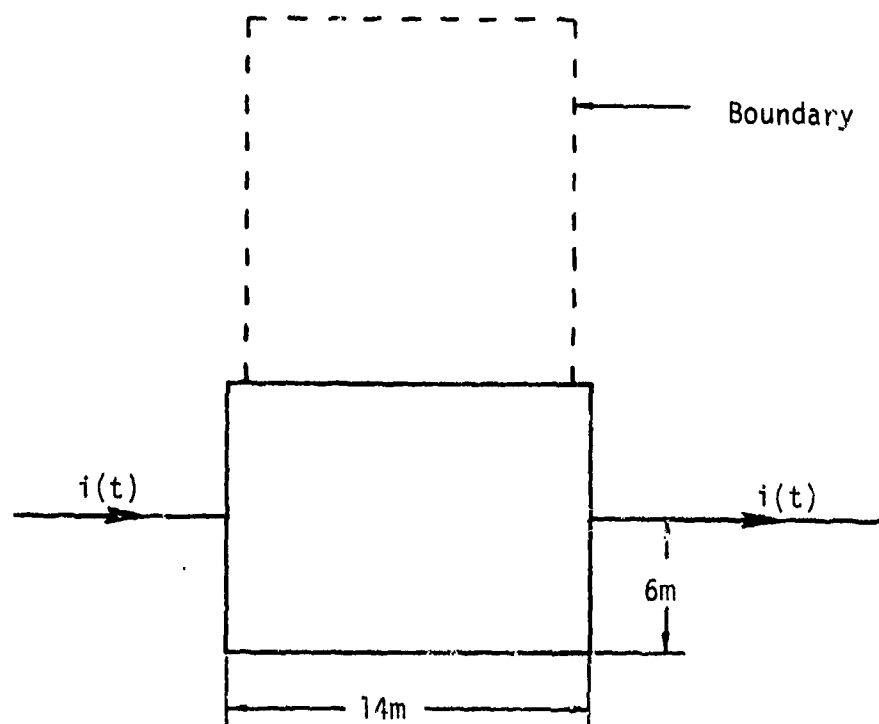
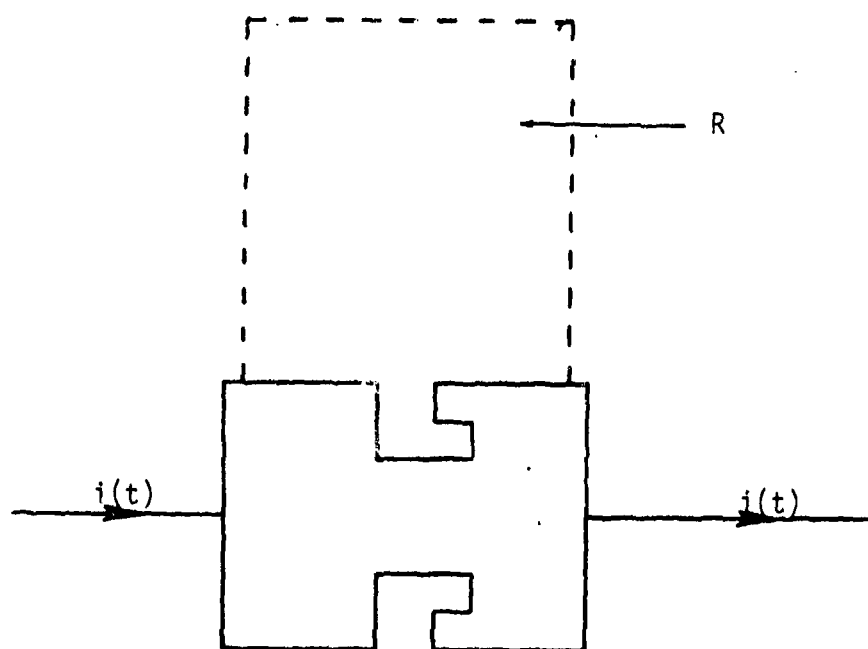


Figure 4.3 Application of Uniqueness Theorem to Aperture Problems



a. Smooth Cylinder



b. Cylinder with Annular Reentrant Cavity

Figure 4.4 Example of Uniqueness Theorem Applied to an Annular Reentrant Cavity in Two Dimensions



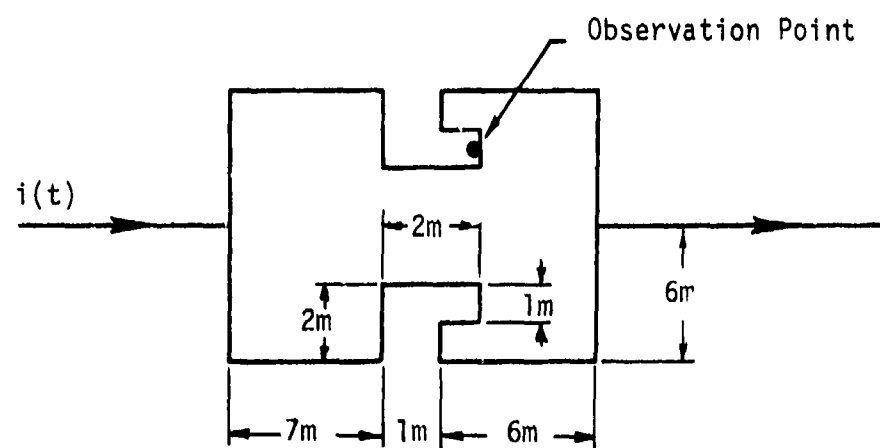
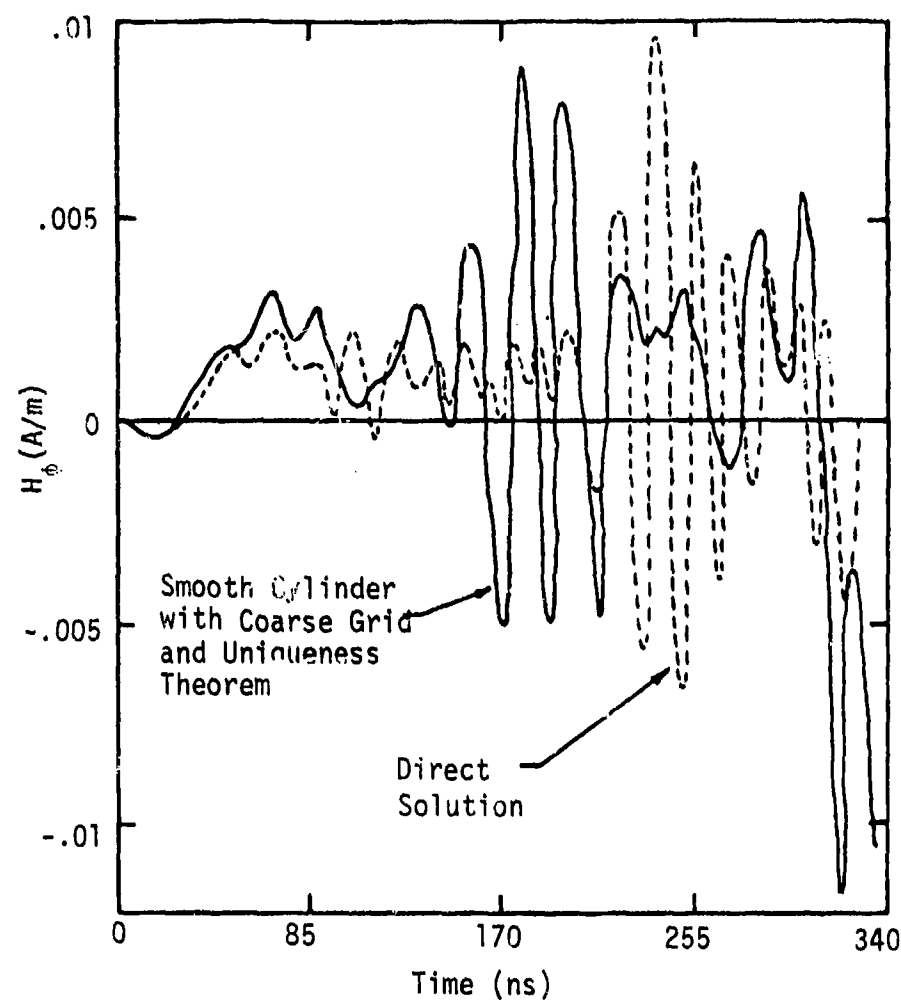


Figure 4.5  $H_\phi$  Comparison

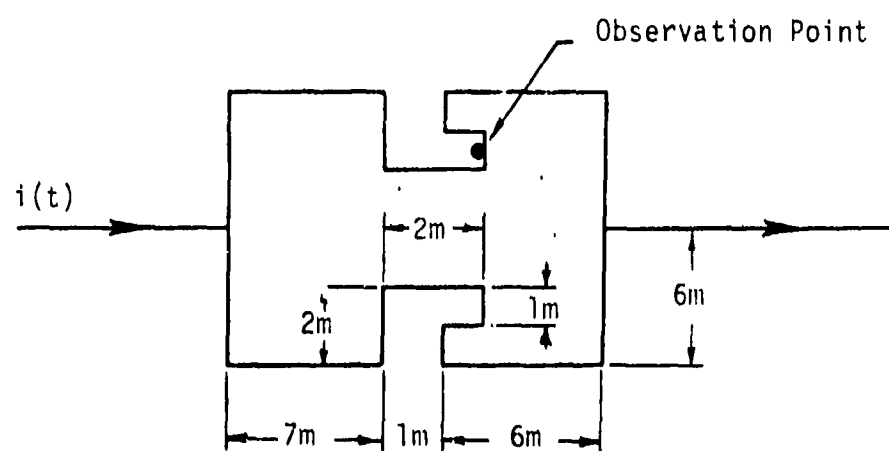
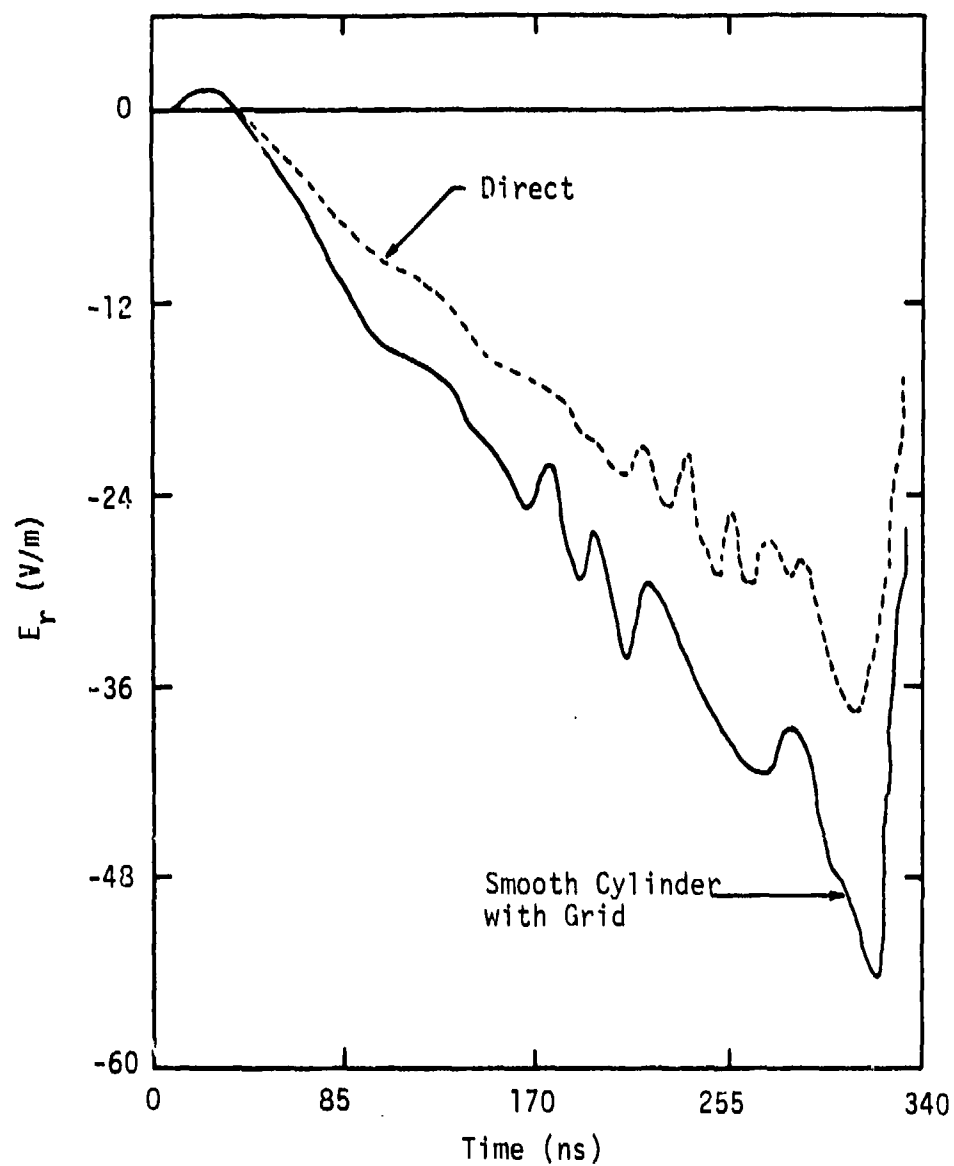


Figure 4.6  $E_r$  Comparison

Finally, it should be noted that both of these proposed techniques can include wires in the cavity by the methods described in [17]. Also, in Section 5.3.2, a three dimensional computation of an aircraft cockpit with wires is given.

One other approach to the cavity-backed aperture problem that has been used is to apply a three dimensional (3D) correction factor to a two dimensional (2D) aperture [112]. In this approach, a cavity aperture cross section (e.g., a cockpit) can be modeled in two dimensions by a Laplace's equation method and a field distribution can be so obtained. Measurements of 3D apertures with the same cross section dimensions (in 2D) can give a correction factor which relates the 3D aperture excitation to the 2D aperture excitation. Thus a family of curves can be developed and a solution to future apertures can be done in 2D along with application of a corrective factor. Clearly, this method would give a good approximation to the low frequency/late time static solution, but cavity or aperture resonances would not be included.

#### 4.2 Seams and Joints

Seams and joints are discontinuities in the aircraft skin which occur between panels. They may be quite conductive, in that they are not open apertures, but they are much less conductive than the metal skin.

In the ideal case, all joints and gaskets are constructed so that they have the same electrical properties as the material around them. In practice, however, this is not the case. Riveted joints usually leave gaps between panels which become entry points. Gaskets, which are flexible conductors introduced into joints to eliminate the gaps, suffer degradation and their impedance increases.

The coupling to interior cables through a seam is usually accomplished in the following manner. Lightning produces a current on the outside of the conducting shield. In the presence of a seam of relatively high impedance there will be a large voltage drop. This voltage drop translates to an electric field just inside the seam and the electric field can then act as a source on a cable which runs near the seam.

The properties of a seam are measured in terms of a transfer impedance,  $Z_t(\omega)$ , which relates the current density,  $J_{ext}(\omega)$ , on the exterior of the shield to the voltage drop  $V(\omega)$  on the inside of the shield,

$$V(\omega)V = Z_t(\omega) J_{\text{ext}}(\omega) \quad (4.2.1)$$

The determination of  $Z_t$  is difficult analytically because of the wide variation and natural irregularities of seam characteristics. Hence  $Z_t$  for seams is normally found empirically [113-115]. The form for  $Z_t(\omega)$  in some cases can be

$$Z_t(\omega) = R + j\omega L, \quad (4.2.2)$$

where  $R$  is the resistive part of the seam transfer impedance, measured in ohm-m,  $L$  is the inductive part, measured in henry-m, and  $\omega$  is the frequency of interest. In the time domain (4.2.2) becomes

$$V(t) = RJ_{\text{ext}}(t) + L \frac{\partial J_{\text{ext}}(t)}{\partial t}. \quad (4.2.3)$$

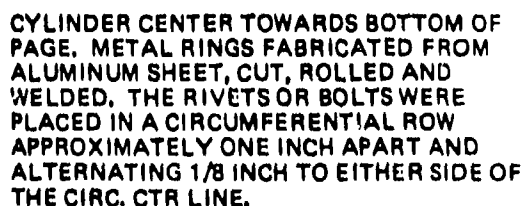
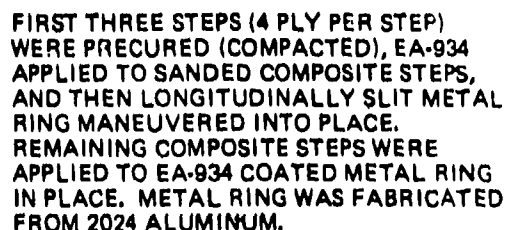
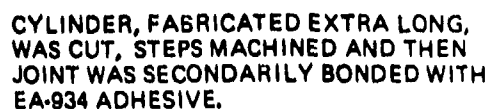
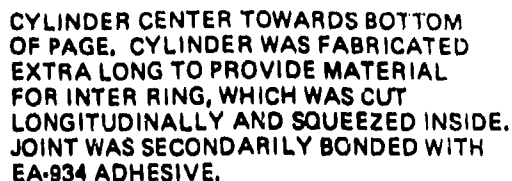
The above analysis assumes that  $J_{\text{ext}}$  is flowing perpendicularly to the seam. If this is not true, then  $J_{\text{ext}}$  in (4.2.1) and (4.2.3) should be read as the perpendicular component of the total external current density.

There is some data on aircraft joints [115]. Some of this is reproduced in Figures 4.8 - 4.9 for the joint configurations of Figure 4.7 as measured with a quadraxial test fixture.

#### 4.3 Slots and Cracks

Slots and cracks are a special type of aperture which is a thin gap in the skin of an aircraft through which energy may enter the body of the aircraft. In theory a slot can be treated as an aperture, the fields behind the aperture calculated, and the coupling to internal cables found from these fields [116]. This is a difficult problem however, so a much simpler method is usually used [117,118]. This method involves treating the slot as a slot antenna, and an internal cable running behind the slot as an impedance loading the antenna (Figure 4.10). The slot antenna is the electromagnetic complement of the strip dipole, so its characteristics can be found from the characteristics of the equivalent strip dipole, both of which are small compared to the incident field wavelength.

## FABRICATION NOTES



208

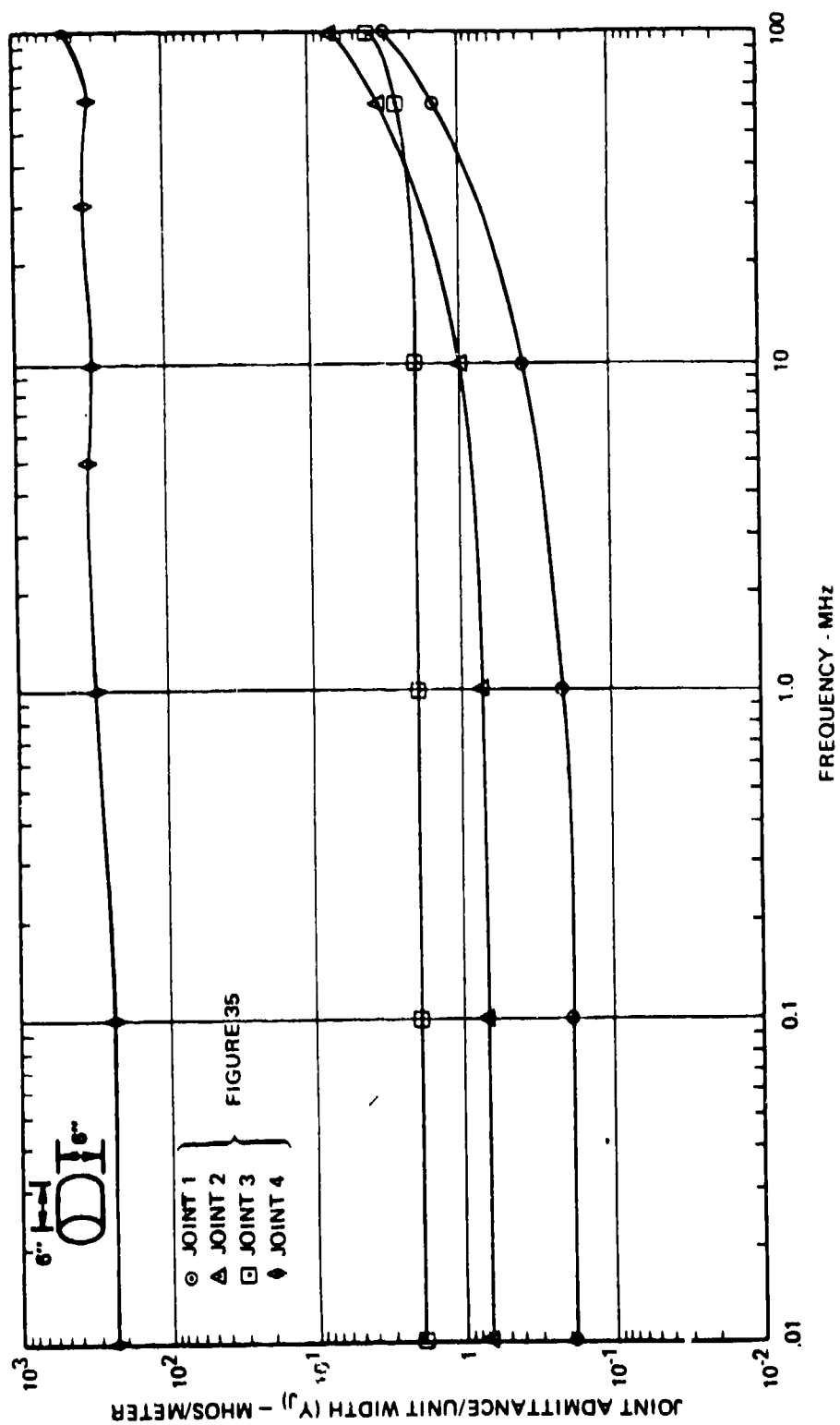
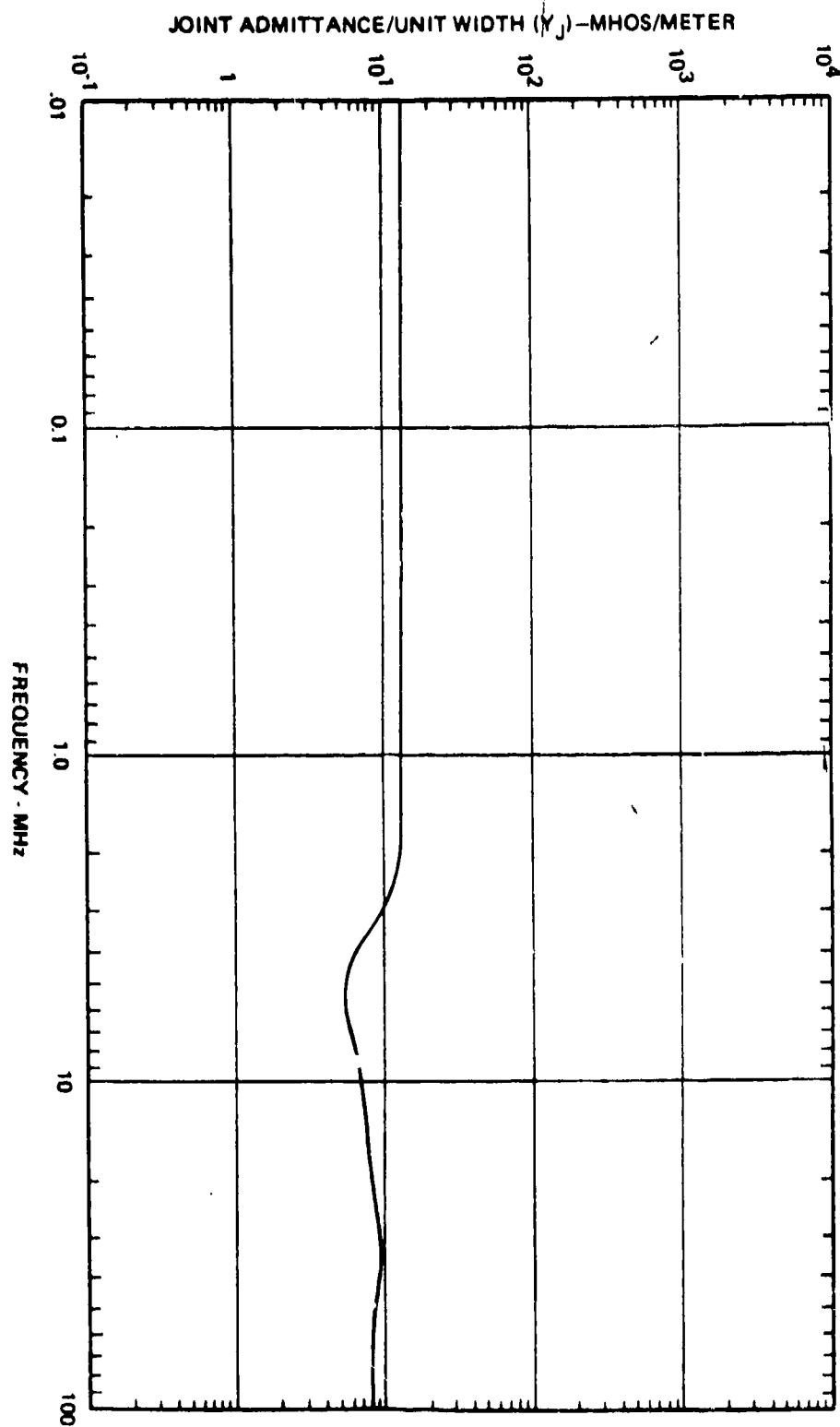
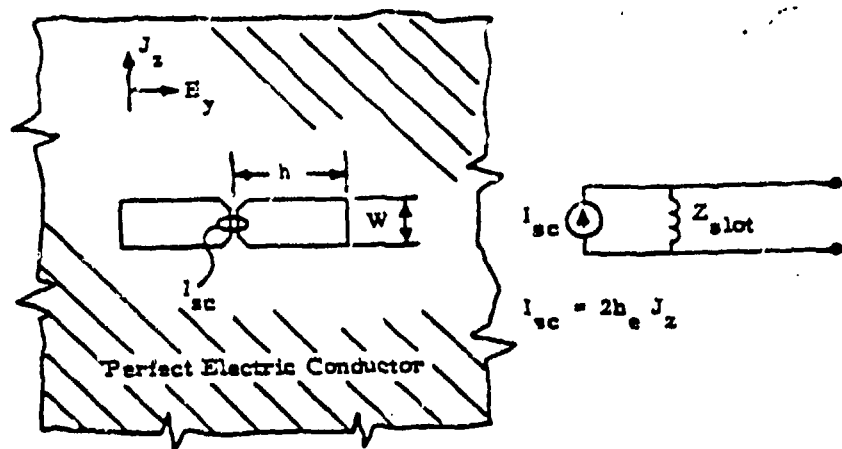


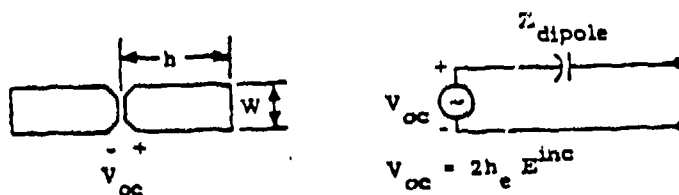
Figure 4.8 Measured Joint Admittance of Structural Joints  
 (Note:  $Z_T = \frac{1}{Y_j}$ ) [115]

Figure 4.9 Measured Joint Admittance of Joint No.5 [115]





a. Slot Antenna.



b. Complementary Strip Dipole.

Figure 4.10 A Slot Antenna and its Complementary Strip Pole

The fatness parameter for strip dipoles is given by

$$\Omega(\text{strip}) = 2 \ln \frac{8h}{w} . \quad (4.3.1)$$

For large fatness parameters the effective height of the slot and its complementary dipole is,

$$h_e(\text{slot}) = h_e(\text{dipole}) = \frac{h}{2} . \quad (4.3.2)$$

Then the short circuit current is,

$$I_{sc} = 2 h_e J_y . \quad (4.3.3)$$

The impedance of the strip dipole is capacitive and is given by,

$$C_{\text{dipole}}(\text{farads}) = \frac{h(\text{meters})}{1.8 \times 10^{10} (\Omega - 3.39)} . \quad (4.3.4)$$



The impedance of the slot antenna is related to the strip dipole impedance according to:

$$Z_{\text{slot}} = \frac{(60\pi \text{ ohms})^2}{Z_{\text{dipole}}} = \frac{(60\pi \text{ ohms})^2}{1/j\omega C_{\text{dipole}}} = (60\pi \text{ ohms})^2 j\omega C_{\text{dipole}} \quad (4.3.5)$$

Hence the impedance of the slot antenna is inductive. To couple to internal cables one can use  $Z_{\text{slot}}$  in (4.3.5) as a transfer impedance and  $I_{\text{sc}}$  as one half the current intercepted by the slot. Then  $V_{\text{int}} = Z_{\text{slot}} I_{\text{sc}}$  gives the internal voltage drop across the slot. This voltage drop is then translated into an internal electric field immediately behind the slot. This electric field is the source which drives the internal cables.

Another possible approach is to construct an equivalent circuit model of the slot-internal cable system. In this model, shown in Figure 4.8, the short circuit current drives the slot and cable inductances, connected in parallel. This model gives the total current flowing on the internal cable, but no information about propagation effects on that cable. It also is only valid at low frequencies where the cable impedance is inductive (assuming it is shorted to the airframe at each end). Otherwise, transmission line theory would be required to effect the solution. In addition, no spatial falloff of the excitation is assumed.

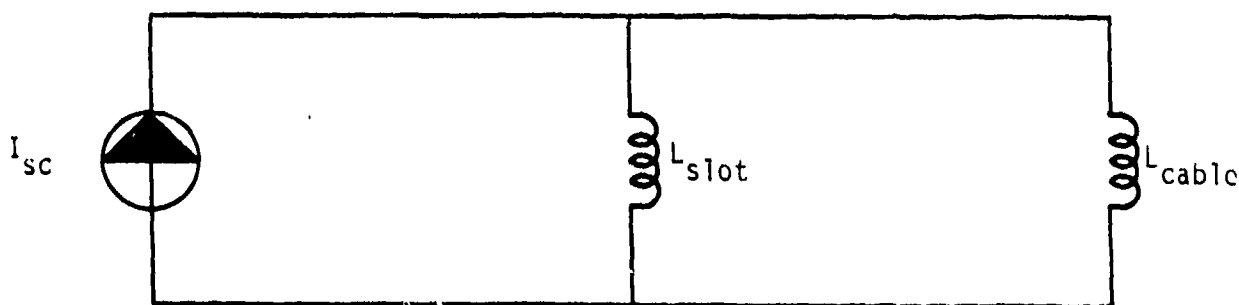


Figure 4.11 Equivalent Circuit Model of the Slot-Internal Cable Coupling

#### 4.4 Diffusion

Diffusion refers to the direct penetration of electromagnetic fields through the skin of an aircraft. Until recently this type of penetration has been of little importance because the skin has been made of highly conducting metals. However, some newer aircraft incorporate lightweight composite materials with much lower conductivities on their skin. For these materials diffusion is an important mechanism, particularly for the low frequency content of lightning return strokes.

Diffusion is basically a three medium problem (Figure 4.12). That is, given an incident electromagnetic field or surface current density, the problem is to find the fields on the other side of the conducting shield. This problem is an old one, but even after much study, exact solutions are available only for simple canonical shapes such as infinite plane shields, infinitely long circular cylinders, and the like [119].

In the frequency domain the problem essentially reduces to finding the transfer impedance  $Z_T(\omega)$  which relates the external surface current density  $J_s(\omega)$  to the internal electric field,  $E_{int}(\omega)$ :

$$E_{int}(\omega) = Z_T(\omega) J_s(\omega) \quad (4.4.1)$$

The function  $Z_T(\omega)$  is generally a complicated function of geometry, shield properties, and frequency, but a few general statements can be made.  $Z_T$  is a monotonically decreasing function of frequency. That is, low frequency fields diffuse through a shield more easily than higher frequency fields. Also  $Z_T$  decreases as  $\sigma$  increases, where  $\sigma$  is the conductivity of the shield. A perfect conductor,  $\sigma$  approaching infinity, allows no field to penetrate, so  $Z_T$  approaches zero for this case.

To illustrate the most straightforward method of deriving  $Z_T$ , consider the case of an infinite plane shield of thickness  $d$  and conductivity  $\sigma$ , as shown in Figure 4.12. There are three regions, labeled I, II, III, which correspond to the outside of the shield, the shield itself, and the

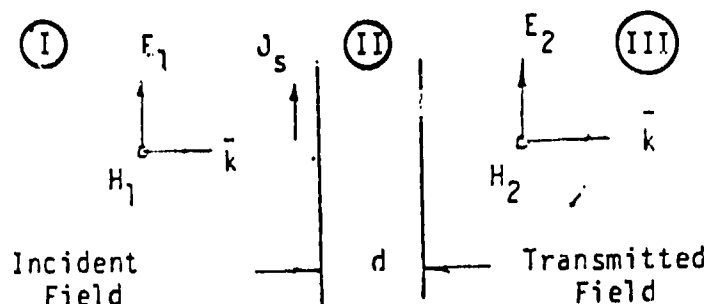


Figure 4.12 Statement of Shielding Problem for a Single Infinite Sheet

inside of the shield, respectively. An electromagnetic wave is incident normally on the shield from region I. Physically, the incident wave induces a current on the shield. Because of the finite conductivity of the shield, this is not strictly a surface current, and fields begin to penetrate the shield. These fields inside the shield (region II) then can act as a source for transmitted fields into region III. Then  $Z_T$  is the ratio of the field in region III to the current density in the shield.

Mathematically, the procedure for this planar case is relatively simple. Maxwell's equations are transformed into a wave equation, which is then solved in each of the three regions. In general, the solutions in regions I and III are non-decaying, while that in region II will be exponentially decaying. The amplitudes of these solutions are determined by appropriately matching fields at the boundaries of the shield.

The solution for  $Z_T(\omega)$  for the case above is,

$$Z_T(\omega) = \frac{K_m / \sigma_m}{\sin K_m d} \quad (4.4.2)$$

where  $K_m$  is the propagation constant of the wave in the shield, and  $\sigma_m$  is the shield conductivity. From (4.4.2), the region III fields can be determined if the current density in the shield, or equivalently, the incident field strength, is known.

The time domain analysis of diffusion consists of transforming (4.4.1) into the time domain. This is not always a trivial problem, and the case for the plane shield is done in Section 5.2.5.

The case of the infinite plane sheet is of course very simple compared to most realistic situations, but does serve very well to illustrate the fundamentals of diffusion calculations. For more complicated situations such as arbitrarily curved shields, geometry plays a large role in determining  $Z_T$ . These situations usually require the introduction of integral equation techniques or approximations based on neglect of displacement current. In the formulation of Franceschetti [120] the problem is stated as a single integral equation in the unknown current in the shield. This equation is numerically solved for the fields on the interior of the shield. Bedrosian and Lee [121] use the diffusion approximation of Kaden [122] to find the frequency domain transfer function for canonical geometries such as infinite extent plane sheets and spherical shells. These transfer functions are then inverse Laplace transformed to give time domain responses for the canonical shapes.

Merewether [123] has developed a technique in which a nonlinear diffusion equation derived from Maxwell's equations is numerically solved for the field distribution inside a conducting sheet. Although the paper deals only with infinite plane sheets, in principle, it should be possible to extend the technique to more arbitrary geometries.

#### 4.5 Radomes

Radomes are particularly difficult structures to model, chiefly because of the large number of cables, antennas, and support structures. A relatively simple example is given in Figure 4.13. Usually only crude models can be developed. Thin wire grid models of aircraft have been extended to include simple models of radome structures [124] with a limited amount of success. Because radomes differ markedly between aircraft, each one would need an individually tailored analysis. Sometimes they can be modelled as electrically small antennas and approximations made in this manner. We note that

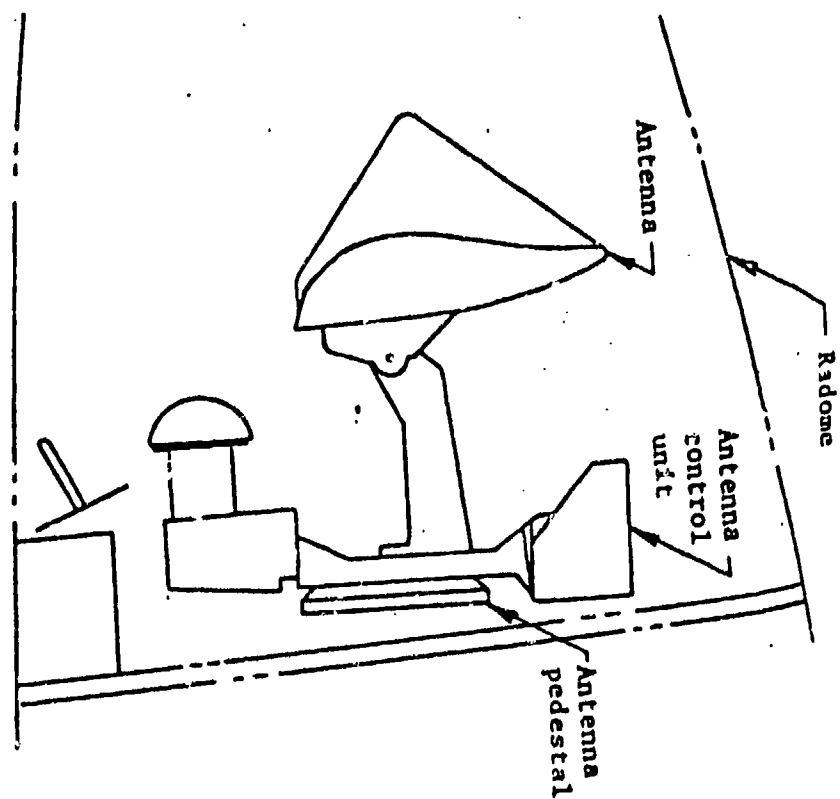
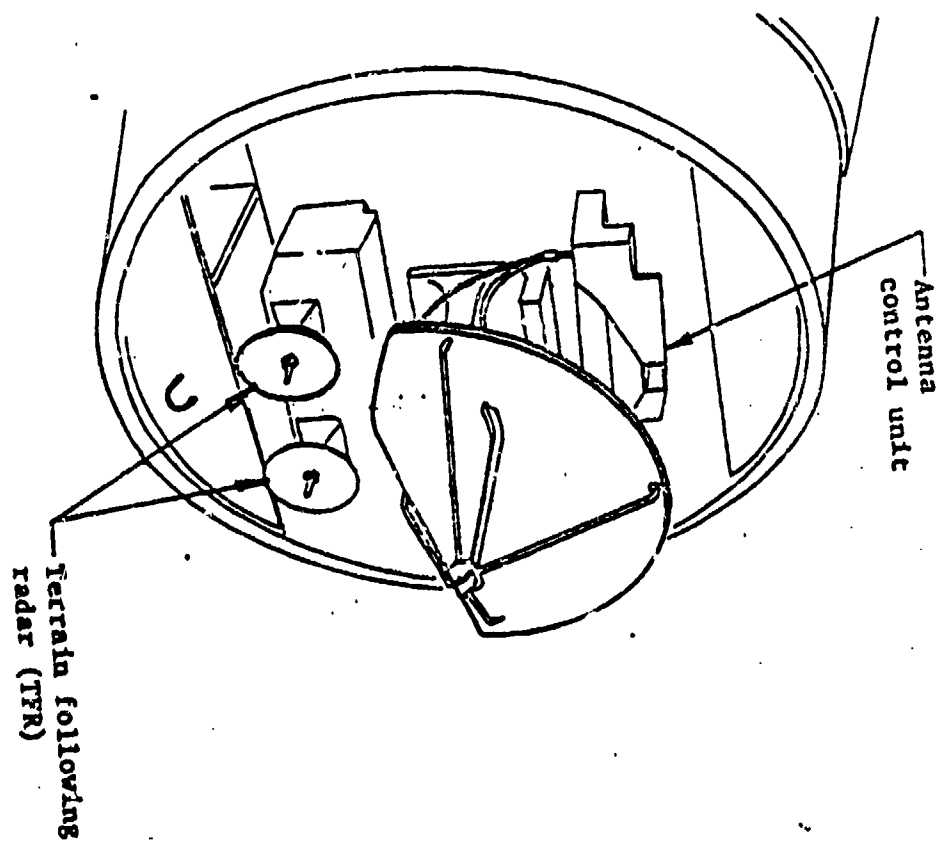


Figure 4.13 Example of Forward Radar Structures [124]

radomes are located such that they can be in a high electric field intensity location.

Finite difference techniques could be extended to account for radomes in much the same manner as discussed for apertures in Section 4.1. However, because of geometric complexity and the "rat's nest" of wiring found in this area, it is unlikely that good accuracy by this method or any other can be obtained. Worst case coupling values may be the best one can do in this problem area.

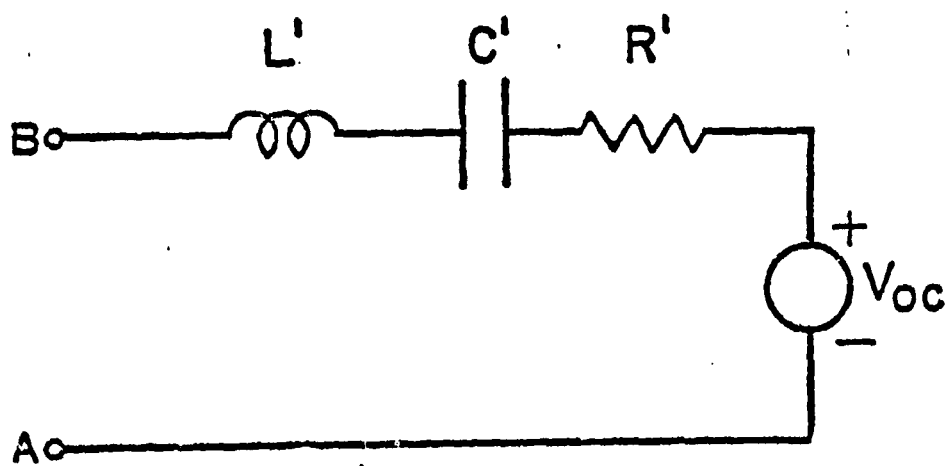
#### 4.6 Deliberate Antennas

Aircraft antennas include many types, such as loops, blades, monopoles, HF wire antennas, slots, and trailing wires. The analysis techniques are as varied as the types of antennas. A good summary of broadband antenna modeling for several antenna types is given in [125, 109]. Thevenin or Norton equivalent circuits are defined, and the sources are defined in terms of the local skin current or charge density as determined from an external coupling analysis. For example, a marker beacon antenna has the equivalent circuit of Figure 4.14. The element values are determined from known geometries of the antenna, and  $V_{ind}$  is, in this particular case, the voltage induced by magnetic flux coupling to the antenna loop. Numerous other antennas can be modeled in a similar fashion.

#### 4.7 Wing Wiring

Wiring and cabling in aircraft wings usually route in the leading and trailing edges. Wires in the leading edge are often shielded to some degree by covers. Wires in the trailing edge are usually electromagnetically exposed, because they are located between the control surfaces and the main part of the wing. The wing electrical wiring is often accompanied by fuel and hydraulic lines and control cables.

The geometry of such wiring readily lends itself to transmission line analysis. The main problem is to obtain the distributed field excitation sources driving the transmission line and the transmission line parameters. An approach which usually works is to use a Laplace's equation solver to obtain both of the parameters. The excitation functions are determined as a scale factor multiplied by the total wing current as determined from an external coupling calculation. This approach assumes that the wing cross section dimensions are small with respect to the wavelength of the highest frequency of interest.



$$L' = L_2 \left[ \frac{\omega M}{\left( \frac{1}{j\omega C} + j\omega L_2 + R \right)} \right]^2$$

$$C' = C \left[ \frac{\omega M}{\left( \frac{1}{j\omega C} + j\omega L_2 + R \right)} \right]^2$$

$$R' = R \left[ \frac{\omega M}{\left( \frac{1}{j\omega C} + j\omega L_2 + R \right)} \right]^2$$

$$V_{oc} = V_{ind} \left[ \frac{j\omega M}{\left( \frac{1}{j\omega C} + j\omega L_2 + R \right)} \right]$$

Figure 4.14 Thevenin Equivalent Circuit of the Marker Beacon Antenna [125]

#### 4.8 Internal Cable Propagation

After electromagnetic fields penetrate into the aircraft interior by means of apertures, diffusion, seams, and slots, they excite internal cables which in turn propagate the energy to other parts of the aircraft. The problem facing the analyst is to predict voltages, currents, powers, and energies on individual connector pins. The common approach to the problem is to model the aircraft cable network as a system of transverse electric and magnetic (TEM) transmission lines. TEM transmission line equations, which are derived from Maxwell's equations, can then be solved in either the frequency or time domain. The transmission line telegrapher's equations are two first order coupled partial differential equations for voltage and current on the lines. There are two commonly used methods for modeling internal cables, the bulk cable model and the multiconductor model. These methods will be discussed in more detail later, and only a brief characterization is necessary here.

Multiconductor modeling requires the specification of capacitance and inductance matrices for multiconductor cable bundles. The transmission line equations become matrix equations and are solved for voltages and currents on each of the individual wires in a bundle.

The derivation of the transmission line equations follows from Maxwell's equations when special restrictions are placed on the field variables [126-128]. The most important restriction is that the separation of the conductors in the line must be small compared with wavelengths of interest. This restriction limits the types of propagating solutions that can exist and allows a unique transverse voltage to be defined between the conductors. It also allows a circuit type of analysis to be applied to short lengths of the conductor, called elements. As the length of these elements approaches zero, the familiar transmission line equations emerge.

$$\begin{aligned}\frac{d[V]}{dx} &= -[Z][I] + [S_V] \\ \frac{d[I]}{dx} &= [Y][V] + [S_I]\end{aligned}\tag{4.8.1}$$



In (4.8.1)  $[V]$  and  $[I]$  represent voltage and current column matrices on the line, respectively,  $[Z]$  the series impedance per unit length,  $[Y]$  the shunt admittance per unit length, and  $[S_V]$ ,  $[S_I]$  voltage and current sources on the line. Clearly the equations are written in the frequency domain, so  $[I]$  and  $[V]$  are functions of  $X$  and  $\omega$ . The transmission line is assumed to run only in the  $X$  direction.

In the time domain (4.8.1) becomes

$$\begin{aligned}\frac{\partial [V]}{\partial X} + \frac{\partial}{\partial t} [L][I] + [R][I] &= [S_V] \\ \frac{\partial [I]}{\partial X} + \frac{\partial}{\partial t} [C][V] + [G][V] &= [S_I]\end{aligned}\tag{4.8.2}$$

Here  $[L]$  is the per unit length inductance matrix,  $[R]$  the per unit length resistance matrix,  $[C]$  the per unit length capacitance matrix, and  $[G]$  the per unit length conductance matrix. Unlike the frequency domain equations, the time domain form almost always must be solved numerically, especially for arbitrary sources.

There are many ways of solving the telegrapher's equations. Frequency domain techniques usually employ the Green's function approach. In this method the source function is replaced by a delta function which simplifies the problem. The solution to the more general problem is then constructed from an integral involving the Green's function and source distribution.

The time domain approach usually employs finite difference techniques in which (4.8.2) is put in a finite difference form in a straightforward manner. The chief advantages of this approach are that the time domain result is obtained directly, non-uniform lines can be treated, and non-linearities and time varying parameters can be included.

In connection with the multiconductor modeling technique the question naturally arises as to how the capacitance and inductance matrices are calculated [142-145]. These are normally calculated as per unit length quantities for a system of infinitely long parallel cylindrical conductors, with or without a dielectric covering. The potential of each conductor is specified, and the charge (bound and free) on conductor and dielectric surfaces is expressed in

terms of expansion functions. This expansion gives the charge per unit length around the surface of the conductor or dielectric in terms of known expansion functions and unknown expansion coefficients. The unknown coefficients are determined by enforcing the boundary conditions that the total potential on each conductor due to all the charge distributions must be the (arbitrary) potential defined earlier, and that the normal component of the displacement vector due to all the charge distributions must be continuous at the dielectric surfaces. This results in a matrix equation for the coefficients which can be straightforwardly solved. Hence the charge distribution is known on each of the conductors. The total charge on each conductor is then calculated by integrating the distribution around the surface. The capacitance matrix  $[C]$  is then found from the matrix equation,

$$[q_f] = [C][V] \quad (4.8.7)$$

where  $q_f$  is the  $N \times 1$  matrix of total free charges on the  $N$  conductors, and  $V$  is the  $N \times 1$  matrix of arbitrary potentials.

The per unit length inductance matrix is calculated in the case when no dielectric is present. This is done because dielectrics have no influence on inductance. First the capacitance matrix is determined, and then the relationship  $L = \mu_0 \epsilon_0 C_0^{-1}$  is applied, where  $C_0^{-1}$  is the inverse of the capacitance matrix with the dielectrics removed, and  $\mu_0$ ,  $\epsilon_0$  are the permeability and permittivity of free space, respectively.

Although multiconductor transmission line theory is sufficiently advanced to permit analysis of aircraft with bundles, it is usually impractical to do so. The main problem is the practical one of identifying how the cable runs are configured in an aircraft. This data is often not readily available from drawings, and is extremely difficult to obtain by a physical inspection. Also, for many aircraft, the layup of individual wires in a bundle is not controlled, and data therefore is not available. In addition, the bundle arrangement and geometry change as a function of position and it would require a great deal of geometrical data to facilitate modeling. Finally, even if all this data could be obtained on a particular aircraft, the data would quite likely be different for another aircraft of the same type.

It thus appears that the best one can hope for in the analysis of aircraft cables is approximate answers which may perhaps be statistically correct.

Therefore one is motivated to find an alternative approach to this problem.

One approach that appears to be helpful is called the bulk model [139,137,140]. In this model, multiconductor cable bundles are approximated by an equivalent single conductor. Simple one-conductor transmission line models can then be used to obtain the total current and average voltage on this single conductor. This so-called bulk response can then be used to estimate the response of a particular wire of interest. There are several ways to do this. It can be done in a worst case fashion, in which one assumes that the individual wire response is the same as the bulk response, although there are certain circumstances for which this is not truly a worst case. Another approach is to relate individual wire response to the bulk response on a statistical basis [23]. The problem here, of course, is that a large data base needs to be developed either numerically or experimentally. A third approach is to separate the individual wire of interest from the bulk cable and solve for its response by treating it as a single wire transmission line whose sources are obtained from the bulk response [137]. This approach is discussed further in Chapter 5.

Finally, studies have been done to identify the effects of a geometrical perturbation such as bends, branches and bulkheads on cable response [146,147]. These are incorporated into transmission line codes as a change in the capacitance and inductance matrices at the spatial location of the perturbation.

## CHAPTER 5

### SELECTED MODELING APPROACHES

#### 5.1 Introduction

In Chapters 3 and 4, various approaches available for lightning interaction modeling were reviewed and discussed. They all have advantages and disadvantages in the context of the lightning problem. In Chapter 5, the models which were actually implemented under this effort are described. These models are installed and operating on the ASD Computer Center at Dayton, Ohio. The theoretical background for these models is presented here, and the actual FORTRAN programs are discussed in detail in the user's manuals which are published separately [1, 2, 3].

#### 5.2 External Coupling Models

The external coupling problem is of particular importance because from it all the internal results are obtained. It is also difficult because no one code has all the desirable features. The big tradeoff is between accuracy and simplicity. The accurate codes require considerable computer resources and user skill, whereas simple codes don't have the desired accuracy. Because of this, two external coupling methods have been implemented, a three-dimensional finite difference code called T3DFD and a simple lumped parameter network (LPN) model.

The T3DFD code is considered to be the best choice for the following reasons:

1. Non-linearities in the attachment process and test configuration can be included;
2. Has demonstrated accuracy on NEMP test programs.
3. All components for  $J_s$  and  $Q_s$  are included.
4. Dielectric and different skin conductivities can be accounted for which is important for advanced composites.
5. Large apertures can be directly analyzed by gridding into them.
6. Small apertures, and thin wires and slots can be included by special techniques.
7. Non-canonical shapes are readily analyzed.

8. Geometrical resolution is better than other methods.
9. Futuristic approach:
  - a. Physics of streamer propagation and corona can be added if known;
  - b. Future computers will allow even better accuracy because the approach has no fundamental approximations or assumptions.

The code also has significant disadvantages:

1. It requires significant computer resources.
2. A skillful user is required.
3. Numerical stability is sometimes a problem (reflection from boundary, accumulation of numerical error).

Because the T3DFD approach severely strains the computer resources at the AFFDL Computing Center, the LPN model was chosen as an alternative.

In order to illustrate the tremendous difference in computer requirements, the two models are compared in Table 5.1. It is clear that the LPN cost and complexity is about two orders of magnitude less than that of T3DFD.

Table 5.1 Comparison of T3DFD and LPN Computer Requirements at AFFDL Computing Center for 300 ns of Problem Time

	3DFD	LPN
Required CP Time	454 seconds	6 seconds
Elapsed Time	2 hours	6 seconds
Central Memory Requirements	44k <sub>10</sub>	12k <sub>10</sub>
Disc Space Required	197k <sub>10</sub>	none
Cost per Run	\$200	<\$1.00

The T3DFD code is similar to that described in Section 3.3.2. The main difference is that it has been adapted to run on the AFFDL computing system. Because of constraints in this system, the radiation boundary conditions had to be removed. Instead, a much simpler approach using a lossy outer boundary (by means of an impressed air conductivity) which absorbs most of the energy, is used.

The details of the code are described in Reference 3.

A generalized LPN model is shown in Figure 5.1. The model can handle 3 different empennage geometries as shown. Both attached and near miss cases can be studied. The LPN model is heuristic in its derivation and is not strictly based on first principles. The model is developed by first computing the total surface area of the aircraft and then finding the capacitance of a sphere having the same area. Then the capacitance of members such as the wings, fuselage, tail, etc. are obtained by multiplying the total capacitance by the ratio of the member area to the total area. Each member is then made into a single conductor transmission line, with the inductances determined from the fact that the waves propagate at the speed of light. Each member can be made into a uniform or non-uniform (spatially varying) transmission line, depending on the option of the user. The model can be excited either by an attached stroke or an incident electric field. For an incident field, the user specifies the angle of incidence and polarization and the code automatically computes the correct source terms for the model.

It should be noted that for an aircraft over a ground plane or in a test fixture, the Laplace equation solver discussed in Section 5.3.8.2 can be used to directly find the capacitances of the various members. This is discussed in more detail in that section.

The question naturally arises of how the results from the LPN and T3DFD models compare. Comparisons have been done for nuclear EMP incident on an F-16 and for a lightning stroke attached to a C-130.

The F-16 is shown in Figure 5.2, and the LPN model is shown in Figure 5.3. Because the fuselage and wing cross sections vary along their lengths, they are modeled as non-uniform transmission lines. When the aircraft is illuminated by an incident field, there are two terms which comprise the total solution. The first term is computed directly by the LPN model. The normal electric field ( $E_n$ ) and the tangential magnetic fields (or the surface current density  $J_s$ ) calculated by the LPN model are obtained from the calculated voltage  $V_n$  and current  $I_n$  according to

$$E_n(t) = \frac{K_s C_n V_n(t)}{\epsilon_0 A_n} \quad (5.1)$$

where  $C_n$  and  $A_n$  are the capacitance and surface areas associated with the  $n$ th node, and  $K_s$  is a shape factor which accounts for the charge distribution over the circumference (e.g., see Figure 5.28). This term is sometimes called the antenna response term.

(A)



(B)



(C)



#### SEGMENTATION:

FUSELAGE: 200 ELEMENTS

WING: 100 ELEMENTS EACH

HORIZONTAL STABILIZER: 100 ELEMENTS EACH

VERTICAL STABILIZER: 100 ELEMENTS EACH

Figure 5.1 Generalized LPN Model

RIGHT WING SUPPORTED WEAPON

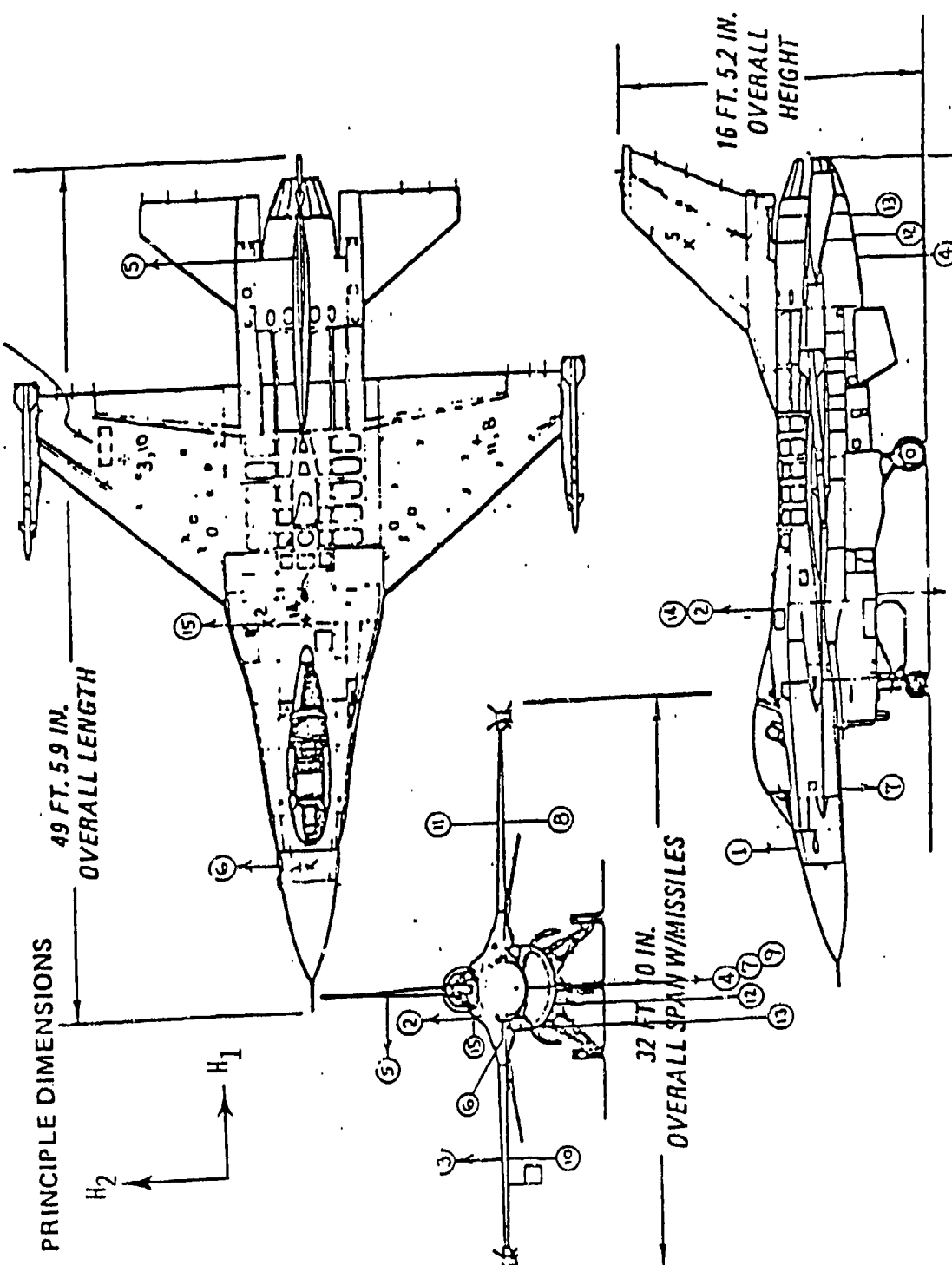
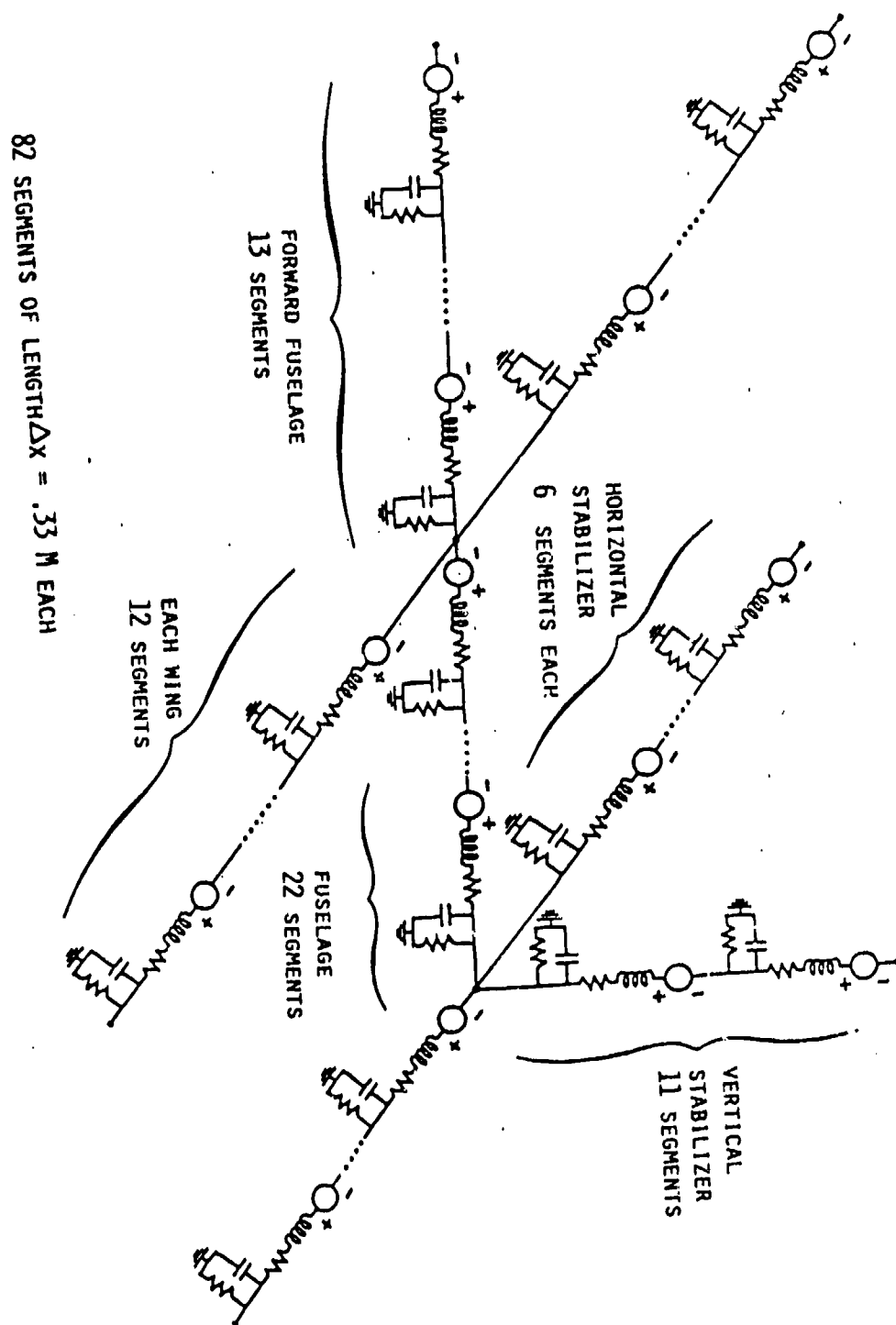


Figure 5.2 F-16 Aircraft System





82 SEGMENTS OF LENGTH  $\Delta x = .33$  M EACH

Figure 5.3 LPN Model of F-16

In addition, there are magnetostatic ( $J_{t1}$ ) and electrostatic ( $E_{t1}$ ) terms approximately given by

$$\begin{aligned} E_{t1} &= 2\vec{n} \cdot \vec{E}_{inc} \\ \vec{J}_{t1} &= 2\vec{n} \cdot \vec{H}_{inc} \end{aligned} \quad (5.2)$$

where  $\vec{n}$  is the outward normal on the surface.

The total normal electric field and the surface current density is then the sum of these terms.

Figures 5.4 to 5.8 illustrate the comparison between the two methods. The excitation is the standard double exponential EMP plane wave given by

$$E_{INC}(t) = 52 \text{ kV/m} (\exp(-4 \times 10^6 t) - \exp(-4.76 \times 10^8 t)). \quad (5.2)$$

The results are encouraging in that there seems to be a fair comparison. There is a difference in waveform details, but if one were interested mainly in peak values and general waveshapes, the LPN approach would probably be adequate.

The two models have also been compared for an attached lightning stroke. Figure 5.9 shows the C-130 outline and the lightning waveform, and the T3DFD model is shown in Figure 5.10. Figure 5.11 shows the comparison of the tangential magnetic fields, and Figure 5.12 shows the comparison of the normal electric fields. While there is a difference in the waveform details, the results have good amplitude agreement and a general agreement in slope.

It is suggested that the 3DFD model be used to "calibrate" the LPN model, as the LPN model can be used to do parameter studies, and the 3DFD also be used to check any conclusions made by the use of the LPN model.

The magnetic fields have better agreement than the electric fields, and although the large features of the responses are similar, there are differences from the two methods. This is, of course, to be expected because there is about three orders of magnitude less physics in the LPN model than in the T3DFD model. The results can be interpreted in terms of aircraft geometry. For test point 1, for example, the dip in electric field after 100 ns or so is caused by the reflection from the wire junction. There is also a corresponding current increase.

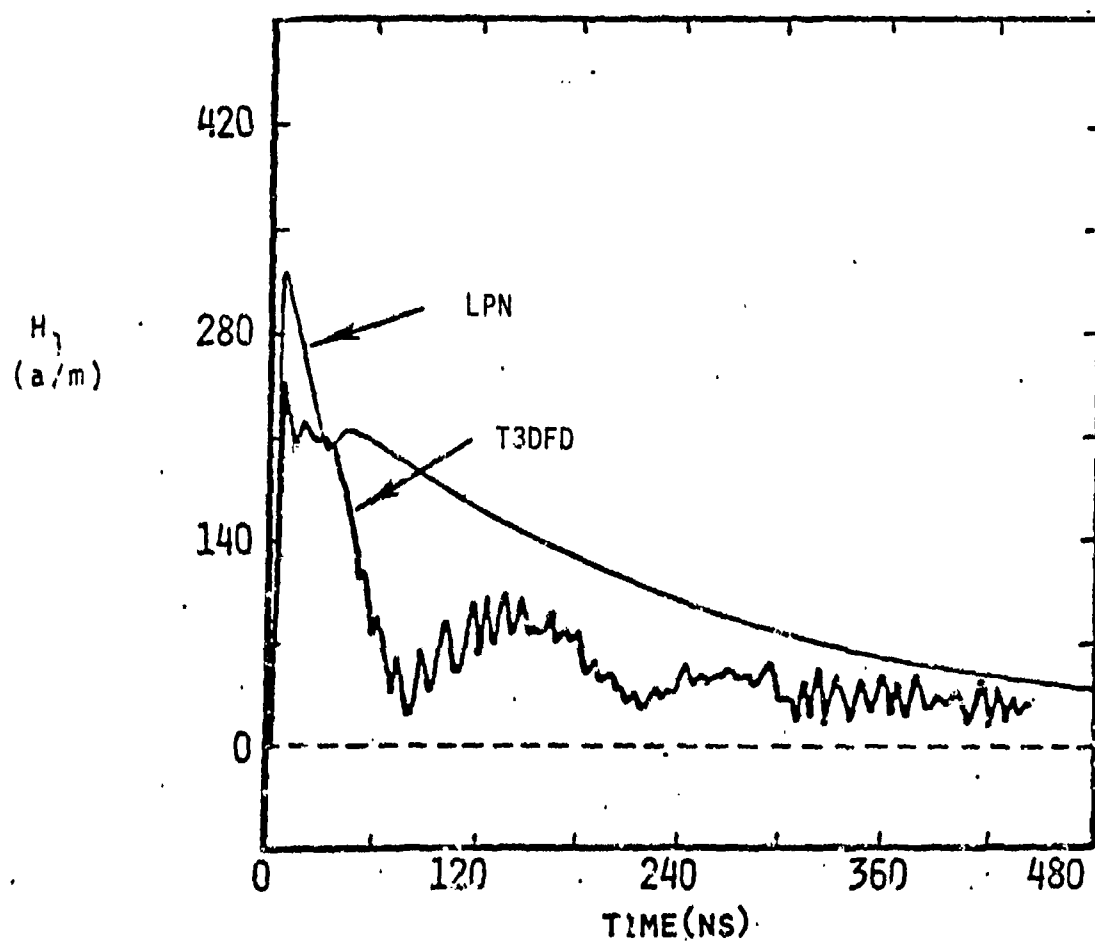


Figure 5 4 Overlay of Finite-Difference and Circuit Model Results for EMP Excitation of F-16 at Test Point 3, for Incident E Field Parallel to Fuselage

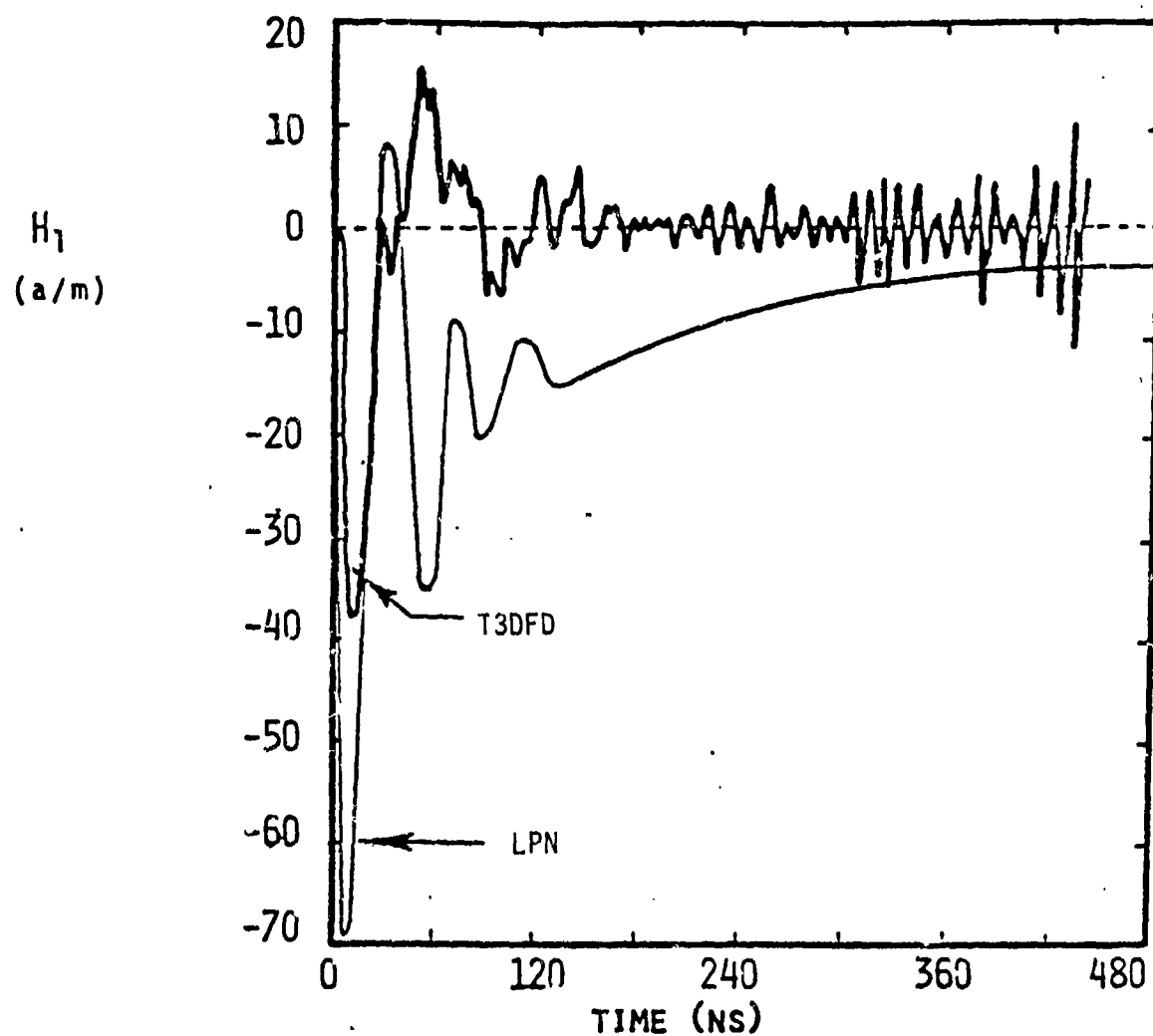


Figure 5.5 Overlay of Finite-Difference and Circuit Model Results for EMP Excitation of F-16 at Test Point 3, for Incident E Field Perpendicular to Fuselage

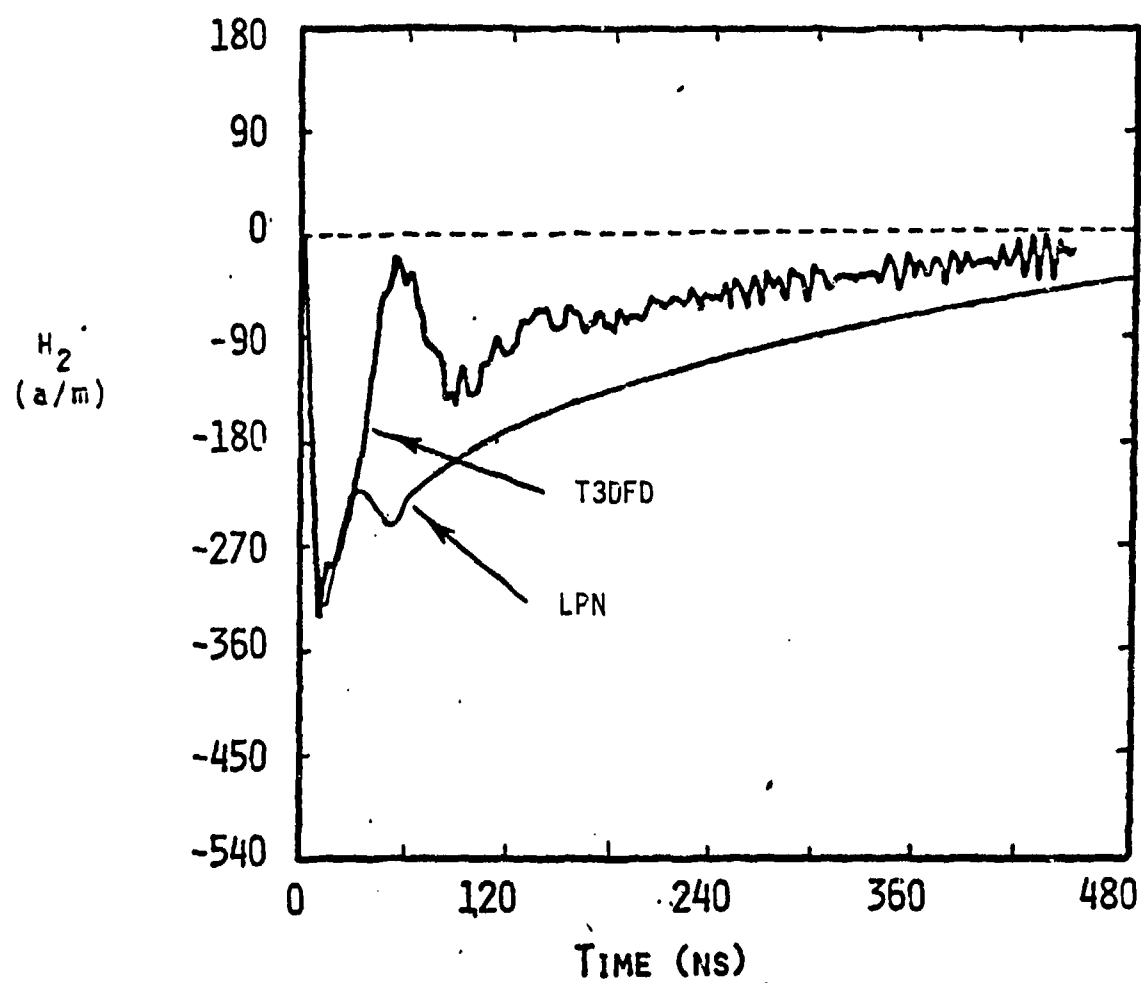


Figure 5.6 Overlay of Finite-Difference and Circuit Model Results for EMP Excitation of F-16 at Test Point 3, for Incident E Field Perpendicular to Fuselage

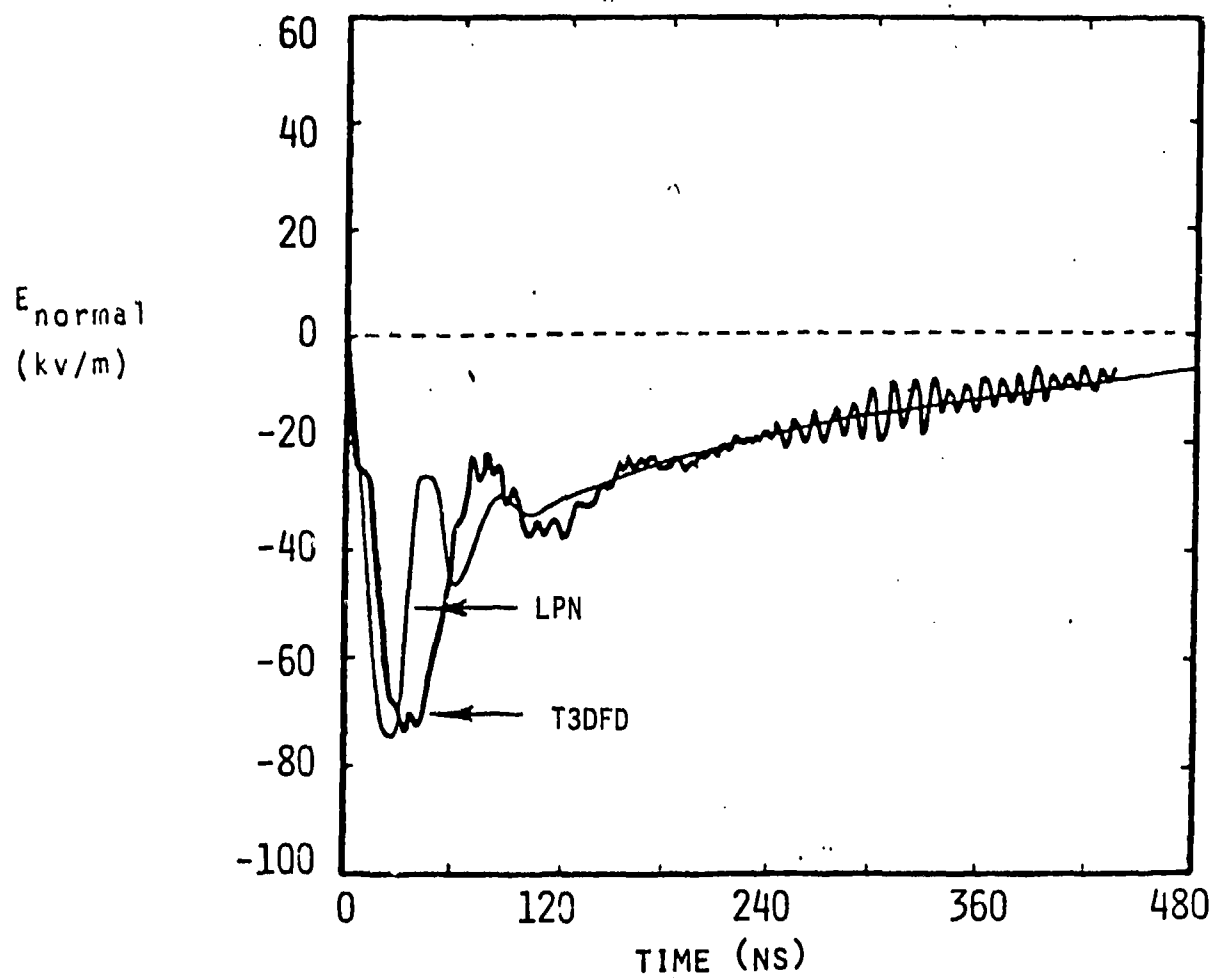


Figure 5.7 Overlay of Finite-Difference and Circuit Model Results for EMP Excitation of F-16 at Test Point 3, for Incident E Field Perpendicular to Fuselage

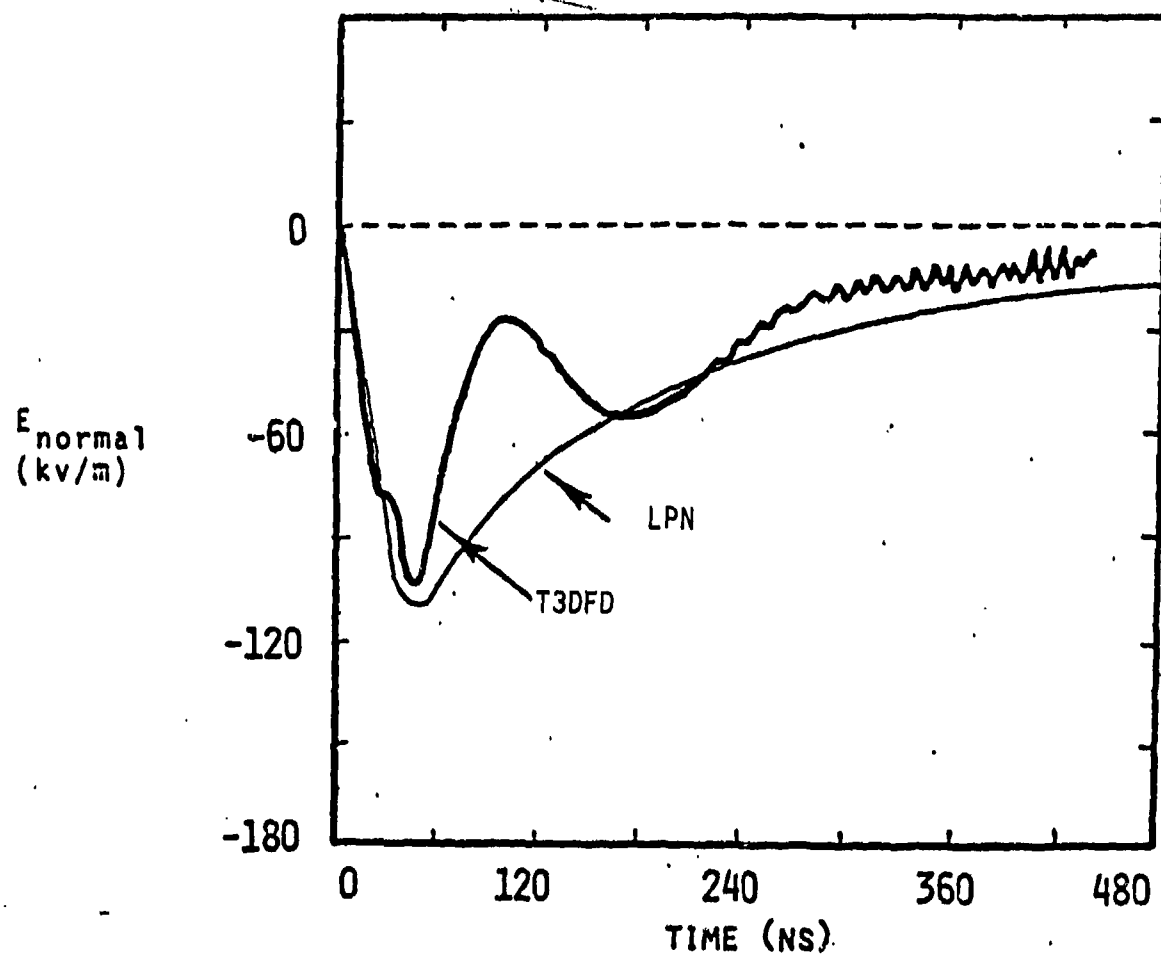


Figure 5.8 Overlay of Finite Difference and Circuit Model Results for EMP Excitation of F-16 Test Point 14, for Incident E Field Parallel to Fuselage

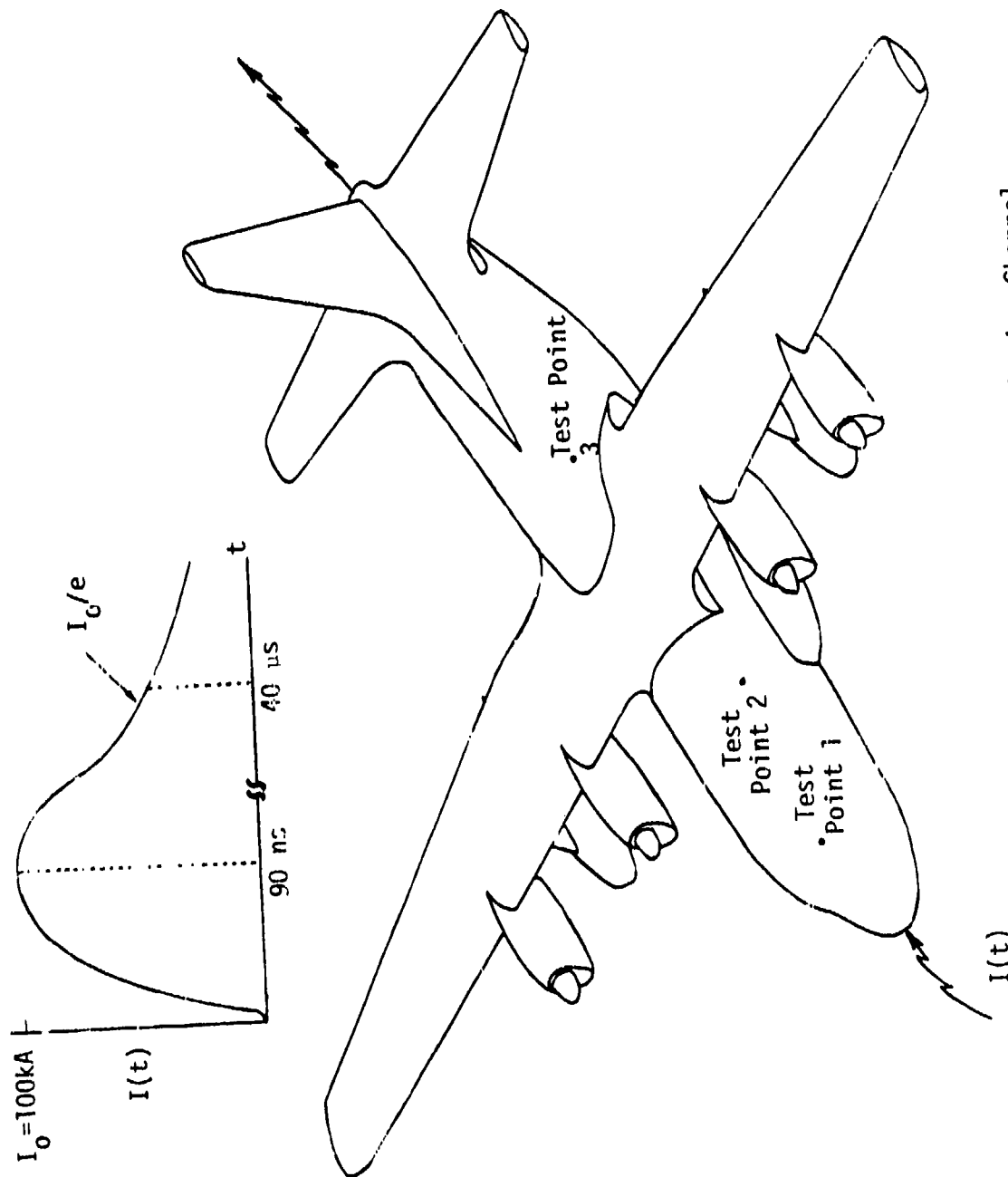


Figure 5.9 C-130 in an Attached Lightning Channel



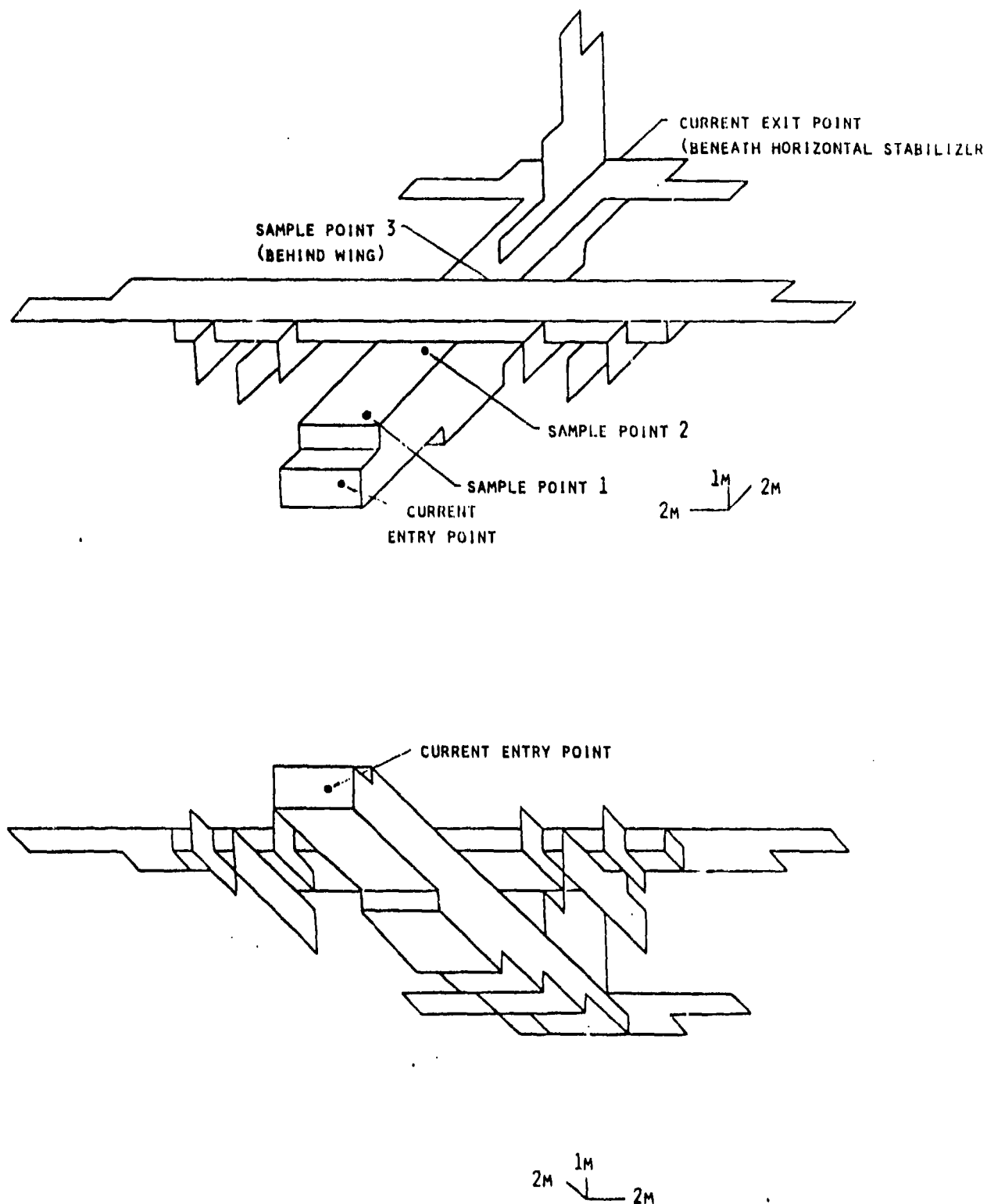


Figure 5.10(a) Three-Dimensional Finite-Difference Representation of a C-130

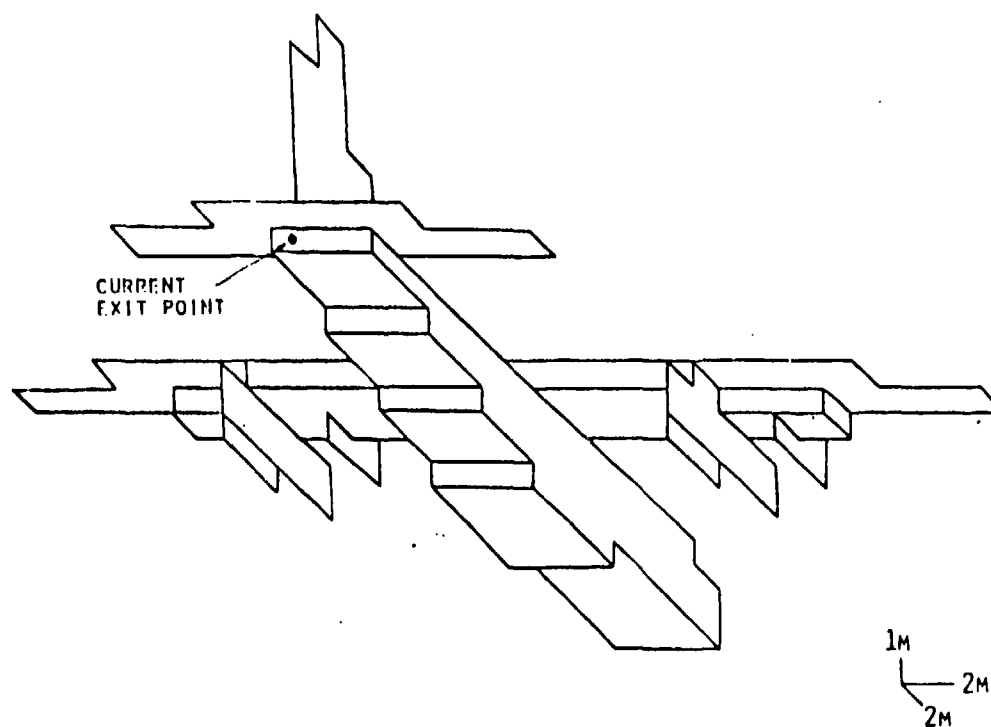
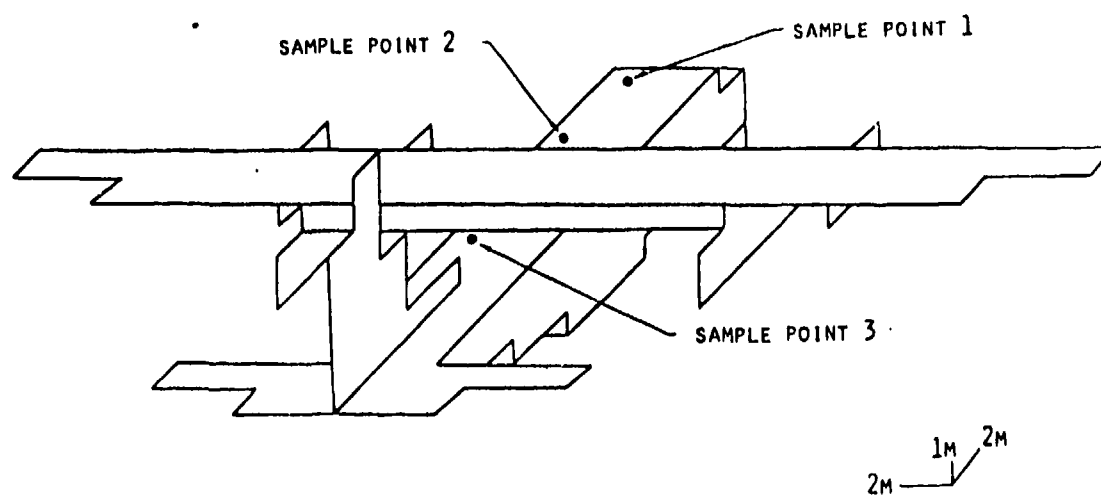


Figure 5.10(b) Three Dimensional Finite-Difference Representation of a C-130

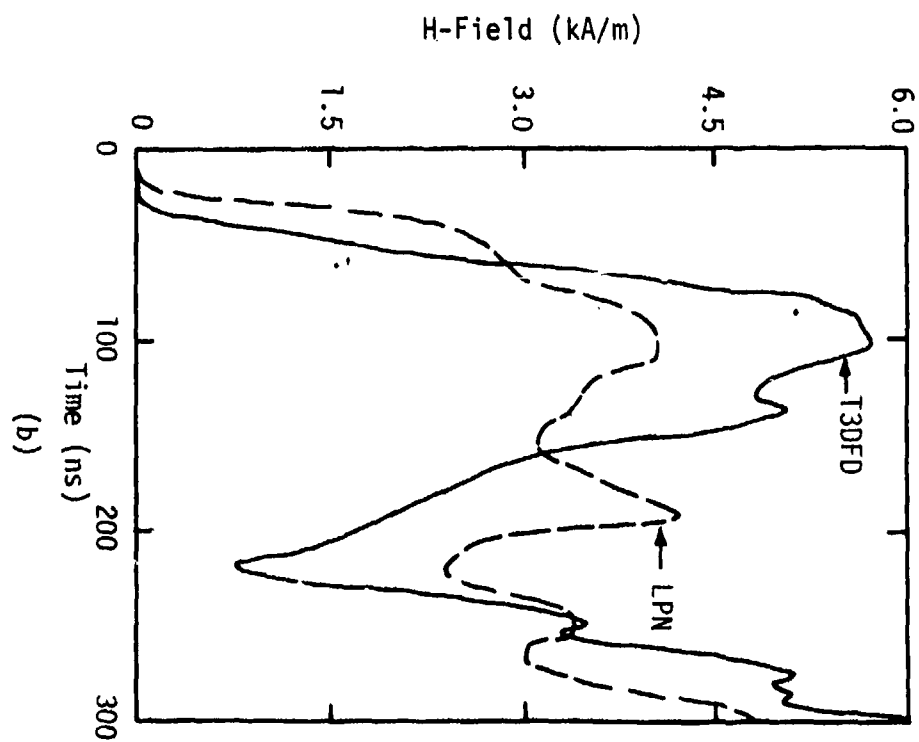
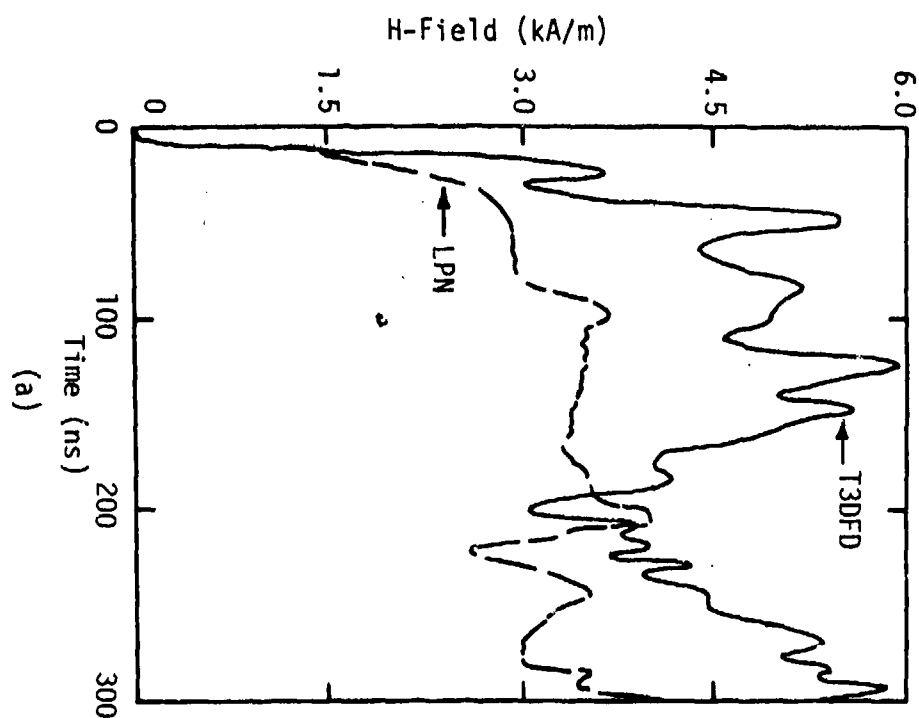


Figure 5.11 Comparison of Theoretical LPN and T3DFD H-Field Calculations at Sample Points 1(a) and 2(b)

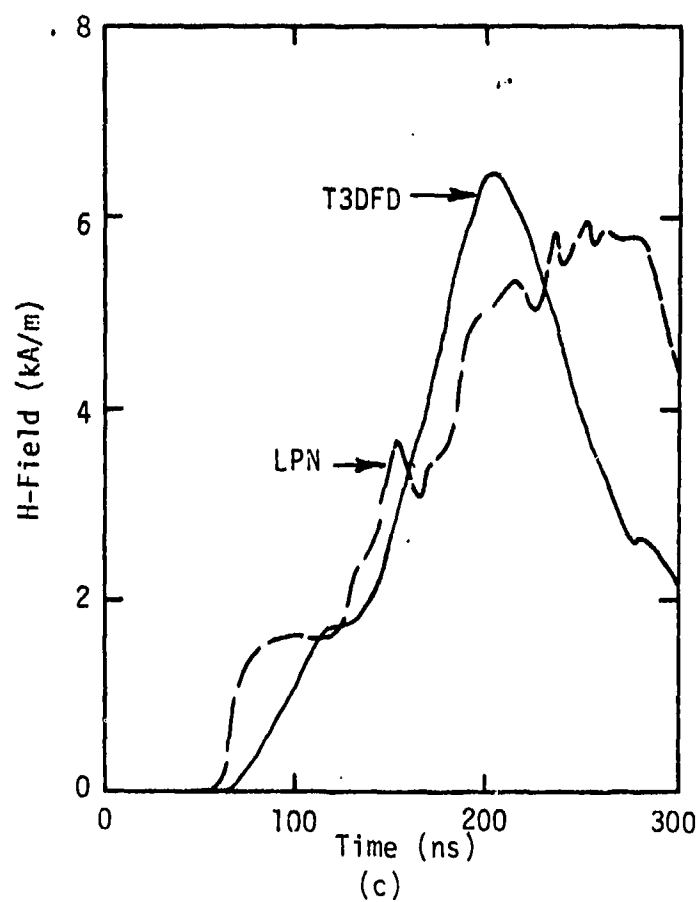


Figure 5.11 (cont'd) Comparison of Theoretical T3DFD and LPN H-Field Calculations at Sample Point 3

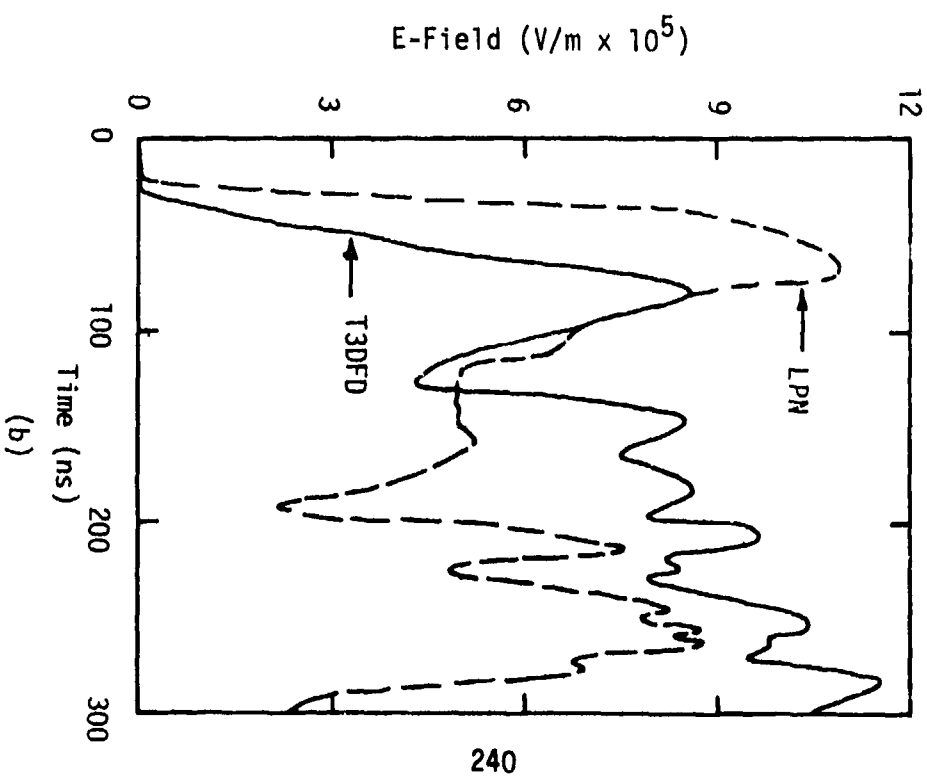
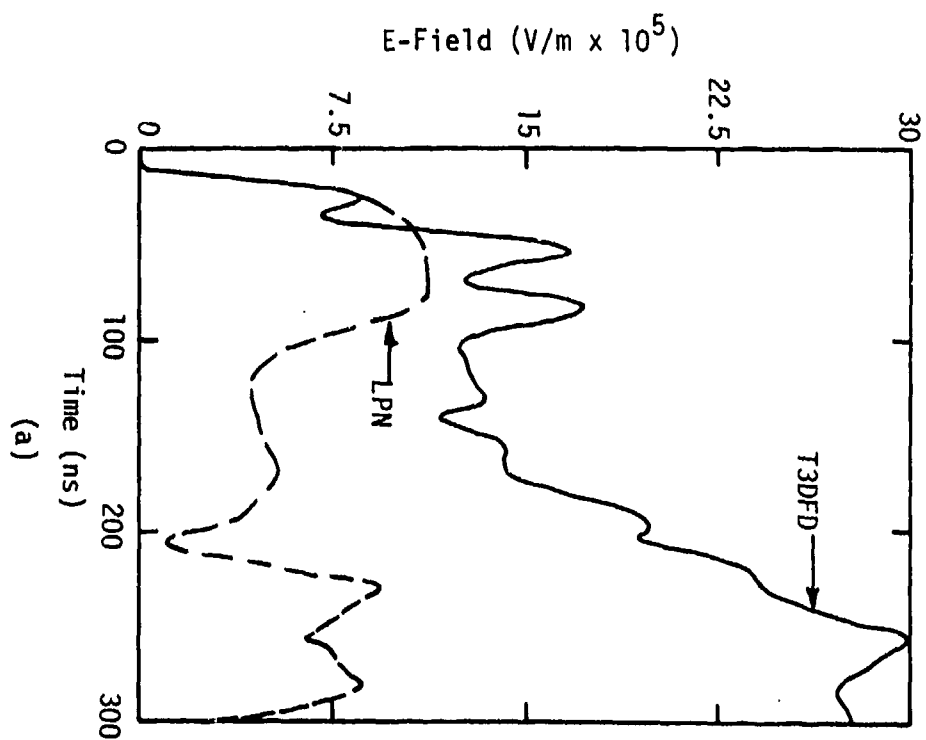


Figure 5.12 Comparison of Theoretical LPN and T3DFD E-Field Calculations at Sample Points  
1(a) and 2(b)

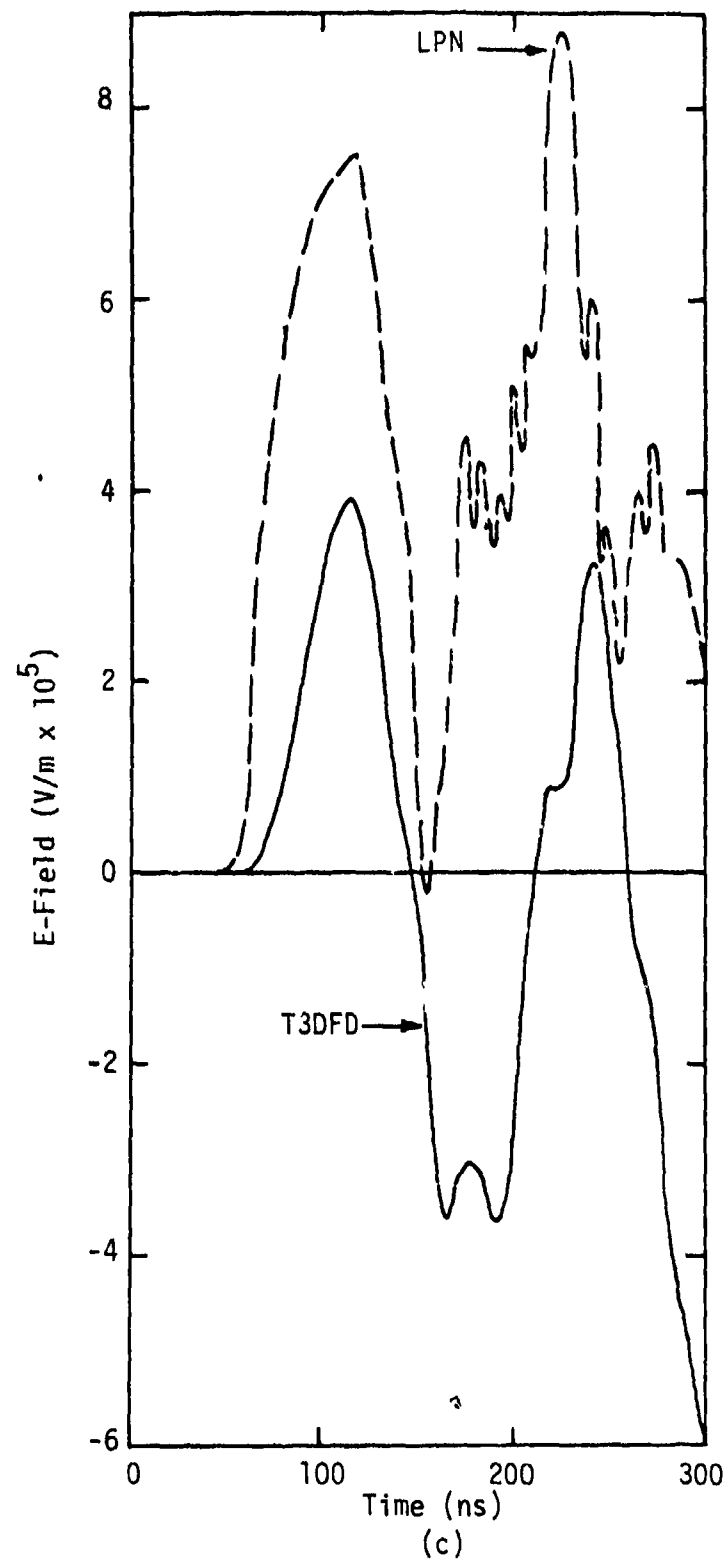


Figure 5.12 (cont'd) Comparison of Theoretical LPN and T3DFD E-Field Calculations at Sample Point 3

Parameter studies were also done with T3DFD to determine the sensitivity of the response to lightning current rise time. Normal electric field and tangential magnetic field responses are shown in Figures 5.13 and 5.14, respectively. Obviously, the resonance behavior is greatly affected by the rise time as is seen in these figures. The effects on aperture coupling are demonstrated in the next section.

### 5.3 Internal Coupling

#### 5.3.1 Background

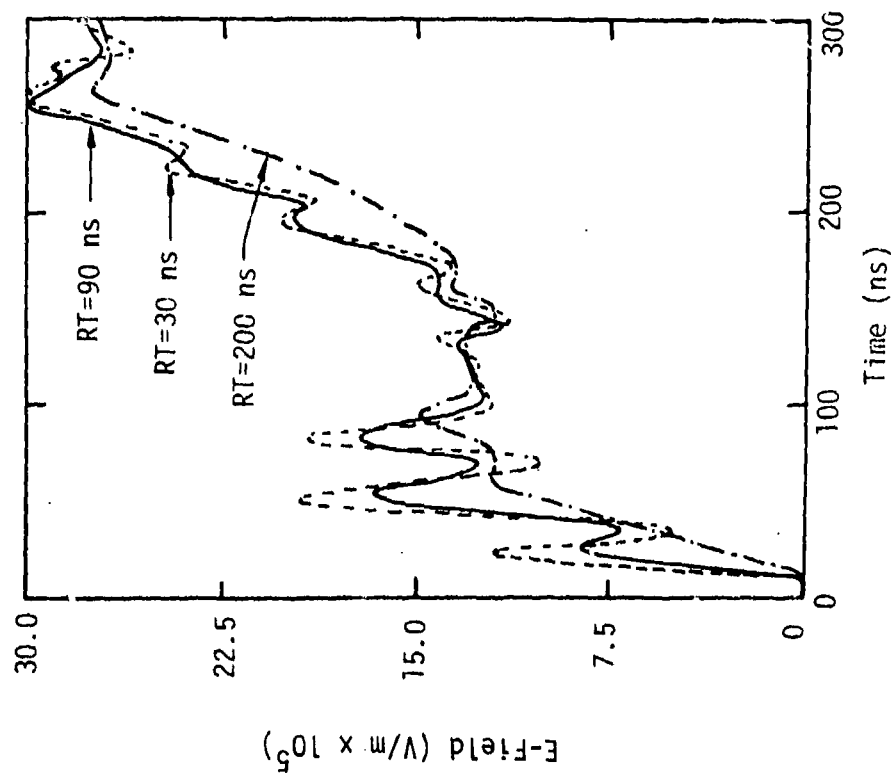
The internal coupling model consists of an executive code, EXEC, a propagation code, PROP, and a code which solves Laplace's equation, CAPCODE. EXEC uses operator supplied data to generate files which contain the necessary geometric, electrical, and source information to define the cable network. CAPMAT computes the capacitance matrices for multiconductor cables. PROP reads these files and also the data files generated by the external coupling codes to perform the calculations which determine propagation of voltages and currents along the network. To do this PROP uses subroutines associated with the various source types. These subroutines include DIFFUS, SEAM, SLOT, APERT, and WNGWIR. The type of source each deals with is evident by the names. The Laplace's equation solver, CAPCODE, takes operator supplied data of wing and wing cable cross-sections to calculate the coupling between wing surface currents and wing cables. CAPCODE's output is to the data files which EXEC initially creates.

The logical flow of the internal coupling model is shown in Figure 5.15.

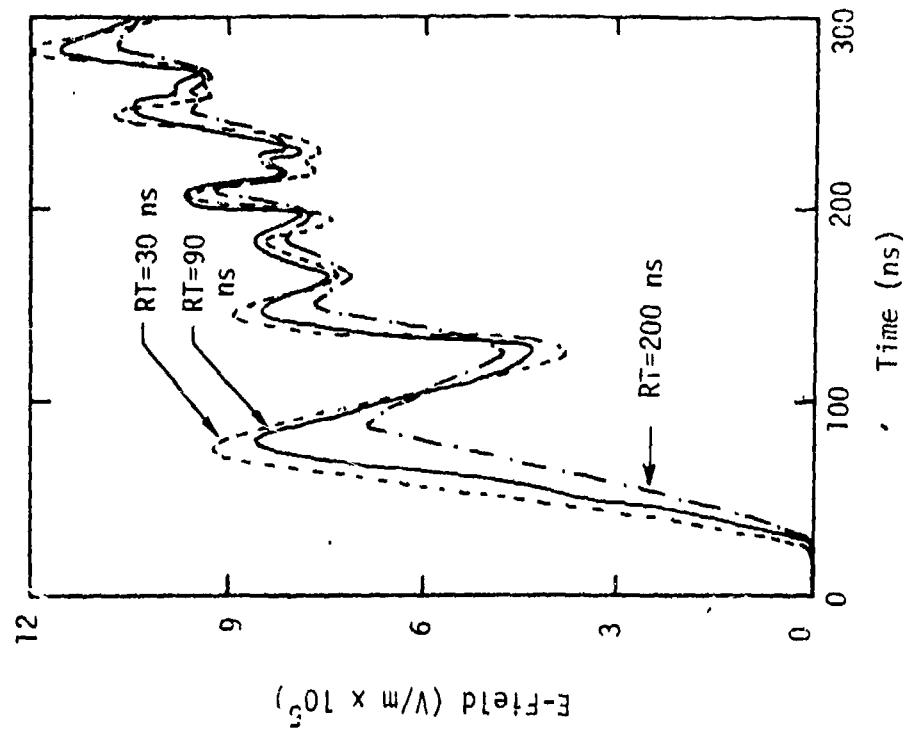
#### 5.3.2 Apertures

The problem of choosing an aperture model is similar to that of selecting an external coupling model. There simply is not a model that has all of the desirable features. Again, the main tradeoff is between having a relatively accurate complex approach or an inaccurate simple approach. As in the external coupling case, two approaches are selected.

The first approach involves the use of the uniqueness theorem and the finite difference approach as discussed in Section 4.1. This approach is complex and does not lend itself to be a readily user oriented approach. That is, a



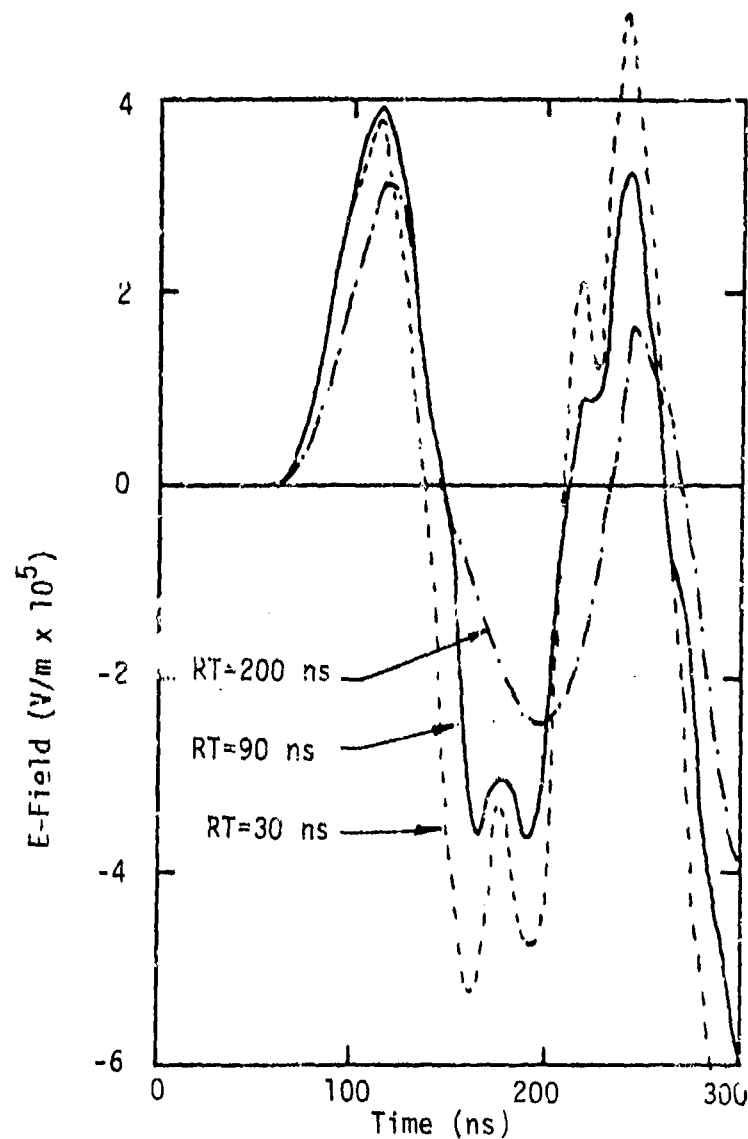
(a) E-Field at Test Point 1



(b) E-Field at Test Point 2

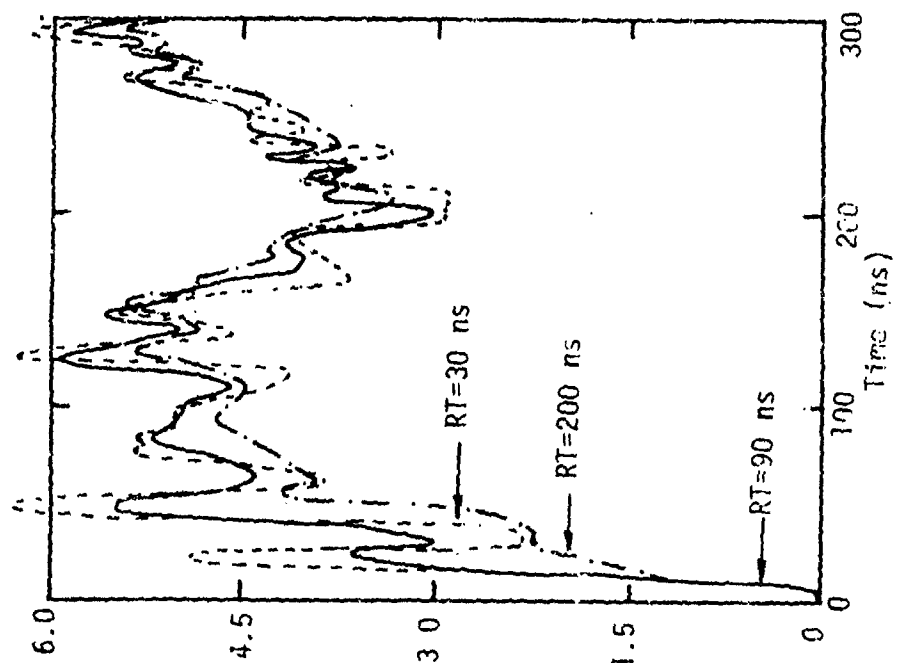
Figure 5.13 Comparison of Electric Field Response for Different Risetimes



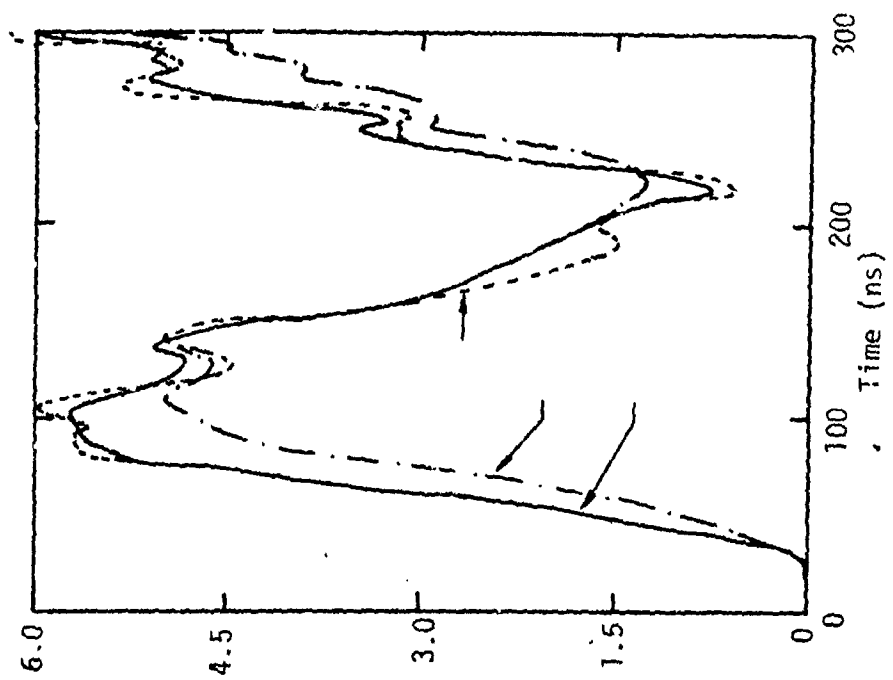


(c) E-Field at Test Point 3

Figure 5.13 (cont'd) Comparison of Electric Field Response for Different Risetimes

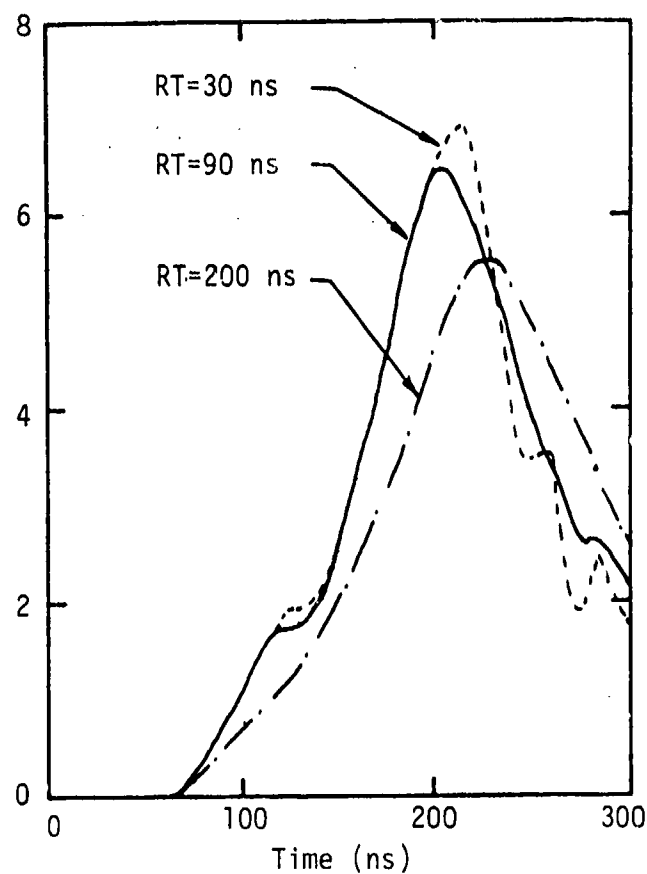


(a) H-Field at Test Point 1



(b) H-Field at Test Point 2

Figure 5.14 Comparison of Magnetic Field Response for Different Risetimes



(c) H-Field at Test Point 3

Figure 5.14 (cont'd) Comparison of Magnetic Field Response at Different Risetimes

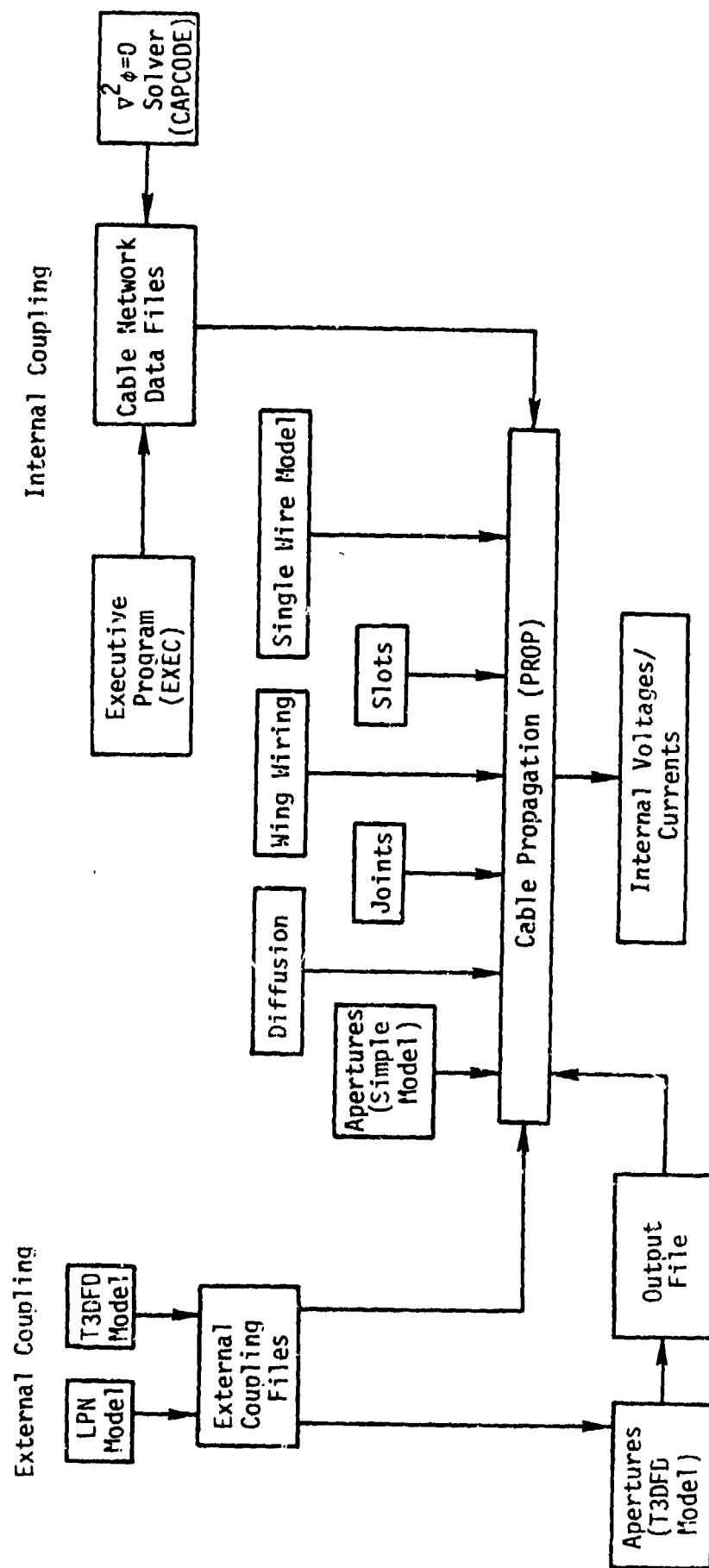


Figure 5.15 Coupling Model Architecture

universal code that can cover all cases of interest without sophisticated modifications cannot yet really be developed. The basic structure of the finite difference equations can be provided, but the user has to implement the boundary conditions and determine the size of his problem space for the aperture.

The other approach is much simpler, but does not accurately represent the problem geometry. This approach assumes the presence of a line conductor near a single aperture. The line conductor and the conducting sheet containing the aperture form a transmission line. For an electrically small aperture the effect of the aperture on the transmission line model can be represented by an equivalent circuit. Figure 5.16 shows the physical geometry and the equivalent circuit. The sources can be written,

$$\begin{aligned} V_{eq} &= \frac{\partial}{\partial t} \mu_0 \frac{h}{\pi R_0^2} \hat{e}_x \cdot \vec{\alpha}_m \cdot \vec{H}_{sc} \\ I_{eq} &= \frac{\partial}{\partial t} \epsilon_0 \frac{h}{\pi R_0^2} \frac{\alpha_e Z_0}{Z_c} E_{sc} \end{aligned} \quad (5.3.2.1)$$

The inductance and capacitance of the aperture are given by,

$$\begin{aligned} L_a &= \mu_0 \alpha_{m,xx} \frac{h}{\pi R_0^2} \\ C_a &= -\mu_0 \frac{\alpha_e}{Z_c^2} \frac{h}{\pi R_0^2} \end{aligned} \quad (5.3.2.2)$$

In the above equations,  $Z_c$  is the characteristic impedance of the transmission line and  $Z_0$  the free space impedance.  $\alpha_m$  and  $\alpha_e$  are the magnetic and electric aperture polarizabilities, examples of which are shown in Table 5.2. The tensor product in the equation for  $V_{eq}$  is simply a geometric factor combining the orientations of wire, aperture, and surface current to reduce the voltage source to the appropriate value.

The lumped circuit elements  $L_a$  and  $C_a$  are neglected in the model used by the propagation code, as they produce only minor perturbations in the lumped transmission line elements.

An example calculation has been done by employing the uniqueness theorem to solve for a cable response inside a C-130 aircraft struck by lightning.

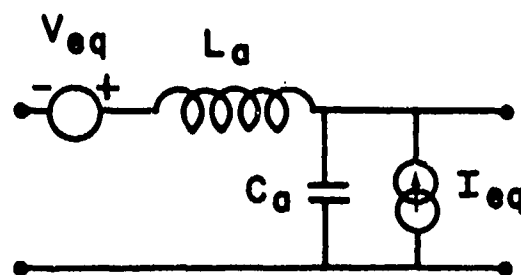
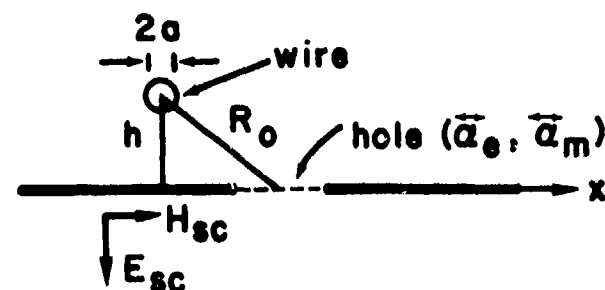


Figure 5.16 Equivalent Circuit of a Small Hole ( $R_0 \gg$  Hole's Dimensions) [109]

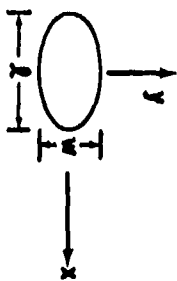
The analytical procedure followed consists of three main steps. The first step is to short the aperture and solve for the fields external to the structure. This is done with a finite difference code using a rather coarse gridding. At each time step of the finite difference code the fields on a surface surrounding the eventual position of the aperture are stored. These stored fields are necessary to determine boundary conditions when the aperture is opened.

The second step is to shrink the gridding down to a size that is compatible with adequate modeling of the aperture. Hence it should be fine enough that several grid points fall within the now open aperture. The stored fields from step one serve as boundary conditions for the finer grid. Shrinking the grid introduced two problems. The first is that the finer grid has more points on its boundary than the coarse grid that was stored, so it is necessary to interpolate for the additional points. Secondly, the finer gridding usually

Table 5.2 Aperture Polarizabilities [109]

Shape	$\alpha_{e,zz}$	$\alpha_{m,xx}$	$\alpha_{m,yy}$
Circle (d = Diameter)	$\frac{1}{12} d^3$	$\frac{1}{6} d^3$	$\frac{1}{6} d^3$
Ellipse *	$\frac{\pi}{24} \frac{w^2 l}{E(m)}$	$\frac{\pi}{24} \frac{l^3 m}{K(m) - E(m)}$	$\frac{\pi}{24} \frac{l^3 m}{(l/w)^2 E(m) - K(m)}$
Narrow Ellipse ( $w \ll l$ )	$\frac{\pi}{24} w^2 l$	$\frac{\pi}{24} \frac{l^3}{\ln(4l/w) - 1}$	$\frac{\pi}{24} w^2 l$
Narrow Slit ( $w \ll l$ )	$\frac{\pi}{16} w^2 l$	$\frac{\pi}{24} \frac{l^3}{\ln(4l/w) - 1}$	$\frac{\pi}{16} w^2 l$

\* Ellipse eccentricity  $e = \sqrt{1 - (w/l)^2}$ ,



K and E are the complete elliptic integrals of the first and second kind,  $m = e^2$ .

demands a smaller time step in the finite difference process, thus interpolation between stored time steps is necessary.

The third step in the analytic procedure is to again solve for the fields inside the cavity in a finite difference fashion using the finer grid and the stored, interpolated boundary conditions. The uniqueness theorem implies that the internal fields are correct, assuming that the presence of the aperture does not significantly affect the boundary fields. This approximation should be valid if the boundary is kept far from the aperture.

In theory the procedure just described is easy to follow. Practically, however, there are difficulties, the largest of which concerns the shrinking of the finite difference grid. Because of boundary condition considerations, external codes are written using tangential magnetic fields on the boundaries as shown in Figure 5.17. The code which solves for the internal fields in step three above is written most conveniently in terms of tangential electric field boundary conditions, since these are zero on the metal walls. This method for solving Maxwell's equations is shown in Figure 5.18. The transformation from Figure 5.17 to Figure 5.18 involves a shifting of one-half a spatial cell size in each of the orthogonal directions. This introduces a difficulty in determining exactly where the boundaries and the metallic structure are positioned, and in making sure all edges mesh together correctly.

The example presented here is that of the cockpit of a C-130 aircraft. The code used to solve for the external fields was T3DFDB which is essentially the external code T3DFD with a patch to store the needed boundary fields. A listing of T3DFDB is given in Appendix A of Reference 3. The boundary chosen for the example is shown in Figure 5.19. The aperture used, the cockpit window, is the patched area in the figure. The code EXPAND, also listed in Appendix A of Reference 3, was used to interpolate the boundary fields in time. The resulting data file containing the boundary fields at each time step contained approximately 300  $k_{10}$  words; clearly storage requirements for this method are somewhat extensive. The interior code COCKPIT, also given in Appendix A of Reference 3, was used to solve for fields at various points inside the cockpit. COCKPIT also incorporates a cable bundle two inches in diameter running vertically in the cockpit approximately 1.3 meters behind the window. Matching resistances were placed on the ends, and the voltage and current at the top end of the wire were calculated.



Assumptions: None

Maxwell's Equations

$$-\mu \frac{\partial H_x}{\partial t} = \left( \frac{\partial E_z}{\partial y} - \frac{\partial E_y}{\partial z} \right)$$

$$H_x^n(1,j,k) = H_x(x_0(1), y_0(j), z_0(k), t_H(n))$$

$$-\mu \frac{\partial H_y}{\partial t} = \left( \frac{\partial E_x}{\partial z} - \frac{\partial E_z}{\partial x} \right)$$

$$H_y^n(1,j,k) = H_y(x_0(1), y_0(j), z_0(k), t_H(n))$$

$$-\mu \frac{\partial H_z}{\partial t} = \left( \frac{\partial E_y}{\partial x} - \frac{\partial E_x}{\partial y} \right)$$

$$H_z^n(1,j,k) = H_z(x_0(1), y_0(j), z_0(k), t_H(n))$$

$$\epsilon \frac{\partial E_x}{\partial t} + \sigma E_x = \left( \frac{\partial H_z}{\partial y} - \frac{\partial H_y}{\partial z} \right) - J_x$$

$$E_x^n(1,j,k) = E_x(x_0(1), y_0(j), z_0(k), t_E(n))$$

$$\epsilon \frac{\partial E_y}{\partial t} + \sigma E_y = \left( \frac{\partial H_x}{\partial z} - \frac{\partial H_z}{\partial x} \right) - J_y$$

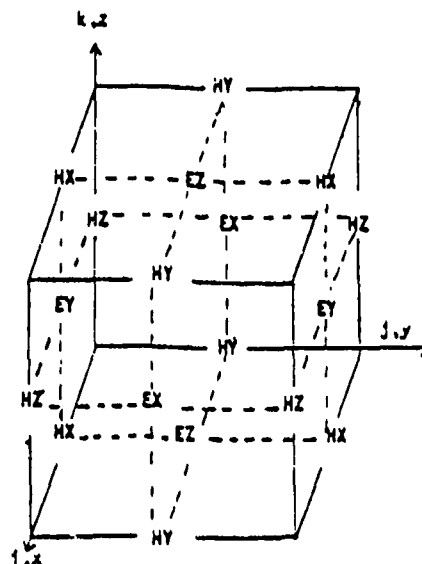
$$E_y^n(1,j,k) = E_y(x_0(1), y_0(j), z_0(k), t_E(n))$$

$$\epsilon \frac{\partial E_z}{\partial t} + \sigma E_z = \left( \frac{\partial H_y}{\partial x} - \frac{\partial H_x}{\partial y} \right) - J_z$$

$$E_z^n(1,j,k) = E_z(x_0(1), y_0(j), z_0(k), t_E(n))$$

$$x_0(1) = (1-1)\Delta x, y_0(j) = (j-1)\Delta y, z_0(k) = (k-1)\Delta z, t_H(n) = (n-1)\Delta t$$

$$x(1) = 1/2\Delta x, y(j) = (j-1/2)\Delta y, z(j) = (k-1/2)\Delta z, t_E(n) = (n-1/2)\Delta t$$



Finite Difference Equations (non-uniform grid allowed)

$$H_x^{n+1}(1,j+1,k+1) = H_x^n(1,j+1,k+1) - \frac{\Delta t}{\mu} \left( \frac{E_z^n(1,j+1,k+1) - E_z^n(1,j,k+1)}{y(j+1) - y(j)} \right) + \frac{\Delta t}{\mu} \left( \frac{E_y^n(1,j+1,k+1) - E_y^n(1,j+1,k)}{z(k+1) - z(k)} \right)$$

$$H_y^{n+1}(1+1,j,k+1) = H_y^n(1+1,j,k+1) - \frac{\Delta t}{\mu} \left( \frac{E_x^n(1+1,j,k+1) - E_x^n(1+1,j,k)}{z(k+1) - z(k)} \right) + \frac{\Delta t}{\mu} \left( \frac{E_z^n(1+1,j,k+1) - E_z^n(1,j,k+1)}{x(1+1) - x(1)} \right)$$

$$H_z^{n+1}(1+1,j+1,k) = H_z^n(1+1,j+1,k) - \frac{\Delta t}{\mu} \left( \frac{E_y^n(1+1,j+1,k) - E_y^n(1,j+1,k)}{x(1+1) - x(1)} \right) + \frac{\Delta t}{\mu} \left( \frac{E_x^n(1+1,j+1,k) - E_x^n(1+1,j,k)}{y(j+1) - y(j)} \right)$$

$$B \cdot E_x^{n+1}(1,j,k) = A \cdot E_x^n(1,j,k) - J_x + \left( \frac{H_z^{n+1}(1,j+1,k) - H_z^{n+1}(1,j,k)}{y_0(j+1) - y_0(j)} \right) - \left( \frac{H_y^{n+1}(1,j,k+1) - H_y^{n+1}(1,j,k)}{z_0(k+1) - z_0(k)} \right)$$

$$B \cdot E_y^{n+1}(1,j,k) = A \cdot E_y^n(1,j,k) - J_y + \left( \frac{H_x^{n+1}(1,j,k+1) - H_x^{n+1}(1,j,k)}{z_0(k+1) - z_0(k)} \right) - \left( \frac{H_z^{n+1}(1+1,j,k) - H_z^{n+1}(1,j,k)}{x_0(1+1) - x_0(1)} \right)$$

$$B \cdot E_z^{n+1}(1,j,k) = A \cdot E_z^n(1,j,k) - J_z + \left( \frac{H_y^{n+1}(1+1,j,k) - H_y^{n+1}(1,j,k)}{x_0(1+1) - x_0(1)} \right) - \left( \frac{H_x^{n+1}(1,j+1,k) - H_x^{n+1}(1,j,k)}{y_0(j+1) - y_0(j)} \right)$$

$$\text{where } A = \left( \frac{\epsilon}{\Delta t} - \frac{\sigma}{2} \right), B = \left( \frac{\epsilon}{\Delta t} + \frac{\sigma}{2} \right), J_x = J_x(t_H(n+1)), J_y = J_y(t_H(n+1)), J_z = J_z(t_H(n+1))$$

all evaluated at desired E component location

Externally supplied values are tangential electric fields on outer surface of problem space:

$$H_x^n(1,j,1), H_y^n(1,j,1), H_x^n(1,j,k_{can}+1), H_y^n(1,j,k_{can}-1) \quad \text{all } 1 \leq j \leq j_{can}, 1 \leq k \leq k_{can}$$

$$H_x^n(1,1,k), H_y^n(1,1,k), H_x^n(1,j_{can}+1,k), H_y^n(1,j_{can}-1,k) \quad \text{all } 1 \leq j \leq j_{can}, 1 \leq k \leq k_{can}$$

$$H_y^n(1,j,k), H_z^n(1,j,k), H_y^n(1,j_{can}+1,k), H_z^n(1,j_{can}-1,k) \quad \text{all } 1 \leq j \leq j_{can}, 1 \leq k \leq k_{can}$$

Figure 5.17 3-D Finite Difference Equations in Rectangular Coordinates Set Up with Externally Supplied H Fields [17]

### Maxwell's Equations

$$-\mu \frac{\partial H_x}{\partial t} = \left( \frac{\partial E_z}{\partial y} - \frac{\partial E_y}{\partial z} \right)$$

$$-\mu \frac{\partial H_y}{\partial t} = \left( \frac{\partial E_x}{\partial z} - \frac{\partial E_z}{\partial x} \right)$$

$$-\mu \frac{\partial H_z}{\partial t} = \left( \frac{\partial E_y}{\partial x} - \frac{\partial E_x}{\partial y} \right)$$

$$c \frac{\partial E_x}{\partial t} + \sigma E_x = \left( \frac{\partial H_z}{\partial y} - \frac{\partial H_y}{\partial z} \right) - j_x$$

$$c \frac{\partial E_y}{\partial t} + \sigma E_y = \left( \frac{\partial H_x}{\partial z} - \frac{\partial H_z}{\partial x} \right) - j_y$$

$$c \frac{\partial E_z}{\partial t} + \sigma E_z = \left( \frac{\partial H_y}{\partial x} - \frac{\partial H_x}{\partial y} \right) - j_z$$

$$H_x^n(i, j, k) = H_x(x_0(i), y_0(j), z_0(k), t_H(n))$$

$$H_y^n(i, j, k) = H_y(x_0(i), y_0(j), z_0(k), t_H(n))$$

$$H_z^n(i, j, k) = H_z(x_0(i), y_0(j), z_0(k), t_H(n))$$

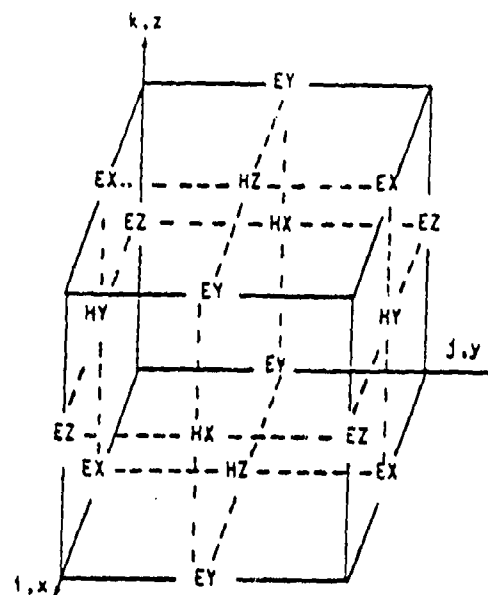
$$E_x^n(i, j, k) = E_x(x_0(i), y_0(j), z_0(k), t_E(n))$$

$$E_y^n(i, j, k) = E_y(x_0(i), y_0(j), z_0(k), t_E(n))$$

$$E_z^n(i, j, k) = E_z(x_0(i), y_0(j), z_0(k), t_E(n))$$

$$x_0(i) = (i-1)\Delta x, y_0(j) = (j-1)\Delta y, z_0(k) = (k-1)\Delta z, t_H(n) = (n-1)\Delta t$$

$$x(i) = (i-1/2)\Delta x, y(j) = (j-1/2)\Delta y, z(k) = (k-1/2)\Delta z, t_E(n) = (n-1/2)\Delta t$$



### Finite Difference Equations (non-uniform grid allowed)

$$H_x^{n+1}(i, j, k) = H_x^n(i, j, k) - \frac{\Delta t}{\mu} \left( \frac{E_z^n(i, j+1, k) - E_z^n(i, j, k)}{y_0(j+1) - y_0(j)} \right) + \frac{\Delta t}{\mu} \left( \frac{E_y^n(i, j, k+1) - E_y^n(i, j, k)}{z_0(k+1) - z_0(k)} \right)$$

$$H_y^{n+1}(i, j, k) = H_y^n(i, j, k) - \frac{\Delta t}{\mu} \left( \frac{E_x^n(i, j, k+1) - E_x^n(i, j, k)}{z_0(k+1) - z_0(k)} \right) + \frac{\Delta t}{\mu} \left( \frac{E_z^n(i+1, j, k) - E_z^n(i, j, k)}{x_0(i+1) - x_0(i)} \right)$$

$$H_z^{n+1}(i, j, k) = H_z^n(i, j, k) - \frac{\Delta t}{\mu} \left( \frac{E_y^n(i+1, j, k) - E_y^n(i, j, k)}{x_0(i+1) - x_0(i)} \right) + \frac{\Delta t}{\mu} \left( \frac{E_x^n(i, j+1, k) - E_x^n(i, j, k)}{y_0(j+1) - y_0(j)} \right)$$

$$B \cdot E_x^{n+1}(i, j+1, k+1) = A \cdot E_x^n(i, j+1, k+1) - j_x + \left( \frac{H_z^{n+1}(i, j+1, k+1) - H_z^{n+1}(i, j, k+1)}{y(j+1) - y(j)} \right) - \left( \frac{H_y^{n+1}(i, j+1, k+1) - H_y^{n+1}(i, j+1, k)}{z(k+1) - z(k)} \right)$$

$$B \cdot E_y^{n+1}(i+1, j, k+1) = A \cdot E_y^n(i+1, j, k+1) - j_y + \left( \frac{H_x^{n+1}(i+1, j, k+1) - H_x^{n+1}(i+1, j, k)}{z(k+1) - z(k)} \right) - \left( \frac{H_z^{n+1}(i+1, j, k+1) - H_z^{n+1}(i, j, k+1)}{x(i+1) - x(i)} \right)$$

$$B \cdot E_z^{n+1}(i+1, j+1, k) = A \cdot E_z^n(i+1, j+1, k) - j_z + \left( \frac{H_y^{n+1}(i+1, j+1, k) - H_y^{n+1}(i, j+1, k)}{x(i+1) - x(i)} \right) - \left( \frac{H_x^{n+1}(i+1, j+1, k) - H_x^{n+1}(i+1, j, k)}{y(j+1) - y(j)} \right)$$

where

$$A = \left( \frac{c}{\Delta t} - \frac{\sigma}{2} \right), B = \left( \frac{c}{\Delta t} + \frac{\sigma}{2} \right), j_x = j_x(t_H(n+1)), j_y = j_y(t_H(n+1)), j_z = j_z(t_H(n+1))$$

all evaluated at desired E component location

Externally supplied values are tangential electric fields on outer surface of problem space:

$$E_x^n(i, j, 1), E_y^n(i, j, 1), E_x^n(i, j, k_{can}+1), E_y^n(i, j, k_{can}+1) \quad \text{all } i \in [1, i_{can}], j \in [1, j_{can}]$$

$$E_x^n(1, 1, k), E_y^n(1, 1, k), E_x^n(1, j_{can}+1, k), E_y^n(1, j_{can}+1, k) \quad \text{all } i \in [1, i_{can}], k \in [1, k_{can}]$$

$$E_x^n(1, j, k), E_y^n(1, j, k), E_x^n(i_{can}+1, j, k), E_y^n(i_{can}+1, j, k) \quad \text{all } j \in [1, j_{can}], k \in [1, k_{can}]$$

Figure 5.18 3-D Finite Difference Equations in Rectangular Coordinates Set Up with Externally Supplied E Fields [17]

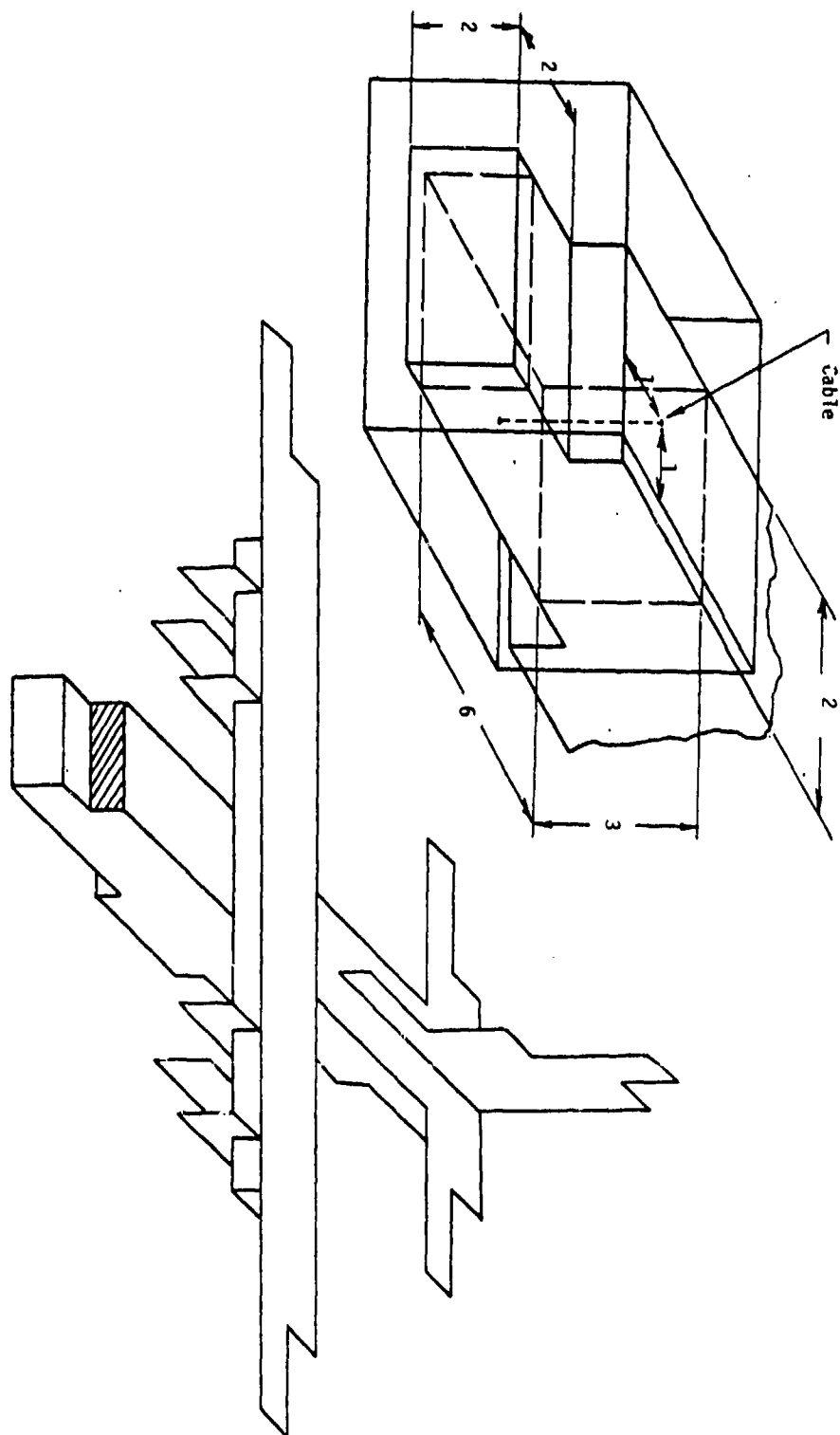


Figure 5.19 Geometry for Cockpit Aperture Example  
(Dimensions in Meters)

The example was run for three lightning current wave shapes, all current injected at the nose of the aircraft, exiting the tail, and of peak magnitude 53 kA. The three wave shapes had rise times of 30, 90, and 200 nsec. It was expected that the largest response would be seen inside the cockpit for the 30 nsec pulse because its high frequency components should most easily penetrate the aperture. This proved to be the case, as Figures 5.20 and 5.21 illustrate. These figures show the voltage and current at the top end of the wire described previously. It should also be noted that the source rise time affects both the amplitude and the wave shape. Inspection of the responses shows cycle times which can be related to the cavity dimensions shown in Figure 5.19. It is also evident that there are modal interference patterns in the response, which may tend to obscure individual modal frequencies.

### 5.3.3 Seams and Joints

The interior cable propagation code uses a very simple model for seams. The transfer impedance of the seam,  $Z_T$ , is an operator defined quantity which is then combined with the calculated external current density to produce an internal voltage drop across the seam:

$$V_{int} = Z_T J_{ext} \quad (5.3.3.1)$$

$$Z_T = R + j\omega L. \quad (5.3.3.2)$$

Here,  $R$  is the resistive part of  $Z_T$  in ohm-m, and  $L$  the inductive part in henry-m. In the time domain, the voltage becomes

$$V_{int}(t) = RJ_{ext}(t) + L \frac{\partial}{\partial t} J_{ext}(t). \quad (5.3.3.3)$$

The model assumes that an interior cable is running near the seam, so  $V_{int}(t)$  is transformed to an electric field and acts on the cable as a driving source. The transformation of  $V_{int}(t)$  is accomplished by assuming that this voltage acts uniformly on the nearest spatial element of the finite-differenced interior cable. Hence the electric field affecting that element is given by

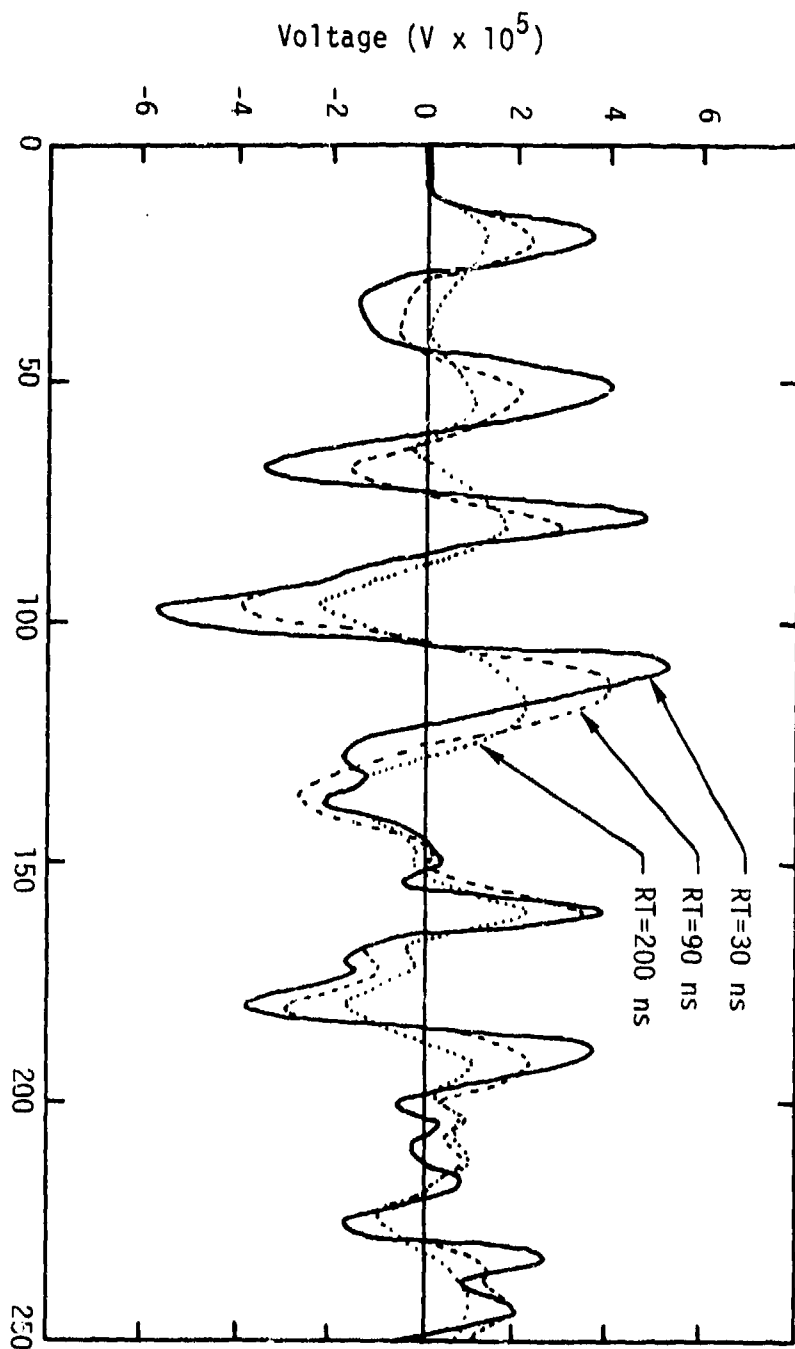


Figure 5.20 Voltage on Wire Inside Cockpit as a Function of Stroke Risettime

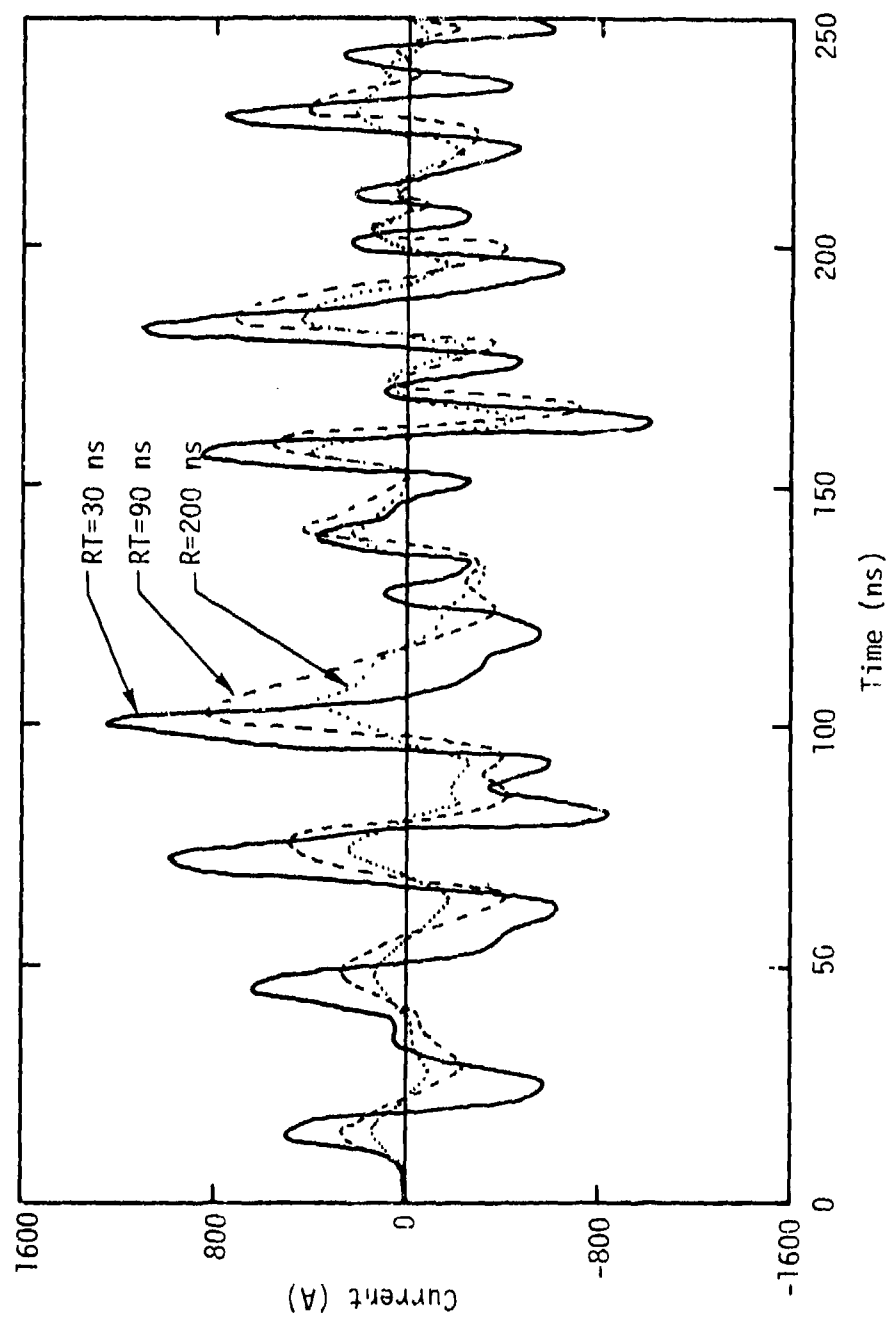


Figure 5.21 Current on Wire Inside Cockpit as a Function of Stroke Risetime

$$E_{int}(t) = V_{int}(t)/\Delta X, \quad (5.3.3.4)$$

where  $\Delta X$  is the length in meters of the spatial element. This electric field is assumed to be tangential to the cable and is the seam source that is used by the transmission line equations.

#### 5.3.4 Cracks and Slots

The slot model used by the internal propagation code is described in detail in Section 4.3.

The user defines the slot width and height in meters. The code calculates the fatness parameter given by

$$\Omega = 2\pi \frac{8h}{w},$$

where  $h$  is the slot height, and  $w$  its width. The code then calculates the slot inductance using the formula,

$$L_{slot}(\text{henries}) = \frac{1.97 \times 10^{-6} h (\text{meters})}{\Omega - 3.39}$$

The internal field implied by the voltage drop across the slot is then calculated from

$$E_{int} = 2hL_{slot} \frac{\partial J_{ext}}{\partial t} \frac{1}{\Delta X},$$

where  $J_{ext}$  is the external current density read from the external coupling file, and  $\Delta X$  is the length in meters of the spatial cell of the internal cable. This electric field is then used as a source for one spatial cell in the transmission line equations. The cable is assumed to run directly behind the slot, and the slot field acts uniformly on the spatial cell nearest the slot and not on any other spatial cells.

#### 5.3.5 Diffusion

The diffusion model used by the internal propagation code assumes a locally plane shield of conductivity  $\sigma$  and thickness  $d$ . The subroutine DIFFUS uses these parameters as input data along with the current density on the shield and calculates the induced electric field on the interior of the shield. This electric field is then used as a source to drive the internal cables which run behind the shield.

The basis for the model is the transfer impedance for a planar shield. In the frequency domain this transfer impedance has the form,

$$Z_T(\omega) = \frac{K_m / \sigma_m}{\sin K_m d} \quad (5.3.5.1)$$

where  $K_m$  is the propagation constant in the shield,  $\sigma_m$  the shield's conductivity, and  $d$  its thickness. The first step is to transform  $Z_T(\omega)$  into the time domain. Equation (5.3.5.1) is not in a convenient form to do this, so it needs to be rewritten. The sine can be written in infinite product form to give

$$Z_T(\omega) = \frac{R_0}{\prod_{n=1}^{\infty} (1 + j\omega/\omega_n)} = \sum_{n=1}^{\infty} \frac{A_n}{1 + j\omega/\omega_n}, \quad (5.3.5.2)$$

where  $\omega_n = \frac{n^2 \pi^2}{\tau}$ ,  $\tau = d^2 \mu \sigma_m$ , and  $\mu$  is the permeability. The  $A_n$ 's are determined by allowing  $\omega$  to approach  $j\omega_n$ .

This results in

$$A_n = 2(-1)^{n+1} R_0 \quad (5.3.5.3)$$

The  $Z_T(\omega)$  can be written

$$Z_T(\omega) = 2R_0 \sum_{n=1}^{\infty} \frac{(-1)^{n+1}}{1 + j\omega/\omega_n} \quad (5.3.5.4)$$

The electric field response on the inside of the shield is, from the definition of transfer impedance,

$$E(\omega) = Z_T(\omega) J_s(\omega) = \sum_{n=1}^{\infty} \frac{2R_0 (-1)^{n+1}}{1 + j\omega/\omega_n} J_s(\omega) \quad (5.3.5.5)$$

Now artificially split  $E(\omega)$  into separate terms, with each term corresponding to a given  $n$ . This allows equation (5.3.5.5) to be rewritten:

$$E(\omega) = \sum_{n=1}^{\infty} E_n(\omega) = \sum_{n=1}^{\infty} \frac{2R_0 (-1)^{n+1}}{1 + j\omega/\omega_n} J_s(\omega) \quad (5.3.5.6)$$



Then equating terms of equal index,

$$E_n(\omega) = \frac{2R_0(-1)^{n+1}}{1+j\omega/\omega_n} J_s(\omega), \quad (5.3.5.7)$$

or,

$$(1+j\omega/\omega_n) E_n(\omega) = 2R_0(-1)^{n+1} J_s(\omega), \quad (5.3.5.8)$$

Equation (5.3.5.8) is finally in an appropriate form to transform to time domain. Recognizing that  $j\omega$  transforms to  $\frac{\partial}{\partial t}$ , (5.3.5.8) becomes

$$\frac{1}{\omega_n} \frac{\partial}{\partial t} E_n(t) + E_n(t) = 2R_0(-1)^{n+1} J_s(t) \quad (5.3.5.9)$$

This is a first order linear differential equation and is therefore readily integrable.

$$E_n(t) = e^{-\int_0^t \omega_n dt'} \left[ E_n(0) + \int_0^t 2\omega_n R_0(-1)^{n+1} J_s(t') e^{\int_0^{t'} \omega_n dt''} dt' \right] \quad (5.3.5.10)$$

Assuming  $E_n(0) = 0$ ,

$$E_n(t) = 2\omega_n R_0(-1)^{n+1} \int_0^t J_s(t') e^{-\omega_n(t-t')} dt'. \quad (5.3.5.10)$$

To find the total electric field the  $E_n$ 's are summed over all  $n$ .

$$E(t) = \sum_{n=1}^{\infty} E_n(t) = \sum_{n=1}^{\infty} 2\omega_n R_0(-1)^{n+1} \int_0^t J_s(t') e^{-\omega_n(t-t')} dt' \quad (5.3.5.11)$$

$$E(t) = 2\alpha R_0 \int_0^t J_s(t') \left[ \sum_{n=1}^{\infty} (-1)^{n+1} \alpha^2 e^{-\alpha n^2(t-t')} \right] dt' \quad (5.3.5.12)$$

In (5.3.5.12),  $\omega_n = \alpha n^2$ . The quantity in square brackets is simply a function of  $\alpha(t-t')$ , which can be relabelled  $f(t-t')$ .  $f$  has been evaluated numerically and tabulated by EMA. The subroutine DIFFUS deals with  $f$  by piece-wise approximating the tabulated values of  $f$ , which are internally stored.

It may be noted that the total electric field in the time domain is simply the convolution integral of the surface current density over the function  $f$ . A general property of the integral is that response of the interior

field lags behind the driving surface current density by some time  $\Delta t$ . This corresponds physically to the time necessary for the field to diffuse through the shield.

It should also be noted that the function  $f$  is not solely dependent on  $t-t'$ , but also on  $\alpha$ , which is a parameter depending on the properties

of the shield. Specifically,  $\alpha = \frac{\pi^2}{d^2 \mu_0 \sigma_m}$ , so the time lag mentioned above

depends strongly on the shield characteristics, as would be expected.

### 5.3.6 Radomes

Because of geometric complexity, it is probably not possible to accurately analyze a given particular conductor in a radome area. The only approach that appears useful is to try to obtain a typical or worst case response. In such an approach, the analyst would obtain the electric and magnetic fields in the radome region from the external coupling approach. This then could be combined with a simple small loop or monopole antenna model for a conductor in the radome region and currents and voltages can thus be estimated. This approach can be done by simple hand analysis, once the external coupling response has been determined.

### 5.3.7 Deliberate Antennas

Because of many different types of deliberate antennas which are deployed on aircraft it is not possible to incorporate such a myriad of models in the general coupling case. Specific models for several types of antennas are given in [109]. It is likely that an antenna other than that discussed there may require analysis. In that case, a specific model would have to be developed.

### 5.3.8 Wing Wiring

#### 5.3.8.1 Introduction

The calculation of coupling between currents flowing on aircraft wings and exposed wing wiring is done using CAPCODE, a computer code which numerically solves Laplace's equation for arbitrarily shaped two-dimensional

conductors. The input required by CAPCODE is the shape of the conductors, and its output includes the per-unit-length capacitance matrix, charge density distributions, and coupling parameters. These outputs are used by the internal propagation code PROP to calculate source terms for wires running along the wings.

#### 5.3.8.2 Theoretical Basis for CAPCODE

CAPCODE is a computer program which calculates the per-unit-length capacitance matrix for an arbitrary multiconductor transmission line. The code's main use is in determining the coupling between wing currents and exposed wing wiring. Another possible use is in the calculation of capacitance and inductance elements for lumped parameter network (LPN) modeling.

CAPCODE solves for the capacitance matrix of an arbitrary array of two dimensional conductors by numerically solving Laplace's equation in two dimensions. The discussion of analytical procedure follows that of Licking [145].

For a multiconductor transmission line of  $N+1$  conductors where the  $N+1$  th conductor is chosen as the reference conductor (ground), the elements of the per-unit-length capacitance matrix are defined as follows:

$C_{ii}$  = the per-unit-length self capacitance of the  $i$ 'th conductor and is numerically equal to the charge per unit length on the  $i$ 'th conductor when it is at one volt potential, and all other conductors are at zero potential with respect to the reference conductor.

$C_{ij}$  = the per-unit-length mutual capacitance between the  $i$ 'th and  $j$ 'th conductors and is numerically equal to the charge per unit length on the  $i$ 'th conductor when the  $j$ 'th conductor is at one volt potential, and the rest of the conductors are at zero potential with respect to the reference conductor.

The capacitance matrix elements are further constrained by the following:

$$C_{ii} \geq 0 \text{ for all } i$$

$$C_{ij} \leq 0 \text{ for all } i \neq j$$

$$\sum_{j=1}^N C_{ij} \geq 0 \text{ for all } i$$

The solution of Laplace's equation proceeds by assuming that each conductor boundary consists of a finite number of line charges and using Gauss' law to solve the resulting potential problem. From Gauss' law, the potential at an observation point  $(x_v, y_v)$  due to a line charge of density  $\rho_l$  at  $(x_o, y_o)$  (Figure 5.22) is,

$$\phi_v(x_v, y_v) = \frac{\rho_l}{4\pi\epsilon} \ln \frac{(x_o - x)^2 + (y_o - y)^2}{(x_v - x)^2 + (y_v - y)^2} \quad (5.3.8.1)$$

where  $\epsilon$  is the permittivity of the dielectric material and  $(x_o, y_o)$  is a point where the potential is zero.

Now consider a conductor of arbitrary cross-section, uniform along the conductor (Figure 5.23), with a surface charge density  $\rho(x, y)$  which is constant along the length of the line. Then the potential at the observation point is,

$$\phi_v(x_v, y_v) = \int_C \frac{\rho_s(x, y)}{4\pi\epsilon} \ln \frac{(x_o - x)^2 + (y_o - y)^2}{(x_v - x)^2 + (y_v - y)^2} dl \quad (5.3.8.2)$$

This is now a line integral around the closed contour  $C$  defined by the cross-section of the conductor. For a system of  $N+1$  conductors (Figure 5.24), the potential at the observation point becomes,

$$\phi_v(x_v, y_v) = \frac{1}{4\pi\epsilon} \sum_{i=1}^{N+1} \int_C \rho_i(x, y) \ln \frac{(x_o - x)^2 + (y_o - y)^2}{(x_v - x)^2 + (y_v - y)^2} dl \quad (5.3.8.3)$$

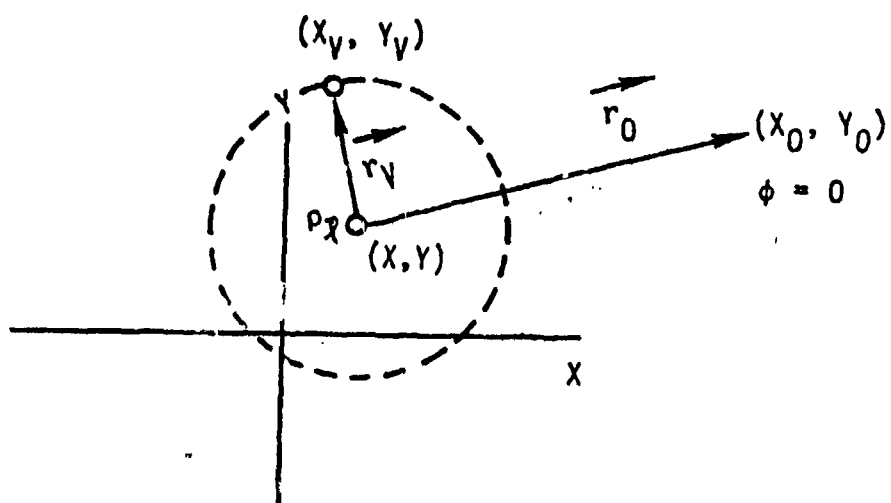


Figure 5.22 Geometry Near the Line Charge  $\rho_\ell$

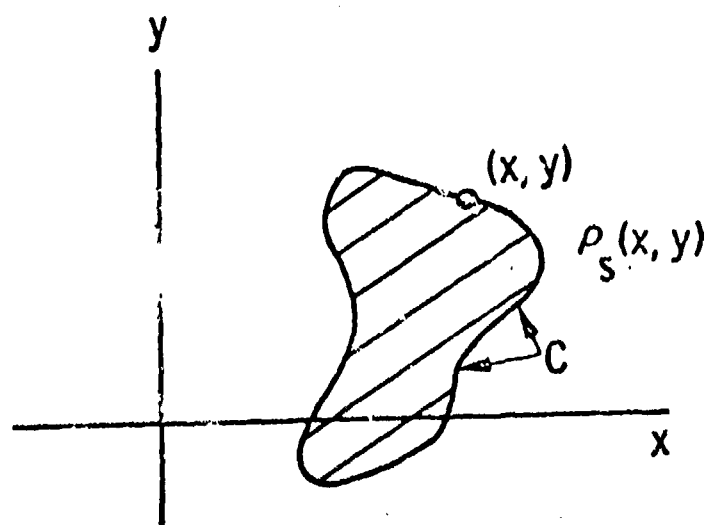


Figure 5.23 Cross-Section of a Conductor

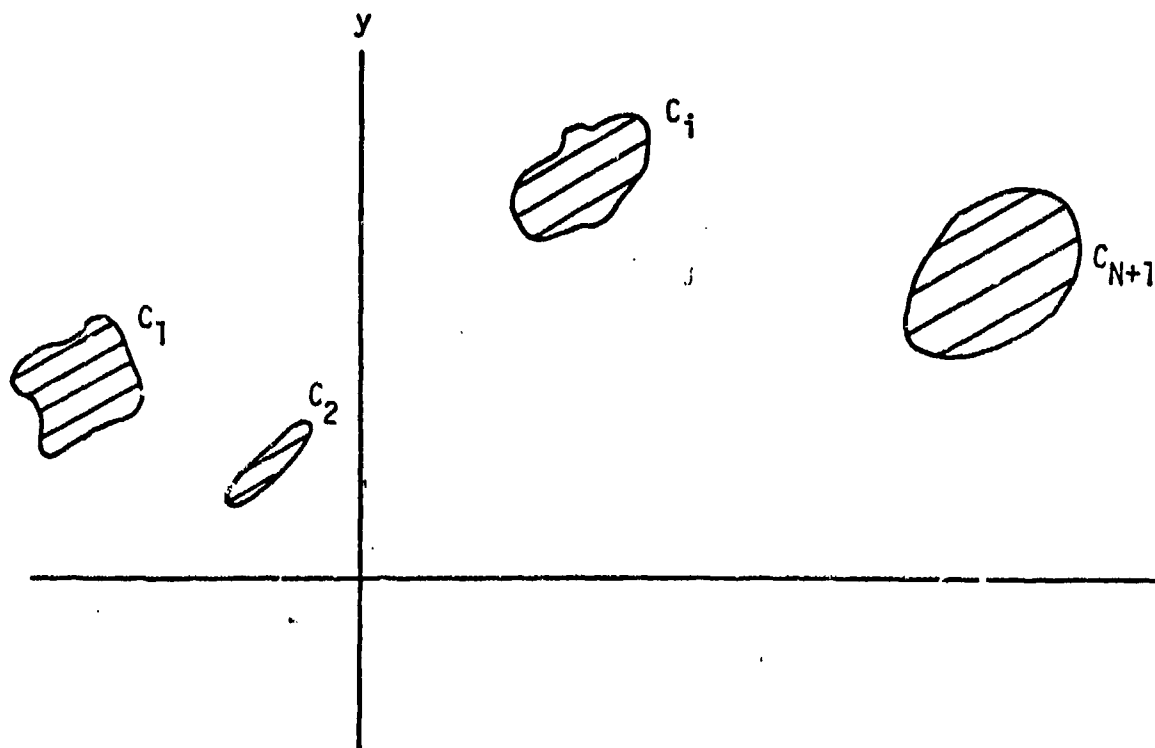


Figure 5.24 Cross-Section of  $N+1$  Conductors

If  $x_0$  and  $y_0$  are chosen such that  $x_0, y_0 \gg r_c$ , where  $r_c$  is the radius of a circle that encloses all the conductors, equation (5.3.8.3) can be simplified:

$$\begin{aligned} & \sum_{i=1}^{N+1} \int_{C_i} \rho_i(x, y) \ln \left[ (x_0 - x)^2 + (y_0 - y)^2 \right]^{1/2} d\mathbf{l} \\ & \approx \sum_{i=1}^{N+1} \int_{C_i} \rho_i(x, y) \ln(x_0^2 + y_0^2) d\mathbf{l} \end{aligned}$$

$$\begin{aligned}
&= \ln(x_0^2 + y_0^2) \sum_{i=1}^{N+1} \int_{C_i} \rho_i(x, y) dl \\
&= \ln(x_0^2 + y_0^2) \sum_{i=1}^{N+1} q_i
\end{aligned} \tag{5.3.8.4}$$

In (5.3.8.4)  $q_i$  is the total charge per unit length on the  $i$ 'th conductor. By requiring that the total charge of the system of conductors be zero, (5.3.8.3) simplifies to,

$$\phi_v(x_v, y_v) = -\frac{1}{4\pi\epsilon} \sum_{i=1}^{N+1} \int_{C_i} \rho_i(x, y) \ln[(x_v - x)^2 + (y_v - y)^2] dl \tag{5.3.8.5}$$

This equation is an integral equation for the unknown  $\rho_i(x, y)$ ,  $i = 1, 2, \dots, N+1$ . By placing the observation point on the surface of the  $k$ 'th conductor and observing that its potential is constant over its surface, a system of  $N+1$  integral equations can be written,

$$V_k = -\frac{1}{4\pi\epsilon} \sum_{i=1}^{N+1} \int_{C_i} \rho_i(x, y) \ln[(x_k - x)^2 + (y_k - y)^2] dl, \tag{5.3.8.6}$$

for  $k = 1, 2, \dots, N+1$

Here  $V_k$  is the constant potential of the  $k$ 'th conductor.

Capacitance calculations are done by dividing the  $N+1$  conductors into two groups and assigning a potential difference of one volt between the two groups (all conductors in a group are held at the same potential). To determine the capacitance matrix, one conductor at a time is raised to the one volt potential with all the rest being held at the reference potential.

To solve the system of integral equations (5.3.8.6) the following procedure is used. Focusing on the  $i$ 'th conductor, the contour  $C_i$  is broken into  $m_i$  subcontours (Figure 5.25) and  $\rho_i(x, y)$  is assumed to be uniform and equal to  $\rho_{iq}$  over the subinterval  $C_{iq}$  for  $q = 1, 2, \dots, m_i$ . By placing the observation point at  $(x_{kp}, y_{kp})$  in the  $q$ 'th subinterval of  $C_p$ , the following set of linear equations is obtained:

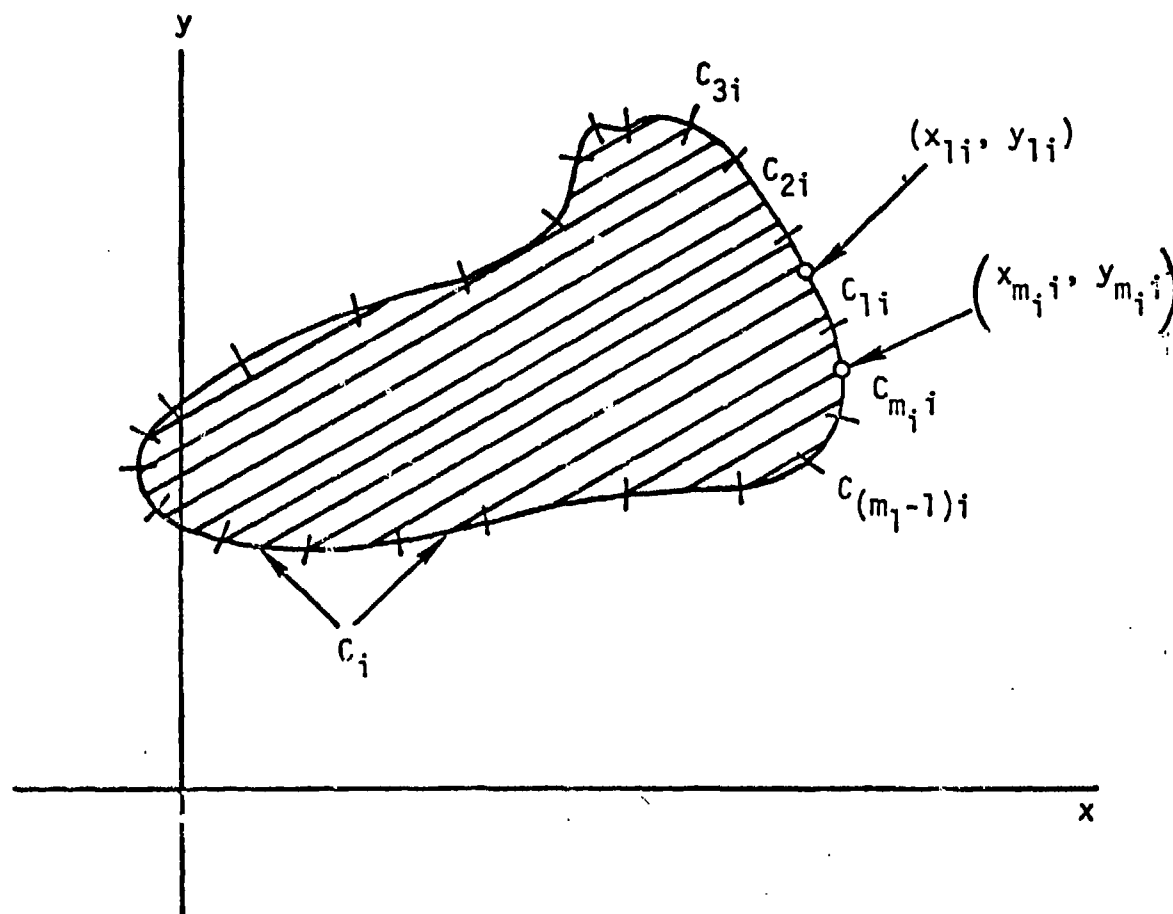


Figure 5.25 Subcontours of the Contour  $C_i$

$$-4\pi\epsilon V_{lp} = \sum_{i=1}^{N+1} \sum_{q=1}^{m_i} \rho_{qi} \int_{C_{qi}} \ln \left[ (x_{lp} - x)^2 + (y_{lp} - y)^2 \right] dl \quad (5.3.8.7)$$

$$p = 1, 2, 3, \dots, N+1$$

$$l = 1, 2, 3, \dots, m_p$$

$$0 = \sum_{i=1}^{N+1} \sum_{q=1}^{m_i} \rho_{qi} \int_{C_{qi}} dl$$

$$V_{11} = V_{21} = \dots = V_{m_1 1} = \dots = V_{ij} = \dots = V_{m_j j} = V_1$$

$$V_{1(j+1)} = V_{2(j+1)} = \dots = V_{m_{j+1}(j+1)} = \dots =$$

$$V_{1n} = V_{m_{N+1} N+1} = V_2$$

$$1 = V_1 - V_2$$



The desired capacitance is given by

$$C = \sum_{i=1}^j \sum_{q=1}^{m_j} \rho_{qi} \int_{C_{qi}} d\ell \quad (5.3.8.8)$$

Define  $\gamma_{\ell p qi}$  by,

$$\gamma_{\ell p qi} \equiv \int_{C_{qi}} \ln \left[ (x_{\ell p} - x)^2 + (y_{\ell p} - y)^2 \right] d\ell \quad (5.3.8.9)$$

(5.3.8.7) can now be written as a matrix equation and is shown as (5.3.8.10) on the next page.

(5.3.8.10) is a set of simultaneous linear algebraic equations and is solved by the Gauss-Jordan elimination method. The solution of (5.3.8.10) gives the distribution of charge density on the conductors from which the desired capacitance can be calculated using (5.3.8.8).

The generalized conductor shapes are read into CAPCODE as a series of points and the shape reconstructed by drawing straight lines between the points. Because of this (5.3.8.9) for  $\gamma_{\ell p qi}$  can be performed analytically, since the line integral is done along a straight line. If the line integral is done between points  $(x_1, y_1)$  and  $(x_2, y_2)$ , and the line is represented by  $y = ax + b$ ,  $\gamma$  can be written,

$$\begin{aligned} \gamma_{\ell p qi} &= \left[ u \ln(u^2 + k^2) - 2u + 2k \tan^{-1} \frac{u}{k} \right] \left| \frac{\sqrt{1+a^2}}{\sqrt{1+a^2}} \frac{x_2 + h}{x_1 + h} \right|, k^2 > 0 \\ &= \left[ u \ln(u^2 + k^2) - 2u + k \ln \left( \frac{x + \sqrt{-k^2}}{x - \sqrt{-k^2}} \right) \right] \left| \frac{\sqrt{1+a^2}}{\sqrt{1+a^2}} \frac{x_2 + h}{x_1 + h} \right|, k^2 < 0 \end{aligned} \quad (5.3.8.11)$$

where  $n = \frac{1}{\sqrt{1+a^2}} (ab - ay_{\ell p} - x_{\ell p})$

$$k^2 = \frac{1}{1+a^2} (b^2 + y_{\ell p}^2 + a^2 x_{\ell p}^2 + 2ab x_{\ell p} - 2ax_{\ell p} y_{\ell p} - 2by_{\ell p})$$

$$\begin{bmatrix}
 \gamma_{1111} & \gamma_{1121} & \dots & \gamma_{11m,j} & \gamma_{111}(j+1) & \dots & \gamma_{11m} & 4\pi\epsilon & 0 & \rho_{11} & 0 \\
 \gamma_{2111} & \gamma_{2121} & \dots & \gamma_{21m,j} & \gamma_{211}(j+1) & \dots & \gamma_{21m} & 4\pi\epsilon & 0 & \rho_{21} & 0 \\
 \gamma_{m,j11} & \gamma_{m,j21} & \dots & \gamma_{m,jm,j} & \gamma_{m,j1}(j+1) & \dots & \gamma_{m,jm} & 4\pi\epsilon & 0 & \rho_{m,j} & 0 \\
 \gamma_{1(j+1)11} & \gamma_{1(j+1)21} & \dots & \gamma_{1(j+1)m,j} & \gamma_{1(j+1)1}(j+1) & \dots & \gamma_{1(j+1)m} & 0 & 4\pi\epsilon & \rho_{1(j+1)} & 0 \\
 \gamma_{m,N+1(N+1)11} & \gamma_{m,N+1(N+1)21} & \dots & \gamma_{m,N+1(N+1)m,j} & \gamma_{m,N+1(N+1)1}(j+0) & \dots & \gamma_{m,N+1(N+1)m}(N+1) & 0 & 4\pi\epsilon & \rho_{m,N+1(N+1)} & 0 \\
 \int_{c_{11}}^{d_1} & \int_{c_{21}}^{d_1} & \dots & \int_{c_{m,j}}^{d_1} & \int_{c_{1(j+1)}}^{d_1} & \dots & \int_{c_{m,N+1(N+1)}}^{d_1} & 0 & 0 & \gamma_1 & 0 \\
 0 & 0 & \dots & 0 & 0 & \dots & 0 & 1 & -1 & \gamma_2 & 1
 \end{bmatrix}
 \quad (10)$$

Equation (5.3.8.10)

Equation (5.3.8.10)

The special case for which  $x_1 = x_2$  is handled separately. For this case,

$$\begin{aligned} \gamma_{\ell p q i} = & u \ln[u^2 + (x_2 - x_{\ell p})^2] - 2u + 2(x_2 - x_{\ell p}) \\ & + 2(x_2 - x_{\ell p}) \tan^{-1} \left( \frac{u}{x_2 - x_{\ell p}} \right) \Bigg|_{y_1 - y_{\ell p}}^{y_2 - y_{\ell p}} \end{aligned} \quad (5.3.8.12)$$

The details of the implementation of CAPCODE are described in the user's manual for the internal propagation codes.

### 5.3.8.3 Example Problem Using CAPCODE

An example problem of an airfoil shape with a circular cable is presented here to demonstrate the usefulness of CAPCODE. Figure 5.26 illustrates the dimensions used in the calculation. Not shown in the figure is the reference conductor which was taken to be a large square enclosing the airfoil and approximately 20 meters from it in all directions. The cable is modeled with 20 points equally spaced around the perimeter. The airfoil is modeled by 39 points. These are clustered more densely around sharp edges and near the cable in order to adequately resolve the expected concentration of charge in these areas. The reference square is modeled by 16 points which are again equally spaced around the perimeter.

CAPCODE calculates the capacitance matrix by first impressing one volt on the cable and holding the airfoil at the reference potential. The charge distributions which then result determine one column of the capacitance matrix. The other column is obtained by impressing one volt on the airfoil and holding the cable at the reference potential. The resulting matrix is below.

$$C = \begin{bmatrix} 9.3116 \times 10^{-11} & -9.3045 \times 10^{-11} \\ -9.3045 \times 10^{-11} & 1.1016 \times 10^{-10} \end{bmatrix} \quad (5.3.8.13)$$

The charge density distributions for the case of the cable at one volt and the airfoil at the reference potential are shown in Figures 5.27 and 5.28. The abscissa represents distance along the perimeter of the conductor, and the letters are provided for position references. The letter key for the airfoil distribution is provided in Figure 5.26.

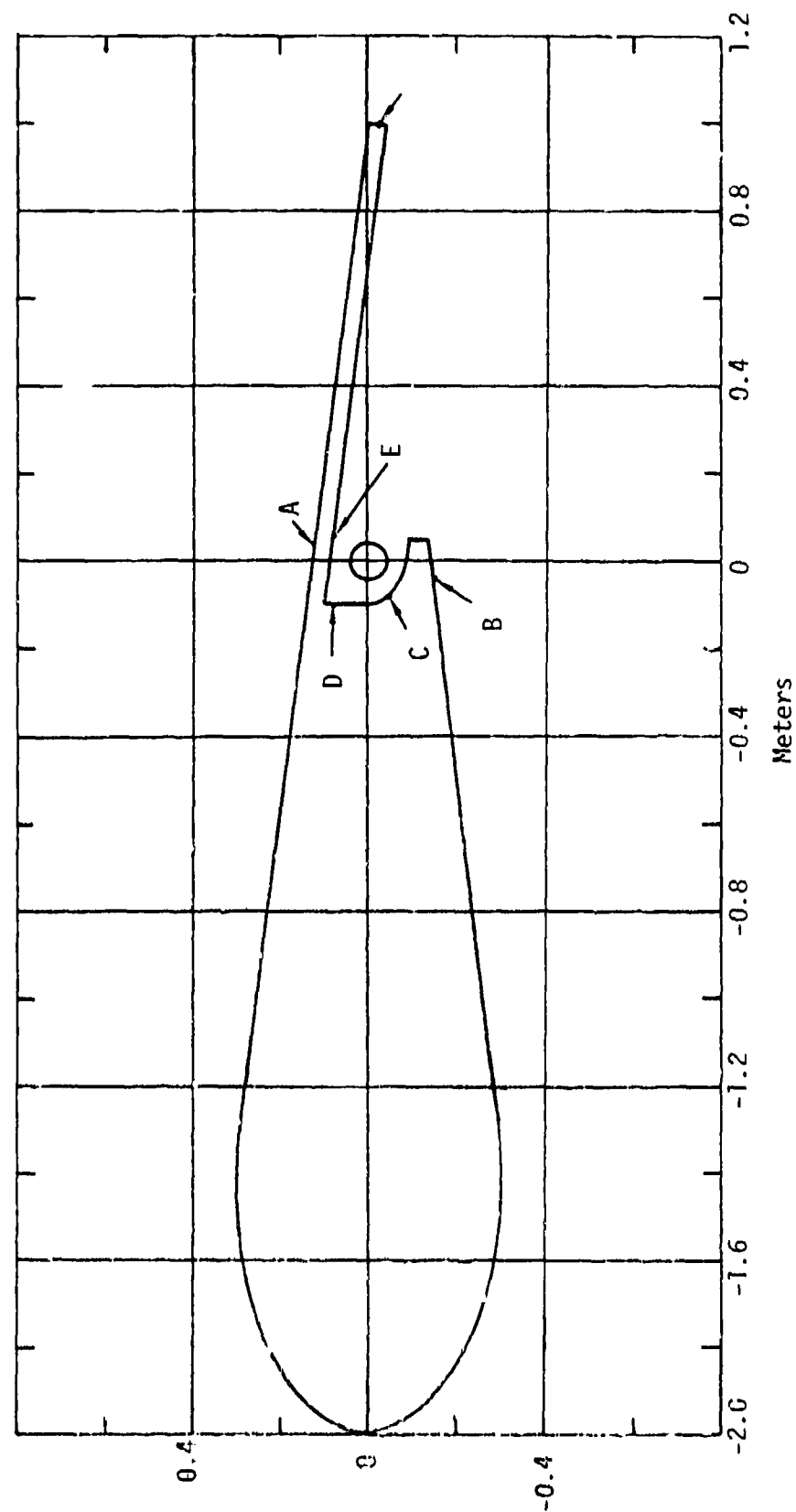


Figure 5.26 Example Conductor Cross-Sections

To determine the actual charge distribution on the airfoil when a current is flowing along the wing, CAPCODE impresses one volt potential with respect to the reference on both the airfoil and the cable. The calculated distributions are shown in Figures 5.29 and 5.30. The letter keys are the same as in Figures 5.27 and 5.28. Figure 5.30 confirms the well known result that the charge tends to concentrate at sharp edges, and most of the current will flow along these edges. Distributions of this type are used to calculate the coupling parameters between the external wing currents and the wing cable as is discussed in the next section.

#### 5.3.8.4 Determination of Coupling Parameters

The source on the wing cable is a voltage source per unit length,  $V_s(t)$ , which is determined by the time derivative of the magnetic flux linking the airfoil and the cable. This can be written,

$$V_s(t) = K_s \mu_0 \frac{\partial I(t)}{\partial t} \quad (5.3.8.14)$$

The parameter  $K_s$  is determined from the charge distribution on the airfoil and is a measure of the fraction of the total current which is flowing on the wing near the cable and relates the magnetic field to the total current. Only the current near the cable contributes significantly to the magnetic flux linking the cable and the wing, so  $K_s$  is included in (5.3.8.14) to reflect this fact.  $K_s$  is calculated by normalizing the integral of the charge distribution on the airfoil (Figure 5.30) to unity, then reading the charge density from the normalized distribution at the point nearest the cable. This is the parameter  $K_s$ . This procedure is somewhat arbitrary, and it may be more accurate to take an average value for all points on the airfoil near the cable. The method outlined here is used for reasons of simplicity. The right hand scale of Figure 5.30 gives the parameter  $K_s$  for all points on the airfoil. Values of  $K_s$  in the vicinity of C and D need to be obtained from the computer output directly, because they are too small to be read from the graph.

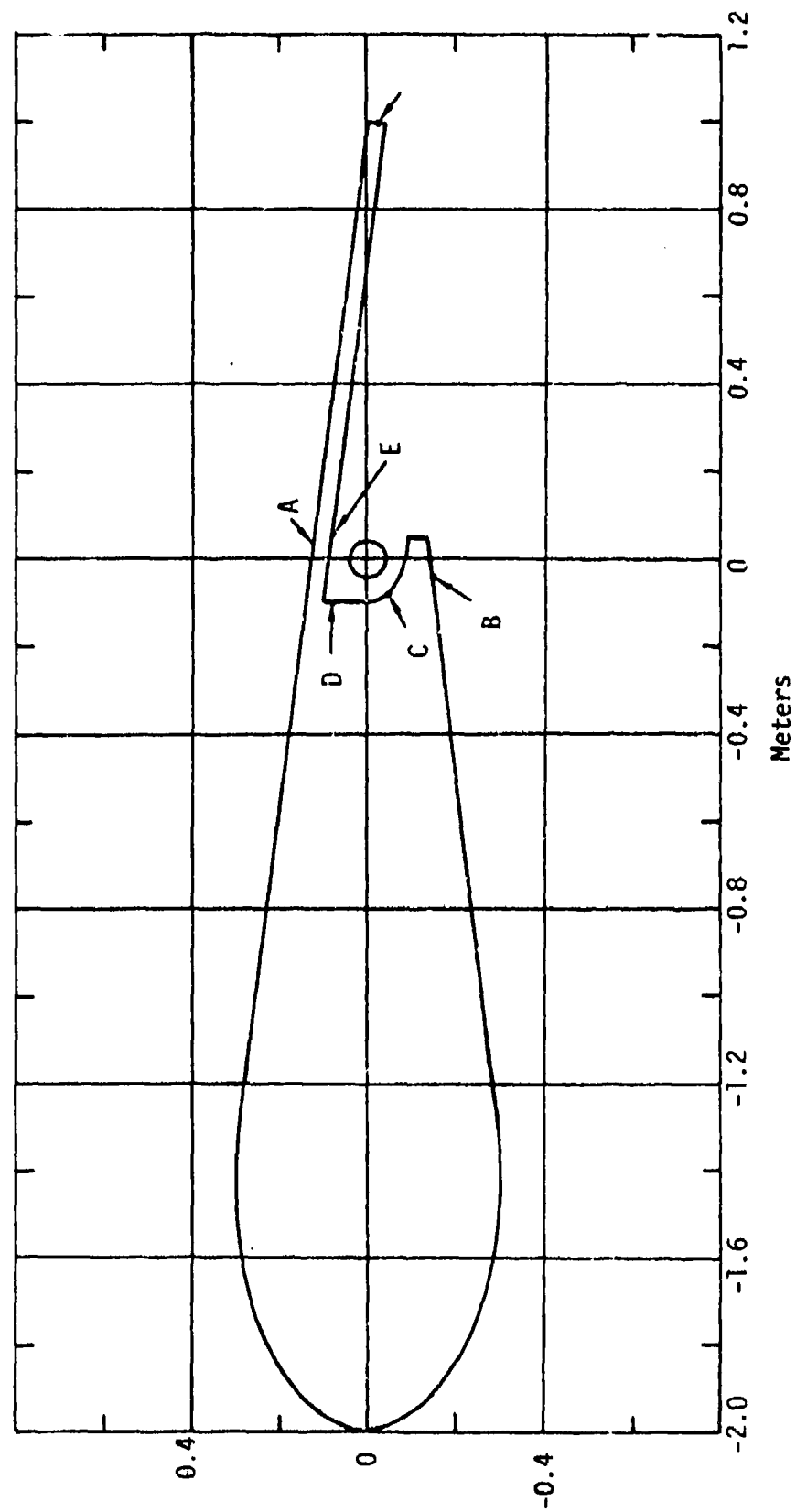


Figure 5.26 Example Conductor Cross-Sections

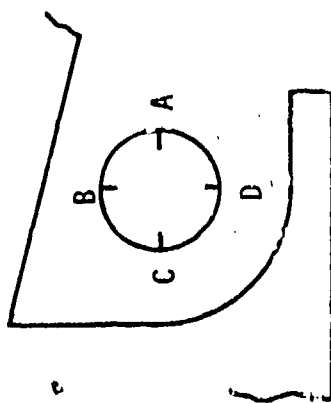
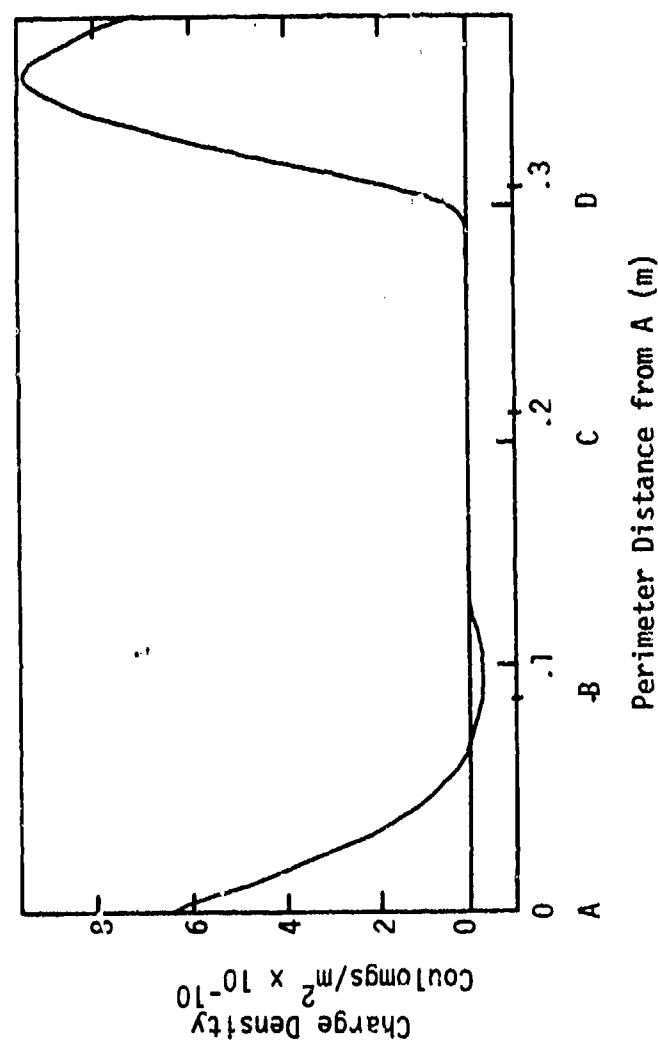


Figure 5.27 Charge Density Distribution on Cable (Cable = 1 Volt,  
Airfoil = 1 Volt)

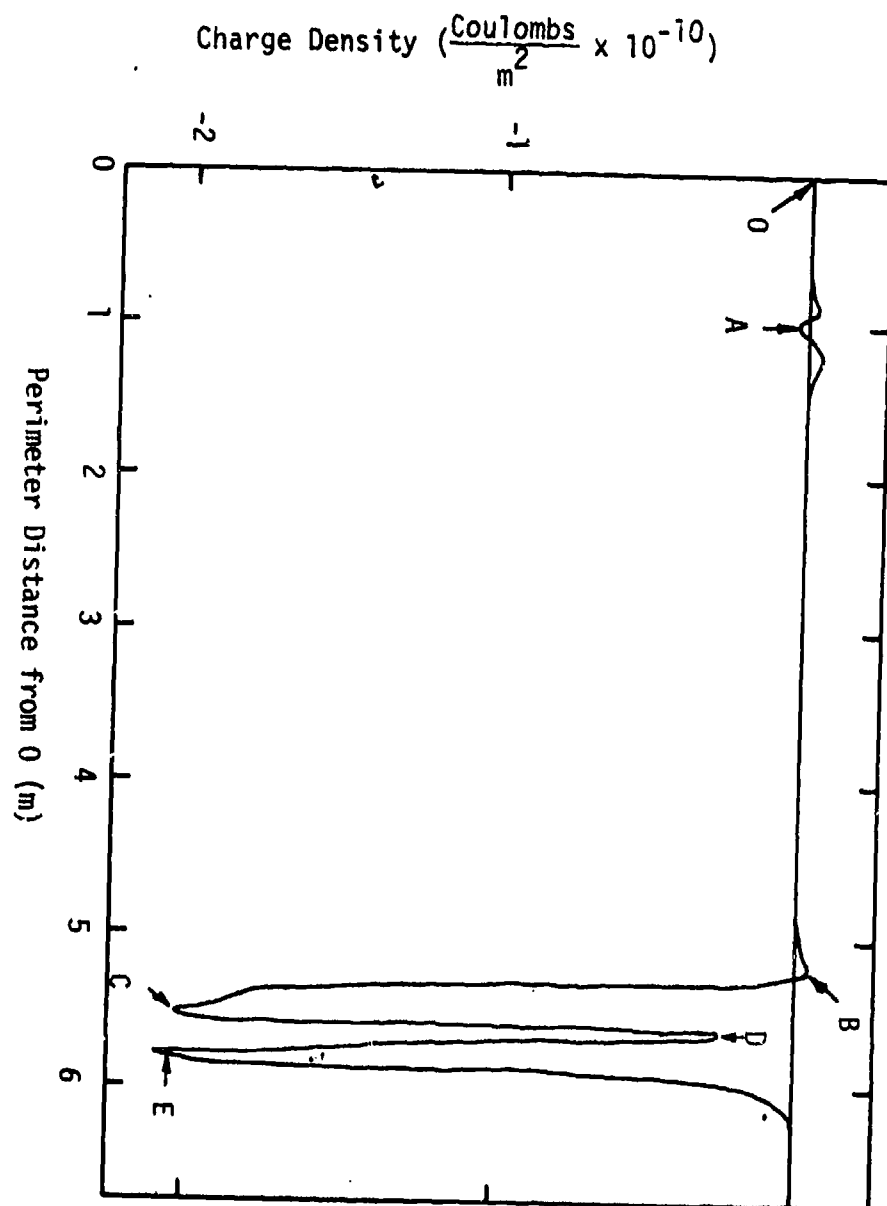


Figure 5.28 Charge Density Distribution on Airfoil  
(Cable = 1 Volt, Airfoil = 0 Volt)



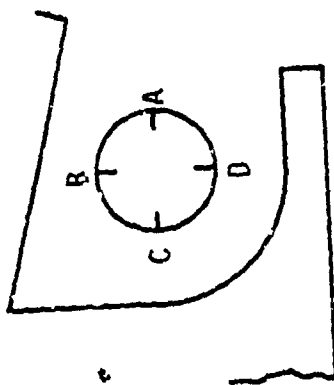
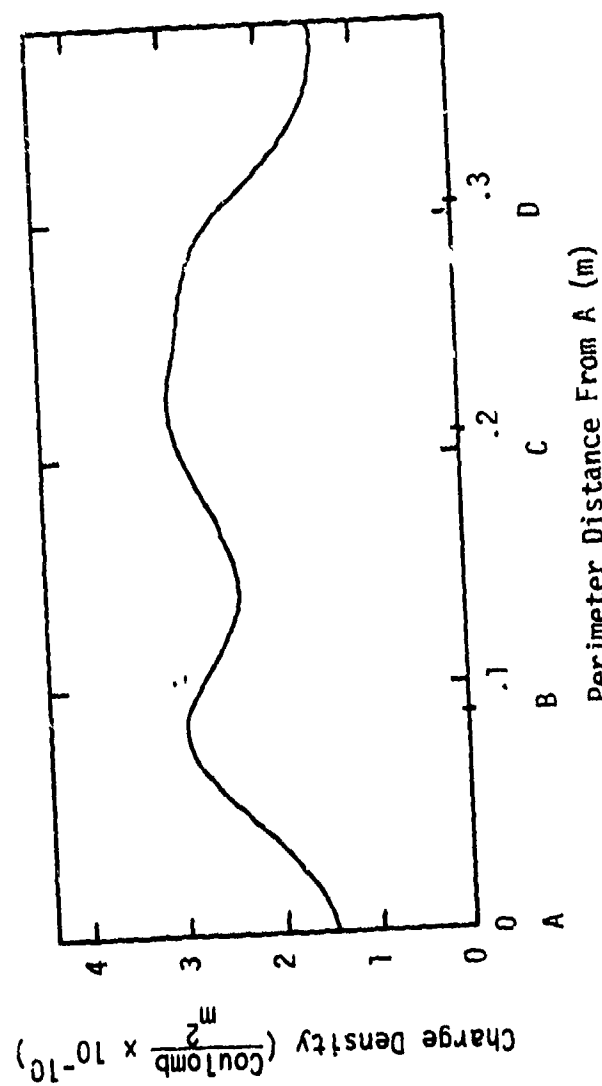
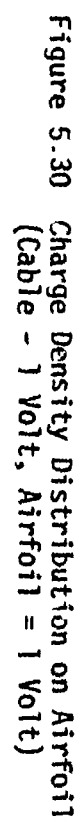


Figure 5.29 Charge Density Distribution on Cable (Cable = 1 Volt, Airfoil = 0 Volt)



### 5.3.9 Internal Cable Propagation Model

The method used by the internal propagation codes PROP and EXEC is that of a single wire transmission line. The characteristics of the single wire are chosen in such a way that the response of the single wire line approximates that of the bulk or common mode response of a more realistic cable bundle. The response of a single wire in the bundle is then determined by assuming weak coupling between the bulk cable and the single wire.

The response of the bulk cable network is determined by solving the time dependent transmission line equations:

$$\begin{aligned} L_B \frac{\partial I_B}{\partial t} + R_B I_B &= - \frac{\partial V_B}{\partial x} + E_x^{inc} \\ C_B \frac{\partial V_B}{\partial t} + G_B V_B &= - \frac{\partial I_B}{\partial x} \end{aligned} \quad (5.3.9.1)$$

In these equations  $L$ ,  $R$ ,  $C$ ,  $G$ ,  $V$  and  $I$  refer to inductance, resistance, capacitance, conductance, voltage, and current, respectively. The subscript  $B$  refers to bulk quantities, and  $L$ ,  $C$ ,  $R$ , and  $G$  are per unit length quantities.  $E_x^{inc}$  refers to the tangential electric field in the position of the wire, which acts as the source.

To be absolutely correct, (5.3.9.1) are not solved for the network as a whole, but for each individual cable segment in the network. Branch points and terminations must be treated somewhat differently. Branch points are dealt with by doing a Kirchhoff analysis of the currents flowing into and out of the point. Terminations use the equations  $I_{term} = \pm G_{term} V_{term}$ , where the sign depends on which end of the cable segment includes the termination.

To solve these equations, central differencing is done on the variables  $I_B$  and  $V_B$ . Then the resulting difference equations are stepped forward in time. These equations are written below.

$$\begin{aligned} I_B^{n+1}(i) &= \left\{ I_B^N(i) \left( \frac{L_B}{\Delta t} - \frac{R_B}{2} \right) - E_x^{inc} - \frac{1}{\Delta x} \left[ V_B^n(i+1) - V_B^n(i) \right] \right\} / \left( \frac{L_B}{\Delta t} + \frac{R_B}{2} \right) \\ V_B^{n+1}(i) &= \left\{ V_B^N(i) \left( \frac{C_B}{\Delta t} - \frac{G_B}{2} \right) - \frac{1}{\Delta x} \left[ I_B^{n+1}(i) - I_B^{n+1}(i-1) \right] \right\} / \left( \frac{C_B}{\Delta t} + \frac{G_B}{2} \right) \end{aligned} \quad (5.3.9.2)$$

In the above equations  $n$  refers to the number of the time step, and  $i$  to the spatial element that is being advanced. The procedure followed is to advance all the currents one  $\Delta t$  by using the previous currents and previous voltages. Then all the voltages are advanced using the previous voltages and the currents which were just calculated. The scheme is stable as long as  $\frac{\Delta x}{\Delta t} > V$ , where  $V$  is the speed of propagation of the signal along the line. The condition simply states that the numerical speed of propagation must be greater than the physical speed in order for equation (5.3.9.2) to give a stable solution.

The bulk transmission line parameters can be entered into the propagation codes in either of two ways. The first is for the user to simply make some estimate of their values and define them. The second is to make use of subroutine CAPMAT and have the code calculate the bulk capacitance and inductance. The details on how to accomplish this are described in the user's manual for the internal propagation codes. CAPMAT first calculates the Maxwell capacitance matrix for the multiconductor cable including the dielectric, then sums the elements of this matrix to get  $C_B$ . The calculation is then redone for the wires without the dielectric and another capacitance matrix is found. This matrix is also summed to get  $C_{B0}$  for the bare wires. In this case the propagation velocity is  $c$ , the speed of light, so  $L_B$  can be found from  $L_B = \frac{1}{c^2 C_{B0}}$ . Because the inductance is unaffected by the presence of the dielectric, this  $L_B$  also applies to the case with dielectric covered wires. The propagation velocity for the dielectric covered wires can be found from

$$V = \frac{1}{\sqrt{L_B/C_B}}, \text{ and the bulk impedance from } Z_B = \sqrt{L_B/C_B}.$$

After the bulk cable response has been determined the voltage and current on a single wire can be found by applying the assumption of weak coupling. The assumption made is that the single wire response is solely determined by coupling to the bulk cable, but the bulk cable is unaffected by the single wire.

The starting point in the derivation of the single wire equations is the multiconductor transmission line equations:

$$\begin{aligned}\frac{\partial}{\partial x} I_n &= -C_{nm} \frac{\partial}{\partial t} V_m \\ \frac{\partial}{\partial x} V_n &= -L_{nm} \frac{\partial}{\partial t} I_m\end{aligned}\tag{5.3.9.3}$$

The capacitance and inductance matrices are here represented in indicial notation, and no sources are included, because the single wire will be driven solely by coupling to the bulk cable.  $I$  and  $V$  are now  $N \times 1$  matrices for the individual wire currents and voltages, where  $N$  is the number of wires in the cable bundle. To study the response of a single wire, let  $n = 1$ , in equations (5.3.9.3):

$$\begin{aligned}\frac{\partial}{\partial x} I_1 &= -C_{1m} \frac{\partial}{\partial t} V_m \\ \frac{\partial}{\partial x} V_1 &= -L_{1m} \frac{\partial}{\partial t} I_m\end{aligned}\tag{5.3.9.4}$$

Separating out the contribution from  $m = 1$  on the right,

$$\begin{aligned}\frac{\partial}{\partial x} I_1 + C_{11} \frac{\partial}{\partial t} V_1 &= -\sum_{m=2}^N C_{1m} \frac{\partial}{\partial t} V_m \\ \frac{\partial}{\partial x} V_1 + L_{11} \frac{\partial}{\partial t} I_1 &= -\sum_{m=2}^N L_{1m} \frac{\partial}{\partial t} I_m\end{aligned}\tag{5.3.9.5}$$

The assumption is now made that the cable is random lay, meaning diagonal elements of  $C_{nm}$  and  $L_{nm}$  are averaged, as are the off-diagonal elements.

$$\begin{aligned}\frac{\partial}{\partial x} I_1 + C_{11} \frac{\partial}{\partial t} V_1 &= -C_o \frac{\partial}{\partial t} \sum_{m=2}^N V_m \\ \frac{\partial}{\partial x} V_1 + L_{11} \frac{\partial}{\partial t} I_1 &= -L_o \frac{\partial}{\partial t} \sum_{m=2}^N I_m\end{aligned}\tag{5.3.9.6}$$

In (5.3.9.6)  $C_o$  and  $L_o$  are the average off-diagonal elements of  $C_{nm}$  and  $L_{nm}$ . Because the bulk current and voltage on the cable are given by

$$\begin{aligned}I_B &= \sum_{m=1}^N I_m \\ V_B &= \frac{1}{N} \sum_{m=1}^N V_m\end{aligned}\tag{5.3.9.7}$$

the single wire equations can be rewritten.

$$\frac{\partial}{\partial x} I_1 + (C_{11} - C_0) \frac{\partial}{\partial t} = -NC_0 \frac{\partial}{\partial t} V_B \quad (5.3.9.8)$$

$$\frac{\partial}{\partial x} V_1 + (L_{11} - L_0) \frac{\partial}{\partial t} I_1 = -L_0 \frac{\partial}{\partial t} I_B$$

These equations use the bulk current and voltage, calculated earlier from (5.3.9.2) as sources for the single wire response. The single wire equations are also very similar formally and could be solved in much the same way as the bulk equations. However, the fact that the sources are time derivatives allows one time integration to be done. Integrating from 0 to t,

$$\begin{aligned} \frac{\partial}{\partial x} \int_0^+ I_1 dt' + (C_{11} - C_0) V_1 &= -NC_0 V_B \\ \frac{\partial}{\partial x} \int_0^+ V_1 dt' + (L_{11} - L_0) I_1 &= -L_0 I_B \end{aligned} \quad (5.3.9.9)$$

These equations allow V and I to be evaluated directly provided their integrals over time are known. The integrals can be evaluated in a running fashion if one again time steps the equations, evaluating  $V_1$  and  $I_1$  at each time step. The advantage of this method is that fewer calculations need to be done at each time step. The solutions are identical to those obtained by straightforward finite-differencing techniques, and therefore the above technique is used to reduce run time.

Examples of internal propagation calculations are contained in the user's manual [1].

## CHAPTER 6

### CONCLUSIONS

The problem of modeling the electromagnetic coupling aspects of the lightning/aircraft interaction event is just beginning to get the attention it requires. Even apart from the usual problems associated with linear electromagnetic scattering, the lightning interaction problem poses fundamental questions yet to be addressed in a significant manner. The largest issue is that of corona and streamer formation and their effects upon coupling. These are nonlinear problems whose physical processes do not yet allow satisfactory, proven models. The big gap, of course, is the lack of definitive experimental data which can be used to check any theories which are advanced. Obtaining such data is of course a difficult task, yet this is the objective of on-going flight test programs, and it is hoped that proper interpretation of this test data will lead to new insights in this area.

In addition, the whole process of attachment is similarly inadequately understood. In addition to the nonlinear aspects just mentioned, there are fundamental questions regarding how large the rate of change of electric field is or can be during this event. Such information is needed if a meaningful specification is ever to be developed. Again, experimental data is lacking.

The requirements that lightning imposes on coupling modeling are severe. In addition to the nonlinear problem, there also is the problem of early and late time effects, both of which can provide real hazards to aircraft. Including the arc channel impedance in the model is also a problem, in that the channel's electromagnetic properties are ill defined. Apart from nonlinearities, the external coupling problem is more understood than the internal coupling or cable propagation problems. The internal coupling problem is not as technologically advanced, and suffers from the inability to model real geometries associated with apertures, radomes, and other penetrations. Although the formalism for cable propagation is fairly mature, it really cannot be used to obtain accurate answers because of the problem of obtaining meaningful input data (i.e., cable geometry and source terms), so that approximate methods are appropriate here also.

## CHAPTER 7

### REFERENCES

1. Rudolph, T.H., "User's Manual for EXEC and PROP Internal Propagation Codes," EMA-81-R-22, April, 1981.
2. Rymes, M.D. and T.H. Rudolph, "LPN User's Manual," EMA-81-R-23, April, 1981.
3. Rymes, M.D., "T3DFD User's Manual," EMA-81-R-24, April, 1981.
4. Uman, M.A. and E.P. Krider, "Lightning Environment Modelling," Volume I of "Atmospheric Electricity Hazards Analytical Model Development and Application," Electro Magnetic Applications EMA-81-R-21, April 1, 1981.
5. Robb, J.D., "Simulation of the Lightning/Aircraft Interaction Event," Volume II of "Atmospheric Electricity Hazards Analytical Model Development and Application," Electro Magnetic Applications EMA-81-R-21, April 1, 1981.
6. Golde, R.H., Lightning Protection, Edward Arnold, London, 1973.  
Golde, R.H. (ed.), Lightning, Vol. 1, Physics of Lightning;  
Vol. 2, Lightning Protection, Academic Press, New York, 1977.
7. Serhan, G.I., M.A. Uman, D.G. Childers and Y.T. Lin, "The RF Spectra of First and Subsequent Lightning Return Strokes in the 1-200 km Range," Radio Science, 1980.
8. Nanevicz, J.E., R.T. Bly and R.C. Adams, "Airborne Measurement of Electromagnetic Environments Near Thunderstorm Cells (TRIP-76)," AFFDL-TR-77-62, August 1977.
9. Little, P.F., "Models for Assessing Hazards Due to Lightning," AGARD Lecture Series 110, Atmospheric Electricity-Aircraft Interaction, Menlo Park, CA, June 1980.
10. Perala, R.A., et al., "An Evaluation of Test Methods for Assessing Lightning Effects on Missile X," Electro Magnetic Applications EMA-80-R-14, September 1980.
11. Rosich, R.K., F.J. Eriksen and M.D. Rymes, "Models of Lightning Channel Impedance," published in the Proceedings of the 1981 International Symposium on Electromagnetic Compatibility, August 1981.



12. Wagner, C.F. and A.R. Hileman, "Surge Impedance and its Application to the Lightning Stroke," IEEE Trans., February 1962.
13. Mittra, R., "Integral Equation Method for Transient Scattering," Topics in Applied Physics, V. 10, ed. by L.B. Felsen (Spring-Verlag, New York, 1976), pp. 73-128.
14. Harrington, R.F., Field Computation by Moment Methods, MacMillan, New York, 1968.
15. Yee, K.S., "Numerical Solution of Initial Boundary Value Problems Involving Maxwell's Equation in Osotropic Media," IEEE Trans. Ant. & Propagat., AP-14, May 1966, pp. 302-307.
16. Holland, R., THREDE: "A Free-Field EMP Coupling and Scattering Code," IEEE Trans. Nuc. Sci., Vol. NS-24, December 1977.
17. Merewether, D.E. and R. Fischer, "Finite Difference Solution of Maxwell's Equations for EMP Applications," EMA-79-R-4, April 22, 1980.
18. Kunz, R.S., B.W. Torres, R.A. Perala and J.M. Hamm, "Surface Current Injection Technique: A Theoretical Investigation," IEEE Trans. Nuc. Sci., Vol. NS-25, December 1978.
19. Perala, R.A., K. Lee and R. Cook, "Induced Effects of Lightning on an All Composite Aircraft," Proceedings of Third Symposium and Technical Exhibition on Electromagnetic Compatibility, Rotterdam, Holland, May 1-3, 1978.
20. Holland, R., L. Simpson and R.H. St. John, "Code Optimization for Solving Large 3D EMP Problems," IEEE Trans. Nuc. Sci., Vol. NS-26, No. 6, December 1979.
21. Kunz, K.S., B.W. Torres and K.M. Lee, "THREDE User's Manual," AMRC-R-105, Mission Research Corporation, Albuquerque, NM 87108.
22. Kunz, K.S., B.W. Torres and K.M. Lee, "THREDE Maintenance Manual," AMRC-R-112, Mission Research Corporation, Albuquerque, NM 87108.
23. Merewether, D.E., R.W. Cox, J.R. Jablonski, R.B. Cook and K.S. Cho, "F-16 Aircraft EMP Analysis and Test Support Program," Electro Magnetic Applications EMA-80-R-12, July 1980.

24. Taflove, Alan, "Time Domain Solutions for Electromagnetic Coupling," TADC-TR-78-142, Rome Air Development Center, Griffiss Air Force Base, New York, June 1978.
25. Taflove, A. and M.E. Brodwin, "Numerical Solution of Steady-State Electromagnetic Scattering Problems Using the Time Dependent Maxwell's Equations," IEEE Trans. Microwave Theory and Techniques, Vol. MTT-23, August 1975, pp. 623-630.
26. Schuman, H.K. and D.E. Warren, "Coupling Through Rotationally Symmetric Apertures in Cavities of Revolution," Document No. RADC-TR-77-214, Griffiss Air Force Base, New York.
27. Bennett, C. Leonard Jr. and Walter L. Weeks, "A Technique for Computing Approximate Electromagnetic Impulse Response of Conducting Bodies," Purdue University School for Electrical Engineering, Lafayette, IN, June 1968.
28. Bennett, C. Leonard Jr. and Walter L. Weeks, "A Technique for Computing Approximate Electromagnetic Impulse Response of Conducting Bodies," Electromagnetic Pulse Interaction Note 222, ed. by C.E. Baum, AFWL, Kirtland AFB, NM, June 1968.
29. Bennett, C.L., "S3T-CLB," in Electromagnetic Computer Codes Newsletter, ed. by R.M. Bevensee, LLL, Livermore, CA, V. 3, p. 15, April 1976.
30. Perala, Rodney A., "Integral Equation Solution for Induced Surface Currents of Bodies of Revolution," IEEE Transactions on Electromagnetic Compatibility, EMC-16, p. 172, August 1974.
31. Sancer, M.I., S. Siegal and A.D. Varvatisis, "Foundation of the Magnetic Field Integral Equation Code for the Calculation of Electromagnetic Pulse External Interaction with Aircraft," AFWL Interaction Note 320, December 1976.
32. Bennett, C.L. and Gerald Ross, "Time-Domain Electromagnetics and its Applications," IEEE Proceedings, V. 66, p. 299 (1978).
33. Bennett, C. Leonard, "The Numerical Solution of Transient Electromagnetic Scattering Problems," in Electromagnetic Scattering, New York: Academic Press (ed. P. Uslenghi), 1978.
34. Bennett, C.L., H. Mieras, S.L. Teeter and J.P. Toomy, "Low EM Signature Response Techniques," RADC-TR-78-287, Griffiss AFB, NY, March 1979.

35. Bevensee, R.M., James N. Brittingham, F.J. Deadrick, Theodore N. Lehman, K. Edmund and A.J. Poggio, "Computer Codes for EMP Interaction and Coupling," IEEE Transactions on Antennas Propagation, AP-26, p. 156 (1978).
36. Bevensee, R.M., Editor, "Electromagnetic Computer Code Newsletter of the Electromagnetic's and System's Research Group," Lawrence Livermore Laboratory, Vol. 3, No. 1, April 1, 1976.
37. Garthwaite, F.G.L. and T.W. Armour, "Wire-Grid Modelling and the Response of Aircraft to EMP," NATO Research Group Seminar on EMP Vulnerability of Military Systems, Wiltshire, UK, 15-17 April 1980.
38. Sancer, M.I., "Fundamental Errors Associated with the Gross Modelling of the Physical Features of Metallic Enclosures," Interaction Note 298, ed. by C.E. Baum, AFWL, Kirtland AFB, December 1976.
39. Burton, R.W., R.W.P. King and D. Blejer, Surface Currents and Charges on a Thick Conducting Tube in an E-Polarized Plane-Wave Field, II. Measurements, progress report on contract F29601-75-C-0019, Air Force Weapons Laboratory/ELPE, Kirtland Air Force Base, New Mexico, 1976.
40. Sancer, Maurice I., Scott Siegel and A.D. Varvatsis, "Formulation of Electromagnetic Pulse External Interaction Above a Lossy Earth/Comparison of Numerical Results with Experimental Data for Limiting Cases," Electromagnetic Pulse Interaction Note 304, ed. by C.E. Baum, AFWL, Kirtland AFB, NM, October 1978.
41. Burke, G.J. and A.J. Poggio, "Numerical Electromagnetic Code (NEC), Method of Moments, Volume I - Program Description Theory," Electromagnetic Pulse Interaction Note 363, ed. by C.E. Baum, AFWL, Kirtland AFB, NM, July 1977.
42. Burke, G.J., A.J. Poggio, J.C. Logan and J.W. Rockway, "Numerical Electromagnetic Code - A Program for Antenna System Analysis," Third Symposium on Electromagnetic Compatibility, Rotterdam, Holland, May 1979, p. 39.
43. Burke, G.J., A.J. Poggio, J.C. Logan and J.W. Rockway, "Numerical Electromagnetic Code (NEC)," Fourth Symposium on Electromagnetic Compatibility, San Diego, CA, October 1979, p. 46.

44. Burke, G.J. and A.J. Poggio, "Numerical Electromagnetic Code (NEC) - Part I, Part II, Part III," Navelix Technical Document 1L, ELEX 3041, Naval Electronic Systems Command, San Diego, CA, July 1977.
45. M. B. Associates, "Antenna Modeling Program, Supplementary, Computer Program (AMP2)," MB-R-75/4, M. B. Associates, San Ramon, CA 94583.
46. Albertsen, N.C., J.E. Hansen and N.E. Jensen, "Computation of Spacecraft Antenna Radiation Patterns," The Technical University of Denmark, Lyngby, Denmark, June 1972.
47. Chao, Hu H. and Bradley J. Strait, "Computer Programs for Radiation and Scattering by Arbitrary Configurations of Bent Wires," Electromagnetic Pulse Interaction Note 191, ed. by C.E. Baum, AFWL, Kirtland AFB, NM, September 1976.
48. Chao, Hu H. and Bradley J. Strait, "Computer Programs for Radiation and Scattering by Arbitrary Configurations of Bent Wires," AFCRL Scientific Report No. 7, Contract F19628-68-C-0180, Syracuse University, Syracuse, NY, September 1970.
49. Garthwaite, F.G.L., T.W. Armour and J. Moore, "Calculation of Surface Current Distributions on Aircraft Structures," 1978 Nuclear EMP Meeting, University of New Mexico, Albuquerque, NM, 8 June 1978.
50. Garthwaite, F.G.L. and T.W. Armour, "Wire-Grid Modelling and the Response of Aircraft to EMP " NATO Research Group Seminar on EMP Vulnerability of Military Systems, Wiltshire, UK, 15-17 April 1980.
51. Castillo, J.P., K.C. Chen and B.K. Singaraju, "Calculation of Currents Induced on a Disk by a Wire Grid Code," Electromagnetic Pulse Interaction Note 203, ed. by C.E. Baum, AFWL, Kirtland AFB, NM, February 1975.
52. Miller, E.K., R.M. Bevensee, A.J. Poggio, R. Adams, F.J. Deadrick and J.A. Landt, "An Evaluation of Computer Programs Using Integral Equations for the Electromagnetic Analysis of Thin Wire Structures," Lawrence Livermore Laboratory, UCRL-75566, Rev. 1 (Reprint), Livermore, CA.
53. Richmond, J.H., "An Integral-Equation Solution for TE Radiation and Scattering from Conducting Cylinders," Electromagnetic Pulse Interaction Note 201, ed. by C.E. Baum, AFWL, April 1973.

54. Richmond, J.H., "Radiation and Scattering by Thin-Wire Structures in the Complex Frequency Domain," Electromagnetic Pulse Interaction Note 202, ed. by C.E. Baum, AFWL, Kirtland AFB, NM, May 1974.
55. Richmond, J.H., "Computer Program for Thin-Wire Structures in a Homogenous Conducting Medium," Electromagnetic Pulse Interaction Note 203, ed. by C.E. Baum, AFWL, Kirtland AFB, NM, June 1974.
56. Richmond, J.H., "Computer Program for Thin Wire Antenna Over a Perfectly Conducting Ground Plane," Electromagnetic Pulse Interaction Note 204, ed. by C.E. Baum, AFWL, Kirtland AFB, NM, October 1974.
57. Rumsey, V.H., "Reaction Concept in Electromagnetic Theory," Physical Review, V. 94, p. 1483 (1954).
58. Schelkunoff, S.A., "On Diffraction and Radiation of Electromagnetic Waves," Physical Review, V. 56, August 15, 1939.
59. Curtis, W.L., "Radar Cross Section of Arbitrarily Shaped Wires," Boeing Company, Tech. Note 2-5453-30-55, October, 1967.
60. Curtis, W.L., "Current and Charge Distributions on Aircraft," Joint EMP Technical Meeting, Kirtland AFB, September 1973.
61. Curtis, W.L., "Charge Distribution on a Dipole with a Stepped Change in Radius," 1976 Int. IEEE/AP-S Symposium and USNC/URSI Meeting, October 10-15, 1976.
62. Strawe, D.F., M. O'Byrne and S. Sandberg, "Electromagnetic Coupling Analysis of a Learjet Aircraft," Air Force Flight Dynamics Lab, AFFDL-TR-78-121, Wright-Patterson AFB, Ohio, June 1978.
63. Vincent, M.C., W.L. Curtis, C.K. Furukawa, J.R. Grozinsky, B.E. Smith, D.E. Young and L.W. Parker, "External Coupling of an Electromagnetic Pulse to the B-1 Aircraft Final Report," Air Force Weapons Lab, AFWL-TR-75-154, Kirtland AFB, NM, June 1975.
64. Bevensee, R.M., "WF-SYR/LLL1: A Thin-Wire Computer Code for Antennas or Scatterers with Pulse Expansion Functions for Current," UCRL 52028, Lawrence Livermore Laboratory, Feb. 1976.
65. Miller, E.K., A.J. Poggio and G.D. Burke, "An Integro-Differential Equation Technique for the Time-Domain Analysis of Thin Wire Structures. I. The Numerical Method," J. of Comp. Physics 12, 24-48 (1973).

66. Poggio, A.J., E.K. Miller and G.J. Burke, "An Integro-Differential Equation Technique for the Time-Domain Analysis of Thin-Wire Structures, II. Numerical Results," J. Comp. Physics 12, 210-233 (1973).
67. Landt, J.A., E.K. Miller and M. Van Blaricum, "WT-MBA/LLLIB: A Computer Program for the Time Domain Electromagnetic Response of Thin-Wire Structures," UCRL-51585, Lawrence Livermore Laboratory, Livermore, CA, May 1974.
68. Lee, K.S.H., Lennart Marin and J.P. Castillo, "Limitation of Wire-Grid Modeling of a Closed Surface," Electromagnetic Pulse Interaction Note 231, ed. by C.E. Baum, AFWL, Kirtland AFB, NM, May 1975.
69. Baum, C.E., "The Singularity Expansion Method," Ch. 3 in Transient Electromagnetic Fields, L. Felsen, ed., Springer-Verlag, New York, 1976.
70. Crow, T.T., C.D. Taylor and M. Kumbale, "The Singularity Expansion Method Applied to Perpendicular Crossed Wires over a Perfectly Conducting Ground Plane," AFWL Sensor and Simulation Note 258, June 1979.
71. Perala, R.A., R.B. Cook and J.D. Robb, "Support of Lightning Analysis and Testing on the Solid Rocket Booster Vehicle," Mission Research Corporation, AMRC-R-122, March 1978.
72. Perala, R.A. and J.D. Robb, "The Experimental Verification of Circuit Modeling Techniques Used to Determine Lightning Current Distribution as Applied to the NASA Space Shuttle Vehicle," 1977 Proceedings of the IEEE International Symposium of Electromagnetic Compatibility, Seattle, 1977.
73. Mangan, D.L. and R.A. Perala, "SGEMP Low-Level Simulation of the FLT SATCOM," Mission Research Corporation, AMRC-R-49, August 1975.
74. Perala, R.A. and L.D. Scott, "Analysis of A-6E and Cylinder Coupling Data and a Recommended Overall Program," AMRC-N-40, Mission Research Corporation, August 1976.
75. Fischer, F.A., "Analysis and Calculations of Lightning Interactions with Aircraft Electrical Circuits," AFFDL-TR-78-106, August 1978.
76. Maxwell, K.J., F.A. Fischer, J.A. Plumer and P.R. Rogers, "Computer Programs for Prediction of Lightning Induced Voltages in Aircraft Electrical Circuits," AFFDL-TR-75-36, Vol. 1, April 1975.

77. Bedrosian, Gary, "Stick-Model Characterization of the Natural Frequencies and Natural Modes of the Aircraft," Electromagnetic Pulse Interaction Note 326, ed. by C.E. Baum, AFWL, Kirtland AFB, NM, September 1977.
78. Bedrosian, G., "Stick-Model of the Total Axial Current and Linear Charge Density on the Surface of an Aircraft Subjected to an EMPI Frequency Domain External-Interaction Current and Charge Transfer Functions," Electromagnetic Pulse Interaction Note 327, ed. by C.E. Baum, AFWL, Kirtland AFB, NM, September 1977.
79. Chang, Shu-Kong and Kenneth K. Mei, "Application of the Unimoment Method to Electromagnetic Scattering of Dielectric Cylinders," IEEE Transactions on Antennas and Propagation, AP-24, p. 35 (1976).
80. Mei, Kenneth K., "Unimoment Method of Solving Antenna and Scattering Problems," Electromagnetic Pulse Interaction Note 205, ed. by C.E. Baum, AFWL, Kirtland AFB, NM, September 1973.
81. Mei, Kenneth K., "Unimoment Method of Solving Antenna and Scattering Problems," IEEE Transactions on Antennas and Propagation, AP-22, p. 760 (1974).
82. Wilton, D.R., S.S.M. Rao and A.W. Glisson, "Electromagnetic Scattering by Surfaces of Arbitrary Shape," preprint, Rome Air Development Center, Griffiss AFB (D. Wilton, U. of Miss., University, MS 38677).
83. Podasky, W.A., "An Examination of the Adequacy of the Three Species Air Chemistry Treatment for the Prediction of Surface Burst EMP," DNA 3880T, December 1975.
84. Merewether, D.E. and T.F. Ezell, "The Interaction of Cylindrical Posts and Radiation Induced Electric Field Pulses in Ionized Media," IEEE Transactions on Nuclear Science, Vol. NS-21, No. 5, October 1974.
85. Perala, R.A. and S.R. Rogers, "The Effects of Corona on the EMP Response of Insulated Cables Lying on the Surface of the Earth," IEEE Transactions on Nuclear Science, Vol. NS-27, No. 6, December 1980.
86. Perala, R.A. and R.B. Cook, "The Effects of Air Breakdown on Antenna Response," EMA-79-R-1, October 27, 1978.

87. Cook, R.B. and R.A. Perala, "Transient Nonlinear Circuit Models of Scattering Antennas with Corona," Accepted for Presentation at the 1981 Nuclear Science Meeting, Seattle, July 1981.
88. Collin, R.E., "Field Theory of Guide Waves," McGraw-Hill Book Company, Inc., pp. 29-34, 1960.
89. Lord Rayleigh, "On the Incidence of Aerial and Electric Waves on Small Obstacles in the Form of Illipsoids or Elliptic Cylinders, on the Passage of Electric Waves Through a Circular Aperture in a Conducting Screen," Phil. Mag., Vol. 44, pp. 28, 1897.
90. Bethe, H.A., "Theory of Diffraction by Small Holes," Physical Review, V. 66, p. 168 (1944).
91. Bouwkamp, C.J., "Diffraction Theory," Rep. Prog. Phy., Vol. 17, pp. 35-100, 1954.
92. Bouwkamp, C.J., "Theoretical and Numerical Treatment of Diffraction Through a Circular Aperture," IEEE Trans. A.P., Vol. AP-18, pp. 152-176, 1970.
93. Umashankar, K.R. and Chalmers M. Butler, "A Numerical Solution Procedure for Small Aperture Integral Equations," Electromagnetic Pulse Interaction Note 212, ed. by C.E. Baum, AFWL, Kirtland AFB, NM, July 1974.
94. Rahmat-Samii, Y. and R. Mittra, "A New Integral Equation Solution of Electromagnetic Aperture Coupling and Thin Plate Scattering Problems," Electromagnetic Pulse Interaction Note 224, ed. by C.E. Baum, AFWL, Kirtland AFB, NM, February 1975.
95. Taylor, C.D., T.T. Crow and K.T. Chen, "On the Singularity Expansion Method Applied to Aperture Penetration," AFWL Interaction Note 134, May 1973.
96. Taylor, C.D., T.T. Crow and K.T. Chen, "On the Electromagnetic Field Penetration Through Apertures," AFWL Interaction Note 199, August 1974.
97. Wilton, D.R. and O.C. Dunaway, "Electromagnetic Penetration Through Apertures of Arbitrary Shape: Formulation and Numerical Solution Procedure," Electromagnetic Pulse Interaction Note 214, ed. by C.E. Baum, AFWL, Kirtland AFB, NM, July 1974.



98. Menger, K.S., C.L. Bennett, D. Peterson and C. Maloy, "The Space-Time Integral Differential Equation Solution of Scattering of Open, Thin Surface," 1974 URSI Meeting, Atlanta, Georgia, 11-13 June 1974.
99. Bombardt, J.N. and L.F. Libelo, "Scattering of Electromagnetic Radiation by Apertures: IV Slotted Cylinders and Cylindrical Strip in the Rayleigh Limit," Harry Diamond Laboratories, HDL-TR-1607, August, 1972.
100. Bombardt, J.N. and L.F. Libelo, "Scattering of Electromagnetic Radiation by Apertures: V Surface, Currents Tangential Aperture Electric Field, and Back Scattering Cross-Section for Axially Slotted Cylinder at Normally, Symmetric Incidence," Naval Surface Weapons Center, N.S.W.C./WOL-TR 75-39, April, 1975.
101. Kligman, R.L. and L.F. Libelo, "Scattering of Electromagnetic Radiation by Apertures VIII: The Normally Slotted Cylinder Theory," Naval Surface Weapons Center, NOLTR 74-35, June 1974.
102. Senior, T.B.A., "Field Penetration into a Cylindrical Cavity," Electromagnetic Pulse Interaction Note 221, ed. by C.E. Baum, AFWL, Kirtland AFB, NM, January 1975.
103. Chang, S. and T.B.A. Senior, "Scattering by a Spherical Shell with a Circular Aperture," A.F.W.L. Interaction Note 141, April 1969.
104. Chen, L.W., "On Cavity Excitation Through Small Apertures," A.F.W.L. Interaction Note 45, January 1970.
105. Lin, J.L., W.L. Curtis and M.C. Vincent, "Electromagnetic Coupling to a Cable Through Apertures," 1974 International IEEE AP-S Symposium, Atlanta, Georgia, pp. 196-199, June 1974.
106. Butler, Chalmers, M. and R. Umashankar Korada, "Electromagnetic Excitation of a Wire Through an Aperture-Perforated, Conducting Screen," Electromagnetic Pulse Interaction Note 251, ed. by C.E. Baum, AFWL, Kirtland AFB, NM, June 1975.
107. Seidel, D.B., D.G. Dudley and C.M. Butler, "Aperture Excitation of a Wire in a Rectangular Cavity," Electromagnetic Pulse Interaction Note 345, ed. by C.E. Baum, AFWL, Kirtland AFB, NM, June 1977.

108. Umashankar, K.R. and J.R. Wait, "Electromagnetic Coupling to an Infinite Cable Placed Behind a Slot Perforated Screen," Electromagnetic Pulse Interaction Note 330, ed. by C.E. Baum, AFWL, Kirtland AFB, NM, June 1977.
109. Lee, K.S.H. (editor), "EMP Interaction: Principles, Techniques, and Reference Data (A Complete Concatenation of Technology from the EMP Interaction Notes)," AFWL-TR-80-402, December 1980.
110. Brittingham, J.N., "A Literature Review of EMP Effects on Apertures," Lawrence Livermore Laboratory Report, UCID-17321, November 1976.
111. Merewether, D.E., "Finite Difference Analysis of the Fields Inside Aperture Driven Cavities," Submitted to IEEE Transactions on Electromagnetic Compatibility.
112. Burrows, B.J.C., "Induced Voltage Programme," CLSU Memo No. 46, Culham Laboratories, November 1976.
113. Ricketts, L.W., J.E. Bridges and J. Miletta, "EMP Radiation and Protective Techniques," John Wiley, New York, 1976.
114. Lowell, R.A., "Shielding Component Evaluation Test Program Final Data Report," TRW, February 1981; also partially published in the Proceedings of the 1981 Conference on Electromagnetic Compatibility, August 1981.
115. Strawe, D. and L. Piszker, "Interaction of Advanced Composites with Electromagnetic Pulse (EMP) Environment," AFWL-TR-75-141, September 1975.
116. Kraus, J.D., "Antennas," McGraw-Hill, New York, 1950.
117. Merewether, D.E., et.al., "Electromagnetic Pulse Handbook for Missiles and Aircraft in Flight," SC-M-710346, Sandia Laboratories, September 1972.
118. Cook, R.B. and R.A. Perala, "Coupling of Lightning Stroke Currents to F-18 Balanced Twisted Shielded Pair Cables," Electro Magnetic App. Report EM-79-R-5, March 1979.
119. Miller, D.A. and J.E. Bridges, "Review of Circuit Approach to Calculate Shielding Effectiveness," IEEE Trans. on Electromagnetic Compatibility, Vol. EMC-10, March 1968.

120. Franceschetti, G., "Fundamentals of Steady-State and Transient Electromagnetic Fields in Shielding Enclosures," AFWL Interaction Note 365, October 1977.
121. Bedrosian, G. and K.S.H. Lee, "EMP Penetration Through Metal Skin Panels and Into Aircraft Cavities," AFWL Interaction Note 314, August 1976.
122. Kaden, H., "Wirbelströme und Schirmung in der Nachrichtentechnik," Springer-Verlag, Berlin, 1959.
123. Merewether, D.E., "Electromagnetic Pulse Transmission Through a Thin Sheet of Saturable Ferromagnetic Material of Infinite Surface Area," IEEE Trans. on Electromagnetic Compatibility, Vol. EMC-11, November 1969.
124. Vincent, M.C., et.al., "EMP Response of the B-1 Aircraft for Inadvertent Penetration Coupling," Vol. 1, Final Report, AFWL-TR-75-164, July 1975.
125. Liu, T.K., et.al., "Broadband Response of Aircraft Antennas, Part I," AFWL Interaction Note 228, May 1975.
126. Weeks, W.L., "Electromagnetic Theory for Engineering Applications," John Wiley, New York, 1964.
127. Taylor, C.D., R.S. Satterwhite and C.W. Harrison, Jr. "The Response of a Terminated Two-Wire Transmission Line Excited by a Nonuniform Electromagnetic Field," IEEE Trans. Antennas Propagat., Vol. AP-13, pp. 987-989, November 1965.
128. Perala, R.A., "Excitation Functions for Multiconductor Transmission Lines Illumined by Nonuniform Electromagnetic Fields," AMRC-R-24, June 1974.
129. Agrawal, A.K., H.M. Fowles and L.D. Scott, "Experimental Characterization of Multiconductor Transmission Lines in Inhomogeneous Media Using Line Domain Techniques," AFWL Interaction Note 332, February 1978.
130. Agrawal, A.K., H.M. Fowles, L.D. Scott and L.T. Simpson, "Time Domain Analysis of Multiconductor Transmission Lines with Branches in Inhomogeneous Media," AFWL Interaction Note 333, February 1978.
131. Baum, C.E., T.K. Liu and F.M. Tesche, "On the Analysis of General Multiconductor Transmission Line Networks," AFWL Interaction Note 350, November 1978.

132. Frankel, S., "Response of a Multiconductor Cable to Excitation by an Arbitrary Single-Frequency, Constant-Impedance Source," AFWL Interaction Note 79, April 1971.
133. Frankel, S., "Response of a Multiconductor Transmission Line to Excitation by an Arbitrary Monochromatic Impressed Field Along the Line," AFWL Interaction Note 80, April, 1971.
134. Frankel, S., "Response of a Multiconductor Cable to an External Electromagnetic Field," AFWL Interaction Note 83, August 1971.
135. Harrison, C.W. Jr., "Generalized Theory of Impedance Loaded Multiconductor Transmission Lines in an Incident Field," AFWL Interaction Note 82, July 1971.
136. Keyser, R.C., "Modeling Techniques for Multiconductor Cables: Theory and Practice," AFWL Interaction Note 285, March 1973.
137. Liu, T.K., "Electromagnetic Coupling Between Multiconductor Transmission Lines in a Homogeneous Medium," AFWL Interaction Note 309, December 1976.
138. Merewether, D.E., et.al., "Electromagnetic Pulse Handbook for Missiles and Aircraft in Flight," SC-M-710346, Sandia Laboratories, September 1972.
139. Tesche, F.M., M.A. Morgan, B. Fishbine and E.R. Parkinson, "Internal Interaction Analysis: Topological Concepts and Needed Model Improvements," AFWL Interaction Note 248, July 1975.
140. Tesche, F.M. and T.K. Liu, "Selected Topics in Transmission-Line Theory for EMP Internal Interaction Problems," AFWL Interaction Note 318, March 1977.
141. Tesche, F.M., T.K. Liu, S.K. Chang and D.V. Giri, "Field Excitation of Multiconductor Transmission Lines," AFWL Interaction Note 351, September 1978.
142. Paul, C.R. and A.E. Feather, "Computation of the Transmission Line Inductance and Capacitance Matrices from the Generalized Capacitance Matrix," IEEE Transactions on Electromagnetic Compatibility, Vol. EMC-18, No. 4, November 1976.
143. Clements, J.C., C.R. Paul and A.T. Adams, "Computation of the Capacitance Matrix for Systems of Dielectric Coated Wires," IEEE Transactions on Electromagnetic Compatibility, Vol. EMC-17, No. 4, November 1975.

144. Paul, C.R., "Connection to 'Computation of the Capacitance Matrix for Systems of Dielectric Coated Cylindrical Conductors'," IEEE Transactions on Electromagnetic Compatibility, May 1976.
145. Licking, Leonard, Capacitance Analysis for Arbitrary Cylindrical Geometries; Application to Electromagnetic Coupling into Sub-systems through Cables, Sandia Laboratories, SC-RR-72 0299, May 1972.
146. Lam, J., "Equivalent Lumped Parameters for a Bend in a Two-Wire Transmission Line: Part I. Inductance," AFWL Interaction Note 303, December 1976.
147. Lam, J., "Equivalent Lumped Parameters for a Bend in a Two-Wire Transmission Line: Part II, Capacitance," AFWL Interaction Note 304, January 1977.

## APPENDIX A

### BIBLIOGRAPHY OF EXTERNAL AND INTERNAL COUPLING LITERATURE

The references included here were found useful in evaluating the current NEMP literature in the context of lightning/aircraft interaction, and come mainly from reports of various institutions, from the AFWL Electromagnetic Pulse Note series, and from the IEEE Transactions on Antennas and Propagation, Microwave Theory and Techniques, and Electromagnetic Compatibility. This bibliography is intended to be a guide to the current literature but is not intended to be a complete listing of all work in any of the areas.

#### OUTLINE

1. External Coupling
  - 1.1 Reviews
  - 1.2 Singularity Expansion Method
  - 1.3 Finite Difference Method
  - 1.4 Electric Field Integral Equation
  - 1.5 Magnetic Field Integral Equation
  - 1.6 Hybrid Methods
  - 1.7 Unimoment Methods
  - 1.8 Analytical Stick Model
  - 1.9 Eigenfunction Expansion
  - 1.10 Finite Element Method
  - 1.11 Zero Reaction Method
  - 1.12 Wire Grid Modeling
  - 1.13 LPN Modeling
  - 1.14 Miscellaneous
2. Internal Coupling
  - 2.1 Apertures
  - 2.2 Deliberate Antennas

## 1.1 Reviews

Baum, Carl E., "Emerging Technology for Transient and Broad-Band Analysis and Synthesis of Antennas and Scatterers," IEEE Proceedings, Invited Paper, v. 64, p.156, (1976).

Beversee, R.M., James N. Brittingham, F.J. Deadrick, Theodore N. Lehman, K. Edmund, and A.J. Poggio, "Computer Codes for EMP Interaction and Coupling," IEEE Transactions on Antennas and Propagation, AP-26, p.156, (1978).

Felsen, L.B., editor, "Transient Electromagnetic Fields," Topics in Applied Physics, v.10, New York: Springer-Verlag, 1976.

IEEE Transactions on Antennas and Propagation, AP-26, 1978; IEEE Transactions on Electromagnetic Compatibility, EMC-20, 1978.

## 1.2 Singularity Expansion Method

Barnes, P.R., "On the Singularity Expansion Method as Applied to the EMP Analysis and Simulation of the Cylindrical Dipole Antenna," AFWL Interaction Note 146, Nov., 1973.

Baum, C.E., "Emerging Technology for Transient and Broad-Band Analysis and Synthesis of Antennas and Scatterers," AFWL Interaction Note 300, Nov., 1976.

Baum, C.E., "Further Developments in the Application of Contour Integration to the Evaluation of the Zeros of Analytic Functions and Relevant Computer Programs," AFWL Mathematics Note 42, March 1976.

Baum, C.E., "Interaction of Electromagnetic Fields with an Object which Has an Electromagnetic Symmetry Plane," AFWL Interaction Note 63, March, 1971.

Baum, C.E., "Electromagnetic Reciprocity and Energy Theorems for Free Space Including Sources Generalized to Numerous Theorems, to Combined Fields, and to Complex Frequency Domain," AFWL Mathematics Note 33, Dec., 1973.

Baum, C.E., "Singularity Expansion of Electromagnetic Fields and Potentials Radiated from Antennas or Scattered from Objects in Free Space," AFWL Sensor and Simulation Note 179, May, 1973.

Baum, C.E., "On the Use of Contour Integration for Finding Poles, Zeros, Saddles, and Other Function Values in the Singularity Expansion Method," AFWL Mathematics Note 35, Feb., 1974.

Baum, C.E., "On the Singularity Expansion Method for the Case of First Order Poles," AFWL Interaction Note 129, Oct., 1972.

Baum, C.E., "Single Port Equivalent Circuits for Antennas and Scattering," AFWL Interaction Note 295, March 1976.

Baum, C.E., "On the Singularity Expansion Method for the Solution of Electromagnetic Interaction Problems," AFWL Interaction Note 88, December, 1971.

Baum, C.E., "On the Eigenmode Expansion Method for Electromagnetic Scattering and Antenna Problems, Part I: Some Basic Relations for Eigenmode Expansions, and Their Relation to Singularity Expansion," AFWL Interaction Note 229, January, 1975.

Baum, C.E., "The Singularity Expansion Method," in Topics in Applied Physics, v.10, ed. by L.B. Felsen (Springer-Verlag, Berlin, 1976, Chapter 3.

Cho, K.S. and R.T. Cordaro, "Calculation of the Singularity Expansion Method Parameters from the Transient Response of a Thin Wire," AFWL Interaction Note 379, Sept., 1979.

Cordaro, J.T., "Comparison of Three Techniques for Calculating Poles and Residues from Experimental Data," AFWL Mathematics Note 61, Aug., 1978.

Cordaro, T., "A Note on Presenting a Transient Waveform by a Finite Sum of Complex Exponentials," AFWL Mathematics Note 46, July, 1977.

Crow, T.T., C.D. Taylor and M. Kumbale, "The Singularity Expansion Method Applied to Perpendicular Crossed Wires over a Perfectly Conducting Ground Plane," AFWL Sensor and Simulation Note 258, June, 1979.

Crow, T.T., Jhi-Chung Kuo and C.D. Taylor, "The Singularity Expansion Method Applied to Perpendicular Crossed Wires over an Imperfect Ground Plane: A Sommerfeld Integral Formulation," AFWL Sensor and Simulation Note 269, June, 1980.

Crow, T.T., B.D. Graves and C.D. Taylor, "The Singularity Expansion Method as Applied to Perpendicular Crossed Cylinders in Free Space," AFWL Interaction Note 161, Oct., 1973.

Crow, T.T., B.D. Graves and C.D. Taylor, "Numerical Techniques Useful in the Singularity Expansion Method as Applied to Electromagnetic Interaction Problems," AFWL Mathematics Note 27, Dec., 1972.

Henderson, T.L., "Matrix Methods for Determining System Poles from Transient Response," AFWL Mathematics Note 66, May, 1980.

Lager, D.L., H.G. Hudson and A.J. Poggio, "User's Manual for SEMPEX: A Computer Code for Extracting Complex Exponentials from a Time Waveform," AFWL Mathematics Note 45, March, 1977.

Lee, S.W. and B. Leung, "The Natural Resonance Frequency of a Thin Cylinder and Its Application to EMP Studies," AFWL Interaction Note 96, Feb., 1972.

Lee, K.S.H., et al., "EMP Interaction: Principles, Techniques, and Reference Data," AFWL-TR-80-402, Dec., 1980.



Lee, K.S.H., and Yang, F.C., "A Wire Passing by a Circular Aperture in an Infinite Ground Plane," Interaction Note 317, Feb., 1977.

Marin, L., "Application of the Singularity Expansion Method to Scattering from Imperfectly Conducting Bodies and Perfectly Conducting Bodies Within a Parallel Plate Region," AFWL Interaction Note 116, June, 1972.

Marin, L. and R.W. Latham, "Analytical Properties of the Field Scattered by a Perfectly Conducting, Finite Body," AFWL Interaction Note 92, Jan., 1972.

Marin, L. and R.W. Latham, "Analytical Properties of the Field Scattered by a Perfectly Conducting, Finite Body," Proc. IEEE 60, 640 (1972).

Marin, L., "Analytical Properties of the Field Scattered by a Perfectly Conducting, Finite Body," IEEE Trans. AP-21, 809 (1973).

Marin, L., "Natural-Mode Representation of Transient Scattering from Rotationally Symmetric, Perfectly Conducting Bodies and Numerical Results for a Prolate Spheroid," AFWL Interaction Note 119, Sept., 1972.

Marin, L., "Natural-Mode Representation of Transient Scattering from Rotationally Symmetric, Perfectly Conducting Bodies and Numerical Results for a Prolate Spheroid," IEEE Trans. AP-22, 266 (1974).

Martinez, J.P., Z.L. Pine and F.M. Tesche, "Numerical Results of the Singularity Expansion Method as Applied to a Plane Wave Incident on a Perfectly Conducting Sphere," AFWL Interaction Note 112, May, 1972.

Martinez, J.P., Z.L. Pine and F.M. Tesche, "Numerical Results of the Singularity Expansion Method as Applied to a Plane Wave Incident on a Perfectly Conducting Sphere," AFWL Interaction Note 112, May, 1972.

IEEE Min. Symposium on Model Analysis of Experimental Data, 1977.  
AFWL Mathematics Note 59, November 1973.

Pearson, L.W., and L.R. Wilton, "The SEM Description of Interaction of a Transient Electromagnetic Wave with an Object," "Lightning Technology", NASA Conference Publication 2128, FAA-RD-80-30, April, 1980.

Pearson, L.W. and R. Mittra, "The Singularity Expansion Representation of the Transient Electromagnetic Coupling through a Rectangular Aperture," AFWL Interaction Note 296, June, 1976.

Price, Harold, J., "An Improved Prony Algorithm for Exponential Analysis," AFWL Mathematics Note 59, November 1978.

Sancer, M.I. and A.D. Varvatsis, "Toward an Increased Understanding of the Singularity Expansion Method," AFWL Interaction Note 398, May, 1980.

Sarkar, Tapan, K., Vijay K. Jain, Joshua Nebat and Donald D. Weiner, "A Comparison of the Pencil-of-Function Method with Prony's Method, Wiener Filters and Other Identification Techniques," AFWL Mathematics Note 54, December 1977.

Shumpert, T.H., "EMP Interaction with a Thin Cylinder above a Ground Plane Using the Singularity Expansion Method," AFWL Sensor and Simulation Note 182, June, 1973.

Singaraju, Bharadwaja K., D.V. Giri and Carl E. Baum, "Further Developments in the Application of Contour Integration to the Evaluation of the Zeros of Analytic Functions and Relevant Computer Programs," AFWL Mathematics Note 42, March 1976.

Taylor, C.D., T.T. Crow and K.T. Chen, "On the Singularity Expansion Method Applied to Aperture Penetration: Part I, Theory," AFWL Interaction Note 134, May, 1973.

Tesche, F.M., "On the Singularity Expansion Method as Applied to Electromagnetic Scattering from Thin Wires," AFWL Interaction Note 102, April, 1972.

Tesche, F.M., "On the Singularity Expansion Method as Applied to Electromagnetic Scattering from Thin Wires," IEEE Trans. AP-21, 53 (1973).

Tesche, F.M., "Application of the Singularity Expression Method to the Analysis of Impedance Loaded Linear Antennas," AFWL Sensor and Simulation Note 177, May, 1973.

Umashankar, K.R. and D. R. Wilton, "Analysis of an L-Shaped Wire Over a Conducting Ground Plane Using the Singularity Expansion Method," AFWL Interaction Note 174, March, 1974.

Van Blaricum, M.L. and R. Mittra, "A Technique for Extracting the Poles and Residues of a System Directly from its Transient Response," AFWL Interaction Note 245, Feb., 1975.

Van Blaricum, M.L. and R. Mittra, "Technique for Extracting the Complex Resonances of a System Directly from its Transient Response," AFWL Interaction Note 301, Dec., 1975.

Vincent, P., "Singularity Expansion for Cylinders of Finite Conductivity," AFWL Interaction Note 329, June 1977

Wilton, D.R. and K.R. Umashankar, "Parametric Study of an L-Shaped Wire Using the Singularity Expansion Method," AFWL Interaction Note 152, Nov., 1973.

### 1.3 Finite Difference Methods

Holland Richard, Larry Simpson, and R.H. St. John, "Techniques for Solving Large 3-D EMP Problems; MRC," presented at IEEE Conference on Nuclear and Space Radiation Effects, Santa Cruz, CA, July 1979.

Holland, Richard, "THREDE: A Free-Field EMP Coupling and Scattering Code," IEEE Nuclear Science, December 1977.

Holland, Richard, "THREDE: A Free-Field EMP Coupling and Scattering Code." AMRC-R-85, Mission Research Corporation, Albuquerque, NM 87108.

Kunz, K.S., and B.W. Torres, "THREDE User's Manual," AMRC-R-113, Mission Research Corporation, Albuquerque, NM 87108.

Kunz, K.S., J.M. Hamm, and B.W. Torres, "Final Report: Alternate Aircraft Simulation Techniques," AMRC-R-115, Mission Research Corporation, Albuquerque, NM 87108.

Kunz, K.S., and Kuan-Min Lee, "A Three-Dimensional Finite-Difference Solution of the External Response of an Aircraft to a Complex Transient EM Environment: Part I - The Method and Its Implementation," IEEE Transactions on Electromagnetic Compatibility, EMC-20, p. 328 (1978).

Kunz, K.S., and Kuan-Min Lee, "A Three-Dimensional Finite Difference Solution of the External Response of an Aircraft to a Complex Transient EM Environment: Part II - Comparison of Predictions and Measurements," IEEE Transactions on Electromagnetic Compatibility, EMC-20, p.333 (1978)

Kunz, K.S., B.W. Torres, and K.M. Lee, "THREDE Maintenance Manual," AMRC-R-112, Mission Research Corporation, Albuquerque, NM 87108.

Kunz, Karl, and Kuan-Min Lee, "A Comparison of Measured and Predicted Surface Currents and Charges on an Aircraft Immersed in a Complex EM Environment," AMRC-N-52 (Revised), Mission Research Corporation, Albuquerque, NM 87108.

Kunz, K.S., B.W. Torres, and K.M. Lee, "THREDE User's Manual," AMRC-R-105, Mission Research Corporation, Albuquerque, NM 87108.

Lee, Kuan-Min, Richard Holland, and Karl Kunz, "Calculation of the Transient Currents Induced on an Aircraft by 3-D Finite Difference Method," AMRC-N-45, Mission Research Corporation, Albuquerque, NM 87108.

Merewether, David E., and Robert Fisher, "Finite Difference Solution of Maxwell's Equations for EMP Applications," Electromagnetic Applications, Inc., EMA 79-R-04.

Perala, R.A., K. Lee, and R. Cook, "Induced Effects of Lightning on all Composite Aircraft," Proceedings of Third Symposium and Technical Exhibition on Electromagnetic Compatibility, Rotterdam, Holland, May 1-3, 1978.

Simpson, Larry, "Development and Optimization of the 50x50x50 Version of THREDE," Mission Research Corporation, Albuquerque, NM.

Taflove, A., and M.E. Brodwin, "Numerical Solution of Steady-State Electromagnetic Scattering Problems Using the Time-Dependent Maxwell's Equations," IEEE Transactions on Microwave Theory and Techniques, MTT 23, p. 623, 1975.

Taflove, Alan, "Time Domain Solutions for Electromagnetic Coupling," RADC-TR-78-142, Rome Air Development Center, Griffiss Air Force Base, New York, June 1978.

Yee, Kane S., "Numerical Solution of Initial Boundary Value Problems Involving Maxwell's Equations in Isotropic Media," IEEE Transactions on Antennas and Propagation, AP-14, p.302 (1966).

#### 1.4 Electric Field Integral Equation

Burke, G.J., E.S. Selden, "Antenna Modeling Program Systems Manual," MB-R-74/62, M.B. Associates, San Ramon, CA 94583.

Chao, Hu H., and Bradley J. Strait, "Computer Programs for Radiation and Scattering by Arbitrary Configurations of Bent Wires," Electro Magnetic Pulse Interaction Note 191, ed. by C.E. Baum, AFWL, Kirtland AFB, NM, September 1976.

Chao, Hu H., and Bradley J. Strait, "Computer Programs for Radiation and Scattering by Arbitrary Configurations of Bent Wires," AFCRL Scientific Report No. 7, Contract F19628-68-C-0180, Syracuse University, Syracuse, NY, September 1970.

Hill, J. Rober, "Transient Currents Induced on an Airplane in Free Field and EMP Simulator Geometry," AMRC-R-6, Mission Research Corporation, Albuquerque, NM 87108.

Landt, J.A., E.K. Miller, and F.J. Deadrick, "Time Domain Computer Models of Thin-Wire Antennas and Scatterers," UCRL-74848, (preprint) Lawrence Livermore Laboratory, Livermore, CA, November 1973.

Landt, J.A., and E.K. Miller, "EMP-Induced Skin Currents on Aircraft," UCRL-75426 (preprint), Lawrence Livermore Laboratory, Livermore, CA, February 1974.

Landt, J.A., E.K. Miller, and M. Van Blaricum, "WT-MBA/LLLIB: A Computer Program for the Time Domain Electromagnetic Response of Thin-Wire Structures," UCRL-51585, Lawrence Livermore Laboratory, Livermore, CA, May 1974.

M.B. Associates, "Antenna Modeling Program Engineering Manual," MB-R-74/62, M.B. Associates, San Ramon, CA 94583.

Miller, E.K., and J.A. Landt, "Direct Time-Domain Techniques for Transient Radiation and Scattering," UCRL-52315, Lawrence Livermore Laboratory, University of California, Livermore, CA, July 1, 1976.

Miller, E.K., A.J. Poggio, and G.J. Burke, "An Integro-Differential Equation Technique for the Time-Domain Analysis of Thin-Wire Structures," Journal of Computational Physics, v.12, p.24 (1973).

Selden, E.S., and G.J. Burke, "Antenna Modeling Program, Composite User's Manual," MB-R-74/46, M.B. Associates, San Ramon, CA 94583.

#### 1.5 Magnetic Field Integral Equation

Bennett, C. Leonard Jr., and Walter L. Weeks, "A Technique for Computing Approximate Electromagnetic Impulse Response of Conducting Bodies," Purdue University School for Electrical Engineering, Lafayette, IN, June 1968.

Bennett, C. Leonard Jr., and Walter L. Weeks, "A Technique for Computing Approximate Electromagnetic Impulse Response of Conducting Bodies," Electromagnetic Pulse Interaction Note 222, ed. by C.E. Baum, AFWL, Kirtland AFB, NM, June 1968.

Bennett, C.L., "S3T-CLB," in Electromagnetic Computer Codes Newsletter, ed. by R.M. Bevensee, LLL, Livermore, CA, v.3, p.15, April 1976.

Perala, Rodney, A., "Integral Equation Solution for Induced Surface Currents of Bodies of Revolution," IEEE Transactions on Electromagnetic Compatibility, EMC-16, p.172, August 1974.

Sancer, Maurice I., "Fundamental Errors Associated with the Gross Modeling of the Physical Features of Metallic Enclosures," Electromagnetic Pulse Interaction Note 298, ed. by C.E. Baum, AFWL, Kirtland AFB, NM, December 1976.

Sancer, Maurice I., Scott Siegel, and A.D. Varvatsis, "Formulation of Electromagnetic Pulse External Interaction Above a Lossy Earth/Comparison of Numerical Results with Experimental Data for Limiting Cases," Electromagnetic Pulse Interaction Note 354, ed. by C.E. Baum, AFWL, Kirtland AFB, NM, October 1978.

## 1.6 Hybrid Methods

Bennett, C. Leonard, and Gerald Ross, "Time-Domain Electromagnetics and its Application," IEEE Proceedings, v.66, p.299 (1978).

Bennett, C. Leonard, "The Numerical Solution of Transient Electromagnetic Scattering Problems," in Electromagnetic Scattering, New York: Academic Press (ed. P. Uslenghi), 1978.

Bennett, C.L., H. Mieras, S.L. Teeter and J.P. Toomy, "Low EM Signature Response Techniques," RADC-TR-287, Griffiss AFB, New York, March 1979.

Burke, G.J. and A.J. Poggio, "Numerical Electromagnetic Code (NEC), Method of Moments, Volume I - Program Description Theory," Electromagnetic Pulse Interaction Note 363, ed. by C.E. Baum, AFWL, Kirtland AFB, NM, July 1977.

Burke, G.J., A.J. Poggio, J.C. Logan, and J.W. Rockway, "Numerical Electromagnetic Code - A Program for Antenna System Analysis," Third Symposium on Electromagnetic Compatibility, Rotterdam, Holland, May 1979, p.39.

Burke, G.J., A.J. Poggio, J.C. Logan, and J.W. Rockway, "Numerical Electromagnetic Code (NEC)," Fourth Symposium on Electromagnetic Compatibility, San Diego, CA, October 1979, p.46.

Burke, G.J., and A.J. Poggio, "Numerical Electromagnetic Code (NEC) - Part I, Part II, Part III," Navelix Technical Document 1L, ELEX 3041, Naval Electronic Systems Command, San Diego, CA July 1977.

Ersoy, L., and N. Wang, "Surface Current and Charge Density Induced on an Infinite, Perfectly Conducting Circular Cylinder in the Presence of Finite Axial Thin Wire Transverse Magnetic Case," Electromagnetic Pulse Interaction Note 338, ed. by C.E. Baum, AFWL, Kirtland AFB, NM, June 1977.

M.B. Associates, "Antenna Modeling Program, Supplementary, Computer Program (AMP 2)," MB-R-75/4, M.B. Associates, San Ramon, CA 94583.

## 1.7 Unimoment

Chang, Shu-Kong, and Kenneth K. Mei, "Application of the Unimoment Method to Electromagnetic Scattering of Dielectric Cylinders," IEEE Transactions on Antennas and Propagation, AP-24, p.35 (1976)

Mei, Kenneth, K., "Unimoment Method of Solving Antenna and Scattering Problems," Electromagnetic Pulse Interaction Note 205, ed. by C.E. Baum, AFWL, Kirtland AFB, NM, September 1973.

Mei, Kenneth, K., "Unimoment Method of Solving Antenna and Scattering Problems," IEEE Transactions on Antennas and Propagation, AP-22, p.760 (1974).

## 1.8 Analytical Stick Models

Bedrosian, Gary, "Stick-Model Characterization of the Natural Frequencies and Natural Modes of the Aircraft," Electromagnetic Pulse Interaction Note 326, ed. by C.E. Baum, AFWL, Kirtland AFB, NM, September 1977.

Bedrosian, G., "Stick-Model of the Total Axial Current and Linear Charge Density on the Surface of an Aircraft Subjected to an EMPI Frequency Domain External-Interaction Current and Charge Transfer Functions," Electromagnetic Pulse Interaction Note 327, ed. by C.E. Baum, AFWL, Kirtland AFB, NM, September 1977.

## 1.9 Eigenfunction Expansion

Burton, R.W., and R.W.P. King, "Measured Currents and Charges on Thin Crossed Antennas in a Plane-Wave Field," AFWL Interaction Note 258, September 1975.

Burton, R.W., and R.W.P. King, "Induced Currents and Charges on Thin Cylinders in a Time-Varying Electromagnetic Field," Electromagnetic Pulse Interaction Note 257, ed. by C.E. Baum, AFWL, Kirtland AFB, NM, August 1975.

King, Ronald W.P., R.W. Burton, and L.C. Shen, "Induced Currents and Charges on Cylinders and Crossed Cylinders by an Electromagnetic Field," Electromagnetic Pulse Interaction Note 335, ed. by C.E. Baum, AFWL, Kirtland AFB, NM, December 1976.

Taylor, Clayborne D., and Charles W. Harrison, Jr., "Charge Density Induced on the Surface of a Prolate Spheroid Illuminated by a Plane Wave Electromagnetic Field," Electromagnetic Pulse Interaction Note 263, ed. by C.E. Baum, AFWL, Kirtland AFB, NM, January 1976.

## 1.10 Finite Element Method

Adams, A.T., T.E. Baldwin, Jr., and D.E. Warren, "Near Fields of Thin-Wire Antennas - Computation and Experiment," IEEE Transactions on Electromagnetic Compatibility, EMC-20, p. 259, (1978).

Daly, P., "Polar Geometry Waveguides by Finite Element Techniques," IEEE Transactions on Microwave Theory and Techniques, MTT-22, p.202, (1974)

Hazel, T.G., and A. Wexler, "Variational Formulation of the Dirichlet Boundary Condition," IEEE Transactions on Microwave Theory and Techniques, MTT-20, p. 385 (1972).

McAulay, A.D., "Variational Finite Element Solution for Dissipative Waveguides and Transportation Application," IEEE Transactions on Microwave Theory and Techniques, MTT-25, p.382, (1977)

McDonald, B.H., M.Friedman, and A. Wexler, "Variation Solution of Integral Equations," IEEE Transactions on Microwave Theory and Techniques, MTT-22, p. 237 (1974).

McDonald, Bruce, H., and Alvin Wexler, "Finite Element Solution of Unbounded Field Problems," IEEE Transactions on Microwave Theory and Techniques, MTT-20, p. 841, December 1972.

McIsaac, P.R., "A General Reciprocity Theorem," IEEE Transactions on Microwave Theory and Techniques, MTT-27, p.340, (1979).

Konrad, A., "High-Order Triangular Finite Elements for Electromagnetic Waves in Anisotropic Media," IEEE Transactions on Microwave Theory and Techniques, MTT-25.

Konrad, A. "Vector Variational Formulation of Electromagnetic Fields in Anisotropic Media," IEEE Transactions on Microwave Theory and Techniques, MTT-24, p. 553 (1976).

Kunsner, W., and E. Ella Torre, "An Interactive Approach to the Finite-Element Method in Field Problems," IEEE Transactions on Microwave Theory and Techniques, MTT-22, p. 221 (1974).

Silvester, P., and M.S. Hsieh, "Finite-Element Solution of 2-Dimensional Exterior Field Problems," Proceedings IEE, v. 118, p. 1743 (1971).

### 1.11 Reaction Integral Method

Richmond, J.H., "An Integral Equation Solution for TE Radiation and Scattering from Conducting Cylinders," Electromagnetic Pulse Interaction Note 201, ed. by C.E. Baum, AFWL, April 1973.

Richmond, J.H., "Radiation and Scattering by Thin-Wire Structures in the Complex Frequency Domain," Electromagnetic Pulse Interaction Note 202, ed. by C.E. Baum, AFWL, Kirtland AFB, NM, May 1974.

Richmond, J.H., "Computer Program for Thin-Wire Structures in a Homogeneous Conducting Medium," Electromagnetic Pulse Interaction Note 203, ed. by C.E. Baum, AFWL, Kirtland AFB, NM, June 1974.

Richmond, J.H., "Computer Program for Thin Wire Antenna Over a Perfectly Conducting Ground Plane," Electromagnetic Pulse Interaction Note 204, ed. by C.E. Baum, AFWL, Kirtland AFB, NM, October 1974.

Rumsey, V.H., "Reaction Concept in Electromagnetic Theory," Physical Review, v. 94, p. 1483 (1954)

### 1.12 Wire Grid Models

Armour, T.W., B.N. Foot, F.G.L. Garthwaite, and J. Moore, "Electromagnetic Interaction with Simple Structures by Wire Grid Modeling," AWRE Report No. G 43/77, AWRE, Aldermaston, Berkshire, December 1977.

Castillo, J.P., K.C. Chen, and B.K. Singaraju, "Calculation of Currents Induced on a Disk by a Wire Grid Code," Electromagnetic Pulse Interaction Note 230, ed. by C.E. Baum, AFWL, Kirtland AFB, NM, February 1975.

Lee, K.S.H., Lennart Marin, and J.P. Castillo, "Limitation of Wire-Grid Modeling of a Closed Surface," Electromagnetic Pulse Interaction Note 231, ed. by C.E. Baum, AFWL, Kirtland AFB, NM, May 1975.

Marin, Lennart, and Tom K. Liu, "A Simple Way of Solving Transient Thin-Wire Problems," Electromagnetic Pulse Interaction Note 253, ed. by C.E. Baum, AFWL, Kirtland AFB, NM, October 1975.

Sancer, Maurice, I., "Fundamental Errors Associated with the Gross Modeling of the Physical Features of Metallic Enclosures," Electromagnetic Pulse Interaction Note 298, ed. by C.E. Baum, AFWL, Kirtland AFB, NM, December 1976.

Sancer, Maurice I., Scott Siegel, and A.D. Varvatsis, "Formulation of Electromagnetic Pulse External Interaction Above a Lossy Earth/Comparison of Numerical Results with Experimental Data for Limiting Cases," Electromagnetic Pulse Interaction Note 354, ed. by C.E. Baum, AFWL, Kirtland AFB, NM, October 1978.

### 1.13 LPN Modeling

Fisher, F.A., "Analysis and Calculations of Lightning Interactions with Aircraft Electrical Circuits," AFFDL-TR-78-106, August 1978.

Higgins, D.F., "Quasi: A Hybrid Quasi-Static Code for Calculating SGEMP Structural Replacement Currents - Theory and Results," Mission Research Corporation, MRC-R-180, March 1975.

Higgins, D.F., and Robert N. Marks, "User's Manual for the Quasi Computer Code," Mission Research Corporation, MRC-N-193, March 1975.

Longmire, C.L., "Note on Equivalent Circuits for Conducting Sphere," Mission Research Corporation, MRC-N-152, September 30, 1974.

Mangan, D.L., and R.A. Peralta, "SGEMP Low-Level Simulation of the FLTSATCOM," Mission Research Corporation, AMRC-R-49, August 1975.

Maxwell, K.J., F.A. Fisher, J.A. Plummer and P.R. Rogers, "Computer Programs for Prediction of Lightning Induced Voltages in Aircraft Electrical Circuits," AFFDL-TR-75-36, Vol. 1, April 1975.



Messier, A.M., "The Quasi-Static Method Applied to Satellite Structural Return Current Analysis: Surface Note Analysis," Mission Research Corporation, MRC-R-179, March 1975.

Perala, R.A., R.B. Cook and J.D. Robb, "Support of Lightning Analysis and Testing and the Solid Rocket Booster Vehicle," Mission Research Corporation, AMRC-R-122, March 1978.

Perala, R.A. and L.D. Scott, "Analysis of A-6E and Cylinder Coupling Data and a Recommended Overall Program," AMRC-N-40, Mission Research Corporation, August 1976.

Perala, R.A. and J.D. Robb, "The Experimental Verification of Circuit Modeling Techniques Used to Determine Lightning Current Distribution as Applied to the NASA Space Shuttle Vehicle," 1977 Proceedings of the IEEE International Symposium of Electromagnetic Compatibility, Seattle, 1977.

#### 1.14 Miscellaneous

Bach, Henning, "GeF-TUD1," in Electromagnetic Computer Code Newsletter, ed. by R.M. Bevensee, LLL, Livermore, CA, v.3, p.4, April 1976.

Lam, John, "Theoretical Study of the Electrical Corona on a Long Wire," Electromagnetic Pulse Interaction Note 305, ed. by C.E. Baum, AFWL, Kirtland AFB, NM, June 1976.

Merewether, D.E., J.A. Cooper, and R.L. Parker, "Electromagnetic Pulse Handbook for Missiles and Aircraft in Flight," EMP Interaction 1-1, Sandi Laboratories for AFDL, AFWL, TR 73-68, Kirtland AFB, NM, September 1972.

Perala, R.A., and L.D. Scott, "Analysis of A-6E and Cylinder Coupling Data," Addendum to AMRC-R-69, Mission Research Corporation, April 1976.

Schuman, H.K., "SA3F-SYRI," in Electromagnetic Computer Code Newsletter, ed. by R.M. Bevensee, LLL, Livermore, CA, v.4, p.4, January 1977.

Taylor, Clayborne D., and Charles W. Harrison, Jr., "Charge Density Induced on the Surface of a Prolate Spheroid Illuminated by a Plane Wave Electromagnetic Field," Electromagnetic Pulse Interaction Note 263, AFWL, Kirtland AFB, NM, January 1976.

Varvatsis, A.D., and M.I. Sancer, "Electromagnetic Pulse Penetration Through Dielectric Skin Panels on the Leading-Edge of Aircraft Wings," Electromagnetic Pulse Interaction Note 325, ed. by C.E. Baum, AFWL, Kirtland AFB, NM, May 1977.

Vincent, M.C., W.P. Hansen, W.L. Curtis, J.L. Lin, E.I. Piatkowski, B.E. Smith, and J.R. Gozinsy, "EMP Response of the B-1 Aircraft for Inadvertent Penetration Coupling, Volume I, Final," Boeing Aerospace Company for AFWL, AFWL-TR-75-164, (Boeing), Seattle, WA, July 1975.

#### 2.1 Apertures

Baum, Carl E., Kenneth C. Chen, and Bharadwaja K., Singaraju, "Categorization of the Types of Apertures," Electromagnetic Pulse Interaction Note 219,

ed. by C.E. Baum, AFWL, Kirtland AFB, NM, January 1975.

Baum, Carl E., and Bharadwaja K. Singaratu, "Generalization of Babinet's Principle in Terms of the Combined Field to Include Impedance Loaded Aperture Antennas and Scatterers," Electromagnetic Pulse Interaction Note 217, ed. by C.E. Baum, AFWL, Kirtland AFB, NM, September 1974.

Bedrosian, G., and K.S.H. Lee, "EMP Penetration Through Metal Skin Panels and into Aircraft Cavities," Electromagnetic Pulse Interaction Note 314, ed. by C.E. Baum, AFWL, Kirtland AFB, NM, August 1976.

Bethe, H.A., "Theory of Diffraction by Small Holes," Physical Review, v. 66, p. 168 (1944).

Bombardt, J.N., and Libelo, L.F., "Scattering of Electromagnetic Radiation by Apertures: IV Slotted Cylinders and Cylindrical Strip in the Rayleigh Limit," Harry Diamond Laboratories, HDL-TR-1607, August, 1972.

Bombardt, J.N., and Libelo, L.F., "Scattering of Electromagnetic Radiation by Apertures: V Surface, Currents Tangential Aperture Electric Field, and Back Scattering Cross-Section for Axially Slotted Cylinder at Normally, Symmetric Incidence," Naval Surface Weapons Center, N.S.W.C./WOL-TR 75-39, April, 1975.

Bouwkamp, C.J., "Diffraction Theory," Rep. Prog. Phys., Vol. 17, pp. 35-100, 1954.

Bouwkamp, C.J., "Theoretical and Numerical Treatment of Diffraction Through a Circular Aperture," IEEE Trans. A.P., Vol. AP-18, pp. 152-176, 1970.

Brittingham, J.N., "A Literature Review of EMP Effects on Apertures," Lawrence Livermore Laboratory Report, UCID-17321, November, 1976.

Brittingham, J.N., F.J. Deadrick, and D.K. Lager, "An Experimental Study of the Use of Bethe Hole Theory for Wires Behind Apertures," UCRL-52443, Lawrence Livermore Laboratory, Livermore, CA March 1978.

Butler, Chalmers M., and Korada R. Umashanker, "Electromagnetic Excitation of a Wire Through an Aperture-Perforated, Conducting Screen," Electromagnetic Pulse Interaction Note 251, ed. by C.E. Baum, AFWL, Kirtland AFB, NM, June 1975.

Case, K.F., "EMP Penetration Through Advanced Composite Skin Panels," Electromagnetic Pulse Interaction Note 315, ed. by C.E. Baum, AFWL, Kirtland AFB, NM, December 1976.

Chang, S., and Senior T.B.A., "Scattering by a Spherical Shell with a Circular Aperture," A.F.W.L. Interaction Note 141, April, 1969.

Chen, L.W., "On Cavity Excitation Through Small Apertures," A.F.W.L. Interaction Note 45, January 1970.

Cheng, David K., and C.A. Chen, "On Transient Electromagnetic Excitation of a Rectangular Cavity Through an Aperture," Electromagnetic Pulse Interaction Note 237, ed. by C.E. Baum, AFWL, Kirtland AFB, NM, February 1975.

Collin, R.E., Field Theory of Guide Waves", McGraw-Hill Book Company, Inc., pp. 29-34, 1960.

Enader, B., "Scattering by a Spherical Shell with a Small Circular Aperture," Electromagnetic Pulse Interaction Note 77, ed. by C.E. Baum, AFWL, Kirtland AFB, NM, August 1971.

Fletcher, Harvard, and Alan Harrison, "Electromagnetic Penetration Through a Circular Aperture in a Plane Screen Separating a Conducting Medium and a Non-Conducting Medium," Electromagnetic Pulse Interaction Note 346, ed. by C.E. Baum, AFWL, Kirtland AFB, NM, October 1976.

Fletcher, H.J., and Alan Harrison, "Diffraction Through a Circular Aperture in a Screen Separating Two Different Media," Electromagnetic Pulse Interaction Note 352, ed. by C.E. Baum, AFWL, Kirtland AFB, NM, December 1978.

Fletcher, H.J., and Alan K. Harrison, "Fields in a Rectangular Cavity Excited by a Plane Wave on an Elliptical Aperture," Electromagnetic Pulse Interaction Note 342, ed. by C.E. Baum, AFWL, Kirtland AFB, NM, June 1978.

Graves, Billy D., Terry T. Crow, and Clayborne D. Taylor, "On the Electromagnetic Field Penetration Through Apertures," IEEE Transaction on Electromagnetic Compatibility, EMC-18, p. 154 (1976).

Graves, Billy D., T.T. Crow, and C.D. Taylor, "SA3F-MSU1," in Electromagnetic Computer Code Newsletter, ed. by R. M. Bevensee, LLL, Livermore, CA, v.4, p.21, January 1977.

Graves, B.D., T.T. Crow, and C.D. Taylor, "On the Electromagnetic Field Penetration Through Apertures," Electromagnetic Pulse Interaction Note 199, ed. by C.E. Baum, AFWL, Kirtland AFB, NM, August 1974.

Jaggard, D.L., and C.H. Papas, "On the Application of Symmetrization to the Transmission of Electromagnetic Waves Through Small Convex Apertures of Arbitrary Shape," Electromagnetic Pulse Interaction Note 324, ed. by C.E. Baum, AFWL, Kirtland AFB, NM, October 1977.

Jaggard, D.L., "Transmission Through One or More Small Apertures of Arbitrary Shape," Electromagnetic Pulse Interaction Note 323, ed. by C.E. Baum, AFWL, Kirtland AFB, NM, September 1977.

Kajfez, Darko, and Donald R. Wilton, "Small Aperture on a Multiconductor Transmission Line Filled with Inhomogeneous Dielectric," Electromagnetic Pulse Interaction Note 347, ed. by C.A. Baum, AFWL, Kirtland AFB, NM, November 1977.

Kligman, R.L., and Libelo, L.F., "Scattering of Electromagnetic Radiation by Apertures VIII: The Normally Slotted Cylinder Theory," Naval Surface Weapons Center, NOLTR 74-35, June 1974.

Kouyoumjian, Robert G., "The Geometrical Theory of Diffraction and Applications," in Numerical Techniques for Antenna and Electromagnetics, v. VI, University of Southern California, Los Angeles, CA, June 1973.

Latham, R.W., "Currents Induced on an Impedance Within a Slotted Sphere," AFWL-TR-74-295, AFWL, Kirtland AFB, NM, July 1975.

Lee, K.S.H., F.C. Yang, and K.C. Chen, "Cavity Excitation Via Apertures," Electromagnetic Pulse Interaction Note 316, ed. by C.E. Baum, AFWL, Kirtland AFB, NM, February 1977.

Lee, K.S.H., and F.C. Yang, "A Wire Passing By a Circular Aperture in an Infinite Ground Plane," Electromagnetic Pulse Interaction Note 317, ed. by C.E. Baum, AFWL, Kirtland AFB, NM, February 1977.

Lee, S.W., "Geometric Theory of Diffraction in Electromagnetics," Electromagnetic Pulse and Interaction Note 364, ed. by C.E. Baum, AFWL, Kirtland AFB, NM, May 1978.

Lin, J.L., Curtis, W.L., and Vincent, M.C., "Electromagnetic Coupling to a Cable Through Apertures," 1974 International IEEE AP-S Symposium, Atlanta, Georgia, pp. 196-199, June 1974.

Marin, Lennart, "Quasi-Static Field Penetration into a Two-Dimensional Rectangular Well in a Ground Plane," Electromagnetic Pulse Interaction Note 171, ed. by C.E. Baum, AFWL, Kirtland AFB, NM, March 1974.

Mautz, Joseph R., and Roger F. Harrington, "SA3F-SYR2," in Electromagnetic Computer Code Newsletter, ed. by R.M. Bevensee, LLL, Livermore, CA, v.4, p.12, January 1977.

Menger, K.S., Bennett, C.L., Peterson, D., and Maloy, C., "The Space Time Integral Differential Equation Solution of Scattering of Open, Thin Surface," 1974 URSI Meeting, Atlanta, Georgia, 11-13 June 1974.

Mittra, R., and L. Wilson Pearson, "Penetration of Electromagnetic Pulses Through Larger Apertures in Shielded Enclosures," Electromagnetic Pulse Interaction Note 240, ed. by C.E. Baum, AFWL, Kirtland AFB, NM, February 1975.

Morgan, G.E., "EMP Hardening of Aircraft by Closing the Points-of-Entry," Electromagnetic Pulse Interaction Note 255, ed. by C.E. Baum, AFWL, Kirtland AFB, NM, October 1975.

Morgan, M.A., and F.M. Tesche, "Statistical Analysis of Critical Load Excitations Induced on a Random Cable System by an Incident Driving Field: Basic Concepts and Methodology," Electromagnetic Pulse Interaction Note 249, ed. by C.E. Baum, AFWL, Kirtland AFB, NM, July 1975.

Papas, C.H., "An Application of Symmetrization to EMP Penetration Through Apertures," Electromagnetic Pulse Interaction Note 299, ed. by C.E. Baum, AFWL, Kirtland AFB, NM, December 1976.

Pearson, L. Wilson, and Raj Mittra, "The Singularity Expansion Representation of the Transient Electromagnetic Coupling Through a Rectangular Aperture," Electromagnetic Pulse Interaction Note 296, ed. by C.E. Baum, AFWL, Kirtland AFB, NM, June 1976.

Rahmai-Samii, Y., and R. Mittra, "Electromagnetic Coupling Through Small Apertures in a Conducting Screen," IEEE Proceedings of Antennas and Propagation.

Rahmai-Samii, Y., and R. Mittra, "A New Integral Equation Solution of Electromagnetic Aperture Coupling and Thin Plate Scattering Problems," Electromagnetic Pulse Interaction Note 224, ed. by C.E. Baum, AFWL, Kirtland AFB, NM, February 1975.

Lord Rayleigh, "On the Incidence of Aerial and Electric Waves on Small Obstacles in the Form of Ellipsoids or Elliptic Cylinders, on the Passage of Electric Waves Through a Circular Aperture in a Conducting Screen," Phil. Mag., Vol. 44, pp. 28, 1897.

Safavi-Naini, S., S.W. Lee, and R. Mittra, "Transmission of an E.M. Wave Through the Aperture of a Cylindrical Cavity," IEEE Transactions of Antennas and Propagation.

Schuman, H.K., in Electromagnetic Computer Code Newsletter ed. by R.M. Bevensee, vol. 4, Lawrence Livermore Laboratory, CA, January 1977.

Seidel, D.B., D.G. Dudley, and C.M. Butler, "Aperture Excitation of a Wire in a Rectangular Cavity," Electromagnetic Pulse Interaction Note 345, ed. by C.E. Baum, AFWL, Kirtland AFB, NM, June 1977.

Senior, T.B.A., "The Spherical Cavity Problem," Electromagnetic Pulse Interaction Note 220, ed. by C.E. Baum, AFWL, Kirtland AFB, NM, January 1975.

Senior, T.B.A., "Field Penetration into a Cylindrical Cavity," Electromagnetic Pulse Interaction Note 221, ed. by C.E. Baum, AFWL, Kirtland AFB, NM, January 1975.

Smith, Albert A., Jr., "Coupling of External Electromagnetic Fields to Transmission Lines," (John Wiley, New York, 1977).

Taylor, Clayborne D., "Electromagnetic Pulse Penetration Through Small Apertures," Electromagnetic Pulse Interaction Note 74, ed. by C.E. Baum, AFWL, Kirtland AFB, NM, March 1971.

Taylor, Clayborne D., and Charles W. Harrison, Jr., "On the Excitation of a Coaxial Line Through a Small Aperture in the Outer Sheath," Electromagnetic Pulse Interaction Note 104, ed. by C.E. Baum, AFWL, Kirtland AFB, NM, January 1972.

Taylor, C.D., Crow, T.T., and Chen, K.T., "On the Singularity Expansion Method Applied to Aperture Penetration," A.F.W.L. Interaction Note 134, May 1973.

Taylor, C.D., Crow, T.T., and Chen, K.T., "On The Electromagnetic Field Penetration Through Apertures," A.F.W.L. Interaction Note 199, August 1974.

Tesche, F.M., M.A. Morgan, B. Fishbine, and E.R. Parkinson, "Internal Interaction Analysis: Topological Concepts and Needed Model Improvements," Electromagnetic Pulse Interaction Note 248, ed. by C.E. Baum, AFWL, Kirtland AFB, NM, July 1975.

Umashanker, Korada, R., and Carl E. Baum, "Transient Electromagnetic Characterization of Arbitrary Conducting Bodies Through an Aperture-Perforated Conducting Screen," Electromagnetic Pulse Interaction Note 343, ed. by C.E. Baum, AFWL, Kirtland AFB, NM, March 1978.

Umashanker, Korada, R., and James R. Watt, "Electromagnetic Coupling to an Infinite Cable Placed Behind a Slot Perforated Screen," Electromagnetic Pulse Interaction Note 330, ed. by C.E. Baum, AFWL, Kirtland AFB, NM, June 1977.

Umashanker, K.R., and Chalmers M. Butler, "A Numerical Solution Procedure for Small Aperture Integral Equations," Electromagnetic Pulse Interaction Note 212, ed. by C.E. Baum, AFWL, Kirtland AFB, NM, July 1974.

Varvatsis, A.D., and M.I. Sancer, "Electromagnetic Pulse Penetration Through Dielectric Skin Panels on the Leading-Edge of Aircraft Wings," AFWL Interaction Note 325, May 1977.

Wilton, D.R., and O.C. Dunaway, "Electromagnetic Penetration Through Apertures of Arbitrary Shape: Formulation and Numerical Solution Procedure," Electromagnetic Pulse Interaction Note 214, ed. by C.E. Baum, AFWL, Kirtland AFB, NM, July 1974.

Wilton, Donald R., Chalmers M. Butler, and K.R. Umashanker, "Penetration of Electromagnetic Fields Through Small Apertures in Planar Screens: Selected Data," Electromagnetic Pulse Interaction Note 213, ed. by C.E. Baum, AFWL, Kirtland AFB, NM, September 1974.

## 2.2 Deliberate Antennas

Burton, R.W., and R.W.P. King, "Measured Currents and Charges on Thin Crossed Antennas in a Plane-Wave Field," Electromagnetic Pulse Interaction Note 258, ed. by C.E. Baum, AFWL, Kirtland AFB, NM, September 1975.

Coe, R.J., and W.L. Curtis, "Deliberate Antenna Modeling Study," prepared by Boeing Company, D224-10025-1, AFWL, Kirtland AFB, NM, October 1973.

Jordan, E.C., and Keith Balmain, Electromagnetic Waves and Radiating Systems, 2 SD ed. (Prentice-Hall, Englewood Cliffs, NJ, 1968).

King, R.W.P. and Charles W. Harrison, Antennas and Waves: A Modern Approach, (MIT Press, Cambridge, 1969).

Liu, Tom K., Kelvin S.H. Lee, and Lennart O. Marin, "DM CN18-1 UHF/L - Band Blade Antenna on AABNCP," EMP Technology File, DAA Memo 22, December 1975.

Liu, Tom K., K.S.H. Lee, and Lennart Marin, "Broadband Responses of Deliberate Aircraft Antennas, Part I," Electromagnetic Pulse Interaction Note 228, ed. by C.E. Baum, AFWL, Kirtland AFB, NM, May 1975.

Marin, Lennart, "Currents Induced on the VLF/LF Antenna Wires on the E-4 in the Resonance Region of the Aircraft," DAA Memo 31, Dikewood Corporation, (Westwood Research Branch), Los Angeles, CA, December 1976.

Mei, K.K., "On the Integral Equations of Thin Wire Antennas," IEEE Transactions on Antennas and Propagation, p. 374 (1975)

Merewether, David E., Rober B. Cook and Robert Fisher, "The Receiving Properties of the Small Annular Slot Antenna," Electromagnetic Pulse Interaction Note 353, ed. by C.E. Baum, AFWL, Kirtland AFB, NM, September 1978.

Messier, Michael. A. "Coupling to Antennas [Revision of Chapter 10 of DNA-2114 EMP Handbood]," Mission Research Corporation, Santa Barabara, CA.

Singaraju, Bharadwaja K., and Robert L. Gardner, "Transient Response of a Helical Antenna," Electromagnetic Pulse Interaction Note 297, ed. by C.W. Baum, AFWL, Kirtland AFB, NM, July 1976.

Thiele, G.A., "Wire Antennas," in Computer Techniques for Electrodynamics, ed. by R. Mittra, (Pergamon Press, Oxford, 1973) Chapter 1.

### 2.3 Diffusion

Bedrosian, G., and Lee, K.S.H., "EMP Penetration Through Metal Skin Panels and Into Aircraft Cavities," AFWL Interaction Note 314, Aug., 1976.

Franceschetti, G., "Fundamentals of Steady-State and Transient Electromagnetic Fields in Shielding Enclosures," AFWL Interaction Note 365, Oct., 1977.

Harrison, C.W. Jr., "Transient Electromagnetic Field Propagation Through Infinite Sheets, Into Spheric Shells, and Into Hollow Cylinders," IEEE Trans. Antennas and Propagation, Vol. AP-12, p. 319-334, May, 1964.

Kaden, H., "Wirbelströme und Schirmung in der Nachrichtentechnik," Springer-Verlag, Berlin, 1959.

Kinsler, L.E., and Frey, A.R., "Fundamental of Acoustics," John Wiley, New York, 1950.

Merewether, D.E., "Electromagnetic Pulse Transmission Through a Thin Sheet of Saturable Ferromagnetic Material of Infinite Surface Area," IEEE Trans. on Electromagnetic Compatibility, Vol. EMC-11, Nov., 1969.

Miller, D.A., and Bridges, J.E., "Review of Circuit Approach to Calculate Shielding Effectiveness," IEEE Trans. on Electromagnetic Compatibility, Vol. EMC-10, March, 1968.

### 2.4 Cable Propagation

Agrawal, A.K., Fowles, H.M., Scott, L.D., "Experimental Characterization of Multiconductor Transmission Lines in Inhomogeneous Media Using Line Domain Techniques," AFWL Interaction Note 332, Feb., 1978.

Agrawal, A.K., Fowles, H.M., Scott, L.D., Simpson, L.T., "Line Domain Analysis of Multiconductor Transmission Lines With Branches in Inhomogeneous Media," AFWL Interaction Note 333, Feb., 1978.

Baum, C.E., Liu, T.K., Tesche, F.M., "On the Analysis of General Multiconductor Transmission Line Networks," AFWL Interaction Note 350, Nov., 1978.

Chang, S.K., Liu, T.K., Tesche, F.M., "Calculation of the Per-Unit-Length Capacitance Matrix for Shielded Insulated Wires," AFWL Interaction Note 319, Apr., 1977.

Frankel, S., "Response of a Multiconductor Cable to Excitation by an Arbitrary Single-Frequency, Constant-Impedance Source," AFWL Interaction Note 79, Apr., 1971.

Frankel, S., "Response of a Multiconductor Transmission Line to Excitation by an Arbitrary Monochromatic Impressed Field Along the Line," AFWL Interaction Note 80, Apr., 1971.

Frankel, S., "Response of a Multiconductor Cable to an External Electromagnetic Field," AFWL Interaction Note 83, Aug., 1971.

Harrison, C.W. Jr., "Generalized Theory of Impedance Loaded Multiconductor Transmission Lines in an Incident Field," AFWL Interaction Note 82, Jul., 1971.

Keyser, R.C., "Modeling Techniques for Multiconductor Cables: Theory and Practice," AFWL Interaction Note 285, Mar. 1973.

Lam, J., "Equivalent Lumped Parameters for a Bend in a Two-Wire Transmission Line: Part I. Inductance," AFWL Interaction Note 303, Dec., 1976.

Lam, J., "Equivalent Lumped Parameters for a Bend in a Two-Wire Transmission Line: Part II, Capacitance," AFWL Interaction Note 304, Jan., 1977.

Liu, T.K., "Electromagnetic Coupling Between Multiconductor Transmission Lines in a Homogeneous Medium," AFWL Interaction Note 309, Dec., 1976.

Merewether, D.E., et al., "Electromagnetic Pulse Handbook for Missiles and Aircraft in Flight," SC-M-710346, Sandia Laboratories, Sept., 1972.

Merewether, D.E., Fisher, R., "Finite Difference Solution of Maxwell's Equations for EMP Applications," EMA Report EMA-79-R-4, Apr., 1980.

Tesche, F.M., Morgan, M.A., Fishbine, B., Parkinson, E.R., "Internal Interaction Analysis: Topological Concepts and Needed Model Improvements," AFWL Interaction Note 248, Jul., 1975.

Tesche, F.M., Liu, T.K., "Selected Topics in Transmission-Line Theory for EMP Internal Interaction Problems," AFWL Interaction Note 318, Mar., 1977.

Tesche, F.M., Liu, T.K., Chang, S.K., Giri, D.V., "Field Excitation of Multiconductor Transmission Lines," AFWL Interaction Note 351, Sept., 1978.

Weeks, W.L., "Electromagnetic Theory for Engineering Applications," John Wiley, New York, 1964.